Carbon nanotubes grown on stainless steel for supercapacitor applications

Luis Fernando Pantoja Suárez

Doctoral Thesis

Carbon nanotubes grown on stainless steel for supercapacitor applications

Luis Fernando
Pantoja Suárez

Directors
Enric Bertran Serra
Roger Amade Rovira

UNIVERSITAT DE BARCELONA

UNIVERSITAT DE BARCELONA

Department of Applied Physics

C/Martí i Franquès 1, 08028 Barcelona

Carbon nanotubes grown on stainless steel for supercapacitor applications

A thesis submitted for the degree of Doctor of Philosophy

Presented by

Luis Fernando Pantoja Suárez

PhD Program: Nanoscience

Directors: Enric Bertran Serra and Roger Amade Rovira

Tutor: Enric Bertran Serra

Barcelona, July 2019

Dedicated to Paola, Sami and Joaquín

Acknowledgements

To Paola, Sami and Joaquín, who gave meaning to all this adventure. You are the fuel of my life. During this period in Barcelona our family has strengthened. Thank you for your sincere love and infinite energy.

To my parents, Alicia and Alexander, who instilled in me patience, perseverance, curiosity and, above all, ethics. Thank you for all you lovingly taught me as a child, now the phrase "You reap what you sow" has taken on full meaning. I would like to thank my parents-in-law Nelly and Eduardo: their wise words, advice and constant support have allowed this life project, which began almost four years ago, to come to fruition. Many thanks to my sister Lilia and my brothers Lander and Darwin. I'm the youngest of the four and I have a little of each of you. Many things that I have used during this time I learned as a child with you. Sylvia, Cristina and Edison thank you for your words of encouragement and affection that have always been there to strengthen me. I must also thank all my nephews and nieces, who by the way are many, were always aware of the progress of this work. You too are part of this achievement. In general, I thank all my family and friends who have supported me along the way.

Special thanks to Prof. Enric Bertran. Enric, thank you for accepting me into your research group. Much of the knowledge acquired during this time of my life has been thanks to you. My stay in the Department of Applied Physics at the University of Barcelona was gratifying. Thank you for giving me intellectual freedom in my work, for your support to attend several conferences, and of course, thank you for involving me in new and challenging ideas, always demanding a high quality of my work. I benefited greatly from your scientific insight, your ability to solve seemingly insoluble practical difficulties, and your ability to put complex ideas into simple terms.

I would like to thank Dr. Roger Amade, who patiently taught me different methods to functionalize and characterize the samples obtained. Rogers worked closely with me on the electrochemical results that I present in this thesis. It was an extremely reliable source of knowledge in chemistry and electrochemistry. I also thank Dra. Ester Pascual and Dr. José Luis Andújar for their pertinent comments, observations and recommendations that always contributed positively to my stay in the research group.

The results described in this thesis were achieved with the help and support of laboratory colleagues and collaborators. Islam Alshaikh and I worked together in the laboratory to obtain the carbon nanotubes and without their help my work would have been more difficult. With Joan Martí and Arevic Musheghyan, we were able to form a good working group on the synthesis of carbon-based materials. Thank you for the academic and non-academic talks, I have greatly benefited from your different points of view. In ad-

dition, Francisco Romero provided immediate support for any computer problems we encountered. I would be negligent if I did not thank Maite Fraile, who deserves credit for providing much-needed help with administrative tasks, reminding us of imminent deadlines and keeping our work going without problems. I must also mention the technicians of the Scientific and Technological Centers (CCiTUB) of the Universitat de Barcelona, especially David Artiaga, Eva Prats, Javier García, Lorenzo Calvo, Tariq Jawhari, Xavier Alcobe and Josep Bassas. I've learned a lot from your knowledge in different characterization techniques. I must thank Joaquim Puigdollers, from the Universitat Politècnica de Catalunya, for allowing me to use the profilometer.

I want to thank the mechanical workshop staff, with whom we made many components that were used in the repotentiation of the systems used for the development of this thesis. Especially Javier Badenas, who always had a positive attitude towards the constructive challenges that Enric and I were constantly proposing to him.

Finally, I am grateful for the sources of funding that allowed me to continue my doctoral studies: the Escuela Politécnica Nacional and the National Secretary of Science, Technology and Innovation (SENESCYT) of Ecuador, through the Scholarship Program-2014. In particular, I must highlight the state policy established during the government of Econ. Rafael Correa, who greatly supported Ecuadorian citizens to study master's degrees and doctorates in foreign countries.

Outline of this thesis

The ability of humans to study, manipulate and understand matter at the nanoscale has enabled us to develop materials that can combine physical, chemical, optical, magnetic and mechanical properties that bulk materials do not possess. One of the materials that triggered interest in the world of Nanoscience and Nanotechnology was carbon nanotubes (CNTs). These nanostructures had already been reported more than forty years ago, but it is not until the beginning of the 90s that Dr. Sumio Iijima manages to produce them under stable conditions in his laboratory. From that time onwards, the resources devoted to the research and production of these carbon-based materials were on the rise. Although today they do not capture the same scientific interest as they did until 2010, their importance in the scientific world and especially in the market is relevant. In fact, since the technology for the production of CNTs on an industrial scale has matured, they are found in an infinite number of applications, such as reinforcing polymers, acting as scaffolds for the growth of artificial tissue, in the manufacture of conductive inks or as part of new generation battery electrodes and supercapacitors. It is precisely in this last application that scientific interest has been focused with special attention. Together with other carbon-based materials, such as graphene, they are excellent support materials for materials with high capacitance. Research groups and companies around the world are spending a lot of resources to obtain electrodes that have a three-dimensional architecture at the nanoscale and whose specific surface is high.

In that sense, the objective of this work was to synthesize CNTs on the surface of a flexible and conductive material: 304 stainless steel. We focused on optimizing the growth processes by plasma enhanced chemical vapor Deposition (PECVD) and water assisted chemical vapor deposition (WACVD) with and without the contribution of external catalyst material. In addition, as will be seen in the development of this work there is an important effort to understand the effects that thermal processes, necessary for CNTs growth, produced on the properties of steel. Especially the influence on corrosion resistance, since the final use of stainless steel CNTs is the manufacture of electrodes exposed to corrosive environments.

Chapter 1, by way of introduction, talks about Nanoscience and Nanotechnology. The classification of carbon-based materials is also briefly described. An extensive section of the chapter is used to cover the different manufacturing processes of CNTs. In addition, the growth mechanisms commonly used to explain the CNT growth are also included. The final part of the chapter includes some of the properties and applications in which these nanostructures are used. Some health problems that can occur due to improper handling of these nanostructured materials are cited.

The experimental description is included in Chapter 2. In general, some of the fundamental principles of vacuum technology and plasma technology, basic pillars of the processes used for the growth of CNTs, are presented. A number of chemical vapor deposition (CVD) and physical vapor deposition (PVD) processes, such as sputtering or PECVD, are covered in detail. The description of the two reactors used during this work, as well as the changes made to them, is included at the end of the chapter. The PID temperature control system recalibration process is also included, which plays an important role in controlling the temperature of the growth process.

All the characterization techniques used in this work are described in Chapter 3. The basic concepts of each of the techniques are included. The characterization of the substrate and nanostructures obtained by PECVD and WACVD involved electrical, optical, spectroscopic and X-ray measurements.

Chapter 4 shows the parameters and growth results of CNTs directly on stainless steel. The native oxide layer of the steel was removed without the need for mechanical nor chemical processes. In addition, no external catalyst was used. In its replacement were used the alloy steel elements. A detailed study is presented of the effects caused on the steel substrate by the reduction process of the native oxide layer. The results of substrate and CNT characterization by different microscopic, spectroscopic and X-ray techniques have been included. The catalytic activity of the substrate has been demonstrated by both PECVD and WACVD.

The process of obtaining uniform forests of CNTs over a diffusion barrier system obtained from thin nitrided layers is described in Chapter 5. The characterization of nitride layers obtained from a target of 304 stainless steel and a target of aluminium, by magnetron sputtering, is presented in this chapter. Its chemical composition, crystalline structure, deposition rate and electrical resistivity are discussed in this section. The results of the dependence of the CNTs morphology in function of the temperature at which they grow are also included. The characterization techniques used were X-ray photoelectron spectroscopy, X-ray diffraction, resistivity measurements by the Van der Pauw method, thickness measurement with profilometer and Raman characterization of carbon-based structures.

Finally, Chapter 6 shows the results of the electrochemical characterization of the electrodes obtained during this research. The CNTs obtained by the process described in Chapter 5 were electrochemically characterized. In addition, the results obtained are compared with others from samples of CNTs decorated with graphene nanowalls (GNWs) and functionalized with MnO_2. In this chapter it is shown that CNTs can be used as scaffolding for other structures. It includes the study of the influence of deposition time on the formation of MnO_2 nanoparticles and how the morphology of the substrate influences its nucleation. The final part of the chapter deals with the issue of electrode instability during electrochemical characterization. Scanning electron microscopy and Raman characterization results which allowed to identify the products of electrode corrosion are included in this section.

Contents

List of Figures

List of Tables

Chapter 1

Introduction

1.1 Nanoscience and Nanotechnology

Certainly, nano is a term that is now frequently used in the scientific world, especially in the fields of materials, physics, chemistry, computer science and engineering. Not for less, in the more than 20 years that the nanoscience and nanotechnology (NST) has been developing, the advances achieved have incredibly revolutionized the academic and nonacademic world (Parak et al. 2015). But before giving examples of their contribution, it is worth mentioning the definition given by the International Society for Standardization (ISO) for these terms:

Nanoscience is defined as the *"study, discovery and understanding of matter where size- and structure-dependent properties and phenomena manifest, predominantly in the nanoscale (length range approximately from 1 nm to 100 nm), distinct from those associated with individual atoms or molecules, or extrapolation from larger sizes of the same material"*.

Nanotechnology is defined as *"application of scientific knowledge to manipulate and control matter (includes material synthesis) predominantly in the nanoscale to make use of size- and structure-dependent properties and phenomena distinct from those associated with individual atoms or molecules, or extrapolation from larger sizes of the same material"*.

The ability of humans to study, understand and manipulate matter at the nanoscale has allowed, for example, the development of materials that can combine physical, chemical, optical and mechanical properties that bulk materials do not possess. Perhaps the most representative of these materials today is graphene (single-carbon hexagonal networks within the structure of the graphite) (T. Gupta 2018). Another example where NST has contributed is the miniaturization of electronic devices. Smaller and improved energy storage systems (ultra-fast load, longer autonomy), hard and hydrophobic displays, higher resolution cameras and processor architectures with higher processing capacity are the result of research and development in the nano field. Note that to produce such nanostructures (graphene, electrodes for batteries or supercapacitors, patterns on silicon wafers), two main approaches are carried out: bottom-up approach often utilizes solution-phase chemistry, that is, wet chemical synthesis and top-down approach usually employs physical methods, for example, lithography.

NST are also related to medical science, environmental science, biotechnology, agriculture, etc. In fact, the list is very extensive. Manipulation in small dimensions has given NST an inter and multidisciplinary character, since understanding, synthesis, analysis and modification of the nanoscale require skills and knowledge from many different

fields. To understand it character, several research groups, using bibliometric techniques, have published useful information on how the NST is found on the science map (M. Jiang et al. 2018; Porter and Youtie 2009; Stopar et al. 2016). For example, (Stopar et al. 2016), using a database of more than 95,000 articles (Web of Science Core Collection), identified four big groups related with NST: (1) materials, physics, chemistry, computer sciences, engineering; (2) environmental sciences, geosciences, agriculture; (3) biological, medical sciences; (4) economics, social sciences and humanities. According with that research, the first group is the one that provides the most scientific information in the NST area. Information that is then used by the areas included in the three remaining groups. Precisely in this work, the knowledge provided by the fields of physics, chemistry and materials science was used to obtain nanostructures of carbon-based materials.

1.2 Carbon-based materials

Carbon is one of the most versatile elements on our planet. Its use has provided many benefits for human beings (since 3750 BC by Egyptians) (Patrick 1995). For instance, we know that in the past this element was widely used in the manufacture of iron tools, utensils and also weapons. Perhaps those who used it were not clear how carbon improved the properties of their tools. Today we know that thanks to carbon those ferrous materials was improved. For example, the Damascus blades had better performance than other blades of their time. The carbon nanotubes content inside the iron matrix allowed them to be both hard and flexible (Reibold et al. 2006). If we jump in time, we find carbon in an event that significantly marked the development of our society. As we well know, the industrial revolution meant a great change in the human history (Wyczalek 2006). The man put to his service the thermal energy. That energy allowed to activate steam machines that in turn moved a set of mechanisms that until that time (end of the XVIII century) had not been seen. Great Britain was the place where that industrial revolution originated and then spread to Europe and North America. Mineral and vegetable coal was used as an energy source, while burning it releases the chemical energy stored in its structure. Then the discovery and exploitation of large deposits of oil and natural gas increased humanity's dependence on carbon. That dependence on fossil fuels has pushed us to a new inflection point. Now the large amount of gases emitted into the atmosphere are seriously affecting the environment. Greenhouse gases, most of which are produced by the combustion of fossil fuels, are responsible for global warming. By the way, there are divided opinions about this phenomenon. Some say that the global behaviour of the climate is due to a normal cycle (on the earth's geological scale), while the other side points mainly to one culprit: fossil fuels. At this point, although it sounds ironic, carbon has leapt onto the world scene to help us again. Thanks to constant research around the world, we have realized that by dominating carbon at a nanometric scale, we can also improve the health of our planet. How? because now carbon is the key element in the development of new materials that allow us to produce energy (solar hydrogen production, water splitting, the blades of windmills consist of carbon fiber reinforced composites) (Bellani et al. 2019; Inagaki et al. 2014), harvest energy (photovoltaic cells) (Z. Wu et al. 2017; Zhu et al. 2009) and if it were not enough to store it (carbon electrodes for lithium-ion rechargeable batteries, electrochemical supercapacitors) (González et al. 2016; Poonam et al. 2019; Linlin Zhang et al. 2019). Moreover, the use of carbon-based materials is not limited to the energy field. They are widely used in different areas (see currently marketed products in **Figure 1.1**). In the aircraft and aerospace fields, carbon

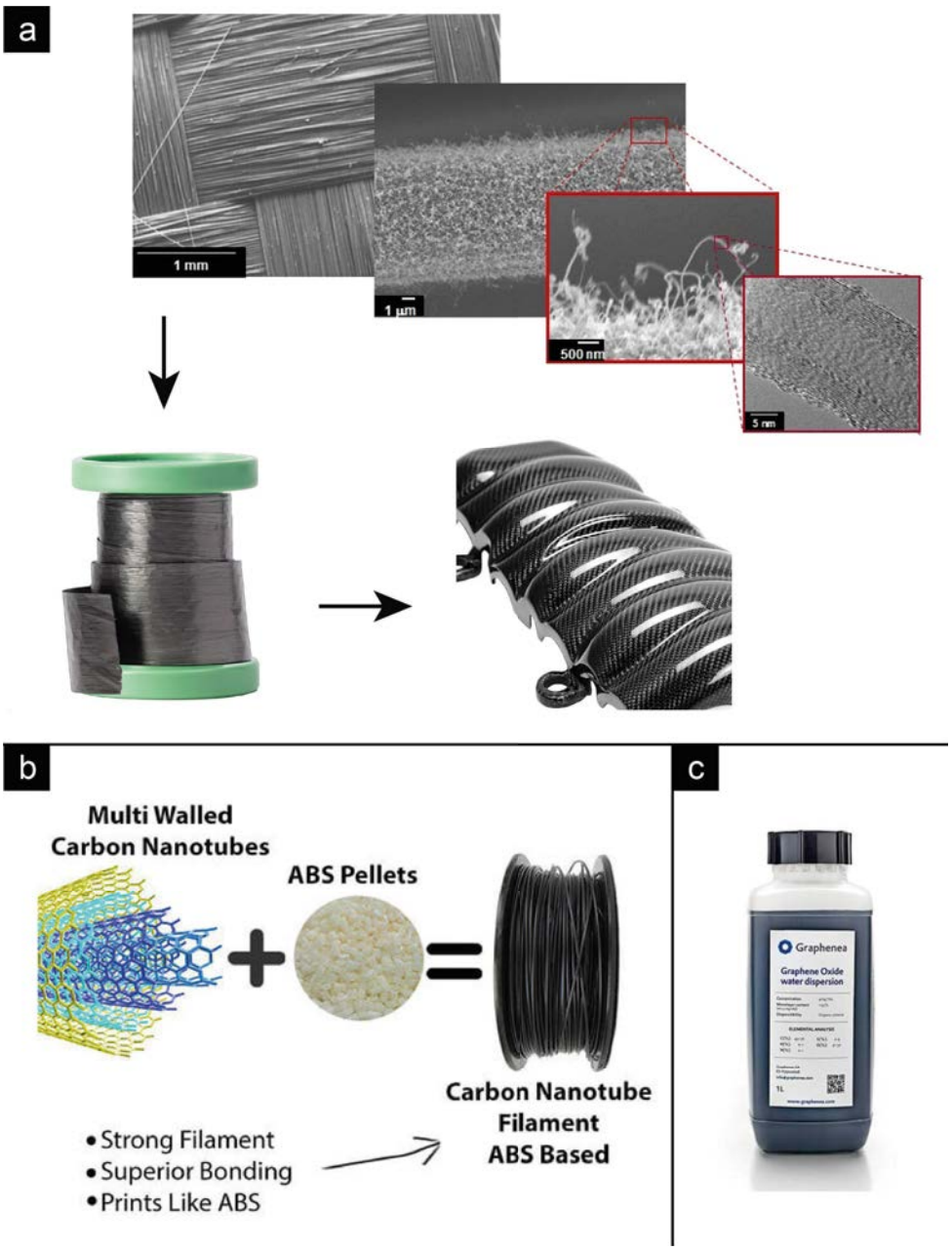

Figure 1.1: Some products currently marketed from carbon-based materials. (a) Carbon nanotubes fibers (Dexmat 2018; UDEL 2019), (b) Filament composite between ABS and carbon nanotubes (Cheaptubes 2019), (c) Graphene oxide water dispersion (Graphenea 2019)

fiber-reinforced plastics are used in body parts. In automobiles, carbon fiber reinforced carbons are used in brakes; carbon/metal composites in brushes; carbon blacks in tires; and activated carbons to create comfortable space in the car, and also in the canister to save gasoline and to avoid air contamination. In the building and civil engineering fields, carbon-fiber-reinforced concrete is successfully used in buildings and bridges exposed to sea water to avoid erosion by salts. Carbon fibers are used for reinforcing the piers of expressways. Note that carbon nanotubes and fullerenes are promoting the development of nanotechnology in various fields of science and engineering (Inagaki et al. 2014).

In the early 1990s, research into carbon-based materials for energy applications was

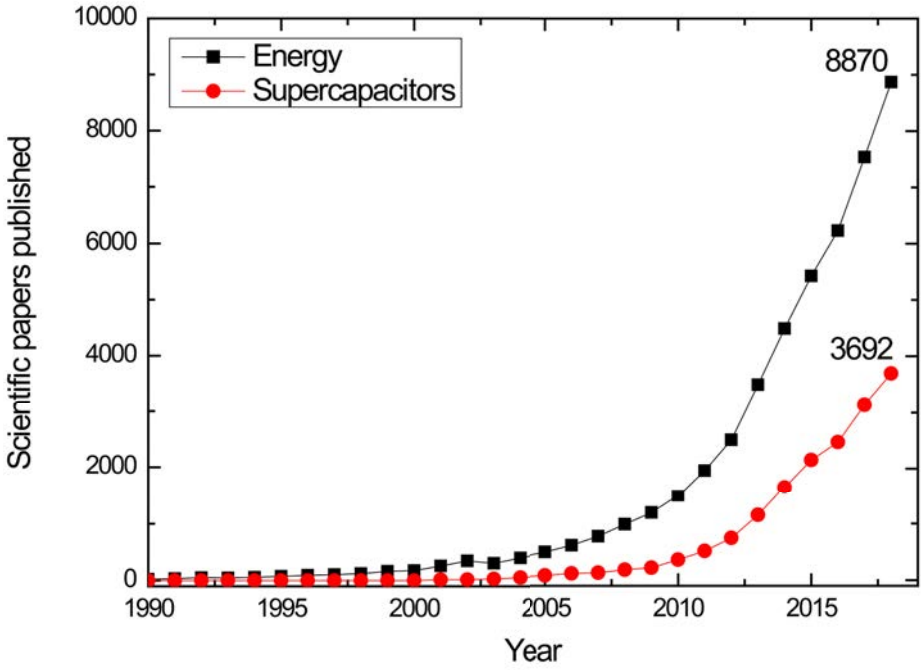

Figure 1.2: Scientific papers related to carbon-based materials in the areas of energy and supercapacitors, published over the past 29 years

almost non-existent. While today, it is a very fruitful field of research. In 2018, 8870 papers related to the use of carbon-based materials in the energy field were published. **Figure 1.2** also includes an evolution curve for the scientific production of supercapacitors made with carbon-based materials. The tendency is the same, in the last 8 years has become a field of great scientific interest.

Figure 1.3 shows the production of scientific papers related to the research of supercapacitors from carbon-based materials by country. China is the nation that undoubtedly leads the research in the area of supercapacitors. This is the country that has gained the most advantage over other nations, such as the United States, Japan, Korea and the countries of the European Union. It seems that this disparity, not only in this field of research, but also in others, has resulted in a trade war between the two great powers of the world: China and the United States (Forbes 2018).

In any case, research into carbon-based materials is booming, and it will definitely grow even more. If this translates into economic benefits, the numbers speak for themselves. For example, it is estimated that only the market for CNTs in 2018 was USD 4.55 billion, and is expected to grow to USD 9.84 billion by 2023. Key players operating in the carbon nanotubes market include Arkema S.A. (France), Arry International Group LTD. (China), Carbon Solutions Inc. (US), Cheap Tubes Inc. (US), CNT Co., Ltd. (Korea), Ocsial Llc (US), Hanwha Chemical Corp. (South Korea), Nano-C Inc. (US), Cnano Technology Ltd (US), Toray International Group Limited (Japan), Showa Denko K.K. (Japan), and Continental Carbon Company (US) (Markets&Markets 2019).

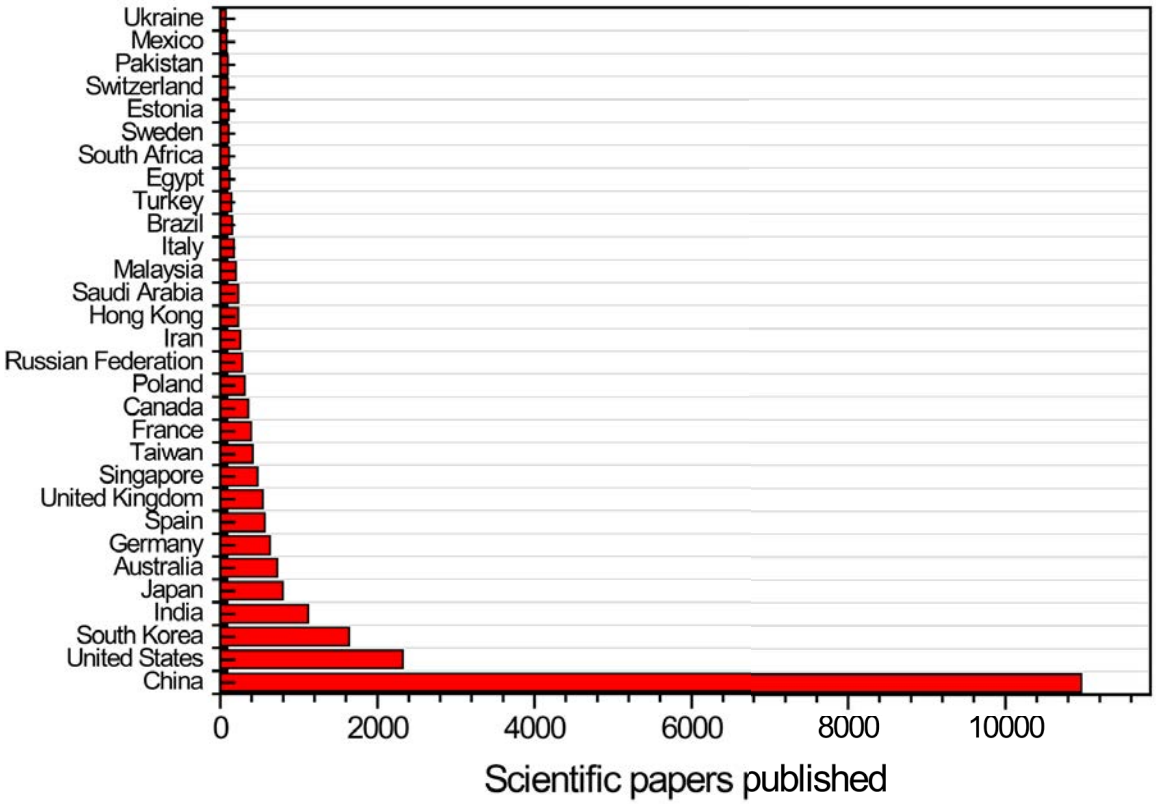

Figure 1.3: Scientific papers related to carbon-based materials in the area of supercapacitors, published in the last 29 years by country

1.2.1 Classification of carbon-based materials

Carbon materials are predominantly composed of carbon atoms, only the single element, but they have widely diverse structures and properties. Diamond has a three-dimensional structure, graphite has a two-dimensional nature, while carbon nanotubes are one dimensional, and buckminsterfullerene, C_{60}, is zero-dimensional. Fullerenes behave as molecules, although other carbon materials do not. Graphite is an electrical conductor and its conductivity is strongly enhanced by AsF_5 intercalation, becoming almost comparable to that of metallic copper, whereas diamond is completely insulating. Diamond, the hardest material, is used for cutting tools, and graphite is so soft that it can be used as a lubricant (Inagaki et al. 2014).

As can be seen, the diversity of carbon-based materials is quite broad and different criteria have been used for their classification. One of them depends on the type of carbon hybridization. This classification takes into account the types of chemical bonds in carbon, with each valence state corresponding to a certain form of simple substance. Elemental carbon can exist in three bonding states corresponding to sp^3, sp^2, and sp^1 hybridization of the atomic orbitals, and the corresponding three carbon alloptropes with an integer degree of carbon bond hybridization are diamond, graphite, and carbyne. In 1931, chemist Linus Pauling first developed the hybridization theory to explain the structure of the simple molecules like methane (CH_4) using atomic orbitals (Weinhold and Landis 2005) (see **Figure 1.4**). It is worth mentioning that in the area of energy conversion and storage one variety of carbon hybridization dominates, it is called $sp^2 - carbon(sp^2 - C)$. $sp^2 -$

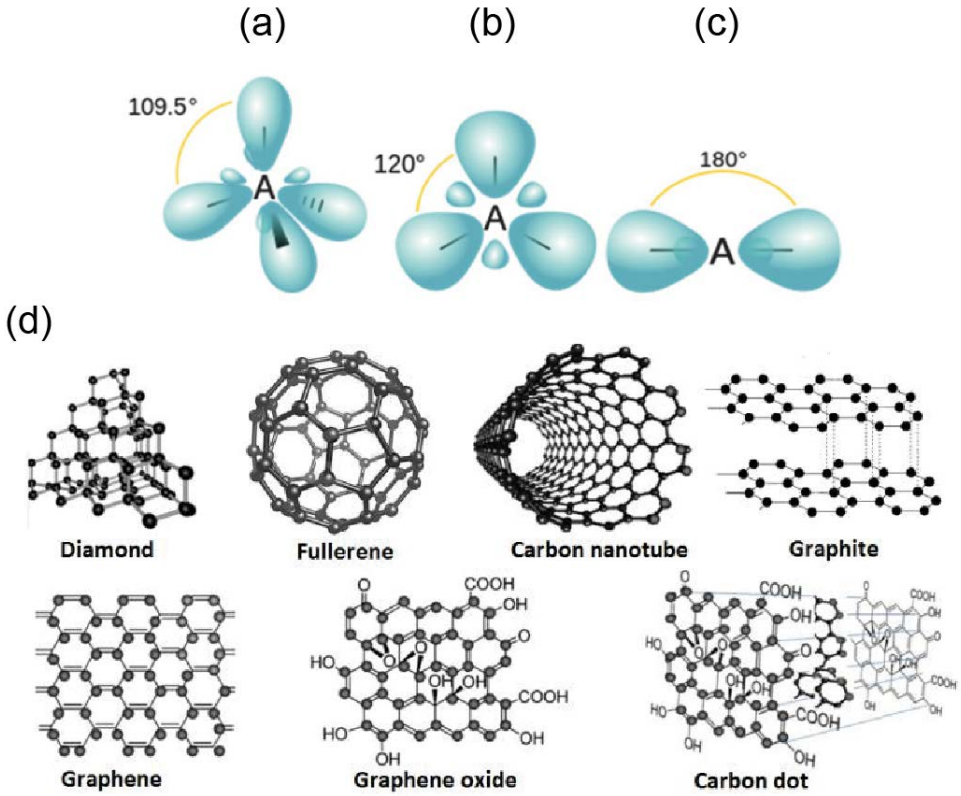

Figure 1.4: Orbital hybridization of carbon (a) four sp^3 orbitals, (b) Three sp^2 orbitals (c) Two *sp* orbitals. (d) Illustration of various forms of carbon nanomaterials

C based carbonaceous materials, featured by its inherent unit structural characteristics of chemical tunability, conjugated network, as well as the topological structure of the carbon-carbon double bond, have been considered as a dazzling star in both scientific research and industrial applications. Compared with defect-free $sp^2 - carbon$ bonded carbon materials, $sp^2 - C$ dominant carbonaceous materials with abundant functionalities and tunable pore structures are more attractive as a candidate for energy storage and conversion systems due to their synergistic effects of the conjugated sp^2 carbon network and the introduced extra functions induced by defects, heteroatoms, many other structure characters, thereby resulting in the combination of the firm and flexible skeleton network, improved electron/ion transport, as well as the rich and exposed active sites (Kong et al. 2019).

All other carbon forms constitute the so-called transitional forms that can be divided into two big groups. The first group comprises mixed short-range order carbon forms, and the second group includes intermediate carbon forms with a noninteger degree of carbon bond hybridization, sp^n. When the value of n is in between 1 and 2 ($1 < n < 2$), it forms a monocyclic carbon. On the other hand, when n lies between 2 and 3 ($2 < n < 3$), it forms closed-shell carbon structures such as fullerene, carbon onions, and nanotubes (Shenderova et al. 2002). In **Figure 1.5**, a tentative ternary carbon allotropy diagram based on carbon valence bond hybridization is shown.

Carbon has three naturally occurring isotopes, ^{12}C, ^{13}C, and ^{14}C. The isotope ^{13}C is stable, while ^{14}C is radioactive, decaying with half-life of about 5730 years (Phatak 2018). It is a first row element with a small ($1s^2$) core having the valence electron 4. This means

carbon has four available atoms for covalent bonding. The overlap between p orbitals perpendicular to C−C bond direction is very sensitive to bond length and the ability of two carbons to approach each other closely enables π bonds to form. It is this fact which gives carbon its unique energetic degeneracy in allotropes with radically different bonding topologies (sp^3/*tetrahedral* of diamond phase and sp^2/*planar* and *curved* graphite nanotubes, or fullerene-like phases) (see **Figure 1.5**).

Another way to classify carbon-based materials is through the production process. It can be classified into artificial graphite, intercalation compounds, activated carbons, carbon/carbon composites, etc. Most carbon materials that have been produced on an industrial scale belong to the graphite family. The fundamental structural unit is a stack of layers of carbon hexagons, i.e. graphite-like hexagonal carbon layers. These hexagonal carbon layers have strong anisotropy because of strong covalent bonding due to sp^2 orbitals in the layer, but weak bonding of Van der Waals force between π electron clouds of stacked layers. When these layers are large enough, they stack with specific regularity: $ABAB$ stacking results in graphite crystals belonging to the hexagonal crystal system and $ABCABC$ stacking results in graphite crystals belonging to the rhombohedral crystal system; the latter crystals being in metastable phase under atmospheric pressure. When the layers are too small, there is no stacking regularity even though they stack in parallel. The structure, where layers are just stacked without regularity, cannot be called graphite and has been named turbostratic. The spacing between two layers that stack without regularity (turbostratic stacking), is larger than that of graphitic stacking. Interlayer spacing

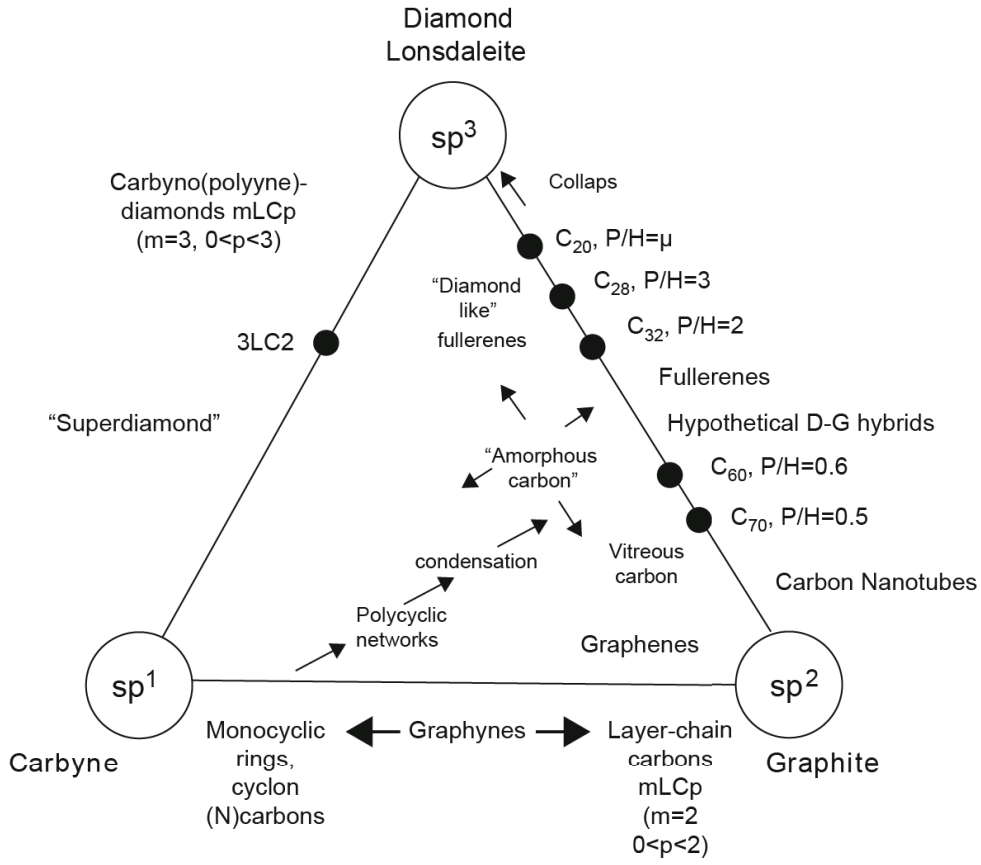

Figure 1.5: Ternary phase diagram of carbon allotropes. Adapted from (Heimann et al. 1997)

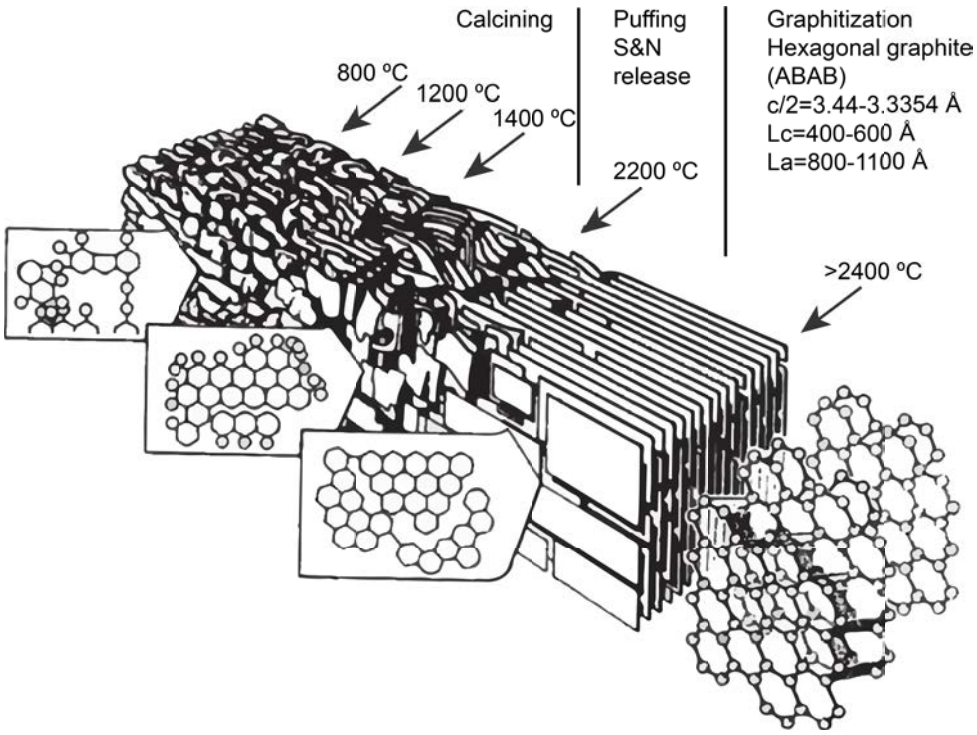

Figure 1.6: Graphite lattice formation. Adapted from (Poco 2015)

of graphite crystals has been accurately determined to be 0.3354 nm. Interlayer spacing of turbostratic stacking is reported to be 0.344 nm, but now it is understood not to be a unique value, because of the presence of foreign atoms at the edges of layers (see **Figure 1.6**). A turbostratic structure is commonly observed after the carbonization of many carbon precursors, because carbonization occurs at temperatures as low as $700 - 1300\,°C$. By heat treatment at higher temperatures, carbon layers grow in both directions, parallel to the layers (increase in the crystallite size L_a) and perpendicular to the layers (increase in the thickness of parallel stacking, which is measured as crystallite size L_c). This crystallite growth was known to depend strongly on carbons prepared at low temperatures, and it was proposed to classify carbons into two groups, graphitizing and non-graphitizing carbons (Inagaki et al. 2014). L_a and L_c can be calculated from the information obtained of the Raman spectra deconvolution (Merlen et al. 2017). X-ray diffraction (XRD) is also commonly used (Z. Q. Li et al. 2007).

1.2.2 Nanotexture of carbon materials

Anisotropic carbon layer's preferred orientation in a carbon material is known to be important for understanding properties and structural changes at high temperatures. The nanotexture of carbon materials has been used to classify them into two groups, random and oriented, and the second into three others: planar, axial and punctual orientations (see **Figure 1.7**).

Graphitized materials have a nanotexture with a planar orientation. Highly oriented pyrolytic graphite (HOPG) is almost 100 % oriented. The degree of planar orientation depends on the preparation conditions and the heat treatment to which they are subjected. In the case of cokes, they may have planar and axial orientations. The degree of orientations mix depends on the heat treatment used. On the other hand, the CNTs present

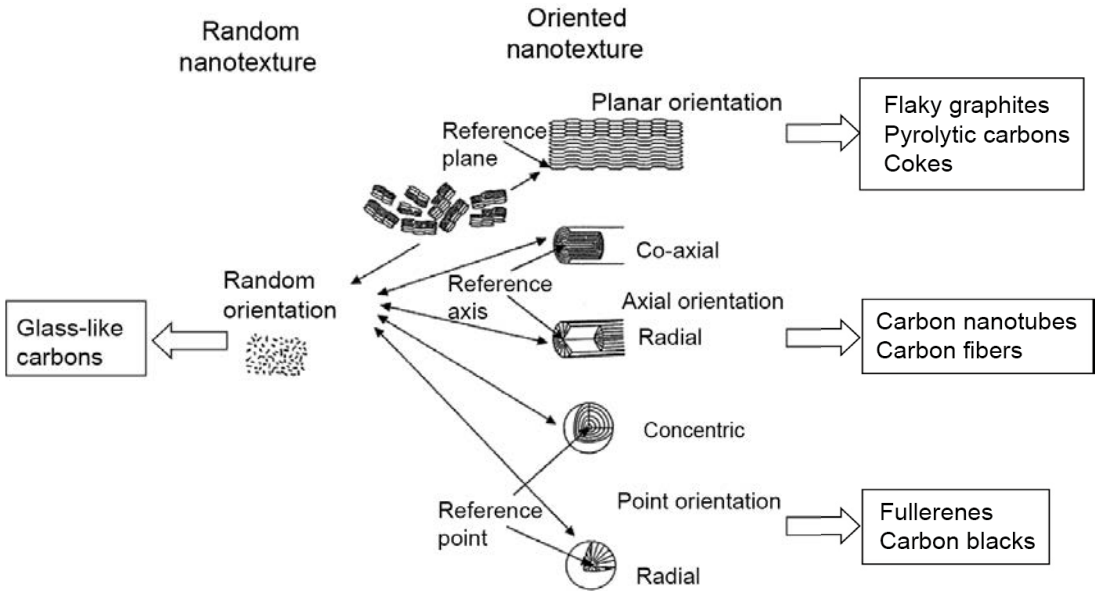

Figure 1.7: Classification of the nanotexture of carbon materials, with examples (Inagaki et al. 2014)

an extreme co-axial orientation (degree of orientation 100 %). Carbon fibers may have co-axial and radial orientations. The fullerenes present punctual orientations. It should be noted that even in carbon-based materials that have a random orientation, the fundamental structure of honeycomb (hexagonal) is present. Note that nanotexture is highly dependent on the precursor used. The thermoplastic precursors provide oriented nanotextures while the thermosetting random nanotextures. Other parameters (e.g. heating rate, pressure) influence the final nanotexture (Inagaki et al. 2014).

1.2.3 Microtexture of carbon materials

In **Figure 1.7**, many of the planar and axially oriented nanotextured particles are also anisotropic and different microtextures can be obtained when agglomerated. Therefore, in order to understand the properties of carbon-based materials it is not only necessary to know their degree of graphitization, it is also necessary to take into account nanotexture and microtexture. The texture due to the preferred orientation of anisotropic particles may be called the microtexture, because the particles are often of micrometer or millimeter size. The microtexture is usually created during the forming process of bulky carbon materials. Some mechanical properties (e.g. Young's modulus, strength), physical properties (e.g. thermal conductivity, electrical conductivity) are directly related to the microtexture of these materials. At the industrial level, tends to play with the orientation and percentage of these particles in the preparation of reinforced fibers (see **Figure 1.8**). Thus, for example, the mechanical properties of automotive parts (composites) are improved. These are stronger and lighter than those made from 100% polymers (e.g. ABS) or aluminum alloys. What's more, in 2018 a Swedish research group went further. They presented a work about the use of automobile structure (made with carbon-based material fibers) to store energy (Fredi et al. 2018).

Two methods have been employed for realizing the isotropy of the bulk of carbon materials that fundamentally consist of anisotropic structural units or crystallites: (1)

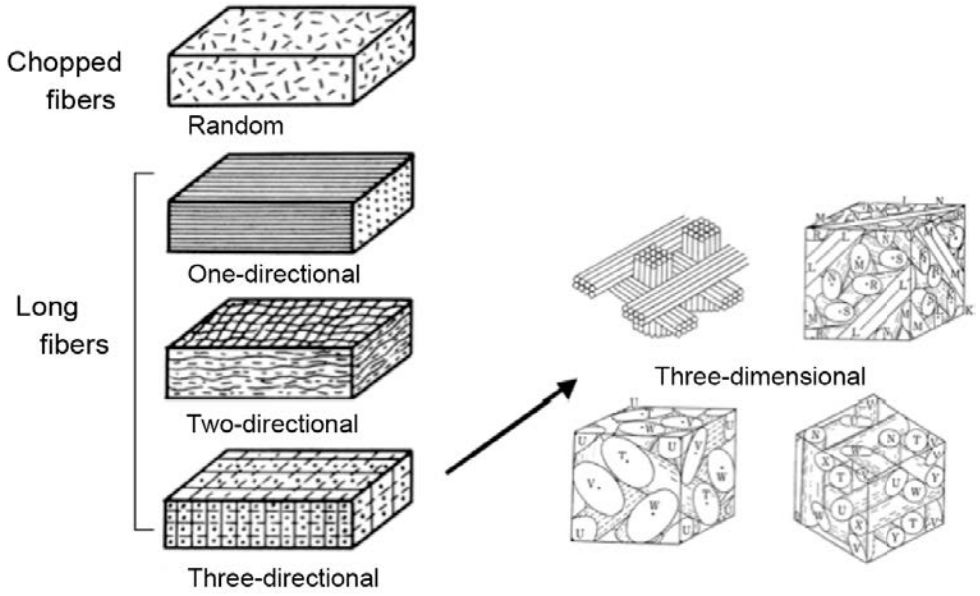

Figure 1.8: Microtextures formed by carbon fibers (Inagaki et al. 2014)

the random aggregation of micrometer or millimeter-sized particles, even though those particles are anisotropic, and (2) the random agglomeration of nanometer-sized crystallites in the bulk (Inagaki et al. 2014).

There is another approach to classifying carbon-based materials. This depends on the time they were discovered, like this: classic carbons, new carbons, and nanocarbons. Classic carbons include synthetic graphite blocks mainly used as electrodes, carbon blacks, and activated carbons, for which production procedures were developed before the 1960s. In the 1960s, carbon materials different from these classic carbons were invented: carbon fibers from various precursors, including vapor-grown carbon fibers; pyrolytic carbons produced via chemical vapor deposition processes; glass- like carbons with high hardness and gas impermeability; high-density isotropic carbons produced by isostatic pressing; intercalation compounds with different functionalities, such as high electrical conductivity; and diamond-like carbons as transparent carbon sheets. These newly developed carbon materials are classified as new carbons. Since the 1990s, various fullerenes with closed-shell structure, carbon nanotubes with nanometer diameters, and graphene flakes of only a few atoms' thickness have attracted attention from nanotechnology; these are classified as nanocarbons (Inagaki et al. 2014).

As seen in this short summary, the family of carbon-based materials is broad and their use in science and engineering is extensive. Its use as a structural part is often reported, but in recent years its use as part of the devices has become more important. For this reason, when working with these materials it is necessary to know the family of carbon to which it belongs, its nanotexture, and other parameters necessary to correctly understand the carbon-based material being produced and/or studied.

1.3 Carbon Nanotubes

Carbon nanotubes (CNTs) are carbon allotropes and currently one of the most interesting members of the carbon family due to their physical, chemical, mechanical, optical and electronic characteristics. The past two decades have witnessed their spread in a range of

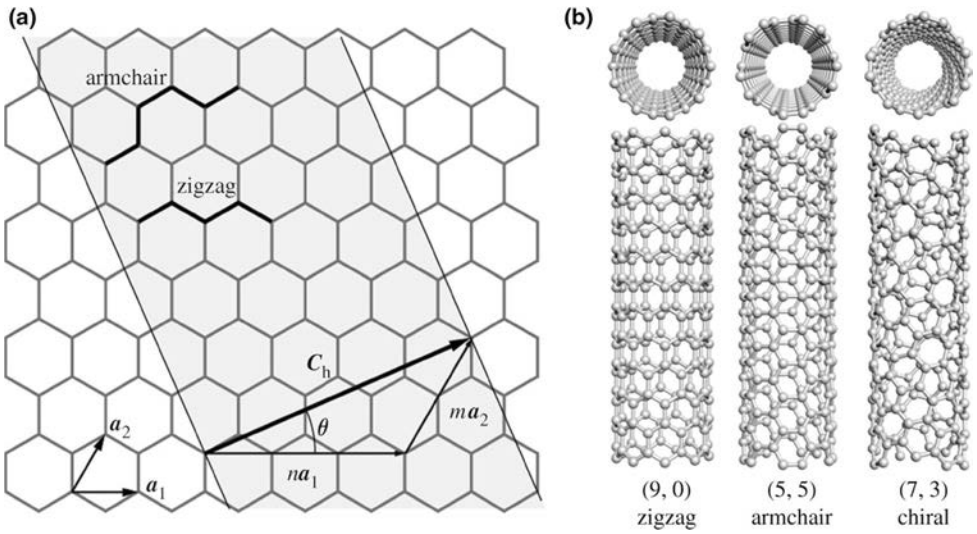

Figure 1.9: An illustration of the structures of a unrolled sheet of (a) SWCNT, (b) zigzag, armchair, and chiral SWCNTs (Ghasemi et al. 2017)

applications including building blocks in modern electronics, field emission sources, photodetectors, nonvolatile memory, ultrasensitive chemical and biosensors, and transparent conductive membranes (An et al. 2016).

A single CNT (without cap) is composed entirely of sp^2 bonds similar to the flat structure of graphite. On the other hand, fullerenes and CNTs (with cap) have hybrid link orbitals between sp^2 and sp^3. However, CNTs that have a low percentage of sp^3 bonds are in this sense closer to graphite. The difference in chemical activity between the CNT caps and the sidewalls, as well as between the straight and curved CNTs, is determined by the sp^2-sp^3 bonding ratio (Kong et al. 2019). CNT name is derived from their long, hollow structure with the walls formed by one atomic layer sheets of carbon called graphene. These sheets are rolled at specific and discrete (chiral) angles, and the combination of rolling angle and radius decides the carbon nanotube (CNT) properties. CNTs are categorized as single-walled (SWCNT) or multiple-walled nanotubes (MWCNTs).

Most SWCNTs have a diameter of approximately 1 nm with a tube length that can be many millions of times longer (high aspect ratio). The structure of SWCNT can be conceptualized by wrapping a one atom thick layer of graphene into a seamless cylinder. The way the graphene sheet is folded is represented by a pair of indices (n, m). The integer n and m denote the number of unit vectors along two directions in honey-comb crystal lattice of graphene. If $m = 0$, the nanotube is called zigzag nanotube, and if $n = m$, it is called armchair; otherwise, the nanotube is called chiral (R. J. Chen et al. 2001; Lieber et al. 1998). The diameter and helicity of a defect-free SWNT are uniquely characterized by the vector:

$$\mathbf{c}_\mathrm{h} = n\mathbf{a}_1 + m\mathbf{a}_2 \equiv (n, m)$$

that connects crystallographically equivalent sites on a two-dimensional gra- phene sheet, where a_1 and a_2 are the graphene lattice vectors (**Figure 1.9a**).

Electronic band structure calculations predict that the (n, m) indices determine the metallic or semiconducting behaviour of SWNTs. Zigzag $(n, 0)$ SWNTs should have two distinct types of behaviour: the tubes will be metals when $n/3$ is an integer, and otherwise

semiconductors. As c_h rotates away from $(n, 0)$, chiral (n, m) SWNTs are possible with electronic properties similar to the zigzag tubes; that is, when $(2n + m/3)$ is an integer the tubes are metallic, and otherwise semiconducting. The gaps of the semiconducting $(n, 0)$ and (n, m) tubes should depend inversely on diameter. Finally, when c_h rotates 30° relative to $(n, 0)$, $n = m$. The (n, n) or armchair tubes are expected to be truly metallic with band crossings at $k = \pm 2/3$ of the one-dimensional Brilluoin zone (Lieber et al. 1998).

The diameter (d) of an individual nanotube can be calculated from its indices as follows:

$$d = (a/\pi)\sqrt{(n^2 + nm + m^2)}$$

where $a = 0.246\,\text{nm}$.

There is a strong dependence of SWCNTs bandgap with (n, m) values, their value can vary from 0 to about 2 eV. Note that, the integers (n, m) uniquely determine the tubule diameter and the chiral angle θ. The chirality predestinates the electrical, mechanical, optical, and other properties of CNTs (M. S. Dresselhaus et al. 1995; M. Dresselhaus et al. 2012). The single atomic layer of graphene wrapped in different configurations of SWCNTs, armchair $(m = n)$, zigzag $(n, 0)$, and chiral (n, m), according to the arrangements of the unit vectors (n, m) along the honeycomb lattice of graphene is shown in **Figure 1.9b**.

1.3.1 Synthesis of carbon nanotubes

Carbon nanotubes (CNTs) are synthesized at the first stage of growth of so-called vapor grown carbon fibers as shown in **Figure 1.10**, and are found in the carbon deposits on graphite anodes during arc discharge. Under similar arc discharge conditions, fibrous carbon composed of a scroll of carbon layers was obtained in 1960, and was called "graphite whisker". Arc discharge between graphite electrodes forms carbon nanotubes together with other forms of amorphous carbon, such as carbon blacks and pyrolytic carbons, but with difficulty in controlling the structure of CNTs, i.e. thickness (single-, double-, or multi-walled), diameter, and length (Inagaki et al. 2014). However, since its discovery in 1991 by Sumio Iijima, other techniques have been developed to obtain CNTs free of defects. In fact, it is a carbon-based material whose production technology has matured a lot and now several processes are known that allow to obtain only single , double- and multi walled CNTs on a large scale. Diameters and lengths may vary depending on the application.

Figure 1.11 shows some of the most recently adopted methods to produce CNTs. Each of them has some advantages and disadvantages resulting in different growth results, which predestinates a choice of specific method for preparation of CNTs with requested properties. There are two main avenues to synthesize CNTs. The first one consists of sublimation of graphite and subsequently desublimation of the product. The second one is the decomposition of carbon-containing compounds. The first one requires very high temperatures ($\sim$ 4000 °C which can be achieved by electric arc furnace, laser ablation, focused solar radiation, or by resistive heating of graphite (T. Gupta 2018).

As we can see, in order to obtain CNTs of high purity, different techniques such as laser abrasion, modified arc discharge, and catalytic chemical vapor deposition have been proposed. Since catalytic chemical vapor deposition (CCVD) was thought to be practical for large-scale production, it has been applied using various carbon precursors and various

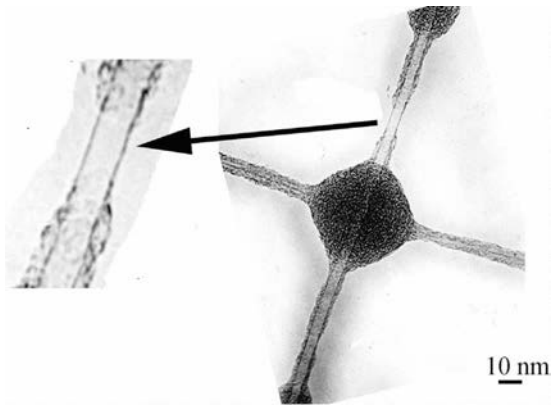

Figure 1.10: Single-walled Carbon Nanotube Formed at the First Stage of Growth of Vapor- grown Carbon Fibers (Prof. M. Endo of Shinshu University, Japan)

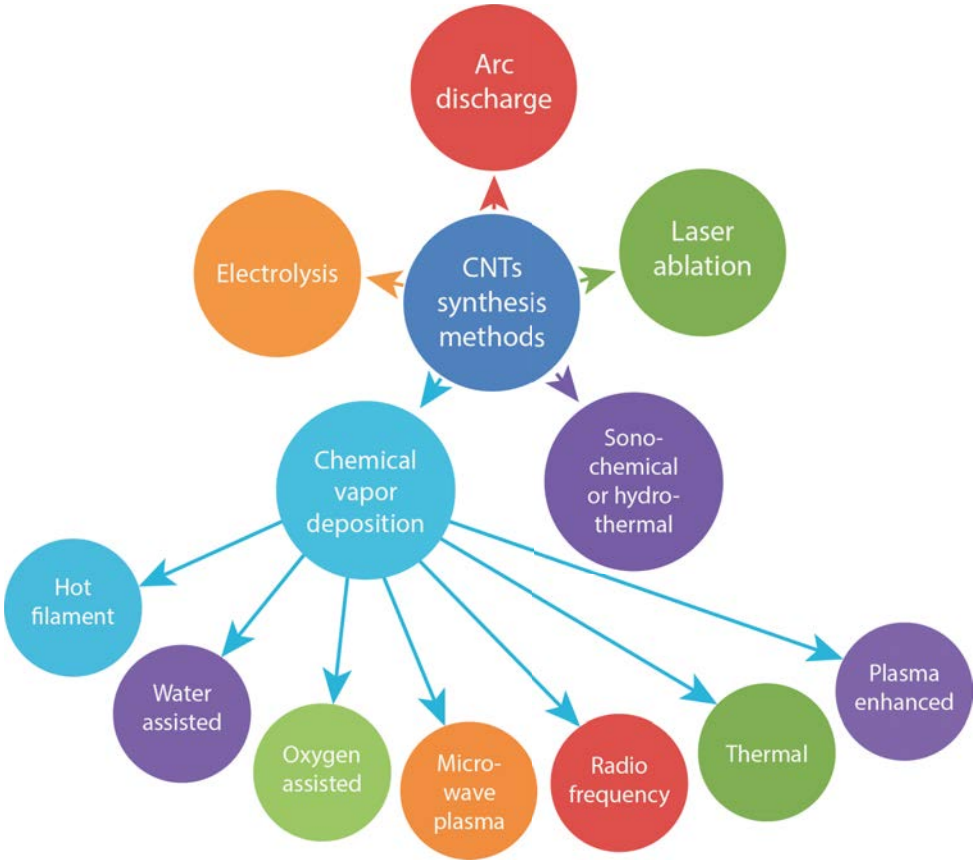

Figure 1.11: Some of the most recently adopted methods to produce CNTs. Adapted from (Prasek et al. 2011)

catalytic metals, either supported on a substrate or floating as fine particles (Inagaki et al. 2014). The following is a summary of some of the processes used for the production of CNTs. Of course, more emphasis will be placed on the process employed in this work: plasma enhanced chemical vapor deposition (PECVD).

Arc discharge

This method which can be operated either by alternating or direct current (AC/DC) is the one by which CNTs were produced by Iijima (Sumlo Iijima 1991). **Figure 1.12a** shows DC arc discharge and **Figure 1.12b** shows the AC arc discharge systems.

In this process a voltage of 10 to 20 V and a current in the range of $20-100\,A$ (approx.) is established between two cylindrical graphite electrodes separated by a distance of the order of 1 mm. The graphite electrodes (rods) used in the arc discharge systems are usually between 6 and 12 mm in diameter and are water-cooled. The chamber is kept at a subatmospheric pressure. Gram-scale synthesis of MWCNTs by arc discharge has been achieved in the presence of helium (He) and CH_4 gases at a pressure of ~ 7 kPa. An arc current of 20 A is applied to the anode with a diameter of 6 mm (Ebbesen and Ajayan 1992). Other sub products like amorphous carbon, fullerenes and nanoparticles are also obtained. The inert gas drags and cools the synthesized products, so the growth is affected by the speed of the existing flow, as well as by the thermal conductivity of the gas. CNTs are normally deposited on the cathode while the rest of the carbonaceous species are deposited mostly on the walls of the chamber. A graphite rod containing a metal catalyst (Fe, Co, etc.) is used as the anode with a pure graphite cathode to produce SWNTs in the form of soot (Bethune et al. 1993; Iijima and Ichihashi 1993). H_2 use during the process results in better graphitization of CNTs as well as better process performance. This is due to the fact that hydrogen forms C-H bonds with the atoms at the ends of the CNT, which prevents the CNT from closing with a fullerenic cap (X. K. Wang et al. 1995).

(Y. Jiang et al. 2009) demonstrated that the use of NH_3 during the arc discharge

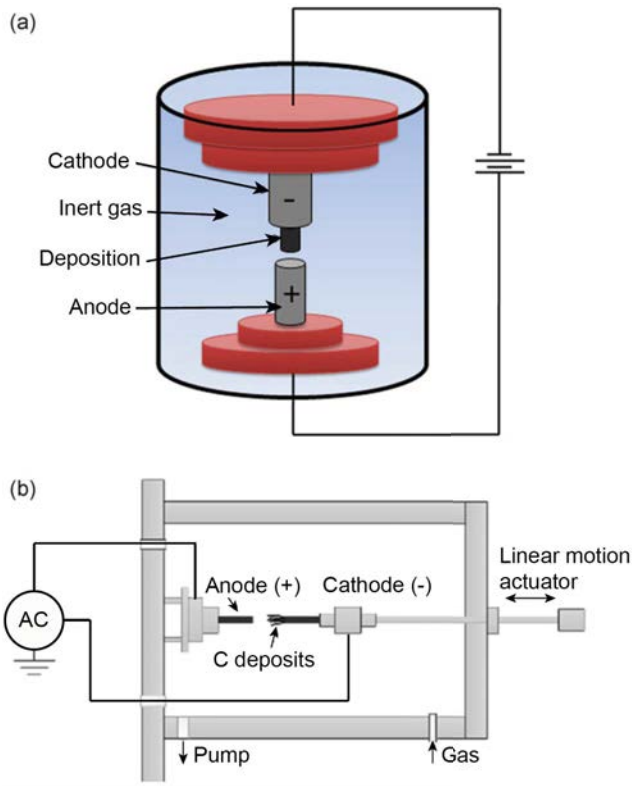

Figure 1.12: (a) DC arc discharge apparatus for CNT growth, (b) AC arc discharge systems. Adapted from (T. Gupta 2018)

process improves the production efficiency of CNTs. Besides arc discharge, single-pulse arc discharge has been successfully applied in the production of near-vertically oriented MWCNTs on Ni/glass using a graphite counter-electrode in an ambient air (Parkansky et al. 2004; Prasek et al. 2011).

The growth of SWCNTs can be done by arc discharge method with or without the use of catalyst precursors. On the other hand, the MWCNTs are produced without a catalyst precursor. In SWCNTs, the anode is made of graphite and a metal catalyst such as nickel (Ni), cobalt (Co), palladium (Pd), titanium (Ti), or platinum (Pt), or the mixtures of Co–Ni, Fe–Ni, Ni–Ti, etc. is used. The metal catalyst plays an important role in the process yield. The gap distance between the electrodes is held constant to ensure high efficiency. The production of CNTs is mostly affected by the presence of impurities. Calcination in air at 400 °C for 2 h is very effective in the removal of carbon nanoparticles deposited during DC arc discharge. Heating by IR irradiation in air at 500 °C is also being used to remove the unwanted carbon nanoparticles (T. Gupta 2018).

Laser Ablation

High temperature preparation techniques such as arc discharge or laser ablation were first used to produce CNTs but nowadays these methods have been replaced by low temperature chemical vapour deposition (CVD) techniques (< 800 °C), since the orientation, alignment, nanotube length, diameter, purity and density of CNTs can be precisely controlled in the latter (Prasek et al. 2011).

The process consists of vaporizing the carbon from a graphite target by irradiation with a pulsed or continuous laser (Nd:YAG and CO_2). The reaction takes place inside a quartz tube, which is typically heated between 1000 and 1500 °C (**Figure 1.13**). A flow of an inert gas (He or Ar) under atmospheric pressure (~ 70 kPa) is passed through the tube, dragging the vaporized material into a cold trap. There the carbon nanostructures are condensed, among which are mostly MWCNTs, and to a lesser extent, fullerenes and amorphous carbon. SWCNTs can be obtained by using a target with a mixture of catalyst metal and graphite in the form of compacted powder. Ni, Co and Fe are the most used catalytic materials to obtain SWCNTs (Maser et al. 1998).

The properties of CNTs prepared by the pulsed laser deposition process (PLD) are

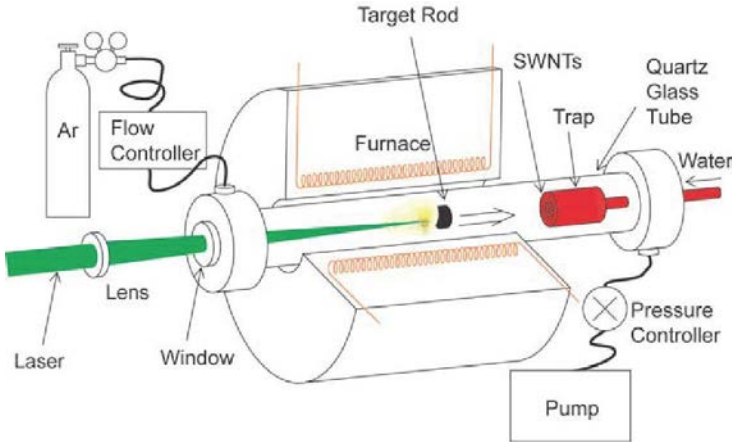

Figure 1.13: Schematic diagram of the laser-furnace apparatus (Ando et al. 2004)

strongly dependent on many parameters such as: the laser properties (energy fluence, peak power, continuous work versus pulse, repetition rate and oscillation wavelength), the structural and chemical composition of the target material, the chamber pressure and the chemical composition, flow and pressure of the buffer gas, the substrate and ambient temperature and the distance between the target and the substrates. Laser ablation, as crucial step of PLD, is one of the superior methods to grow SWNTs with high-quality and high-purity (Prasek et al. 2011). The high level of control over the deposition parameters, as well as the variety of these, allows greater control over the final characteristics of the CNTs and as many nanostructures produced with this method (García Cespedez 2008).

There are some commercial applications of producing CNTs using this process. For example, (Stramel et al. 2010) have successfully applied commercial MWNTS and MWNTs polystyrene targets (PSNTs) for deposition of composite thin films onto silicon substrates using PLD with a pulsed, diode pumped, Tm:Ho:LuLF laser (a laser host material LuLF ($LuLiF_4$) is doped with holmium and thulium in order to reach a laser light production in the vicinity of 2 mm). They found that usage of pure MWNTs targets gives rise to a thin film containing much higher quality MWNTs compared to PSNTs targets. Similarly, Bonaccorso et al. prepared MWNTs thin films deposited by PLD techniques (with Nd:YAG laser) ablating commercially polystyrene-nanotubes pellets on alumina substrates (Bonaccorso et al. 2007).

Chemical Vapor Deposition of CNTs

Catalytic chemical vapour deposition (CCVD), either thermal or plasma enhanced (PE), is now the standard method for the CNTs production. Moreover, there are trends to use other CVD techniques, like water assisted CVD (S. Hussain et al. 2012; L. X. Kang et al. 2016), alcohol assisted CVD (Yang Li et al. 2015), oxygen assisted CVD (Hye et al. 2007), hot-filament (HFCVD) (Varshney et al. 2010), microwave plasma (MPECVD) (Brown et al. 2011) or radiofrequency CVD (RF-CVD) (Y. Xu et al. 2011). CCVD is considered to be an economically viable process for large scale and quite pure CNTs production compared with laser ablation.

The main advantage of this approach is the versatility to obtain CNTs on a multitude of different supports (conducting, semiconducting, and insulating materials) and geometries. In addition, in CVD processes it is possible to easily control the reaction course and the high purity of the obtained material. Chemical vapor deposition (CVD) is practiced in different formats. These formats generally differed in the means by which chemical reactions are performed. They are classified as follows:

- Atmospheric pressure CVD (APCVD), low-pressure CVD (LPCVD), and ultrahigh vacuum CVD (UHVCVD), when the operation depends on the chamber pressure.
- Aerosol-assisted CVD(AACVD), direct liquid injection CVD(DLICVD), when the operation depends on the physical characteristics of vapor.
- Plasma-enhanced CVD (PECVD), atomic layer CVD (ALCVD), microwave plasma-assisted CVD (MPCVD), when the operation is controlled by plasmas.
- Hot filament CVD, rapid thermal CVD, and flame pyrolysis CVD in open air. All these operations are performed by following combustion technology.

CVD processes involve the catalytic decomposition of a solid, liquid or gaseous precursor rich in C atoms on nanometric-sized metal particles (catalyst) at temperatures

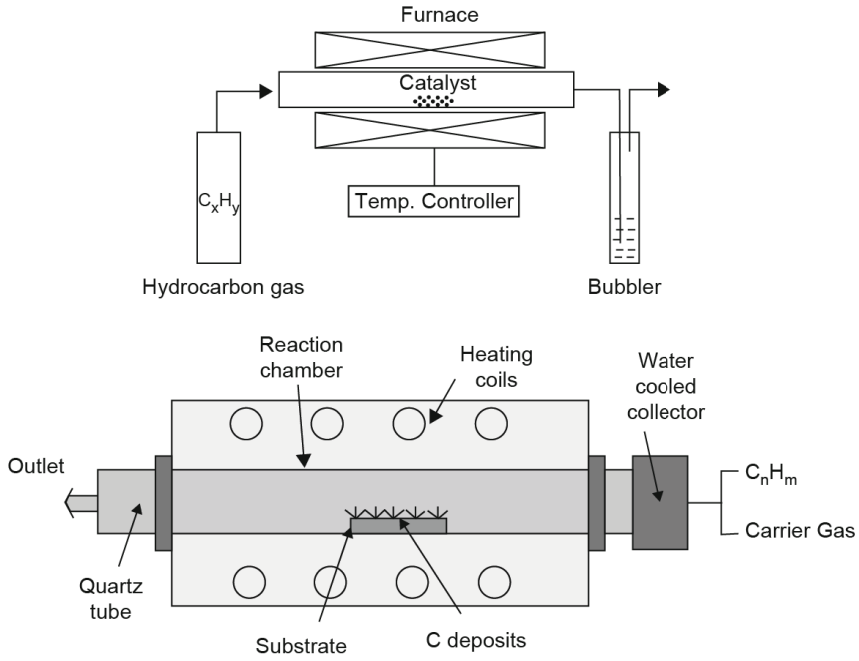

Figure 1.14: Schematic diagram of a CVD setup used for CNT growth (T. Gupta 2018)

between 600 and 1200 °C. As an example, the tubular configuration of CVD reactor is shown in **Figure 1.14**. The method involves passing a hydrocarbon gas (CH_n) (typically $15-60$ min) through a tubular reactor in the presence of a catalyst material. The tube is heated to a high temperature to decompose the hydrocarbon. The function of the catalyst in the CVD process is the decomposition of the carbon source by applying heat (T. Gupta 2018).

1.3.2 Growth Mechanism

The mechanism known as vapor-liquid-solid (VLS) is widely accepted. VLS model was introduced for explaining the growth of silicon whiskers. For CNTs, this model was first adapted for explaining the formation of sea-urchin-like structures (Loiseau et al. 2003). According with this mechanism (**Figures 1.15a-c**), the growth process includes the dissociation of gaseous hydrocarbon on the catalyst, the diffusion of adsorbed carbon atoms into the bulk of the nanoparticle, carbon precipitation, and the nucleation of cap structures of nanotubes (Y. Chen and J. Zhang 2014; Yan Li et al. 2010). Since the caps that are initially formed around the catalyst define the diameter and the chirality of the growing nanotube, it is extremely effective to control the diameter and chirality by tuning the size, shape, and composition of the catalyst nanoparticles.

It should be noted that CNTs can also be obtained using non-metallic particles. In this case, the growth of CNTs is explained by the mechanism known as vapor-solid-solid (VSS, illustrated in **Figures 1.15a,d,e**) (Tessonnier and Su 2011). It was (Rümmeli et al. 2007) who noticed that oxide particles (which met certain requirements) could be used to obtain CNTs. This approach results in better diameter control and chirality control. The nonmetal catalysts, such as metal oxide and diamond, have high melting points so that their structure and morphology remain unchanged at high growth temperature. Such stable catalysts are superior templates for cap nucleation, thereby defining the diameter and

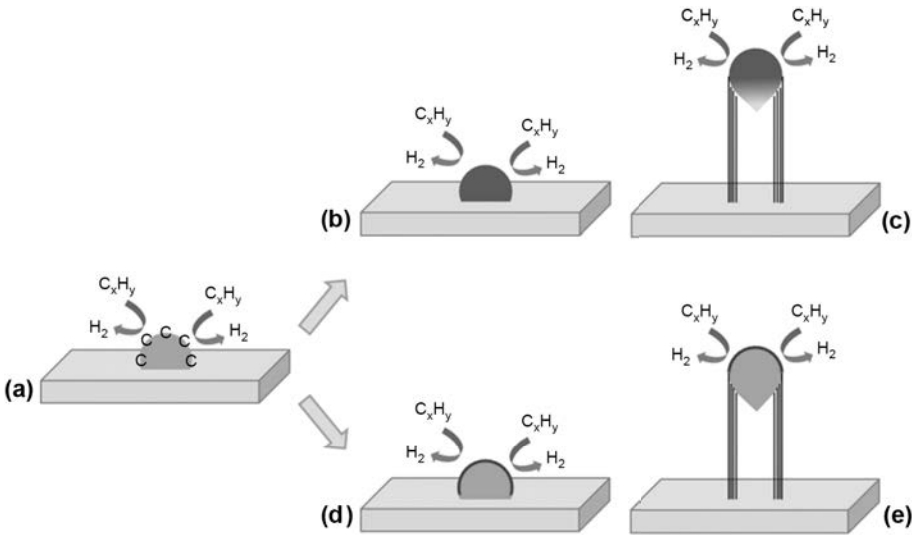

Figure 1.15: Schematic demonstration of growth dynamics of carbon nanotubes (CNTs). Vapor-liquid-solid (VLS) growth model (a-c) vs. vapor-solid-solid (VSS) growth model (a, d, and e) (Tessonnier and Su 2011)

chirality of the growing nanotube. Additionally, these solid nonmetal catalysts have little activity of carbon feed stock decomposition, resulting in the tendency of carbon atoms to diffuse along the particle surface (surface diffusion) instead of within the nanoparticle (bulk diffusion) (An et al. 2016).

The growth of CNTs by CVD ends when the catalyst loses its activity, which occurs when the diffusion of new C atoms into the particle becomes impossible. This may occur due to the formation of a stable carbide in the metal particle (Hernadi et al. 1996), or after total coverage of the metal particle by concentric graphitic shells (Guo et al. 2005; Yang Li et al. 2015).

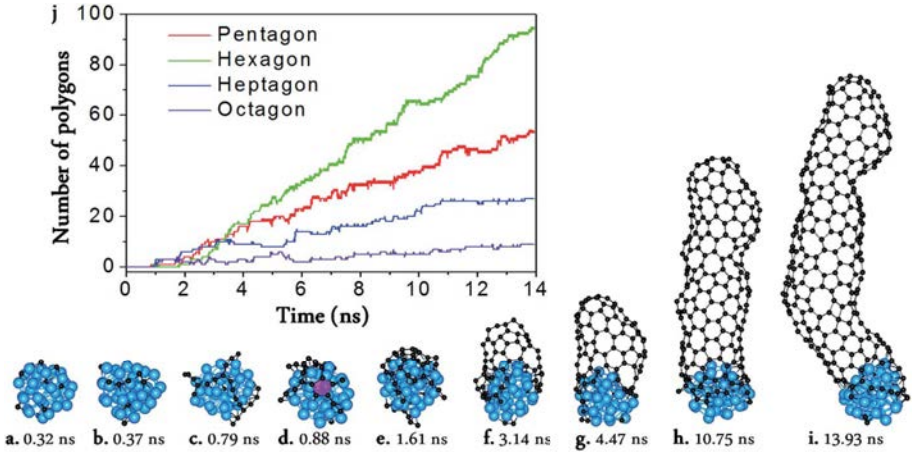

Figure 1.16: Molecular dynamic (MD) simulation of SWCNT growth from a Ni32 catalyst surface. (a–i) Snapshots taken from the MD trajectory. (j) The numbers of the pentagons, hexagons, heptagons, and octagons vs. MD simulation time. The pink polygon in (d) is the pentagon which firstly appeared in the MD simulation (Z. Xu et al. 2015)

It is important to highlight the effort of many research groups to better understand the intrinsic processes of obtaining CNTs. Thanks to the computational processing capacity and atomic simulation methods, the growth mechanisms of nanocarbon materials (such as carbon nanotubes and graphite) can be explored in depth. **Figure 1.16** shows the molecular dynamic (MD) simulation of SWCNT growth from a Ni_{32} catalyst surface. (Z. Xu et al. 2015) were capable of simulating the nucleation and growth of SWCNTs with fairly good quality. That simulation results were in agreement with most experimental observations, and shows that the chirality-selected growth of SWCNTs is very hard to achieve on liquid catalyst particles. In addition, it is interesting to observe how the number of hexagons (honey-comb) imposes itself, during the growth time, to the other arrangements of carbon atoms.

1.3.3 Plasma enhanced chemical vapor deposition of CNTs

The plasma enhanced chemical vapor deposition (PECVD) is a low temperature operation and can be also used in several different modes (radio frequency (RF), direct current (DC), diffusion (D), or microwave (MW)). The major difference between RF and DC mode PECVD is the higher concentration of reactive radicles in the former (T. Gupta 2018). Obtaining CNTs at lower temperatures than thermal CVD processes is vital when substrates sensitive to high temperatures are used (above 900 °C), especially in the manufacture of electronic devices.

In comparison to the thermal CVD, with the PECVD it is possible:

- To have an extra contribution of precursor species due to the dissociation of the gases produced by the plasma.
- Obtain alignment perpendicular to the substrate of the CNTs, regardless of their density.
- Reduce the activation energy for the growth of CNTs.
- Lower growth rate with respect to thermal CVD.

The plasmatic energy efficiently dissociates gas molecules at lower temperatures, and the synthesis of carbon nanotubes might occur at lower temperature. PECVD has been investigated for its ability to produce vertically aligned nanotubes. It has been suggested that in PECVD only VACNTs grown from the tip are aligned specifically due to the presence of the plasma electric field in the growth process, whereas VACNTs grown from the base are aligned mainly due to the crowding effect. The electrostatic force F creates a uniform tensile stress across the entire particle/CNT interface, regardless of where the particle is located tip or at base. The plasma is composed of electrons, charged species and ions, and neutral atoms and molecules. The plasma remains electrically neutral as the ion density is balanced by the electron density. The electron density in the radio frequency (RF) generated plasma is typically $\sim 10^8 - 10^9\,\mathrm{cm}^{-3}$ for a pressure range of $0.1 - 133\,\mathrm{mbar}$. The electron temperatures are $\sim 1 - 11\,\mathrm{eV}$, while the ion temperatures are lower at $\sim 50 - 100\,\mathrm{meV}$. There is also a spontaneous but nonequilibrium conversion of neutral species into long lived radicals. The plasma forms "sheaths", dark regions of very low electron density, with the electrodes (Shahzad Hussain 2014).

Note that according to the VLS growth mechanism, the catalyst particles must be in liquid phase. Carbon nanotubes were precipitated from the supersaturated eutectic liquid (Grüneis et al. 2006). The activated energy for thermal CVD ($\leq$ 700 °C) was

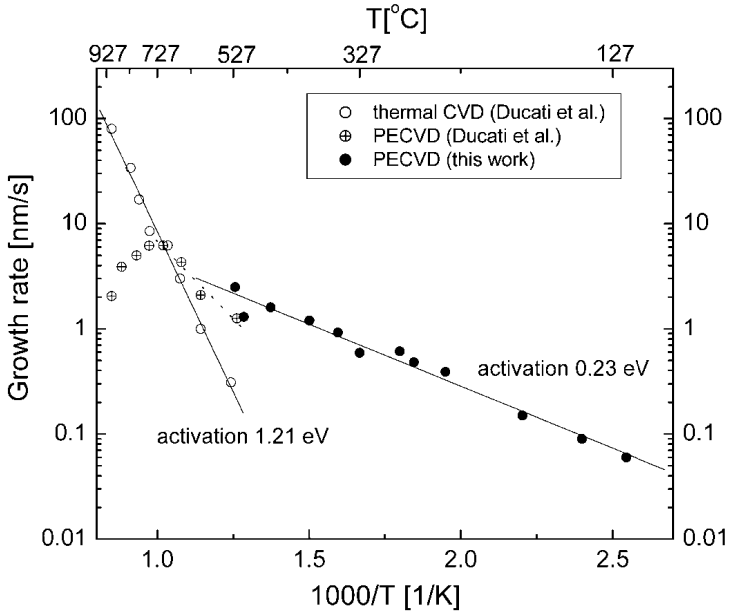

Figure 1.17: The growth rate variation with temperature for thermal CVD and PECVD (Hofmann et al. 2003)

reported to be $\sim$ 1.21 eV, while in the case of PECVD, the activation energy is much lower (0.23 eV) (Hofmann et al. 2003). The differential fact that the PECVD technique allows such a low temperature for the synthesis of these nanostructures is the dissociation of species produced in the plasma, which increases the contribution of precursors to the catalyst (García Cespedez 2008). At high temperatures ($>$ 700 °C approx.) CNTs grown by PECVD have a lower growth rate than their counterparts grown under thermal CVD conditions. While at low temperatures, given that CNTs grown by PECVD present a lower activation energy, the growth rate is higher compared to thermal CVD **Figure 1.17**. Moreover, in general terms, the contribution of carbon atoms cannot be as high in PECVD as in thermal CVD, whose working pressure can be atmospheric. In a PECVD system, the technical difficulties in creating a stable discharge limits the working pressure to values below 5×10^3 Pa (Meyyappan et al. 2003).

1.3.4 Catalyst material

Most important catalysts are transition metal alloys. Ni, Fe and Co are the most commonly used metals, because of their strong activity in catalyzing the decomposition of carbon feedstock and sufficient carbon solubility (Yan Li et al. 2010) . However, other metals and their alloys can also be used: Mo, Pd, Cu, Au, Ag, Mn, Cr, Sn, and Al, and their combinations, have been employed as catalysts in the form of nanoparticles, nanoclusters, or single crystals (An et al. 2016).

According with the iron-carbon phase diagram, the eutectic temperature for the Fe-C in the bulk phase is 1153 °C but it decreased down to 732 °C significantly at the nanometer scale (Harutyunyan et al. 2005). At higher temperature catalyst particle is more active and stay in liquid phase for longer time but it is important to grow the nanotubes at the temperature well below self-pyrolysis temperature and slightly above the eutectic point. The self-pyrolysis temperature depends on the stability of the carbon source used and the eutectic point decreases for all metals with the film thickness. The catalyst deactivation

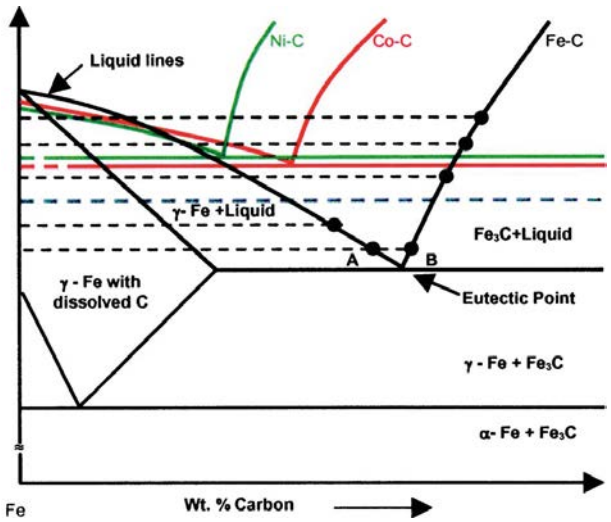

Figure 1.18: Scheme of the iron-carbon phase diagram (Harutyunyan et al. 2005)

due to the amorphous carbon is a major problem which is the result of the self-pyrolysis of hydrocarbon or excessive carbon concentration (Shahzad Hussain 2014). **Figure 1.18** represents the iron-carbon phase diagram and it shows the eutectic points of other two metals used commonly as catalysts (Co and Ni). Note that Fe is the metal with the lowest eutectic point. Indeed, eutectic means easy to melt. The carbon content at the eutectic points of cobalt-carbon and nickel carbon phases is approximately two times lower and the temperature significantly higher than for the iron-carbon phase. Additionally, the solidification of cobalt-carbon and nickel-carbon phases occurs at relatively low concentration of carbon, at a given temperature. These can terminate the growth of SWCNTs at early stages. Therefore, cobalt and nickel catalysts will require higher synthesis temperatures, as in the cases of laser ablation or arc-discharge methods (Harutyunyan et al. 2005). It is important to take into account that the catalyst particle diameter largely determines the diameter of the CNTs formed from them. It is relatively easy to control the diameter and number of walls of the CNTs by tuning the size of the catalyst nanoparticles.

As shown in **Figure 1.19**, when iron is used as catalyst, the number of graphitic walls in a CNT is dependent on CNT diameter, which is dependent on catalyst thickness. The mean CNT diameter is proportional to the thickness of the Fe thin film, and thin CNTs have a strong tendency to be SWCNTs while thick CNTs tend to be double-walled carbon nanotubes (DWCNTs) or MWCNTs. SWCNTs occupied the majority of the nanotube population within a diameter range of $1.0 - 2.5$ nm, and DWCNTs account for the majority of CNTs with a diameter in the range of $3.0 - 4.0$ nm, while MWCNTs have a higher percentage for the diameter larger than 4.5 nm. Maximum DWCNT selectivity was reached at an Fe thin film thickness of 1.69 nm. It is generally believed that during catalyst annealing, thin (thick) metal films break up into smaller (larger) catalytic nanoparticles, which, in turn, produce smaller (larger) tubes. Empirically, it is well established that a thin catalytic metal film (around 1 nm) is required to grow SWNTs.

In addition to the thickness of the thin film, the formation of the catalyst nanoparticles depends on many parameters, such as pressure, gas used, temperature, surface energy of the substrate, among others. (Dervishi et al. 2009) studied the thermal effect from an MgO supported Fe-Co catalyst system. It was found that the diameter distribution was

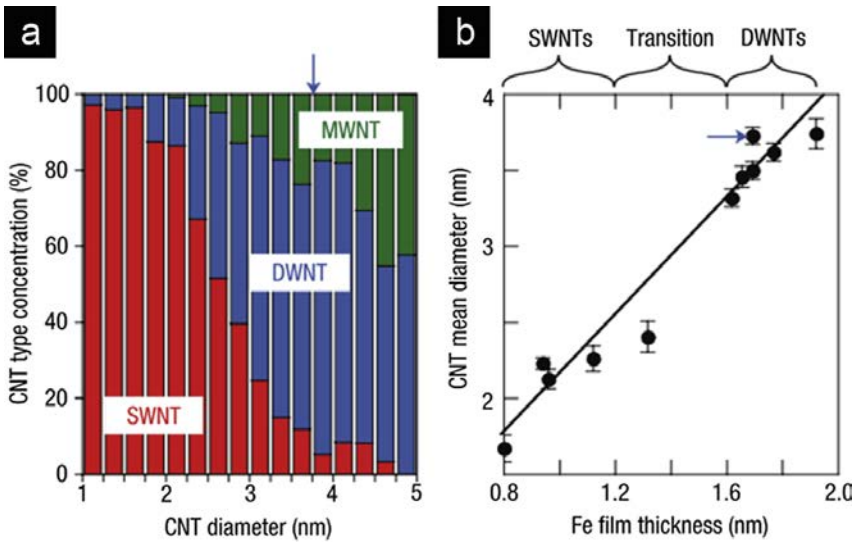

Figure 1.19: Trends in carbon nanotube (CNT) type and diameter. (a) Concentrations of single walled carbon nanotube (SWNT), double-walled carbon nanotube (DWNT), and multiwalled carbon nanotube (MWNT) as a function of the CNT diameter; (b) CNT mean diameter as a function of Fe film thickness (An et al. 2016)

broadened when raising the growth temperature from 800 to 1000 °C. These results are normally explained by particle coalescence or Ostwald ripening (Wen et al. 1996). At the CNT growth temperatures, catalyst sintering by coalescence modifies the particle size distribution and consequently the CNT diameter distribution. Some supports, in particular MgO and Al_2O_3, seem to keep the particles in a dispersed state. Another approach to solve the sintering problem is to embed the transition metal species in a matrix. Several groups showed that mixed oxide catalysts, that is, oxides with several elements present as cations in the structure, are efficient catalysts to grow MWCNTs. Mixed oxides with perovskite- and spinel-type oxide structures led to particularly interesting results (Tessonnier and Su 2011). Feeding gas is another factor that affects diameter and chirality. It is believed that the diameter is tightly related to the carbon feeding rate because of the selective activation of catalyst nanoparticles.

1.3.5 Precursor gases to obtain CNTs

The selection of the gas(s) influences the characteristics of the CNTs. From the formation of the catalyst nanoparticles, through the orientation of the nanotubes, to the amount of amorphous carbon are strongly related to the gases used during the production of these carbon-based materials. Among the precursor materials of CVD growth of CNTs, a distinction can be made between those that are used as sources of C atoms, and those that have a catalytic, or simply carrier, function. The precursors traditionally used as sources of C are acetylene (C_2H_2) and methane (CH_4). However, there are many other gaseous precursors such as ethane (C_2H_6), ethylene (C_2H_4), 1,2-propandiene (C_3H_4), carbon monoxide (CO); solid C sources such as camphor ($C_{10}H_{16}O$); and liquid precursors such as benzene (C_6H_6), toluene ($C_6H_5CH_3$), iso-octane or ethanol (C_2H_5OH) or 2,2,4-trimethyl-pentane (C_8H_{18}) among others (García Cespedez 2008).

It can be said that the ideal precursor is the one that allows a synthesis of CNTs in

high quantity, with greater crystallinity, at lower temperature, with low percentage of amorphous carbon, in a cheaper and safer way. However, no gas meets all these requirements. C_2H_2 is the most widely used precursor for obtaining low temperature CNTs, with which MWCNTs are mainly obtained. At temperatures above 900 °C its thermal decomposition generates large amounts of amorphous carbon that makes it impossible for SWCNTs to use. This is why CH_4 and CO are more used for this purpose, due to their greater stability at these temperatures. However, this problem has been solved by introducing C_2H_2 in short insufflations of $\sim$ 5 s at 1000 °C (Lacerda et al. 2004). But high-pressure carbon monoxide (HiPco) process is the most successful CVD variant to date for the production of high quality SWCNTs in large quantities. Iron pentacarbonyl is used to produce iron nanoparticles that provide a nucleation surface for the transformation of carbon monoxide into carbon during the growth of the nanotubes. Experiments use in the range of milligrams to grams of material. Waste material is regularly picked up by a professional waste disposal company, and the waste material is incinerated, avoiding environmental release (Bronikowski et al. 2002). Note that precursor gas can affect diameter and chirality. It is believed that the diameter is tightly related to the carbon feeding rate because of the selective activation of catalyst nanoparticles. (Lu and J. Liu 2006) reported that small diameter SWNTs were preferentially obtained at a low carbon feeding rate. In contrast to this, (T. Saito et al. 2008) found that increasing the flow rate of the carbon source would lead to a smaller diameter. The type of carbon source may lead to the change in chirality distribution. (B. Wang, L. Wei, et al. 2007) utilized four different carbon precursors, CO, C_2H_5OH, CH_3OH, and C_2H_2, to synthesize SWNTs on CoMo catalysts. It was discovered that narrowly (n, m) distributed SWNTs could be obtained only under high-pressure CO or vacuumed C_2H_5OH and CH_3OH. The same group also reported that SWNTs with enriched three dominant chiralities could be obtained by changing the pressure of the carbon precursor (B. Wang, Poa, et al. 2007).

Catalytic or carrier gases are mainly gases such as Ar, H_2, N_2 or NH_3. The role of H_2 and NH_3 is usually to maintain the catalytic particle in a reduced state (Ci et al. 2001), while the hydrogen atoms that decompose on the surface help prevent the formation of the graphitized shell, which would deactivate the catalyst. On the other hand, an excess of H atoms can lead to a reduction in the growth rate in the CVD method by ferrocene injection (Singh et al. 2003), which could be due to the formation of CH_4 atoms (K. L. Yang and R. T. Yang 1986) that cut off the contribution of C atoms to the formation of CNTs. In addition, it has been found that the presence of NH_3 during a CVD process by decomposition of C_2H_2, as a consequence of its action on the catalyst, favors the growth of vertically aligned CNTs (Choi et al. 2001).

1.3.6 Alignment control of CNTs and patterning

CNTs aligned in parallel with each other have been prepared from different hydrocarbon gases on different metal catalysts. The growth of aligned carbon nanotube forests is studied extensively because it represents one of the highest yield methods of nanotube growth. The aim of several works is to fabricate vertically aligned CNTs with homogeneous distribution on the surfaces and high uniformity. It is evident to use nanolithography to create pattern of the catalyst on the surface on which CNTs are formed using CVD methods. It was (Xie et al. 1996) who reported the first vertically aligned MWCNTs using Fe nanoparticles as a catalyst. They used mesoporous silica as support. Since then the processes of obtaining vertically aligned CNTs have been constantly improved, especially for their applications in many areas. CNTs must be effectively assembled into macroscopic prod-

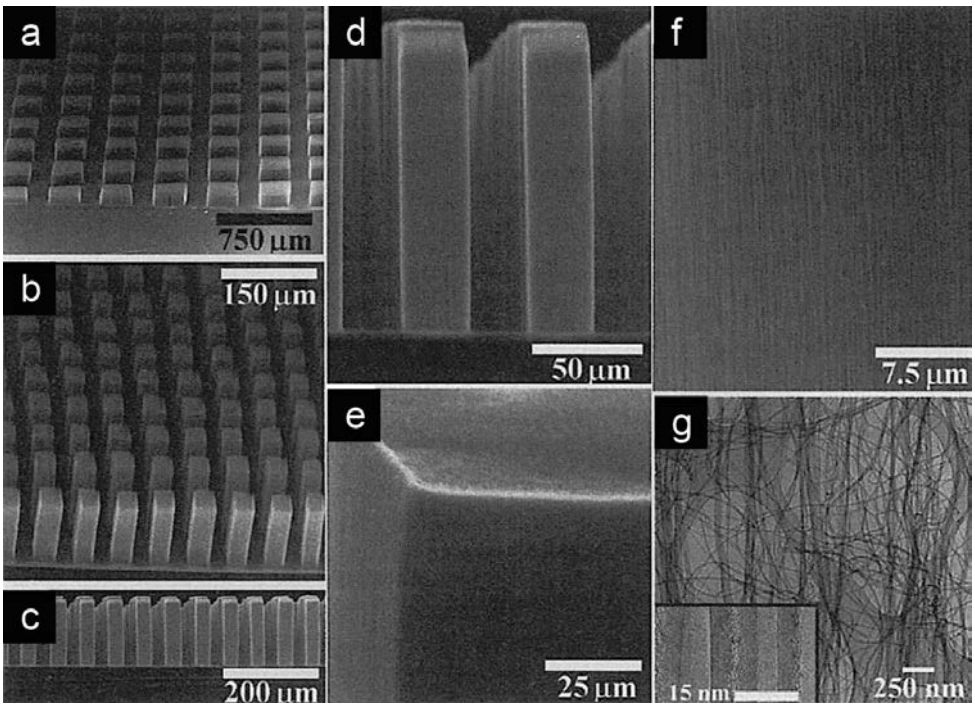

Figure 1.20: Carbon nanotube arrays. (a-f) SEM images with different magnifications, (g) TEM images of carbon nanotubes in the array (Inagaki et al. 2014)

ucts, so that their excellent properties can be retained at a larger scale. Aligned CNTs could be used to derive 1D CNT fibers, 2D CNT sheets/films, and 3D foams, and the processability or spinnability of converting a aligned CNT into a macroscopic assembly is found strongly dependent on the alignment of the CNTs. A good alignment in CNTs is believed to be the prerequisite to full exploitation of CNTs potentials (An et al. 2016).

CNTs aligned perpendicularly to the substrate (called "arrays") with well-defined patterns were synthesized by CVD at 700 °C under a flow of ethylene at 1000 standard cm^3/min (SCCM) on a P-doped porous Si(100) wafer, on which an Fe thin film (5 nm thick) was patterned by electron beam evaporation, as shown in **Figure 1.20**.

The resultant CNTs were multi-walled and had diameters of 16 ± 2 nm. Growth rate of CNTs was very high; the length of CNTs, i.e. the height of the arrays, reached 30 and 240 μm after 5 and 60 min CVD, respectively. In the arrays, CNTs aligned almost perfectly perpendicularly to the substrate, as shown in **Figure 1.20f**, although CNTs formed on a porous Si wafer without an Fe film were not aligned **Figure 1.20g**. The CNT arrays can be formed with a well-defined pattern **Figures 1.20a-c**, of which the edges and corners are very sharp **Figures 1.20d-e**. Instant addition of inert gas (Ar) into the supply of the precursor gas (acetylene), as shown in **Figure 1.20d**, was found to give a distinct straight line on the scanning electron microscopy (SEM) image of the as-grown CNT array **Figure 1.20e**, and so the growth kinetics and mechanism of the multi-walled CNT (MWCNT) array were discussed with relation to these marks (K. Liu, K. Jiang, et al. 2005). Growth rate of CNTs by CVD of acetylene was almost constant at 600 °C, c. 3 μm/min, but at 680 °C it increased from 17 to 23 μm/min during the first 15 min and then tended to be saturated. The growth process was well approximated by the first order reaction $E_a = 159 \pm 5$ kJ/mol. The diameter corresponding to its maximum population tended to shift to larger sizes with increasing thickness of Fe catalyst: 6.2 nm (3-4 walls)

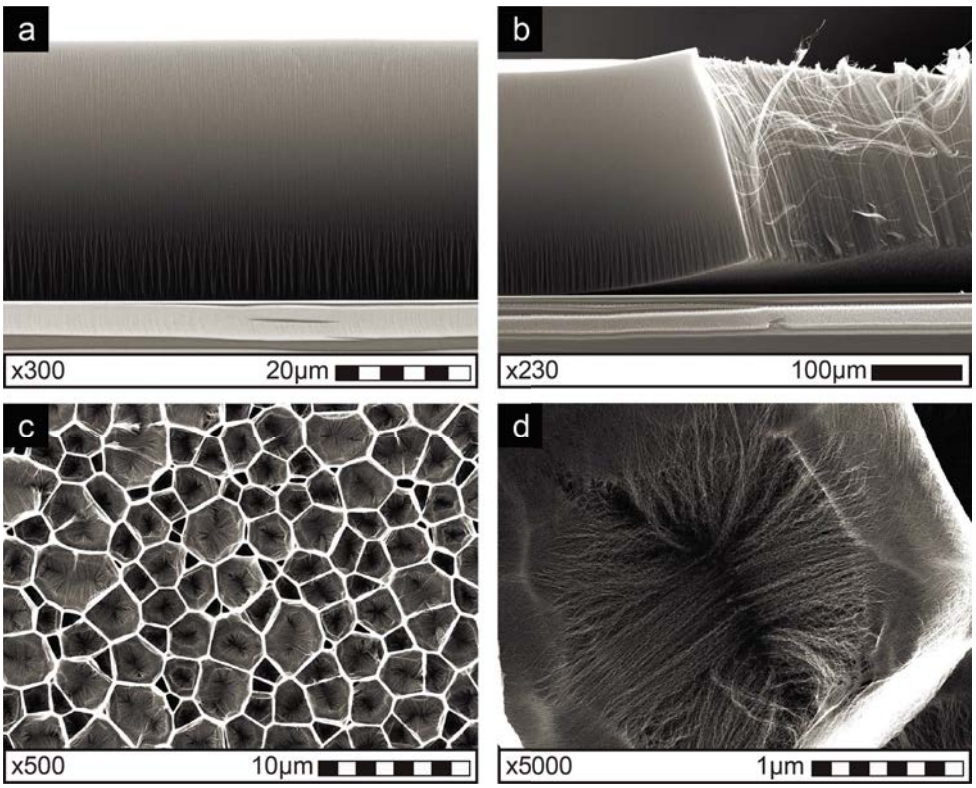

Figure 1.21: Vertical aligned CNTs obtained by WACVD on Si substrate. (a,b) lateral view of CNTs on silicon wafer. (c,d) Top view of CNTs forest patterned by water spray

to 9.2 nm (6-9 walls) with increase in Fe thickness from 0.2 to 5.0 nm (K. Liu, Yinghui Sun, et al. 2008). The presence of a buffer layer of Al_2O_3 or SiO_2 in between the substrate and catalyst layer was essential for the synthesis of CNT arrays, no formation of CNT array being observed on a flexible stainless steel foil either with or without a thin film of iron (Lepró et al. 2010a).

Following the process reported by (Shahzad Hussain, Amade, and Bertran 2014), vertically aligned CNTs on silicon wafers can be obtained in our research group. The water assisted chemical vapor deposition (WACVD) process was used for this purpose. **Figures 1.21a-b** shows the uniformity of the structures obtained. The nanotube forests shown in that figure were obtained using an Al_2O_3 diffusion barrier. A thin layer of Fe 2 nm thick was deposited by sputtering and then annealing in hydrogen atmosphere.

Figures 1.21c-d shows the result of exposing the forests of CNTs to a water spray. It is a simple method of making a pattern, however, there is an agglomeration of CNTs, which gives rise to the patterns that are observed. These phenomena can be explained as the self-assembly of carbon nanotubes as a result of the capillary action of water. Probably, the evaporation of liquids from the interstices of the ordered nanotubes forest produces remarkable cellular structures. Similar structures were formed with a variety of liquids including acetone, toluene, dimethylformamide, tetrahydrofuran, and methanol. The cellular structures were stable once formed despite the significant deformation of the constituent elastic nanotubes; the patterns were not affected by annealing the sample in vacuum at 800 °C (Chakrapani et al. 2004; Correa-Duarte et al. 2004; H. Liu et al. 2004). This process to make patterns is really easy and economical. However, control of the

patterns is poor. On the other hand, with the use of techniques, such as lithography, well-defined patterns can be obtained.

In summary, the selection of the growth process of the CNTs depends on the final use that these materials will have. For some applications it is necessary to have defect-free SWCNTs (e.g. electronic devices), in other cases it is more appropriate to have long MWCNTs (e.g. fibers), and in other applications short nanotubes (e.g. conductive inks) are required. Obviously, the potential applications of these nanostructures are linked to their properties.

1.3.7 Properties of CNTs

Individual carbon nanotubes are a type of quantum wires. They are long but extremely narrow conductors with diameters in the range of several atomic distances, and additionally are hollow. The electron wavevectors are quantized along the circumferences of the nanotubes and the charge carriers are free to travel only along the axial directions. Similarly, to other quantum wires, the CNTs may show ballistic electron transport i.e. without scattering, which has been confirmed experimentally. According to theoretical calculations, electrons in CNTs should travel over micrometer range distances without experiencing scattering at room temperature. The maximum mean free path measured experimentally at room temperature amounted to $1\,\mu m$. For comparison, electrons in copper at room temperature have mean free paths of only $40\,nm$. The resistivity in the individual SWNT, at room temperature, can be as low as $1 \times 10^{-6}\,\Omega \cdot \mathrm{cm}^{-1}$, which exceeds conventional conductive metals. The lowest resistivity reported for MWNT amounted to $5 \times 10^{-6}\,\Omega \cdot \mathrm{cm}^{-1}$ which was lower than SWNT probably due to the fact that MWNTs have higher diameters than typical SWNTs.

The density of carbon nanotubes amounts to about $1.3\,\mathrm{g} \cdot \mathrm{cm}^{-3}$ for SWNT and $2.1\,\mathrm{g} \cdot \mathrm{cm}^{-3}$ for MWNT, whereas for Cu and Al about $8.96\,\mathrm{g} \cdot \mathrm{cm}^{-3}$ and $2.7\,\mathrm{g} \cdot \mathrm{cm}^{-3}$ respectively. If the length of CNT is larger than the ballistic regime then diffusive transport will be observed. Ballistic transport may also be suppressed owing to increased temperature or high electric fields. Nonetheless, the maximum current density measured experimentally in individual SWNT at room temperature amounted to $10^9 - 10^{10}\,\mathrm{A} \cdot \mathrm{cm}^{-2}$, which is higher than even the critical current density of superconductors.

Regarding the factors which may impede the electrical performance of CNTs, it was found that electron transport in CNTs may be changed by disorders such as structural defects formed during synthesis processes or physical distortions, for example, evoked by strong mechanical forces. However, it was found that semiconducting nanotubes are the most sensitive to disorder. For armchair nanotubes, only defects with a potential shorter than the distance between carbon atoms, such as vacancy, considerably decrease the conductance at the Fermi level. The weak vulnerability to electron scattering in armchair nanotubes is related to their high symmetry and a decrease of the defect potential averaged over the circumference of the nanotube.

In addition, the CNTs, are characterized by excellent mechanical performance. The experimentally measured values of tensile moduli amounted to approximately $0.3 - 0.95\,\mathrm{TPa}$, tensile strengths approximately $10 - 100\,\mathrm{GPa}$ and tensile strains approximately $6 - 12\,\%$. The values of modulus and strength under uniform compression, measured by embedding the nanotubes in polymer or epoxy matrix, were even higher. Due to low density, nanotubes have very high specific mechanical properties (strength or stiffness divided by density), far exceeding steel or other high-performance materials.

Moreover, the thermal conductivity of CNTs in the axial direction exceeds the best-

known bulk heat conductors including diamond. Experimentally measured thermal conductivities of isolated SWNT and MWNT, in the axial direction, were 3500 and 3000 $W \cdot m^{-1} \cdot K^{-1}$ respectively. Such extremely high thermal conductivity contributes to the effective heat removal, which is also facilitated by the extremely high surface area of CNTs. All the above presented data show that carbon nanotubes are very interesting materials for electrical engineering applications as they have all the characteristics of a perfect electrical conductor, very high conductivity, current carrying capacity, strength, and thermal conductivity, all combined with very low weight (Lekawa-Raus et al. 2014).

1.3.8 Applications of Carbon Nanotubes

Some applications of carbon-based materials were described in the opening part of the chapter. In this section some of the applications in which aligned CNTs are used are listed. The aligned feature provides a new way to develop transistors, harvesting and energy storage devices, and super-strong composite materials. By considering the ways to align CNTs, the horizontal array and vertical forest have also great differences in their applications.

Electronic Transistors

Thanks to its high carrier mobility and current-carrying capacity, its use in electronic devices is increasing. The superior electrostatics were experimentally verified via the fabrication of $sub - 10\,nm$ gate length transistors that show superior transport properties to that of silicon devices, while operating at substantially lower voltages (Franklin et al. 2012). In terms of manipulation and integration of nanotubes for device applications, aligned nanotube arrays possess an apparent advantage. (S. J. Kang et al. 2007) reported the use of dense, perfectly aligned arrays of long, perfectly linear SWNTs as an effective thin-film semiconductor suitable for integration into transistors with a top gate. The large number of SWNTs enables excellent device-level performance characteristics and good device to-device uniformity, even with SWCNTs that are electronically heterogeneous. Though these SWCNT electron devices still leave much to be desired, complex SWCNT field-effect transistor (FET)-based digital systems can now be realized. For example, a general-purpose fully programmable processor has been experimentally demonstrated (Shulaker et al. 2013). It consists of 178 nanotube FETs, each comprising 10-200 SWCNTs (depending on the FET sizes), and is created using the highly scalable fabrication techniques and design flows. This SWCNT computer can be used to execute any arbitrary program and it was a significant development for the advancement of CNT circuits.

Scientists at the IBM research center, being a longtime leader of carbon nanoelectronics, have clearly claimed that the desired SWNT arrays should have a density of 125 nanotubes/mm and metallic impurity of less than 0.0001% (Franklin 2013). Without doubt, this ultimate target for SWCNT sample preparation presents tremendous challenges, and the essential prerequisite is how to realize the orientation-controlled synthesis of SWNTs.

Thin-Film Devices

Besides the horizontal CNT arrays that can be grown directly on substrates, 50 nm-thick CNT sheets can be drawn out from spinnable forest and then laid on various substrates, rigid or flexible, opaque or transparent, and flat or rough. The drawn-out CNT sheet

is also electronically conductive because CNT entanglement still exists. Therefore, the forest-based CNT sheets can serve as transparent electrodes to replace the resource limited and brittle indium tin oxide (ITO) electrodes for high-performance optoelectronic devices (K. Jiang et al. 2011). They can also act as conducting scaffolds with large surface area for semiconductors to prepare functional devices. (Di, Yong, X. Zheng, et al. 2013) report a way to use forest based CNT sheets to develop solar cells. CNT sheet was directly laid on silicon wafer with the interfacial contact strengthened with ethanol treatment. The aligned CNTs formed a high CNT-Si junction density and provided efficient charge-transport paths. As a result, the power conversion efficiency reached 10.5%, even higher than that of solar cells fabricated using pristine and random CNT networks. Besides the photovoltaic property, these aligned CNTs were also applied in photoelectrochemical cells (Di, Yong, Yao, et al. 2013). The ability to conduct electric current opened a way to design a smart window with switchable transparency (Meng et al. 2011). When the aligned CNTs were fabricated inside a polyurethane (PU) film, the electroheating effect caused a rapid crystal melting of the soft segments in the PU. As a result, the film can be switched from opaque to transparent in just several seconds, and also can reverse to opaque after tuning off the voltage.

High-Strength Composite Materials

The development of the spinnable CNT forest opened a new way to design high-strength nanocomposites, because the super alignment provides a way to fully utilize the extraordinary mechanical property of CNT. The CNT sheets can be first assembled into a preform and then infiltrated with epoxy resin (Q. F. Cheng et al. 2010). The CNTs with a loading up to 16.5 wt% were homogeneously dispersed and highly aligned in the matrix. Because of the reinforcement, the Young's modulus and tensile strength of the composites reached 20.4 and 231.5 MPa, respectively. Although it was already 160% stronger than the pure epoxy, the low CNT content still hindered the future mechanical strengthening. To overcome this problem, the aligned CNT sheets were layer-by-layer stacked with the aid of solution spraying (W. Liu et al. 2011). The as-drawn CNT sheets were continuously wound onto a rotating mandrel under the spray of a polymer solution. Various polymers can be used to act as interfacial strengthening agents, such as polyvinyl alcohol (PVA), nylon, epoxy, and polyimide. By tuning the polymer content in the range of $0 - 40$ wt%, aligned CNT/polymer composites with different tensile properties were obtained. For example, the CNT/PVA composite film exhibited a strength of 1.8 GPa at a CNT content of 65 wt%. Furthermore, because of the alignment, the composite film had also a high modulus (40-96 GPa) and toughness ($38 - 100$ J/g), and was electrically conductive (conductivity of 780 S/cm). By using a high-performance polyimide, bismaleimides, the composite film can be even as strong as 3.8 GPa with a modulus of 293 GPa (Liwen Zhang et al. 2015), showing the superb advantages of the aligned CNTs.

The layer-by-layer stacking allowed a more uniform penetration of polymer molecules compared to the prepreg method and thus could improve the interfacial properties under the lowest polymer loadings. Furthermore, this approach can produce composite structures in one step, can be controlled by the rotating motion, and thus is easy to be scaled up for industrial production. By further reducing the tube diameter and number of walls, the self-packing between CNTs allows a fabrication of strong CNT films without introducing polymer matrix. For example, when $2 - 3-$walled, $4 - 6$ nm-diameter CNTs were drawn out from their spinnable forests, they can be densely packed just with the aid of ethanol wetting (Di, Hu, et al. 2012). The CNT films had a smooth and shining surface,

were flexible, and exhibited tensile strengths of $1.1 - 1.9\,\text{GPa}$ and Young's modulus of $40 - 90\,\text{GPa}$. By further introducing a stretching treatment in a liquid environment on the dry-stacked CNT films (Y. Wang et al. 2015) or by microcombing (Liwen Zhang et al. 2015). These two methods improved both the tensile strength up to $\sim 3.2\,\text{GPa}$ and the modulus up to $124 - 172\,\text{GPa}$, respectively.

Supercapacitors (SCs)

Over the past few years, research focused on energy storage devices has increased considerably. As mentioned in the introductory part, this is mainly due to the search for environmentally friendly and high-performance renewable energy storage devices. Electrochemical energy is an unavoidable part of the clean energy portfolio. Batteries, supercapacitors (SCs) and fuel cells are unconventional energy devices working on the principle of electrochemical energy conversion. SCs have gained much attention on account of high specific capacitance (C_s), long life cycle, high power density (P_d), being almost maintenance free, experiencing no memory effect, safe and function as a bridge for power-energy difference that exists between capacitor (high P_d) and fuel cells/batteries (large energy storage) (Kandalkar et al. 2010). These present a viable solution for providing energy in rural areas, where no public grids are available or where a heavy cost of wiring and providing electricity is involved. SCs can also be utilized as power supplies for portable devices like mobile phones, notebook computers, digital cameras etc. -being small, light- weight and flexible. In electric and hybrid vehicles, SCs may be used to offer high P_d required for short-term acceleration along with recuperation of energy during braking, hence saving energy and shielding the batteries from the high frequency rapid charging-discharging process (dynamic operation). The P_d and energy density (E_d) are represented by Ragone plot **Figure 1.22**. This plot explains that the fuel cells are high-energy systems; whereas SCs are high-power systems. Batteries have intermediary power and energy capabilities.

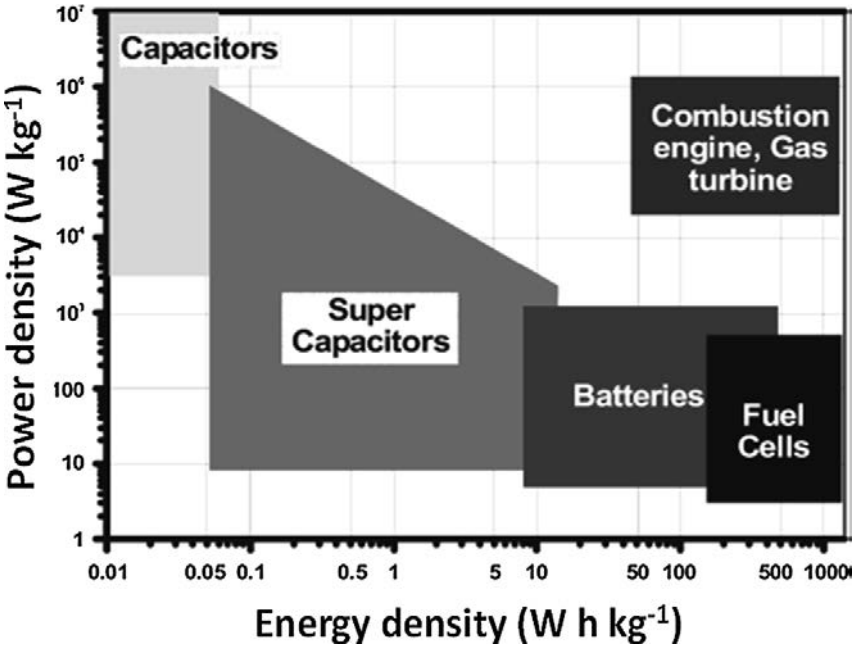

Figure 1.22: Ragone plot of different electrochemical energy conversion systems, combustion engine, turbines and traditional capacitors

There exists some overlap in Ed and Pd of fuel cells and SCs with batteries. Also, it is apparent from the figure that any single electrochemical device cannot compete with an internal combustion engine. So, E_d and P_d of electrochemical devices have to be increased to compete with the combustion engine (Winter and Brodd 2004).

Supercapacitors are called with several names such as *electrochemical capacitors*, *ultra capacitors* and *electrochemical double-layer capacitors*. The first electrolytic capacitor came in the 1920s. In 1957, the first super- capacitor (electric double layer capacitors-EDLCs) was patented by General Electric using activated charcoal as the plates. In EDLCs, charge storage takes place electrostatically (non-Faradaic) i.e. no shifting of charge takes place between electrode and electrolyte (which makes them highly reversible along with high cycling stability). Carbon nanomaterials, like carbon aerogels, activated carbons (ACs), carbon nanotubes (CNTs), graphene, carbide derived carbon (CDC) etc. are unique structures for EDLCs with the huge specific surface area (SSA), great mechanical and chemical stability and good electrical conductivity. To increase the C_s of SCs, new electrochemically active materials had been investigated for pseudocapacitors (Faradaic charge transfer). During 1975–1980, B. E. Conway explored RuO_2 pseudocapacitors extensively. These capacitors store charge through electrosorption, oxidation-reduction reactions and intercalation mechanism (Conway 1991).

These faradaic processes would let pseudocapacitors attain higher C_s and E_d compared to EDLCs. Pseudocapacitance is linked to the electron charge-transfer among electrolyte and electrode impending from de-solvated and adsorbed ion. The adsorbed ions do not react with the atoms of the material, but only the transfer of charge occurs. The capacity of electrodes to achieve pseudocapacitance effect depends on the chemical affinity of materials to the ions adsorbed on the surface of the electrode along with the structure and the dimension of the electrode pores. The charge storage increases linearly with the applied voltage. Materials that exhibit redox behaviour and used in pseudocapacitors are transition-metal oxides (TMOs), such as IrO_2, RuO_2, Fe_3O_4, IrO_2, MnO_2, V_2O_5, NiO, Co_3O_4, etc. transition metal sulphides and conducting polymers CPs), such as polyaniline (PANI), polythiophene, polypyrrole (PPy), polyvinyl alcohol (PVA), poly (3,4-ethylene dioxythiophene) (PEDOT), poly- acetylene, poly (4-styrene sulfonate) (PSS), polyphenylene-vinylene (PPV), etc. (Borenstein et al. 2017).

Li-ion capacitors (hybrid capacitors) were explored by FDK in 2007. In such capacitors, a carbon electrode was combined with a Li-ion electrode which increased the capacitance, lowered the anode potential with enhanced cell voltage and hence increased the E_d. In such systems, the faradaic electrode, with high C_s, provides higher E_d and the non-faradaic electrode provides higher P_d. Hence, research has been focused on hybrid capacitors such as composites (coupling of carbon materials with either CPs or TMOs) and battery type (coupling a supercapacitor (SC) electrode with a battery electrode), etc. (Zhi et al. 2013).

As already mentioned, one of the carbon-based materials widely used in the manufacture of SCs is CNTs. CNTs can be of great interest to design composite electrodes for supercapacitors, since they have a unique internal structure, excellent physical and chemical stability, low gravimetric density and excellent electronic conductivity (X. Sun et al. 2013) . However, their gravimetric and volumetric capacitances are quite low compared to other materials, like metallic oxides. For that reason, these carbon nanostructures are used to support materials that have high capacitance. The performances that can be reached between the CNTs and the metallic oxides, are really amazing.

There were also recent attempts to combine two different nanocarbons: composite materials comprising CNTs with graphene were tested for SC applications. Their synthesis

however was rather complicated: CNTs were attached to the edges and surface of graphene sheets, thereby acting as spacers to increase the electrolyte solution-accessible surface area and to provide 3D electrical conduction pathways (Jung et al. 2013).

1.3.9 Toxicity of CNTs

As commented above, carbon-nanotubes have found profound applications in a wide range of diverse domains as single or multiwalled carbon nanotubes. Past studies have reported that the cytotoxic effects of carbon-based materials have a direct correlation to their size (Herzog et al. 2007). Multiwalled carbon nanotubes were shown to induce carcinogenicity after entering the peritoneal cavity as observed in animals under experimental trials. Besides that, single walled carbon nanotubes, which are accumulated in the liver for prolonged durations, have significantly impacted numerous parameters, including chemicals: glutathione, enzymes: aspartate transaminases, malondialdehyde, lactate dehydrogenase, and organ indices (S. T. Yang et al. 2008). Higher concentrations of single-walled carbon nanotubes have been indicated to generate reactive oxidative stress, lipid peroxidation, and may alter mitochondrial functions after in vitro incubation with bronchial epithelial cells (De Jong and Borm 2008). Both single- and multiwall carbon nanotubes have been reported to promote platelet aggregation, chronic lung inflammation, interstitial fibrosis, and lung granulomas. Inhalable carbon nanotubes are indicated to cause severe lung inflammation, which can lead to malignancy as a consequence of extended exposure (Eun and Myung 2007; Firme and Bandaru 2010). As compared to ultrafine carbon black, carbon-based nanotubes were found to be more toxic as many workers were diagnosed with lung lesions after being exposed to single-walled carbon nanotubes beyond the safe exposure limit (Chalupa et al. 2004).

Although small quantities of these materials are produced in research laboratories, the risks involved in handling these types of nanostructured materials must always be taken into account. Risks that also exist when handling other substances such as chemical reagents.

Chapter 2

Experimental Description

The cleaning surfaces, the thin layer deposition processes and the growth and functionalization of the nanotubes (CNTs) were carried out in two reactors. These reactors essentially employ two types of technology: vacuum technology and plasma technology. They are not the only ones, but they did play an important role during the experimental stage. The concepts related to these technologies, their advantages and disadvantages in comparison with other processes of experimental and industrial use, are briefly presented below. In addition, the configuration of our reactors is presented. Through several years of research, they have improved and allow us to continually carry out new research work.

2.1 Vacuum

The standard definition of vacuum is "the state of a gas at which its pressure in a vessel and therefore its particle density is lower than that of the ambient surrounding atmosphere or in which the pressure of the gas is lower than 300mbar, i.e. lower than the pressure of the atmosphere on the Earth's surface" (Pfeiffer 2019a). In ancient civilizations, the concept of "emptiness" had already been raised. However, it was not until the middle of the seventeenth century that the first studies of vacuum and its properties were considered. The first to theorize about the properties of the vacuum was the scientist and jurist Otto von Guericke, who established the basis for the development of modern technology that is now used every day in many industries (Vacuum Daily.net 2011).

Today, the vacuum levels that can be reached have allowed the development of a wide variety of techniques for processing and obtaining new materials. The same technology is used for packing as well as for simulating space conditions. It all depends on the level of vacuum to be reached. In general, higher vacuum means that the pumps required to obtain it are more complex, and therefore more expensive. Different types of vacuum pumps are used on Earth to generate a vacuum. An overview of the working ranges of the most important types of vacuum pumps and vacuum instruments is given in **Figure 2.1**. In our case, in order to assure the quality of the samples, before performing any process, the vacuum must be around 10^{-6}mbar (high vacuum). This ensures that a great amount of the potential contaminants present in the atmosphere (oxygen, water vapor) can be removed from the reactor chamber. Thus, under the protective environment of vacuum, reactive materials can be stored and their special properties utilized. The relative absence of molecules in a vacuum allows particles present in vacuum (atoms, molecules, ions, electrons and radicals) to travel long distances without colliding. This is of particular interest when it comes to charged particles such as electrons, ions and protons whose

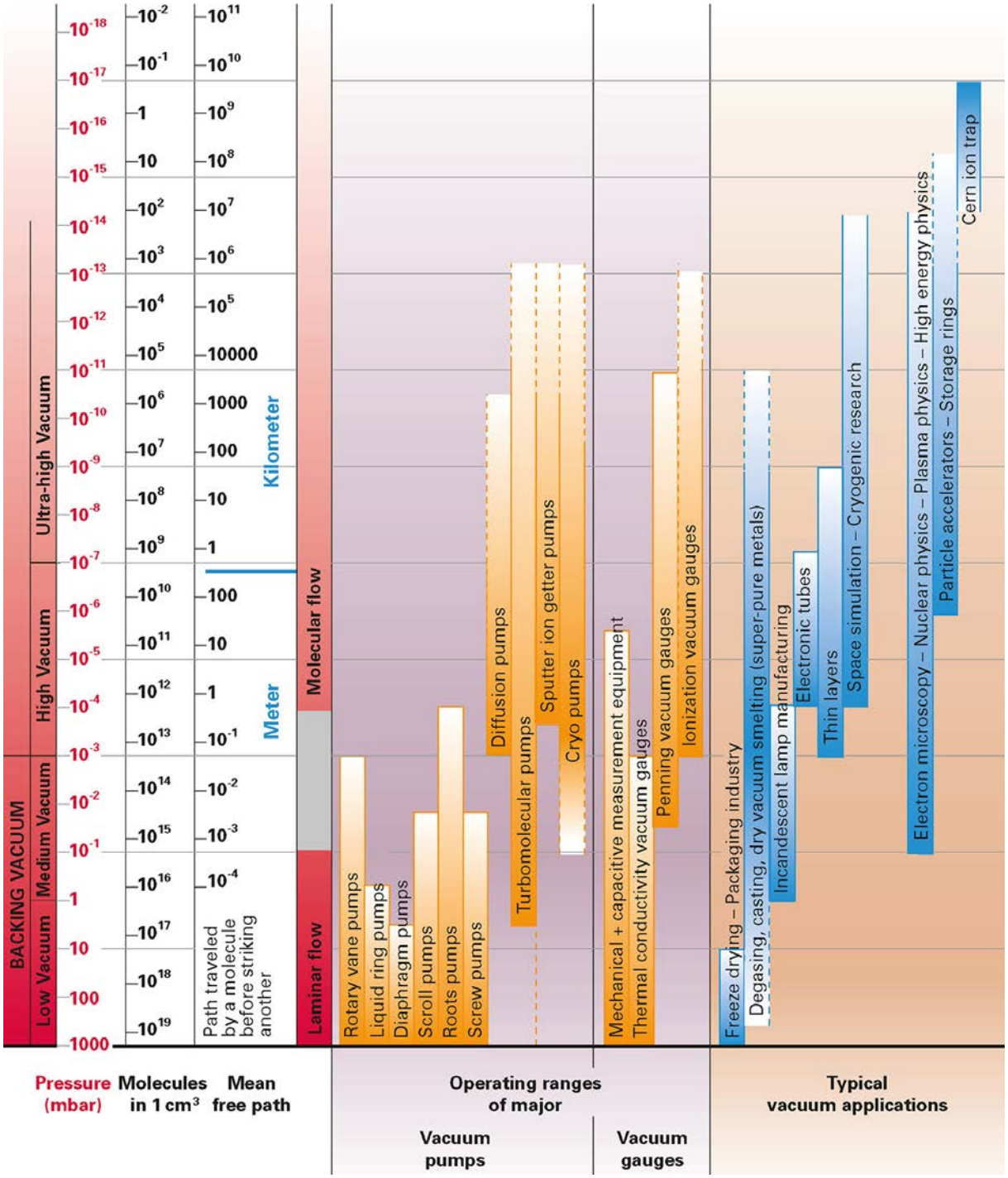

Figure 2.1: Overview of vacuum, adapted from (Pfeiffer 2019a)

precise path in the absence of collisions can be controlled by electric and/or magnetic fields (Weston 1985).

Theoretical support behind this technology allows us to understand the behavior of fluids at low pressures. Let us remember that laminar flow theory is not useful in vacuum, since at low pressures molecular flow dominates. Physical processes such as heat transfer, sound and even the movement of the gas itself, which take place through interaction between the particles of the gas under atmospheric conditions, change dramatically when the density of the gas is reduced, to the point where the interaction of gas molecules

is not anymore the predominant transport mechanism (Weston 1985). In addition, it is important to keep in mind the concept of pressure and the pressure units frequently used in vacuum technology. Pressure is defined as the force applied over the unit area. In the international system, it has as unit the newton per m^2 (N/m^2), or also known as *Pascal* (Pa) (Kovalevsky and Quinn 2004). Outside the international system, there are also other pressure units, such as the bar ($1\,bar = 10^5 Pa$), the *atmosphere* ($1atm = 1.01 \times 10^5\,Pa$), and the Torr ($1\,Torr = 1.33 \times 10^5\,Pa$).

2.1.1 Important parameters of vacuum

The relationship between the pressure (P) absolute temperature (T), of the molecules of a gas contained in a chamber of volume (V), is given by the equation of state of the gases:

$$P \cdot V = n \cdot k \cdot T \tag{2.1}$$

Where n represents the number of molecules per unit volume and k the Boltzman constant. The above equation can also be written as a function of the number of moles of the gas (N) and the universal constant of ideal gases (R).

$$P \cdot V = N \cdot R \cdot T \tag{2.2}$$

According to this last equation, the concentration of gas molecules in a confined space is $2.69 \times 10^{25}/m^3$ under standard conditions of pressure and temperature ($10^5\,Pa$ and $298.15\,K$). The atoms or molecules of the gas move at very high speeds ($\sim 500 - 1000\,m/s$) and constantly collide each other and on the walls of the container, in a process of exchange of kinetic energy. Depending on the gas pressure, different vacuum ranges from atmospheric pressure to an extremely low level are distinguished. As the pressure decreases, so does the concentration of molecules per unit volume.

An important parameter of the kinetic theory of gases is the mean free path (λ). It is defined as the average distance travelled between two consecutive collisions of a molecule with other molecules in the medium. This parameter is inversely related with the container pressure, according to the following expression:

$$\lambda = \frac{kT}{\sqrt{2}P\pi\sigma^2} \tag{2.3}$$

when we consider that T equals the ambient temperature, we have:

$$\lambda(\text{mm}) \approx \frac{6.6}{P(\text{Pa})} \tag{2.4}$$

In studies related to vacuum, it is important to know the number of molecules (Ni), which per unit of time (t), affect the surface unit of an enclosure at a given system pressure. Calculations based on gas kinetic theory lead to the following expression (Albella 2018):

$$\frac{dNi}{dt} = \frac{P}{(2\pi mkT)} = \frac{P \cdot 2.63 \cdot 10^{22}}{(M \cdot T)^{\frac{1}{2}}} \frac{\text{molec}}{\text{cm}^2 \cdot \text{s}} \tag{2.5}$$

where M is the molecular weight in grams. It is necessary to note that not all molecules that hit the walls of the chamber are adsorbed. Assuming that all incident molecules will be fixed to the surface, the above expression allows the time required to form a monolayer of adsorbed gas on a surface inside a vacuum chamber to be estimated by a simple calculation. Thus, in the case of atoms or molecules of a gas, with a diameter of 4.5 Å,

Vacuum level	Pressure (mbar)	n (molecules/cm^3)	λ (cm)	Time of monolayer formation (s)
Low	$1x10^{3}$	$2.46x10^{19}$	$6.6x10^{-6}$	$2.9x10^{-9}$
Medium	$1x10^{0}$	$2.46x10^{16}$	$6.6x10^{-3}$	$2.9x10^{-6}$
High	$1x10^{-3}$	$2.46x10^{13}$	$6.6x10^{0}$	$2.9x10^{-3}$
Ultra high	$1x10^{-7}$	$2.46x10^{9}$	$6.6x10^{4}$	$2.9x10^{1}$
	$1x10^{-12}$	$2.46x10^{4}$	$6.6x10^{9}$	$2.9x10^{6}$

Table 2.1: Vacuum levels and some important vacuum parameters (Albella 2018)

enclosed at a pressure of 10^{-6} mbar, the time to form a monolayer is ~ 1 s, as indicated in **Table2.1**. This fact emphasizes the importance to maintain a low residual pressure in a vacuum system in order to maintain good cleaning conditions in the chamber walls and to avoid contamination of the adsorbed layers on its surface. **Table2.1** also includes the parameter values of the behaviour of gases at different pressures, calculated according to the above equations in the different vacuum ranges. Note that the mean free path of the gases, in the region of 10^{-5} mbar, commonly used in the thermal evaporation process is in the range of the typical dimensions of a vacuum chamber ($\sim 60 - 70$ cm) which implies that the evaporated molecules follow rectilinear trajectories from the source of evaporation to the substrate (Albella 2018).

It is also important to mention that molecules that are adsorbed on the reactor walls (when exposed to the atmosphere) must be removed. The process by which molecules are desorbed is known as degassing. It is of great importance to determine the quality of the materials obtained or deposited. There are some strategies to achieve an effective degassing of the vacuum chamber. The most commonly used is heating the reactor walls.

Types of flow

The ratio of the mean free path, λ, to the flow channel diameter, d, can be used to describe types of flow. This ratio is referred to as the Knudsen number (Kn):

$$Kn = \frac{\lambda}{d} \tag{2.6}$$

The value of the Knudsen number characterizes the type of gas flow and assigns it to a particular pressure range. **Figure 2.2** shows the profiles of the various types of flow regimes.

In the continuous flow regime (laminar), the current lines remain parallel and the gas circulates in the form of layers that slide on top of each other, slowing down the speed of the molecules from the center to the wall, where it becomes zero as a result of friction with the walls. The laminar flow and the turbulent flow (which is not illustrated in **Figure 2.2** are grouped in the viscous regime, in which the collision frequency of some molecules with others is much higher than that of the collisions with the pipe walls, with a Knudsen number value lower than the 0.01. When the Knudsen number is greater than 0.5 (very fine pipe and/or very low pressure), the gas flows are in molecular regime, in which the mean free path of the molecules is so high that the collision of the molecules with the pipe walls prevails. In this case, the movement of each particle is completely independent of the others. The molecular regime is the most common in high vacuum systems. Note that the transition range between viscous regime and molecular regime is $0.01 < Kn < 0.5$,

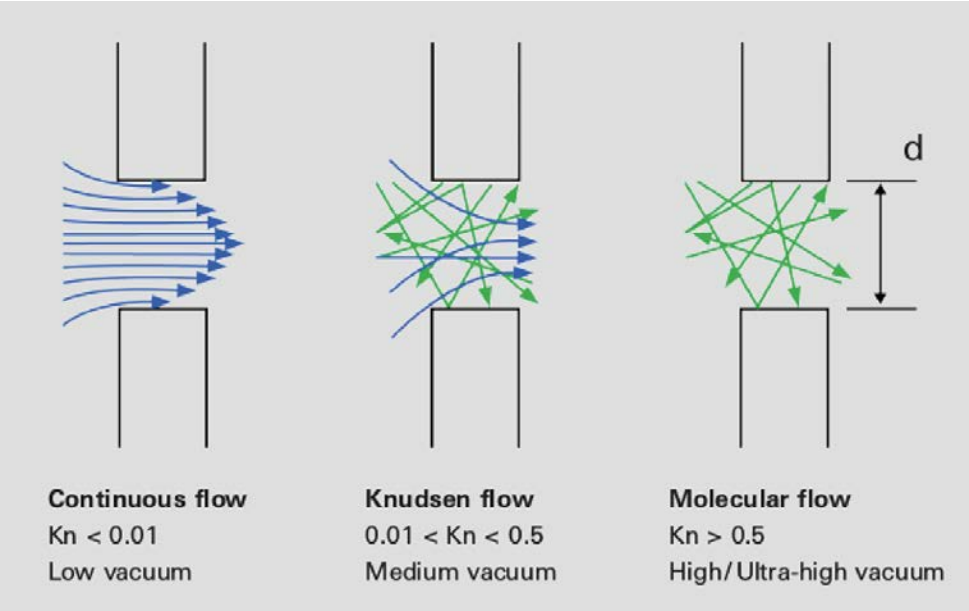

Figure 2.2: Profiles of the various types of flow regimes (Pfeiffer 2019b)

also known as Knudsen flow. Since many process pressures are in the medium vacuum range, this type of flow occurs with corresponding frequency (Pfeiffer 2019b).

Conductance

When a gas flows through a pipe, it is important to know the rate or flow of gas transferred in the unit of time from one region of the system to another (by pressure difference). The mass flow of gas (Q) (also named "troughout"), represents the number of molecules crossing a normal plane to the direction of flow in the unit of time at pressure (P). It can be expressed as follows:

$$Q = P \cdot (dV/dt) = P \cdot S \tag{2.7}$$

where $S = dV/dt$ represents the volumetric flow rate, that is, the volume of gas flowing per unit of time, measured at the temperature T and pressure P of the gas. According to the above expression, mass flow is expressed in units of mbar $\cdot$ l/s or, more frequently, in cm^3/s at standard pressure and temperature conditions (sccm).

It should also be noted that Q depends on the temperature of the system. Thus, through the equation of state of perfect gases ($PV = NkT$) is obtained:

$$Q = kT \cdot (dN/dt) \tag{2.8}$$

This expression indicates that Q is proportional to the number of molecules per unit time (dN/dt) that pass through the plane in which the pressure is measured.

According to these magnitudes, the conductance (C), of an orifice or pipe for the transport of gases is defined by the relation:

$$C = Q/(P_2 - P_1) \tag{2.9}$$

which represents the resistance that the pipe or orifice opposes to the gas circulation. In the above equation, Q is the mass flow of the gas molecules circulating through the pipe

and P_2 and P_1 are the inlet and outlet pressures of the pipe, respectively. The measure of C is expressed in m^3/s.

When two or more pipes or holes, with conductance Ci (with $i = 1, 2, ...n$) are connected in parallel or in series the final conductance is given respectively by:

$$C = C_1 + C_2 + \ldots + C_n \tag{2.10}$$

$$1/C = (1/C_1) + (1/C_2) + \ldots + (1/C_n) \tag{2.11}$$

The determination of the conductance of a pipe is very important in vacuum systems, because it allows to obtain, for example, the real evacuation rate of a vacuum pump induced by the coupling pipes of the pump(s) to the system. This fact is essential when dimensioning the equipment and accessories used in the processes. In this regard, it is important to mention that conductance depends on a number of factors, including: the geometry of the pipe/chamber (including geometrical dimensions), the circulation regime, the nature of the gas and its temperature. In turbulent conditions, it also depends on the internal pressure of the pipe/chamber. On the other hand, when the transport of the gas takes place in molecular regime, the conductance does not depend on the pressure, since the dominant factor in this case is the mean free path (Albella 2018; VacAero 2015).

There are several parameters that should be taken into account when working with vacuum systems. Some of them, mentioned above, are the mean free path, the conductance and the gas flow regime (type of flow). For this reason, it is essential to understand the theory behind this technology. In this way, the results that can be obtained when processing materials in vacuum will be outstanding. It has been mentioned that this technology is present in innumerable applications. More than 70 general industrial applications use vacuum processing, with new ones emerging on a regular basis. These, in turn, can be broken down into hundreds of specific applications, which can have very different requirements. Specifically, electronics, flat-panel displays, solar manufacturing, and scientific instrumentation are likely to drive developments in vacuum technology in the coming years (Stephen and Nigel 2014).

When processing materials (for example in thin films deposition), there are great advantages when working in vacuum. Perhaps the main advantage of using vacuum is that high purity films can typically be deposited from a high purity target. Another point in favor of this technology is the reduction of pollutants. Compared to conventional processes (e.g. electroplating), vacuum processes are more efficient in the use of raw materials. However, despite the great advantages of this technology, there are also certain disadvantages. One of the main drawbacks is the complexity of the equipment and its scalability. This, of course, influences the cost of the equipment and accessories.

2.1.2 Safety aspects of vacuum technology

It is important to take into account the potential risks involved in the use of this technology, so it is recommended to follow some safety recommendations (Mattox 2009).

- Hazardous gases can accumulate in pump oils and cryosorption pumps. This can lead to problems during maintenance and disposal.

- Pumping pure oxygen using hydrocarbon pump oils in mechanical pumps can lead to an explosion (Diesel effect).

- Floating surfaces in contact with a plasma can attain a high electrical potential if the plasma is in contact with a high potential at some other point in the system. Surfaces that can be touched by personnel should be grounded

- Quartz vacuum windows allow UV radiation, which that may cause eye damage, to be transmitted from a plasma.

2.2 Plasma

Plasma is an ionized gas, a distinct fourth state of matter. "Ionized" means that at least one electron is not attached to an atom or molecule, converting atoms or molecules into positively charged ions. As the temperature increases, the molecules become more energetic and transform the matter following the sequence: solid, liquid, gaseous and finally plasma, which justifies the title "fourth state of matter" (Shahzad Hussain 2014).

2.2.1 Fundamental concepts

Plasmas used in materials technology have many properties in common with the gaseous state. In fact, it is a set of particles formed by neutral atoms or molecules, ions, electrons and chemical radicals, confined in a reactor, where Coulomb forces long range give rise to effects of collective interaction. In a general sense it can be said that plasma occurs in any state of matter containing sufficient free charged particles, so that its collective behavior is dominated by electromagnetic forces. Thus, the plasma state includes, within the solid state, for example, metals and semiconductors in which the positive ions occupy fixed positions. However, the phenomena of load redistribution and shielding of interior regions in metals occur at extremely fast times (in the order of 10^{-19} s) due to the high density of free charges (Albella 2018).

Stochastic processes taking place in a plasma require a statistical description. The species present in a plasma have a wide range of velocities and collide with each other. Its most probable distribution is determined by the Maxwell-Boltzmann function. Usually, three parameters are required to define the state of the gases: pressure, density (concentration of particles per unit volume) and temperature. However, it is also necessary to know other parameters. In the case of a plasma composed of electrons, neutrons and different types of ions, it is necessary to give the density of each species. For the described case, a temperature (T_s), is assigned to each particle group, which is directly proportional to the mean kinetic energy (E_m), of the particles:

$$k_B T_s = \frac{2E_m}{3} \tag{2.12}$$

where k_B corresponds to the Boltzmann constant.

Something similar happens for the electrons of a plasma, characterized by their density and temperature. The electron temperature (T_e), can vary over a wide range of values. Most plasmas of practical significance, have electron temperatures of $1 - 20\,\text{eV}$, with electron densities in the range $10^{12} - 10^{24}\text{m}^{-3}$. Note that high temperatures are conventionally expressed in electron volts; 1 eV approximately equals $11,600\,\text{K}$. For any gas, the temperature in the plasma is determined by the average energies of the plasma particles (neutral and charged) and their corresponding degrees of freedom (translational, rotational, vibrational and those related to electronic excitation). Thus, plasmas, as multicomponent systems, are capable of displaying multiple temperatures. In common

electric discharges for plasma generation in the laboratory, the energy from the electric field is first accumulated by electrons between collisions and then transferred from the electrons to the heavy particles (Shahzad Hussain 2014).

2.2.2 Degree of ionization

In gases, the degree of ionization (α), refers to the proportion of neutral particles that are ionized into charged particles:

$$\alpha = \frac{n_e}{n_e + n_n} \tag{2.13}$$

where n_e is the electron density and n_n the neutral density (in particles per cubic meter). It is a dimensionless number, most of the time expressed as a percentage. Most laboratory plasmas are macroscopically neutral, the density of positive ions is neither equal to that of electrons, i.e. $n_i \approx n_e$.

In the thermodynamic equilibrium, there are two reactions: direct reaction leading to ionization and a back reaction leading to recombination. In the case considered, the direct reaction is the electron impact ionization and back reaction is the recombination involving three particles. In other words, the stochiometric equation will have the form:

$$\mathrm{a} + \mathrm{e} \leftrightarrow \mathrm{i} + 2\mathrm{e} \tag{2.14}$$

with the rate of ionization being $k_i \cdot n_n \cdot n_e$ and the rate of recombination being $k_r \cdot n_i \cdot n_e^2$ where k_i and k_r are the ionization and recombination coefficient, respectively. We shall define the ionization equilibrium as a state in which ionization and recombination rates are equal (Michael Keidar and Beilis 2013).

In a plasma, the electron-ion collision frequency (v_{ei}) is much greater than the electron neutral collision frequency (v_{en}) because the higher cross section of ions. The term fully ionized gas introduced by Lyman Spitzer does not mean the degree of ionization is unity, but only that the plasma is in a Coulomb-collision dominated regime, i.e. when $v_{ei} > v_{en}$ which can correspond to a degree of ionization as low as 0.01 %. A partially or weakly ionized gas means the plasma is not dominated by Coulomb collisions, i.e. when $v_{ei} < v_{en}$.

A particular case of fully ionizes gases are very hot thermonuclear plasmas, such as plasmas artificially produced in nuclear explosions or naturally formed in our sun and all stars in the universe. Stars contain largely hydrogen and helium gases that are fully ionized into electrons, protons (H^+) and helium ions (He^{++}). Equations to characterize such very hot, fully ionized thermonuclear plasmas in the presence of stellar magnetic fields can be approximated to ideal magnetohydrodynamics laws with high magnetic Reynolds number (Michael Keidar and Beilis 2013).

2.2.3 Quasi-neutrality and Debye length

The study of the plasma state is complex due to different causes:

- Although the movement of charged particles is governed by electromagnetic fields, these fields are affected by the presence and movement of the particles themselves.

- Atomic processes such as ionization, excitation, recombination and charge exchange come into play and compete with each other in a complicated way, depending on the densities and energies of the particles of each type.

- The movement of charged particles gives rise to a variety of transport phenomena related to short-range and long-range (coulombian) interactions between different particles.

- Long-range forces in turn give rise to different collective phenomena, such as electrostatic oscillations and instabilities.

Plasmas tend to be neutral (in macroscopic volume). That is, with equal concentration of free, positive and negative charges. If this equilibrium is disturbed (e.g. by separation of charges) it causes the instant manifestation of electrostatic forces that act to restore neutrality. Similarly, if an external electric field acts on the plasma, the free charges are adjusted to shield the external electric field. To consider a plasma as an ionized gas, it must have a sufficiently large number of charged particles, so that it can shield itself electrostatically within a distance less than any other length of physical interest. A shielding measure is the so-called Debye length.

In an ionized gas where particle collisions are important, plasma oscillations can develop only if the mean time between the collisions (τ_n), is longer than the oscillation period, that is, $\omega_p \tau_n > 1$. The frequency of oscillation of the plasma (ω_p), defines the time scale of the plasma, and depends on the electron density by equation:

$$\omega_p = \left(\frac{n_e e^2}{m_e \varepsilon_0} \right)^{1/2} \tag{2.15}$$

Where ε_0 is the vacuum permittivity, e is the electron charge and m_e is the electron mass.

Debye's length measures the distance needed for the plasma to shield itself from external perturbations. Its value is given by:

$$\lambda_D = \left(\frac{e_0 k_B T_e}{n_e e^2} \right)^{1/2} \tag{2.16}$$

Debye length corresponds to the distance at which a significant deviation from quasi neutrality occurs. This length defines the state of plasma, since it cannot exist in a spatial region that has dimensions smaller than Debye's length. According to the above expression, λ_D increases with the equivalent temperature of the electrons and decreases with increasing plasma density. Depending on these magnitudes, in typical laboratory plasmas, its value oscillates between 10^{-3} and 10^{-6} m, approximately (Albella 2018).

2.2.4 Influence of uniform magnetic fields on the movement of charged particles. Magnetic confinement of electrons

The ability of an ionized gas to maintain an electric current is accentuated in the presence of magnetic fields. According to the laws of electrostatics, a particle with charge q and mass m in the presence of an electric field of intensity E moves in the direction of the field in an accelerated movement associated with force: $F_E = q_E$. Under these conditions, the presence of a magnetic induction B perturbs the movement of the particle due to the so-called Lorentz force. In the case that the field is perpendicular to velocity v, this force is given by $F_B = q \cdot v \cdot B$, and forces the particle into a rotational motion around the magnetic field. The joint action of both fields gives rise to a complex movement, which depends on the speed and initial direction of the particle. In the most general case, in which the E and B fields are stationary with a constant value with time(**Figure 2.3**),

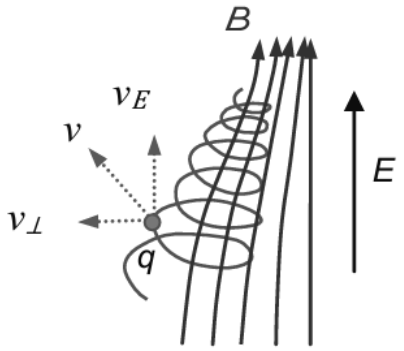

Figure 2.3: Cyclotronic movement of a charged particle, q, in presence of an electric field E, and a magnetic field, B, of variable intensity (Albella 2018)

the particle describes a trajectory described by a helical curve around the magnetic field, with a constant radius, whose value is given by the so-called Larmor radius, R_L given by:

$$R_L = \frac{mv_\perp}{qB} \tag{2.17}$$

where $v_\perp$ is the velocity perpendicular to the magnetic field. The corresponding angular frequency, ω_L, called cyclotronic frequency is given by:

$$R_L = \frac{v_\perp}{r_L} = \frac{qB}{m} \tag{2.18}$$

Magnetic confinement is very important in industrial applications. The magnetron sputtering is one of these applications. Its use is widespread in physical vapor deposition (PVD) processes.

2.2.5 Collisional and radiative processes in plasmas

The behavior of plasmas, in applications related to the treatment of materials, depends to a considerable degree on the density and temperature (mean energy) of the electrons and their energy distribution function. These parameters greatly influence the surface properties of the treated material. Collisions between electrons and heavy particles have a dual function: they maintain plasma and determine the densities of reactive species. In addition, these collisions affect the flow of particles into the substrate. There are three types of collisions: elastic, inelastic and super-elastic.

In elastic collisions the involved particles exchange the kinetic momentum, while the kinetic energy is conserved according to the relationship:

$$e_{\text{fast}} + A_{\text{slow}} \rightarrow e_{\text{less fast}} + A_{\text{less slow}} \tag{2.19}$$

On the other hand, in inelastic collisions, the amount of movement is redistributed among the particles, but a fraction of the initial kinetic energy is transferred to the internal energy of one or more particles, through the formation of excited states or ions:

$$e_{\text{fast}} + A \rightarrow e_{\text{slow}} + A^*_{\text{excited}} \rightarrow e_{\text{slow}} + A^+ + e \tag{2.20}$$

In super-elastic collisions there is an exchange of kinetic energy and internal energy between chemical species. The amount of motion of the whole is preserved, but the

First ionization energy (eV)			
Ar	15.7	O	13.6
Al	6.0	CH_4	14.1
Au	9.8	C_2H_2	11.6
Cl	12.9	C_6H_6	9.6
Cr	6.7	Cl_2	13.2
F	17.3	F_2	17.8
H	13.5	H_2	15.6
He	24.4	HCl	13.8
Hg	10.3	NO	9.5
Na	5.1	N_2O	12.9
Ne	21.4	O_2	12.5
Second ionization energy (eV)			
Ar	27.76	Na	47.0
O	34.93	Cr	16.6
Metastable energy levels (eV)			
He		19.82, 20.61	
Ne		16.62, 16.71	
Ar		11.55, 11.72	
Kr		9.91, 9.99	
Xe		8.31, 8.44	

Table 2.2: Ionization and metastable excitation energies of various materials (Mattox 2009)

internal energy of the particles involved in the collision is transferred in the form of kinetic energy, that is:

$$A^*_{\text{slow}} + B_{\text{slow}} \rightarrow A_{\text{fast}} + B_{\text{fast}} \tag{2.21}$$

A typical example is the collisions between different excited states of the Ar atom in a plasma:

$$\text{Ar}_m + e \rightarrow \text{Ar}^*_{\text{excited}} + e \tag{2.22}$$

which corresponds to a conversion between metastable states, Ar_m, and radiative states, $\text{Ar}^*_{\text{excited}}$, by super-elastic collisions of argon with electrons (Albella 2018). Excitation is the elevation of outer-shell electrons of the atom to a higher energy state.

Excitation may be very short-lived where the electrons return spontaneously to the ground energy state and emit optical radiation, or may be stable where some collision process is necessary to de-excite the atom. These long-lived states are called metastable states. **Table2.2** gives the ionization and metastable excitation energies of some atoms.

2.3 Plasma chemistry

Plasma is an energetic environment in which a number of chemical processes may occur. Many of these chemical processes occur because of electron-atom collisions. In a sustained plasma, electrons are accelerated in an electric field. The sources of electrons are:

- Secondary electrons from an ion- or electron-bombarded surface.

- Ionizing collisions in which an atom loses an electron.

- Electrons from a hot thermoelectron-emitting source (hot cathode).

- Electrons from a hollow cathode source.

On the other hand, some surfaces (i.e. tungsten and thoriated tungsten) emit copious amounts of electrons (thermoelectron emission) when heated. Hot surfaces of these materials are used as electron sources in some ion and plasma sources (Mattox 2009).

A plasma source, which in most laboratory conditions is a gas represents the physical and engineering basis of plasma chemistry. To simplify, an electric discharge can be seen as two electrodes inserted into a glass tube and connected to a power source. The tube can be filled with various gases or evacuated. As the voltage applied across the two electrodes increases, the current suddenly increases sharply to a certain voltage required for sufficiently intense electron avalanches. If the pressure is low, of the order of a few Torr, and the external circuit has a great resistance to prohibit a large current, a glow discharge develops. It is a low-current high voltage discharge widely used to generate non-thermal plasma (Fridman 2008).

In gases the process begins when a stray electron near the cathode carrying an initial current i_0 is accelerated toward the anode by the applied electric field (E). After gaining sufficient energy the electron collides with a neutral gas atom (A) converting it into a positively charged ion (A^+). During this impact ionization process, charge conservation indicates that two electrons are released, according to the relationship:

$$e^- + A \rightarrow 2e^- + A^+ \tag{2.23}$$

These are accelerated and now bombard two other neutral gas atoms, which generate more ions and electrons, and so on. Meanwhile, the electric field drives the ions in the opposite direction where they collide with the cathode, ejecting, among other particles, secondary electrons. These now also undergo the multiplication of charges. The effect of snowballs until a sufficiently large avalanche current finally causes the gas to breakdown. For breakdown to occur, the distance (d) between the electrodes must be large enough to allow the electrons to gain the energy needed for an ionization cascade. In addition, the electrodes must be wide enough to prevent the loss of electrons or ions through sideways diffusion out of the gaps between electrodes.

The critical breakdown voltage (V_B) can be calculated as expressed by Paschen's Law:

$$V_B = \frac{APd}{\ln(Pd) + B} \tag{2.24}$$

where A and B are constants. At low values of Pd there are few electron-ion collisions and the secondary electron yield is too low to sustain ionization in the discharge. On the other hand, at high pressures there are frequent collisions, and since electrons do not acquire sufficient energy to ionize gas atoms, the discharge is quenched. Thus, at either extreme, ion generation rates are low and high voltages are required to sustain the discharge. In between, at typically a few hundred to a thousand volts, the discharge is self-sustaining. In most sputtering discharges the Pd product is well to the left of the minimum value (Shahzad Hussain 2014).

2.4 Sputtering

There are some methods for obtaining thin layers. One of them is called sputtering. It is a technique that has improved during more than 150 years and belongs to the physical vapor deposition (PVD) processes. In general, unlike other techniques, such as thermal evaporation or laser ablation, a target is bombarded by ions generated in a plasma. Thus, it is possible to remove material (atom by atom) from the target and deposit it on the substrate surface. Prior to this process, a vacuum must be created in the chamber containing the substrate. Contaminants (e.g. oxygen or water vapor) which can affect the properties of the deposited layers, especially their purity, are thus eliminated. This technique uses the two technologies that have already been revised: vacuum technology and plasma technology. So, we can imagine the number of parameters involved in this process. The previous vacuum of the chamber, the working pressure, the temperature, the power used during the process, among others, are parameters that determine the deposition rate, the purity of the layers, the adherence of the layers and also their morphology.

When a high energy electron (approximately 40 eV) collides with an Ar atom, it has a high probability of producing an Ar^+ ion and an additional electron that is:

$$e^- + \mathrm{Ar} = e^- + \mathrm{Ar}^+ + e^- \tag{2.25}$$

In a sputtering process the cathode or target surface is bombarded by the high energy ions (usually, Ar^+). The incident ion actually becomes a neutral atom because Auger neutralization before impact; that is, it picks up an electron from the target, so that energetic Ar atom that shares its kinetic momentum with target atoms (see **Figure 2.4**). The target atom will obtain kinetic energy from the atom incident in a collision and will be displaced from its deepest position within the material and will transfer its energy to other material atoms that will also move from their positions. With the continuous impact and transfer of the kinetic momentum of the incident energy atoms to the target, the atoms close to the surface can be emitted by overcoming the surface binding energy. These ejected atoms are called sputtered atoms. In sputtering actually a transfer of momentum process occurs between the incident Ar atom and the target atom (Shahzad Hussain 2014). Most of the transferred energy ($> 95\,\%$) appears as heat in the target surface region and near surface region. Some of the bombarding particles are reflected as high energy neutrals and some are implanted into the target surface (Rossnagel et al. 1990). The theory of kinetic momentum transfer has been substantiated since several effects have been detected. These effects include the following:

- The sputtering yield (ratio of atoms sputtered to the number of high energy incident particles) depends on the mass of the bombarding particle as well as its energy.

- The sputtering yield is sensitive to the angle-of-incidence of the bombarding particle.

- There is a “threshold energy” below which sputtering does not occur no matter how high the bombarding flux.

- Many sputtered atoms have kinetic energies much higher that than those of thermally evaporated atoms.

- Atoms ejected from single crystals tend to be ejected along directions of the close packed planes in the crystal.

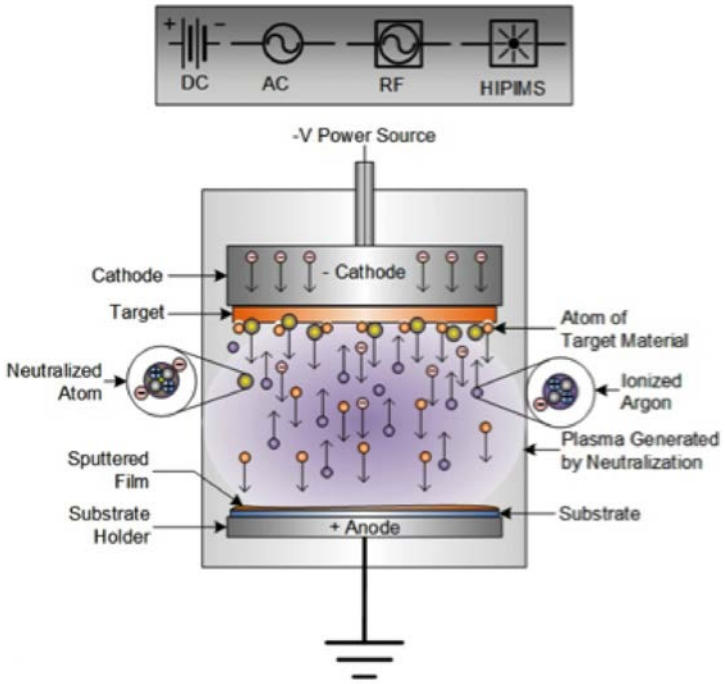

Figure 2.4: Diagram of the sputtering process (Hughes 2014)

- When sputtering a polycrystalline material, some crystallographic planes are sputtered faster than others (preferential sputter etching).
- Atoms sputtered from an alloy surface are deposited in the ratio of the bulk composition.
- Sputtering yields decrease at very high energies because the ions lose much of their energy far below the surface.
- The sputtering yield is rather insensitive to the temperature of the sputtering target.
- There is no sputtering by electrons, even at very high temperatures.
- The secondary electron emission by ion bombardment is low, whereas high rates from thermoelectron emission would be expected if high temperatures were present.

Effects one through seven above are important to the growth of films by sputter deposition. This is particularly true for low pressure ($< 6.7 \times 10^{-3}$ mbar) sputtering where the energetic sputtered atoms and reflected high energy neutrals are not "thermalized" by collision between the sputtering source (target) and the substrate (Mattox 2009).

When the atoms removed from the target (sputtered atoms) reach the substrate surface they interact with the surface atoms and eventually form clusters, then the clusters form islands (coalescence process) and finally the islands form uniform layers. The formation of clusters, islands and uniform layers depends on several factors. It mainly depends on the interaction of the sputtered atoms with the substrate surface. Thus, it is necessary to take into account the surface energy, the surface roughness, the substrate temperature and the affinity with the substrate.

Typically, argon ($40amu$) is used for inert gas sputtering since it is a relatively inexpensive inert gas. Other gases useful to increase the sputtering yield are krypton ($84amu$),

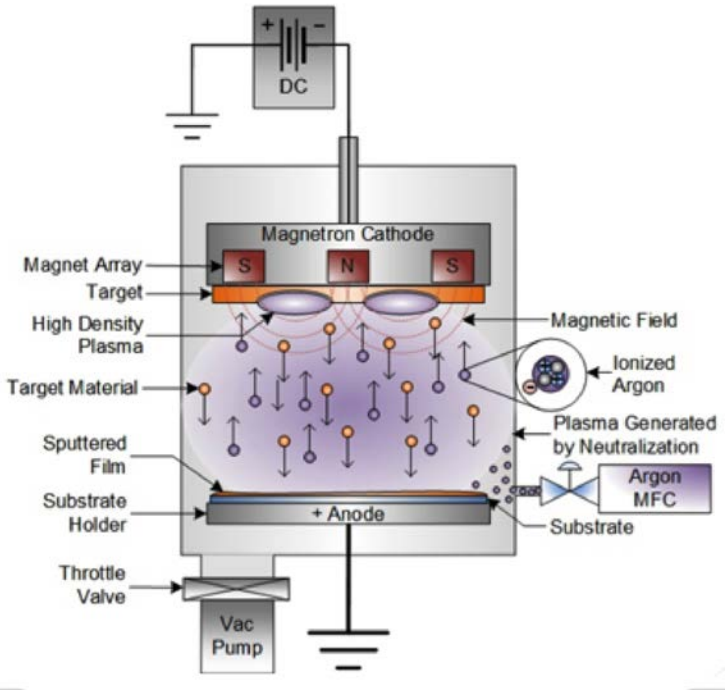

Figure 2.5: Diagram of the DC magnetron sputtering process (Hughes 2014)

xenon ($131amu$), and mercury ($201amu$) (Mattox 2009). However, in addition to its expensive price compared to the Ar, its environmental impact must also be considered. Mixtures of argon and nitrogen, argon and oxygen, or argon and methane/acetylene are used in the reactive sputter deposition of oxides, nitrides, and carbides. Several different methods of physical vapor deposition are widely used in sputter coaters, including ion beam and ion-assisted sputtering, reactive sputtering and magnetron sputtering (Hughes 2014).

In magnetron sputtering, a magnet (permanent magnets or electromagnets) that generates a constant magnetic field (E) is introduced into the sputtering head. In this way, the free electrons are stabilized (confined), and consequently the sputtering yield increases. Also, this design allows to protect the target material from electron contact, and increase the likelihood that the electrons will ionize the argon atoms. **Figure 2.5** shows a useful illustration of magnetron sputtering configuration. Magnetron sputtering offers higher ionization rates and less electron damage to the target material than traditional sputter deposition techniques. The magnet creates a field that keeps the electrons restrained and trapped above the target material where they cannot harm it. Since the magnetic field lines are curved, the path of the electrons in the chamber is extended through the stream of argon, improving ionization rates and decreasing the time until the thin film is complete. In this way, magnetron sputtering is able to counteract the initial problems of time and target material damage that had occurred with traditional sputtering (Walker 2019). Besides, using a magnetron configuration, plasmas can be sustained at a few tenths of an mTorr in Ar (Mattox 2009).

One reason that this process is considered versatile is its adaptability to different types of power sources. DC sources and their pulsed-DC variant can be used. Also, MF Mid Frequency AC Sputtering Power, radio frequency (RF) and high-power impulse magnetron sputtering (HIPMS) sources. DC power is generally used with electrically

conductive target materials. It is easy to control and a low-cost option. Pulsed DC (variable frequency) has found broad application in reactive sputtering applications where a positive voltage spike, induced at some frequency on the power waveform can be used to clean the target face and eliminate the buildup of a thick dielectric layer which can be prone to arcing. Frequency ranges from 40 to 200 KHz are typically used. This approach is commonly referred to as uni-polar pulsed sputtering. Another option known as bi-polar pulsed sputtering uses two pulses ,180 degrees out of phase, that are applied to two adjacent magnetrons in which each magnetron alternates as both a cathode and anode, mitigating the effects of dielectric build-up and greatly reducing the disappearing anode effect. This technique has also found wide industrial use. On the other hand, MF sputtering is typically used to deposit non-conductive materials. Two cathodes in a dual configuration are used and the AC current is switched between each cathode allowing the target surface to be cleaned with each reverse of the cycle. This reduces arcing by charge build up and eliminates the need for anode cleaning which provides long term process stability. MF sputtering is widely used in many in line production systems today. RF power can be used with all materials, but generally finds most use in depositing films from dielectric target materials. The deposition rate (driven by the relative duty cycle) when compared to DC is generally quite low and the electron flux (due to the mobility difference of electrons and ions in a plasma) on the substrate is much higher and may cause significant heating. Due to the major cost considerations of RF power supplies, RF deposition is generally limited to smaller substrate sizes. Finally, HIPMS is an emerging process which uses a high current pulse to greatly increase the ionization of the sputtering material. These ionized atoms have much higher energies than sputtered atoms in conventional magnetron sputtering and have been found to yield very dense and stable films (Angstrom Sciences 2019). For all thin layers deposited in this work the pulsed-DC power supply was used.

Normally the targets used are pure metals. However, alloys and compounds are also used. For alloys, since sputtering is generally done from a solid surface, ideally, if there is no diffusion, each layer of atoms must be removed from the surface before the next layer is subject to sputtering. This means that the flux of sputtered atoms has the same composition as the bulk composition of the sputtering target, although, at any instant, the surface layer of the target will be enriched with the material having the lower sputtering yield. In some cases where the mixture is of materials having significantly different masses or sputtering yields, the sputtered composition may be different from the target composition. An additional aspect to consider when using this process is the potential deterioration of the target. The "poisoning" of the target surface can be due to contaminant gases in the system or can develop during reactive sputter deposition from the deliberately introduced process gases (Sundgren et al. 1983). In addition, the sputtering target generally is actively cooled. The cold surface minimizes the amount of radiant heat in a sputtering system and this may be an advantage over thermal evaporation in vacuums, where the radiant heat load can be appreciable. The low level of radiant heat is one factor that allows thermally sensitive surfaces to be placed near the sputtering target (i.e. polymers). Cooling also prevents diffusion in the target, which could lead to changes in the elemental composition in the surface region when alloy sputtering targets are used (Mattox 2009). Refrigeration systems must be used to ensure that the target temperature is adequate. The designs of refrigeration systems can vary considerably depending on the scale (laboratory or industry).

Advantages and disadvantages of sputter deposition

As mentioned above, this is a versatile process by which different types of materials can be deposited on different types of substrates and with different power supply technology. Its extensive use in research laboratories and in industry has allowed the identification of innumerable advantages over other PVD processes. Simultaneously, disadvantages have been identified that may condition their use. Mattox summarizes them as follows:
Advantages in some cases

- Any material can be sputtered and deposited (i.e. an element, alloy, or compound).
- The sputtering target provides a stable, long-lived vaporization source.
- Vaporization is from a solid surface and can be up, down, or sideways.
- In some configurations, the sputtering target can provide a large-area vaporization source.
- In some configurations, the sputtering target can provide specific vaporization geometries, e.g. line source from an extended planar magnetron sputtering source.
- The sputtering target can be made conformal to a substrate surface such as a cone or sphere.
- Sputtering conditions can easily be reproduced from run to run.
- There is little radiant heating in the system compared to vacuum evaporation.
- In reactive deposition, the reactive species can be activated in a plasma.
- When using chemical vapor precursors, the molecules can be dissociated or partially dissociated in the plasma.
- Utilization of sputtered material can be high, e.g. rotatable cylindrical magnetron.
- In situ surface preparation is easily incorporated into the processing.

Disadvantages in some cases

- In many sputtering configurations the ejection sputter pattern is non-uniform and special fixturing, tooling, or source design must be used to deposit films with uniform properties.
- Most of the sputtering energy goes into heat in the target and the targets must be cooled.
- Sputter vaporization rates are low compared to those that can be achieved by thermal vaporization.
- Sputtering is not energy-efficient. Sputtering targets are often expensive.
- Sputter targets, particularly those of insulators, may be fragile and easily broken in handling or by non-uniform heating.
- Utilization of the target material may be low. Substrate heating from electron bombardment can be high in some configurations.

- Substrates and films may be bombarded by short-wavelength radiation and high energy particles that are detrimental to their performance.
- Contaminants on surfaces in the deposition chamber are easily desorbed in plasma-based sputtering due to heating and ion scrubbing.
- Gaseous contaminants are "activated" in plasma-based sputtering and become more effective in contaminating the deposited film.
- When using chemical vapor precursors, the molecules may be dissociated or partially dissociated in the plasma to generate "soot".
- High energy reflected neutrals in low pressure and vacuum sputtering can be an important, but often uncontrolled, process variable.

2.5 Chemical Vapor Deposition

Another process that uses vacuum technology is the one known as chemical vapor deposition (CVD). In addition to being a useful process for obtaining carbon-based materials, CVD is a basic tool of manufacturing (used in everything from sunglasses to potato-chip bags) and is fundamental to the production of much of today's electronics. The majority of its applications involve applying solid thin-film coatings to surfaces, but it is also used to produce high-purity bulk materials and powders, as well as fabricating composite materials via infiltration techniques. It has been used to deposit a very wide range of materials (Creighton and Ho 2001). It is also a technique subject to constant refining and expansion, pushing materials research in new directions, such as the production of large scale sheets of graphene, or the development of solar cells that could be "printed" onto a sheet of paper or plastic (Chandler 2015).

In physical deposition processes the material deposited is physically moved on to the substrate. There is no chemical reaction which forms the material on the substrate. Chemical deposition techniques exploit the creation of solid materials directly from chemical reactions in gas and/or liquid compositions or with the substrate material. The solid material is usually not the only product formed by the reaction. By products can include gases, liquids and even other solids. Like PVD process, the CVD process is performed in vacuum condition to reduce the undesirable physical or chemical reactions from air constituents (oxygen or water vapors) and to increase the mean free path of the precursor gases to form uniform material on the substrate.

CVD reaction can be classified into several major categories such as:

- Thermal decomposition, in which a molecule is broken apart into its constituents or more elementary molecule (e.g. CNTs or graphene structures).
- Hydrogen reduction. Reduction is the process in which an element gains an electron. Hydrogen reduction has a major advantage in that the reaction generally takes place at lower temperature than equivalent decomposition reaction. CVD reactor main function is to heat the sample (Pierson 1999).

Advantages and disadvantages of CVD

As discussed in the first chapter, CVD has pros and cons. Below are some general advantages and disadvantages of this deposit process:
Advantages

- One of the primary advantages is that CVD structures are generally quite conformal, i.e., that the film thickness on the sidewalls of features is comparable to the thickness on the top. This means that films can be applied to elaborately shaped pieces and that high-aspect ratio holes and other features can be completely filled. In contrast, physical vapor deposition (PVD) techniques, such as sputtering or evaporation, generally require a line-of-sight between the surface to be coated and the source.

- Another advantage of CVD is that, in addition to the wide variety of materials that can be deposited, they can be deposited with very high purity. This results from the relative ease with which impurities are removed from gaseous precursors using distillation techniques.

- Other advantages include relatively high deposition rates, and the fact that CVD often doesn't require as high a vacuum as PVD processes.

Disadvantages

- One of the primary disadvantages lies in the properties of the precursors. Ideally, the precursors need to be volatile at near-room temperatures. This is non-trivial for a number of elements in the periodic table, although the use of metal-organic precursors has eased this situation.

- CVD precursors can also be highly toxic $Ni(CO)_4$, explosive B_2H_6, or corrosive $SiCl_4$. The byproducts of CVD reactions can also be hazardous (CO, H_2, or HF). Some of these precursors, especially the metal-organic precursors, can also be quite costly.

- The other major disadvantage is the fact that the films are usually deposited at elevated temperatures. This puts some restrictions on the kind of substrates that can be coated.

- More importantly, it leads to stresses in films deposited on materials with different thermal expansion coefficients, which can cause mechanical instabilities in the deposited films (Creighton and Ho 2001).

2.6 Plasma-enhanced chemical vapor Deposition

As discussed in the first chapter, plasma-enhanced chemical vapor deposition (PECVD) is a deposition technique that allows for tunable control over the chemical composition of structures. PECVD allows the process to proceed at relatively lower temperatures due to the assistance of plasma compared to other types of thermal CVD that utilize, e.g., hot-wall reactor, cold-wall reactor, and laser.

Remember that in PECVD processes, deposition/growth is achieved by introducing reactant gases between parallel electrodes, i.e. a grounded electrode and an RF energized electrode. The capacitive coupling between the electrodes excites the reactant gases into a plasma, which induces a chemical reaction and results in the reaction product being deposited on the substrate. The substrate, which is placed on the grounded electrode, is typically heated, depending on the specific structure requirements. In comparison, CVD requires higher ranges of temperature. The lower deposition temperatures are critical in many applications where CVD temperatures could damage the substrate or devices being fabricated (Plasma-Therm 2019).

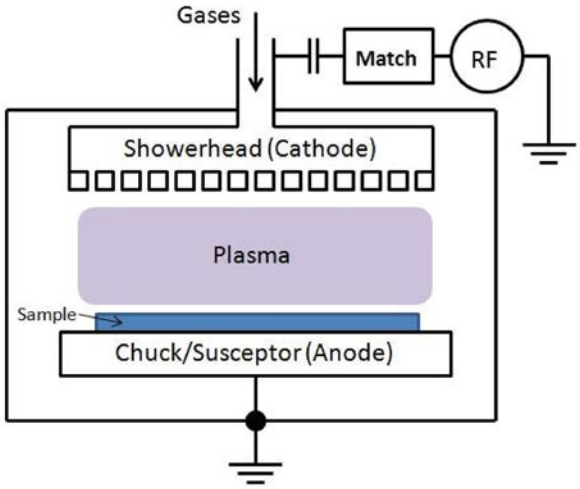

Figure 2.6: PECVD chamber configuration

The current used high frequencies are radio frequency (RF) at 13.45 MHz and microwave (MW) frequency at 2.45 GHz (Shahzad Hussain 2014). **Figure 2.6** shows a typical configuration of the PECVD system.

Advantages and disadvantages of PECVD

While some specific advantages and disadvantages of PECVD were already included in the first chapter in the production of CNTs, a general summary of these is given below:
Advantages

- It is capable of forming a deposit at relative low temperatures where, no reaction whatsoever would take place in thermal CVD.
- The effects of thermal expansion mismatch between substrate and coating and resulting stresses are reduced since the temperature of deposition remains low.
- The rate controlling factor is surface kinetics, which leads to greater uniformity.
- The low temperature of deposition also favors the formation of amorphous or very fine polycrystalline deposits which usually have superior properties.
- It is possible to use organic and inorganic precursors.
- The geometry and composition of the substrate do not limit it.

Disadvantages

- It is difficult to obtain a deposit of pure material. In most cases, desorption of by-products and other gases, particularly hydrogen, remains as inclusion in the deposit.
- PECVD tends to create undesirable compressive stresses in the deposit particularly at the lower frequencies. This may not be a problem in very thin films used in semiconductor application, but in thicker films typically metallurgical applications, the process carries peeling and cracking.

- The equipment is generally more complicated and more expensive than another CVD process.

- Toxic, explosive and/or highly corrosive gases may be produced depending on the precursor gases.

During this work the PECVD was the main process used to produce uniform forests of nanotubes (CNTs) on the substrates used. Thus, it has been worked in temperature ranges from 500 to 800 °C. In addition, in this temperature range was also performed the reduction of the native oxide layer of 304 stainless steel. Definitely, PECVD was one of the processes that has played a pillar for the culmination of this work. We have dedicated many hours of work to improve this technique. The work done in the PECVD system of the CNTs reactor will be explained in the next section.

2.7 Reactors used in the experiments

Our reactors integrate PVD and PECVD processes. This has allowed our group to venture into new areas of research. Thin layers of ultra hard materials (i.e. carbides, oxides, diamond like carbon) have been deposited on metals and polymers. Furthermore, the production and functionalization of nanostructures (single wall and multi walled carbon nanotubes) was carried out using different materials as substrates. The availability of the reactors together with the existence of various precursor gases, substrates and targets of different materials (pure metals, alloys and compounds) have facilitated in our research group the activities of investigation and education.

2.7.1 Thin film deposition reactor

Our research group has different reactors to obtain nanostructures. The most versatile, due to its configuration, is undoubtedly the multi-process reactor (**Figure 2.7**). This reactor was named PEDRO (Plasma Etching and Deposition ReactOr) due to the amount of processes that can be performed inside it. Magnetron sputtering (14) and plasma enhanced chemical vapor deposition (PECVD) (15) heads were used during this research work. Due to its configuration, this unit allows working with different sized substrates. In addition, since there is an RF and a pulsed-DC power source, it is possible to work with conductive and insulating materials. Basically, the reactor is constituted by two sections: the main chamber and the pre-chambers (12,13,17). Two prechamber (13,17) are to load samples and the remaining one (12) serves to place the target. This reactor consists in a 304 stainless steel spherical chamber capable of reaching very high vacuum (10-5 Pa). The seals are mainly of ISO-CF type (copper).

The magnetron sputtering and PECVD heads have a water-cooling system. This prevents the heads from heating up during operation. Elevated temperatures can lead to efficiency loss of magnetron sputtering. The magnets are cooled by water, because the ionic bombardment could raise its temperature above Curie's temperature, and the magnetron would then lose its permanent magnetization irreversibly. In addition, without cooling system, it would be impossible to place samples with a low melting point (e.g. polymers). The gases used during the different processes are introduced through 316 stainless steel lines. The flow control of the gases is carried out using a pneumatic system (pneumatic valves) that is complemented with mass flow controllers (MFCs). The reactor is pumped down by means of a turbomolecular pump (LEYBOLD TMP360C), and the

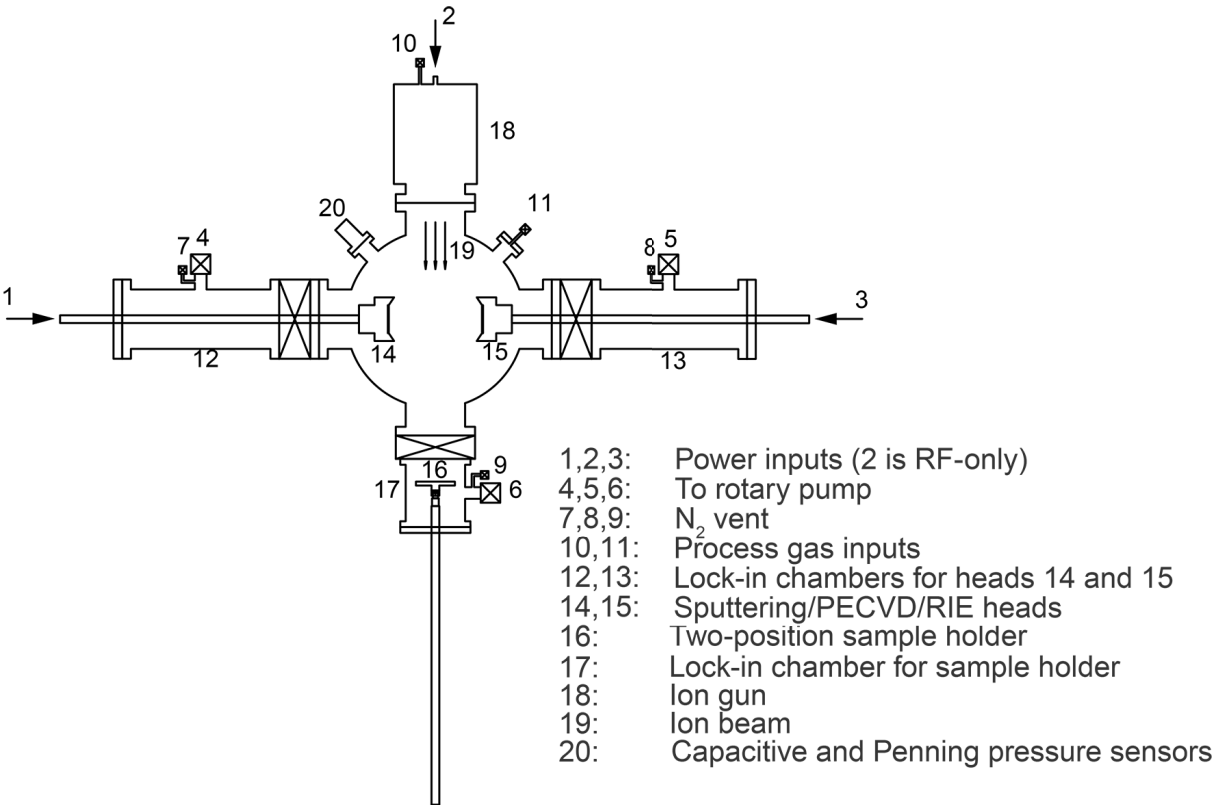

Figure 2.7: Schematic figure of PEDRO reactor. Several techniques can be used, including magnetron sputtering, PECVD, reactive ion etching (RIE) or ion beam etching (IBE)

load-lock chambers are evacuated by rough pumping (up to $\sim 10^{-2}$ mbar before opening the chamber valve). The pressure inside the principal chamber reactor is measured using penning and capacitive vacuum gauges.

In addition, during the processes carried out with this reactor, independent of the gas or gas mixture used, a wide range of pressures could be selected. For that, a butterfly valve located between the turbomolecular pump and the main chamber made it possible to control the process pressure. One of the strong points of this reactor is that the aforementioned systems are controlled through a computer software. Gas valves, pressure gauges, and mass flow controllers are operated with a LABVIEW interface, which can be programmed for the deposition process. Thus, the control of the different parameters during the operation of the system is more reliable. The repeatability and reproducibility of the experiments is high. In this case, computer control has made it possible to reduce human error. The LabVIEW program has two tabs: the "Control center" and the "Sequence configuration tab". The software can operate in two modes: manual or automatic. In the former, the following elements can be controlled as desired at any time:

- Bottle-side, bypass and reactor-side valves of the six different gas lines available.
- Valve for the cold cathode pressure gauge.
- Main valve between turbomolecular pump and chamber.
- Valves between turbomolecular pump and backing pumps.

- Butterfly valve: fixed position or pressure regulation.
- MFCs' setpoint, on/off state and zero adjustment.

In addition, all pressure and flow readings are available all time and updated every two seconds:

- Full scale of the MFCs and actual flow.
- Valve open/closed state.
- Pressure in the chamber (two capacitive gauges with full scale of 133 Pa).
- 13 Pa plus one full range Pirani + cold cathode for down to 10^{-6} Pa with numeric displays and a graphic plot of time evolution.
- Pressure in the entry port of both backing pumps.

Manual mode includes a security switch in the "Sequence configuration" tab that watches over bad operation of the reactor by disabling certain actions:

- Open the bottle-side valve of a gas that could damage the cold cathode if its valve is opened.
- Open the cold cathode valve if the bottle-side valve of any harmful gas is opened.
- Open the bypass valve of any line if the bottle-side valve is also opened.
- Entering combustible gases when pumping with the comburent pump and vice versa.

When automatic mode is started, the program is run. Every step of the program defines the flow setpoint for every MFC, the pressure setpoint for the butterfly valve, the duration of the step and the state of the pulsed-DC power supply. In addition, every step has a "Gradient" switch. When on, flow setpoints are changed in the MFC linearly from the initial value to the defined setpoint. With this feature, layers with varying mixtures of different gases can carried out. PEDRO reactor was used to sputter various thin films (SS304, AlN, Al_2O_3) on different substrates such as silicon wafer, glass and 304 stainless steel foil.

2.7.2 Carbon nanotubes reactor

This is a reactor, which unlike the previous one, was created exclusively to obtain carbon nanotubes (CNTs). The original design consisted of a cylindrical chamber, in which the substrate (one holder) was placed on a rotating platform (like-carousel). The main advantage of that configuration is the integration of all treatments involved in the deposit of CNTs in a single sequential process, without break the vacuum. On the same sample can be deposit thin films (by magnetron sputtering) and growth of CNTs (CVD or PECVD). In one stage, plasma and heating systems for CVD and PECVD processes are placed. The other stages are equipped with two homemade magnetron sputtering systems (600 W of nominal RF power, water cooled and 3" targets of iron and 304 stainless steel, respectively. In addition, the reactor has a load-lock prechamber system to avoid atmospheric contamination of the main chamber during the sample introduction.

The plasma in PECVD stage is achieved via electrically connecting the sample holder (cathode) to the RF power supply and matching network. The same RF power supply and

matching network is also used in the sputtering processes. The heating system consists in a graphite resistance (1.70 Ω) connected to a DC power supply with a maximum voltage output of 60 V. The temperature is measured through an external pyrometer. It can only be measured in the PECVD stage where there is a quartz window (viewport).

The vacuum system is composed for three pumps. A primary rotatory pump for the first vacuum, a Roots pump with a butterfly valve to maintain the low-pressure conditions during the processes and a turbomolecular pump for high vacuum. The final pressure that the system can achieve is $\sim 2 \times 10^{-4}$ Pa. The atmosphere composition is selected with six gas lines connected to the reactor; all equipped with mass flow controllers. The flux of gas, the different valves and the power of the heating and plasma systems are computer controlled with a LabView interface. The software interface permits to control different actuators independently. Also, a specific schedule can be programmed in way that the actions with the reactor actuators are performed automatically during the process.

Since it was the reactor with which most work was done during this research and the one that presented the most technological challenges, the changes and improvements made will be exposed. In order to improve the process of obtaining CNTs samples, all the changes described in this work, were made on my own initiative, always under the direction of Prof. Enric Bertran. Much emphasis has been placed on minimizing human error, so many changes were made in the reactor to try to "automatize" the process.

A view of the reactor can be seen in **Figure 2.8**. Several changes were made on the outside of the reactor. The first was to replace the old elevation system of the reactor cover. Estimated weight of the cover, which includes the magnetron sputtering heads and the heating system (graphite resistance), was $\sim 130\,kg$. The old elevation system was continuously blocked. The main cause identified was the wear and plastic deformation of the worm screw. Because of this, the entire elevation system was replaced by a new one. The reactor now has an electro mechanical linear actuator (SKF system) which is a more reliable elevation system **Figure 2.9**. In addition, since the elevation system does not act on the center of gravity of the cover, a counterweight system was also included. As a

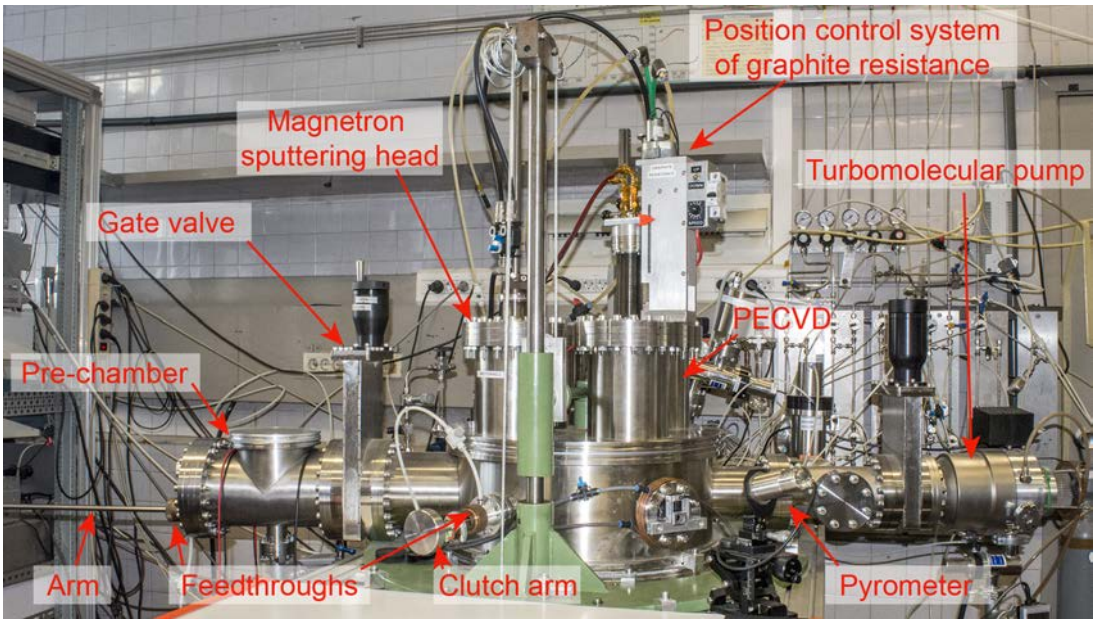

Figure 2.8: Plasma enhanced chemical vapour deposition (PECVD) reactor for CNTs growth

result, loads that could damage the anchorage elements are avoided.

The elevation system has great importance in the operation and maintenance of the reactor. By removing the reactor cover, the internal mechanisms can be calibrated. In addition, it is possible to replace old parts, check the state of the heating element, check the state of the PECVD electrode, clean the vacuum chamber and also change the targets.

Another significant modification was to replace the position control systems of the heating element (graphite resistance) and the PECVD electrode. These systems allow to introduce and extract the graphite resistance and the PECVD electrode according to the requirements of each process. Being manual, it depended a lot on the user's skill. In addition, position control accuracy was low. So, it was decided to replace them with semi automatic systems (homemade) that facilitate the control of the position of those elements **Figure 2.10**. Each system is made up of an electric motor that acts on a ball screw (NKS), a current changeover switch, a current limiter, a speed control, a guide and other mechanical elements that give the design its robustness. Thus, the repeatability and reproducibility of the CVD and PECVD experiments were improved.

The static pyrometer support was also replaced. This support did not allow the tilt of the pyrometer to be properly controlled. Like other factors, temperature control is critical in CVD and PECVD processes. It is worth mentioning that depending on the sample with which it is working, the angle of the pyrometer may vary. In other words, the geometry of the sample influences the optimal position of the pyrometer. It was decided to mount the temperature measuring device on a platform with more degrees of freedo m. It is now possible to move the pyrometer both vertically and horizontally, with the plus that the inclination can also be controlled (see **Figure 2.11**).

In addition to the changes mentioned above, the feedthroughs used in the reactor were also replaced. A new generation of feedthroughs were designed and their performance has been satisfactory to date. The feedthroughs with one o-ring did not maintain vacuum

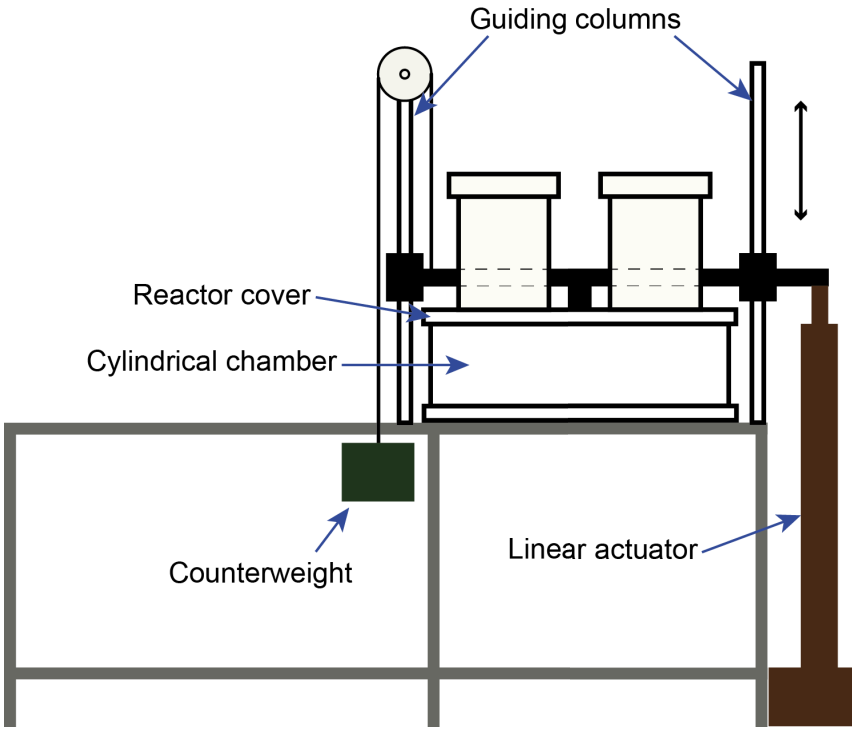

Figure 2.9: Illustration of elevation system

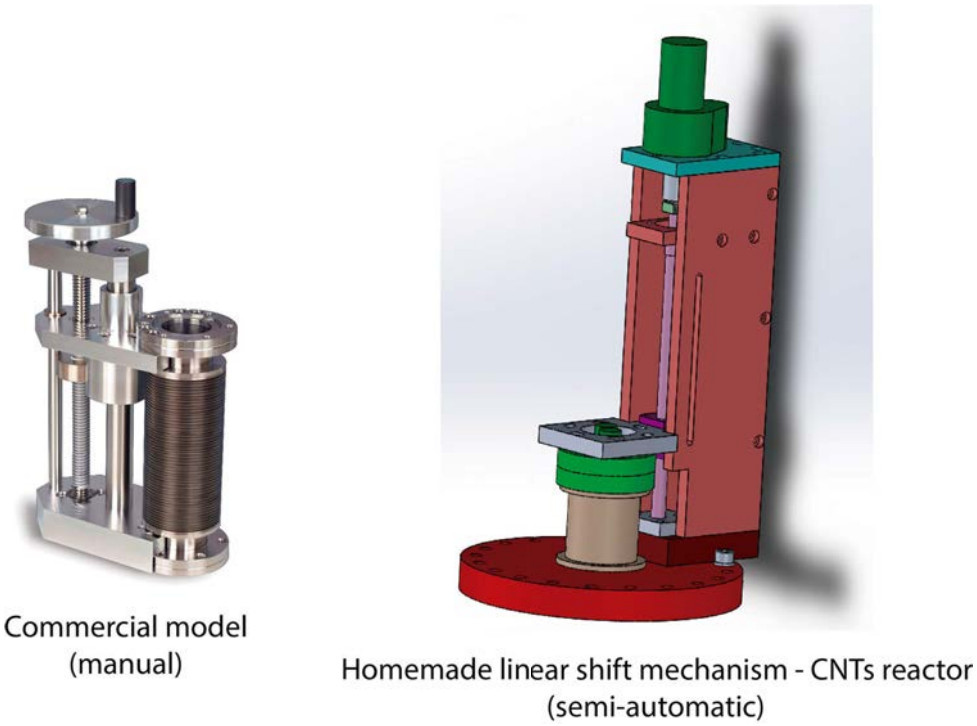

Figure 2.10: Illustration of position control systems

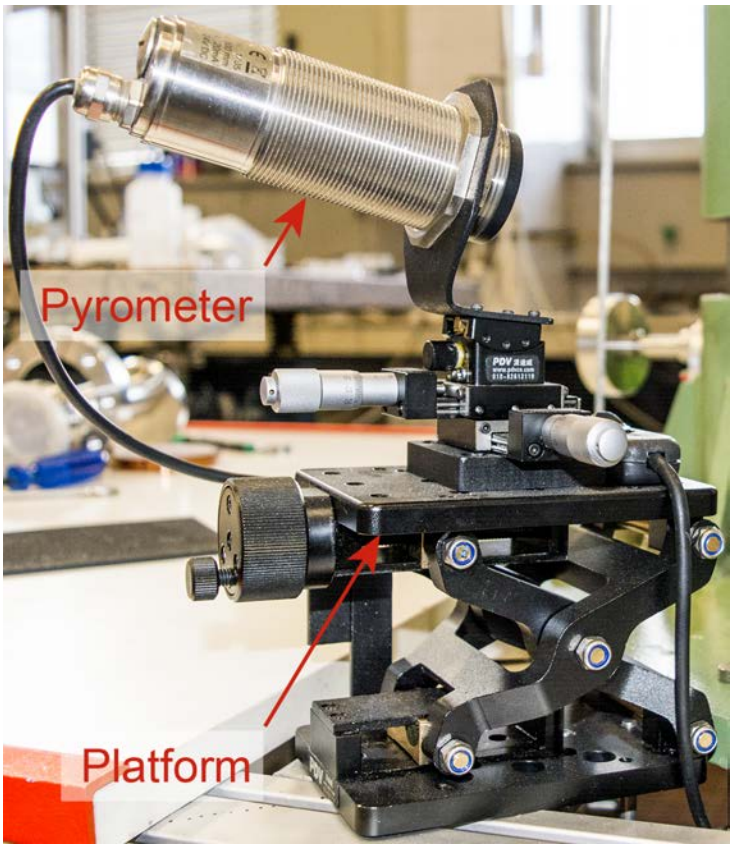

Figure 2.11: Pyrometer mounted on a mobile precision platform

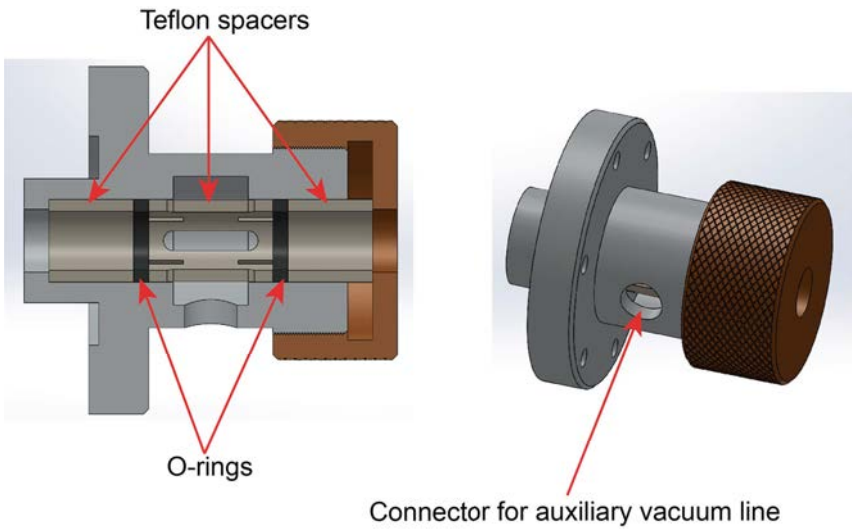

Figure 2.12: New design of feedthroughs

property, especially when there were movements (linear or rotational) of the shafts. This type of movement is normal in this type of reactor and is in fact inevitable. When the sample was introduced or when the sample was being positioned, if the feedthrough did not work properly, the vacuum was not adequate. In contrast to the design used in the old feedthroughs, a double o-ring system was implemented in the new design. Between the two o-rings there is a small cavity connected to an auxiliary vacuum line (**Figure 2.12**). Thus, air that can pass a firs o-ring (exposed to atmospheric pressure) is immediately purged through the auxiliary vacuum line. It is an economical and at the same time a good performance feedthrough design. The implementation of the new elements has considerably improved the reactor's sealing.

With respect to the changes made in the internal part of the reactor, two can be mentioned: the design and build of the rail system for the introduction of the samples, the design and build of the sample positioning system.

The sample loading system had to be improved as it was identified as one of the reasons why vacuum was not adequate. As soon as the gate valve of the reactor was opened (**Figure 2.8**) the vacuum deteriorated. In Addition to identifying that the function of the feedthrough was not correct, it was identified that the rotational, linear and angular movement of the loading arm allowed air to enter the reactor. The sample holder (due to its weight) produced a moment in the loading arm. The angular movement caused deformed and damaged the internal elements of the feedthrough, resulting in the loss of vacuum.

When these problems were identified, the new sample loading system was proposed. Basically, two rails were placed: one in the pre-chamber and the other inside the main chamber of the reactor. We used two sections as it was necessary to leave a space for the gate valve. The fixation of the rails was achieved using internal rings (two rings for each rail) that were adapted to the cylindrical shape of where they were placed. With this new design, it was also necessary to redesign the loading arm and sample holder. The new system for loading samples using rails is shown in **Figure 2.13**.

As mentioned at the beginning of this section, the original design of the reactor consisted of a like-carousel system to position a sample under the different heads. One drawback of this configuration is that, as with the loading arm, the weight of the holder

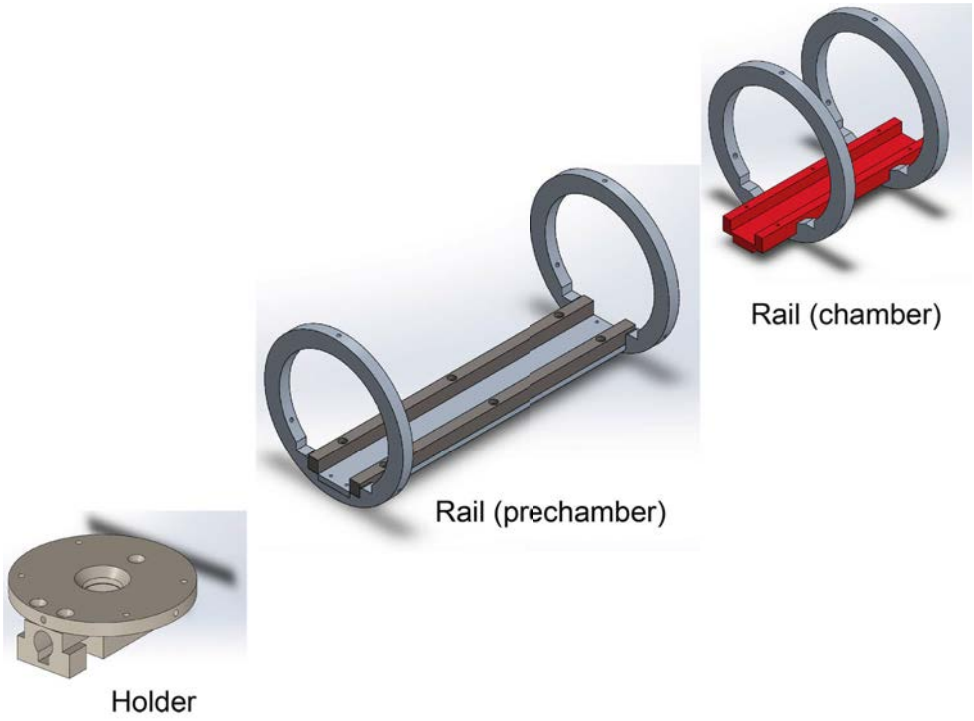

Figure 2.13: System for loading samples using rails

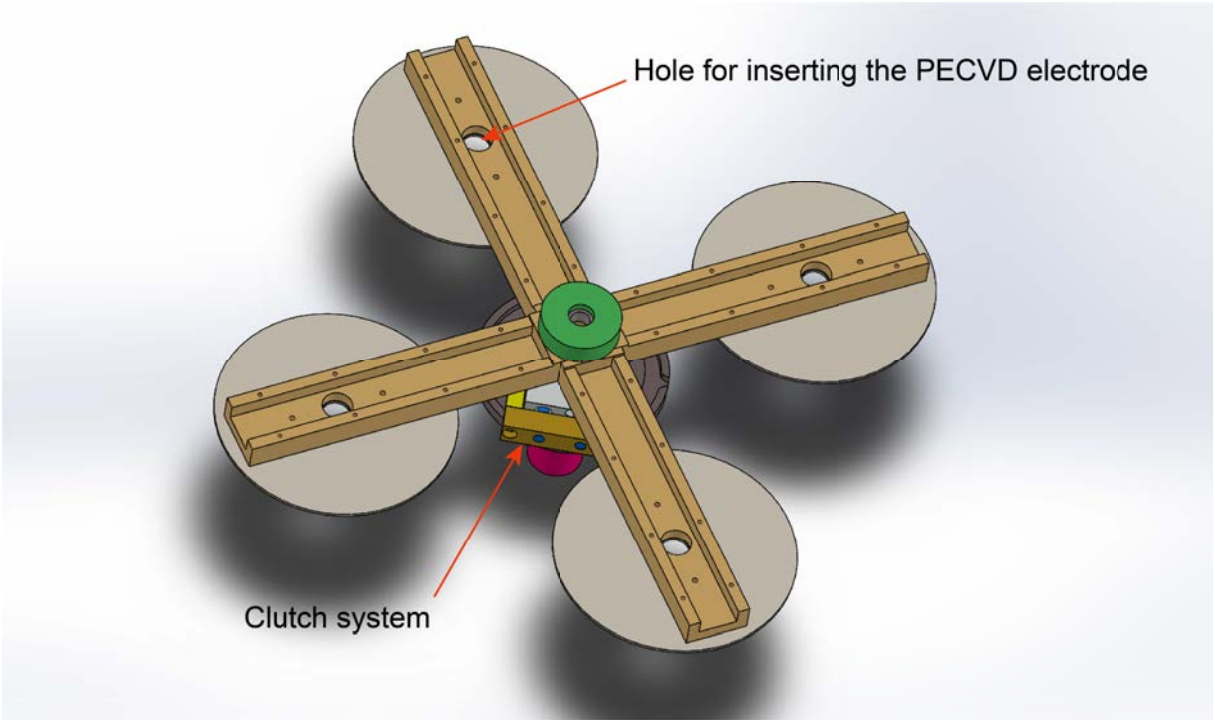

Figure 2.14: Sample positioning system like-carousel

and the system itself generated a moment in the rotation shaft (which affected the integrity of the feedthrough). In addition, the preparation of samples and their subsequent extraction required a long time, especially if CVD or PECVD processes were carried out. It was necessary to wait at least one hour to extract the sample from the reactor in order

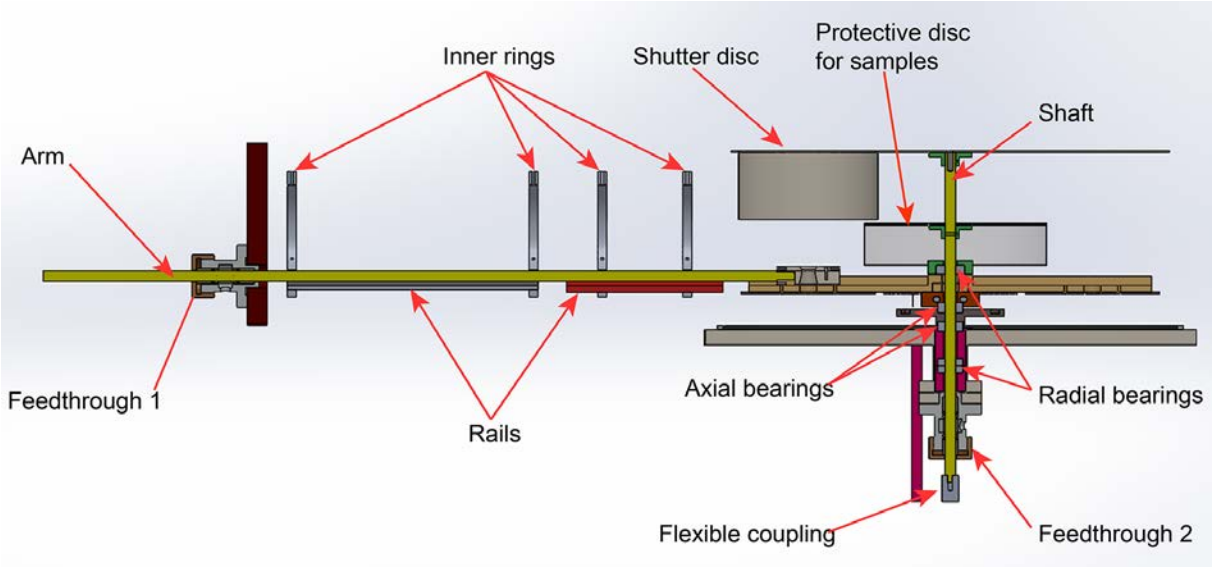

Figure 2.15: Sample loading and positioning systems

to avoid contamination (basically oxidation). To avoid these inconveniences, we decided to implement a new like-carousel system with four ports (**Figure 2.14**). A set of bearings (axial and radial) supports the additional weight of the system that was placed. Thus, it was possible to eliminate the moment and to reduce the time of obtaining the samples.

At the same time, it is possible to have the other samples inside the reactor. If one sample is being utilized, the other three can be protected under as special shelter. The main advantage of this configuration is to avoid constantly breaking the vacuum.

Certainly, one of the challenges in the design presented the way to select the working port. It should be mentioned that the original design included a disc. That forced us to look for a mechanism that would attach to that protection system. The solution was to include a clutch mechanism, which is operated by an external arm. So, it was necessary to relocate one of the vacuum sensors. By implementing all of the reactor design changes and improvements, new accessories such as graphite sample holders, PECVD electrode, graphite resistance and molybdenum radiation shields were also redesign. **Figure 2.15** shows in detail the sample loading and positioning systems. All the detailed plans elaborated during the reactor repowering can be found in the annexes section.

Despite all the modifications described in this section, during much of this work there was a serious drawback: the repeatability and reproducibility of the experiments was not as expected. We achieved a lot with the change of the feedthroughs and the redesign of the different systems, but we didn't understand what factor or factors influenced in our experiments. The other support systems were considered suspicious. We reviewed the pneumatic system, the gas supply system, the vacuum gauges, in the heating system we redesigned the graphite resistance, we also reviewed the control program (LabVIEW) and nevertheless we did not find the culprit. It was during some experiments with the optical emission spectroscopy (OES) probe that we found the cause of this lack of reproducibility. As a result of the increase in reactor productivity (due to the incorporation of the like-carousel), the contamination rate of the viewport where the radiation signal collects also increased. **Figure 2.16** shows the previous configuration of the platform on which the optical pyrometer was located at the front of the viewport. It seems that the PID temperature control system was affected by this contamination. This was detected because

the OES spectra, obtained during reduction process, did not show the typical OH peaks on oxidized surfaces. When the viewport was disassembled, a layer of amorphous carbon was found on the quartz that acted as a filter for the signals required to be collected. In order to counteract this contamination, different actions have been taken. The first is to periodically clean the quartz surface of the viewport.

A new accessory was also designed that allows the viewport to be away from the area where the plasma is produced (see **Figure 2.17**). In order to check that the working conditions did not change, a calibration of the PID temperature control system was carried out before and after the modification using a clean viewport.

For this purpose, a sample coated with CNTs was annealing up to 900 °C with a

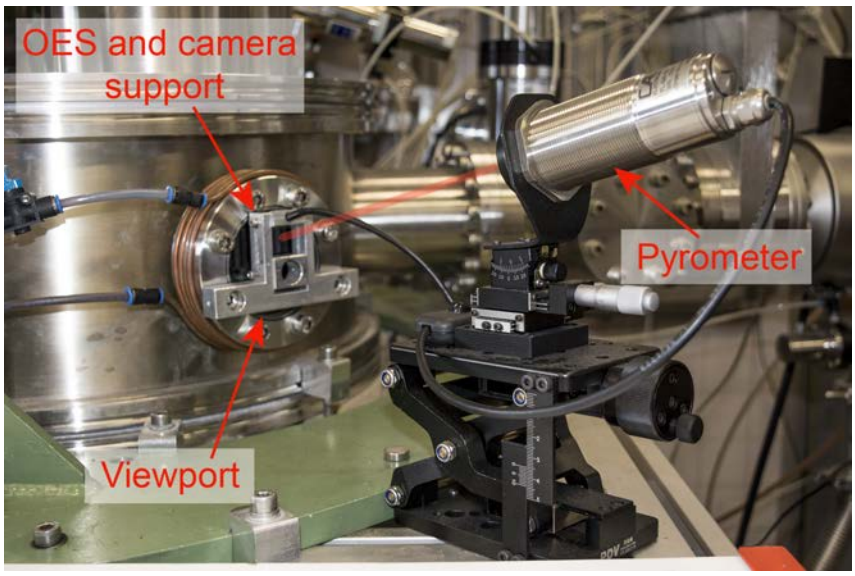

Figure 2.16: Optical pyrometer position with respect to the viewport

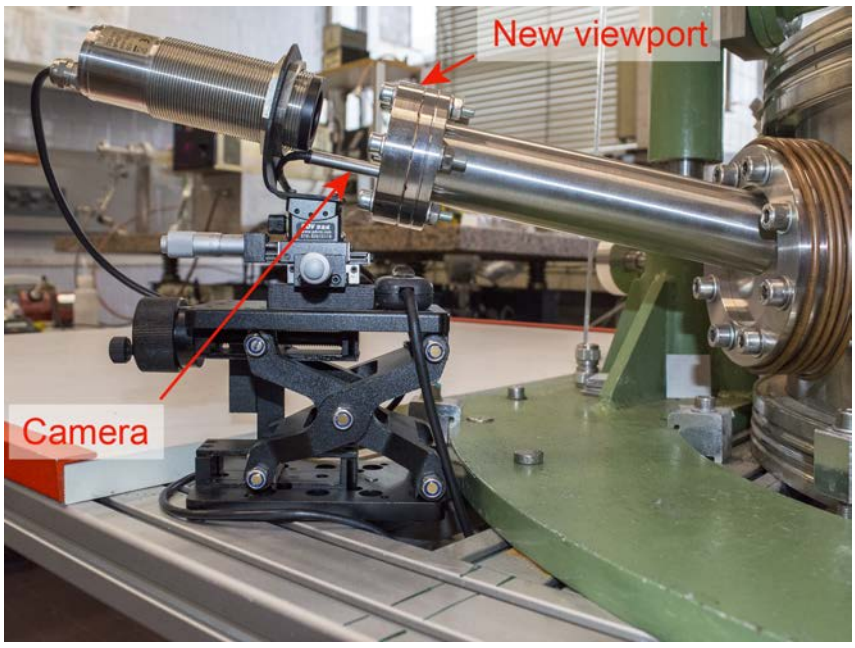

Figure 2.17: New viewport configuration

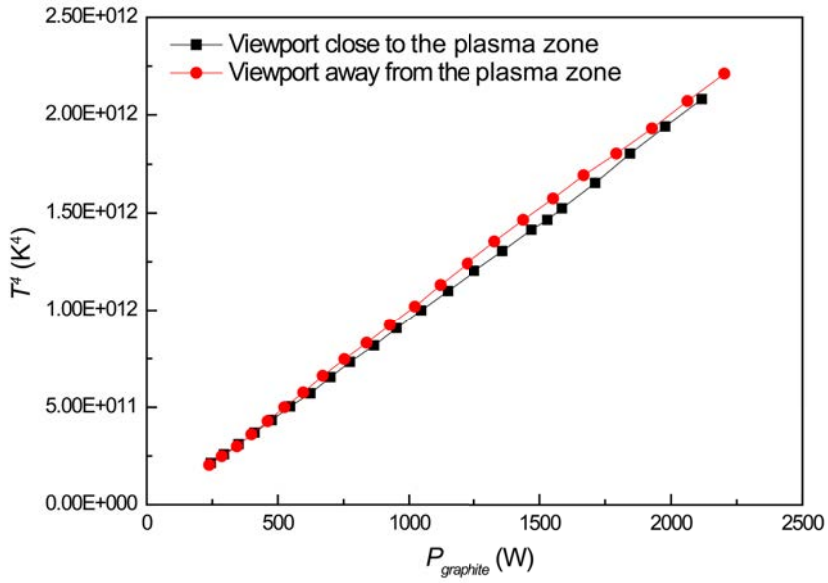

Figure 2.18: T^4 **vs power provided to the graphite resistance externally by the power supply**

heating rate of $\sim 5.5\,°C/min$. Since the surface coated with CNTs is very close to an ideal blackbody, we can employ the blackbody radiation theory. A modified Stefan Boltzmann formula would provide the net power density radiated per graphite resistance as:

$$P_{\text{graphite}} = K \cdot \varepsilon \cdot \sigma \cdot T^4 \tag{2.26}$$

where K is a constant that depends of the experimental conditions of our reactor, ε is the emissivity, T is the sample temperature in Kelvin registered by the pyrometer and $\sigma = 5.67{\times}10^{-8} W/(m^2 \cdot K^4)$ (C. C. Lee et al. 2006). During the heating several parameters were recorded: temperature, voltage and intensity (direct current source) and pressure inside the reactor chamber. It is worth mentioning that during the heating process, the reactor chamber was normally evacuated with the turbomolecular vacuum system and no gas was introduced. However, some degassing gases were produced increasing the total pressure as plotted in **Figure 2.21**. Initial pressure was 3×10^{-3}Pa.

The resistance of the cables/accessories and the resistance of the heating element (graphite resistance) were also determined, the values were 0.04Ω and 1.67Ω (measured at 800°C), respectively. Thus, the effective power provided to the graphite resistance for heating the sample was calibrated. The effective electrical power provided to the graphite resistance is distributed in several forms: a) to heat the resistance itself (its value is low and has been underestimated because the heat capacitance of graphite is low and $m_{graphite} \approx 15\,g$), b) to heat the walls of reactor by direct radiation, c) and to heat the sample and sample holder by radiation. Then, when plotting the pyrometer temperature T4 as a function of the effective power Pgraphite (calculated from the measured I and V values) a linear dependence is received (see **Figure 2.18**). This behavior can be explained in the base of the Stefan Boltzmann's law for blackbodies, because the emitted power by the sample seems to be proportional to the emitted radiation of the graphite resistance. So, by considering that ε is equal to the unit (ideal blackbody) it was possible to determine the constant K for each measurement point. Equation 1.26 can be expressed as follows:

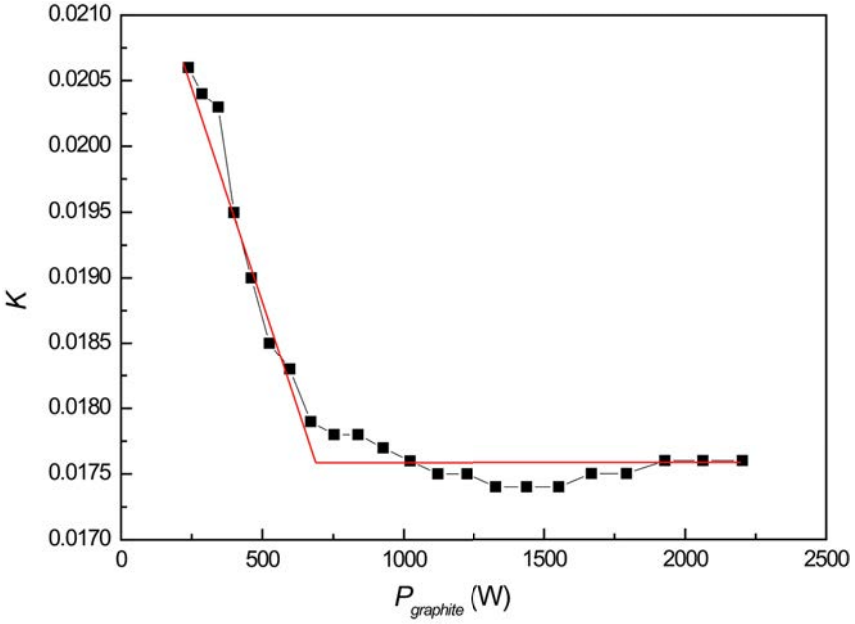

Figure 2.19: K **dependence vs power radiated per graphite resistance**

$$K = \frac{P_{\text{graphite}}}{\sigma \cdot T^4} \tag{2.27}$$

However, when the K value was plotted as a function of the power, it was observed that K changes depending on the radiated power a 18% at temperatures below 700°C (corresponding to 700 W of effective power supplied to the graphite resistance). Above 700 W, the K value keeps constant within the range of 2%, while under 700 W the value of K decreases with increasing the supplied power (see **Figure 2.19**). For practical applications, the value of the constant K that explains the behavior of our system at working temperatures is $1.76 \times 10^{-2}\,(\text{m}^2)$. This is the average of values calculated from 700 W and up to 2200 W. It is important to mention that, based on these results, it was possible to establish an expression that allows the temperature of the substrate to be predicted independently of the temperature recorded by the pyrometer. Thus, using the modified law of Stefan Boltzmann and with the value of K, the resulting expression was:

$$T = \sqrt[4]{9.98 \cdot 10^{10} P_{\text{graphite}}} \tag{2.28}$$

Figure 2.20 shows the measured T and $P_{graphite}$ values before and after the modification. In addition, the values calculated using Equation 1.28 are included. The deviation of the calculated curve from the other two curves is small, so it is a valid expression to estimate the substrate temperature independently of the pyrometer reading.

During the PID calibration experiments, it was also observed that the pressure inside the reactor chamber remained constant at around 700 °C (see **Figure 2.21**). As we passed that threshold, the pressure began to increase. This can be explained by the degassing phenomena that occur on the reactor walls. Or perhaps, under these conditions of pressure and temperature, they coincide with the vapour pressure of some internal elements of the reactor (graphite resistance –working temperatures between 2000-4000 °C– or molybdenum sheets –working temperatures < 1000 °C–). In any case, this phenomenon must be kept in mind so that it does not influence the experiments.

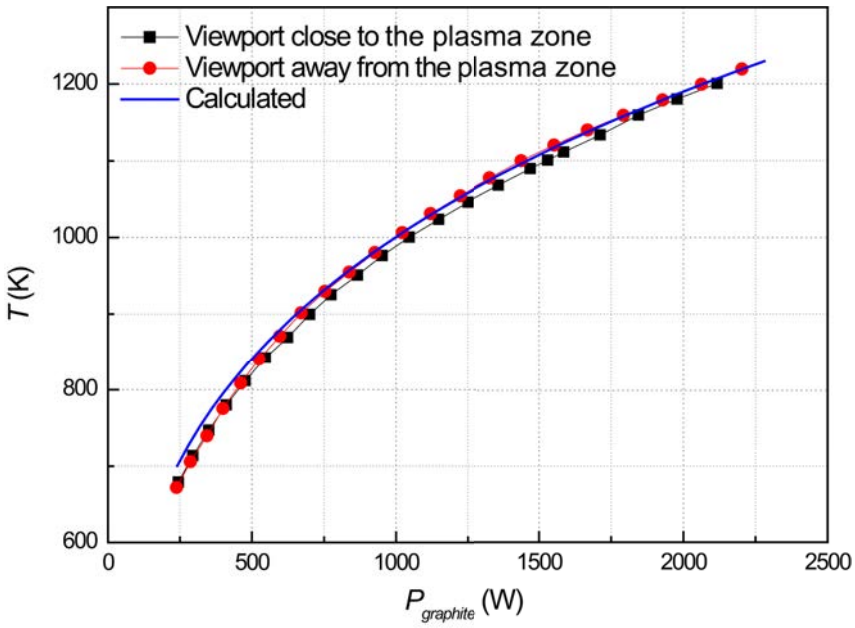

Figure 2.20: Surface sample temperature vs power radiated per graphite resistance (measured and calculated) based on blackbody radiation theory

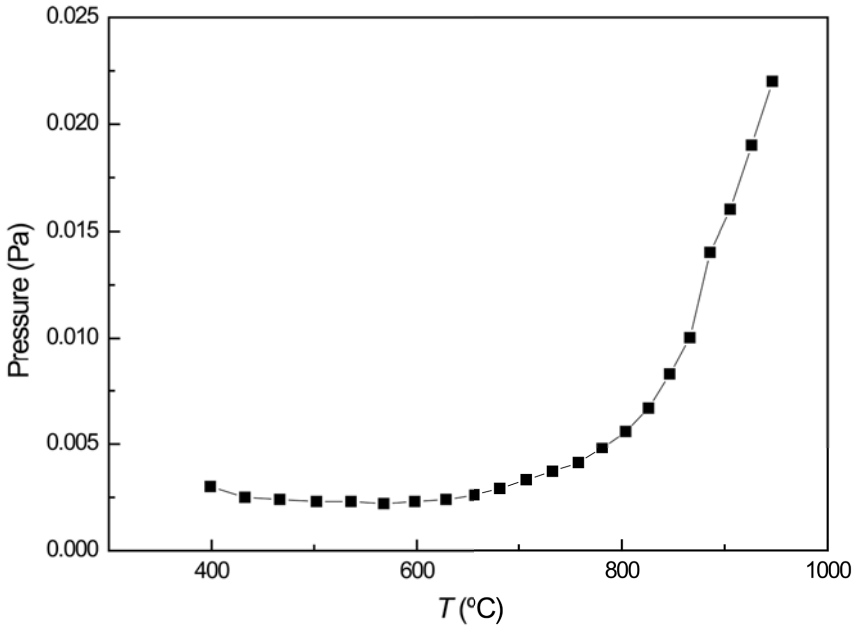

Figure 2.21: Pressure variation inside the reactor chamber

2.7.3 The power source used to generate plasmas

During this work, two sources have been used for the production of plasma in the experiments carried out. For magnetron sputtering processes in the PEDRO reactor: pulsed-DC source, ENI Reactive Plasma Generator RPG-50. For magnetron sputtering processes to deposit a thin Fe layer (catalyst material): RF (13.56MHz), Hütinger TIS 0.5/13 560. For the CNTs growth by PECVD the same RF source was used. In addition, XANTREX XDC 60-100 Digital DC Power Supply was used for the heating system.

2.7.4 CNT growth process

In general, two approaches to CNT growth were used. The first consisted in obtaining the nanotubes directly on the substrate, without the need to deposit the catalyst layer (iron). Using the CVD or PECVD process it was possible to obtain forests of CNTs on stainless steel. For this purpose, prior to growth, the surface of the substrate was subjected to a reduction process (under a hydrogen atmosphere).

The other approach followed to obtain CNTs was to deposit thin layers on steel. The sputtering process was carried out in both inert and reactive atmosphere inside the multi process reactor (PEDRO). After the deposit of the thin layers, the samples were introduced into the reactor for the growth of CNTs. In this case the catalyst was deposited using the magnetron sputtering head. Finally, using the PECVD process, the CNT forests were obtained.

It is worth mentioning that hybrid samples were also obtained between CNTs and GNWs. We collaborated with a member of our research group. These samples were prepared using an inductively coupled plasma (ICP) reactor. This type of reactor is a type of plasma source in which the energy is supplied by electric currents which are produced by electromagnetic induction, that is, by time-varying magnetic fields. The samples are listed in the part of the annexes of this work. Samples made with multi process reactor (PEDRO) and samples made in the CNT reactor are included.

As a general recommendation, regular maintenance of equipment and systems should be taken into account. Above all, those who are exposed to ammonia (rubbers become fragile), to loading stresses (the Teflon of the feedthroughs is deformed), control windows (are contaminated by exposure to species produced in plasmas). The cables and their connections should also be checked periodically, especially after the reactor has been opened. A general cleaning of the reactor interior is also recommended. Special emphasis should be placed on gate valves, as contamination often accumulates and decreases the tightness of the system. Finally, basic safety rules must be followed when operating reactors and characterization units. Avoid touching heated surfaces, energized cables and rotating elements. Due to the noise level in the laboratory, it is recommended to use hearing protection. Noise levels above 80dB can affect our hearing system in the long term. The use and disposal of chemical reagents must be done according to the University's regulations and obviously according to the recommendations of those who produce these materials.

Chapter 3

Characterization techniques

The results presented in this work were obtained by characterization techniques that are frequently used for the study of this type of materials. Among the most used are scanning electron microscopy (SEM), Raman spectroscopy, chemical analysis of surfaces by X-Ray Photoelectron Spectroscopy (XPS) and the study of crystalline structure using X-ray diffraction (XRD). These and other techniques have been used in a considerable amount of the literature consulted to characterize nanostructures. However, since one of the objectives of this research was to obtain CNTs on stainless steel, special interest has been placed on learning about the phenomena that occur on the surface and inner of that material. As can be seen in the next chapters, there are considerable changes in the properties of the substrate that can favorably or negatively affect the performance of the electrodes obtained. Therefore, special emphasis has been placed on the characterization of the substrate without neglecting the characterization of nanostructures. The characterization techniques used are reviewed below.

3.1 Electron Microscopy

The minimum distance (resolution or resolving power) between two points that can be resolved by human eyes is about $0.1 - 0.2\,\text{mm}$. **Figure 3.1** shows a comparison of seeing objects between the human eye, light microscopy and electron microscopy. A microscope could be used to study the details of the finer objects below the size of $0.1\,\text{mm}$. Electron microscopy (EM) is widely used technique that uses a beam of electrons to produce a highly magnified image of a specimen. An EM has greater resolving power than a light microscope and can reveal the structure of smaller objects because electrons have wavelengths about $100,000$ times shorter than visible light photons.

In an electronic microscope, magnetic lenses are used to direct electrons much as the optical lens is used to direct light in an optical microscope. The resolution of an optical microscope depends on two factors, wavelength of the illumination source (λ) and the numerical aperture of the lens (NA) (Law of Ernst Abbé). So, the limits of resolution (LR) can be calculated as follows:

$$LR = \frac{0.61\lambda}{NA} \tag{3.1}$$

The maximum value of NA for light microscope is approx. 1.4; it is obvious, therefore, that even the short blue light ($\lambda = 436\,\text{nm}$) of the visible spectrum will yield a resolution of only $190\,\text{nm}$. The electron microscope, however, utilizes electrons for illumination. Electrons have the characteristics of both particles and waves. The wavelength λ of the

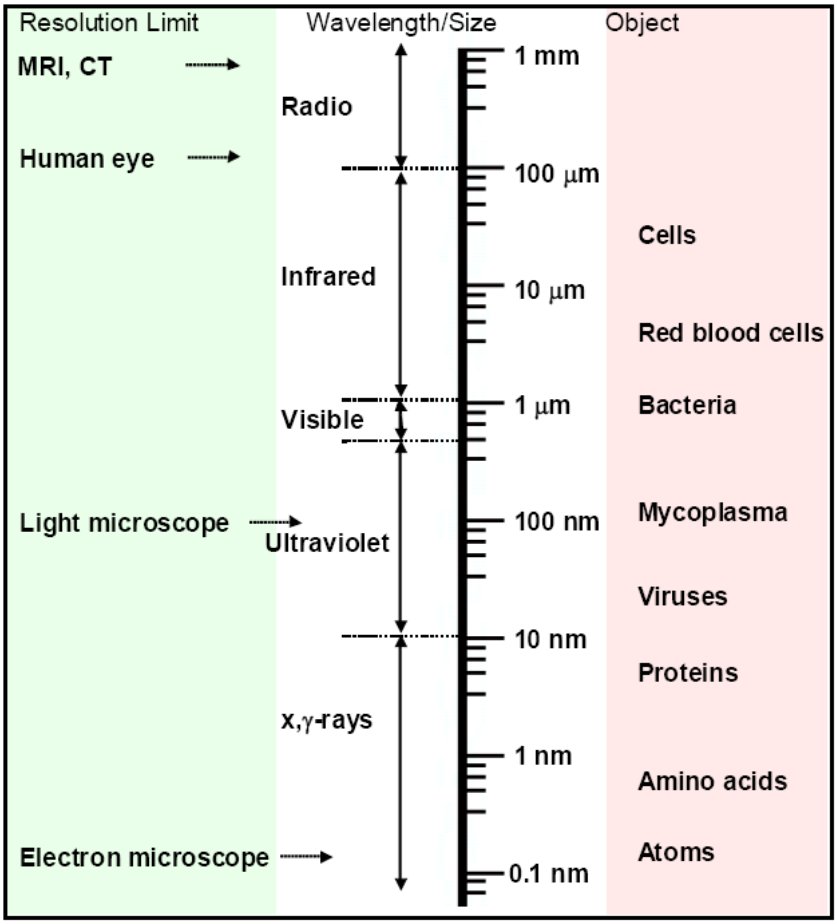

Figure 3.1: Resolution limitations of different imaging techniques, involved radiation and size of biological objects (Kaech 2013)

incident electron can be determined by the kinetic energy of the electrons, k, which follow the Broglie's expression:

$$\lambda = \frac{h}{p} = \frac{h}{\sqrt{2m_e k}} \tag{3.2}$$

where h is the Planck's constant, p is the momentum of the electron, and m_e is the electron mass.

3.1.1 Scanning Electron Microscopy (SEM)

SEM technique allows the observation of objects much smaller than those observed in the optical microscope.

As previously mentioned, this is because the wavelength associated with electrons is much lower than that of visible light, depending on their kinetic energy, according to the relationship between wavelength and momentum found by De Broglie (Equation 3.2). Taking into account the relativistic effects associated with high energies, the following expression should be considered:

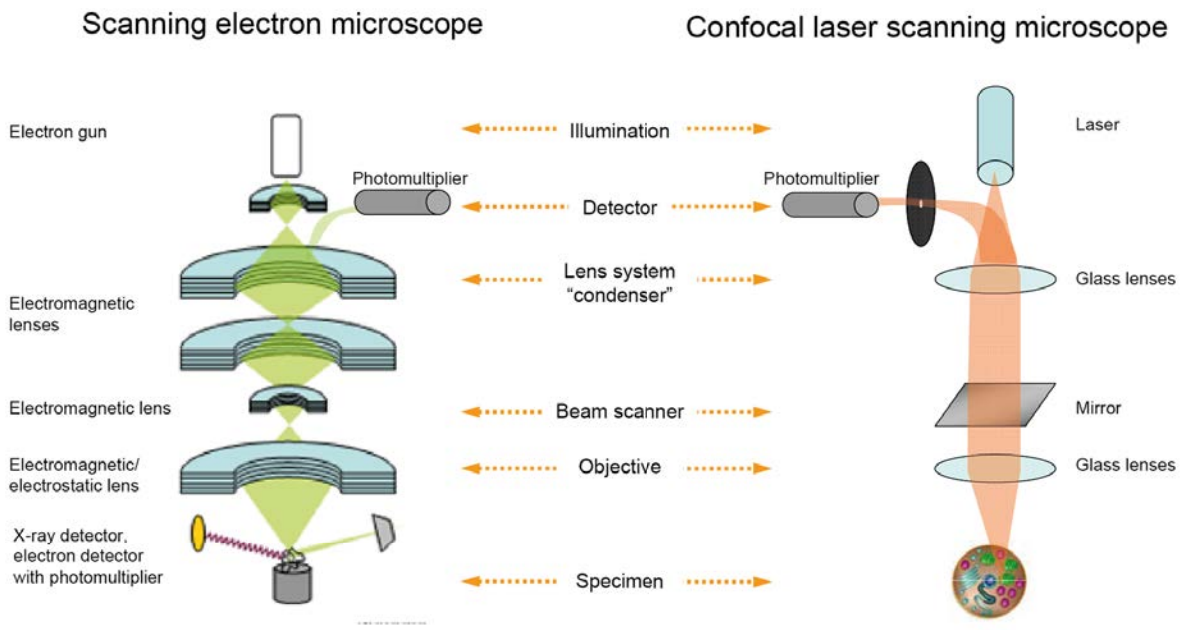

Figure 3.2: Similarity of a scanning electron microscope with a confocal laser scanning microscope (Kaech 2013)

$$\lambda = \frac{h}{\sqrt{2m_e eV_e\left(1+\frac{eV_e}{2m_e c^2}\right)}} \tag{3.3}$$

where c is the speed of light, V_e is the acceleration potential of the microscope, m_e is the mass of the electron and e is its charge.

The disposition of the elements of a scanning electron microscope is illustrated in **Figure 3.2**. Note that there is similarity between a scanning electron microscope and a confocal laser scanning microscope (Kaech 2013).

To obtain an SEM image, an electron beam is incident on the sample to be observed. This beam is generated from the emission of a hot filament or field emission source, and is accelerated by potentials typically ranging from 0.1 to 50 keV. The environmental conditions for this to be possible must be ultra-high vacuum ($< 10^{-5}$ Pa). In this way, the possibility of the residual gas affecting the observation is minimized, and the electrons of the beam are prevented from suffering any collision on their way from the source to the sample. The electrons pass through a series of magnetic lenses to obtain a coherent and collimated electron beam. The interaction between the electron beam and the sample produces several types of emissions, which are captured by different detectors within the microscope (**Figure 3.3**).

If the secondary electrons (SE) emitted (energy < 50 eV, although most of them have around 5 eV) are selected to form the image, images are obtained with topological and morphological information of the sample (**Figure 3.4a**). On the other hand, if backscattered electrons (BSE, energy > 50 eV) are used to form the image it will provide compositional information (**Figure 3.4b**). The signal coming from the electron detector (SE or BSE) is used to modulate the intensity of the electron beam on a monitor, which in turn is scanned on the monitor screen in a synchronized way with the scanning of the electron beam on the sample, creating the image. The resolution obtained in modern

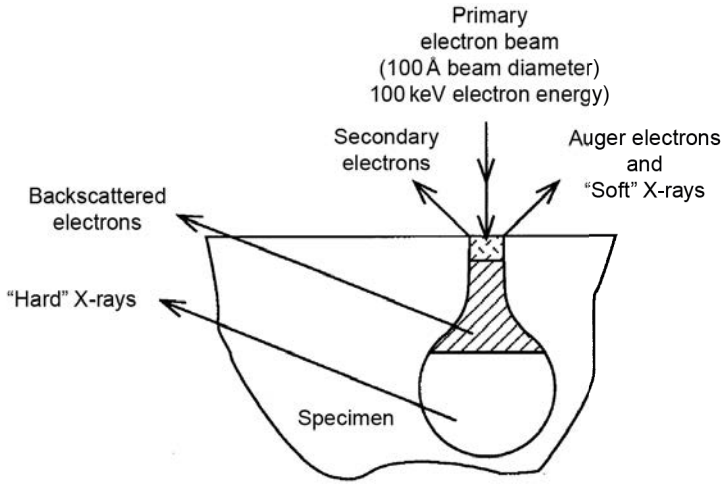

Signal	Escape depth (Å)	Effective diameter (Å)
Photoelectrons	3	100
Auger electrons/"Soft" X-rays	10	100
Secondary electrons	100	100
Backscttered electrons	3 000–10 000	3 000–10 000
"Hard" X-rays	5 000–30 000	5 000–30 000

Figure 3.3: Escape depths of various species formed by high energy electrons penetrating into a solid (Mattox 2009)

systems ranges from 50 to 20 Å. Resolutions below the nanometer can even be achieved using field emission electron sources (Albella 2018). The sample must be electrically conductive in order to be observed under such a microscope and, if it is not, it must be coated with a thin film of gold or carbon.

Every atom has a unique number of electrons that reside under normal conditions in specific positions (**Figure 3.5**). These positions belong to certain shells, which have different, discrete energies. The generation of the X-rays in a SEM is a two-step process. In the first step, the electron beam hits the sample and transfers part of its energy to the atoms of the sample. This energy can be used by the electrons of the atoms to "jump" to an energy shell with higher energy or be knocked-off from the atom. If such a transition

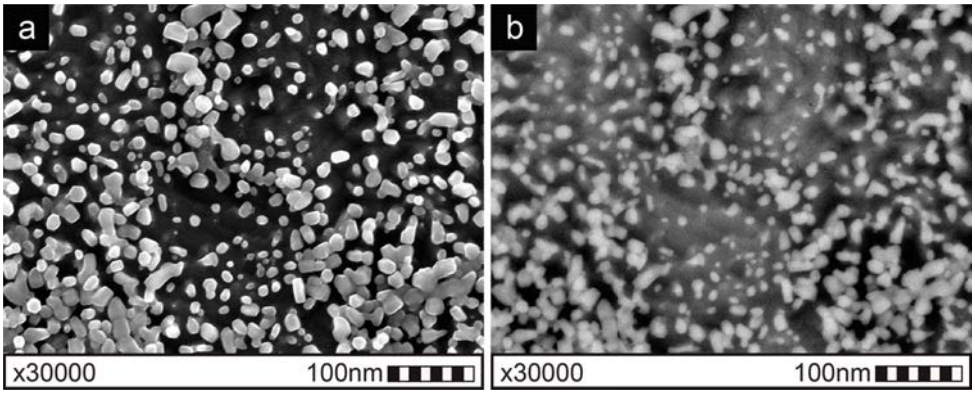

Figure 3.4: SEM images of carbide particles on ferrous alloy substrate (a) secondary electrons (b) backscattered electrons

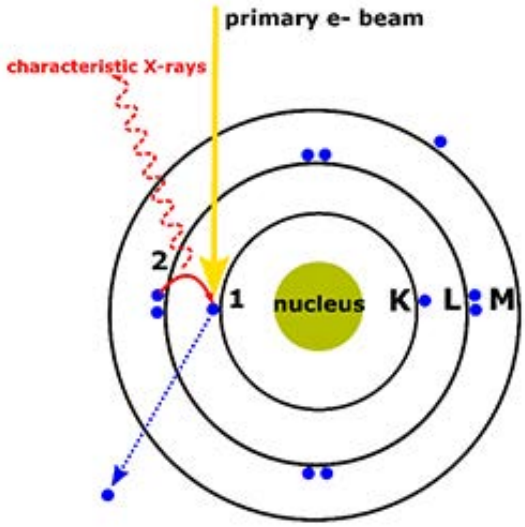

Figure 3.5: X-ray generation process: (1) The energy transferred to the atomic electron knocks it off leaving behind a hole, (2) Its position is filled by another electron from a higher energy shell and the characteristic X-ray is released (Nanakoudis 2018)

occurs, the electron leaves behind a hole. Holes have a positive charge and, in the second step of the process, attract the negatively-charged electrons from higher-energy shells. When an electron from such a higher-energy shell fills the hole of the lower energy shell, the energy difference of this transition can be released in the form of an X ray.

This X-ray has energy which is characteristic of the energy difference between these two shells. It depends on the atomic number, which is a unique property of every element. In this way, X-rays are a "fingerprint" of each element and can be used to identify the type of elements that exist in a sample.

This type of microscope may also include microanalysis tools as energy dispersive

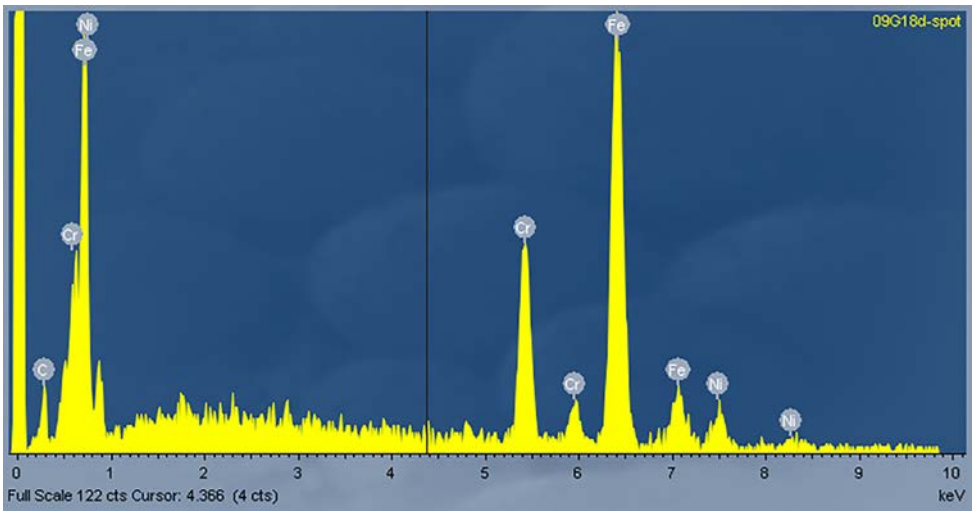

Figure 3.6: Typical EDX spectrum: y-axis depicts the number of counts and x-axis the energy of the X-rays

spectroscopy (EDX) detector. To obtain the EDX spectrum the detectors are placed under an angle, very close to the sample, and have the ability to measure the energy of the incoming photons that belong to the X-rays. The higher the solid angle between the detector and the sample, the higher the X-ray's detection probability, and therefore the likelihood of acquiring the best results.

The data that is generated by EDX analysis consists of spectra with peaks corresponding to all the different elements that are present in the sample (**Figure 3.6**). Every element has characteristic peaks of unique energy, all extensively documented. The peak height helps in the quantification of each element's concentration in the sample.

Furthermore, EDX can be used for qualitative (the type of elements) as well as quantitative (the percentage of the concentration of each element of the sample) analysis. In most SEMs, dedicated software enables auto-identification of the peaks and calculation of the atomic percentage of each element that is detected. One more advantage of the EDX technique is that it is a non-destructive characterization technique, which requires little or no sample preparation (Nanakoudis 2018). The typical applications of this technique include (Lucideon 2019):

- Characterization of material structures.

- Assessment of reaction interfaces, service environment and degradation mechanisms.

- Characterization of surface defects, stains and residues on metals, glasses, ceramics and polymers.

- Measurement of the thickness of layered structures, metallized layers, oxide films, composite materials using cross sectional imaging.

- Particulate and contaminant analysis on and within materials.

One thing that particularly caught my attention is the fact of being able to give color to SEM images. Using software like Photoshop or GIMP it is possible to easily distinguish different parts of an image. Among the research areas where this strategy has more use is in geology and life sciences. **Figure 3.7** include a couple of images where the difference

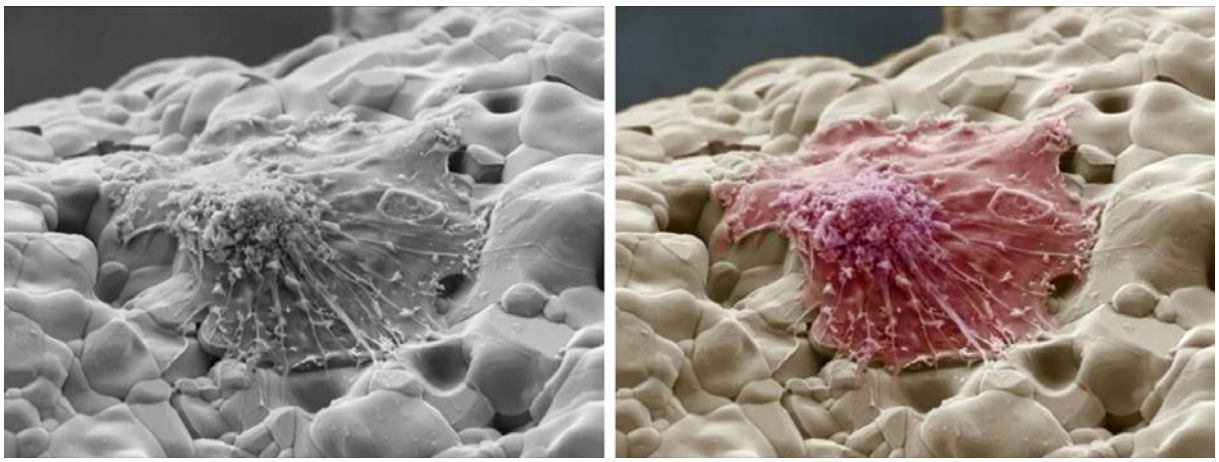

Figure 3.7: Coloring SEM images. Cell growing on a new bone repair ceramic (Myscope 2019)

between a grayscale SEM image and a colored one can be appreciated. The realism is surprising.

In this work, secondary and backscattered electrons were used to obtain SEM images. The superficial modification of the substrates used to support the forests of CNTs, after the different treatments to which they were exposed, could be observed. SEM images also allowed us to study the morphology and distribution of the nanoparticles and microparticles produced during the experiments. In addition, it allowed to observe the morphology and distribution of the CNTs. Together with the EDX detector, it was possible to have a semi quantitative and qualitative idea of the chemical composition of the substrate surface and the nanostructures produced by the PVD and PECVD processes.

3.1.2 Transmission Electron Microscopy (TEM)

In contrast with SEM, where images are obtained using secondary (SE) and backscattered (BSE) electrons, the images obtained by transmission electron microscopy (TEM) are generated from the electrons that pass through the sample, so for this type of analysis it is necessary that it is transparent to the electrons (thickness $\leq 100\,\text{nm}$). **Figure 3.8** shows the interaction of the electron beam with the specimen.

The primary electron beam passes through the thin specimen and generates non diffracted (unscattered) and diffracted electromagnetic waves (elastically and inelastically electrons). The objective lens collates the diffracted and non-diffracted waves in the image plane and forms the primary image.

Note that the TEM system is similar to a wide field light microscope (**Figure 3.9**). An electron beam is formed at the tip of a heated filament. The electrons are accelerated with high voltages ($60 - 1200\,\text{kV}$ depending on the type of TEM) and are guided through the

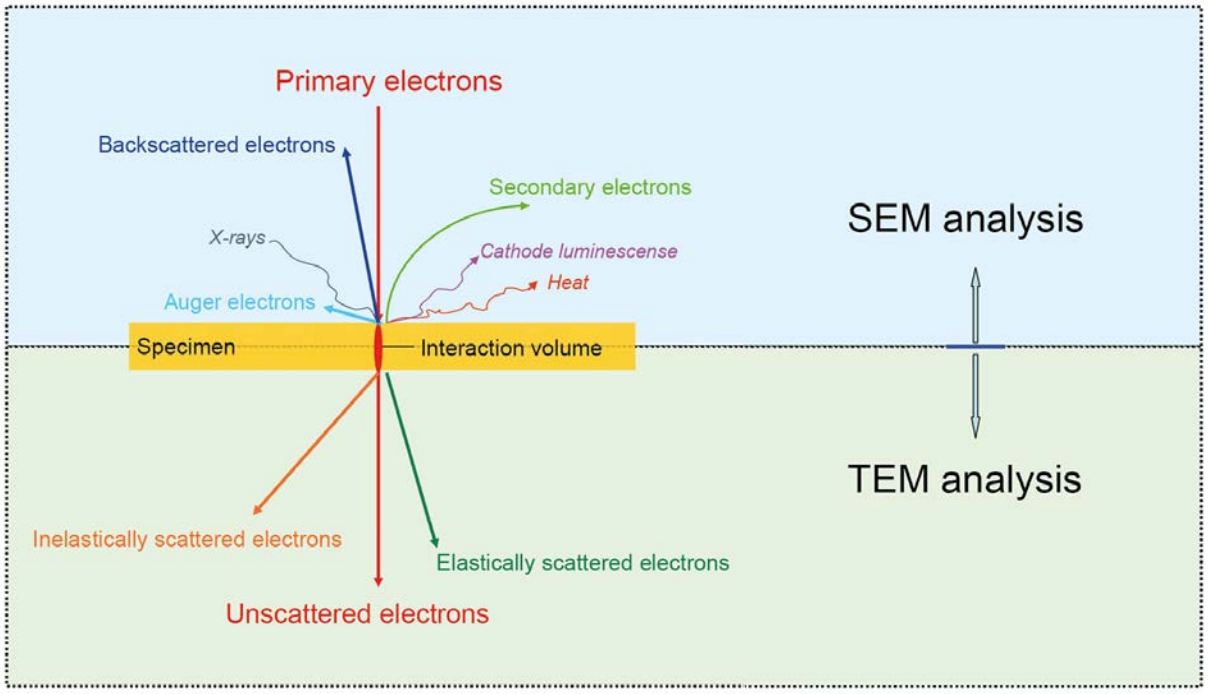

Figure 3.8: CInteraction of electrons with specimen/matter, induced radiation and emission (Kaech 2013)

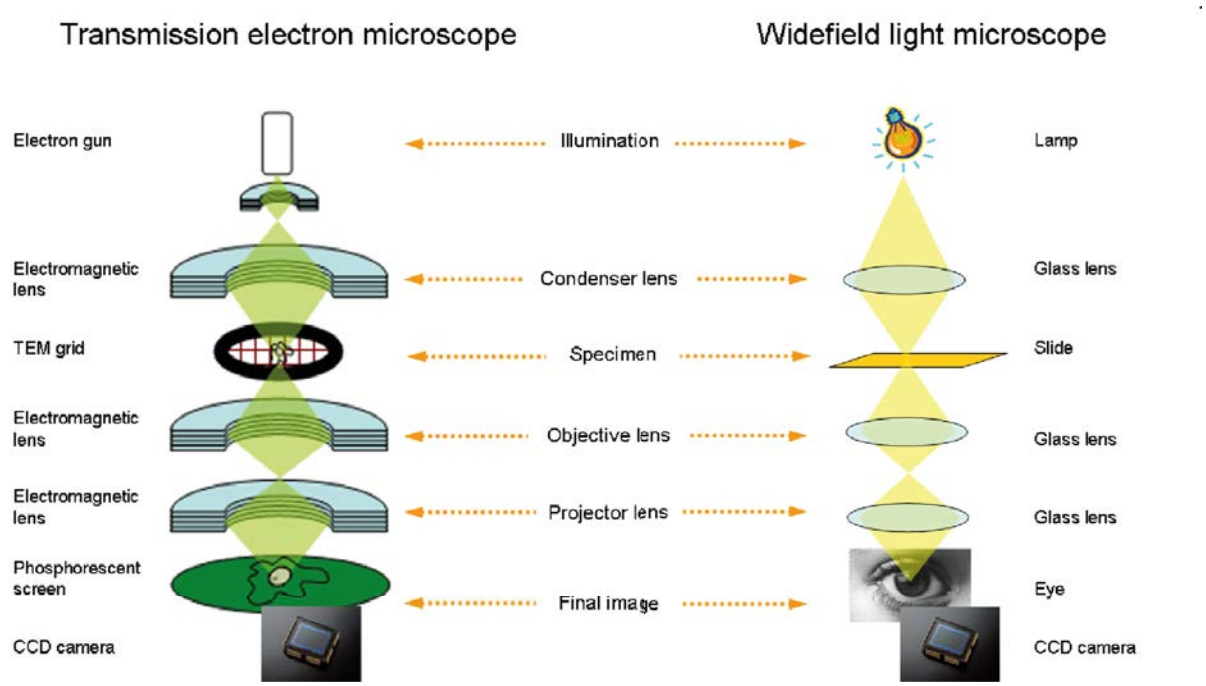

Figure 3.9: Similarity of a transmission electron microscope with a wide field light microscope (Kaech 2013)

electron microscope column by electromagnetic lenses. The beam penetrates and interacts with the specimen and leads to an image. The image is monitored on a phosphorescent screen or specially designed CCD camera and recorded (Kaech 2013). The TEM has a higher spatial resolution than the SEM ($0.1 - 1\,\text{nm}$), and can provide information at an atomic scale (in a range of several nanometers). TEM is a technique used for morphological, crystallographic and even compositional analysis of a sample.

TEM can basically operate in normal mode, HRTEM mode and SAED mode. High resolution transmission electron microscopy (HRTEM) is an imaging mode that allows for direct imaging of the atomic structure of the specimen. Selected area electron diffraction (SAED) is particularly useful as only a small area of specimen is used, and this can afterward be imaged to view the diffracting species and establish the relationship between the structure and the diffraction pattern (Meurig Thomas and Midgley 2004)

In addition, this type of microscopy may also include microanalysis tools, the most well known being the EDX technique, which is usually associated with the scanning transmission electron microscopy (STEM) visualization mode (Choi et al. 2001), and the electron energy loss spectroscopy (EELS) technique. As for SEM microscopes, the EDX technique allows the qualitative and quantitative analysis of the elements present in a sample through the X-rays emitted as a consequence of the electronic bombardment of the material. The EELS technique measures the energy lost by the electrons that disperse inelastically in the sample, and is also used for the identification and quantification of the elements present in the sample. The main difference between the two techniques is that the EELS technique offers higher spatial resolution than the EDX technique, while providing supplementary information about how the atoms in the sample are bonded. On the other hand, the EDX technique is insufficient for the detection of elements with $Z < 4$.

On the other hand, it is possible to differentiate two work modes in which images are obtained in brightfield and in darkfield. In brightfield mode, images are generated from

transmitted electrons only, i.e., electrons that retain their trajectory as they pass through the sample. However, in darkfield mode the images are generated from a diffracted beam, which is achieved by shifting the target aperture in the focal plane so that electrons whose trajectory has been varied are allowed to pass through the sample. When observing a crystalline sample, it is convenient to always specify the diffracted beam in question. Qualitatively, darkfield images are very useful for differentiating between the amorphous and crystalline phases of a material.

In this thesis samples for HRTEM were prepared as follows. CNTs which were grown by the plasma enhanced chemical vapor deposition (PECVD) technique were scratched from the stainless steel and dispersing in the absolute ethanol using an ultrasound bath. The dispersed nanotubes were deposited on the holy carbon TEM grid and analyzed by HRTEM JEOL 2100. The EDX detector was also used to perform an elemental analysis of an isolated CNT obtained directly on stainless steel surface.

3.2 Confocal microscopy

As a non-destructive technique, the confocal microscope is widely used to study the surface topography (roughness) of materials. Roughness of surfaces is of interest to a wide range of researchers in materials science. The basic key to the confocal approach is the use of spatial filtering techniques to eliminate out-of-focus light or glare in specimens whose thickness exceeds the immediate plane of focus (Olympus 2019).

Similar to the widefield microscope, the confocal microscope uses fluorescence optics. Instead of illuminating the whole sample at once, laser light is focused onto a defined spot at a specific depth within the sample (**Figure 3.10**). This leads to the emission of fluorescent light at exactly this point. A pinhole inside the optical pathway cuts off signals that are out of focus, thus allowing only the fluorescence signals from the illuminated spot to enter the light detector. By scanning the specimen in a raster pattern, images of one

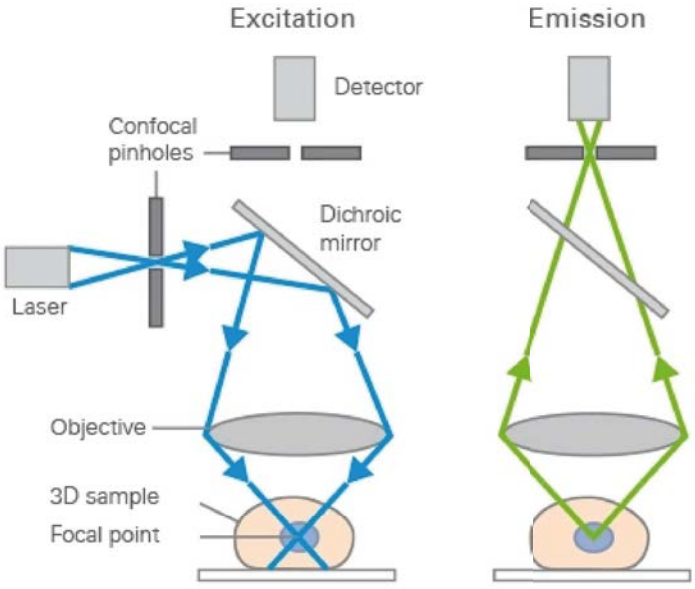

Figure 3.10: Excitation and emission light pathways in a basic confocal microscope configuration (Ibidi 2019)

single optical plane are created. 3D objects can be visualized by scanning several optical planes and stacking them using a suitable microscopy deconvolution software (z stack) (Ibidi 2019).

Compared with conventional widefield optical microscopy, confocal microscopy offers several advantages, including the ability to control depth of field, elimination or reduction of background information away from the focal plane (that leads to image degradation), and the capability to collect serial optical sections from thick specimens. In addition, operating a confocal microscope is relatively easy, and images can be developed quickly. The technique produces high quality images of a specific area of a specimen. A limitation of confocal microscopy is that it can lose intensity due to light passing through small pinholes so long exposure is needed (Cavanagh et al. 1994).

Each confocal microscope is usually controlled through a dedicated software for that purpose. For example, our research group has a SENSOFAR microscope and the software used to collect and process the data is called SensoMap. With this type of software, it is possible to obtain a variety of surface parameters. A powerful tool available in this software is the generation of Abbott-Firestone curve or also known as the bearing area curve (BAC) analysis. This statistical method makes it possible to know the surface texture of an object (Jurečka et al. 2018). The distribution of the material can be known through a curve. The parameters that can be obtained from the BAC are varied (Keyence 2019). The PECVD effect on substrate topography was studied using this technique. Additionally, some Abbott-Firestone curves were generated which were very useful to analyze the evolution of the topography according to each process used.

3.3 X-ray Photoelectron Spectroscopy (XPS)

X-ray Photoelectron Spectroscopy (XPS) also known as Electron Spectroscopy for Chemical Analysis (ESCA) is the most widely used surface analysis technique because it can be applied to a broad range of materials and provides valuable quantitative and chemical state information from the surface of the material being studied. The average depth of analysis for an XPS measurement is approximately 5 nm (PhysicalElectronics 2019).

A target solid material is irradiated by the X-ray photons whose energy ($h\nu$) is high

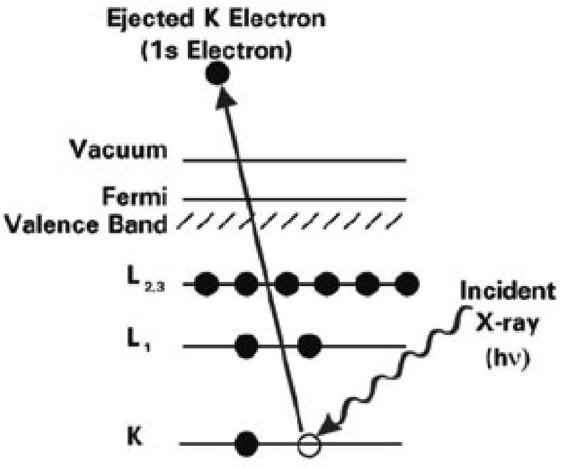

Figure 3.11: The photoemission process involved for XPS surface analysis

enough to knock out the electron from the K shell of the atom (**Figure 3.11**). The $K - shell$ electron would be ejected from the surface as a photoelectron with a kinetic energy E_k. We can calculate the binding energy of the atom's photoelectron (E_B) by the following expression:

$$E_B = hv - E_k - \phi \tag{3.4}$$

Where h is Plank's constant, v is the frequency, ϕ represents the energy required for an electron to escape from the material. The ϕ depends on both the sample material and the spectrometer.

XPS is performed in the environment with a vacuum pressure range of 10^{-8}–10^{-10} mbar to keep the surface of the sample free from contaminants and reduce the chance of low energy electrons being scattered by gas molecules on their way to reach the detector. Scattering will reduce signals intensity and increase background noise in spectra. In XPS soft characteristic X-ray Al Kα and Mg Kα are generated by X-ray anode materials, Al and Mg, whose energies 1.4866 and 1.2536 keV are used. XPS requires a line width less than 1.0 eV to ensure good energy resolution. Both AlKα and MgKα exhibits line width less than 1.0 eV and also have sufficient energies. An XPS spectrum can have three types of peaks on a background: photo-emission from core electron levels, photo emission from valance levels and Auger emission excited by X-rays. As can be seen in **Figure 3.12**, XPS spectra have a step like background, increasing with binding energy. They result from inelastic scattering of photoelectrons in a solid. The XPS spectrum can also include extra, or satellite, peaks associated with a main core level peak. Note that the nomenclature used to identify the XPS peaks refers to the level from which the electron is emitted. Following this nomenclature, the main quantum number appears first, followed by the corresponding value of: $l = 0, 1, 2, 3,$ andsoon. (designated by the letters $s, p, d, f,$ etc., respectively) and finally, the values of j are assigned as suffixes. Thus, the state corresponding to level L_3 in X-ray notation, in which $n = 2, l = 1$ and $j = 3/2$, is expressed as 2 $p_{3/2}$ in XPS spectroscopy. Auger transitions are named after the same X-ray nomenclature (Albella 2018).

XPS spectra are, for the most part, quantified in terms of peak intensities and peak

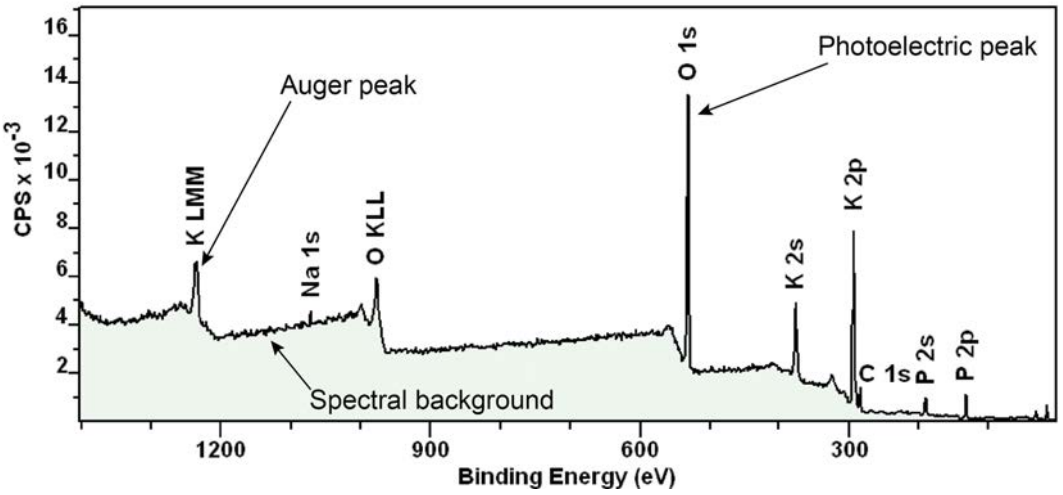

Figure 3.12: Example of a survey spectrum with multiple elements within the sample surface.

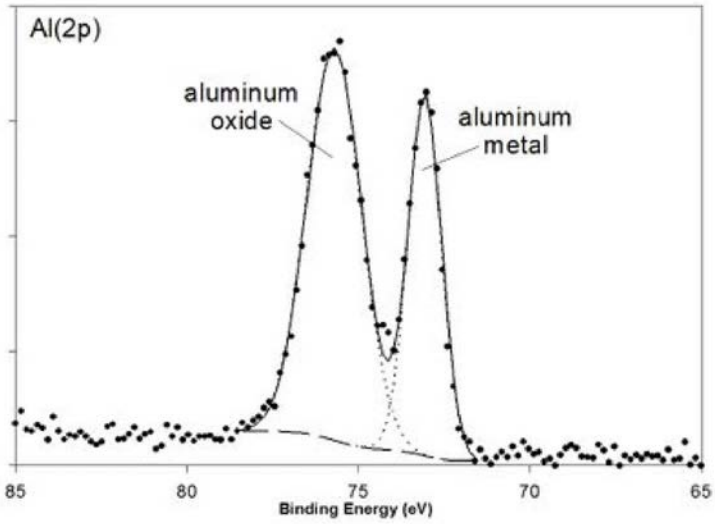

Figure 3.13: Al $2p$ XPS spectrum of a thin film Al oxide on Al metal (M. Biesinger 2018)

positions. The peak intensities measure how much of a material is at the surface, while the peak positions indicate the elemental and chemical composition. Other values, such as the full width at half maximum (FWHM) are useful indicators of chemical state changes and physical influences. That is, broadening of a peak may indicate: a change in the number of chemical bonds contributing to a peak shape, a change in the sample condition (x-ray damage) and/or differential charging of the surface (localized differences in the charge-state of the surface) (CasaXPS 2013).

In addition, it is possible to quantify isolated peaks of the survey spectrum. For this purpose, XPS high resolution spectrum must be obtained (**Figure 3.13**). XPS high resolution spectrum, depending on their complexity, can be adjusted (deconvoluted) using one or several subpeaks. Special care must be taken in quantification, especially when selecting relative sensitivity factors (RSF). The processing of the data obtained during the XPS characterization can be performed using a variety of options. The CASA XPS software has been used for this work.

Definitely the study of the chemical composition of surfaces is of great interest for an infinite number of applications. In this sense, the XPS characterization is impresicindible in the study of surfaces. The surface represents a discontinuity between one phase and another and, therefore, the physical and chemical properties of the surface are different from those of the bulk material. These differences affect the topmost atomic layer of the material to a large extent. In the bulk of the material, an atom is surrounded on all sides in a regular manner by atoms composing that material. Because a surface atom is not surrounded by atoms on all sides, it has bonding potential, which makes the surface atom more reactive than atoms in the bulk (ThermoFisher 2019).

Figure 3.14 summarizes some of the properties and processes (related with the depth) that take place on the surface of materials. Through XPS technique, it is possible to obtain very valuable information to properly understand the phenomena that occur on the surface. In contrast to SEM/EDX which has a typical analysis depth of $1 - 3\,\mu$m, XPS is a surface analysis technique with a typical analysis depth of less than 5 nm (few number of atomic layers) and is therefore better suited for the compositional analysis of

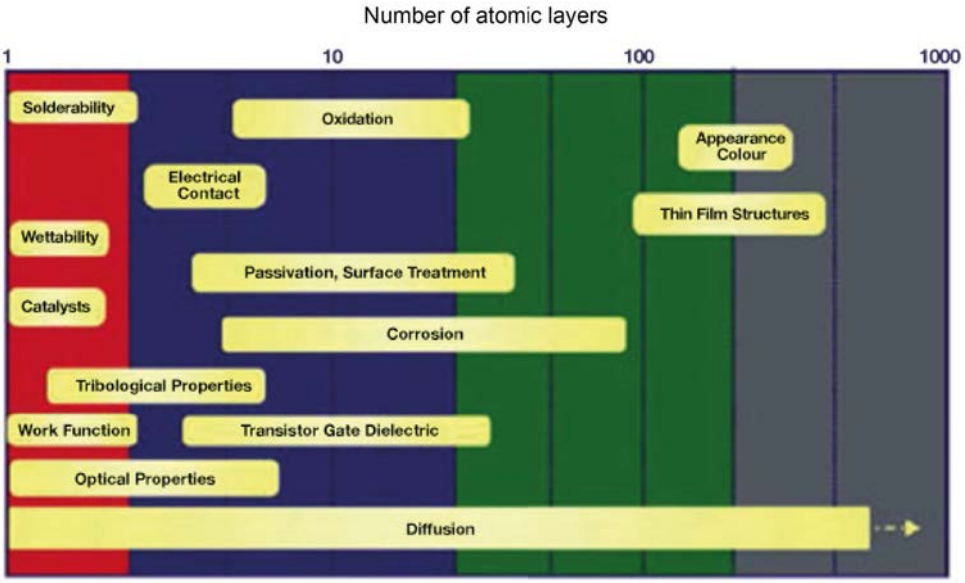

Figure 3.14: Common properties and processes as a function of the depth or thickness (ThermoFisher 2019)

ultra-thin layers and thin microscale sample features.

With this technique it is also possible to study the chemical composition in depth (depth profile) (**Figure 3.15**). Using a sputtering process, Ar gas is normally used, the first atomic layers of material are removed, allowing regions of the material previously covered to be exposed. The sputtering process can be repeated as many times as necessary. At the end a chart of chemical composition (at.%) as a function of sputtering time or depth is obtained. This approach is widely used to characterize thin film structures. The information that XPS provides about surface layers or thin film structures is important for

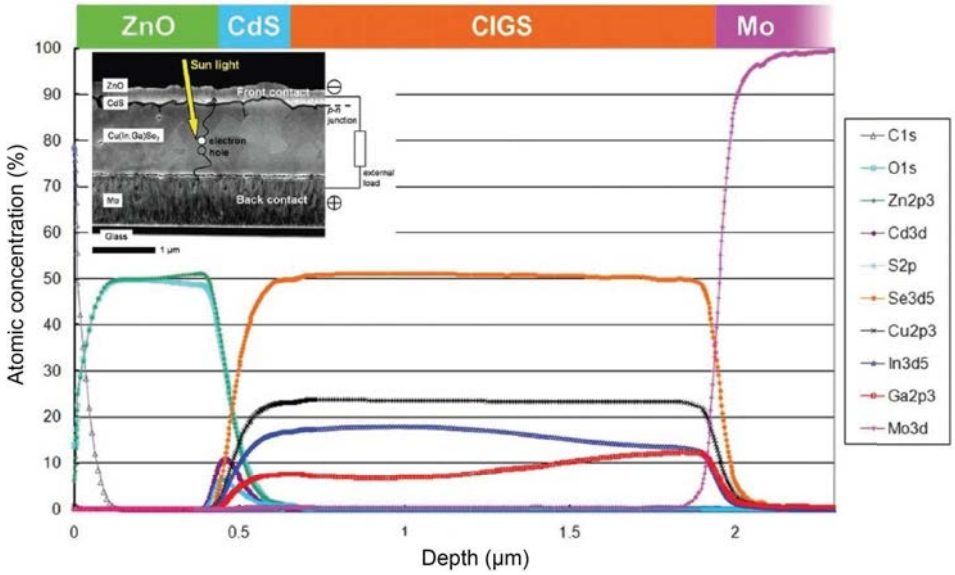

Figure 3.15: Compositional analysis of solar cell (multilayer structure) (AmericanLaboratory 2010)

many industrial and research applications where surface or thin film composition plays a critical role in performance including: nanomaterials, photovoltaics, catalysis, corrosion, adhesion, electronic devices and packaging, magnetic media, display technology, surface treatments, and thin film coatings used for numerous applications.

In our case, the chemical composition of the surface and the depth profile of the stainless steel were obtained through this technique, after being reduced (PECVD). In addition, the chemical composition of thin layers deposited by reactive magnetron sputtering (PVD) was identified.

3.4 X-ray diffraction (XRD)

X-ray diffraction is a nondestructive technique that is used to determine the detailed structure of a material (size and shape of diffracting domains, distribution of size, lattice deformation, the nature of dislocations and the occurrence of faults or "mistakes" in the structure) (Mittemeijer and Scardi 2004), which leads to knowledge of the positions occupied in space by the atoms, ions or molecules that make it up. This arrangement, together with the periodicities and symmetries involved, determines to a significant part of the physical, mechanical and chemical properties of the materials. A clear and well known example is the two allotropic structures of carbon: diamond and graphite, which have radically different properties despite having identical chemical composition. **Figure 3.16** shows simulated spectra of diamond and graphite compared to soot. Although they

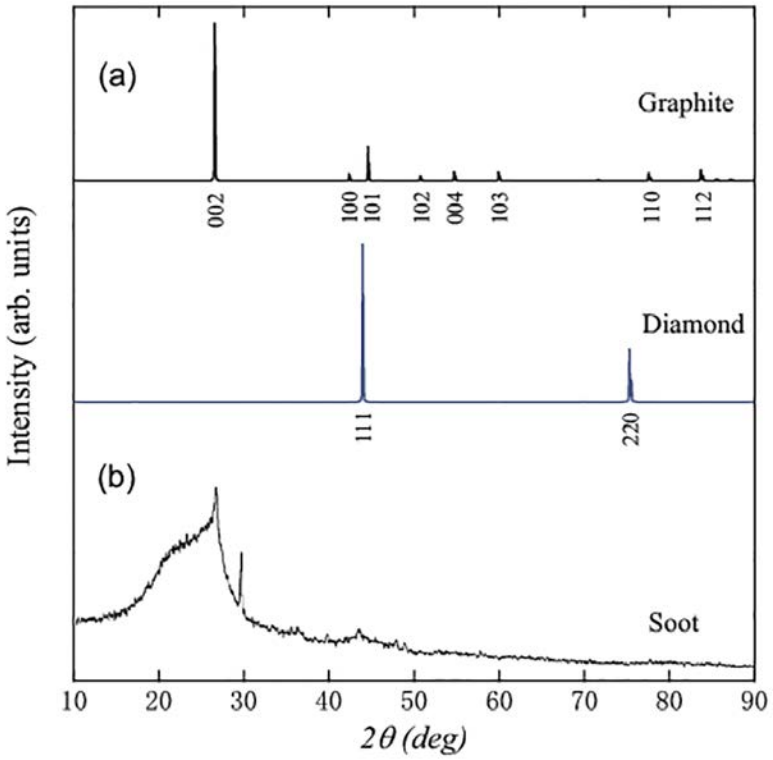

Figure 3.16: X-ray diffraction (XRD) patterns. (a) Simulated XRD patterns for graphite and diamond. (b) Experimental XRD patterns for TNT/diesel oil detonation soot. X-ray wavelength is 1.5406 Åwith a copper source (J.-T. Wang et al. 2015)

have the same chemical composition, the characteristic X-ray diffraction patterns of each material differ from each other.

XRD is definitely a powerful technique for discerning between materials with same chemical composition. Therefore, a good structural characterization of a material is essential to understand its properties and, consequently, be able to develop materials with the correct properties depending on the application planned.

In addition to the structure at the atomic level, a determining aspect is the structure at the nanometric level. The properties of a material can and do change when it is obtained with nanometric dimensions, i.e. some of its dimensions are in the order of the nanometer or a few tens of nanometers $10^{-9} - 10^{-7}$ m (Albella 2018).

X-ray diffractometers consist of three basic elements: an X-ray tube, a sample holder, and an X-ray detector (**Figure 3.17**). X-rays are generated in a cathode ray tube by heating a filament to produce electrons, accelerating the electrons toward a target by applying a voltage, and bombarding the target material with electrons. When electrons have sufficient energy to dislodge inner shell electrons of the target material, characteristic X-ray spectra are produced. These spectra consist of several components, the most common being K_α and K_β. K_α consists, in part, of $K_{\alpha 1}$ and $K_{\alpha 2}$. $K_{\alpha 1}$ has a slightly shorter wavelength and twice the intensity as $K_{\alpha 2}$. The specific wavelengths are characteristic of the target material (Cu, Fe, Mo, Cr). Filtering, by foils or crystal monochrometers, is required to produce monochromatic X-rays needed for diffraction. $K_{\alpha 1}$ and $K_{\alpha 2}$ are sufficiently close in wavelength such that a weighted average of the two is used. Cu is the most common target material for single crystal diffraction, with Cu K_α radiation=1.5418 Å. These X-rays are collimated and directed onto the sample. As the sample and detector are rotated ($\theta/2\theta$ scanning method), the intensity of the reflected X-rays is recorded. The instrument used to maintain the angle and rotate the sample is termed a goniometer (Dutrow 2019).

When the geometry of the incident X-rays impinging the sample satisfies the Bragg's Law, constructive interference occurs and a peak in intensity occurs. A detector records and processes this X-ray signal and converts the signal to a count rate which is then output to a device such as a printer or computer monitor.

Note that Bragg's Law relates the wavelength (λ) of electromagnetic radiation to the diffraction angle (θ) and the lattice spacing in a crystalline sample (d) defined by the

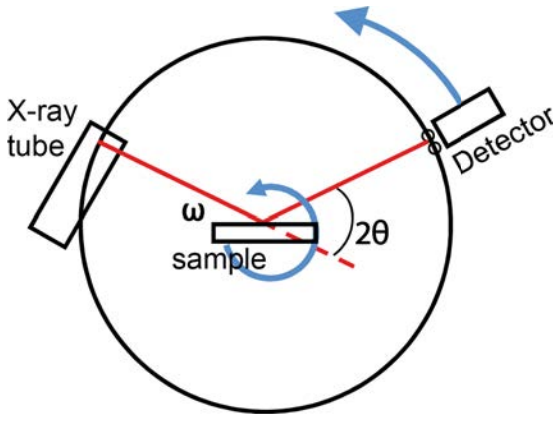

Figure 3.17: Illustration of the system to obtain XRD pattern. Diffraction pattern is a plot of the intensity of X-rays scattered at different angles by a sample (Speakman 2011c)

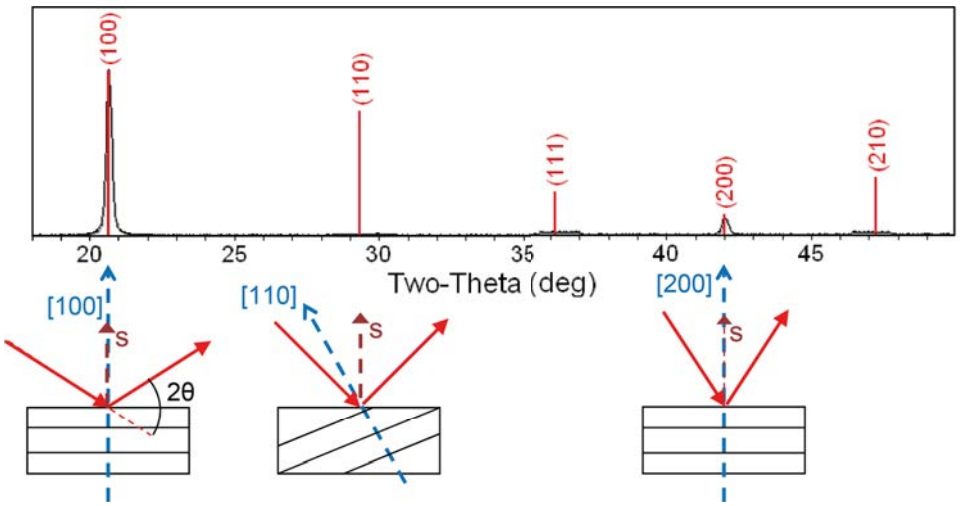

Figure 3.18: X-ray diffraction (XRD) pattern of monocrystal material (Speakman 2011a)

Miller indices hkl, as follow:

$$n\lambda = 2d \sin\theta \tag{3.5}$$

The wavelength of X-rays is in the order of the interatomic distances of the crystals, which act as diffraction grids.

The characteristic X-ray diffraction pattern generated in a typical XRD analysis provides a unique "fingerprint" of the crystals present in the sample. When properly interpreted, by comparison with standard reference patterns and measurements, this fingerprint allows identification of the crystalline form (ParticleAnalytical 2019).

The monocrystal materials have a characteristic X-ray diffraction pattern as shown in **Figure 3.18**. A single crystal specimen in a Bragg-Brentano diffractometer would produce only one family of peaks in the diffraction pattern. At 20.6° 2θ, Bragg's law fulfilled for the (100) planes, producing a diffraction peak. The (110) planes would diffract at 29.3° 2θ; however, they are not properly aligned to produce a diffraction peak (the perpendicular to those planes does not bisect the incident and diffracted beams). Only background is observed. The (200) planes are parallel to the (100) planes. Therefore, they also diffract for this crystal. Since d_{200} is 1/2 d_{100}, they appear at 42° 2θ.

However, when a polycrystalline material is studied with this technique, in the X-ray diffraction pattern appear the signal of more planes (**Figure 3.19**). A polycrystalline sample should contain thousands of crystallites. Therefore, all possible diffraction peaks should be observed. For every set of planes, there will be a small percentage of crystallites that are properly oriented to diffract (the plane perpendicular bisects the incident and diffracted beams). Basic assumptions of diffraction are that for every set of planes there is an equal number of crystallites that will diffract and that there is a statistically relevant number of crystallites, not just one or two.

When diffraction patterns of thin ($1 - 1000$ nm) films are obtained using conventional $\theta/2\theta$ scanning methods generally produces a week signal from the film and an intense signal from the substrate. One of the ways to avoid intense signal from the substrate and get stronger signal from the film itself is to perform a scan with a fixed grazing angle of incidence, popularly known as GIXRD. The fixed angle is generally chosen to

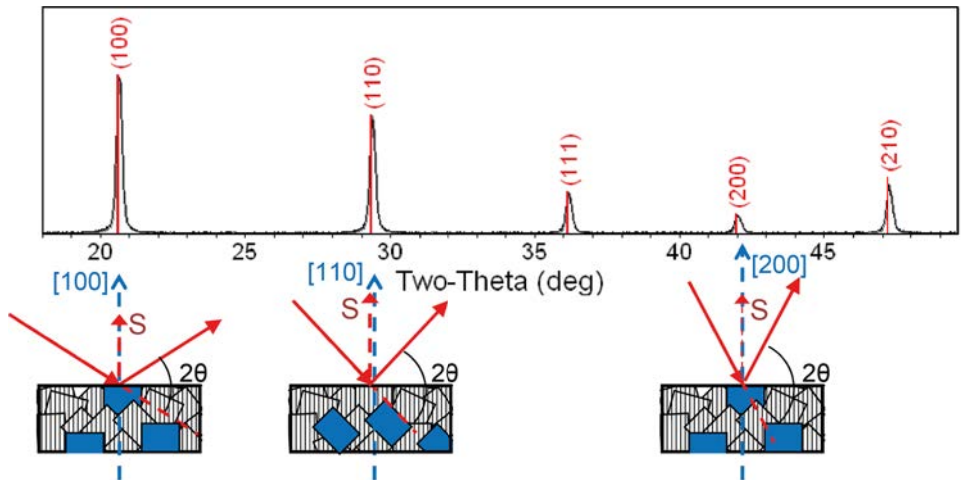

Figure 3.19: X-ray diffraction (XRD) pattern of polycrystal material (Speakman 2011a)

be slightly above the critical angle for total reflection of the film material (Rigaku 2019). The incident angle is fixed at a very small angle ($< 5°$) so that X-rays are focused in only the top most surface of the sample (Speakman 2011a).

There are different ways to extract peak information for quantitative analysis. Numerical methods reduce the diffraction data to a list of discrete diffraction peaks. The peak list records the position, intensity, width and shape of each diffraction peak. Calculations must be executed on the peak list to yield any information about the sample. This list of peaks itself says nothing about the sample. Additional analysis must be done on the peak list to extract information. Thus, from the peak list it is possible to determine (Speakman 2011c):

- Phase composition: by comparison to a database of reference patterns.
- Semi-quantitative phase composition: calculated from peak intensities for different phases.
- Unit cell lattice parameters: calculated from peak positions.
- Crystal system: determined by indexing observed peaks and systematic absences.
- Crystallite size and microstrain: calculated from peak widths and/or shapes.
- A number of engineering indexes are also calculated from peak list information.

Several full pattern fitting methods have been developed over time to extract information from peak list. Those methods refine a model of the sample. In general, the refinement process involves the following tasks:

- A diffraction pattern is calculated from a model.
- The calculated and experimental diffraction patterns are compared.
- The model is refined until the differences between the observed and calculated patterns are minimized.

- The Rietveld, LeBail, and Pawley fitting methods use different models to produce the calculated pattern.

The method proposed by Hugo Rietveld is among the most widely used refining methods. Rietveld refinement is a tool that tries to model a full diffraction profile based on crystal structure data, specimen and instrument effects. This is achieved by introducing certain functions that describe typical phenomena in powder diffraction experiments, like 2θ errors or peak broadening, and by fitting the corresponding parameters afterwards. The parameters are varied using a least-squares procedure, in order to minimize the difference between the calculated and the experimental diffraction pattern (Crystalimpact 2019).

For this work, the crystal size, among the vast information that can be obtained with this characterization technique, was calculated from the diffraction patterns of the substrate and the thin layers deposited by magnetron sputtering. For this, the expression developed by Paul Scherrer was used. Scherrer derived his equation for the ideal condition of a perfectly parallel, infinitely narrow and monochromatic X-ray beam incident on a monodisperse powder of cube-shaped crystallites. The equation is:

$$D_{\mathrm{hkl}} = K\lambda / \left(B_{\mathrm{hkl}} \cos\theta\right) \tag{3.6}$$

where D_{hkl} is the crystallite size in the direction perpendicular to the lattice planes, hkl are the Miller indices of the planes being analyzed, K is a numerical factor frequently, referred to as the crystallite-shape factor, λ is the wavelength of the X-rays, B_{hkl} is the width (full-width at half-maximum-FWHM) of the X-ray diffraction peak in radians and θ is the Bragg angle. In addition to depending on the crystallite shape, the numerical factor K also depends on the definitions of the average crystallite size (for example, if the cube root of the crystallite volume is used instead of the definition above) and the width (for example, if the integral line width is used, as in von Laue's derivation of Scherrer's formula, rather than the full-width at half-maximum, which is usually easier to obtain from experimental data). The structure of the formula is not affected by these definitions, but the numerical value of K may change appreciably (Holzwarth and Gibson 2011). The most common values for K are 0.94 (for FWHM of spherical crystals with cubic symmetry) and 0.89 for integral breadth of spherical crystals with cubic symmetry (Speakman 2011b).

According to Scherrer's equation, peak width due to crystallite size varies inversely with crystallite size. Or which is tantamount to saying that as the crystallite size gets smaller, the peak gets broader. It is important to bear in mind that the crystallite size broadening is most pronounced at large angles 2θ. However, the instrumental profile width and microstrain broadening are also largest at large angles 2θ. As general recommendation, if using a single peak, often get better results from using diffraction peaks between 30 and 50° 2θ (Speakman 2011b).

As can be seen, X-ray powder diffraction is most widely used for the identification of unknown crystalline materials (e.g. minerals, inorganic compounds). Determination of unknown solids is critical to studies in geology, environmental science, material science, engineering and biology. Other applications include: characterization of crystalline materials, identification of fine-grained minerals such as clays and mixed layer clays that are difficult to determine optically, determination of unit cell dimensions and measurement of sample purity. With specialized techniques, XRD can be used to: determine crystal structures using Rietveld refinement, determine of modal amounts of minerals (quantitative analysis). In addition, characterize thin films samples (GIXRD mode) by: determining

lattice mismatch between film and substrate and to inferring stress and strain, determining dislocation density and quality of the film by rocking curve measurements, measuring superlattices in multilayered epitaxial structures, determining the thickness, roughness and density of the film using glancing incidence X-ray reflectivity measurements (Dutrow 2019).

3.5 Optical emission spectroscopy (OES)

Optical emission spectroscopy (OES) is a non-intrusive technique used to characterize a plasma. This technique consists of collecting the light emitted in a discharge and separating it into the different wavelengths that compose it by means of a spectrophotometer, obtaining an emission spectrum. The lines or peaks of which these spectra are composed correspond to the transitions between two energetic states of the atoms and/or molecules, in their neutral or ionic state, which are found in the discharge volume. Since the energy corresponding to these transitions is characteristic of each element or compound, it is possible to identify the species present in the plasma (Bruker 2019).

Emission lines include monoatomic transitions on the one hand and bands associated with molecules on the other. These bands consist of transitions between rotational and vibrational states in addition to atomic transitions (Machala et al. 2007). These peaks are difficult to resolve individually, so the best way to evaluate the resolution of a spectrophotometer is to measure the half width at half maximum (FWHM) of a monoatomic emission peak. With regard to peak width, there are several fundamental mechanisms that contribute to wavelength dispersion (Devia et al. 2015):

- Heisenberg's uncertainty principle

$$\Delta E \cdot \Delta t \geq \hbar/2 \tag{3.7}$$

  There is a fundamental broadening because the half-life of an excited state is limited, from which an uncertainty in the associated energy is deduced. There is a fundamental broadening because the half-life of an excited state is limited, from which an uncertainty in the associated energy is deduced.

- The Doppler effect
  The dispersion in the speed (modulus and direction) of the species with respect to the detector causes the peak to broaden around the maximum wavelength.

- The medium pressure
  The proximity between colliding atoms or molecules causes a shift in the respective energy levels, and therefore in the respective emission lines.

- The Stark effect
  The charged particles (ions or electrons) have an associated electric field, so when colliding with a neutral particle, the electronic levels of these atoms or molecules unfold, which contributes again to the broadening of the lines.

But the fundamental broadening of the transmission lines is usually masked by the resolution of the device. As for the intensity of the peaks, this depends on the density within the plasma of the species that generate them. It is important to know which mathematical function corresponds or comes closest to the shape of the observed peaks, for example, when a band or two very close peaks require deconvolution. The broadening

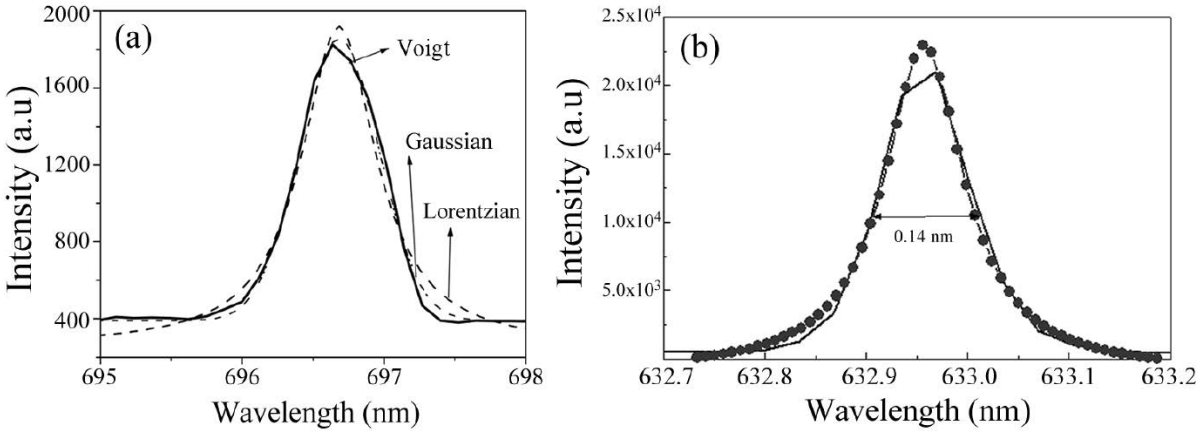

Figure 3.20: (a) Spectral line shape combining both Gaussian and Lorentzian profiles and (b) spectral line shape obtained from a He-Ne laser for determining the instrumental broadening (Devia et al. 2015)

can be Gaussian, Lorentzian or Voigt (a mixture of Lorentzian and Gaussian), as shown in **Figure 3.20a**. In the case where the dominant broadening mechanism is the Doppler effect, the peaks approach Gaussian (low pressure conditions), while the broadening due to collisions induces a Lorentzian shape (high pressure conditions). In the case of an intermediate regime, it is recommended to use a Voigt profile, which is no more than a mixture of the two functions (Payling and Larkins 2002). Note that statistical error is the main source of broadening in common spectrophotometers where the resolution is around the nanometer. **Figure 3.20b** presents an example of a profile measured using a He-Ne laser for determining the instrumental broadening.

Baseline or background is another important element to consider when processing a spectrum. According to (Boss and Fredeen 1997), potential contributions to the baseline may come from:

- The continuous radiation of free electrons that are inelastically dispersed or "captured" by ions.
- Blackbody radiation, when in the discharge volume a radiant element coexists at an elevated temperature. The blackbody radiation spectrum falls in or near the region of the analyzed electromagnetic spectrum.
- Parasitic radiation, such as light produced by fluorescent lights.

This characterization technique was used during reduction process of the native oxide layer of 304 stainless steel. The peaks corresponding to the radicals of hydrogen (monoatomic), argon and especially those corresponding to OH provided valuable information on the effect of H_2/Ar plasma on the substrate surface. Thus, it was possible to know, under our process conditions, the time in which the layer was reduced.

3.6 Raman Spectroscopy

Raman spectroscopy is a common method of studying carbon-based materials such as graphene, CNTs, GNWs and graphite. The Raman effect consists in the inelastic scattering of light by a material, where the transfer of energy may involve modes of vibration,

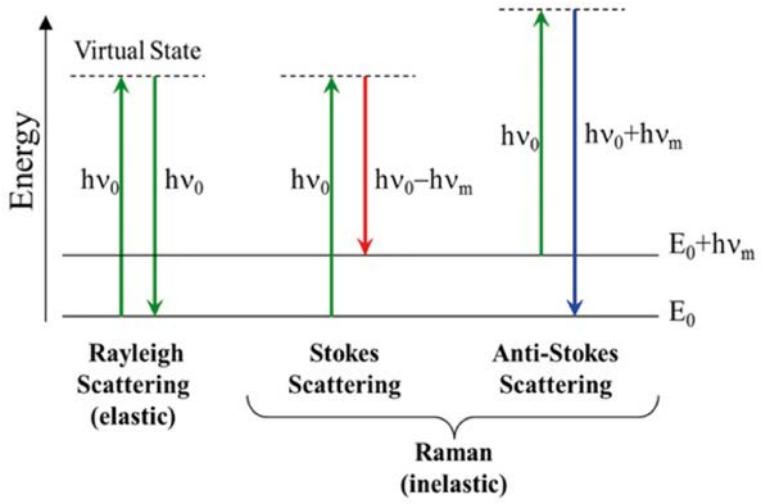

Figure 3.21: Jablonski diagram representing quantum energy transitions for Rayleigh and Raman Scattering

rotation, or in the case of crystalline solids, low frequency collective excitations such as phonons or plasmons (ACS 2019). For carbon-based materials, the study of Raman interaction is limited to the transfer of energy between incident light and crystalline (phonons) or molecular modes of vibration. **Figure 3.21** shows the quantum energy transitions for Raman and Rayleigh scattering. Energy transfer can occur in two ways.

In the first, the incident photon of energy hv_0 induces an excitation in the material which translates into the creation of a quantum of vibrational energy hv_m. The resulting photon has an energy $hv_0 - hv_m$ (Stokes scattering). In the second case, the same energy quantum hv_0 can be annihilated by the photon if the system is in the corresponding excited state, so that the energy of the scattered photon will be $hv_0 + hv_m$ (Anti Stokes scattering).

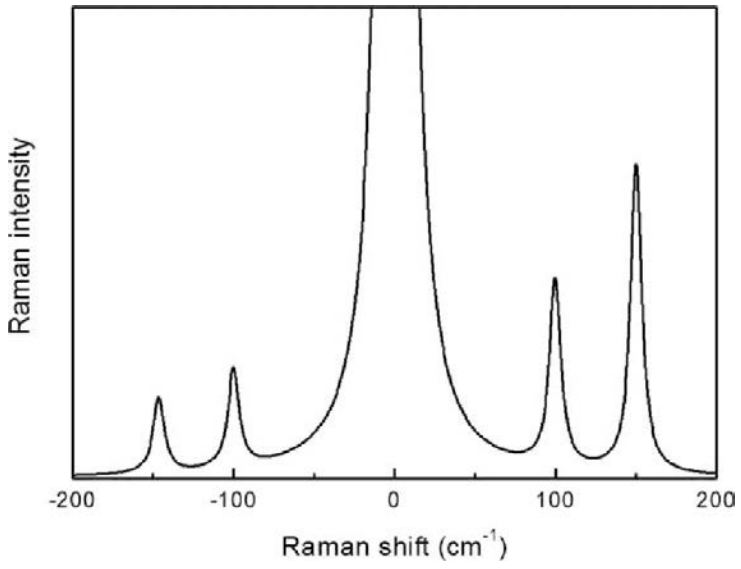

Figure 3.22: Schematics showing the Rayleigh line and the Raman spectrum (R. Saito et al. 2011)

However, most of the light is scattered elastically (Rayleigh scattering) (Merlen et al. 2017).

Figure 3.22 shows the Rayleigh line (at 0 cm^{-1}) and the Raman spectrum. The Rayleigh intensity is always much stronger and it has to be filtered out for any meaningful Raman experiment. The Stokes process (positive frequency peaks) are usually stronger than the anti-Stokes process (negative frequency peaks) due to phonon creation/annihilation statistics (R. Saito et al. 2011). For this reason, interest is generally focused only on the part of the spectrum that corresponds to Stokes radiation, as it is more intense. The advantage of using such a shifted scale is that it allows working with a spectrum that gives directly the frequency of the molecular vibrations.

The excitation of the vibration modes of a material does not depend on the wavelength of the incident light. However, if the energy is close to or equal to some electronic transition allowed in the material, a resonance phenomenon (Raman resonance) is observed, so that the intensity of light scattered by Raman effect can increase from one to several orders of magnitude.

In general, this technique can be considered non-destructive. This means that it can be used as an in-situ characterization technique in the synthesis of certain materials. On the other hand, if a light source with sufficient energy is used to induce chemical or structural changes, Raman spectroscopy can be an advantage when studying the thermal behaviour of a material. This technique is widely used in activities such as the control of manufacturing processes in the petrochemical and pharmaceutical industries. Illegal drugs captured at a crime scene can be analyzed rapidly without breaking the evidence seal on the plastic bag. Chemists can watch paint dry and understand what reactions are occurring as the paint hardens. Using a fiber-optic probe, they can analyze nuclear waste material from a safe distance. Photochemists and photobiologists are using laser Raman techniques to record the spectra of transient chemical species with lifetimes as small as 10^{-11} seconds. Surface-enhanced Raman spectroscopy is used for studying surfaces and reactions on surfaces (ACS 2019). However, the analysis of this technique is non-trivial since recorded spectra may be a convolution of both molecular vibrations and phonon resonances. The energies of these physical processes may occur in the same energy regime, and hence several analytical approaches can be necessary for a full analysis (Düngen et al. 2017).

The Raman band frequency depends on the masses and positions of the atoms, the interatomic forces (i.e. the force constants of the bonds) and the bond length. Therefore, any effect that alters these characteristics will produce a change in the frequency of the band. For example, this is why the position of the band is susceptible to the presence of stresses or tensions: a tensile stress will determine an increase in the spacing of the lattice and, therefore, a decrease in the wave number of the vibrational mode. In addition, the presence of crystalline disorder and chemical impurities in the crystalline network produce changes in the wave number. Raman bandwidth and band shape are closely related to the crystalline order. In principle the bandwidth is related to the lifetime of the phonons. The presence of crystalline disorder produces a decrease of the phonon lifetime, which thus generates an increase of the bandwidth. Therefore, the density of defects can be evaluated from the bandwidth (Shahzad Hussain 2014).

3.6.1 Carbon vibration modes

Among all possible phonon modes for sp^2 carbons, only a limited number of phonons are Raman-active modes (namely those with A_{1g}, E_1 and E_2 symmetry for carbon nanotubes,

and E_{2g} for graphite) (R. Saito et al. 2011). sp^2 carbons presents a characteristic band around $1580\,cm^{-1}$, called G-band, in reference to graphite, which is the stretching of C-C bond in the graphitic materials is the first order Raman peak. This mode does not require the presence of six-fold ring. Radial breathing mode (RBM) at the lower frequencies ($100 - 400\,cm^{-1}$) is a unique phonon mode appears only in carbon nanotubes is the unique feature of G band splitting is direct evidence that sample contains the SWCNTs.

Figure 3.23 contains the Raman spectra from several sp^2 nanocarbon and bulk carbon materials. When sp^3 (diamond type carbon) hybridization is abundant, a very narrow beak around $1330\,cm^{-1}$ can be observed (A. Ferrari and Robertson 2000). D-band $\sim$ $1360\,cm^{-1}$ and G' $\sim$ $2700\,cm^{-1}$ are due to one and two phonon, second order Raman scattering process. The appearance of D mode is due to the defects (vacancies, finite crystal size, curvatures and defects in general), disorder or amorphous carbon in the graphitic material. The D band is the A_{1g} symmetry breathing mode. The G' band spectra are free from defect effects (Shahzad Hussain 2014).

A common metric used to characterize the defect density in a material, specially when MWCNTs are studied, is the ratio of the intensities of the disorder-induced D-band to the symmetry-allowed G-band ratio (I_D/I_G). Study of the D and G-band modes by Raman spectroscopy yields information about the crystal structure of the material and about many of its interesting physical properties (Düngen et al. 2017; R. Saito et al. 2011).

In addition, by deconvolution of the D and G peaks obtained from MWCNTs samples,

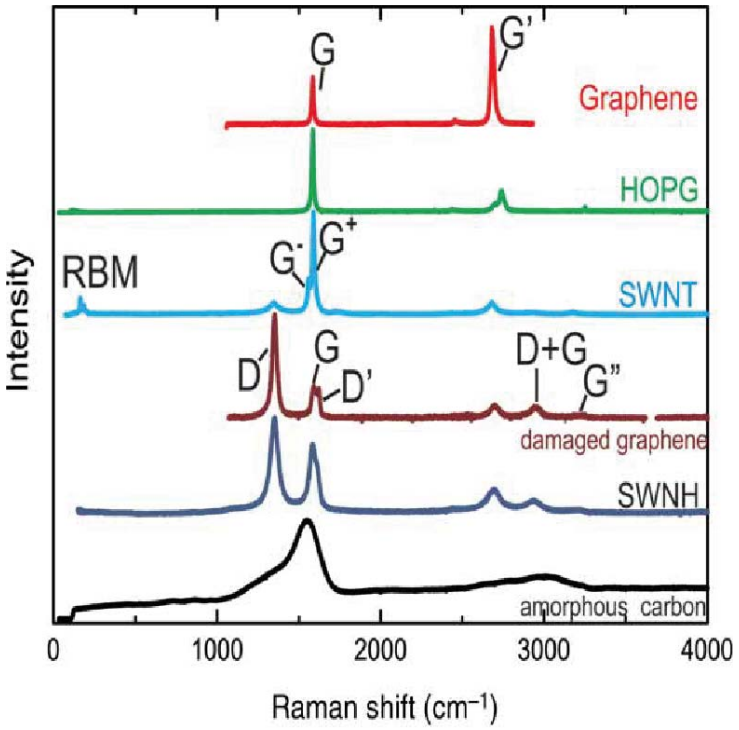

Figure 3.23: Raman spectra from several sp^2 nanocarbon and bulk carbon materials. From top to bottom: crystalline mono-layer graphene, HOPG, an SWNT bundle sample, damaged graphene, single-wall carbon nanohorns (SWNH). The most intense Raman peaks are labeled in a few of the spectra. Note that some authors call the G' by 2D and the G" by 2D' (R. Saito et al. 2011)

two additional bands to those already mentioned have been identified in several studies. One is found $\sim 1200\,\mathrm{cm}^{-1}$ and it is related to impurities in the graphite lattice (Shahzad Hussain, Amade, and Bertran 2014). The other is $\sim 1480\,\mathrm{cm}^{-1}$, related to quantity of amorphous carbon (Düngen et al. 2017). These bands are denoted as D" and A, respectively.

As can be seen, Raman spectroscopy studies of carbon-based materials have provided a great deal of information about their solid-state properties, such us as electronic structure, phonon structure and defects. This characterization technique has been useful for the development of this work. It has allowed to identify and compare the different modes of vibration of the nanostructures obtained by PECVD. Above all, the quality of the carbon-based materials deposited on the 304 stainless steel.

3.7 Electrochemical characterization

This characterization technique has allowed us to evaluate the electrochemical properties of our electrodes and devices. Thus, it is possible to understand the reaction mechanisms at the electrode/electrolyte interface, which occur inside the electrochemical cell.

Electrochemistry is the branch of chemistry concerned with the interrelation of electrical and chemical effects. A large part of this field deals with the study of chemical changes caused by the passage of an electric current and the production of electrical energy by chemical reactions. In fact, the field of electrochemistry encompasses a huge array of different phenomena (e.g., electrophoresis and corrosion), devices (electrochromic displays, electro analytical sensors, batteries, and fuel cells), and technologies (the electroplating of metals and the large-scale production of aluminum and chlorine) (Bard 2001).

In electrochemical systems, the processes and factors affecting charge transport must be understood across the interface between chemical phases (in our case between an electrode and an electrolyte). Charge is transported through the electrode by the movement of electrons (and holes). Some electrode materials include solid metals (e.g., Pt, Au), liquid metals (Hg, amalgams), carbon (graphite), and semiconductors (indium tin oxide, Si). In the electrolyte phase, charge is carried by the movement of ions. Among the most used solutions are liquid solutions containing ionic species, such as, H^+, Na^+, Cl^-, in either water or a nonaqueous solvent. To be useful in an electrochemical cell, the solvent/electrolyte system must be of sufficiently low resistance (i.e., sufficiently conductive) for the electrochemical experiment envisioned (Bard 2001).

According to (Harvey 2019), five important concepts must be considered to understand electrochemistry:

- The electrode's potential determines the analyte's form at the electrode's surface.
- The concentration of analyte at the electrode's surface may not be the same as its concentration in bulk solution.
- In addition to an oxidation–reduction reaction, the analyte may participate in other reactions.
- Current is a measure of the rate of the analyte's oxidation or reduction.
- We cannot simultaneously control current and potential.

Electrochemical measurements are made in an electrochemical cell consisting of two or more electrodes and the electronic circuitry for controlling and measuring the current

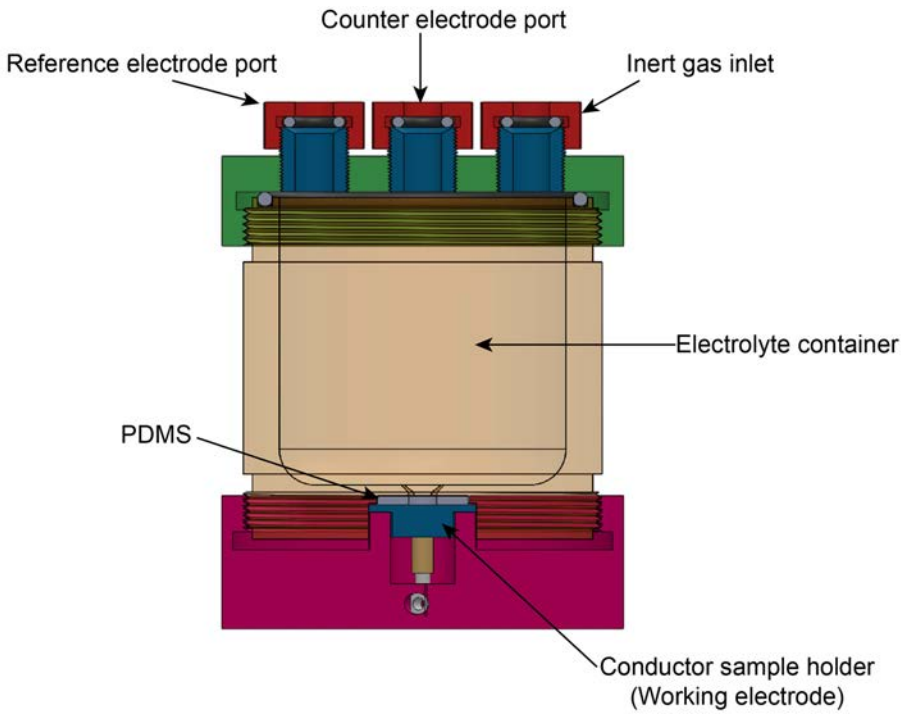

Figure 3.24: Illustration of new three-electrode electrochemical cell

and the potential. The most basic electrochemical cell uses two electrodes. The potential of an electrode is sensitive to the concentration of the solution (electrolyte), and is called the working electrode. The second electrode, called the counter electrode, completes the electrical circuit and provides a reference potential against which the potential of the working electrode is measured. Ideally, the potential of the counter electrode is kept constant, so that any changes in the total potential of the cell can be assigned to the working electrode. If the potential of the counter electrode is not constant, it can be replaced by two electrodes: a reference electrode whose potential remains constant and an auxiliary electrode that completes the electrical circuit (Harvey 2019).

During this work, we developed a new three-electrode cell that has allowed us to optimize the electrochemical characterization of electrodes (see **Figure 3.24**). An Ag/AgCl electrode (3M KCl internal solution) and a Pt-ring electrode were used as the reference and counter electrode, respectively. The working electrodes were the samples to be studied, such as stainless steel/CNTs, stainless steel/MnO_2, among others. The area of the working electrode was set to a constant value of 0.78cm^2. The ease of assembly of the working electrode and the tightness of the system are the main advantages of the new design. In addition, the cell robustness also contributes to more reliable electrochemical measurements.

Note that, since the potential and current cannot be controlled at the same time, there are only three basic experimental designs:

- Measure the potential when the current is zero.

- Measure the potential while controlling the current.

- Measure the current while controlling the potential.

Each of these experimental designs relies on Ohm's law which states that a current (i), passing through an electrical circuit of resistance (R), generates a potential (E).

$$E = iR \tag{3.8}$$

Each of these experimental designs uses a different type of instrument. They are briefly described below.

3.7.1 Potentiometers

To measure the potential of an electrochemical cell under a zero current condition a potentiometer must be used. **Figure 3.25** shows a schematic diagram for a manual potentiometer, consisting of a power supply, an electrochemical cell with a working electrode and a counter electrode, an ammeter for measuring the current passing through the electrochemical cell, an adjustable, slide-wire resistor, and a tap key for closing the circuit through the electrochemical cell.

Using Ohm's law, the current in the upper half of the circuit is:

$$i_{up} = \frac{E_{PS}}{R_{ab}} \tag{3.9}$$

where E_{PS} is the potential of power supply, and R_{ab} is the resistance between points a and b of the slide-wire resistor. In a similar manner, the current in the lower half of the circuit is:

$$i_{low} = \frac{E_{cell}}{R_{cb}} \tag{3.10}$$

where E_{cell} is the potential difference between the working electrode and the counter electrode, and R_{cb} is the resistance between the points c and b of the slide-wire resistor. When $i_{up} = i_{low} = 0$, no current flows through the ammeter and the potential of the electrochemical cell is:

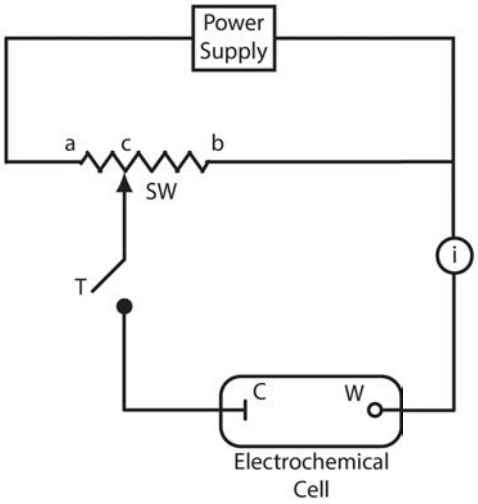

Figure 3.25: Schematic diagram of a manual potentiometer: C is the counter electrode; W is the working electrode; SW is a slide-wire resistor; T is a tap key and i is an ammeter for measuring current (Harvey 2019)

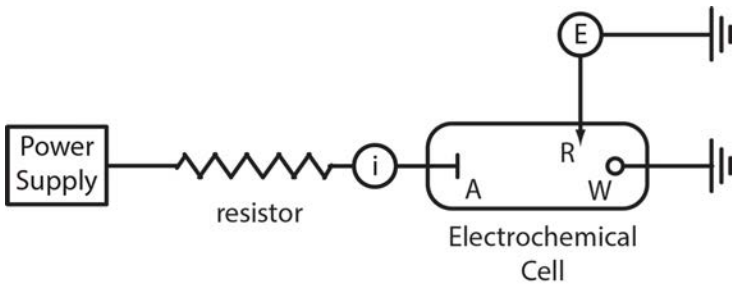

Figure 3.26: Schematic diagram of a galvanostat: A is the auxiliary electrode; W is the working electrode; R is an optional reference electrode, E is a high-impedance potentiometer, and i is an ammeter. The working electrode and the optional reference electrode are connected to a ground (Harvey 2019)

$$E_{cell} = \frac{R_{cb}}{R_{ab}} \times E_{PS} \tag{3.11}$$

To determine E_{cell} it is necessary to momentarily press the tap key and observe the current at the ammeter. If the current is not zero, the slip-wire resistance is moved and the current is measured again, continuing this process until the current is zero. When the current is zero, the last equation should be used to calculate E_{cell}.

Using the tap key to momentarily close the circuit containing the electrochemical cell, minimizes the current passing through the cell and limits the change in the composition of the electrochemical cell.

3.7.2 Galvanostats

A galvanostat allows us to control the current flowing through an electrochemical cell. A schematic diagram of a constant-current galvanostat is shown in **Figure 3.26**.

The current flowing from the power supply through the working electrode is:

$$i = \frac{E_{PS}}{R + R_{cell}} \tag{3.12}$$

where R is the resistance of the resistor, and R_{cell} is the resistance of the electrochemical cell. If $R >> R_{cell}$, then the current between the auxiliary and working electrodes is:

$$i = \frac{E_{PS}}{R} \approx \text{constant} \tag{3.13}$$

To control the potential of the working electrode, which changes as the composition of the electrochemical cell changes, it is possible to include an optional reference electrode and a high impedance potentiometer.

3.7.3 Potentiostat

A potentiostat allows to control the potential of the working electrode. A schematic diagram for a manual potentiostat is shown in **Figure 3.27**. The potential of the working electrode is measured relative to a constant-potential reference electrode that is connected to the working electrode through a high-impedance potentiometer. To regulate the potential of the working electrode, the slid-wire resistor can be adjusted, which is connected

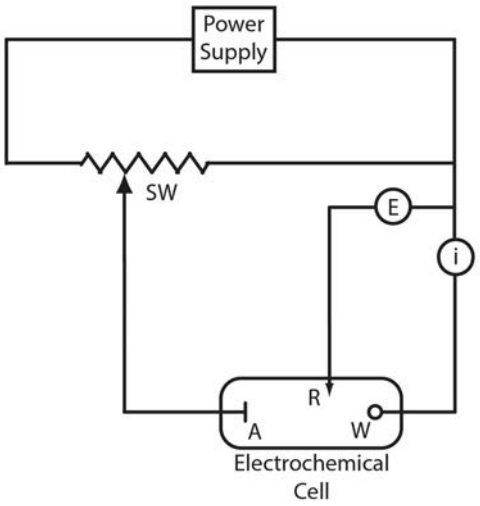

Figure 3.27: Schematic diagram for a manual potentiostat: W is the working electrode; A is the auxiliary electrode; R is the reference electrode; SW is a slide-wire resistor, E is a high impendance potentiometer; and i is an ammeter (Harvey 2019)

to the auxiliary electrode. If the potential of the working electrode starts to drift, the resistance of the slip wire can be adjusted to return the potential to its initial value. The current flowing between the auxiliary electrode and the working electrode is measured with an ammeter. Modern potentiostats include waveform generators that allow us to apply a time-dependent potential profile, such as a series of potential pulses, to the working electrode (Harvey 2019).

Since this work has focused on obtaining devices for energy storage applications, the recently described experiments were used to study the electrochemical behavior of our supercapacitor electrodes.

3.7.4 Double layer capacitance

A standard capacitor consists of two conductive electrodes of equal area A separated at a distance d in vacuum. When a voltage is applied to it, opposing charges accumulate on the surfaces of each electrode. Charges are kept separate by the dielectric, thus producing an electric field that allows the capacitor to store energy.

Supercapacitors store energy in a similar way, but the charge does not accumulate on two conductors separated by a dielectric. Instead, the charge accumulates in the electric double layer at the interface between the surface of a conductor and an electrolyte solution. When charged, the negative ions in the electrolytes will diffuse to the positive electrode, while the positive ions will diffuse to the negative electrodes (Kiamahalleh et al. 2012). The electrochemical process for the double-layer capacitor can be written as:

Positive electrode

$$E_s + A^- \leftrightarrow E_s^+ // A^{-1} + e^{-1} \tag{3.14}$$

Negative electrode

$$E_S + C^+ + e^- \leftrightarrow E_S^+ // C^+ \tag{3.15}$$

Overall reaction

$$E_s + E_s + C^+ A^- \leftrightarrow E_s^+ // A^{-1} + E_s^+ // C^+ \tag{3.16}$$

where E_s represents the surface of electrode under study, // represents the double layer where charges are accumulated on the two sides of the double layer and C and A represent the cation and the anion of the electrolyte, respectively. As shown in (Equations 3.14 and 3.15), during the charge, electrons are forward from the positive electrode to the negative electrode through the external power sources; at the same time, positive and negative ions are separated from the bulk electrolyte and moved to the electrode surfaces. During the discharge, electrons move from the negative electrode to the positive electrode through the load, and ions are released from the electrode surface and moved back into the bulk of the electrolyte. According with the overall reaction (Equation 3.16), the salt (C^+A^-) in the electrolyte is consumed during charge, so the electrolyte can also be considered as an active material (J. P. Zheng 1997). Considering this, only the electrons would be transported to and from the electrode surfaces through the external circuit, and the anions and cations of the electrolyte would move into the solution towards the charged surfaces. Theoretically, there are no chemical or phase changes or no charge transfer at the electrode/electrolyte interface. Due to the purely physical formation of electric double-layer (EDL) without electrochemical reactions, the charging of EDL capacitors (EDLCs) is very fast. While in batteries energy is stored through redox processes. EDLCs can deliver very high-power densities compared to batteries (Béguin et al. 2014).

The double-layer capacitance could be calculated by using the following expression:

$$C = \frac{A\varepsilon}{4\pi d} \tag{3.17}$$

where A represents the surface area of the electrode, d represents the thickness of the double-layer, and ε represents the electrolyte dielectric constant. As shown in **Figure 3.28** , the solution side of the double layer is thought to be made up of several "layers." That closest to the electrode, the inner layer, contains solvent molecules and sometimes other species (ions or molecules) that are said to be specifically adsorbed. This inner layer is also called the compact, Helmholtz, or Stern layer. The locus of the electrical centers of the specifically adsorbed ions is called the inner Helmholtz plane (IHP), which is at a distance x_1. The total charge density from specifically adsorbed ions in this inner layer is σ^i (μC/cm^2). Solvated ions can approach the metal only to a distance x_2; the locus of centers of these nearest solvated ions is called the outer Helmholtz plane (OHP). The interaction of the solvated ions with the charged metal involves only long-range electrostatic forces, so that their interaction is essentially independent of the chemical properties of the ions. These ions are said to be nonspecifically adsorbed. Because of thermal agitation in the solution, the nonspecifically adsorbed ions are distributed in a three-dimensional region called the diffuse layer, which extends from the OHP into the bulk of the solution. The excess charge density in the diffuse layer is σ^d hence the total excess charge density on the solution side of the double layer, σ^s, is given by:

$$\sigma^s = \sigma^i + \sigma^d = -\sigma^M \tag{3.18}$$

The thickness of the diffuse layer depends on the total ionic concentration in the solution; for concentrations greater than 10^{-2} M, the thickness is less than ~ 100 Å(Bard 2001). It is precisely because of the small thickness of the compact molecular interfacial layer that a much larger capacitance could arise for an EDLC, compared to that of a standard capacitor, where the separation distance is within the range of micrometers.

The specific capacitance (C_{sp}) of an electrode in a supercapacitor can be calculated using the following equation:

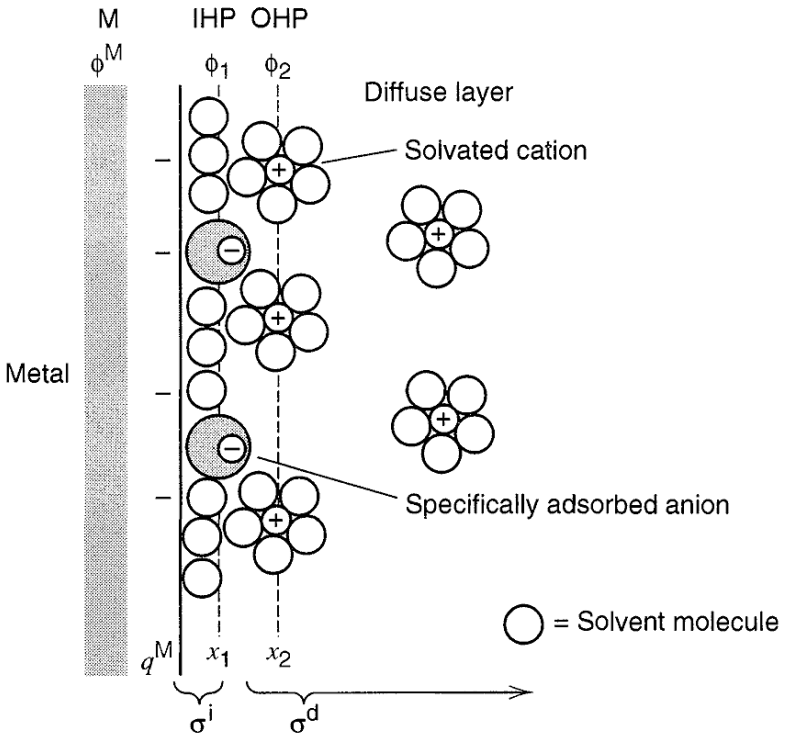

Figure 3.28: Proposed model of the double-layer region under conditions where anions are specifically adsorbed (Bard 2001)

$$C_{sp}\left(Fg^{-1}\right) = \frac{4C}{M} \tag{3.19}$$

where C is the measured capacitance for the two-electrode cell and M is the total mass of the active materials in both electrodes. The stored energy (E) and the power density (P) in a supercapacitor can then be calculated as follows:

$$E = \frac{(CV^2)}{2} \tag{3.20}$$

$$P = \frac{V^2}{(4R_S)} \tag{3.21}$$

where C (Fg^{-1}) is the total capacitance of the cell, V is the cell voltage, and R_S is the equivalent series resistance.

3.7.5 Cyclic voltammetry (CV)

According to the literature reviewed, there are several approaches that can be used to know the electrochemical performance of working electrodes. One of those used in this work was cyclic voltammetry (CV). In a CV experiment, the potentiostat applies a potential ramp to the working electrode to gradually change potential and then reverses the scan, returning to the initial potential. **Figure 3.29a** shows a typical potential-excitation signal. In this example, we first scan the potential to more positive values, resulting in the following oxidation reaction for the species R:

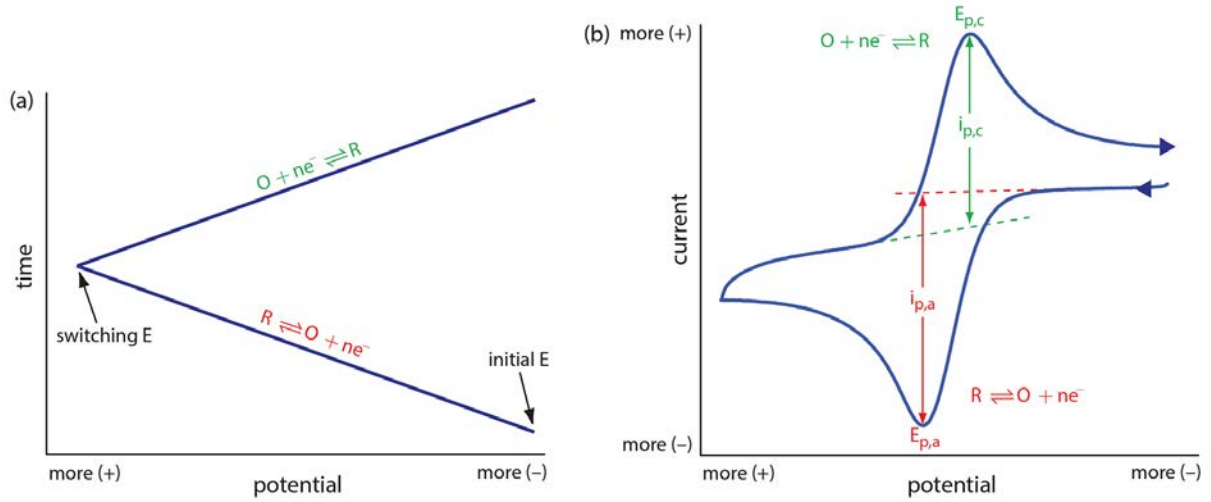

Figure 3.29: Details for cyclic voltammetry. (a) One cycle of the triangular potential excitation signal showing the initial potential and the switching potential. A cyclic voltammetry experiment can consist of one cycle or many cycles. Although the initial potential in this example is the negative switching potential, the cycle can begin with an intermediate initial potential and cycle between two limits. (b) The resulting cyclic voltammogram showing the measurement of the peak currents and peak potentials (Harvey 2019)

$$\mathrm{R} \rightleftharpoons \mathrm{O} + ne^- \tag{3.22}$$

When the potential reaches a predetermined switching potential, we reverse the direction of the scan toward more negative potentials. Because we generated the species O on the forward scan, during the reverse scan it is reduced back to R.

$$\mathrm{O} + ne^- \rightleftharpoons \mathrm{R} \tag{3.23}$$

Because we carry out cyclic voltammetry in an unstirred solution, the resulting cyclic voltammogram, as shown in **Figure 3.29b**, has peak currents instead of limiting currents. The voltammogram has separate peaks for the oxidation reaction and the reduction reaction, each characterized by a peak potential and a peak current.

The peak current in cyclic voltammetry is given by the Randles-Sevcik equation:

$$i_\mathrm{p} = \left(2.69 \times 10^5\right) n^{3/2} A D^{1/2} \nu^{1/2} C = KC \tag{3.24}$$

where n is the number of electrons in the redox reaction, A is the area of the working electrode, D is the diffusion coefficient for the electroactive species, ν is the scan rate, and C is the concentration of the electroactive species at the electrode. For a well behaved system, the anodic and cathodic peak currents are equal, and the ratio $i_{p,a}/i_{p,c}$ is 1.00. The half-wave potential, $E_{1/2}$, is midway between the anodic and cathodic peak potentials.

$$E_{1/2} = \frac{E_\mathrm{p,a} + E_\mathrm{p,c}}{2} \tag{3.25}$$

On the working electrode, electrochemical impedance measurements were also performed. Electrochemical impedance spectroscopy (EIS), measures the dielectric properties of a medium as a function of frequency. This technique is capable of high precision

and is frequently used for the evaluation of heterogeneous charge-transfer parameters and for studies of double-layer structure (Bard 2001). It is based on the interaction of an external field with the electric dipole moment of the sample, often expressed by permittivity. This technique measures the impedance of a system over a range of frequencies, and therefore the frequency response of the system, including the energy storage and dissipation properties, is revealed.

3.8 Resistivity sheet resistance

Measuring the resistivity of thin layers can be a real challenge if the different parameters influencing the measurement are not taken into account. Above all, the geometry of the area where the layer is deposited, the contact between the test tips and the layer, and the measuring devices must be considered.

In our case, to ensure that the measures were correct, the electrical resistivity of thin layers deposited by magnetron sputtering was determined by two techniques.

3.8.1 Van der Pauw technique

One typical low resistance structure used in device characterization is the van der Pauw resistivity structure (Van der Pauw 1958). L. J. van der Pauw described a technique in which the specific resistivity of arbitrarily shaped disks can be measured, but the use of highly symmetrical and flat samples is preferred. The geometries shown in **Figure 3.30** are recommended.

From these measurements on these structures, the resistivity, doping type, sheet carrier density, major carrier mobility, sheet resistance, and line widths can be determined (Keithley 2012). In measuring resistance with Van der Pauw method, we used 4 contacts (2 for current, 2 for voltage) to determine the sheet resistance (R_s) of a layer while minimizing effects of contact resistance (see **Figure 3.31**). The average resistivity ρ and conductivity σ can be calculated as follows:

$$\sigma = \frac{1}{\rho} \tag{3.26}$$

$$\rho = R_s \cdot t \tag{3.27}$$

where t is the film thickness as measured on a profilometer. The sheet resistance R_s expressed in $\Omega/\square$ is later used to calculate the resistivity ρ in $(\Omega \cdot \mathrm{m})$. To calculate R_s

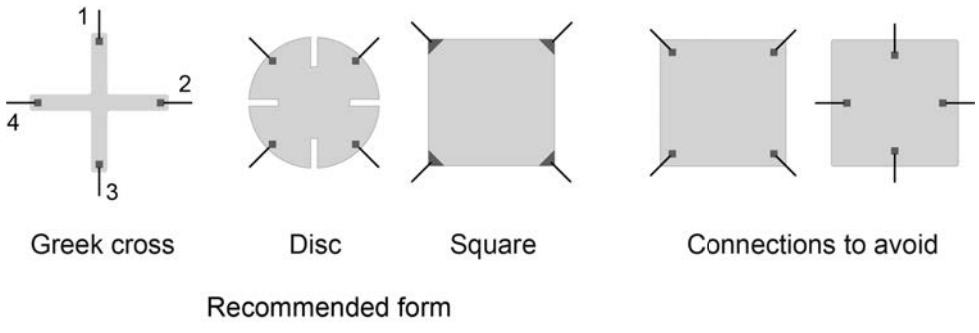

Figure 3.30: Different forms of samples for the Van der Pauw method

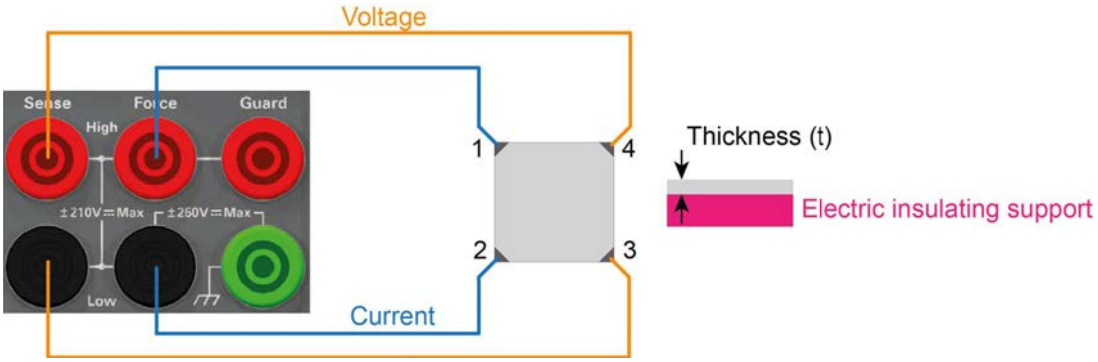

Figure 3.31: Schematic of wire connections for making 4-point van der Pauw measurements. Device contacts are labeled 1 through 4 counter-clockwise

the van der Pauw method makes two measurements. First, it sources current along the horizontal edge of the film and measures the voltage drop across the opposite edge. Then it sources current along the vertical edge of the film and measures the voltage drop across the opposite edge.

From Ohm's law $R = V/I$ so the slope of the $Vvs.I$ curve obtained in the measurement sweep is the resistance. To improve measurement precision by reciprocity, four total measurement sweeps are taken; sourcing current along each of the film edges. To cancel any offset voltages, four additional sweeps can be taken with the polarity of each measurement reversed. Thus, the average vertical and horizontal resistances are calculated:

$$R_{\text{vertical}} = \frac{R_{1243} + R_{2134} + R_{4312} + R_{3421}}{4} \tag{3.28}$$

$$R_{\text{horizontal}} = \frac{R_{1423} + R_{4132} + R_{2314} + R_{3241}}{4} \tag{3.29}$$

Van der Pauw demonstrated in 1958 the following relationship between R_{vertical} and $R_{\text{horizontal}}$ for a given sample:

$$e^{\left(-\frac{\pi R_{\text{vertical}}}{R_s}\right)} + e^{\left(-\frac{\pi R_{\text{horizontal}}}{R_s}\right)} = 1 \tag{3.30}$$

In terms of average resistivity, the Equation 3.30 is:

$$e^{\left(-\frac{\pi t R_{\text{vertical}}}{\rho}\right)} + e^{\left(-\frac{\pi t R_{\text{horizontal}}}{\rho}\right)} = 1 \tag{3.31}$$

Solving the Equation 3.31 for ρ gives:

$$\rho = \frac{\pi t}{ln2} \frac{R_{\text{vertical}} + R_{\text{horizontal}}}{2} f \tag{3.32}$$

where f is a factor that depends on the $R_{\text{vertical}}/R_{\text{horizontal}}$ ratio (**Figure 3.32**). In the case of a symmetrical and isotropic sample, we have $R_{\text{vertical}} = R_{\text{horizontal}} = R$ and the solution gives:

$$\rho = \frac{\pi t}{\ln 2} R \tag{3.33}$$

Combinations to obtain vertical and horizontal resistances can be counterproductive in obtaining reliable resistivity measurements. So, during the investigation a multiplexer

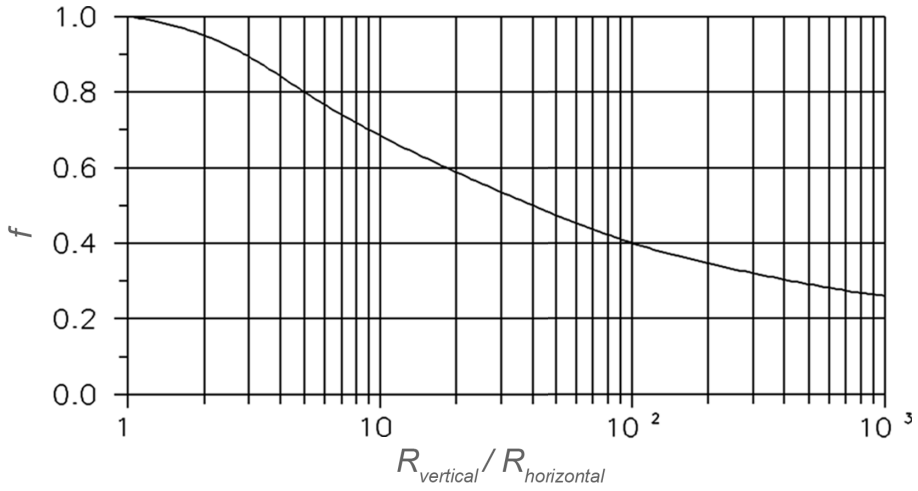

Figure 3.32: Correction coefficient, f, for the relationship between resistivity and Van der Pauw resistance

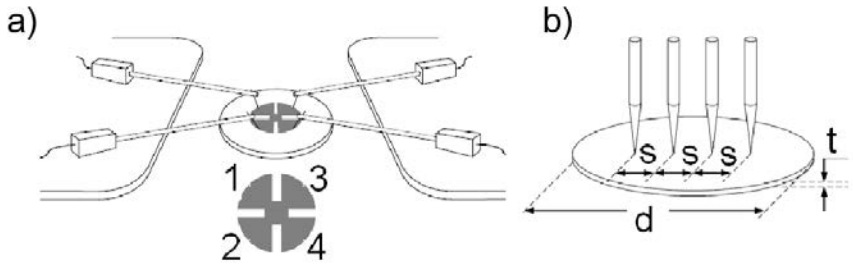

Figure 3.33: (a) Van der Pauw measurement setup with clover-shape sample and (b) 4 points probe measurement setup (Boutry et al. 2010)

was developed. This system allows the combinations to be carried out without any modifications to the connections. We have developed a system that basically consists of relays controlled by an Arduino (Arduino UNO). In addition, the system was controlled via a LabVIEW graphical interface.

To ensure that the contact between the measuring tips and the layers is ohmic, it is highly recommended to use a suitable mechanical or electro-mechanical mounting system, like the ones shown in **Figure 3.33a**. In addition, if materials permit, a soft soldering (e.g. tin) or conductive paint (e.g. silver) can be used to improve contact.

3.8.2 4 points probe measurements

The sputtered layers resistance R_s was also measured using a 4-points probe setup consisting of 4 equally-distant aligned needles (**Figure 3.33b**). A current I is applied to the two outside needles while the potential difference between the two inner needles V is measured (Boutry et al. 2010). For an infinitely large and thin membrane, R_s is given as:

$$R_s = \frac{\pi}{\ln 2 \left(\frac{V}{I}\right)} \tag{3.34}$$

For non-ideal sample, R_s is calculated according to the Smits equation with size correction factor $C(d/s)$ and the thickness correction factor $F(t/s)$ listed in tables in (Smits

1958):

$$R_s = \frac{V}{I} \cdot C(d/s) \cdot F(t/s) \tag{3.35}$$

While simple in principle, there are experimental issues to take into account when using a four-point probe. In particular, the application of a metal to a semiconductor forms a schottky diode rather than an ohmic contact. Very high or very low resistivity samples require adjustment of the drive current to obtain a reliable reading. Samples with as cut or as lapped surfaces are easier to measure than samples with polished surfaces.

The comprehension of the conductivity mechanisms of a material and of its dependencies with respect to different extrinsic factors (e.g. temperature or illumination), or that can affect its intrinsic properties (e.g. thermal treatments or non-uniform impurity concentration), demands to take into account that two contributions appear in the conductivity of a material: the concentration of free carriers and mobility. In metals, the concentration of free carriers is practically constant, so that variations in conductivity with temperature are due solely to variations in mobility. In semiconductors, temperature variation, in addition to affecting mobility, can cause a strong variation in carrier concentration. In the case of polycrystalline semiconductors, there are also specific grain boundary phenomena that can lead to more complex dependencies of mobility and carrier concentration with temperature, lighting, etc. (Department of Applied Physics UB 2001). So, if we need to know these parameters of the free carriers and even their type, positive (p) or negative (n), it is necessary to carry out an additional measure to those already described, called the Hall effect.

Chapter 4

Direct growth of CNTs on stainless steel

4.1 Introduction

Over time, carbon nanotubes (CNTs) have earned a well-deserved reputation. Thanks to their physical, chemical, electronic, thermal, mechanical and optoelectrical properties, research and industrial groups all over the world are constantly improving their production (Ji et al. 2017). It is a versatile material that can be obtained covering surfaces, in powder or even in fibers (An et al. 2016). For example, industrial processes have been developed to form long fibers and then build high-performance mechanical conductive meshes (Lepró et al. 2010b). It is also found in powder form that acts as a reinforcing material (Makowski and Fortuniak 2015). In addition, flexible displays, sensors, and energy storage devices using this material can be manufactured. The development of energy storage devices is one of the applications in which CNTs and other carbon-based materials stand out (L. X. Kang et al. 2016). The new generation battery and supercapacitor industry constantly promotes the development of new materials that meet current standards (Q. Ke and J. Wang 2016).

CNTs have excellent chemical and thermal stability and can be functionalized (Adamska and Narkiewicz 2017). CNTs can also be obtained on different rigid and flexible substrates. One of the most commonly used rigid substrates is silicon (S. Hussain et al. 2012). Silicon wafers, which have a native silicon oxide layer, are coated with a thin layer of catalyst material. The thickness of these layers must be enough to obtain nanoislands when it is heated. The shape, distribution and of course the type of catalyst material present in the nanoislands determine the type of CNTs that will be obtained (Loiseau et al. 2003). The most common materials used as catalysts are iron, nickel, cobalt, among others (Harutyunyan et al. 2005). Plasma enhanced chemical vapor deposition (PECVD) or water assisted chemical vapor deposition (WACVD) processes are used to obtain these nanostructures with outstanding control of density, shape and size (Shahzad Hussain, Amade, and Bertran 2014). Thus, uniform forests of vertically aligned CNTs have been created. In addition, WACVD, unlike PECVD, allows to reach exceptional growth rates, which is also called "supergrowth" in the literature (Yang Li et al. 2015). CNTs with lengths over 5 mm have been reported. However, in many practical cases, rigid substrates are not acceptable. They are incompatible with industrial manufacturing processes, which limits their use in laboratories. For that reason, the attention of research groups is now focused on flexible substrates. There are basically two ways to obtain CNTs on flexible substrates: transfer the CNTs obtained on rigid substrates or grow them directly on flex-

ible substrates (H. A. Moreno et al. 2014). The first option is very cumbersome because there is not enough control. The second approach has been used by numerous researchers and offers better control of CNTs properties. The flexible substrates used are sheets of copper, nickel, aluminum, different types of steel or graphite paper. To avoid the diffusion of catalyst nanoparticles, diffusion barrier systems are used, normally consisting of oxides or nitrides. In addition, between the diffusion barrier and the substrate, multilayer systems are usually inserted that act as buffer layers. The buffer layers compensate the difference of thermal expansion coefficient. However, diffusion barrier and buffer layer systems reduce the electrical contact between the carbon nanotubes and the substrate (J. Yang et al. 2014).

There is another approach that has been used to obtain CNTs on flexible substrates. The growth of these nanostructures on stainless steel has been reported without using diffusion barriers, buffer layers or external catalyst material (Masarapu and B. Wei 2007; Thapa et al. 2018). The main obstacle to do this is remove from the surface the stable layer of chromium oxide. The removal of the native oxide layer can be done by mechanical (grinding and polishing) or chemical processes. Then, when the substrate is heated in a reducing atmosphere, the alloying elements (Fe, Ni, Mn, Cr) act as catalysts and promote the growth of CNTs directly on the metallic substrate. The reported results show that high control of the growth process has been achieved. CNTs with uniform distribution and vertical alignment have been obtained. In addition, there is an ohmic contact between the substrate and the CNTs. The research that has been carried out until now has always focused on improving the growth process of CNTs. But little or nothing is said about the integrity of the substrate. There is enough scientific evidence to support that prolonged exposure of stainless steel to high temperatures in the presence of hydrogen can severely deteriorate its properties (Han et al. 1998; Marchi et al. 2005).

In that sense, in this chapter we present the results related with the reduction of the native oxide layer of 304 stainless steel using hydrogen-argon plasma in the temperature range of 600 to 730 °C. Through several characterization techniques, we have studied the effects that the reduction process has on the surface and inside the material. In addition, the catalytic activity of the reduced surface was evaluated at 730 °C. CNTs of different characteristics were obtained by PECVD and WACVD.

4.2 Experimental section

4.2.1 Native oxide film reduction

The 304 stainless steel samples were cut and introduced into the reactor chamber as received. The area and thickness of each sample was 9cm^2 and 0.1mm, respectively. Before to start the heating process, the pressure inside the reactor was below 6×10^{-4} Pa to ensure clean conditions. The samples were heated up to the annealing temperature (AT) in a hydrogen atmosphere.

The heating rate was 50 °C/min and the AT range was in the range 600 to 730 °C. After reaching the AT, the argon gas was introduced. During three minutes the samples were exposed to a RF hydrogen/argon plasma. Finally, the samples were cooled inside the vacuum chamber, following the thermal inertia of the reactor. **Figure 4.1** represents the reduction process that we followed. Experimental parameters, which has been used during the process, are presented in **Table4.1**.

By definition, materials known as stainless steels (SS) have at least 50% iron and

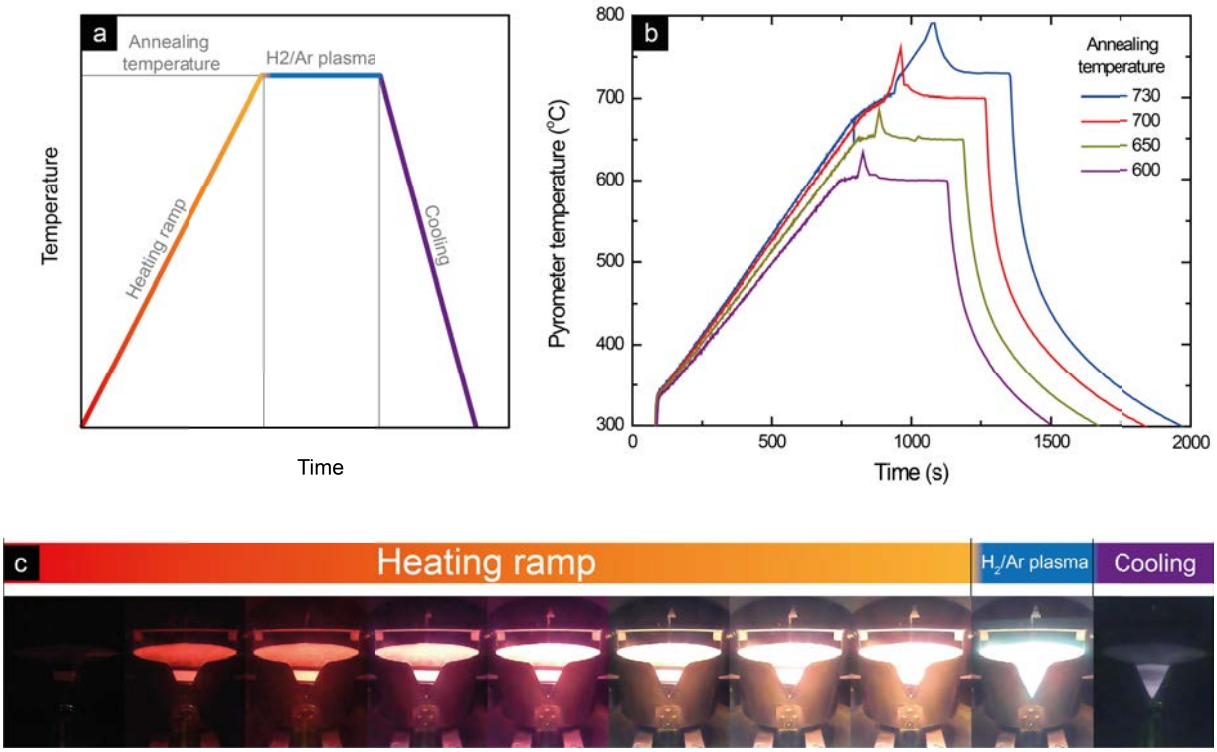

Figure 4.1: (a) Schematic curve for heating samples, (b) real curves obtained by the PID system in the range 600 to 730 °C and (c) photographic sequence of the heating, reduction and cooling process of the samples

10.5% chromium. Corrosion resistance is the result of the protection conferred by a chromium rich passive layer, normally in the range of 3 to 5 nm thick, or about 10-15 monoatomic layers. The passive layer is formed by an oxidation-reduction reaction in which chromium and iron are oxidized and the passivating agent is reduced. If this layer does not form, or if the layer is broken, rapid general and/or galvanic corrosion can develop (Kerber and Tverberg 2000). Several surface analysis of chromium-rich passive layer have determined that it corresponds to Cr_2O_3 (Detroye et al. 1999; Vesel et al. 2016). The chemical stability of Cr_2O_3 allows the use of SS in environments where it is critical to avoid undesired reactions. A particular use is as a substrate for carbon nanotubes (CNTs) forests (Thapa et al. 2018). Hence, it is possible to manufacture electrodes for batteries or supercapacitors that are in contact with liquid electrolytes, which are extremely corrosive environments for other conductive materials like cooper. Several papers use native oxide films as part of the diffusion barrier system to obtain CNTs. However, this film has two drawbacks: low electrical conductivity and shielding of the catalytic activity of metal (iron) nanoparticles (Masarapu and B. Wei 2007).

There are some alternatives to remove the native oxide layer. Mechanical methods such as brushing and polishing with abrasive materials. Chemical reagents can also be used to remove the thin oxide layer (Masarapu and B. Wei 2007; Thapa et al. 2018). However, mechanical and chemical approach produces environmentally unfriendly waste and some chemical substances, as sulfuric or hydrochloric acid, represent a serious problem for users. Another interesting approach to reduce the native oxide layer is through the employment of hydrogen plasma. (Sabat et al. 2014) present details on the reduction of mineral oxides using this method. The reaction of interest is the reduction of a metal

oxide (MeO_x) by hydrogen plasma. The hydrogen gas is supplied in molecular form to the plasma site where the reduction of metal oxide occurs. The plasma changes the molecular hydrogen gas into atomic, ionic or vibration-activated forms and other excited forms.

The reaction in its general form is:

$$MeO_x + xH_2 = Me + xH_2O(g); \quad \Delta G_1 > 0 \tag{4.1}$$

where MeO and Me represent metal oxide and metal, respectively; ΔG is the Gibbs free

	Heating ramp			Reduction					
Substrate	Heating rate (°C/min)	H_2 flow (sccm)	Pressure (Pa)	H_2 flow (sccm)	Ar flow (sccm)	RF Power (W)	Time (min)	Pressure (Pa)	Temperature (°C)
SS304-1	50	100	200	50	50	90	5	100	600
SS304-2	50	100	200	50	50	90	5	100	650
SS304-3	50	100	200	50	50	90	5	100	700
SS304-4	50	100	200	50	50	90	5	100	730

Table 4.1: Conditions to reduce the native oxide of the substrate

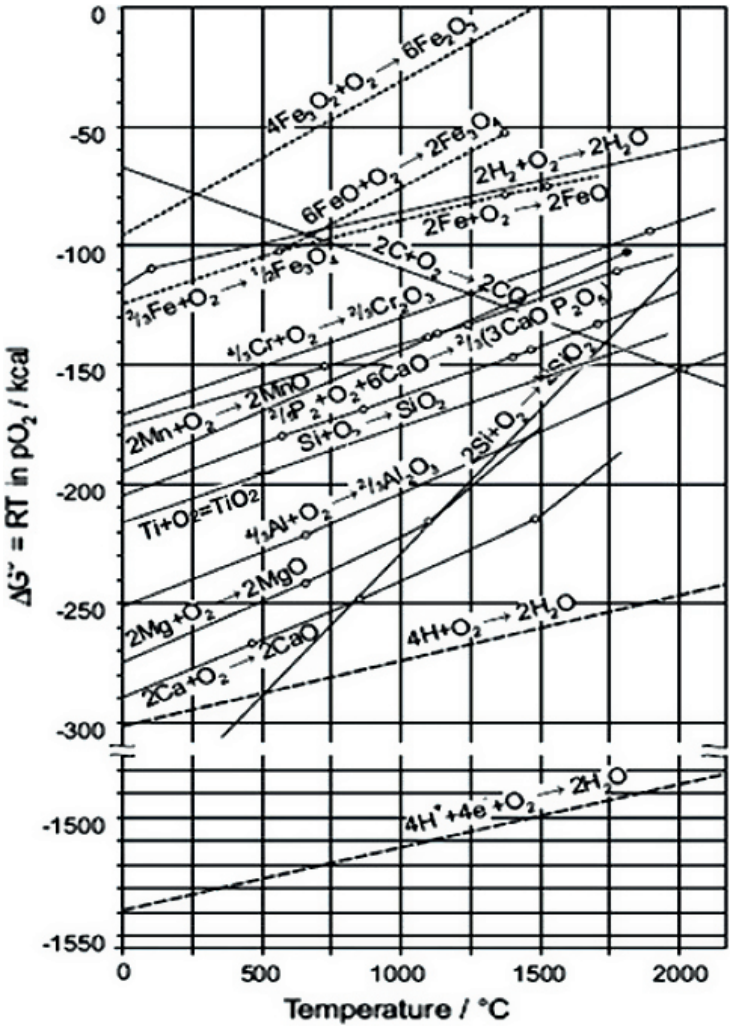

Figure 4.2: Ellingham diagram for different oxides (Sabat et al. 2014)

	Heating ramp				CNTs growth process						
Process	Heating rate (ºC/min)	H_2 flow (sccm)	Pressure (Pa)	Temp. (ºC)	NH_3 (sccm)	C_2H_2 (sccm)	H_2O (sccm)	RF Power (W)	Time (min)	Pressure (Pa)	Temp. (ºC)
PECVD	58	100	200	730	100	50	0	50	10	100	730
WACVD	48	100	200	600	100	50	0.04	0	10	100	730

Table 4.2: Experimental parameters to obtain CNTs on the substrate

energy change. Activation of molecular hydrogen gas by plasma is represented as

$$H_2(g) = \text{ Hydrogen Plasma } \left(2H/2H^+/2H^{2+}/2H^{3+}/H_2^*\right) \quad \Delta G_2 >> 0 \tag{4.2}$$

Thermodynamic coupling of (4.1) and (4.2) leads to

$$MeO_x + \text{ xHydrogen Plasma } \left(2H/2H^+/2H^{2+}/2H^{3+}/H_2^*\right) = Me + xH_2O(g)$$

$$\Delta G_3 = \Delta G_1 - x\Delta G_2 << 0 \tag{4.3}$$

The change of free energy determines the spontaneity or viability of a chemical reaction. To be spontaneous, the free energy change should be negative. The Gibbs free energy change ΔG for reduction of metal oxides with hydrogen plasma becomes negative from positive or more negative even at lower temperatures. **Figure 4.2** shows the Ellingham diagram for metal oxide conversion as MeO–Me, H_2O–H_2, H_2O–H and H_2O–H^+ lines.

The H_2O–H_2 line lies between the MeO-Me lines indicating that molecular hydrogen can reduce only those metal oxides which lie above it but it cannot reduce the metal oxides which are lying below it (Sabat et al. 2014). Thus the different excited forms of monoatomic hydrogen provide an optimal way to reduce the native oxide layer of stainless steel because the H_2O–H and H_2O–H^+ lines lie below all of the metal oxides in the Ellingham diagram for different oxides.

4.2.2 Catalyst activity on the substrate surface

After 15 minutes and without breaking the vacuum, the growth process of carbon nanotubes (CNTs) was carried out to evaluate the catalytic activity of the substrate surface. Two samples reduced at 730 °C were prepared for this phase. Plasma enhanced chemical vapor deposition (PECVD) and water assisted plasma enhanced chemical vapor deposition (WACVD) were the methods used to obtain CNTs. As in the previous step, the annealing was carried out under hydrogen atmosphere. However, during the CNTs growth process, for PECVD and WACVD we used ammonia (NH_3) and water vapor as carrier gas, respectively. Furthermore, acetylene gas (C_2H_2) was used as a carbon source (precursor gas). PECVD and WACVD were done at 730 °C. Experimental parameters are presented in **Table4.2**.

Some researchers reported that stainless steel without its oxide layer allows direct growth of CNTs. (Masarapu and B. Wei 2007) removed the native oxide layer with sulfuric acid solution. Bath time control the ratio of iron oxide and chromium oxide. It was an effective method to control the density and alignment of CNTs. The surface catalytic activity of stainless steel is higher with the presence of iron oxide than with chromium oxide (Masarapu and B. Wei 2007). (Thapa et al. 2018) obtained forest of CNTs on polishing surface of 304 stainless steel. Polishing provides more surface and crystallographic defects

offering more active sites for dissociative adsorption and precipitation of the elemental carbon available from the dissociation of the hydrocarbon source at an elevated temperature (Thapa et al. 2018). When the native oxide layer is removed, and under specific conditions, the stainless steel metal alloy elements allow the dissolution and precipitation of carbon to form nanotubes.

As in the processes for obtaining CNTs on substrates with diffusion barrier (Shahzad Hussain, Amade, and Bertran 2014; Milne et al. 2006; H. A. Moreno et al. 2014), the vapor-liquid-solid (VLS) description for carbon filament growth is also applicable to direct growth on stainless steel (Baker et al. 2009). **Figure 4.3** shows a CNT with bamboo like shape observed by HRTEM and that was obtained in this work. This particular shape consists of regular cone shaped compartments. Compartment formation in the bamboo like structure occurs due to periodic precipitation of graphite sheets at the top of the catalyst particle. NH_3 molecules can dissociate more quickly than H_2 molecules because of their weaker bonds (S. Hussain et al. 2012).

NH_3 is crucial in the formation of the bamboo compartment. When C_2H_2 and NH_3 are introduced during the PECVD process, the gas molecules are broken and different species are produced (H_2, HCN, H_2O, N_2, and CO_2). Nitrogen containing plasma allows the formation of CNTs with bamboo compartment. Furthermore, NH_3 avoids the formation of amorphous carbon. NH_3 has a key role in removing any excess of carbon through the generation of reactive atomic hydrogen species, which combine with and carry away carbon atoms (Milne et al. 2006). It should be noted that the diameter of the CNTs depends on the diameter of the catalyst particle that is previously formed on the substrate. The HRTEM image of **Figure 4.3** shows traces of the catalyst on the walls of the tube. This evidence that during the growth of the CNTs, the catalyst was in liquid phase. This phenomenon is consistent with the vapor liquid solid (VLS) growth method.

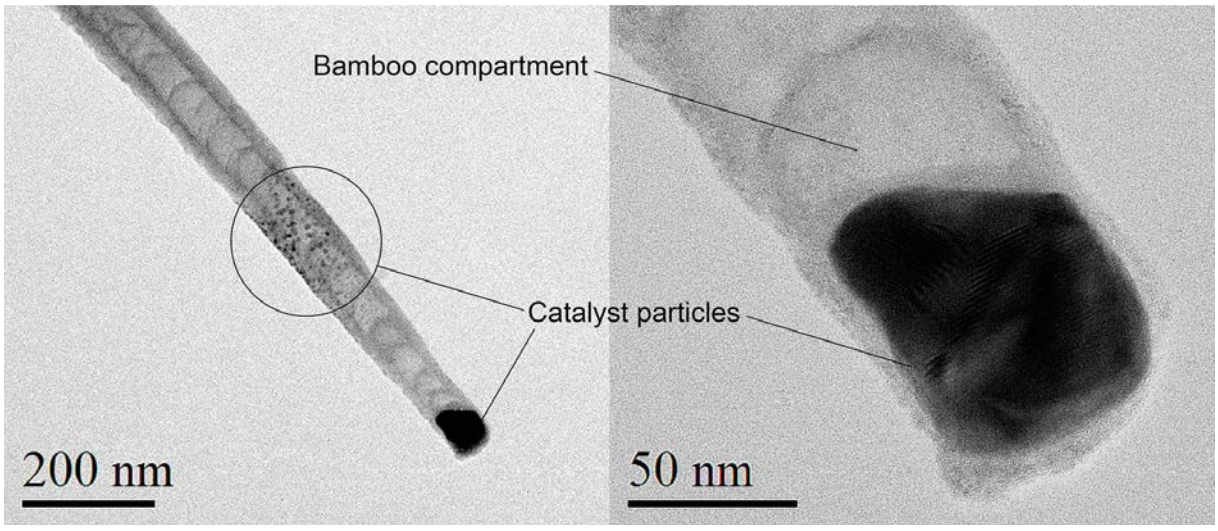

Figure 4.3: HRTEM images of PECVD grown MWCNTs

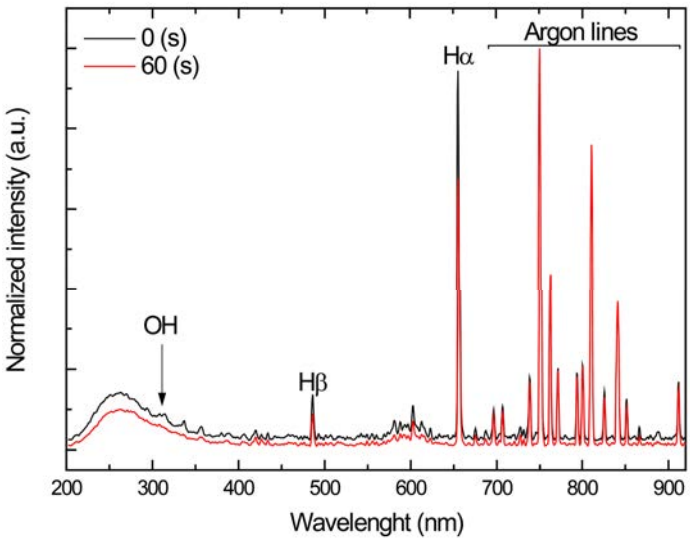

Figure 4.4: Optical emission spectra of hydrogen-argon plasma during the reduction process

4.3 Results and discussion

4.3.1 Optical emission spectroscopy (OES)

This technique allows to identify the signals generated at different optical wavelengths by the chemical species that are produced in the sheath of a plasma. We recorded different spectra of the signal produced during the reduction process. The discharge output light was collected through a quartz optical fiber and led to a spectrophotometer (Stellarnet EPP2000C), which operated in the UV-VIS range ($185 - 850\,\text{nm}$).

Heating the sample in a hydrogen atmosphere results in a prior reduction of the oxide present on the substrate surface. However, it is not enough to remove it completely. We supposed that the low pressure hydrogen-argon plasma (non-thermal plasma) combined with temperature would be enough to break the bonds of the native oxides on the stainless steel. The species generated in the hydrogen-argon plasma (monoatomic hydrogen, ionic hydrogen and ionic argon) allows the complete removal of the remaining oxide. Under our experimental conditions a strong signal of the peaks corresponding to Hβ, Hα and the radicals of Ar were observed **Figure 4.4**. The intensity of these peaks did not change during the reduction period with the exception of the peak corresponding to Hα. In that Figure it can also be observed that the hydrogen-argon plasma has wider continuous UV spectra, in contrast to argon plasma (Lebreton et al. 2016). In addition, the reduction of the OH radical peak intensity in the spectral range of $300 - 357\,\text{nm}$ reveals the complete reduction of the oxide layer. When the evolution of the OH peaks is plotted separately, it can be inferred that approximately 60 s after plasma start the reduction process is completed. Beyond that time there are no significant changes in the shape of the spectra **Figure 4.5**.

One possible explanation for the removal of native oxide from the stainless-steel surface is the formation of compounds that can be desorbed from the surface at the temperatures of the reduction process. The most stable oxide found on stainless steel surface is the Cr_2O_3. This exposed at high temperature and under the action of a hydrogen plasma

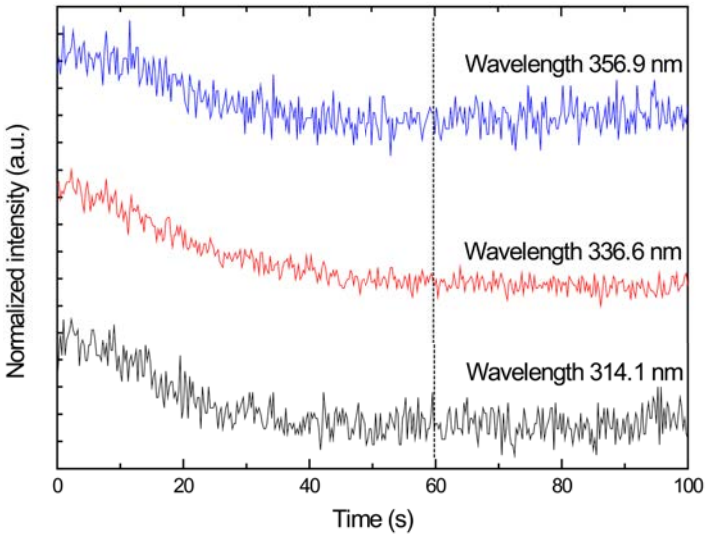

Figure 4.5: Intensity evolution of three OH peaks during the reduction process

can be transformed into hydroxide. Under this assumption, hydrogen interacts with chromium oxide at high temperature forming $Cr(OH)_3$, which is immediately desorbed from the surface after formation. $CrO_2(OH)_2$ is another compound that is normally formed at elevated temperatures when chromium oxide is allowed to interact with water vapor (Mozetič et al. 2015). The vapor pressure of the resulting compounds is higher than the native oxide, so high temperatures allow them to evaporate.

4.3.2 Confocal microscopy

The morphology at micro scale was determined by confocal microscope SENSOFAR. The reduction process by plasma was performed directly on the surface as received. This avoids the use of chemical cleaning or surface polishing processes as in other processes. (Masarapu and B. Wei 2007; H. A. Moreno et al. 2014; Thapa et al. 2018). **Figure 4.6** shows the typical topography of cold metal rolling. The plastic deformation of the material is controlled by the rolling process. The valleys and peaks are oriented perpendicularly to the position of the rolling system. The topography in **Figure 4.6** is also observed in **Figure 4.7a-d**. This evidences that the reduction process used does not eliminate the peaks and valleys produced by the rolling process.

However, if we compare the 3D images and roughness profiles, we can see a variation

Temperature (ºC)	*Sa* (µm)	*Vmp* (nm^3/nm^2)	*Vmc* (nm^3/nm^2)	*Vmv* (nm^3/nm^2)	*Rk* (µm)	S_{SK}	S_{KU}
as received	0.06 ± 0.01	5.0 ± 0.7	43.0 ± 6.2	6.0 ± 0.9	0.21 ± 0.03	1.45	8.27
600	0.09 ± 0.02	8.0 ± 0.7	71.0 ± 6.3	11.0 ± 1.0	0.25 ± 0.02	0.79	5.96
650	0.09 ± 0.02	8.0 ± 0.8	91.0 ± 8.8	18.0 ± 1.7	0.21 ± 0.02	-0.26	5.31
700	0.09 ± 0.02	8.0 ± 0.7	79.0 ± 6.5	12.0 ± 1.0	0.21 ± 0.02	0.46	4.94
730	0.07 ± 0.01	2.0 ± 0.1	36.0 ± 2.7	5.0 ± 0.4	0.21 ± 0.02	0.13	5.1

Table 4.3: Roughness parameters of samples with and without reduction process

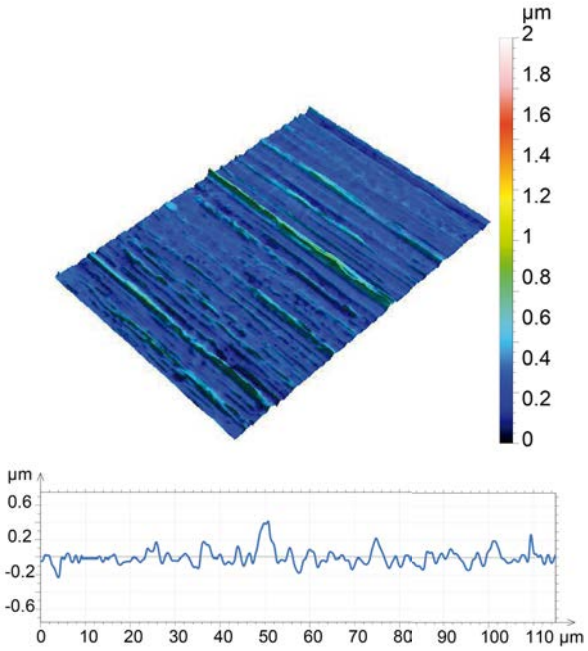

Figure 4.6: 3D topographic image and roughness profile of untreated sample

in the roughness morphology (see data on **Table4.3**).

One of the parameters commonly used to characterize the roughness is the arithmetic mean height of a line (Ra). However, is not enough to compare surfaces. If we look on **Figure 4.8**, we can see that roughness profiles have similar values of Ra, but that the number of peaks and valleys varies considerably. Ra makes no distinction between peaks and valleys, nor does it provide information about spatial structure (Sahay and Ghosh 2018). Sa is the extension of Ra to a surface. It expresses, as an absolute value, the difference in height of each point with respect to the arithmetic mean of the surface. This parameter is generally used to evaluate surface roughness (Mitutoyo 2014). **Table4.3** contains the Sa values for the analyzed samples. According to this roughness parameter, the surface of the samples obtained in the range of 600 to 700 °C have the same morphology. However, when we observe the roughness profiles (**Figure 4.6, 4.7**), certain differences (e.g. height of peaks and valleys) can be appreciated that the Sa parameter does not allow us to detect.

An alternative route to study the surface morphology is using the Abbott-Firestone method or also known as the bearing area curve (BAC) analysis. This statistical method makes it possible to know the surface texture of an object (Jurečka et al. 2018). The distribution of the material can be known through a curve. The parameters that can be obtained from the BAC are varied. For our purposes we have used those represented in **Figure 4.9**. The peak material volume (Vmp). It is the volume of material comprising the surface from the height corresponding to the bearing ratio value "p" to the highest peak. The core material volume (Vmc), is the volume of material comprising the texture between heights corresponding to the bearing ratio values of "p" and "q". The valley material volume (Vmv), is the volume of valley from the height corresponding to the bearing ratio value "q" to the lowest valley. In our case the values selected for "p" and q" were 10% and 80%, respectively. The last parameter that we got from the Abbott-Firestone curve was the core roughness (Rk). It is a measure of the "core" roughness (peak to valley) of the surface with the predominant peaks and valleys removed. Prior

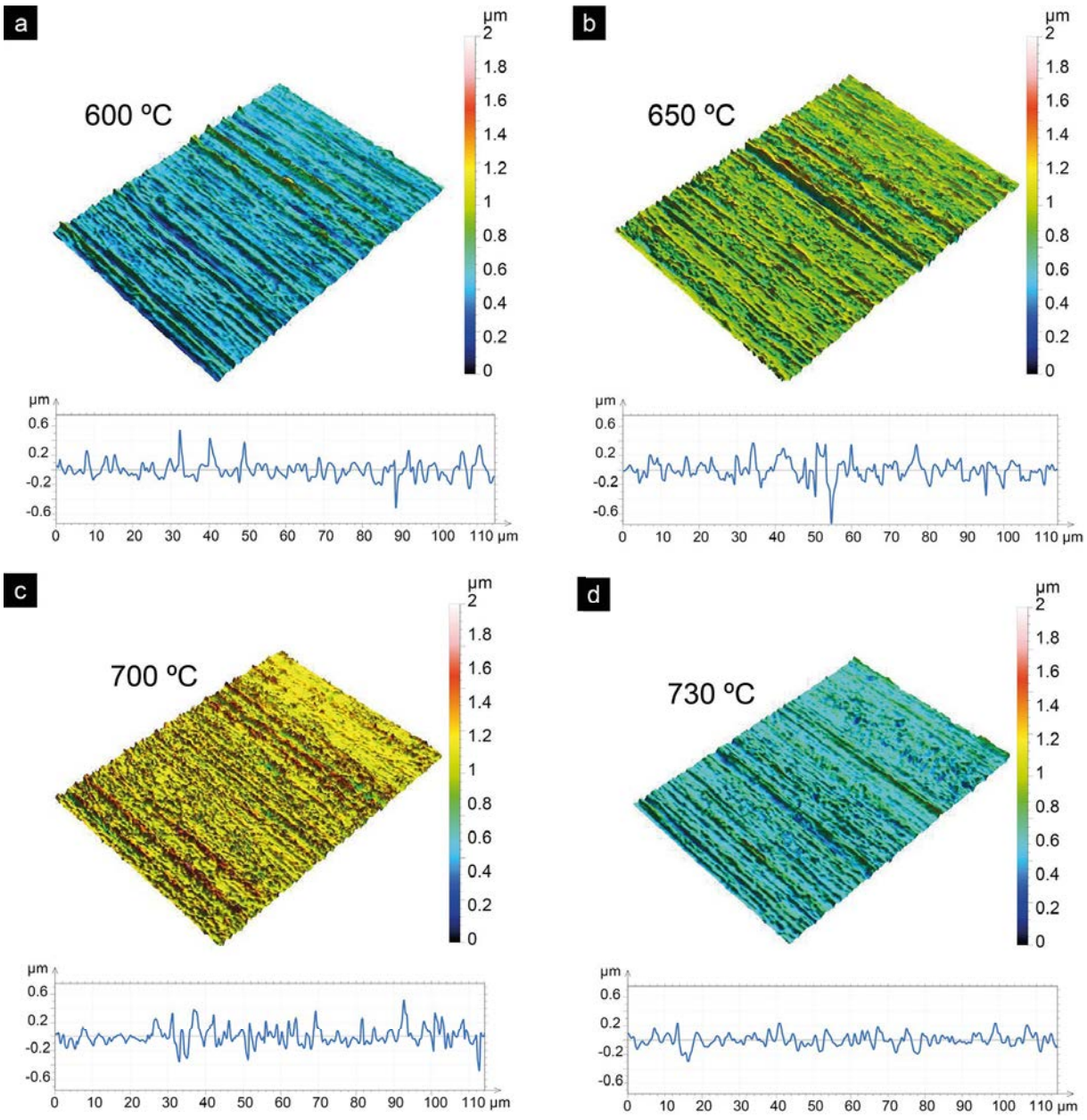

Figure 4.7: 3D topographic image and roughness profile of untreated sample

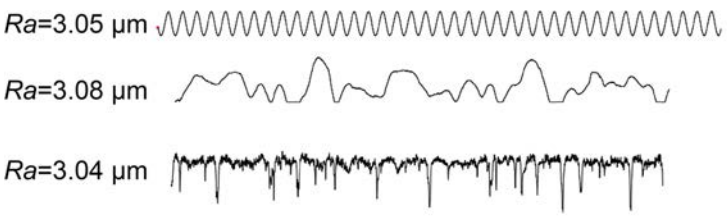

Figure 4.8: Roughness profiles with a similar value of Ra but with different morphology

to establishing the surface parameters, a certain percentage of the peak points (i.e., the peak offset) and valley points (i.e., the valley offset) are eliminated to minimize the effects

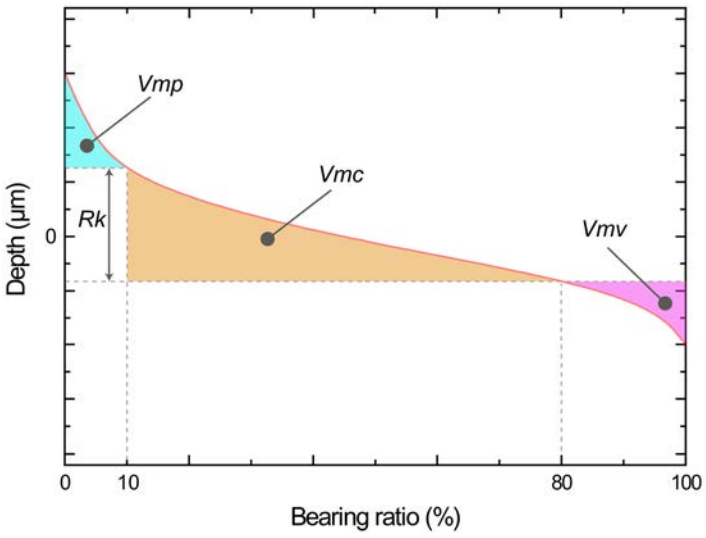

Figure 4.9: Schematic representation of the surface parameters obtained from the Abbott Firestone curve

of outliers (Buj Corral et al. 2010). Typically, the peak offset and valley offset are set to 1%.

Figure 4.10 shows the Abbott-Firestone curves of the analyzed surfaces. This curve and the roughness parameters were obtained with SensoMap software. Hence, for untreated sample the Vmp (10%) = 5 nm^3/nm^2. It means (note how the units nm^3/nm^2 reduce to nm) that a layer 5 nm thick of material over the measured cross section would account for all the material from the highest peak to the 10% point on the bearing area curve. The core material volume for that sample was Vmc (10 − 80%) = 43 nm^3/nm^2. This is tantamount to saying that in the range of 10 to 80% of the bearing ratio there is a core layer with 43 nm thickness. The Vmv (80%) is 6 nm^3/nm^2. Its value corresponds to the valley space in this sample from the 80% point to the lowest peak in the curve of the bearing area. Finally, the core roughness for that sample was $Rk = 0.21\,\mu$m. This value represents the core roughness of the surface over which a forest of CNTs will be distributed after the growth process.

Table4.3 contains the values of Vmp, Vmc and Vmv for all samples. **Figure 4.11** shows more detailed how these parameters change depending on the reduction conditions. At 730 °C, a surface with a morphology similar to the untreated sample is obtained. According to the value of its roughness parameters, we can say that it is the least rough. On the other hand, the reduction at 650 °C produces a greater change on the surface morphology. Treatment at that temperature produced deeper valleys compared to the other reduction temperatures.

In addition to the parameters commented above, **Table4.3** contains the values of Skewness (S_{SK}) and kurtosis (S_{KU}) of the distribution. These provide additional information about observed microstructure properties. High positive values of S_{SK} indicate presence of dominant high peaks on observed area. Kurtosis is a measure of sharpness of observed distribution. High positive values of S_{KU} show presence of high and narrow structure features (Jurečka et al. 2018). If we pay attention to the S_{SK} and S_{KU} values for treated samples, we will notice that regardless of the temperature at which they were reduced, all of them have lower values than the S_{SK} and S_{KU} values of the untreated

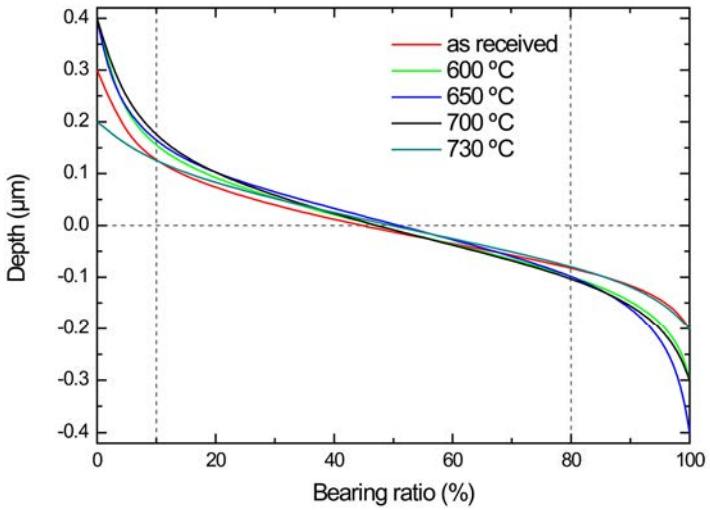

Figure 4.10: Development of the Abbott-Firestone curve with the reduction temperature

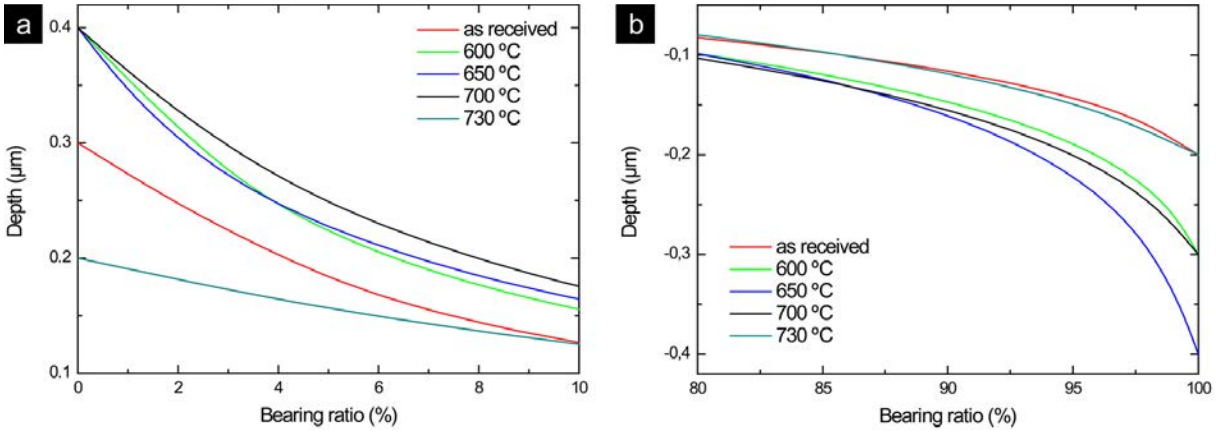

Figure 4.11: Detail of the BAC. (a) Bearing area curve (b) 3D image and surface roughness profile. The peak offsets and valley offsets are applied prior to analysis

sample. The presence of high and narrow structure features and dominant high peaks on observed area was reduced after the reduction process.

The species generated in the hydrogen-argon plasma combined with heating not only reduces native surface oxide, it seems that also modifies the morphology of 304 stainless steel samples. The reduction treatment, during 5 minutes, was enough to change the surface morphology of this material. In the range 600 to 700 °C, there is an increase in core volume compared to the untreated sample. In the same way, the value of the volume of the valleys increases. However, there is no appreciable change in the "core" roughness (peak-to-valley) and peak volume of the surface. With the exception of the sample reduced at 600 °C which has a slightly higher *Rk* than the other samples. The behavior observed in the reduced samples in the above range is not repeated in the sample treated at 730 °C. We presume that there were precipitated iron-rich carbides particles on the surface at temperatures below 700 °C. While above that temperature they evaporated and gave

way to the formation of new precipitates particles which modified the roughness. The new precipitates could correspond to chromium rich carbides. Note that vapor pressure is higher for iron rich carbides than chromium-rich carbides (Shatynski 1979). It is necessary to mention that although the stainless steel samples were extracted from the same sheet metal, the results are not conclusive in themselves, due to the conjecture of possible starting errors. Therefore, inspection with SEM is required to confirm the significant changes in the sample surface as a result of thermal/plasma treatment.

4.3.3 Scanning electron microscopy

The surface morphology of samples reduced with hydrogen-argon plasma was studied by field emission scanning electron microscopy (FE-SEM). The study was performed on a Hitachi S-4100 (Japan) and (FE-SEM) (FEI Nova NanoSEM 230, USA), equipped with an energy dispersive X-ray (EDX) detector. The evolution of the sample surface at nanoscale was revealed under different conditions. The SEM images show the presence of precipitated particles on all the sample surfaces exposed during the reduction process.

Figure 4.12 shows the uniform distribution of these precipitates. However, the size increases as the temperature is higher. This tendency is maintained until 700 °C (**Figure 4.12a-c**). Then at 730 °C (**Figure 4.12d**) the size and shape of the precipitates are similar to those obtained at 600 °C. Therefore, there is a possibility that the particles obtained between 600 and 700 °C the growth of precipitated particles. This behavior is maintained until the vapor pressure of these particles is reached. When this threshold is exceeded, the particles evaporate and are replaced by new particles. Through the energy dispersive X-ray (EDX) microanalysis we did a first approach to understand the chemical nature of precipitated particles. Although it is not a recommended way to study nanoscale structures since the depth it analyzes is around 1 μm^3, it allowed us to know what is the evolution of the chemical composition of surfaces at different temperatures. First the untreated stainless steel sample was analyzed by this technique.

The spectrum obtained by EDX analysis (**Figure 4.13**) is in accordance with the standard composition of this material (see **Table4.4**). Being a stainless steel, this substrate contains Cr, Ni and Fe. The C peak can also be easily identified. The other alloy

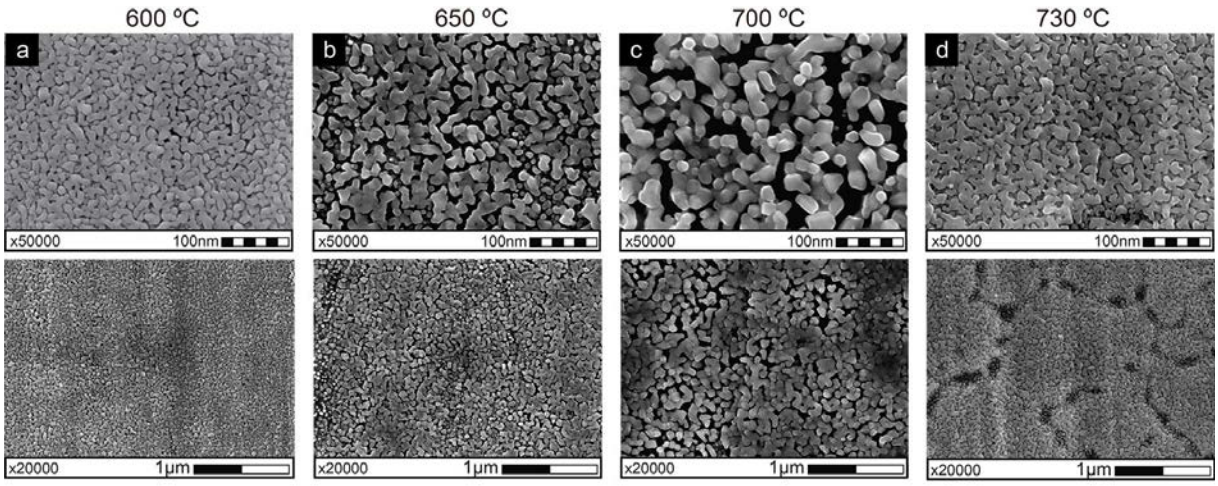

Figure 4.12: Secondary electrons SEM images of reduced samples at diferent temperatures (a) 600 °C, (b) 650 °C, (c) 700 °C, (d) 730 °C

	C	Cr	Ni	Fe	Mn	Si	P	S
%	0-0.07	17.5-19.5	8.0-19.5	balance	0-2.0	0-1.0	0-0.05	0-0.03

Table 4.4: Chemical composition of 304 stainless steel

Temperature (℃)	Fe (Weight %)	Ni (Weight %)	Cr (Weight %)	C (Weight %)
600	65.74 ± 0.74	8.84 ± 0.57	18.32 ± 0.43	7.10 ± 0.61
650	67.40 ± 0.71	8.05 ± 0.54	17.65 ± 0.42	6.90 ± 0.55
700	68.11 ± 0.74	7.49 ± 0.54	15.97 ± 0.40	8.43 ± 0.63
730	61.76 ± 0.72	6.04 ± 0.50	19.78 ± 0.44	9.78 ± 0.59

Table 4.5: Developed of chemical composition with reduction temperature

elements (e.g. Si, P, O, S) normally present in this steel were not detected with this technique. To continue with the study of the EDX characterization of the reduced samples, we plotted the percentage of iron, nickel, chromium and carbon as a function of the process temperature (**Figure 4.14**). **Table4.5** contains the chemical composition values obtained. The assumption that we comment about the chemical nature of the precipitated particles gains importance. One point to highlight is the increment of carbon on the surface (**Figure 4.14d**). During the process we used a reducing atmosphere. This prevented the oxidation of the surface sample but did not prevent the diffusion of the carbon atoms to the surface.

This phenomenon is known as decarburization. Decarburization manifests itself in the formation of carbides on the surfaces of the materials that suffer it. On our case, carbon atoms probably form iron-rich carbides between 600 and 700 ℃. Over this range, that behavior changes. The percentage of iron at 730 ℃ is lower than the value at 600 ℃ (**Figure 4.14a**). The iron-rich carbides reached the vapor pressure and evaporated. On the other hand, the percentage of chromium at 730 ℃ increase abruptly (**Figure 4.14c**). This suggests that chromium-rich precipitate particles prevail on the surface. The only element that did not increase its percentage on the surface was the Ni (**Figure 4.14b**). This element diffuses very well in the stainless steel matrix and contrary to carbon, tends

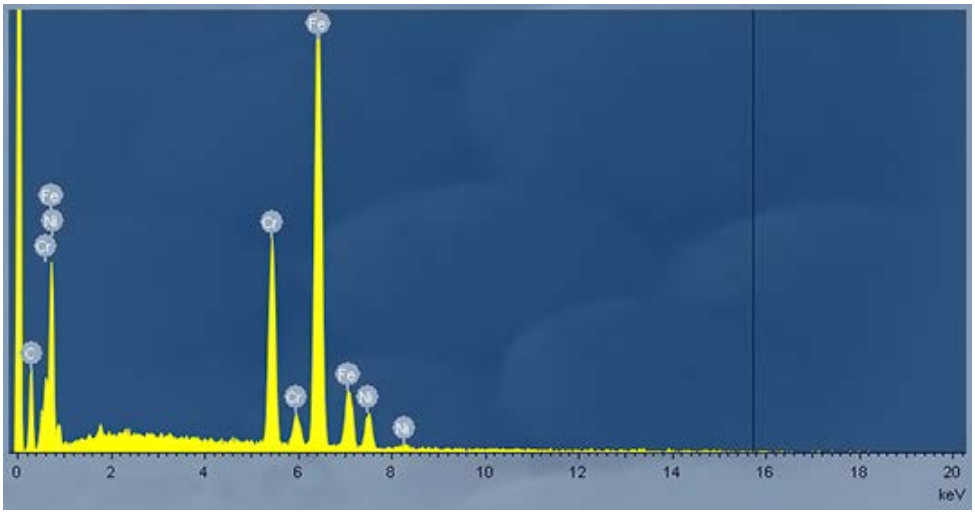

Figure 4.13: EDX spectrum of untreadted 304 stainless steel sample

to diffuse towards the interior of steel (Hedayati et al. 2017).

In order to observe the influence of gas flow ratio on the formation of precipitated particles, the H_2/Ar ratio was changed. Two additional samples were carried out under slightly different reduction conditions to those described until now. The reduction temperature was 730 °C and the plasma conditions were the same. We observe that the distribution of precipitate particles is uniform on the substrate surface. But in the absence of Ar (**Figure 4.15a**), the density of them is lower than when 75/25 (H_2/Ar) ratio was used (**Figure 4.15b**). In both cases the number of particles is lower than that of the samples obtained with the 50/50 (H_2/Ar) ratio, at the same reduction temperature. The H_2 atmosphere inhibits the formation of precipitates. In that case the surface became smoother with only a few precipitate particles. On the other hand, it seems that argon promotes crystalline defects that help chromium to form carbides. At high temperatures this phenomenon is known to take place at the grain boundary of the material (Jinlong et al. 2015). The low particle density allows to distinguish qualitatively the chemical composition between the substrate and the precipitate particles. The number of backscattered electrons (BSE) reaching the detector is proportional to their Z number. This dependence of the BSE number on the atomic number helps to distinguish between the different phases, providing images that transmit information on the sample composition. High average Z appear brighter than those of low average Z. The values for C, Fe, Cr are 6, 24 and 26, respectively. At 730 °C, The EDX detector got more signal from chromium than iron. There is

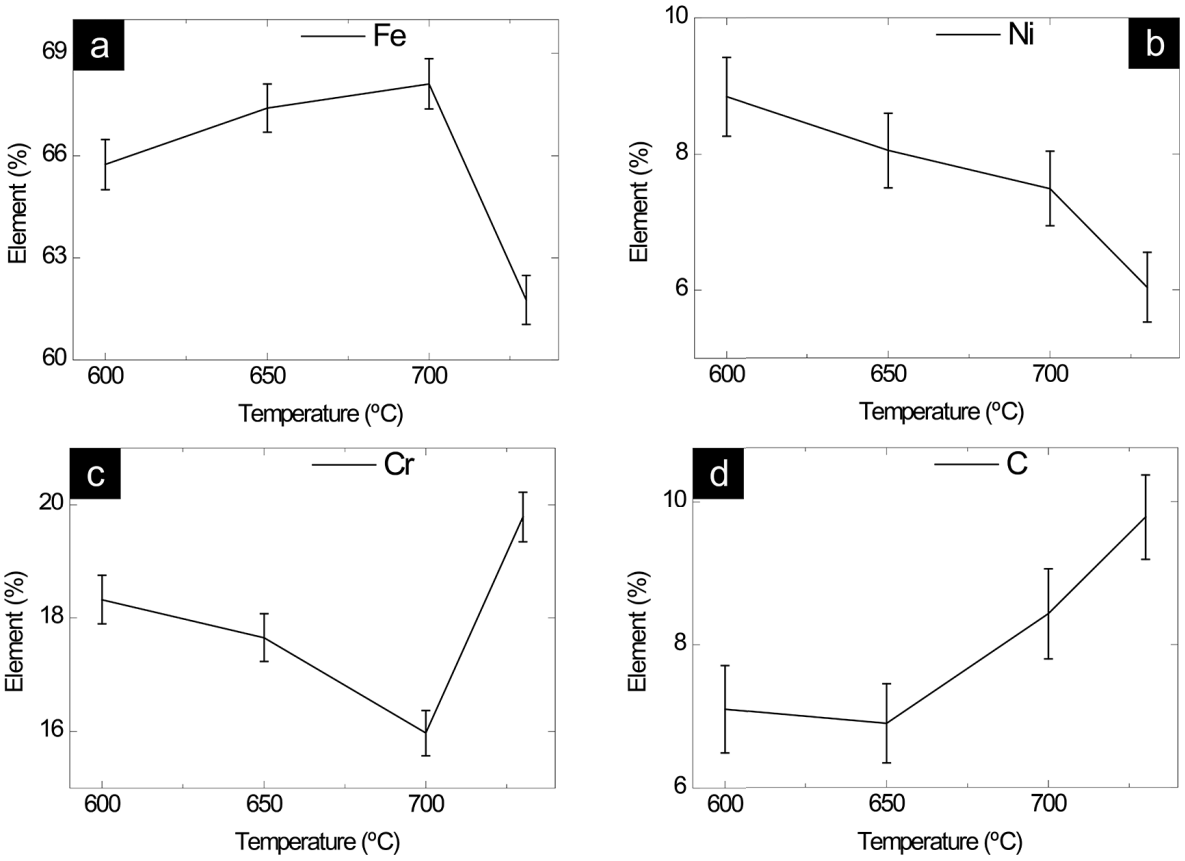

Figure 4.14: Development of chemical composition with reduction temperature. The chemical percentages were obtained by EDX detector (a) for iron, (b) for niquel, (c) for chromium (d) for carbon

more probability that these precipitated particles correspond to chromium-rich carbides. The following section presents in detail the analysis of the surface composition of the samples.

Another interesting aspect that the SEM characterization allowed us was to observe the nucleation of the catalyst particles. This step was very important for our purpose since it determines the morphology and density of carbon nanotubes. Without the presence of oxygen on the surface, the poisoning effect of the particles disappears(Masarapu and B. Wei 2007). Thus, the alloy elements are allowed to act as catalysts. These absorb the carbon atoms that the precursor gas provides, giving place to the growth of carbon nanotubes.

Figure 4.16 shows three kind of structures: the precipitated particles, of which we already discuss, and two new nanostructures. The first one corresponds to the catalyst nanoparticles and the second one is a few quantities of carbon nanotubes. This picture

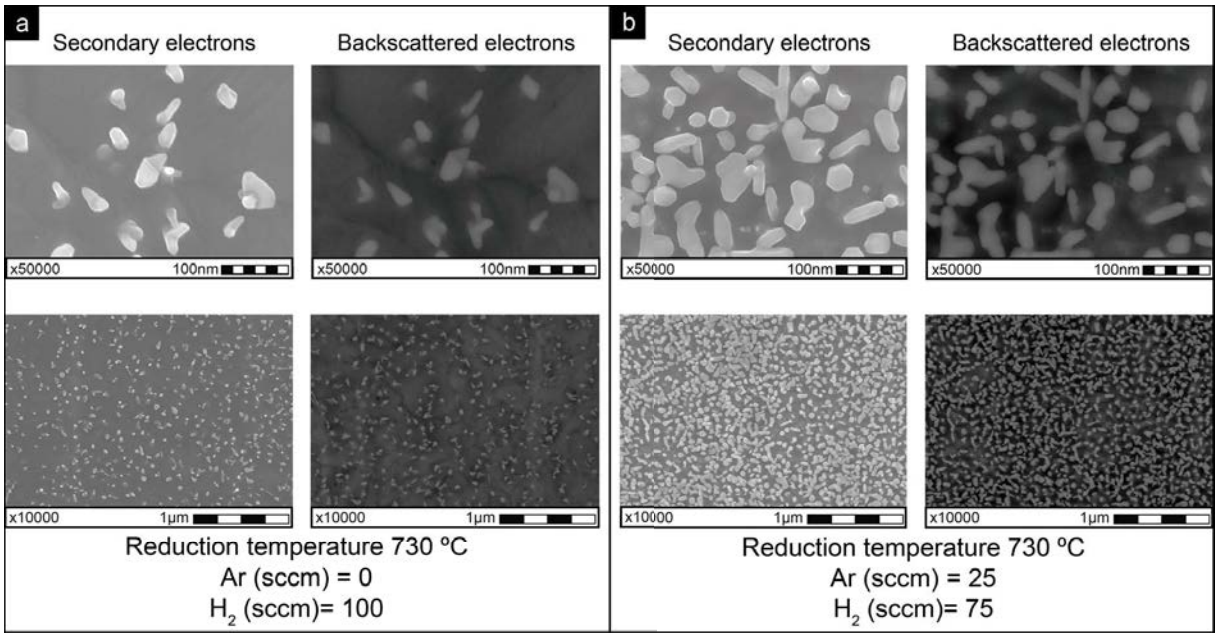

Figure 4.15: Secondary and backscattered electrons SEM images of samples reduced at diferent gases ratio. (a) H_2/Ar=100/0 sccm, (b) H_2/Ar=75/25 sccm

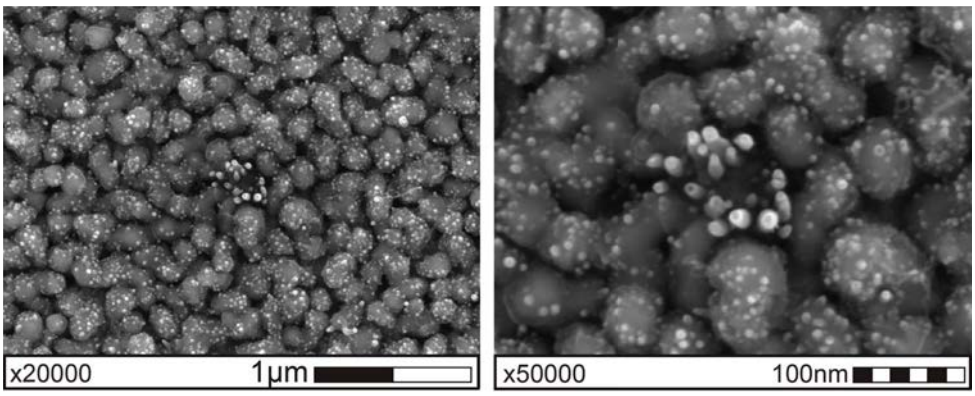

Figure 4.16: Secondary electrons SEM images of catalyst nucleation at 730 °C

provides us interesting information about the nucleation and growth process of CNTs. The catalyst nanoparticles are on the surface of precipitated particles. Until now, we consider the chromium-rich composition of those precipitated. But this does not exclude the possibility that inside of these structures there could be iron, nickel or another alloy element. Iron and nickel are excellent catalysts for the growth of CNTs. The eutectic temperatures of Fe-C, Ni-C and Co-C compounds are compared in the phase diagram reported by (Harutyunyan et al. 2005). As already mentioned in the first chapter, they reported that the carbon content at the eutectic points of cobalt-carbon and nickel carbon phases is approximately two times lower and the temperature significantly higher than for the iron-carbon phase. The reported eutectic temperature for Fe-C compounds is 732 °C. Cobalt and nickel catalysts will require higher synthesis temperatures to become an efficient way to produce CNTs. Under or over this temperature the rate of diffusion of the carbon atoms into the nanoparticles of iron decreases (Harutyunyan et al. 2005). As the growth temperature of our nanotubes is 730 °C, we can expect that at this temperature the nanoislands are formed mostly by iron.

The catalytic activity of the samples, reduced at 730 °C, were tested by PECVD and WACVD processes. Over the last years our research group have acquired a huge experience in the production of CNTs by those methods. Using our reactors CNT forests were obtained on silicon wafers and other materials such as copper or stainless steel. In all cases, a diffusion barrier had always been used. A thin layer of iron or nickel deposited by magnetron sputtering provides the material which acts as a catalyst (S. Hussain et al. 2012; Shahzad Hussain, Amade, and Bertran 2014; Shahzad Hussain, Amade, H. Moreno, et al. 2014). In this work, we present CNT forests growth directly on 304 stainless steel surfaces. **Figure 4.17a-b** show these nanostructures produced by PECVD and WACVD, respectively. At the same process temperature, the differences between the two samples are easily distinguished. With PECVD, the CNTs are short, present a uniform distribution and orientation (vertically aligned). In contrast, with WACVD the CNTs are longer, present a uniform distribution and random orientation. That distribution on the surface looks like wool lint. WACVD process is also called “superwroght” (An et al. 2016). The main purpose of using a water vapor in CVD is to prevent deposition of amorphous carbon over the catalyst nanoparticles and to prolong the catalytic lifetime (Futaba et al. 2009; Hata et al. 2004; Q. Li et al. 2006). In both cases, the density of the CNTs is lower than that of the samples produced in our laboratory on silicon wafers. It is also convenient to remark the plasma influence during the CNTs growth process. The

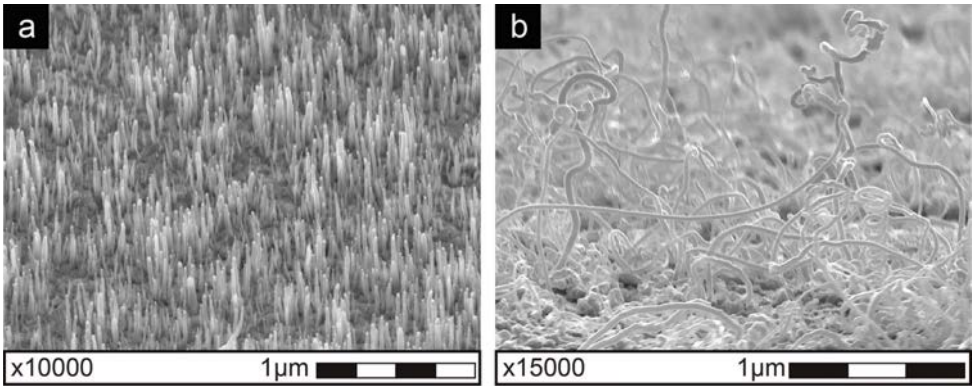

Figure 4.17: Secondary electrons SEM images of carbon nanotubes on 304 stainless steel. (a) Obtained by PECVD (b) obtained by WACVD

use of plasma can significantly reduce the activation energy of the growth of CNTs (Seah et al. 2011). In addition, the self-bias potential has influence on the substrate surface under plasma conditions, because the electric field normal to the cathode surface during the growth of CNTs. The CNTs align with the electric field as they grow (Bower et al. 2000) due to the ion bombardment in the direction of the electric field.

4.3.4 X-ray photoelectron spectroscopy

XPS experiments were performed in a PHI 5500 Multitechnique System (from Physical Electronics) with a monochromatic X-ray source (aluminum Kα line at 1486.6 eV of energy and 350 W), placed perpendicular to the analyzer axis and calibrated using the $3d_{5/2}$ line of Ag with a full width at half maximum (FWHM) of 0.8 eV. The analyzed area was a circle of 0.8 mm diameter, and the selected resolution for the spectra was 187.85 eV of pass energy and 0.8 eV/step for the general spectra and 23.5 eV of pass energy and 0.1 eV/step for the spectra of the different elements.

In order to obtain depth profiles, the untreated and reduced samples were sputtered with Ar. The composition depth profiles were obtained by sputtering the surface with an Ar^+ ion source (4 keV energy). A low energy electron gun (less than 10 eV) was used in order to discharge (neutralize) the surface when necessary. All measurements were made in ultra-high vacuum (UHV) chamber pressure between 5×10^{-9} and 2×10^{-8} Torr.

(CasaXPS 2018) was used to process the data obtained during XPS experiments. In addition, to identify the binding energy of peaks the mean sources of information were the (NIST-Database 2012) and the information presented by (Mark C. Biesinger et al. 2011). The first one has enough information to identify uncomplicated spectra, for example single peaks. However, the transition metal 2p spectra pose a number of complications that NIST Database do not adequately address, specifically, shake-up and plasmon loss structures, and multiplet splitting, all of which can complicate identification of the chemical states present (Mark C. Biesinger et al. 2011). The multiplet splitting occurs when an atom contains unpaired electrons. In these cases, when a core electron vacancy is formed by photoionization, there can be a coupling between the unpaired electron in the core and the unpaired outer shell electron. This can produce a series of final states, which will manifest in the photoelectron spectrum (Moulder et al. 1992). In the first transition series, low spin Fe(II), low-spin Ni(II), Cr(VI) and Mn(VII) species do not have unpaired d electrons and therefore will not exhibit multiplet splitting. Cr(III), Mn(II), Mn(III), Mn(IV), Mn(VI), high spin Fe(II), Fe(III), Co(II), Co(III), high spin Ni(II) and Ni(III) species all contain unpaired d electrons and therefore have multiplet structures (R. P. Gupta and Sen 1975). Also, to identify the binding energy of some oxides and carbides peaks we used additional references (M. C. Biesinger et al. 2004; Detroye et al. 1999; Kerber and Tverberg 2000).

XPS survey spectra are presented in **Figure 4.18** for untreated and reduced samples. As evident in that figure, iron, chromium, oxygen, carbon, manganese and nickel are present at the surface. All spectrum has a low value of nickel, even in the untreated spectrum, there is no peak of this element (red line). Previously, in section of EDX characterization, we commented that this alloy element tends to diffuse into bulk of steel when is subjected to heat treatment.

Another interesting aspect observed in the survey spectra is the evolution of the Mn peak. Note that 304 stainless steel contains Mn as an alloying element (Kerber and Tverberg 2000). Although in the sample without treatment its intensity is weak, as the temperature increases, in the range 600 to 700 °C, its intensity also increases. Then at

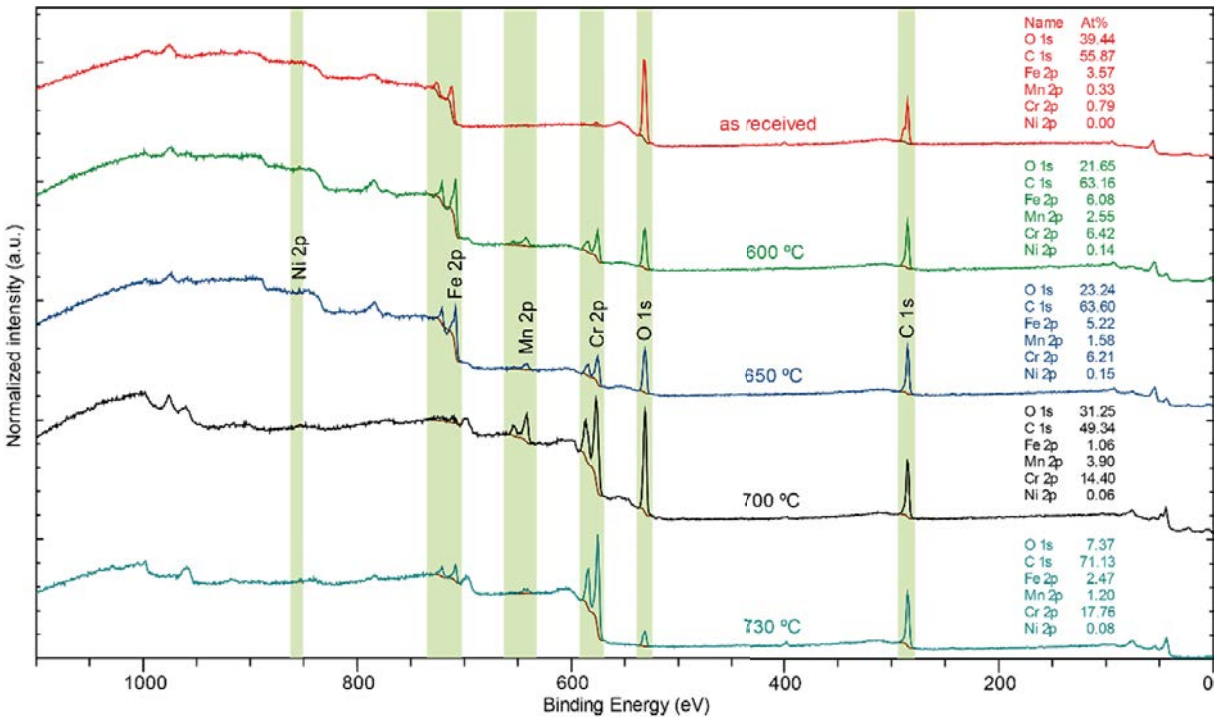

Figure 4.18: Survey spectra of reduced and no reduced samples. The relative error of %at. concentration is $\sim$ 1.5%

730 °C decrease to a value slightly higher than the untreated sample. The phenomenon of segregation of Mn towards the surface of annealed steel takes place in very thin layers, so thin that this is negligible for EDX characterization technique. As the XPS technique reduces the analyzed thickness to only 3 nm, it is an effective tool for detecting segregation phenomena that take place on the surface (Feliu and Pérez-Revenga 2004). Furthermore, it was observed that the presence of manganese and its oxides on the surface of annealed steel tends to significantly inhibit the growth of coatings, i.e. galvanneal (Feliu and Pérez-Revenga 2005).

On the other hand, the evolution of oxygen, carbon, iron and chromium peaks have special importance in this work. For that reason, we present high resolution XPS spectrum for those peaks. In addition, we elaborate bar charts using the data obtained with the Casa XPS software. Thus, the evolution of the surface chemical composition of the samples can be observed in detail and even the comparison between the samples is simplified. The evolution of the atomic concentration for O_{1s} is represented in the bar graph in **Figure 4.19**. All samples before being analyzed by XPS were extracted from our reactor, with the exception of the steel sample as received. This untreated sample of 304 stainless steel has a chromium-rich passive layer formed by an oxidation-reduction reaction in which the chromium and iron are oxidized (Kerber and Tverberg 2000). High percentage of chromium is to be expected for this type of steel, since the passivation layer is given by its stainless nature. Instead, for reduced samples, the percentage of oxygen decreases, but is not completely eliminated. This is because, immediately after breaking the vacuum, the reduced samples were oxidized. In the range of 600 to 700 °C, the oxygen percentage increases.

The possible explanation for this behavior is the shape of the precipitated particles and their distribution on the surface. At 600 °C there is a dense porous layer of iron

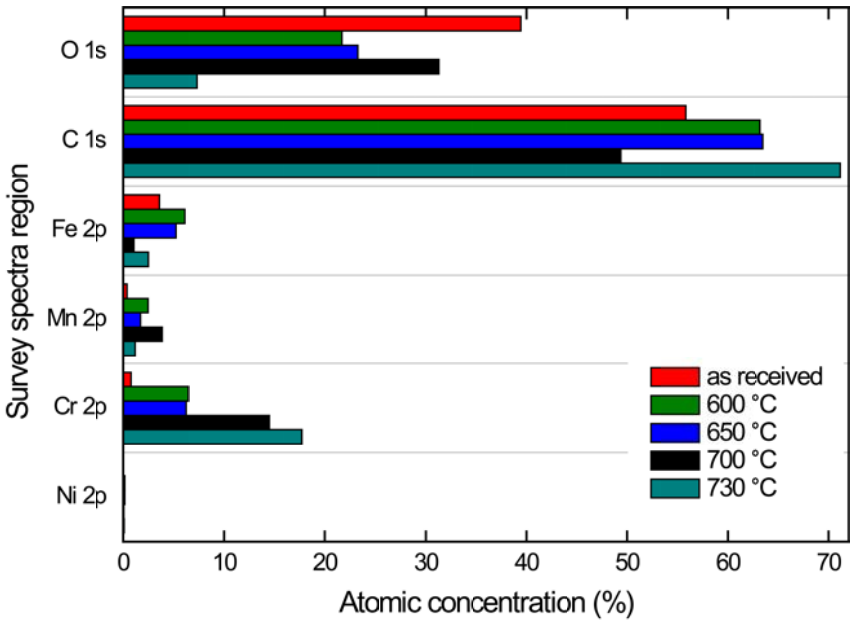

Figure 4.19: Atomic concentration bar chart measured on the surface of reduced and as recieved samples of 304 stainless steel

rich carbide on the surface. When the temperature reaches 700 °C, that layer is more porous, allowing oxygen to react with the iron and chromium-rich areas of the surface under precipitated particles. This behavior changes at 730 °C, the porous layer of iron rich carbide is replaced by a new denser porous layer. It acts as a passivation layer and by the evidence found until now corresponds to chromium-rich carbides. The evolution of the atomic percentage for regions C_{1s}, Fe 2p and Cr 2p supports this interpretation (**Figure 4.19**).

Figure 4.20 shows the O_{1s} high resolution spectra obtained on the surface of untreated and reduced samples. The spectral fitting parameters of these spectra are presented in **Table4.6**. The spectra recorded for surfaces show organic contamination, as is common with samples that were not subject to any in situ cleaning procedures or were exposed to the atmosphere. Carbonate species comes from reaction with CO_2 during air exposure (Mark C. Biesinger et al. 2011). In agreement with the results obtained by (Lothongkum et al. 2003), untreated sample possess a thin multilayer oxide film. A layer containing iron and chromium oxides and hydroxides on the outside and an inner layer containing chromium oxides (Lothongkum et al. 2003). In our sample there are also Mn. On all the studied steels, Mn is the alloying element that is found in the greatest proportion on the annealed steel surface (Feliu and Pérez-Revenga 2004). The binding energy value for the Cr_2O_3 varies between 530.33 and 530.62 eV. For Fe_2O_3, its value varies between 529.80 and 529.90 eV. Contaminants, hydroxides and oxides are present on the surface of the reduced samples. As stated above, this is because the samples were exposed to the atmosphere. In spite of taking care in its storage and transport, contamination and reaction with the surrounding gases was inevitable.

Figure 4.21 shows graphically the evolution of O_{1s} compounds for samples analyzed. For each sample, the oxide bars represent the sum of the oxide percentages. Hydroxides and oxides contribute more to the peak area than other species. The evolution of the hydroxide percentage can be explained by the presence of Mn. This element increases on the surface with temperature, reaching its maximum value at 700 °C. In the range of

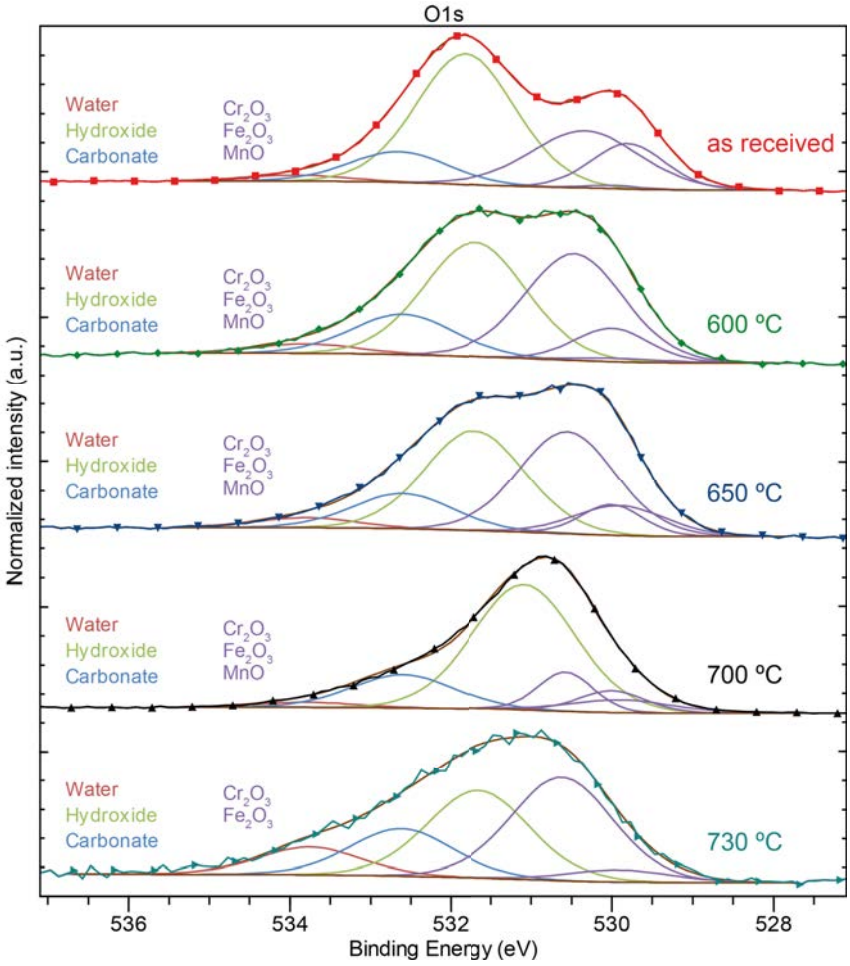

Figure 4.20: O_{1s} high-resolution XPS spectra obtained on the surface of untreated and reduced samples

600 °C to 700 °C the shift of binding energy is 0.61 eV that is large compared to the rest of the peaks. This probably means that Mn could have formed more oxide (Feliu and Pérez-Revenga 2004) and hydroxide on the surface in the same temperature range.

The binding energy for water, hydroxide, carbonate and oxides are in concordance with the results presented by (Dupin et al. 2000). A useful information about the binding energy for the O_{1s} peak can be observed (**Figure 4.22**). Note that in the Figure the transition metals are referred as TM. In general, when the reduction temperature increases,

Compound	as received			600 ºC			650 ºC			700 ºC			730 ºC		
	Position (eV)	FWHM (eV)	%At Conc	Position (eV)	FWHM (eV)	%At Conc	Position (eV)	FWHM (eV)	%At Conc	Position (eV)	FWHM (eV)	%At Conc	Position (eV)	FWHM (eV)	%At Conc
Water	533.92	1.45	2.25	533.80	1.50	3.19	533.80	1.47	3.43	533.80	1.50	2.40	533.76	1.50	9.95
Hydroxide	531.82	1.45	49.29	531.70	1.50	38.83	531.70	1.47	34.54	531.09	1.50	59.25	531.66	1.50	31.63
Carbonate	532.65	1.45	11.53	532.60	1.50	13.71	532.60	1.47	12.14	532.60	1.50	15.66	532.62	1.50	17.02
Cr_2O_3	530.33	1.58	23.54	530.46	1.44	34.83	530.56	1.42	34.07	530.57	0.80	9.92	530.62	1.50	37.14
Fe_2O_3	529.80	1.07	12.72	529.90	1.39	1.10	529.90	1.33	9.36	529.90	1.50	6.04	529.90	1.50	4.26
MnO	530.00	0.78	0.67	530.00	1.10	8.35	530.00	0.90	6.47	530.00	0.98	6.73	530.00	1.10	0.00

Table 4.6: O_{1s} spectral fitting parameters: binding energy (eV), FWHM value (eV) and percentage of atomic concentration. The relative error of FWHM and %at. concentration is $\sim$ 1.5%

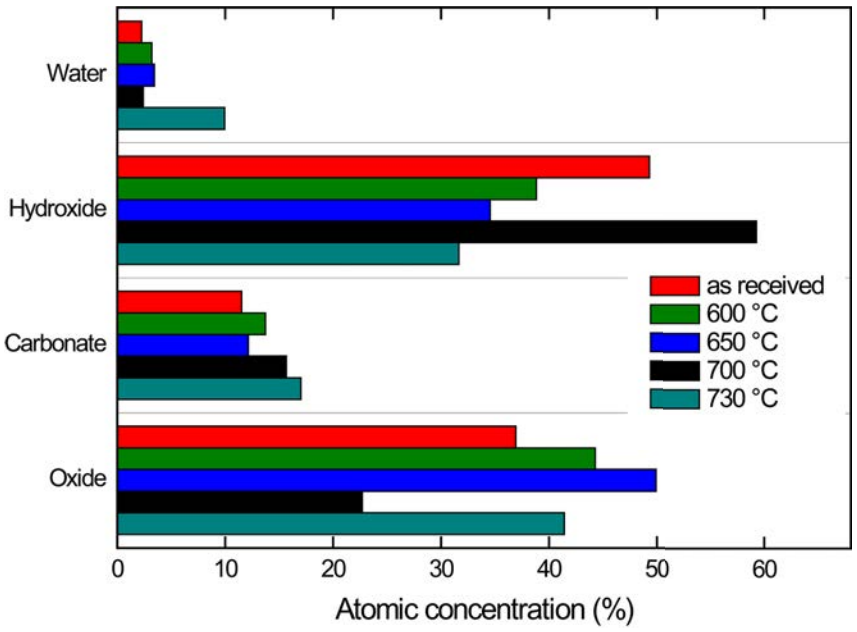

Figure 4.21: O_{1s} atomic concentration bar chart of reduced and as received samples, measured on the surface of the samples

the percentage of oxygen detected on the surface is lower. The surface reacts less with oxygen as it has a new passivation layer.

Figure 4.23 shows the C_{1s} high resolution spectra obtained on the surface of untreated and reduced samples. The spectral fitting parameters of these spectra are presented in **Table4.7**. The peak of adventitious carbon (Barr and Seal 2002) is situated at 284.8 eV and may be attributed to the presence of C–C/C–H groups. At room temperature, the surface of any metal, in contact with the atmosphere, irrespective of its composition, instantaneously becomes coated with a thin film of C–C/C–H groups (with a thickness less than 3 nm) (Feliu and Pérez-Revenga 2004). In addition, the deconvolution shows that the sample of stainless steel without reduction has more carbonate species than the reduced samples.

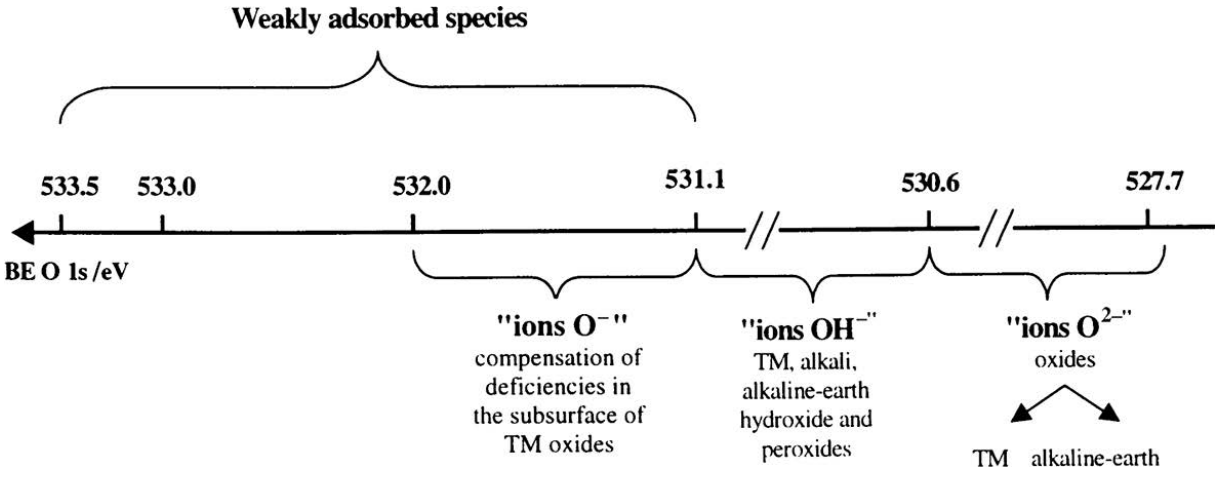

Figure 4.22: A binding energy scale for the O_{1s} peak (Dupin et al. 2000)

Compound	as received			600 ºC			650 ºC			700 ºC			730 ºC		
	Position (eV)	FWHM (eV)	%At Conc	Position (eV)	FWHM (eV)	%At Conc	Position (eV)	FWHM (eV)	%At Conc	Position (eV)	FWHM (eV)	%At Conc	Position (eV)	FWHM (eV)	%At Conc
C-C, C-H	284.80	1.33	68.15	284.80	1.48	75.32	284.80	1.44	76.14	284.80	1.27	77.04	284.80	1.32	71.99
C-OH, C-O-C	286.30	1.33	9.66	286.30	1.48	9.38	286.30	1.44	8.74	286.30	1.27	9.49	286.30	1.32	8.50
C=O	287.80	1.33	2.69	287.80	1.48	3.49	287.80	1.44	2.63	287.80	1.27	3.17	287.80	1.32	2.48
O-C=O	289.16	1.33	2.91	289.64	1.48	0.62	289.31	1.44	0.40	289.51	1.27	0.32	289.31	1.32	0.30
Carbonate	288.65	1.33	16.04	288.84	1.48	4.68	288.80	1.44	4.64	288.82	1.27	3.56	288.87	1.32	1.00
Cr_7C_3	282.95	0.80	0.55	282.95	0.80	0.23	283.04	0.90	0.71	282.98	0.80	2.32	283.06	0.80	5.87
(FeCr)7C3	283.30	1.20	0.00	283.35	1.20	0.00	283.35	1.20	0.68	283.26	0.56	1.85	283.28	0.71	4.44
Fe_3C	283.60	0.50	0.00	283.65	0.65	6.29	283.63	0.62	6.05	283.62	0.50	2.25	283.66	0.50	5.42

Table 4.7: C_{1s} spectral fitting parameters: binding energy (eV), FWHM value (eV) and percentage of atomic concentration. The relative error of FWHM and %at. concentration is $\sim$ 1.5%

The existence of peak at the highest binding energies of the C_{1s} high resolution spectrum may indicate the existence of isolated points of low thickness corresponding to the oils used to protect the steel surfaces during their storage (Feliu and Pérez-Revenga 2004). At 286.30 and 287.80 eV others peaks appear that are attributed to C−OH/C−O−C and C=O groups, respectively. The binding energy for O−C=O groups varies between 289.16 to 289.64 eV. In addition, at low binding energies there are shoulders in the spectra, even

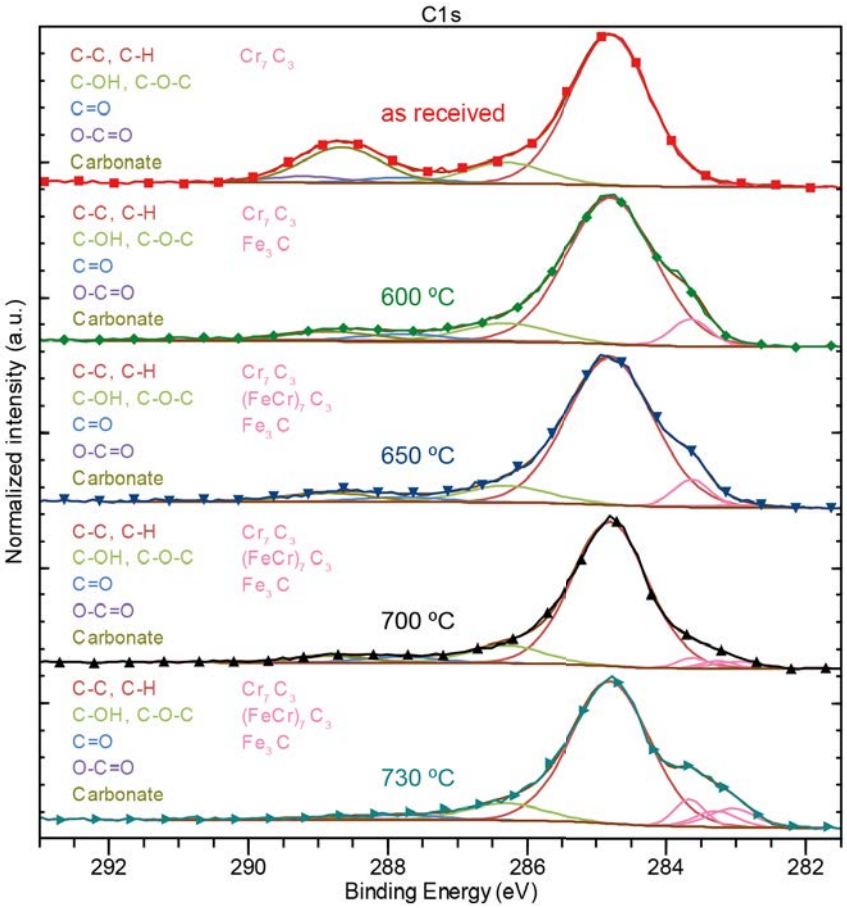

Figure 4.23: C_{1s} high-resolution XPS spectra obtained on the surface of untreated and reduced samples. The relative error of FWHM and %at. concentration is $\sim$ 1.5%.

in the untreated sample. The bond energies for these peaks vary between 282.95 and 283.66 eV, which correspond to carbides (Detroye et al., 1999). At 730 °C, it should be noted that Fe_3C is not removed from the surface. When we compare the atomic concentration % of the three types of carbides we notice that their value differs slightly. The XPS analysis confirms that on the surface of the reduced samples they are iron, chromium and carbon. In other words, the precipitated particles obtained at 730 °C are composed of iron and chromium carbides. As stated above, the carbides form a porous layer on the surface which also acts as a passivation layer. In fact, that layer reacts less with oxygen when exposed to the environment.

Figure 4.24 shows graphically the evolution of C_{1s} compounds for samples analyzed. For each sample, the carbide bars represent the sum of the carbide percentages. For C_{1s} spectra, C−C/C−H groups contribute more to the peak area than other species. But if the sample was not extracted from the vacuum chamber, this behavior would be different. In fact, that is exactly what happens when we continue the whole process. On the samples that are not extracted from the reactor after the reduction process at 730 °C, there are only carbides (cyan bar). The CNTs growth is done after the reduction. Normally, we wait until the substrate temperature drops below 300 °C and then we start the growth process.

We have carried out the deconvolution of the Fe and Cr peaks following the process used by (Mark C. Biesinger et al. 2011). For that, only the $2p_{3/2}$ signal and its associated structure were analyzed. The current databases attempt to assign oxidation states from the binding energy of this $2p_{3/2}$ signal assuming a single identifiable peak maximum. This assumption has been shown to be invalid for many transition metal spectra (Mark C. Biesinger et al., 2011).

Hence, for the Fe $2p_{3/2}$ spectra in **Figure 4.25**, the deconvolution was carried out. The spectral fitting parameters of these spectra are presented in **Table4.8**. In the steel sample without reduction, the left side of the spectrum is the most prominent. The observed peaks show binding energies in the range of 709.75 to 713.25 eV. All the peaks

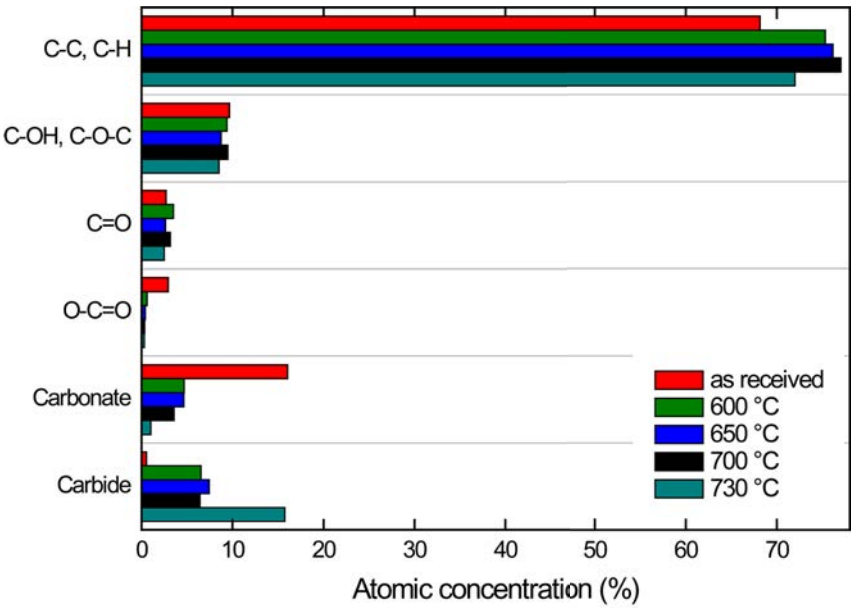

Figure 4.24: C_{1s} atomic concentration bar chart of untreated and reduced samples, measured on the surface of the samples

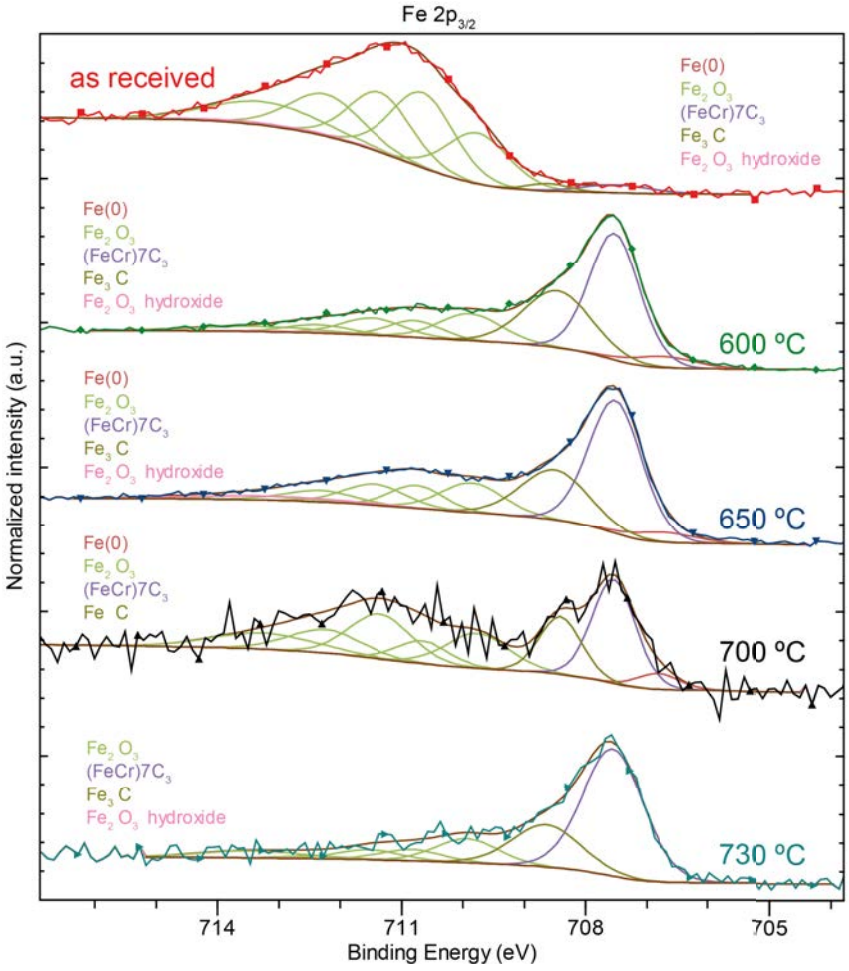

Figure 4.25: Fe $2p_{3/2}$ high-resolution XPS spectra obtained on the surface of untreated and reduced samples

correspond to the Fe_2O_3 (Mark C. Biesinger et al. 2011). At lower energies, on the right side of the spectrum, a small shoulder can be seen. There are three low intensity peaks with binding energies between 706.8 and 708.6 eV. These peaks correspond to the metal and carbide signal (Detroye et al. 1999). On the other hand, all reduced samples have a different spectrum than described above. The main difference lies in the displacement of the Fe $2p_{3/2}$ peak to the right. As we can see, the carbide signal has increased compared to the Fe_2O_3 signal. Two high intensity peaks can be differentiated in the spectra of reduced samples. One has a binding energy between 707.50 and 707.55 eV, which correspond to the $(FeCr)_7C_3$ (Detroye et al. 1999) and the other has a binding energy between 708.41 and 708.60 eV and can be attributed to the Fe_3C. It should be noted that at the temperature at which the CNTs are obtained, the peaks of the carbides present on the surface are clearly differentiated in these spectra. They are not in the same proportion as observed in the C_{1s} spectrum at 730 °C. In the Fe $2p_{3/2}$ spectrum at 730 °C, the carbide prevailing on the surface is $(FeCr)_7C_3$.

In addition, **Figure 4.26** shows the atomic concentration of the peaks. For each sample, the Fe_2O_3 bars represent the sum of the five oxide peaks percentages. In the untreated sample, the bar that dominates the chart corresponds to Fe_2O_3 signal. This compound is part of the native oxide layer of stainless steels. However, as the reduction temperature increases, that signal decreases except at 700 °C. At this temperature, according to SEM

Sample	Compound	Peak 1			Peak 2			Peak 3			Peak 4			Peak 5		
		Position (eV)	FWHM (eV)	%At Conc	Position (eV)	FWHM (eV)	%At Conc	Position (eV)	FWHM (eV)	%At Conc	Position (eV)	FWHM (eV)	%At Conc	Position (eV)	FWHM (eV)	%At Conc
as received	Fe(0)	706.80	1.20	0.06												
	Fe_2O_3	709.75	1.19	17.16	710.65	1.20	25.52	711.35	1.20	20.34	712.25	1.40	16.55	713.25	2.11	14.06
	$(FeCr)7C_3$	707.50	1.30	2.89												
	Fe_3C	708.60	0.80	1.69												
	Fe_2O_3 hydroxide	713.20	3.00	1.71												
600 °C	Fe(0)	706.73	1.20	4.44												
	Fe_2O_3	709.88	1.20	10.64	710.78	1.00	5.55	711.48	1.20	6.75	712.38	1.20	3.28	713.38	2.20	3.83
	$(FeCr)7C_3$	707.52	0.96	40.22												
	Fe_3C	708.45	1.30	24.53												
	Fe_2O_3 hydroxide	713.20	3.00	0.75												
650 °C	Fe(0)	706.70	1.20	3.57												
	Fe_2O_3	709.85	1.20	10.73	710.75	1.00	6.97	711.45	1.20	7.57	712.35	1.33	4.57	713.35	2.20	2.53
	$(FeCr)7C_3$	707.51	1.02	40.86												
	Fe_3C	708.50	1.30	19.63												
	Fe_2O_3 hydroxide	713.20	3.00	3.55												
700 °C	Fe(0)	706.81	0.80	3.83												
	Fe_2O_3	709.76	1.20	12.78	710.66	1.00	6.89	711.36	1.20	16.41	712.26	1.40	10.00	713.26	2.00	9.72
	$(FeCr)7C_3$	707.53	0.83	26.29												
	Fe_3C	708.41	0.80	14.08												
	Fe_2O_3 hydroxide	713.20	3.00	0.00												
730 °C	Fe(0)	706.83	0.80	0.00												
	Fe_2O_3	709.94	1.20	10.48	710.84	1.20	4.87	711.54	1.20	4.33	712.44	1.20	1.24	713.44	2.00	5.20
	$(FeCr)7C_3$	707.55	1.16	53.71												
	Fe_3C	708.64	1.30	19.94												
	Fe_2O_3 hydroxide	713.20	2.00	0.23												

Table 4.8: Fe $2p_{3/2}$ spectral fitting parameters: binding energy (eV), FWHM value (eV) and percentage of atomic concentration. The relative error of FWHM and %at. concentration is $\sim$ 1.5%

images, carbides precipitated on the surface did not completely cover the surface. So, when the sample was taken from the vacuum chamber, the protection of the passivation layer (composed of carbides) was lower. The XPS analysis has also shown that the carbide that prevails at a range of 600 to 700 °C is an iron and chromium-rich carbide.

In order to perform the deconvolution of the Cr $2p_{3/2}$ spectra, the work of (Mark C. Biesinger et al. 2011) has been used as a reference, as for the Fe $2p_{3/2}$ spectra. The spectral fitting parameters of these spectra are presented in **Table4.9**. In all spectra, except that reduced at 600 °C, six curves were used to make the adjustment of the region with the highest binding energy (left side in **Figure 4.27**). Five of them vary between 575.7 and 578.9 eV corresponding to the Cr_2O_3. The binding energy for the other peak is 577.3 eV and is attributed to Cr_2O_3 hydroxide (Mark C. Biesinger et al. 2011). The signal from these six peaks is the dominant in the spectrum of the sample without reduction and also in the reduced sample at 700 °C. The untreated sample has the native oxide layer and that is evidenced in the dominant signal of Cr_2O_3 and its hydroxide. On the other hand, at 700 °C, the oxide and hydroxide signals are high since the surface with few carbide precipitates was exposed to atmosphere gases. The area under the carbide precipitates is more reactive to oxygen. Two additional peaks appear in the region with the lowest binding energy of the Cr $2p_{3/2}$ spectra. These signals are dominant in all spectra of the reduced samples, except for that obtained at 700 °C. Although their signal is less intense,

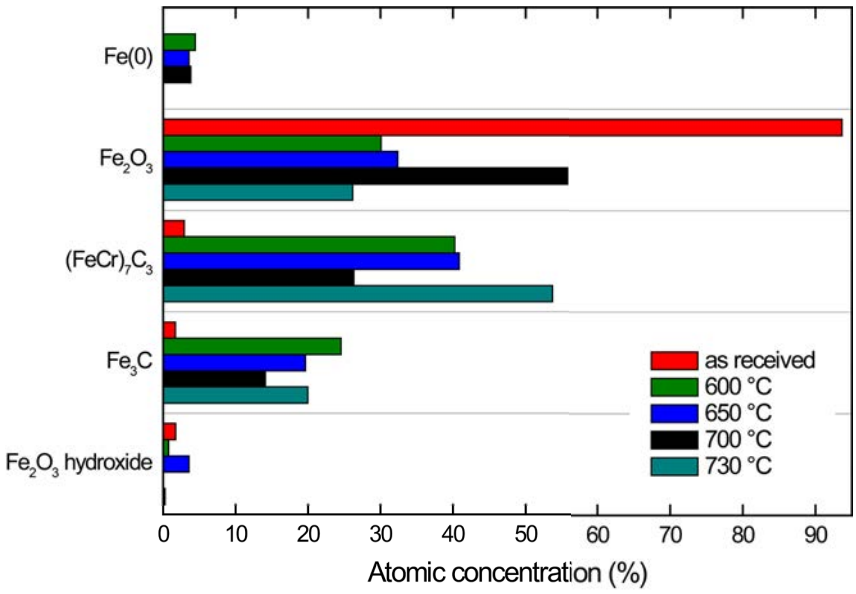

Figure 4.26: Fe $2p_{3/2}$ atomic concentration bar chart of untreated and reduced samples, measured on the surface of the samples

Sample	Compound	Peak 1			Peak 2			Peak 3			Peak 4			Peak 5		
		Position (eV)	FWHM (eV)	%At Conc	Position (eV)	FWHM (eV)	%At Conc	Position (eV)	FWHM (eV)	%At Conc	Position (eV)	FWHM (eV)	%At Conc	Position (eV)	FWHM (eV)	%At Conc
as received	Cr(0)	574.2	0.8	0.05												
	Cr_2O_3	575.7	0.94	25.38	576.71	1.23	27.57	577.49	1.14	24.77	578.49	0.5	3.1	578.9	1.5	12.47
	Cr_7C_3	574.5	1.44	0												
	$(FeCr)_7C_3$	574.2	1	1.22												
	Cr_2O_3 hydroxide	577.3	2.6	5.44												
600 °C	Cr(0)	574.18	0.9	1.05												
	Cr_2O_3	575.7	0.94	18.09	576.71	0.94	6.93	577.49	0.94	0.29	578.49	0.94	0	578.9	0.94	0.24
	Cr_7C_3	574.81	1	33.32												
	$(FeCr)_7C_3$	574.25	0.93	15.66												
	Cr_2O_3 hydroxide	577.3	2.6	24.41												
650 °C	Cr(0)	574.25	0.8	1.14												
	Cr_2O_3	575.7	1.4	20.06	576.71	1.5	9.82	577.49	1.17	1.47	578.49	0.5	0.19	578.9	1.5	1.01
	Cr_7C_3	574.81	1.21	29.47												
	$(FeCr)_7C_3$	574.35	0.94	17.89												
	Cr_2O_3 hydroxide	577.3	2.6	18.96												
700 °C	Cr(0)	574.25	0.8	0												
	Cr_2O_3	575.7	1.5	28.72	576.71	1.5	17.95	577.49	1.5	17.11	578.49	1.5	2.47	578.9	1.5	4.18
	Cr_7C_3	574.75	0.88	10.22												
	$(FeCr)_7C_3$	574.36	1	7.28												
	Cr_2O_3 hydroxide	577.3	2.6	12.07												
730 °C	Cr(0)	574.25	0.8	0												
	Cr_2O_3	575.7	1.49	9.08	576.71	1.5	9.03	577.49	1.5	0	578.49	0.91	0.83	578.9	1.5	0.03
	Cr_7C_3	574.97	1.46	53.53												
	$(FeCr)_7C_3$	574.45	0.88	14.06												
	Cr_2O_3 hydroxide	577.3	2.6	13.44												

Table 4.9: Cr $2p_{3/2}$ spectral fitting parameters: binding energy (eV), FWHM value (eV) and percentage of atomic concentration. The relative error of FWHM and %at. concentration is $\sim$ 1.5%

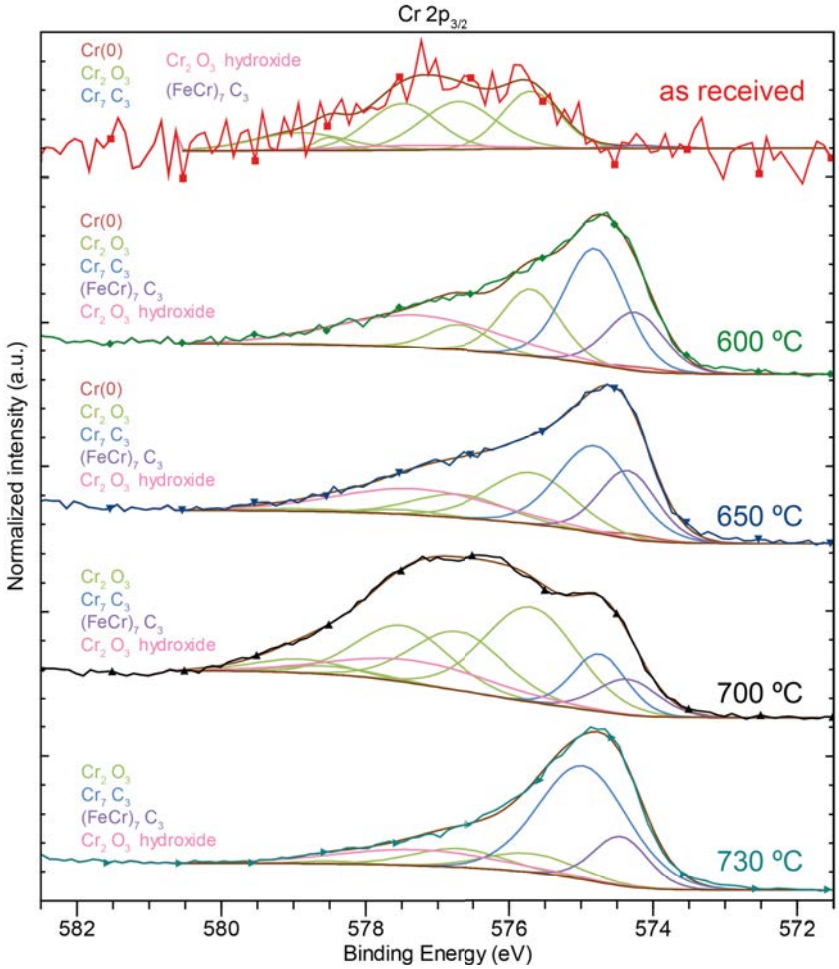

Figure 4.27: Fe $2p_{3/2}$ high-resolution XPS spectra obtained on the surface of untreated and reduced samples

they are also present on the surface of untreated stainless steel. The binding energy of one of them varies between 574.50 and 574.97 eV. With a slightly superior binding energy, the other peak is between 574.20 and 574.45 eV. According to the consulted literature, these peaks are attributed to Cr_7C_3 and $(FeCr)_7C_3$, respectively (Detroye et al. 1999). These results are consistent with the results of the C_{1s} and Fe $2p_{3/2}$ spectra deconvolution. The temperature and the hydrogen-argon plasma promote the formation of carbides on the 304 stainless steel surfaces.

As for the analysis of the previous high-resolution spectra, **Figure 4.28** presents the evolution of the atomic concentration of the compounds identified in the Cr $2p_{3/2}$ spectra. For each sample, the Cr_2O_3 bars represent the sum of the five oxide peaks percentages. Again, the bar representing the oxide of the untreated steel sample is the one that stands out in the graph. This is not surprising, it has already been mentioned that stainless steel has an oxide layer that protects it from external agents. It is also noted that the carbide that prevails on the surface of all samples is the Cr_7C_3. If we complement the information found in the high resolution spectrum of Fe $2p_{3/2}$, it can be stated that at 730 °C the carbides present on the surface are Fe_3C, $(FeCr)_7C_3$ and Cr_7C_3. These are arranged in ascending order according to their percentage on the surface.

In addition to the surface analysis shown until now, the reduced and untreated samples were sputtered with Ar in order to obtain a depth profile. **Figure 4.29** shows the depth

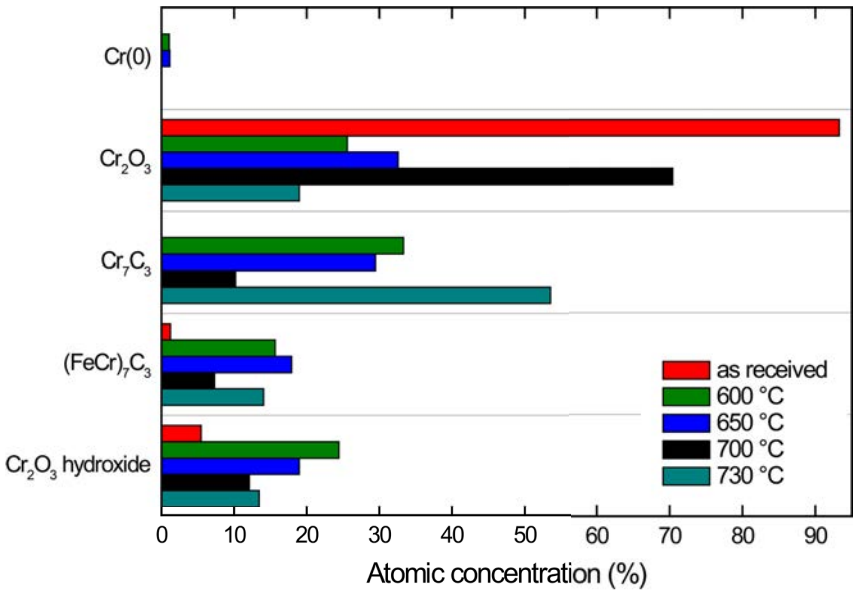

Figure 4.28: Cr $2p_{3/2}$ atomic concentration bar chart of untreated and reduced samples

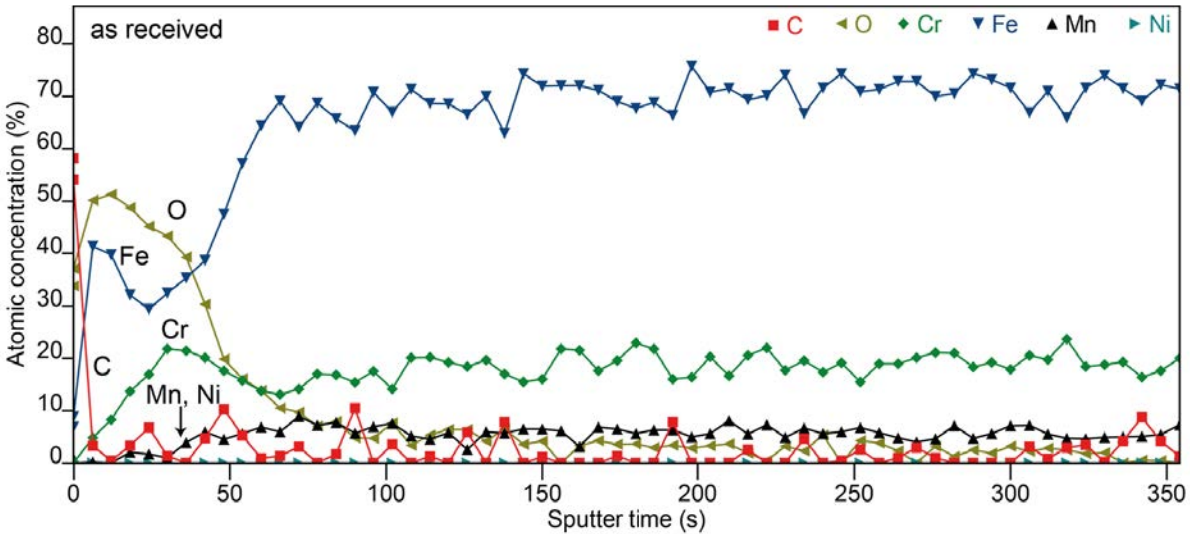

Figure 4.29: Depth profile of the sample without reduction process

profile of the sample without reduction process. Through this analysis we can see that on the surface of the untreated sample there is more Fe, Cr, C and O than Ni and Mn. This had already been observed in the survey spectrum of that sample. From this Figure, the information provided by the inner part of the material must be taken into account. Approximately up to 5 s of the sputter time corresponds to the contamination layer of the stainless steel (~ 0.3 nm thick). From this, the chemical composition of the native oxide layer and the bulk material can be observed. As the material is removed, the amount of oxygen decreases. This abrupt change in oxygen percentage indicates where the native oxide layer ends and where the bulk material begins. If we consider the information provided by (Kerber and Tverberg 2000), it could be said that the point of intersection between the lines of chromium and oxygen is in the range of 3 to 5 nm depth. This value

corresponds to the thickness of the native oxide layer. It is further observed that the native oxide layer has two well defined regions. The external one that is rich in iron and the internal one that is rich in chromium. This is consistent with the results reported by (Lothongkum et al. 2003). On the other hand, if we move deeper into the bulk material, we can see that the values for chromium and iron are as established for this type of steel in the literature. However, the percentage of manganese does not agree with the values that this material normally presents in its core. Manganese, which was only present as an impurity in the bulk material (according to the standard chemical composition, the concentration should be less than 1%), appears on the surface due to the high mobility of the Mn ions compared to other metallic species and the segregation of the surface (Mozetič et al. 2015).

On the other hand, when observing **Figure 4.30**, the reduction process on 304 stainless steel samples is evident. The chemical composition change of the material is shown in its surface and also in its inner part. The main effect to emphasize is that on reduced samples, regardless of temperature, the native oxide layer (3-5 nm thickness) was completely eliminated. The oxygen signal in these profiles is a result of the exposure of the samples to the atmosphere gases. The carbides formed on the surface act as passivation layers, especially at 730 °C (**Figure 4.30d**), but as shown in the SEM images, these layers are also porous (mostly at 700 °C) because it's made up of precipitated particles. This morphological feature probably explains that at 700 °C (**Figure 4.30c**) the percentage of oxygen in the profile is higher than in other samples. There is no sharp interface between the oxides and the bulk material due to the formation of extensive interfaces (Mozetič et al. 2015). Note that atmospheric oxygen could be reacted with Fe and Mn from areas uncoated with carbide particles and that the diameter of incident beam was bigger than the precipitates (0.8 mm), involving a signal coming both from the precipitate and the area supporting them. Chromium (∼40%) is forming carbides, while iron (<10%) and manganese (∼ 10%) are forming oxides and hydroxides. When the **Figures 4.30a-b** are compared we observe that the concentration of chromium and iron are similar. The percentages of Fe and Cr are ∼40% and ∼20%, respectively. This trend varies slightly in the deep profiles corresponding to 600 and 650 °C. This also indicates that on the surface of the reduced samples there are iron and chromium rich carbides. The carbides identified in the high resolution spectra were type Me_7C_3 and also Fe_3C. However, the most significant change in the deep profiles can be found in **Figure 4.30d**. The elements that dominate the surface are Cr and C. Their percentages are around 40% for each one. Iron has a value below 5% and the other alloying elements are almost undetectable. The use of hydrogen-argon plasma at 730 °C had made possible to modify the 304 stainless steel surfaces completely. In addition, from the shape of the profiles we can affirm that a thick layer of carbides lies on the steel. The three carbides that constitute it are Fe_3C, $(FeCr)_7C_3$ and Cr_7C_3. If we consider also the SEM image of the surface obtained at 730 °C, we can say that the carbide layer is porous.

In contrast to **Figure 4.30**, **Figure 4.31** shows the deep profiles for O, C, Fe and Cr independently. Thus, the evolution of these chemical elements can be easily visualized. **Figure 4.31a** shows the passivation effect of carbides on the surface. The samples that were reduced reacts less with oxygen, with the exception of the sample reduced at 700 °C, which has already been mentioned. The decarburization of the material as the reduction temperature increases is shown in **Figure 4.31b**. This fact makes it clear that temperature promotes the formation of carbides on the surface of 304 stainless steel samples. This is not all, it is well known that the formation of chromium precipitates in these materials also occurs at the grain boundaries. If the exposure time of the material is long enough, it

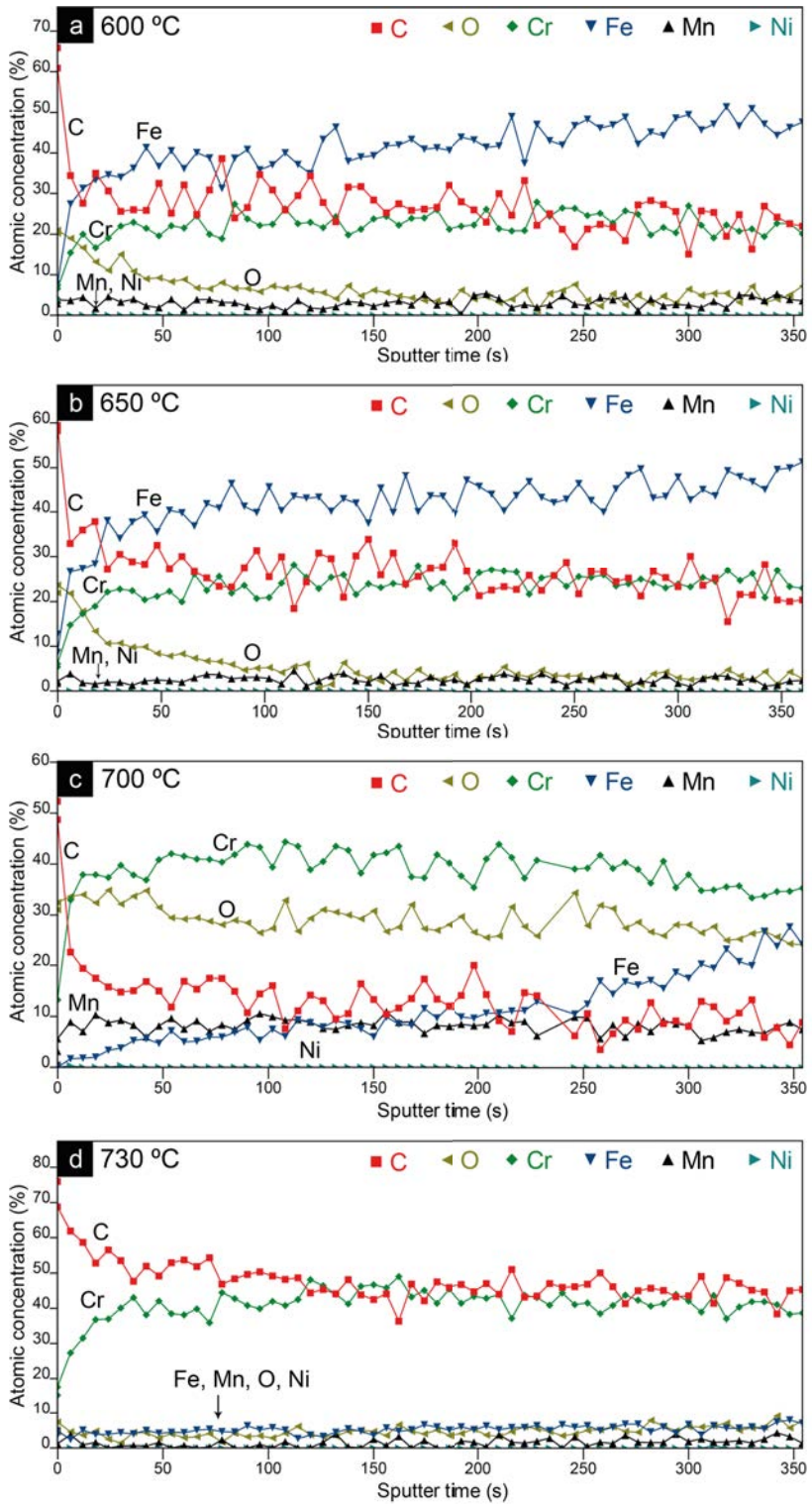

Figure 4.30: Depth profile of the sample reduced at (a) 600 °C, (b) 650 °C, (c) 700 °C, (d) 600 °C

will suffer a significant alteration of its properties. In particular its corrosion resistance, as there is not enough Cr to form the passivation layer. Mechanical properties such as ductility and toughness are also affected (L. F. Li and Celis 2004; Mallick et al. 2017). What is not seen in **Figure 4.31d** is Cr depleted zone (Akita et al. 2015). Perhaps the depth

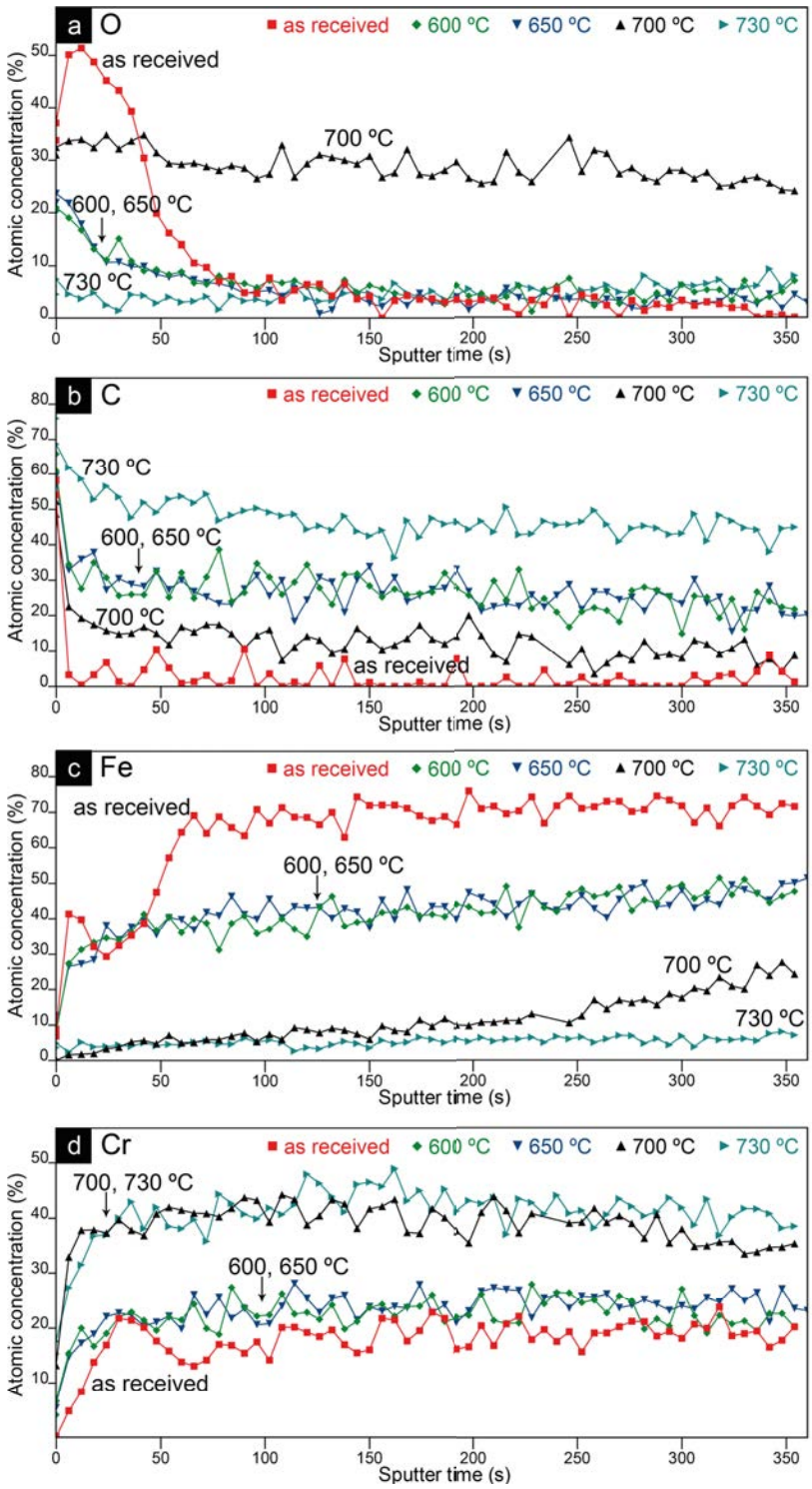

Figure 4.31: Depth profile of samples with and without reduction process for (a) oxygen, (b) carbon, (c) iron, (d) chromium

to which the analysis was performed did not exceed the thickness of the carbide layer. Under that layer is probably a poor chrome zone. Type 304 stainless steel is sensitive to carbide precipitation on grain boundaries between approximately 773 K (500 °C) and 1073 K (800 °C), this phenomenon is called sensitization. A low-carbon grade, designated 304L, is used to moderate this sensitization. Carbides themselves are believed to have

little, if any, effect on susceptibility to hydrogen embrittlement (Han et al. 1998).

In summary, the XPS analysis allowed us to study in detail the surface of the samples. It was possible to identify the different compounds and species present on the surface. Oxides and other contaminants such as hydrocarbons, water and hydroxides contaminated our samples when they were taken from the vacuum chamber, except for the untreated sample which had a native oxide layer. We were also able to observe that the native oxide layer present in 304 stainless steel is a mixture of oxides. More importantly, we now understand what happens on the surface of this material when it is exposed to a hydrogen-argon plasma with temperatures ranging from 600 to 730 °C. Its chemical composition on the surface changes dramatically. Particularly at 730 °C, temperature that we use to grow carbon nanotubes. On the surface there is a thick layer of carbides type Me_7C_3 and Fe_3C. That layer is composed mostly of Cr_7C_3 and even with less than 5% of Fe, allow us to obtain carbon nanotubes.

4.3.5 X-ray diffraction

The crystallinity of the samples was determined by X-ray diffraction. XRD analysis was performed using a PANalytical X'Pert Pro diffractometer (MPD) θ/θ Bragg-Brentano powder diffractometer of 240 millimetres of radius. The diffractometer was operating at 45 kV and 40 mA (Cu Ka_α radiation, λ=1.5418 Å). The X-ray diffraction measurements of q/2q scan were made in the range 5 to 120°θ with step size of 0.017° and measuring time of 50 seconds per step. The X-ray diffraction spectra were analyzed with a PANalytical HighScore Plus software. Crystalline phases were identified by comparison with standard reference patterns (powder diffraction file PDF-2, International Centre for Diffraction Data (ICDD)).

The steel sheets used as substrate were obtained through a cold rolling process. When a material with these characteristics is heat treated it internal structure changes. This is illustrated in **Figure 4.32**. This process is summarized in three well-defined steps for polycrystalline metal samples: recovery, recrystallization and grain growth. In the first one there is a stress relief. These were caused by the rolling process. Then, when the recrystallization temperature is exceeded, new grains begin to grow. The recrystallization temperature is usually estimated to half the melting point of the material. This is also dependent on the amount of internal energy in the material (plastic deformation percent). In other words, a material with a high percentage of plastic deformation requires less temperature to recrystallize. Finally, if the temperature exceeds the recrystallization point and depending on the annealing time, the new grains may grow. **Figure 4.32** also shows the behavior of the ductility and tensile strength of the material when recrystallizing. As new grains appear, the material becomes more ductile as its tensile strength decreases. This is because the new grains have less crystalline defects (William D. Callister and Rethwisch 2013)

We did not know the recrystallization temperature of our substrate, but through this characterization technique we could make an approximation. Our substrate is 304 stainless steel. Type 304 stainless steels are austenitic alloys that have a good combination of machinability, weldability and corrosion resistance. The "austenitic" denomination is due to the predominant presence of gamma iron in the material. Type 304 stainless steel is, however, susceptible to strain induced martensitic transformations during room temperature deformation including machining operations (Marchi et al. 2005).

Using the PANalytical HighScore Plus software, it was possible to compare the XRD spectra with the database patterns. The spectrum of untreated sample has two intense

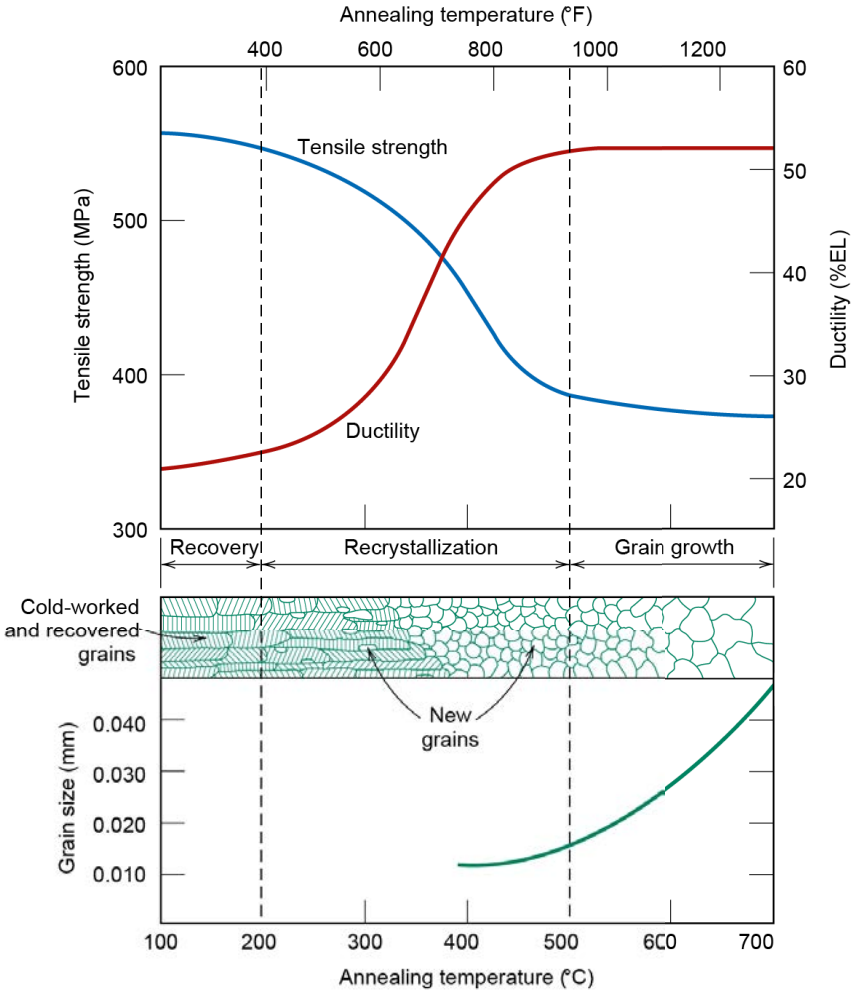

Figure 4.32: The influence of annealing temperature (for an annealing time of 1 h) on the tensile strength and ductility of a brass alloy. Grain size as a function of annealing temperature is indicated. Grain structures during recovery, recrystallization, and grain growth stages are shown schematically (William D. Callister and Rethwisch 2013)

peaks (red line in **Figure 4.33**). They were identified as (111) and (220) austenitic peaks. Other austenitic peaks with less intensity were also identified: (200), (311) and (222). In addition, three peaks of another phase are present in the untreated XRD spectrum. These were identified as (110), (200) and (211). (Mallick et al. 2017) attributed these peaks to strain induced martensite. The trend for Fe-Cr-Ni stainless steels (300-series alloys) is that higher nickel and chromium concentrations suppress the martensitic transformation temperature and thus the strain induced martensite (Mallick et al. 2017). Based on the peak area, that austenitic steel without heat treatment has 80% austenite and 20% strain induced martensite.

In the sample treated at 600 °C a slight narrowing of (111) and (220) austenitic peaks is observed. In addition, the intensity of (110), (200) and (211) strain induced martensite peaks almost disappears. This is in accordance with the stress release process. The number of crystalline defects, accumulated during plastic deformation, decreases (William D. Callister and Rethwisch 2013). At 650 °C the (111) and (220) austenitic peaks move to the left of the spectrum. In addition, the value of FWHM for these peaks increases.

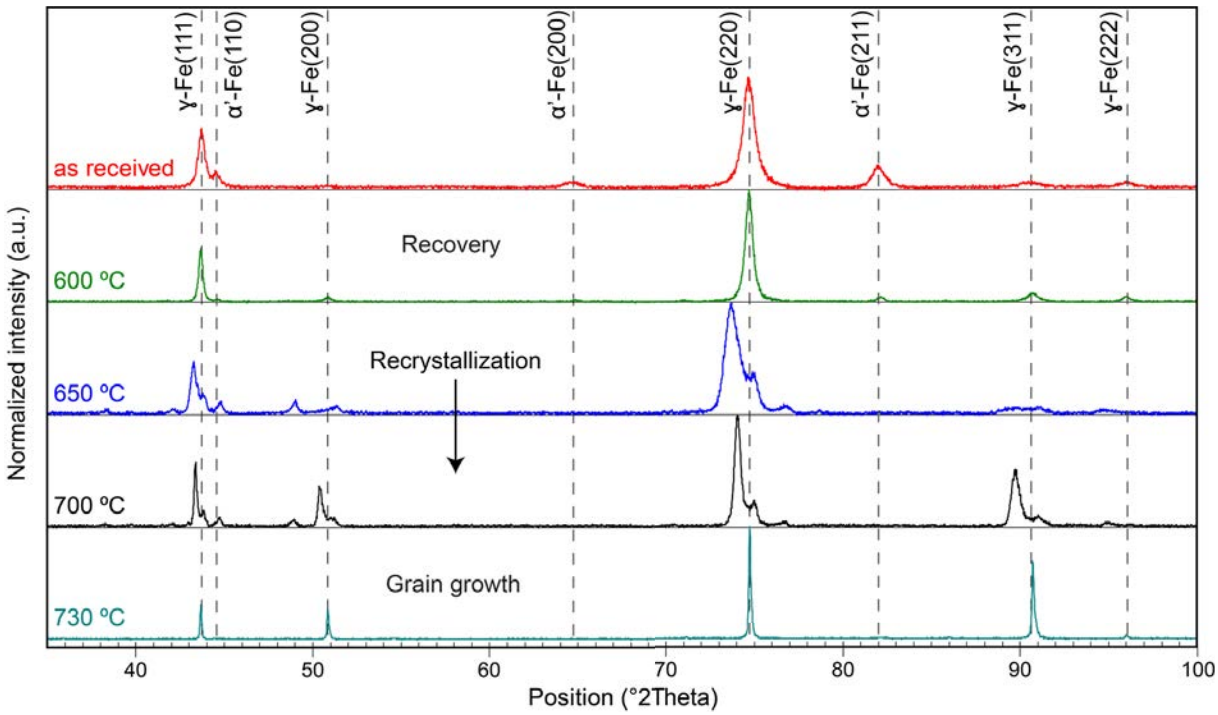

Figure 4.33: XRD patterns of untreated sample and reduced samples at 600 °C, 650 °C, 700 °C and 730 °C

According to Scherrer equation the peak width varies with 2θ as $\cos\theta$:

$$\text{FWHM} = \frac{K \cdot \lambda}{D_{\text{hkl}} \cdot \cos\theta} \tag{4.4}$$

as mentioned in the previous chapter, K is 0.94 for FWHM of spherical crystals with cubic symmetry, λ=1.5418 Å, D_{hkl} is a crystallite size and θ is expressed in radians (Speakman 2011b). A higher value of FWHM means that the crystal size decreases. This XRD spectrum shows that the recrystallization process at 650 °C has already started. At 700 °C, the (111) and (220) austenitic peaks tend to return to their position before recrystallization began. The value of FWHM (0.18) is less than at 650 °C (0.35). This can be attributed to a growth of new grains resulting from recrystallization. Two new peaks are also observed at 700 °C. One located at 50.43 (2θ) and the other located at 89.76 (2θ), may be attributed to (200) and (311) austenitic peaks, respectively. Finally, at 730 °C, the austenitic peaks (111), (220), (200) and (311) move to the original position (before recrystallization) and narrow. They are the only ones in the spectrum. The grain growth is greater than for the sample obtained at 700 °C. The parameters of the (111) and (220) austenitic peaks are listed in **Table4.10**.

Using Scherrer equation the crystal size was calculated for (111) and (220) austenitic peaks. **Figure 4.34** shows the development of crystal size with reduction temperature. In both cases the crystal size increases as the reducing temperature increases. However, between 600 and 650 °C, we see a change in this trend. This suggests that, for this material, the recrystallization temperature is in that range. For this type of stainless steel, the grain size can basically grow by two routes. One can be by using a significant increase in temperature above the recrystallization temperature. Or the other way is by using a temperature slightly higher than recrystallization temperature for a prolonged time (William D. Callister and Rethwisch 2013).

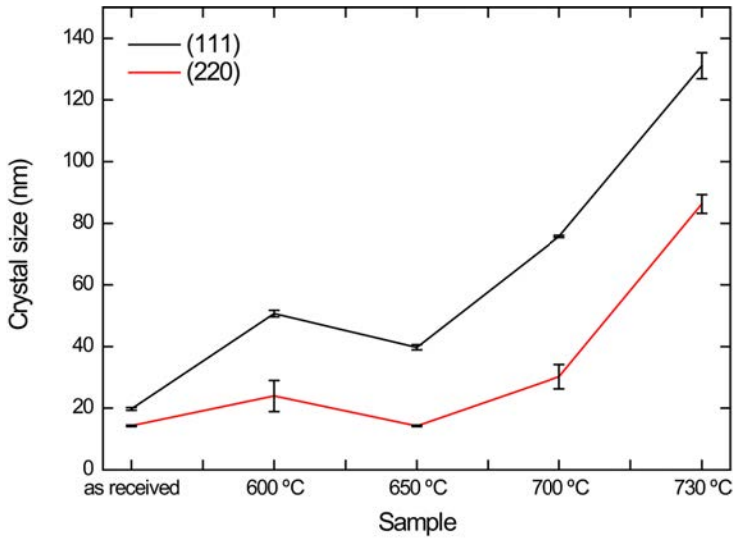

Figure 4.34: Crystal size evolution for (111) and (220) austenitic peaks

It is very important to keep in mind that once the recrystallization temperature is exceeded (for our samples under 650 °C) the size of the grains can grow to dimensions that do not benefit the material. Materials with small grains have better mechanical properties than those with large grains. In addition, the large grain size, the decarburization phenomena, the chromium diffusion to the grain boundaries (sensitization), intergranular corrosion and even the hydrogen embrittlement (Han et al. 1998; Marchi et al. 2005) can seriously deteriorate the properties of 304 stainless steel. Properties for which it has been selected as a substrate for obtaining carbon nanotubes.

4.3.6 High resolution transmission electron microscopy (HRTEM)

High resolution electron microscopy (HRTEM) analysis was performed to see differences in the number of CNT walls. In addition, using the energy dispersive X-ray (EDX) detector, it was feasible to perform an elemental analysis of a carbon nanotube obtained by PECVD. The nanotubes were obtained at 730 °C. The number of layers of this type of nanotubes is in the range of 15 to 50. The nanotubes obtained by PECVD have a

	hkl	Phase	Pos. [°2Th.]	d-spacing [Å]	FWHM [°2Th.]	Crystal size (nm)
as received	111	austenitic	43.72 ± 0.92	2.07 ± 0.04	0.45 ± 0.01	19.76 ± 0.41
	220	austenitic	74.70 ± 0.97	1.27 ± 0.02	0.73 ± 0.01	14.28 ± 0.19
600 °C	111	austenitic	43.68 ± 0.92	2.07 ± 0.04	0.27 ± 0.01	50.67 ± 1.06
	220	austenitic	74.71 ± 15.69	1.27 ± 0.27	0.49 ± 0.10	23.96 ± 5.03
650 °C	111	austenitic	43.27 ± 0.91	2.09 ± 0.04	0.35 ± 0.01	39.74 ± 0.83
	220	austenitic	73.73 ± 1.25	1.28 ± 0.02	0.84 ± 0.02	14.26 ± 0.24
700 °C	111	austenitic	43.38 ± 0.22	2.08 ± 0.01	0.18 ± 0.01	75.74 ± 0.38
	220	austenitic	74.07 ± 9.63	1.28 ± 0.17	0.39 ± 0.01	30.23 ± 3.93
730 °C	111	austenitic	43.68 ± 1.40	2.07 ± 0.07	0.11 ± 0.01	131.10 ± 4.20
	220	austenitic	74.75 ± 2.62	1.27 ± 0.04	0.14 ± 0.01	86.27 ± 3.02

Table 4.10: (111) and (220) austenitic peaks parameters

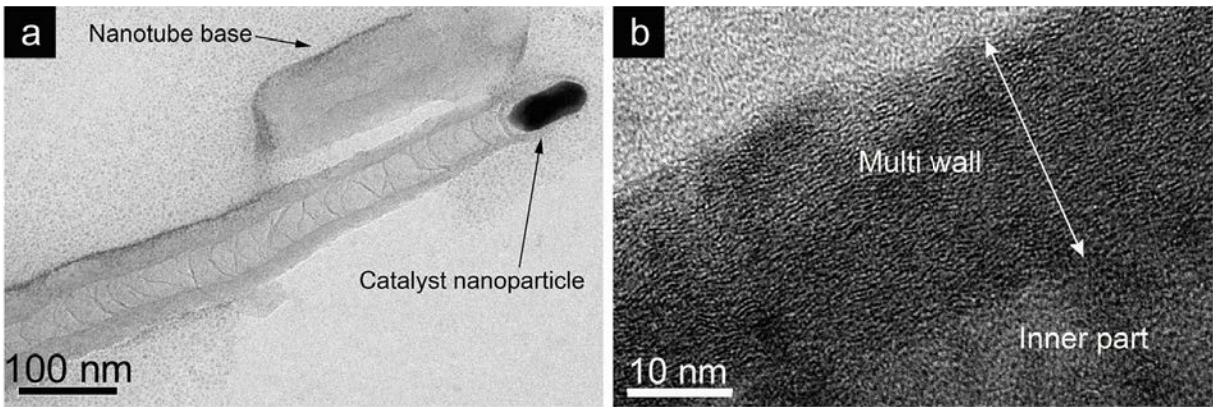

Figure 4.35: TEM images of wulti walled CNT. (a) Catalyst particle at the tip of the CNT, (b) Detail of the multi wall

"conical" shape. So, depending on where we look (base, center or tip), the number of layers changes. In **Figure 4.35a**, two different sections can be distinguished. One section belongs to the base of a CNT, that possibly fractured during sample preparation, and the other corresponds to a CNT tip. The number of layers is lower as we move closer to the catalyst particle. **Figure 4.35b** was taken in a section close to the base so the thickness of the multi-layer wall is greater than the one presented by the nanotube at the tip. In addition, the distance between layers is 0.34 nm. This value is consistent with that previously reported in our research group (Shahzad Hussain 2014).

Figure 4.36 shows the elemental analysis of a carbon nanotube and **Table4.11** contains the weight percentage of the elements detected in the nanostructure. As a carbon nanotube, carbon is the most abundant element (green). It is followed, and by far, by iron (red). This element is present in the catalyst particle. The high value of copper is due to the contribution given to the signal by the grid that supports the nanotube (yellow). It should also be noted that there is an oxygen signal since the nanotube was exposed to atmospheric gases (cyan). On the other hand, the signal from the other alloy elements is negligible. At least in this nanotube, the elements present are carbon and iron.

This is consistent with the results presented by (Thapa et al. 2018). Catalytic nanoparticles are mostly made of iron. They report that also found Mn, Ni, and Cr in some nanoparticles. 304 stainless steel has at least two elements that are commonly used to obtain CNT, iron and nickel. Not surprisingly, these elements are part of the nanoparticles present at the tips of nanotubes. In fact, that is what was expected. To be able to use alloy elements as catalysts for CNTs without depositing external material.

The results obtained through the TEM characterization, together with the results obtained previously, allow us to understand how the carbon nanotubes growth directly on 304 stainless steel. At 730 °C, the hydrogen-argon plasma reduced the native oxide layer of stainless steel and the process also induced the formation of a chrome-rich carbide layer. According to SEM images and XPS analysis, that layer was porous and also had

	C	Fe	Cu	O	Cr	Mn	Ni
Weight %	63.32 ± 0.53	6.60 ± 0.19	29.67 ± 0.42	0.26 ± 0.42	0.06 ± 0.06	0.04 ± 0.06	0.06 ± 0.07

Table 4.11: Chemical composition of CNT obtained at 730 °C

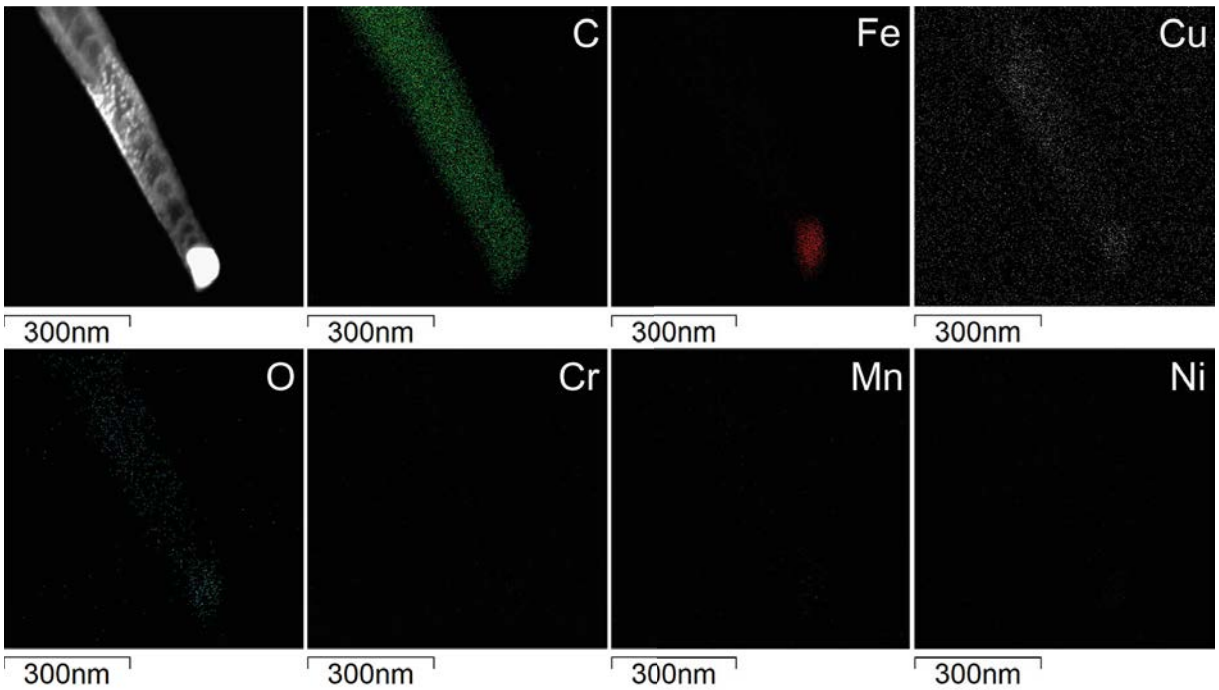

Figure 4.36: EDX elemental analysis of CNT obtained by PECVD at 730 °C

iron. The percentage of iron present in the carbide layer, although small, was enough to be used as a catalyst. So, during the growth process of CNTs, the iron nanoparticles were obtained on carbide surface. That nanoparticles had a high absorption rate and were saturated with carbon when acetylene was introduced in the vacuum chamber. Remember that 730 °C corresponds to the eutectic temperature of iron at nanoscale (Harutyunyan et al. 2005). The structures obtained were multiwalled tubes and were mainly composed of carbon (walls) and iron (catalyst particle in the tip). As described above, no diffusion barriers or other elements different from those found in the alloy substrate were used. This growth method improved the bond between the CNTs and the substrate (Masarapu and B. Wei 2007; Thapa et al. 2018).

4.3.7 Raman Shift Spectroscopy

Raman Spectroscopy was used to evaluate the quality of CNTs in samples obtained by PECVD and WACVD at 730 °C. This kind of carbon-based material displays two characteristic bands, the tangential stretching G mode ($1500 - 1600\text{cm}^{-1}$) and the D mode ($1330 - 1360\,\text{cm}^{-1}$) (Korneva 2008) (see **Figure 4.37**). In addition, multi wall carbon nanotubes (MWCNTs) present a band in the range 1617 to $1625\,\text{cm}^{-1}$ called D'-band that corresponds to defects on the side walls of CNTs (Lehman et al. 2011). D'-band is related with disordered graphitic lattice. These bands are activated by defects due to the breaking of the crystal symmetry that relax the Raman selection rules (Merlen et al. 2017).

The D band, like the D'-band, is a double resonance Raman mode which can be attributed to the presence of disordered graphitic lattice (Düngen et al. 2017), double resonance effects in sp^2 carbon and other defects (Lehman et al. 2011; Osswald et al. 2007). Following the deconvolution process presented by (Sadezky et al. 2005) in Raman spectra were possible identified two additional bands (**Figure 4.38**). One denoted as A-

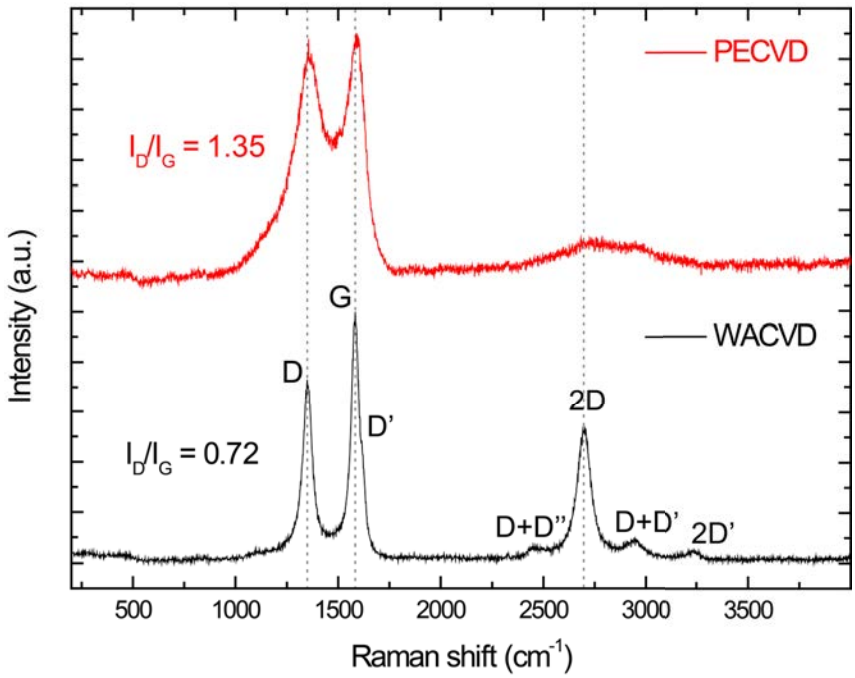

Figure 4.37: Raman spectra for directly growth of CNTs at 730 °C on 304 stainless steel by PECVD and WACVD

Band ($\sim 1500\,\mathrm{cm}^{-1}$), related with amorphous carbon (Düngen et al. 2017), and the other one denoted as D" band ($\sim 1200\,\mathrm{cm}^{-1}$). D" band according with (Venezuela et al. 2011), it is mainly due to phonons associated to the $K\Gamma$ direction in the Brillouin zone. As this band is related with very defective samples, (Couzi et al. 2016) determined the behavior of the D" band, by means the identification of two new bands (D^* and D^{**}) lying close to the D"band on defective aromatic carbons (graphite nanoplatelets, heat treated glassy carbons, pyrograph nanofilaments, and multiwall nanotubes), (Couzi et al. 2016). In our case, for carbon nanotubes, the line shape of the D" mode is significantly broadened due to contributions from different tubes in or close to resonance with the excitation laser (Herziger et al. 2014). It is necessary to take into account that the Raman intensity of the defect-induced lines (e.g., D, D', and D" bands) is proportional to the average number of defects in the material (Venezuela et al. 2011). In that sense, the number of defects in the CNTs can be estimated by using the intensity ratio between D band and G band (I_D/I_G). As the I_D/I_G ratio decreases, so does the number of structural defects present in the CNTs (Shahzad Hussain, Amade, and Bertran 2014). For sample obtained by PECVD the value of the ratio I_D/I_G is 1.35, which if compared for sample obtained by WACVD ($I_D/I_G = 0.72$) is higher. The Raman feature are given in **Table4.12**.

The difference is considerable and is most likely due to the different amount of amorphous carbon present in the first one. A comparison of **Figure 4.38a** and **Figure 4.38b** indicates that the A-band in the CNTs obtained by PECVD is more intense than that observed in the sample obtained by WACVD. However, although A band is related to amorphous carbon, it does not provide information on the type of amorphous carbon. For "pure" amorphous carbons, the Raman spectra can be seen as simpler, because only a broad asymmetric band is seen close to $1500\,\mathrm{cm}^{-1}$. However, this is incorrect, and for several reasons. First, many different kinds of amorphous carbon exist: sp^2 dominated

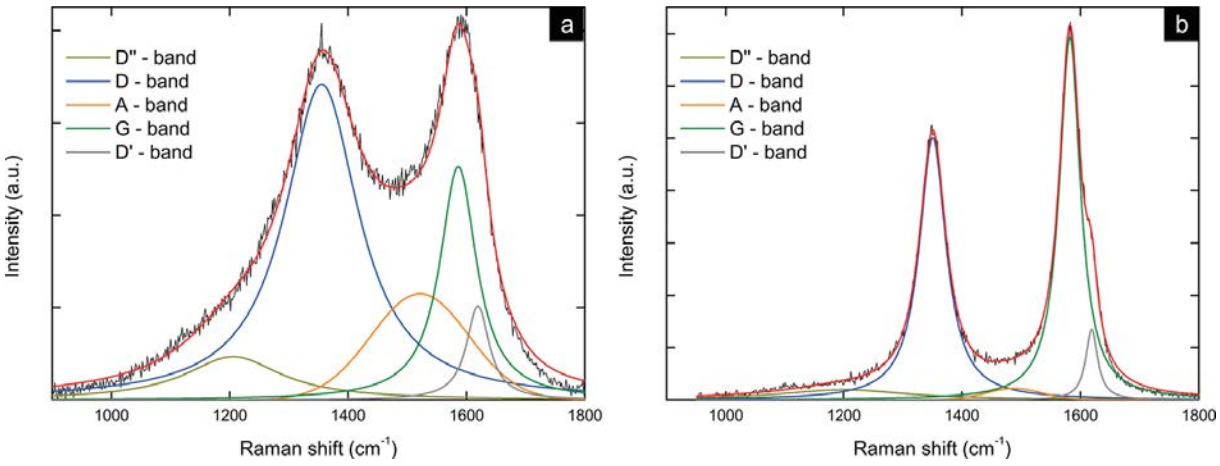

Figure 4.38: D and G band deconvolution for MWCNTs obtained by (a) PECVD and (b) WACVD at 730 °C

ones (a-C), sp^3 dominated ones (ta-C, referring to tetrahedral amorphous carbon), one containing heteroatoms such as H (a-C:H, ta-C:H, an others) or N. Their structure and properties are related but widely varying. Second, as there is some aromatic carbon embedded in their structure, some resonance occurs (Merlen et al. 2017). There is another approach that identifies the type of amorphous carbon. It is possible to discriminate between types of amorphous carbon with the G-band data. (Pardanaud et al. 2014) related the shift and width (FWHM) of the G band with the type of amorphous carbon. We have plotted the data obtained for our samples in **Figure 4.39**. According to this figure, the amorphous carbon for PECVD and WACVD samples correspond to nanocrystalline graphite (nc-G).

If one uses FWHM_G (Γ_G) as an indicator of local disorder close to sp^2 bonds in the material (which can be related to the size of the clusters and/or to the sp^3 content close to sp^2 bonds, one can use this parameter in order to have an idea of where is the sample situated in Ferrari's "three stage model". With this in mind, nc-G is more ordered than aC:H/D which are themselves more ordered than ta-C:H and ta-C. The presence

		D"	D	A	G	D'	2D	I_D/I_G	$I_D/I_{D'}$	I_{2D}/I_G
PECVD	Position (cm^{-1})	1205.86 ± 7.81	1355.31 ± 0.92	1521.50 ± 8.63	1586.20 ± 1.82	1619.35 ± 1.91		1.35	3.35	
	Intensity (a.u.)	0.94 ± 0.02	6.84 ± 0.14	2.30 ± 0.05	5.06 ± 0.10	2.04 ± 0.04				
	FWHM (cm^{-1})	197.33 ± 17.40	152.05 ± 4.61	194.07 ± 10.13	74.98 ± 4.62	46.69 ± 6.96				
WACVD	Position (cm^{-1})	1200.20 ± 10.47	1350.72 ± 0.12	1488.25 ± 5.27	1582.26 ± 0.11	1619.11 ± 0.33	2698.32 ± 0.12	0.72	3.73	0.55
	Intensity (a.u.)	0.38 ± 0.01	10.03 ± 0.20	0.43 ± 0.01	13.86 ± 0.28	2.69 ± 0.05	7.61 ± 0.23			
	FWHM (cm^{-1})	263.38 ± 31.47	54.71 ± 0.50	110.73 ± 14.53	43.44 ± 0.47	24.40 ± 1.28	81.11 ± 0.36			

Table 4.12: Raman feature of MWCNTs obtained by PECVD and WACVD at 730 °C

of hydrogen systematically diminishes the shift of the G band (for ta C/ta-C:H and a C/ta-C:H) (Merlen et al. 2017).

For what has been exposed so far, it can be said that PECVD sample has a greater disorder than WACVD sample. The disorder of the materials is directly related to the defects of the material (e.g. vacancies and boundaries). The $I_D/I_{D'}$ ratio is useful to know which type of defect is predominant in the materials. (Eckmann et al. 2012) showed for graphene that the ID/ID' is very effective to discriminate between different kinds of defects: $I_D/I_{D'} = 3.5$, the minimum value, is found for boundaries, whereas $I_D/I_{D'}$ is close to 7 for vacancy like defects and up to 13 for sp^3 defects (Eckmann et al. 2012). The $I_D/I_{D'}$ ratio is interesting because, according to the resonance Raman theory, it is not sensitive to the number of defects but only to the type of defects (Merlen et al. 2017). In our case, although it is not precisely graphene sheets, the ratio $I_D/I_{D'}$ is close to the value corresponding to 3.5 that is attributed to boundaries type. The value of $I_D/I_{D'} = 3.35$ of sample obtained by PECVD is below the minimum value determined by (Eckmann et al. 2012) for graphene. This may be influenced by the fact that the Raman fingerprint of the material, in the range $900 - 1800\,\mathrm{cm}^{-1}$, was strongly affected by the amorphous carbon (nanocrystalline graphite). In between amorphous materials and perfect crystals, defects play a role in the disturbed Raman scattering process (Merlen et al. 2017). Note that the borders of the crystallites work as defects involved in the double-resonance process, giving rise to the D and D' bands in the Raman spectra of nanographites (Cançado et al. 2007).

The growth process also influences the crystalline state of carbon-based structures. Because of defects implied in this model, Raman spectroscopy can be used to characterize how a graphenic material is far from its crystalline state (Merlen et al. 2017). The value of crystallite size (L_a) for the sample obtained by PECVD is less than that of the sample obtained by WACVD. This can be seen graphically in **Figure 4.40**. We have plotted the values of Γ_D and Γ_G on chart prepared by (Merlen et al. 2017). In this chart the FWHM values of the D and G bands are related. Depending on the characteristic size of the aromatic domain, the data are grouped in three different areas: the lowest rectangle with L_a higher than roughly 10 nm, the intermediate region with La in the range of few to

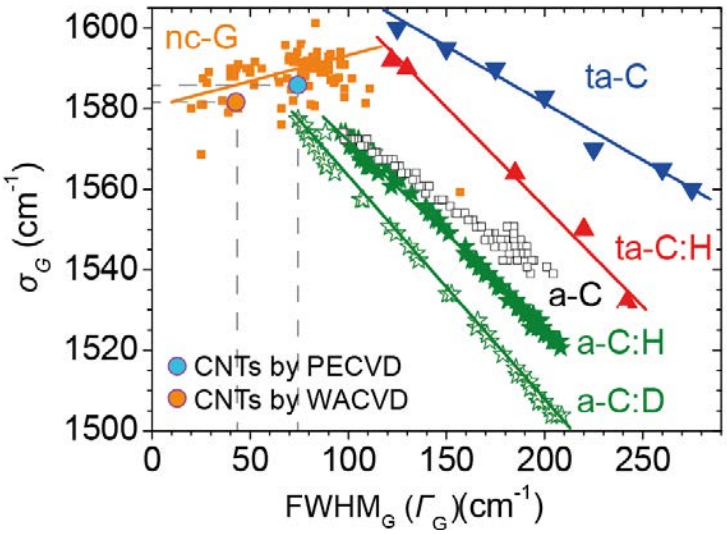

Figure 4.39: Plots of σ_G *vs.* Γ_G for nc-G and different amorphous carbons. Data were recorded with $\lambda_L = 514$ nm. Adapted from (Merlen et al. 2017)

10 nm, and the higher one with L_a close to 1 nm. For PECVD sample L_a is close to 1 nm and for WACVD sample $L_a > 10$ nm. This makes sense, the sample obtained by PECVD, which has more amorphous carbon and therefore more defects, has a smaller crystal size than that obtained for the WACVD sample, which has less amorphous carbon. Besides, this is in accordance with the established by the I_D/I_G ratio, the samples obtained by PECVD have a greater degree of disorder than the samples obtained by WACVD.

Note that for WACVD sample, an additional set of bands in the range of 2350 – 3300 cm^{-1} appears. The most intense and sharp peak is located at 2698.32 cm^{-1} and it

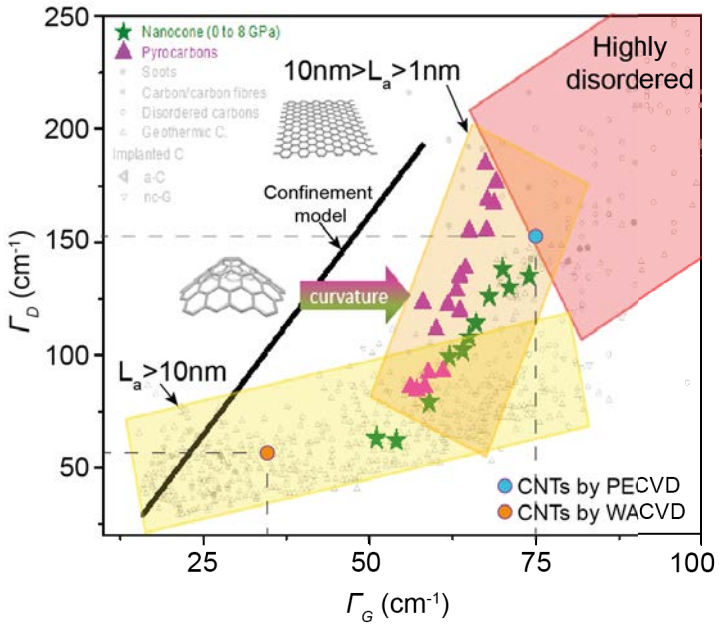

Figure 4.40: Γ_D *vs.* Γ_G plot for a large variety of disordered aromatic carbons. Adapted from (Merlen et al. 2017)

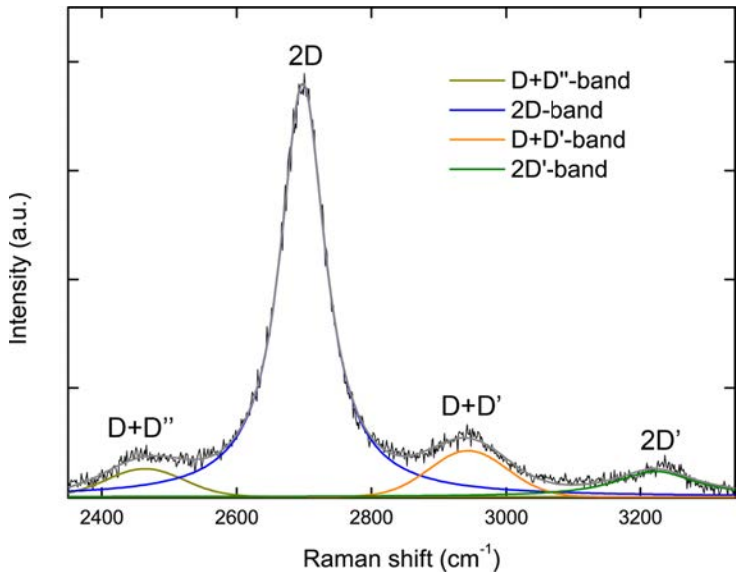

Figure 4.41: 2D band deconvolution for WACVD sample

is attributed to the 2D band (**Figure 4.41**). The 2D band is caused by two-phonon scattering around the K point of the Brillouin zone, and it is active due to the double resonance mechanism (Reich and Thomsen 2004). It must be taken into account that for the D-band, a phonon and a defect are involved. For the 2D-band, only two phonons (without defect) are necessary (Merlen et al. 2017). For graphene, as it has different electronic structures close to the K point, and because the double resonance mechanism connects phonons to the electronic structure, the shift, shape (composed of several overlapped bands), and intensity of the 2-band(s) can be used to distinguish from monolayer up to 5–10 stacked layers. The relative intensity ratio between the 2D and G bands was also found to be dependent on the number of layers: I_{2D}/I_G is close to 3 for monolayer graphene, and falls down to 0.3 for highly oriented pyrolytic graphite (HOPG) (Merlen et al. 2017). For the CNTs produced by WACVD, 2D band is the overtone of D mode, but it does not need the presence of defects to appear since it is sensitive to the strain. The I_{2D}/I_G ratio value (0.55) is in accordance with the above mentioned concerning the lower number of walls in the sample obtained by WACVD. In addition, this is consistent with what was reported by (Shahzad Hussain, Amade, and Bertran 2014). Water vapor removes amorphous carbon and increases the crystallinity of carbon nanotubes.

In **Figure 4.41** it is also possible to distinguish three weak bands that are close to 2D band. In the literature these 2D subbands are denominated D+D", D+D' and 2D' and are found at $\sim$ 2460, $\sim$ 2940 and $\sim$ 3230 cm^{-1}, respectively (Merlen et al. 2017). The number and origin of the 2D sub-bands have been understood for multilayer graphene (A. C. Ferrari et al. 2006) in the framework of the double resonance mechanism and more complex things can occur such as folding (Podila et al. 2012), misorientation (Poncharal et al. 2008), and stacking faults that can modify the intensities and shape (Merlen et al. 2017). In our case these bands can be attributed to the few concentric graphene nanotubes obtained by WACVD. G, 2D and 2D subbands are sensitive to defect density in the MWCNTs, including the ones related to tube diameter and number of walls (Antunes et al. 2007).

In resume, this technique provided enough information to ensure that the CNTs samples have different characteristics. Not only morphological, as could be saw in the SEM images, MWCNTs with different structural quality were obtained. In accordance with the development of the A-band, the PECVD process produced forest of MWCNTs with a large percentage of amorphous carbon. On the other hand, the nanotubes obtained by WACVD had less amorphous carbon. Amorphous carbon was removed during the growth process of MWCNTs (Shahzad Hussain, Amade, and Bertran 2014). This was oxidized by the water vapor used during the process.

4.4 Conclusions

The native Cr_2O_3 layer was completely removed with the hydrogen-argon plasma in the temperature range 600 to 730 °C. Neither mechanical nor chemical preparation of the 304 stainless steel surfaces took place prior to the reduction process. The OES spectra allowed us to estimate that during the first 60 s, after plasma started, the oxide layer was completely reduced. The 5 minutes of process also modified the roughness of the substrate. Firestone Abbot curves proved it. The presence of high and narrow structure features and dominant high peaks on observed area was reduced after the process. In addition, through SEM, EDX and XPS characterization it was determined that carbides were precipitated on the surface of the 304 steel. Between 600 and 650 °C the most common carbides were Fe_3C

and $(FeCr)_7C_3$. In contrast, at 700 and 730 °C, the carbide found was Cr_7C_3 and in low proportion $(FeCr)_7C_3$ and Fe_3C. The removal of the native oxide layer as well as the carbide type change on the surface can be understood by reviewing the Ellingham diagrams. In the first case, one possible explanation is that hydrogen species generated in the plasma modify the stable Cr_2O_3 layer to form hydroxides. The obtained compounds have a higher vapour pressure than the oxide, so at the reduction temperature it evaporates. The same applies to carbides. The Fe_3C has a vapor pressure higher than the Cr_7C_3. At 600 and 650 °C it is the prevailing carbide, however at 700 °C the percentage of Fe decreases abruptly on the surface. This suggests that it is replaced by a more stable carbide at that temperature. At 730 °C, the prevailing carbide is Cr_7C_3. Another thing to note is that precipitated carbides formed a porous thick layer on the surface, under which there probably was a depleted chromium zone. This behavior has been extensively documented for this type of material. Moreover, negative effects of exposing this type of steel to a hydrogen atmosphere at elevated temperatures have also been described. Prolonged exposure can severely change the properties of the material. Our substrate XRD spectra were consistent with that. We check that as the temperature increases, the size of the crystals also does. This is because the recrystallization temperature was exceeded. For the steel sheets used that temperature is in the range of 600 to 650 °C. Special attention must be paid to the time and temperature used in the reduction and growth process of nanotubes on this material. Above all to prevent their flexibility and corrosion resistance from being affected. Finally, we tested that independently of the growth process used, under conditions described in this study, it was possible to obtain MWCNT forests directly on the reduced surface of 304 stainless steel. The amount of iron in the carbide layer obtained at 730 °C was enough to act as a catalyst. The Raman characterization made it possible to evaluate the quality of the CNTs. Clearly there is a difference, the CNTs obtained by WACVD, although with random orientation, have better crystallinity than those obtained by PECVD.

Chapter 5

Growth of CNTs on nitrided stainless steel layers

5.1 Introduction

Nowadays, stainless steel is one of the metallic alloys with a major variety of applications in different productive and research fields. The main applications are in the fields like petrochemical, transport, food, conductors, storage and energy (Alresheedi and Krzanowski 2017; Bogacz et al. 2017; Lepró et al. 2010b; Romero et al. 2015; Saker et al. 1991; X. Yang et al. 2017). The surface modification of this versatile material has different purposes, such as increase of corrosion resistance and hardness, reducing wear rates (Alresheedi and Krzanowski 2017; X. Yang et al. 2017), controlling the wettability behavior (Bogacz et al. 2017) and allowing the growth of nanostructures (Lepró et al. 2010b; Romero et al. 2015). Physical, chemical, mechanical and thermal processes have been used for tuning its surface properties. Modern trends of surface modification include a plasma-based surface treatment. One of the most widespread technologies used in the industry is the magnetron sputtering. It allows the deposition of a great variety of metallic, non-metallic, alloys and compounds. Some researchers have studied mechanical coatings of stainless steel deposited by this technique (Baranowska et al. 2013; Kappaganthu and Y. Sun 2004; Kappaganthu and Y. Sun 2005; Saker et al. 1991; Terwagne et al. 2003). In particular, (Saker et al. 1991) found high nitrogen supersaturation of austenite in the stainless steel layers obtained by sputtering, which presented a rather low compressive stress and a high value of micro hardness. Surface modification allows interesting uses of stainless steel, for example as a substrate to grow nanostructures or even to act as a diffusion barrier. (Romero et al. 2015) modified the native chromium oxide of stainless steel to grow carbon nanotubes (CNTs). In this case, the oxidized layer acted as a diffusion barrier. The rich phases of iron, nickel and chromium on the surface acts as a catalyst to obtain CNTs although there is a considerable amount of amorphous carbon (Romero et al. 2015). Other alternatives allow to obtain CNTs forest on stainless steel with low percentage of amorphous carbon, as an example, using a buffer layer along with a diffusion barrier (Lepró et al. 2010b). These diffusion barriers are usually based on thin layers of Al_2O_3, TiN, TiO_2, AlN, avoid the diffusion of catalyst inside of bulk stainless steel. In order to circumvent the effects of thermal stress an effective buffer layer can be used. Thus, pure Al, Ti, Cr, Ni buffer monolayers and multilayers avoid the formation of cracks in the diffusion barrier surface during thermal process in order to prevent the contamination of catalyst particles (De Los Arcos et al. 2003; Nicolet 1978). The synthetized process of CNTs directly on this conductive substrate, instead of the conventionally silicon wafer,

improves the device performance, makes unnecessary the transfer step of CNTs, prevents the use of any additional material that may increase the total mass of the electrode, and offers a lower contact resistance that improves the electron/thermal transport properties (H. A. Moreno et al. 2014).

The aim of this study is to present an alternative methodology for producing CNTs grown on stainless steel in a simplified way to obtain similar or better results than the described above. This new methodology is based in a direct and gradual nitriding of the buffer layer deposited by reactive DC-magnetron sputtering from a stainless steel target. This gradient nitrided buffer layer has no abrupt interfaces with the bulk material. We have evaluated the efficiency of the gradient 304 stainless steel (G-SS304) buffer layer deposited on bulk 304 stainless steel (SS304) combined with a thin layer of aluminum nitride (AlN). The thin layer of AlN acts as a diffusion barrier to avoid the lost of catalyst into the SS304 substrate. The chemical composition and crystalline structure of the layers were investigated using X-ray photoelectron spectroscopy (XPS) and X-ray diffraction (XRD) analyses. In addition, the development of the deposition rate and resistivity of the nitrided layers are presented. For this study, high purity iron nanoparticles have been used as a catalyst material. Different temperatures were used to obtain a forest of CNTs. The morphology and the quality of the system CNTs/AlN/G−SS304/SS304 were studied using Scanning Electron Microscope (SEM) and Raman spectroscopy. The analysis of the diffusion barrier for the catalyst, built by a multilayer system, was carried out by X-ray photoelectron spectroscopy (XPS).

5.2 Experimental section

5.2.1 Preparation of substrate surface SS304 and deposition process of G-SS304/AlN films

AlN/G−SS304 coatings were deposited on SS304 substrate foil of 0.1 mm thickness. Before deposition, the substrates were cleaned with acetone and isopropanol in an ultrasonic bath for 10 minutes, respectively. The diffusion barrier system (AlN/G−SS304) was deposited using a multifunctional reactor that combines plasma enhanced chemical vapor deposition (PECVD) and magnetron sputtering. A SS304 substrate foil of 0.1 mm thickness and 9 cm^2 of area was fixed on the substrate holder, 8 cm away in front of the sputtering header and cleaned using Ar plasma to etch the native oxide film. **Figure 5.1** shows the multilayer structure that we obtained. The diffusion barrier was deposited by two steps. Firstly, a gradient layer of nitrided steel (G−SS304) was deposited on bulk SS304 substrate by DC-pulsed sputter process (50 W, 100 kHz, duty-cycle 2016 ns) using a SS304 target. The sputtering process started with 20 sccm of mass flow of Ar during 600 s. Progressively, N_2 was introduced and Ar was reduced during 100 s until reaching 3/17 sccm of mass flow ratio of N_2/Ar. This regime was kept during 500 s. During 100 s, the N_2/Ar mass flow ratio was changed again until reaching 7/13 sccm/sccm then it was kept during 500 s. The deposition process was carried out at 1 Pa of total pressure and at room temperature. Secondly, a 17 nm of aluminum nitride (AlN) thin layer was deposited on top of the nitrided steel gradient layer using DC pulsed sputtering (120 W, 100 kHz, duty cycle 2016 ns) with an Al target with 20/30 sccm/sccm of mass flow ratio of N_2/Ar and 3 Pa of total pressure at room temperature. **Table5.1** shows the parameters used during the process to obtain the multilayer diffusion barrier system.

(Nicolet 1978) provided a detailed summary of the different barriers that can be used.

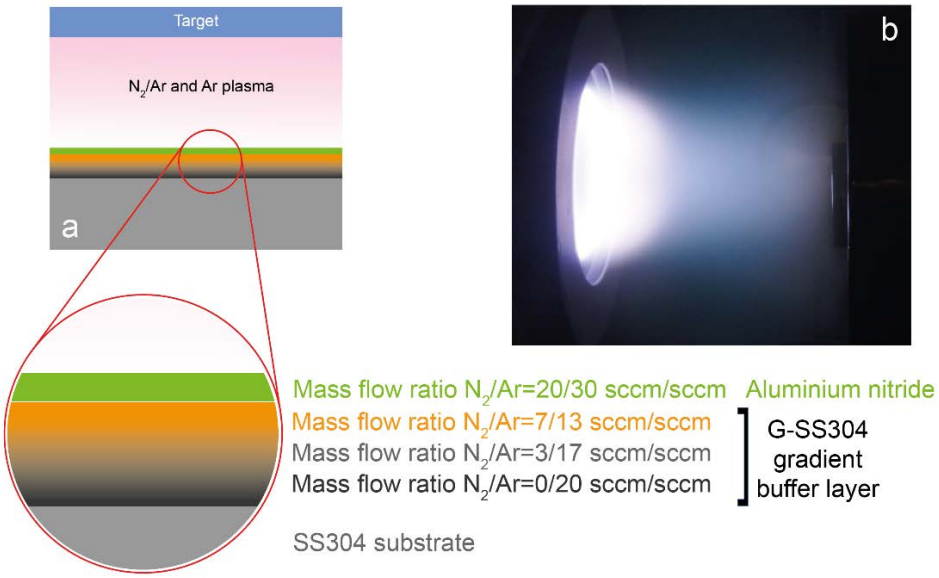

Figure 5.1: Multilayer system configuration (a) illustration of transversal section (b) magnetron sputtering process during SS304 deposition with Ar plasma

Figure 5.2 shows three types of diffusion barriers. The aim is to ensure that materials A and B do not form a compound, so it is necessary to use a diffusion barrier X. One obvious choice for the material of the barrier X is a metal which does not react chemically with A and B and which has negligible mutual solubility with both A and B. Of course, there is no assurance that such a metal can be found, but even if it exists, it is most likely that the metal will not behave as a thin film diffusion barrier if grain limits or other extended defects (surface, texture, internal stress, dislocations) are present (Nicolet 1978). In the case of **Figure 5.2a**, layer X acts as a sacrificial barrier. A and B atoms diffuse towards X through crystalline defects. However, if the thickness of barrier X is suitable, AB compounds are not formed. For a more permanent protection, barrier layer X must be thermodynamically stable against A and B. This means that there are insignificant driving forces for the reactions at the A/X and X/B interfaces. This is a necessary but not sufficient condition for a stable diffusion barrier. It is also necessary to stop or reduce the diffusion of A and B through X by means of fast diffusion paths, as there is still a driving force for A to diffuse into B and vice versa. This can be achieved (1) by eliminating the fast diffusion paths or (2) by filling the easy paths with appropriate atoms/molecules and thus preventing the fast diffusion of A and B (Mešić 2010).

Layer	N_2/Ar (sccm)	N_2 %	Power (W)	DC-pulsed/RF	Frequency (kHz)	Pressure (Pa)	Time (s)
G-SS304	0/20	0	50	DC-pulsed	100 kHz	1	600
	3/17	15	50	DC-pulsed	100 kHz	1	600
	7/1	35	50	DC-pulsed	100 kHz	1	600
AlN	20/30	40	120	DC-pulsed	100 kHz	3	320
Fe	0/128		50	RF	13.56 MHz	2	56

Table 5.1: Deposition parameters used to deposit the thin layers on 304 stainless steel

Crystalline defects, that act as diffusion paths, are a critical factor in determining the atomic transport properties. In general, if the number of defects is high, the diffusion rate will be high. The direct implication is that grain size affects the diffusion processes. The small crystal size allows higher penetration of atoms compared to a larger grain polycrystalline material. In fact, an ideal material to be used as a diffusion barrier should be a monocrystal. However, the use of this type of material is limited. Another interesting approach to producing an efficient diffusion barrier is to introduce between the grain boundaries atoms that act as "stuffing material" (**Figure 5.2b**).

When the atoms of A and B cannot use the short-circuit paths (they are now occupied by the atoms or molecules purposely introduced there), diffusion usually slows down by several orders of magnitude. Elimination of short-circuit paths can also be achieved by eliminating fast paths (Mešić 2010). The other option is to use materials that are amorphous (Figure 2c). However, it should be kept in mind that as the temperature increases the atoms in the amorphous barrier will form crystals, so grain boundaries will appear. The approaches mentioned until now have been used in several studies to obtain diffusion barriers (Borges et al. 2012; García-Céspedes et al. 2009; Iriarte et al. 2010; G. Ke et al. 2015; Keraudy et al. 2015; Ren et al. 2015).

Among these materials, some refractory compounds such as nitrides, borides, oxides and carbides stand out (Nicolet 1978). In spite of having low electrical conductivity, which is a drawback for their use as an electrode, they are useful when it comes to withstanding high temperatures. Normally, in order to allow the passage of electrons by the tunneling effect, the barrier thickness does not exceed few nm (Shahzad Hussain, Amade, H. Moreno, et al. 2014). **Table5.2** lists the properties of some materials with high melting points. In addition, iron, nickel (catalyst materials for CNTs), aluminum, aluminum oxide, aluminum nitride and cooper are included. The materials listed in **Table5.2** are classified according to their melting point value. Tungsten has the highest melting point on this list. While aluminum, the first in the list, is the one that requires less tempera-

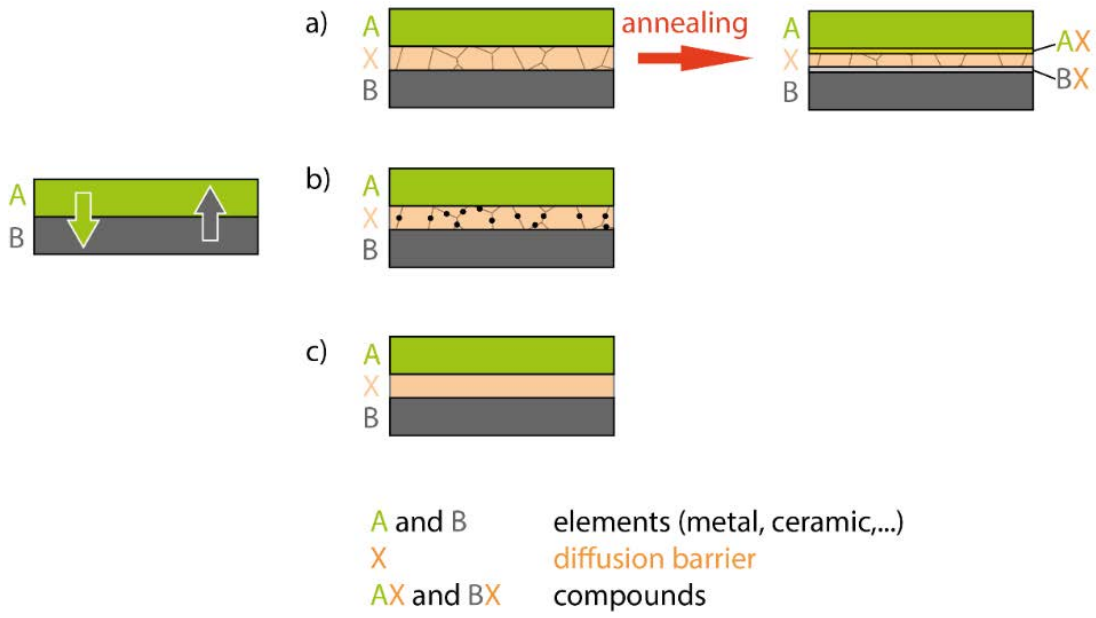

Figure 5.2: Illustration of three types of diffusion barrier: (a) sacrificial, (b) stuffed (c) amorphous barrier. Adapted from (Mešić 2010)

Name	Symbol	Melting Point (ºC)	Density (Kg/m^3)	Thermal expansion coefficient ($\times 10^{-6}$ m / m· K)	Resistivity (ohm.m)	Young`s Modulus (Gpa)
Aluminium	Al	660	2700	23.1	2.8×10^{-8}	70
Cooper	Cu	1084	8960	16.5	16.78×10^{-9}	110-128
Nickel	Ni	1455	8908	13.4	6.9×10^{-8}	200
Iron	Fe	1535	7860	11.8	9.6×10^{-8}	211
Titanum	Ti	1668	4507	8.6	42×10^{-8}	116
Stainless steel 304	SS304	1700	7850	16 - 18	7.6×10^{-8}	205-310
Zirconium	Zr	1852	6520	5.7	42.1×10^{-8}	88
Chromium	Cr	1907	7140	4.9	12.5×10^{-8}	279
Vanadium	V	1917	6160	8.4	19.7×10^{-8}	128
Rhodium	Rh	1963	12410	8.2	4.3×10^{-8}	380
Aluminium oxide	Al_2O_3	2054	4000	8.1	$>10 \times 10^{12}$	300
Hafnium	Hf	2227	13310	5.9	33.1×10^{-8}	78
Ruthenium	Ru	2334	12450	6.4	7.1×10^{-8}	447
Iridium	Ir	2447	22650	6.4	4.7×10^{-8}	528
Niobium	Nb	2468	8570	7.3	15.2×10^{-8}	105
Molybdenum	Mo	2622	10280	4.8	5.3×10^{-8}	329
Tantalum	Ta	2996	16650	6.3	13.1×10^{-8}	186
Aluminium nitride	AlN	3000	3255	4.5 - 5.3	$>10 \times 10^{12}$	330
Osmium	Os	3045	22610	5.1	8.1×10^{-8}	548
Rhenium	Re	3180	21020	6.2	19.3×10^{-8}	463
Tungsten	W	3387	19250	4.5	5.3×10^{-8}	411

Table 5.2: Properties of materials with high melting points

ture to melt. However, if aluminum is combined with oxygen or nitrogen, the resulting compounds have much higher melting points. In fact, two of the most relevant groups of materials used in coatings technology are the metal (Me) nitrides (MeNx) and oxides (MeOy), such as aluminum nitride, AlN, and aluminum oxide, Al_2O_3, whose properties are quite studied and its application widely spread in different technologies (Borges et al. 2012). For our purpose, AlN has exceptional thermal stability in the growth temperature range of CNTs (600 to 730 °C). This nitride is an excellent thermal conductor, with high stability and resistance to caustic chemical etching. In one of its most common structural arrangements, it is a hexagonal (wurtzite) crystalline semiconductor with a large bandgap ($\sim 6.2\,\text{eV}$), with very high electrical resistivity ($> 10^{12}\,\Omega\,\text{m}$) and high hardness (Borges et al. 2012). This approach allows for diffusion barriers to be obtained at low cost compared to those that can be obtained with high cost materials (Moreira et al. 2011).

The integrity of the diffusion barriers is often compromised when their thermal expansion coefficient differs considerably from that of the substrate. It can be noted in **Table5.2** that as the melting point increases, the thermal expansion coefficient decreases. When the difference in the thermal expansion coefficient is substantial and to ensure the integrity of the diffusion barrier, several strategies have been developed. One of the strategies used is to deposit two thin layers whose thermal expansion coefficient values are in the range of the substrate and the diffusion barrier. In this way the layers act as buffer layers. Hussain et al. used a multilayer system to support an Al_2O_3 diffusion barrier. On a copper foil, using a magnetron sputtering head, they deposited a layer of nickel. Then, they deposited a layer of titanium. Finally, Al_2O_3 was deposited on that last layer. They

reported a successful iron catalyst particle support system to obtain CNTs (Shahzad Hussain, Amade, H. Moreno, et al. 2014). Nickel and titanium layers efficiently fulfilled their buffer function.

Another approach by which the time to obtain a buffer layer can be reduced is to produce gradient layers. By exposing a target to different O_2/Ar or N_2/Ar ratios, layers with different chemical composition and therefore different properties can be deposited. Oxygen or nitrogen are two reactive gases that can be mixed with argon to obtain oxides or nitrides, respectively. Precisely this is the approach that has been used in this work. Although instead of using a pure metal target, was selected the same alloy of the substrate, stainless steel 304. This has two advantages for us. With one target of SS304, a gradient buffer layer for the diffusion barrier can be obtained. In addition, the adhesion between the substrate and the gradient buffer layer is optimal, because they are the same material.(Alresheedi and Krzanowski 2017), in their work titled *Structure and morphology of stainless steel coatings sputter-deposited in a nitrogen/argon atmosphere*, report that depending on the temperature at which the magnetron process is performed and the N_2/Ar ratio, layers of different nature can be obtained. In that work, samples were deposited over a temperature range of 150-600 °C. For higher nitrogen gas concentrations ($10N_2$/15Ar and $12N_2$/12Ar) the nitrogen content in the films decreased with increasing the substrate temperature, whereas at lower nitrogen gas concentration ($5N_2$/20Ar) the nitrogen content was relatively constant up to 450 °C and then sharply declined at higher substrate temperatures. Increasing the nitrogen partial pressure increased the nitrogen content in the films, while increasing the bias from -100 V to -140 V had little effect. Films deposited at $5N_2$/20Ar/-100 CrN, bcc−Fe and Ni, whereas films deposited at lower temperatures were primarily S−phase (Alresheedi and Krzanowski 2017). For this study, the buffer layer as well as the diffusion barrier were deposited at room temperature.

5.2.2 Nucleation and carbon nanotubes growth

The substrate, with the diffusion barrier system, was transferred to a CNTs reactor. In this reactor, a 2.5 nm layer of catalyst material was deposited at room temperature on this substrate using RF sputtering process from a high purity Fe target (3 inches of diameter) using Ar (see **Figure 5.3**). The deposited ultrafine iron layer is presumably amorphous, and subsequent thermal treatment in a reducing atmosphere that increases the adatom mobility and facilitates the formation of catalyst iron nanoparticles. This is consistent with the lower surface energy of AlN (assuming the exposed face to be Al) of 0.82 J/m^2, compared to the surface energy of Fe (2.50 J/m^2) (J. Y. Lee et al. 2018). The technological parameters for iron layer were: 2 Pa of Ar (flow rate 128 sccm) and 50 W of RF power (13.56 MHz). Then, the sample was placed under a heating element in order to anneal the catalyst layer and grow the CNTs. **Table5.3** summarizes the parameters that were used at this stage. The CNTs growth process was carried out by two steps: (a) annealing during 870 s (750 s ramp time and 120 s hold time) under H_2 (100 sccm, 200 Pa), hold time is necessary to allow the formation of iron nanoparticles and (b) during 30 s, H_2 was purged and the NH_3 was introduced (100 sccm, 80 Pa). Then, plasma (50 W of RF power) was ignited and 100 sccm of the gas precursor (C_2H_2) was introduced (Shahzad Hussain, Amade, H. Moreno, et al. 2014). The total pressure of the gas mixture was set pointed to 100 Pa. The CNTs growth was carried out for a total time of 900 s. We used different annealing temperatures to obtain CNTs: 680, 700, 715 and 730 °C.

A temperature control during the nucleation and growth process was performed using a PID system. The pyrometer that we use allows us to sense temperatures from 300 °C.

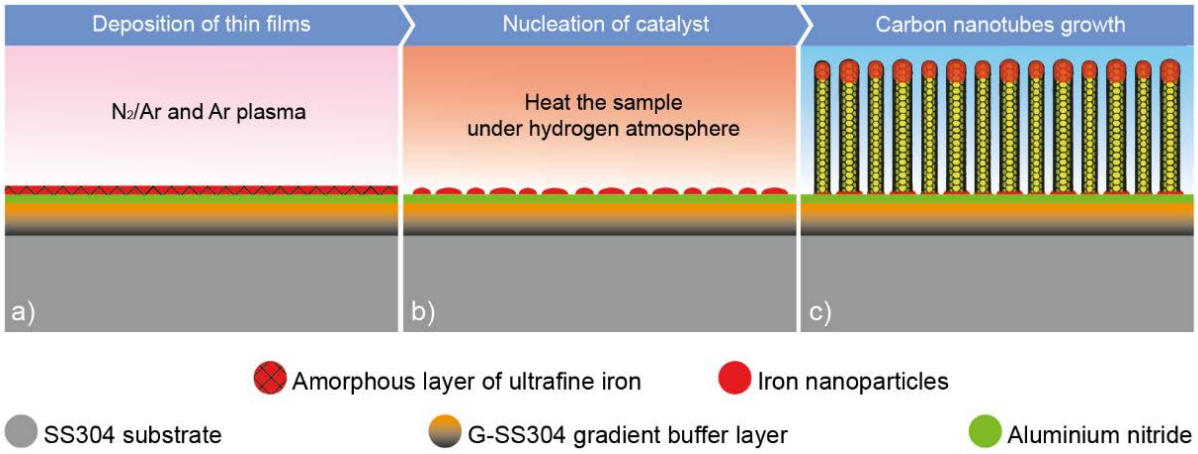

Figure 5.3: Illustration of CNTs growth process. (a) ultrafine iron layer is deposited on AlN/gradient SS304 system, (b) iron nanoislands are formed after annealing period, (c) CNTs are represented on diffusion barrier and SS304 substrate

That is why the curves presented in **Figure 5.4** start at that value. The heating rate of the samples was in the range of 54.4 to 58.4 °C/min. The integrity of the layers that act as diffusion and buffer layers also depends on the proper selection of this heating rate. If its value is high, cracks may be produced, which reduce the performance of the system. When the annealing temperature was reached, in the curves recorded by the pyrometer, two regions are differentiated. The first one corresponds to the hold period, to ensure the formation of the nanoislands. While the second, which covers the final 900 seconds, corresponds to the CNT growth period by PECVD. The discontinuities observed at the

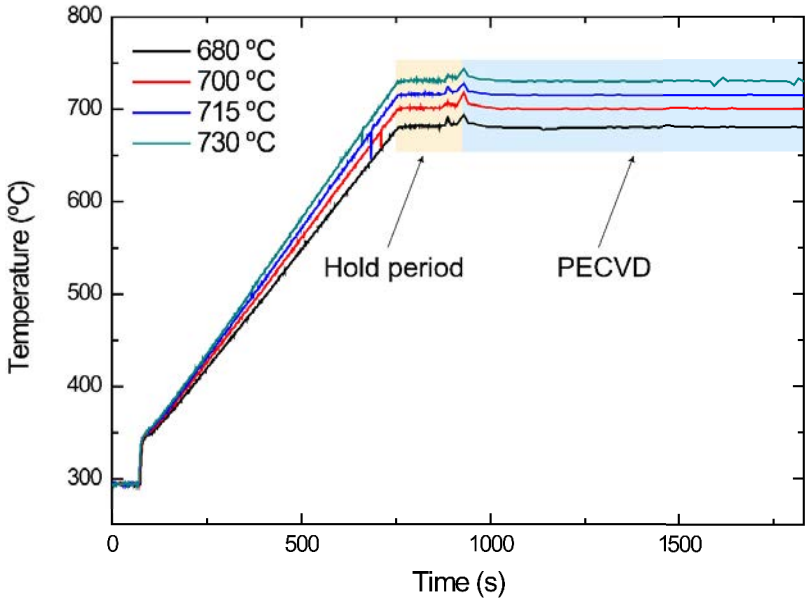

Figure 5.4: Temperature recording during the growth process of CNTs in the range of 680 to 730 °C

	Nucleation of catalyst	H_2 Purging	CNTs growth
Gas	H_2	NH_3	NH_3/C_2H_2
Time (s)	750+120	30	900
Pressure (Pa)	200	80	100
Flux (sccm)	100	100	100/50
RF Power (W)			50

Table 5.3: Parameters used to obtain Fe nanoislands and CNTs

end of the period were due to the replacement of hydrogen by ammonia. In addition, the greatest disturbances were produced by the ignition of the NH_3/C_2H_2 plasma.

5.3 Results and discussion

5.3.1 Chemical composition of nitrided 304 stainless steel layers

In the following two sections we present the chemical composition of surfaces obtained by X ray photoelectron spectroscopy (XPS). XPS experiments were performed in a PHI 5500 Multitechnique System (from Physical Electronics) with a monochromatic X-ray source (Aluminum Kα line of 1486.6 eV energy and 350 W), placed perpendicular to the analyzer axis and calibrated using the $3d_{5/2}$ line of Ag with a full width at half maximum (FWHM) of 0.8 eV. The analyzed area was a circle of 0.8 mm diameter, and the selected resolution for the spectra was 187.85 eV of pass energy and 0.8 eV/step for the general spectra and 23.5 eV of pass energy and 0.1 eV/step for the spectra of the different elements. Two main sources were used in the identification of binding energy peaks: the (NIST-Database 2012) and the research done by (Mark C. Biesinger et al. 2011). In the previous chapter, the approach presented in paper *Resolving surface chemical states in XPS analysis of first row transition metals, oxides and hydroxides: Cr, Mn, Fe, Co and Ni* was also used. Fitting of the peaks obtained for transition metals 2p requires more meticulous work than for single peaks (1s spectrum). For transition metals 2p, NIST Database does not adequately address, specifically, shake-up and plasmon loss structures, and multiplet splitting, all of which can complicate identification of the chemical states present (Mark C. Biesinger et al. 2011). The approach used in that work allowed us to fit and identify the peaks, which would otherwise have been cumbersome. In addition, Casa XPS software was used to process the data obtained during XPS experiments. For 304 stainless steel deposited layers, the results were compared with the nominal concentrations of 304 stainless steel (73 at.%Fe, 18 at.%Cr and 9 at.%Ni).

Although before the analysis was made an etching with argon for a minute, the oxygen and carbon were on the surface. These peaks were the result of the reaction between the

N_2/Ar	Atomic %								Cr/Fe	Ni/Fe	O/(Fe+Cr+Ni)	N/(Fe+Cr+Ni)
(sccm)	%N_2	O 1s	C 1s	N 1s	Mn 2p	Fe 2p	Cr 2p	Ni 2p				
0/20	0	28.09	0.87	0.00	2.13	41.31	11.86	15.75	0.29	0.38	0.53	0.00
3/17	15	12.03	1.05	20.12	2.13	40.26	8.91	15.49	0.22	0.38	0.19	0.31
7/13	35	8.91	0.80	23.08	2.54	40.53	8.89	15.24	0.22	0.38	0.14	0.36

Table 5.4: Composition analysis of deposited layers determined by XPS analysis. The relative error of %at. concentration is $\sim$ 1.5%

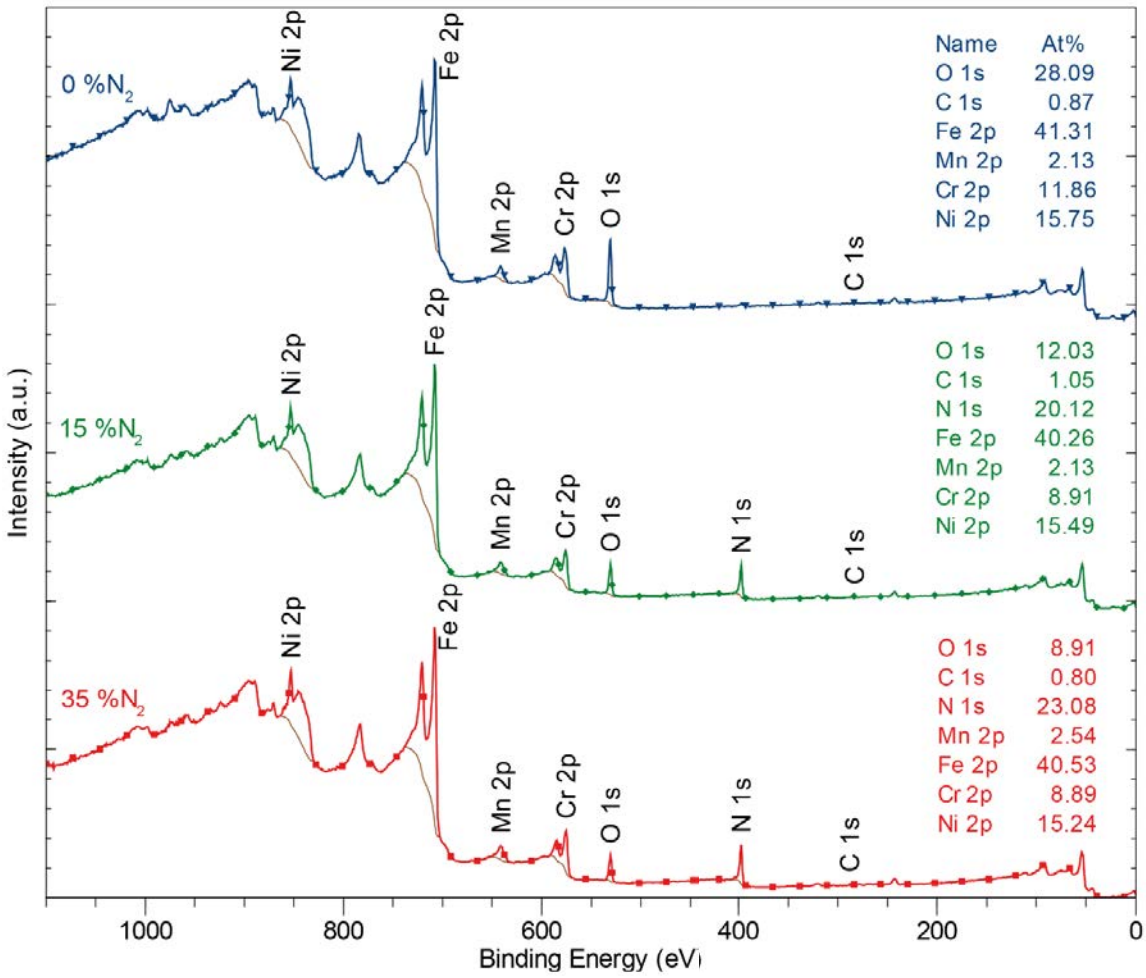

Figure 5.5: Survey spectra of 304 stainless steel deposited layers with different nitrogen content. The relative error of %at. concentration is ∼ 1.5%

layers and the environment (**Figure 5.5**). The layers were deposited on glass substrate and then extracted from the reactor for XPS analysis. Under these conditions, it was impossible to avoid contamination of the samples with these elements. However, these peaks were useful when performing the binding energy calibration. During the fitting process of the high resolution XPS spectra, we used the carbon peak with a binding energy of 284.8 eV as a reference. In addition, the presence of oxygen allowed us to verify the passivation effect that nitrogen has when being part of the layers deposited by sputtering. By calculating the ratio of O/(Fe+Cr+Ni) it was observed that in the absence of nitrogen its value was 0.53 (see **Table5.4**). The addition of nitrogen in the layers reduced that ratio. In the layer with 20.12 and 23.08 at.% N, the O/(Fe+Cr+Ni) ratio dropped to 0.19 and 0.14, respectively. On the other hand, the ratio of N/(Fe+Cr+Ni) for the deposited layers was directly proportional to the atomic percentage of nitrogen. As nitrogen increased, the ratio of N/(Fe+Cr+Ni) also increased. Higher percentage of nitrogen in the chemical composition implied that the sputtered layers were less susceptible to react with oxygen. This can be attributed to the nitrogen forming a stable compound with one or more of the alloying elements. The high resolution XPS spectra were useful to identify the compound(s) that may have formed between the alloy elements and nitrogen.

The relative concentrations of Fe, Cr and Ni should correspond closely with the nom-

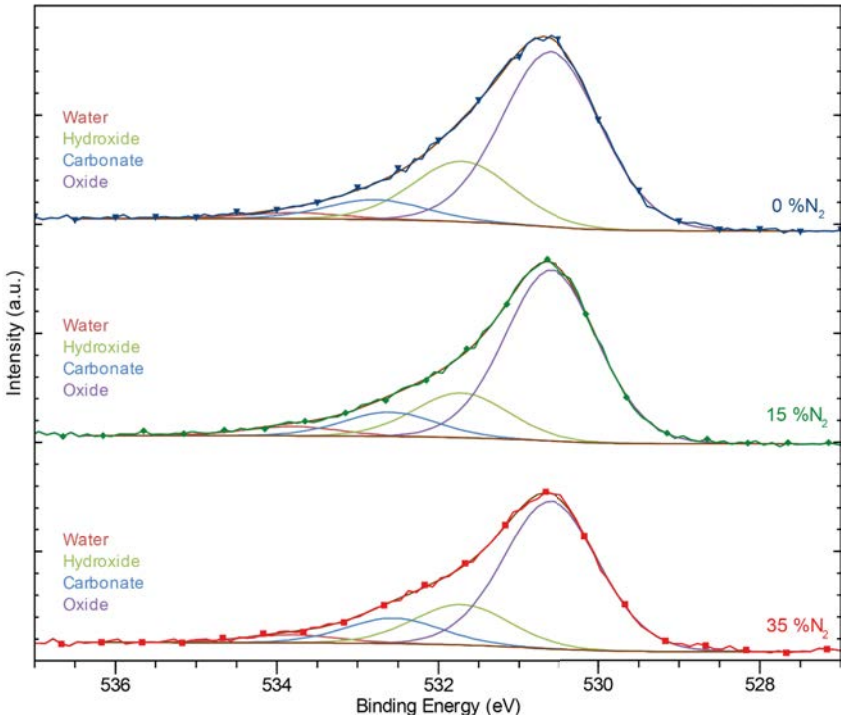

Figure 5.6: O 1s high-resolution XPS spectra of 304 stainless steel deposited layers

inal composition of 304 stainless steel. To test this, the Cr/Fe and Ni/Fe ratios were calculated as shown in the **Table5.4**. The average Cr/Fe ratio was 0.24, while for Ni/Fe the ratio was 0.38. The first ratio corresponds to the nominal value of 0.25 for Cr/Fe. But the Ni/Fe ratio of the sputtered layers is higher than the nominal value of 0.13. This was noted in the sample obtained only with argon and for those obtained with the nitrogen/argon mixture. There was no distinction. Under our experimental conditions, it was possible to obtain a higher percentage of nickel in the layers deposited inside the multi-process reactor PEDRO (described in Chapter 2) by DC magnetron sputtering. This differs from the results presented by (Alresheedi and Krzanowski 2017). In both studies it is reported that the chemical composition of the layers is quite similar to that of the target used (Alresheedi and Krzanowski 2017; Saker et al. 1991). The presence of Mn in the chemical composition of the layers is not surprising. This is an element that is commonly present in ferrous alloys such as 304 stainless steel and its value is within the nominal range (Feliu and Pérez-Revenga 2004).

From now on, in this section, it is presented the results derived from the deconvolution of the high resolution XPS spectra. High resolution scans were performed on the areas around the peaks O 1s, N 1s, Fe $2p_{3/2}$, Cr $2p_{3/2}$ and Ni 2p for the stainless steel deposited layers. Calculating the area under the peaks, and applying the relative sensitivity factors of 2.93 (O 1s), 1.8 (N 1s), 9.82 (Fe $2p_{3/2}$), 6.97 (Cr $2p_{3/2}$) and 20.05 (Ni 2p) for the above peaks gives the atomic concentrations reported in the following tables (**Table5.5** to **Table5.10**).

As mentioned previously, oxygen presence on 304 stainless steel sputtered layers was a consequence of their atmospheric exposure (**Figure 5.6**). We assume that all the subpeaks obtained through O 1s peaks deconvolution are contaminants. To avoid any inclusion of oxides in the sputtered layers, the target surface was cleaned with Ar plasma

$\%N_2$	Compound	O 1s		
		Position (eV)	FWHM (eV)	%At Conc
0	Water	533.80	1.46	2.35
	Hydroxide	531.70	1.46	23.12
	Carbonate	532.78	1.46	7.55
	Oxide	530.59	1.46	66.98
15	Water	533.81	1.36	3.74
	Hydroxide	531.71	1.36	17.92
	Carbonate	532.60	1.36	9.70
	Oxide	530.59	1.36	68.63
35	Water	533.81	1.40	3.58
	Hydroxide	531.71	1.40	18.29
	Carbonate	532.55	1.40	11.45
	Oxide	530.60	1.40	66.69

Table 5.5: O 1s spectral fitting parameters: binding energy (eV), FWHM value (eV) and percentage of atomic concentration. The relative error of FWHM and %at. concentration is ∼1.5%

during 10 min. In this way, we were able to remove the native oxide of the 304 stainless steel and the contaminants that could exist on the surface. This cleaning was carried out prior to each deposit process. The spectral fitting parameters of O 1s spectra are presented in **Table5.5**.

Through the deconvolution of the N 1s peak, two subpeaks were found (**Figure 5.7**). The first one is located at 399.50 eV and corresponds to N 1s. The other peak was identified between 397.77 and 397.80 eV. It can be attributed to the nitrides that were formed in the layers during the sputtering deposition. The prevalence percentage of the nitride peak over the N 1s peak suggests that nitrogen mostly forms nitrides (see **Table5.6**). However, the remaining nitrogen ($11.62 - 12.77$ at.%) suggests that these atoms are retained in the material. One possible explanation is that nitrogen atoms occupy the interstitial spaces in the crystal lattice. As the matrix is constituted by iron, the crystal lattice can be metastable ferrite phase (α) with a body centered cubic (bcc) structure or face centered cubic (fcc) austenitic structure (Kappaganthu and Y. Sun 2005). X ray diffraction (XRD) provides further information. Results of the XRD analysis are presented in the following section.

The percentage of nitrogen introduced in the 304 stainless steel layers differs from that reported in the consulted articles (Alresheedi and Krzanowski 2017; Kappaganthu and Y.

$\%N_2$	Compound	N 1s		
		Position (eV)	FWHM (eV)	%At Conc
15	Nitride	397.77	1.48	87.23
	N 1s	399.50	2.00	12.77
35	Nitride	397.80	1.45	88.38
	N 1s	399.50	2.00	11.62

Table 5.6: N 1s spectral fitting parameters: binding energy (eV), FWHM value (eV) and percentage of atomic concentration. The relative error of FWHM and %at. concentration is ∼1.5%

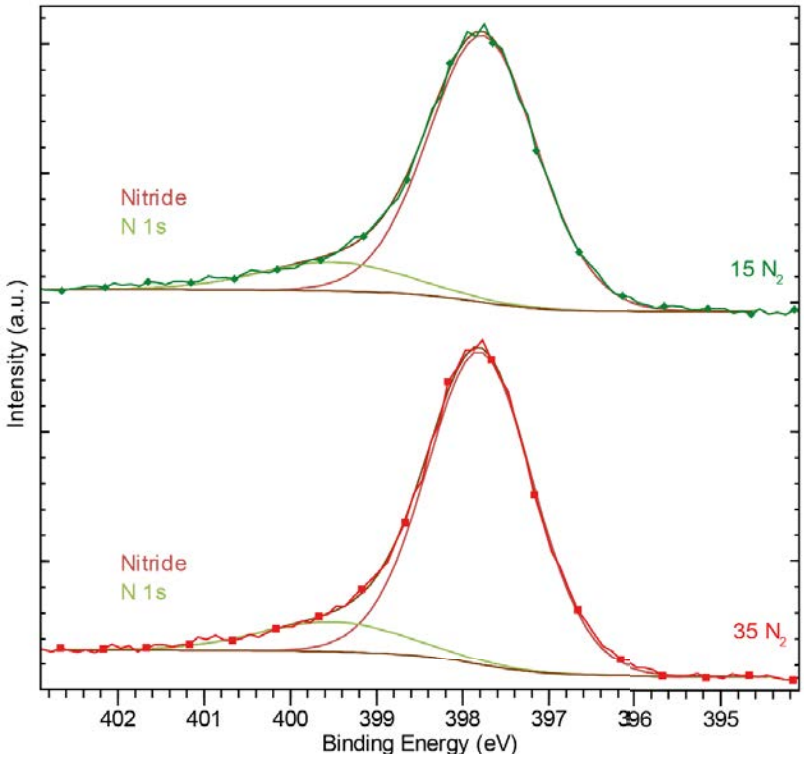

Figure 5.7: N 1s high-resolution XPS spectra of 304 stainless steel deposited layers deposited by sputtering with 15 and 35% of N_2 gas flow

Sun 2004; Kappaganthu and Y. Sun 2005). For example, (Alresheedi and Krzanowski 2017) report values higher than 28.9 at.% N. The main difference with their work is that our layers were obtained at room temperature. At that temperature it is probably a more percentage of amorphous material than that obtained at elevated temperatures. Thus, the nitrogen retention into the amorphous stainless steel layers changes. The formation of amorphous like-phases in thin film deposition is usually due to insufficient thermal energy and adatom energy, as well as the high condensation rates of sputtered species (Kappaganthu and Y. Sun 2005). It is reported that regardless of the N_2/Ar, at higher temperatures the retention of nitrogen atoms decreases. In general, the residence times of the adatoms on the substrate surface obey an Arrhenius relation and decrease as the temperature increases. This suggests that the chemical reaction of nitrogen with atoms on the substrate is weak and that the incorporation of nitrogen into the film is favored by longer residence times at lower temperatures (Alresheedi and Krzanowski 2017). In addition, (Kappaganthu and Y. Sun 2005) reported that if 50% N_2 (percentage of flow) is exceeded, the at.% N in the stainless steel layers obtained by sputtering probably reaches the saturation point.

The peaks O 1s and N 1s were relatively easy to fit. However, the high-resolution spectra of Fe $2p_{3/2}$ and Cr $2p_{3/2}$ presented more difficulty. Probably because the analyzed layers were based on a ferrous alloy. On the other hand, we could not find references that would allow us to compare our results, except for the peaks of Cr_2O_3, Fe_2O_3 and their hydroxides, which were adjusted following the procedure presented by (Mark C. Biesinger et al. 2011). However, we believe that the peaks obtained from deconvolution are coherent and allow us to understand the interaction of alloying the elements with nitrogen.

Figure 5.8 shows the asymmetrical high-resolution spectra. If the points with max-

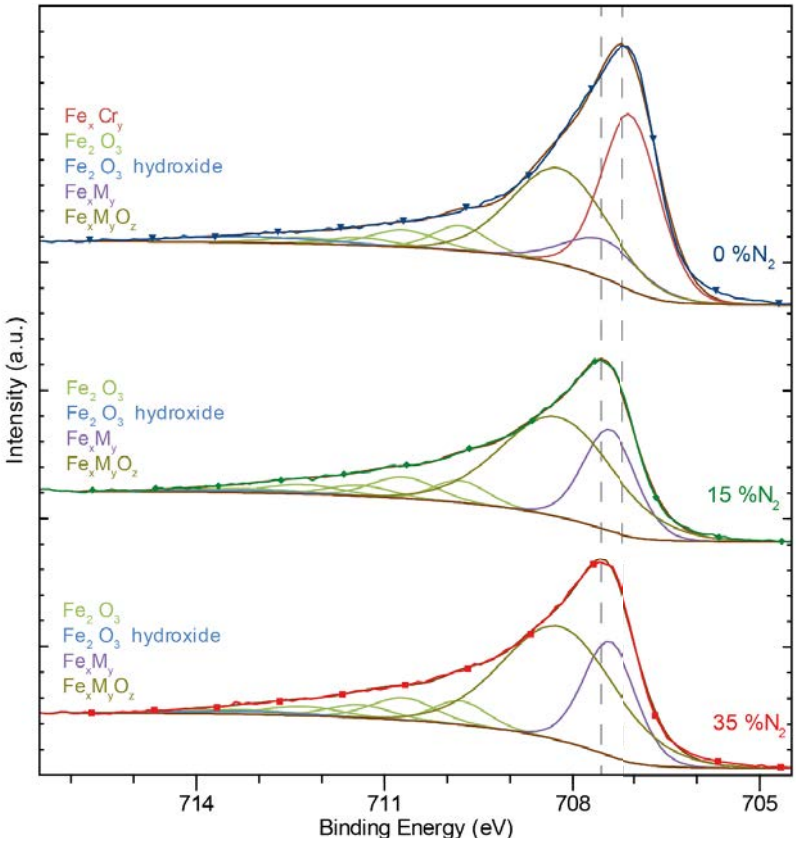

Figure 5.8: Fe $2p_{3/2}$ high-resolution XPS spectra of 304 stainless steel deposited layers

imum intensity are taken as a reference, two regions are differentiated for each of the peaks. The left has a slope that decreases progressively and the right has a steep slope. In general, the subpeaks corresponding to the oxides and hydroxides are located on the left side. The adjustment parameters used for the peaks are included in **Table5.7**. In addition to the subpeaks of Fe_2O_3 ($709.80 - 713.30$ eV) and Fe_2O_3 hydroxide (713.18 eV), a broad and intense subpeak appears. The nomenclature used to identify it was $Fe_xM_yO_z$. According to the (NIST-Database 2012), some Fe metal compound oxides have a binding energy close to the range of 708.21 to 708.24 eV. One of the alloying elements that can be considered is the nickel. All thin layers of 304 stainless steel obtained in this research had $\sim$ 15 at.% of Ni. The value reported by Kishi K., in the (NIST-Database 2012), is 708.2 eV. It is reported that the binding energy was obtained from a multilayer structure.

On the other hand, the shift of Fe $2p_{3/2}$ high resolution XPS spectra can be attributed to the development of two subpeaks with nitrogen content. We identified them as Fe_xCr_y and Fe_xM_y, respectively. The thin layer obtained without nitrogen, presents an intense and broad subpeak Fe_xCr_y (707.07 eV, 45.63 at.%). Mischler, S., Mathieu, H. J., Landolt D. reported, for sputtered specimen, that iron chromium alloy (76-24) present a binding energy of 707.1 eV (NIST-Database 2012). We assume that this compound may be present in our layer. Additionally, when nitrogen is introduced into the gas mixture used during the sputtering process, the Fe_xCr_y subpeak disappears, while the subpeak of Fe_xM_y located at $707.4 - 707.5$ eV. range increases in intensity. Its binding energy corresponds to that reported by Conner G.R. (NIST Database) as sputtered iron. However, the binding energy of Fe(0) is 706.6 eV (Mark C. Biesinger et al. 2011). The shift of binding energy

%N_2	Compound	Peak 1			Peak 2			Peak 3			Peak 4			Peak 5		
		Position (eV)	FWHM (eV)	%At Conc	Position (eV)	FWHM (eV)	%At Conc	Position (eV)	FWHM (eV)	%At Conc	Position (eV)	FWHM (eV)	%At Conc	Position (eV)	FWHM (eV)	%At Conc
0	Fe_xCr_y	707.07	1.10	45.63												
	Fe_2O_3	709.80	1.00	5.86	710.70	1.20	4.89	711.40	1.20	2.21	712.30	1.40	2.01	713.30	2.20	0.11
	Fe_2O_3 hydroxide	713.18	2.78	3.91												
	Fe_xM_y	707.50	1.44	8.57												
	$Fe_xM_yO_z$	708.21	1.80	26.81												
15	Fe_xCr_y	707.10	1.10	0.00												
	Fe_2O_3	709.80	1.00	7.47	710.70	1.20	8.68	711.40	1.20	4.36	712.30	1.40	4.50	713.30	2.20	2.99
	Fe_2O_3 hydroxide	713.18	2.64	1.84												
	Fe_xM_y	707.40	1.00	22.71												
	$Fe_xM_yO_z$	708.24	2.13	47.44												
35	Fe_xCr_y	707.10	1.10	0.00												
	Fe_2O_3	709.80	1.00	7.25	710.70	1.20	8.17	711.40	1.20	4.70	712.30	1.40	3.94	713.30	2.04	2.74
	Fe_2O_3 hydroxide	713.18	2.32	2.00												
	Fe_xM_y	707.40	1.00	22.84												
	$Fe_xM_yO_z$	708.21	2.13	48.36												

Table 5.7: Fe $2p_{3/2}$ spectral fitting parameters: binding energy (eV), FWHM value (eV) and percentage of atomic concentration. The relative error of FWHM and %at. concentration is $\sim$ 1.5%

may be due to iron forming a compound with one or more of the alloying elements. The results suggest us that the dependence of the Fe_xCr_y and Fe_xM_y subpeaks with the N_2/Ar ratio is related with the tendency of nitrogen atoms to form compounds with chromium.

Cr $2p_{3/2}$ high resolution spectra (**Figure 5.9**), like Fe $2p_{3/2}$ spectra, is asymmetrical. Several subpeaks were used to fit it. Especially for compounds with high binding energy (oxides and hydroxide) (Mark C. Biesinger et al. 2011). The fitting parameters are listed in **Table5.8**. Cr_2O_3 subpeaks are between 575.70 and 578.90 eV, while Cr_2O_3 hydroxide is between 577.30 and 577.90 eV. In addition, the subpeak identified as $M_xCr_yO_z$ is between 575.90 and 576.00 eV. According to the (NIST-Database 2012), two compounds present their binding energies in that range. One is the $MnCr_2O_4$ (575.90 eV) and the other is the $NiCr_2O_4$ (576.0 eV). According to the survey spectra (**Figure 5.5**), all thin layers obtained by sputtering have Mn and Ni, so the signal of the subpeak $M_xCr_yO_z$ can be the contribution of the two alloying elements. Certainly, it must be taken into account that the at.% of Ni is higher than the at.% of Mn in the spectra. In that sense, we presume that the $NiCr_2O_4$ signal prevails over the $MnCr_2O_4$ signal.

In addition, in the deconvolution process three other subpeaks were used to fit the Cr $2p_{3/2}$ spectra. The first is between 574.40 and 574.55 eV. It reached its highest intensity in the layer that was deposited in a nitrogen-free atmosphere. However, when nitrogen was introduced, its intensity decreased. In **Figure 5.9** it is identified as Fe_xCr_y. Again, for identification, the (NIST-Database 2012) was used as a reference. The binding energy range matches that reported for $Fe_{76}Cr_{24}$ (575.5 eV). This result is in accordance with the subpeak Fe_xCr_y found in high resolution Fe $2p_{3/2}$ spectra. The second subpeak was the Cr(0) (573.90 − 574.02 eV). Like the previous subpeak, the development of this subpeak with nitrogen was unfavorable. Its atomic concentration decreased as the percentage of nitrogen increased. In contrast, the third subpeak appears in the range of 575.13 − 575.22 eV and only in the spectra corresponding to the nitrided stainless steel layers. This fact allowed us to presume that it corresponds to a compound formed by chromium and nitrogen. When exploring the (NIST-Database 2012), it was found that several compounds present binding energies in that range. The CrN is one of the candidates.

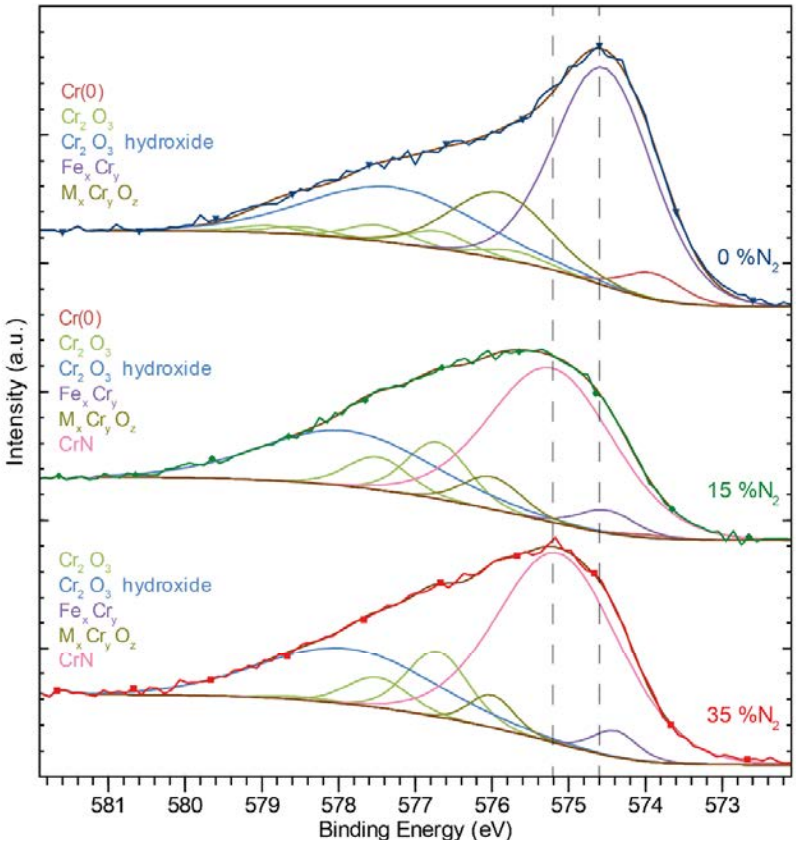

Figure 5.9: Cr $2p_{3/2}$ high-resolution XPS spectra of 304 stainless steel deposited layers

However, the reported binding energy is slightly higher than we found (575.7 eV). Milosev et al. instead reported a binding energy of 574.5 eV. The peaks we found are within the range of 574.5 and 575.7 eV. With the XRD analysis it will be possible to have more evidence to support our suspicion that this is CrN.

To fit the Ni 2p high-resolution XPS spectra, two subpeaks were used (**Figure 5.10**). Their identification was done through the (NIST-Database 2012). The fitting parameters are listed in **Table5.9**. The most intense is between 853.21 and 853.45 eV. That peak corresponds to metallic nickel. The other peak showed binding energy values higher than those of the previous peak (853.96 − 854.62 eV). Within that range there are the oxides that nickel forms in its pure state and when it is forming compounds with other metals. The metals to be considered in this case, as the target used was 304 stainless steel, are Fe and Cr. In general, a small shift of the Ni 2p peak is observed. Although nitrogen does not form compounds with nickel, it influences the development of oxides. Thus, as the at.% N increases, the at% of nickel oxides decreases. At least with nickel, the passivation layer formed between nitrogen and chromium protects it from oxygen.

Since the target is an alloy, the identification of the subpeaks of the O 1s, N 1s, Cr $2p_{3/2}$, Fe $2p_{3/2}$ and Ni 2p XPS high-resolution spectra required special care to avoid misidentifying the species. Perhaps, some species have not been identified in this work. With so many possible species having overlapping binding energies erroneous interpretation can result (Mark C. Biesinger et al. 2011). Thus, caution has been taken in the nomenclature used. However, we are confident that our results will contribute significantly to the understanding of the sputtering process using a 304 stainless steel target.

$\%N_2$	Compound	Peak 1			Peak 2			Peak 3			Peak 4			Peak 5		
		Position (eV)	FWHM (eV)	%At Conc	Position (eV)	FWHM (eV)	%At Conc	Position (eV)	FWHM (eV)	%At Conc	Position (eV)	FWHM (eV)	%At Conc	Position (eV)	FWHM (eV)	%At Conc
0	Cr(0)	573.90	0.90	4.65												
	Cr_2O_3	575.70	0.94	1.93	576.71	0.94	3.26	577.49	0.94	3.00	578.49	0.94	1.43	578.90	0.94	1.35
	Cr_2O_3 hydroxide	577.30	2.60	28.66												
	Fe_xCr_y	574.55	1.50	42.75												
	$M_xCr_yO_z$	575.90	1.50	12.97												
15	Cr(0)	574.00	0.90	0.62												
	Cr_2O_3	575.70	0.94	0.00	576.71	0.94	11.73	577.49	0.94	6.76	578.49	0.94	0.00	578.90	0.94	0.00
	Cr_2O_3 hydroxide	577.90	2.60	31.37												
	Fe_xCr_y	574.50	0.87	2.88												
	$M_xCr_yO_z$	576.00	0.90	4.21												
	CrN	575.22	1.91	42.43												
35	Cr(0)	574.02	0.90	0.00												
	Cr_2O_3	575.70	0.94	0.00	576.71	0.94	12.35	577.49	0.94	5.65	578.49	0.94	0.58	578.90	0.94	0.00
	Cr_2O_3 hydroxide	577.90	2.60	29.14												
	Fe_xCr_y	574.40	0.69	2.41												
	$M_xCr_yO_z$	576.00	0.67	2.87												
	CrN	575.13	1.86	47.00												

Table 5.8: Cr $2p_{3/2}$ spectral fitting parameters: binding energy (eV), FWHM value (eV) and percentage of atomic concentration. The relative error of FWHM and %at. concentration is $\sim$ 1.5%

Excluding oxides and hydroxides, four compounds were clearly identified in this section. Three of them were the product of the interaction between the alloying elements (Ni-Fe, Ni Cr, Fe Cr) and the other was the product of the interaction of Cr and N (CrN).

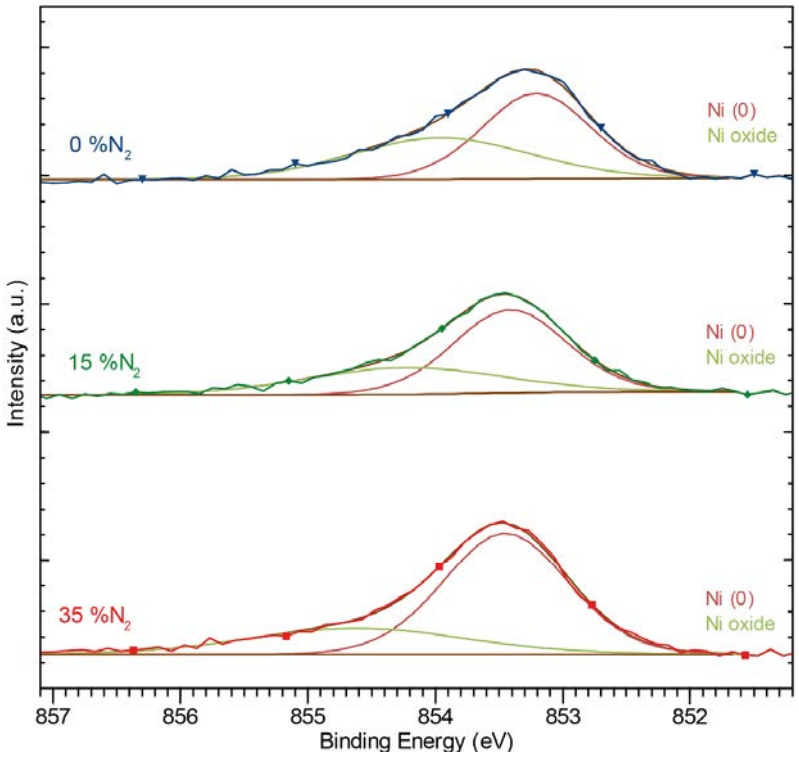

Figure 5.10: Ni 2p high-resolution XPS spectra of 304 stainless steel deposited layers

% N_2	Compound	N 2p		
		Position (eV)	FWHM (eV)	%At Conc
0	Ni (0)	853.21	1.00	55.51
	NiO	853.96	1.65	44.49
15	Ni (0)	853.42	1.04	64.30
	NiO	854.23	1.80	35.70
35	Ni (0)	853.45	1.15	72.49
	NiO	854.62	2.00	27.51

Table 5.9: Ni 2p spectral fitting parameters: binding energy (eV), FWHM value (eV) and percentage of atomic concentration. The relative error of FWHM and %at. concentration is ∼1.5%

Both the Fe $2p_{3/2}$ and Cr $2p_{3/2}$ spectra confirm the presence of Fe_xCr_y. This is the compound that prevailed when the layer was obtained only with Ar. The use of nitrogen, on the other hand, changed the chemical composition of the layers considerably. The prevailing compound was CrN and not Fe_xCr_y. Under our experimental conditions, Cr atoms had a more affinity with N atoms than with Fe atoms. (Saker et al. 1991) mentioned that for deposits with a nitrogen concentration higher than about 20 at.% N, the demixing is associated with a loss of nitrogen indicating that, in the nitride phase CrN, the substitution of chromium by iron or nickel is unlikely: only chromium atoms are able to be combined with nitrogen atoms (Saker et al. 1991). In the consulted literature, the deconvolution of XPS high resolution peaks was poorly reported (Alresheedi and Krzanowski 2017; Kappaganthu and Y. Sun 2005; Mischler et al. 1988; Saker et al. 1991). It was not easy to compare our results. In general, references concerning the deposition of steel layers by sputtering report the structural evolution of these layers at high temperatures. The primary reason for this, it seems, is to obtain thick layers for mechanical applications.

In the face of all this, with the results presented so far, we can state that the use of nitrogen during the sputtering process allowed the thin layers to be nitrided. In addition, the high percentage of Ni can benefit the conductivity of thin layers. This is especially useful to produce electrodes for energy storage devices.

5.3.2 Chemical composition of nitrided aluminum layer

The XPS analysis of the aluminum nitride layer were carried out using the same procedure as for the 304 stainless steel thin layers. Before the analysis was made an etching with argon for a minute. Calculating the area under the peaks, and applying the relative sensitivity factors of 2.93 (O 1s), 1.8 (N 1s) and 0.44 (Al 2p) for the high resolution XPS spectra gives the atomic concentrations reported in **Table5.10**. In addition, we use the carbon peak with a binding energy of 284.8 eV as a reference for analyzing the spectra. In the survey spectrum (Figure 11) there is an intense peak that correspond to oxygen (35.46 at.%). This as well as the carbon peak (5.58 at.%) can be attributed to the contamination that the sample suffered when it was extracted from the reactor vacuum chamber. In addition, as expected, the presence of nitrogen in the sample was confirmed (11.97 at.%). However, the N 1s peak at $\sim$ 399 eV is less intense than that of O 1s. The Al 2p peak is also observed (46.99 at.%). Survey spectrum shows that the deposited aluminum layer, using 20/30 sccm/sccm (N_2/Ar), did not fully react with nitrogen. In other words, a certain percentage of aluminum did not interact with nitrogen atoms. When the sputtered layer was exposed to the atmosphere, a considerable amount

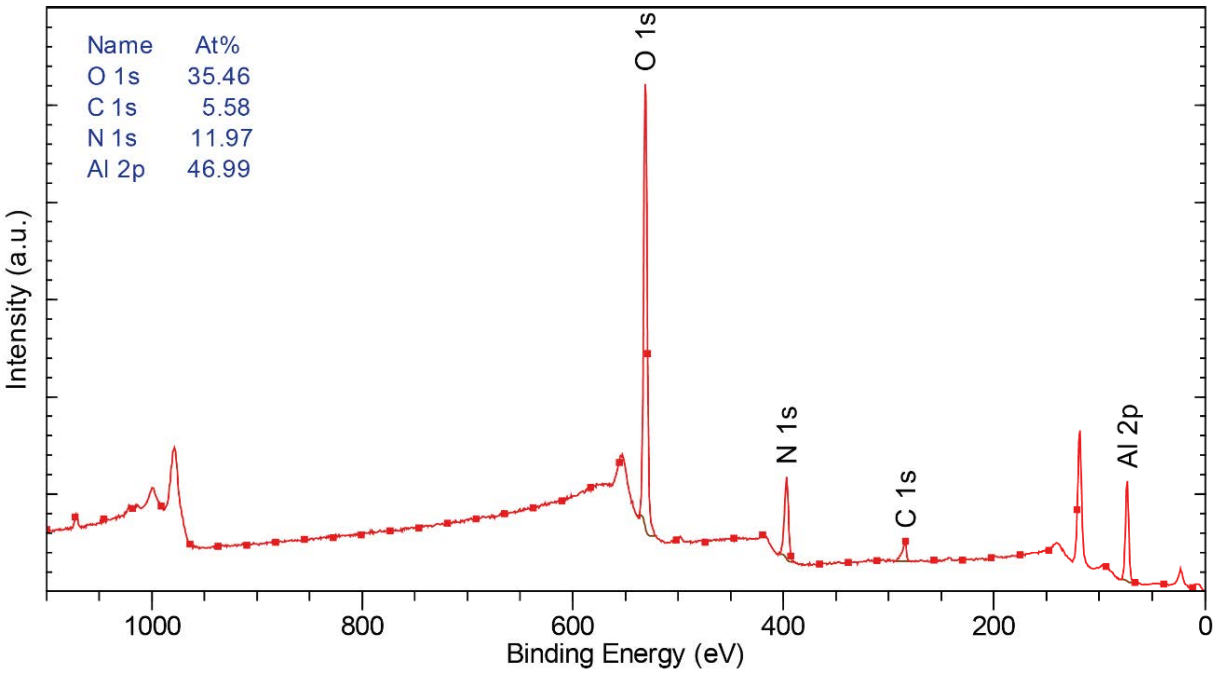

Figure 5.11: Survey XPS analysis of nitrided aluminum deposited layer

of oxides immediately formed on its surface.

The deconvolution of O 1s high-resolution XPS spectrum confirmed our hypothesis. **Figure 5.12a** shows the subpeaks present in the O 1s region. An intense and broad subpeak is at 531.42 eV. According to (Harris et al. 1990), that binding energy corresponds to Al_2O_3. The other two subpeaks correspond to the contamination that reached the surface layer when it was exposed to the atmosphere. The amount of carbon in the surface was very low and indicates that no significant incorporation of carbon containing ligands from the precursors had taken place (Motamedi and Cadien 2014). In the N 1s high-resolution XPS spectrum (**Figure 5.12b**) there is a broad and intense subpeak lying at 397.37 eV and corresponding to AlN (Jose et al. 2010). However, it was not the only subpeak obtained with deconvolution. Spectrum fitting indicates the presence of an additional phase with a binding energy of 399.50 eV attributed to nitrogen (NIST-Database 2012). The subpeaks represent 84.64 and 15.36 at.%, respectively. (Motamedi and Cadien 2014) did not report that nitrogen atoms remain in the deposited layers without reacting with the aluminum. We suppose that this fact was produced by the

Peak	Compound	Position (eV)	FWHM (eV)	%At Conc
O 1s	Water	533.88	2.45	3.03
	Carbonate	532.35	2.45	31.91
	Al_2O_3	531.42	2.45	65.05
N 1s	AlN	397.37	2.78	84.64
	N 1s	399.50	2.00	15.36
Al 2p	AlN	74.06	1.95	54.70
	Al_2O_3	75.01	1.94	45.30

Table 5.10: O 1s, N 1s and Al 2p spectral fitting parameters: binding energy (eV), FWHM value (eV) and percentage of atomic concentration. The relative error of FWHM and %at. concentration is $\sim$ 1.5%

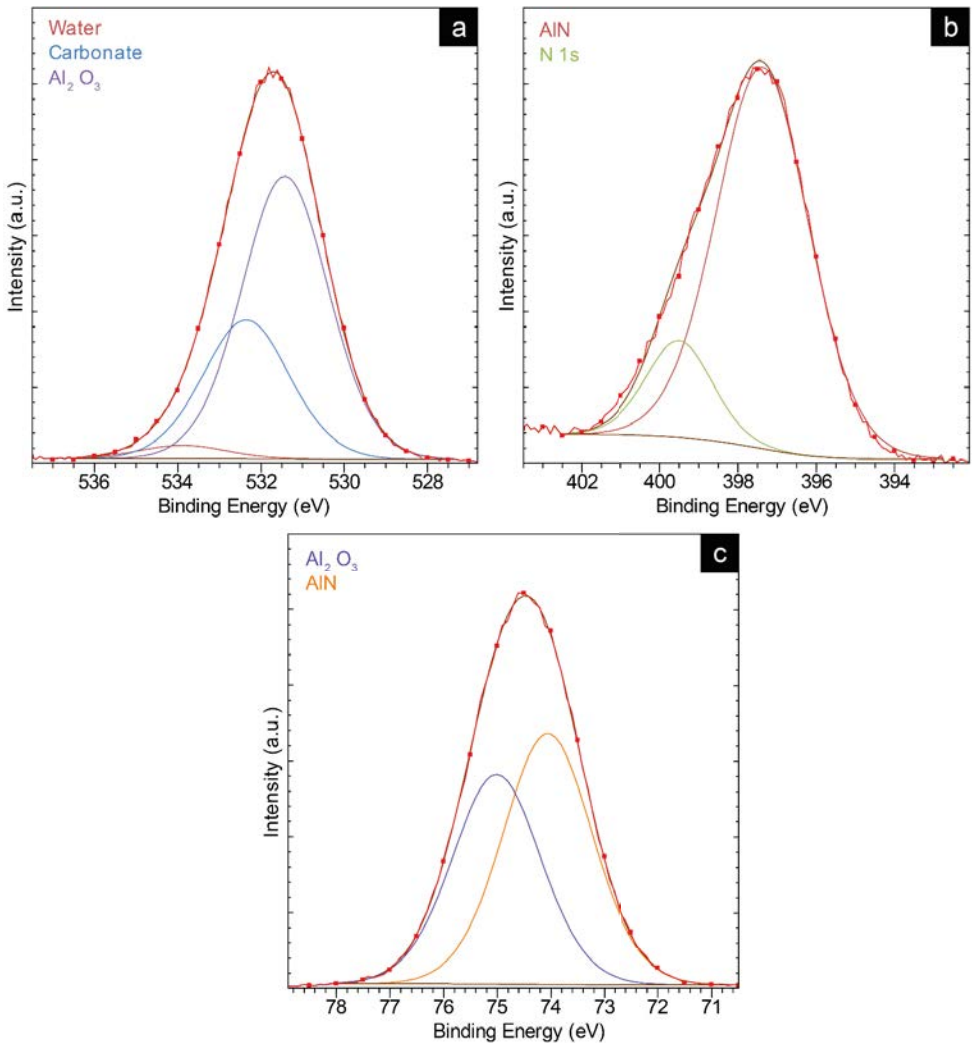

Figure 5.12: O 1s(a), N 1s(b) and Al 2p(c) high-resolution XPS spectra of nitrided aluminum deposited layer

amorphous nature of the layer. This was already observed in the steel layers obtained by sputtering. It is remembered that all the layers we obtained by sputtering were deposited at room temperature. In the previous section, it was mentioned that the residence times of the adatoms on the surface of the substrate obey an Arrhenius relationship and decrease as the temperature increases. This suggests that the chemical reaction of nitrogen with atoms in the substrate is weak and that the incorporation of nitrogen into the film is favored by longer residence times at lower temperatures (Alresheedi and Krzanowski 2017).

Finally, in the Al 2p high-resolution XPS spectrum (**Figure 5.12c**), two subpeaks are clearly differentiated. These correspond to species with different binding energies, one at 74.06 eV and the other at 75.01 eV. It is confirmed that the layer, at least on the surface, is made up of AlN and Al_2O_3 (Jose et al. 2010; Motamedi and Cadien 2014). Aluminum nitride has higher atomic concentration than alumina, 54.70 and 45.30 at%, respectively. Although the difference between the atomic concentration is slight, it seems that the experimental conditions used (N_2/Ar ratio, pressure, substrate temperature and power) were not adequate to obtain a pure AlN layer. However, if we refer to **Table5.1**, Al_2O_3 is a compound that can be used as a diffusion barrier. In fact, some works in our research group were carried out using only this material (Shahzad Hussain, Amade, and Bertran

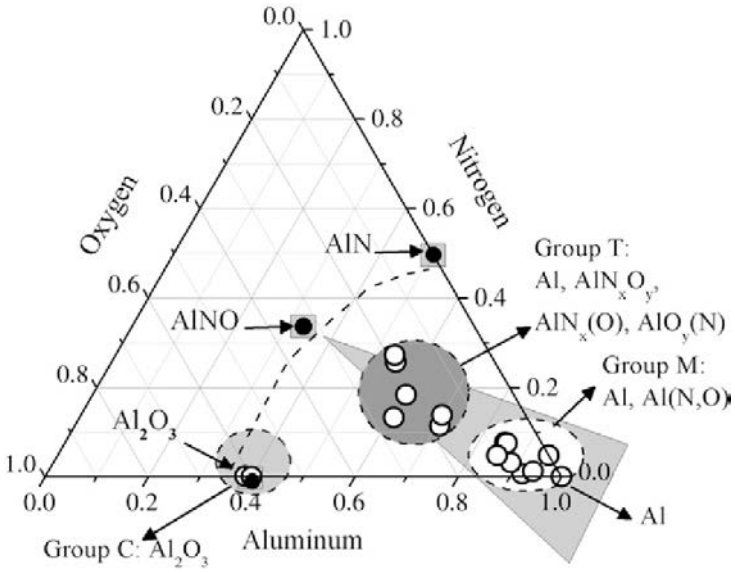

Figure 5.13: Ternary phase diagram for the deposited AlN_xO_y films (Borges et al. 2012)

2014; Shahzad Hussain, Amade, H. Moreno, et al. 2014).

Aluminum layers deposited with N_2/Ar have AlN and Al_2O_3. The first compound was obtained during the sputtering operation. In contrast, Al_2O_3 was formed when the material was exposed to the atmosphere. For our purpose, this contamination was well seen. The residual "pure" aluminum reacting with oxygen improved the performance of the diffusion barrier. In this case, and according to (Nicolet 1978), the oxygen atoms act as stuffing material. Our results differ from those obtained by (Borges et al. 2012) because in that work, besides N_2 and Ar, O_2 was also used during the sputtering process. So, by varying the proportions of those gases, different AlN_xO_y compounds were obtained in the layers. In the ternary diagram of **Figure 5.13** , (Borges et al. 2012) reported three well defined regions. The first belongs to group C (compound-like film), the second to group T (transition zone) and finally the third to group M (metallic-like zone). It is important to emphasize that according to our results, the surface layer obtained clearly shows the phases of AlN and Al_2O_3, as well as carbon resulting from the contamination of the sample when exposed to the atmosphere.

5.3.3 Structure of nitrided layers

The crystalline structure of the thin layers depends to a large extent on the conditions under which they were obtained. In our case, it depends of pressure, power, distance between target and substrate, substrate temperature and N_2/Ar ratio. The difference between an amorphous and a crystalline layer can be strongly influenced by any of the variables mentioned above. For example, the tendency to obtain amorphous layers at low temperatures or when using low power was reported (Kappaganthu and Y. Sun 2005). Until now we know the chemical composition of the nitrided layers, but the structural features are still uncertain. For that reason, X-ray diffraction (XRD) was used to obtain information about the crystalline structure of the layers. Using the same parameters reported in **Table5.1**, thin layers were deposited on glass for about 10 min. The layers obtained were uniform and their adherence was excellent. No collapses were observed.

This can be explained since a pulsed-DC power supply was used. This technology allows to obtain layers with low residual stress. XRD analysis was performed using a PANalytical X'Pert Pro diffractometer (MPD) θ/θ Bragg-Brentano powder diffractometer of 240 mm of radius. The diffractometer was operating at 45 kV and 40 mA (Cu Kα radiation, $\lambda = 1.5418$ Å). For thin layers, grazing angle incidence X-ray diffraction studies were performed. In addition, on four samples of 304 stainless steel were deposited the system of nitrided layers that act as a diffusion barrier. The samples were annealed in the range of temperature 680 to 730 °C. For that samples, the X-ray diffraction measurements of $\theta/2\theta$ scan were made in the range 5 to 120° 2θ with step size of 0.0170° and measuring time of 50 s/step. The X-ray diffraction spectra were examined with a PANalytical HighScore Plus software. Crystalline phases were identified by comparison with standard reference patterns (powder diffraction file PDF-2, International Centre for Diffraction Data (ICDD)). Grazing angle incidence XRD peak parameters of deposited layers and XRD peak parameters of bulk material are presented in **Table5.11** and **Table5.12**, respectively. Using the Scherrer equation, the size of the crystals was calculated. That expression relates the full with at half maximum (FWHM), lambda (λ) and the reflection angle θ to calculate the size of the crystal (D_{hkl}). We select a K value of 0.94.

$$D_{\text{hkl}} = \frac{K \cdot \lambda}{FWHM \cdot \cos\theta} \tag{5.1}$$

In addition, the magnitude of the distance between two adjacent and parallel planes of atoms (d-spacing) is a function of the Miller indices (h, k, and l) as well as the lattice parameter (a). For crystal structures that have cubic symmetry (William D. Callister and Rethwisch 2013), the expression can be written as follows:

$$d - \text{spacing} = \frac{a}{\sqrt{(h^2 + k^2 + l^2}} \tag{5.2}$$

When reviewing grazing angle incidence XRD results, we noted that although the 304 stainless steel target has an austenitic fcc structure, the thin layer obtained with pure Ar, shows a diffraction peak at $2\theta = 44.69°$. This corresponds to metastable bcc ferritic phase (α), with preferential orientation (110) (see **Figure 5.14**). This result is in agreement with those presented by (Kappaganthu and Y. Sun 2005) and (Alresheedi and Krzanowski 2017). However, the diffraction peak of our layer is not narrow and has one shoulder. At $2\theta = 44.12°$, the chromium (210) was also identified. According to the results of the XPS analysis, it is known that the sputtered stainless steel layer obtained without nitrogen has a Fe_xCr_yFxCry compound. This leads us to assume that the broad and high intensity peak observed between $2\theta = 44.12°$ and 44.69° corresponds to that compound. In addition, there are small peaks at $2\theta = 48.98°$ and 53.49°, corresponding to Cr(211) and Ni(200), respectively. These peaks were identified by comparing the XRD spectrum with standard reference patterns. This is consistent with the chemical composition results. The chemical analysis revealed that the layer obtained without nitrogen is rich in nickel and chromium (see **Table5.4**). In addition, under our deposition conditions, it was obtained bigger nickel crystals than those obtained for the other phases. In general, the calculated value of lattice parameter a is equal to the reference value.

On the other hand, the thin layers of nitrided 304 stainless steel presented very different grazing angle incidence XRD patterns to the previous one. Regardless of the N_2/Ar ratio used, different phases were obtained. Peaks corresponding to CrN were identified. Although with low intensity, its position can be easily differentiated. At 37.7, 43.84 and 63.4° 2θ are located the (111), (200) and (220) reflections. This was expected, since with

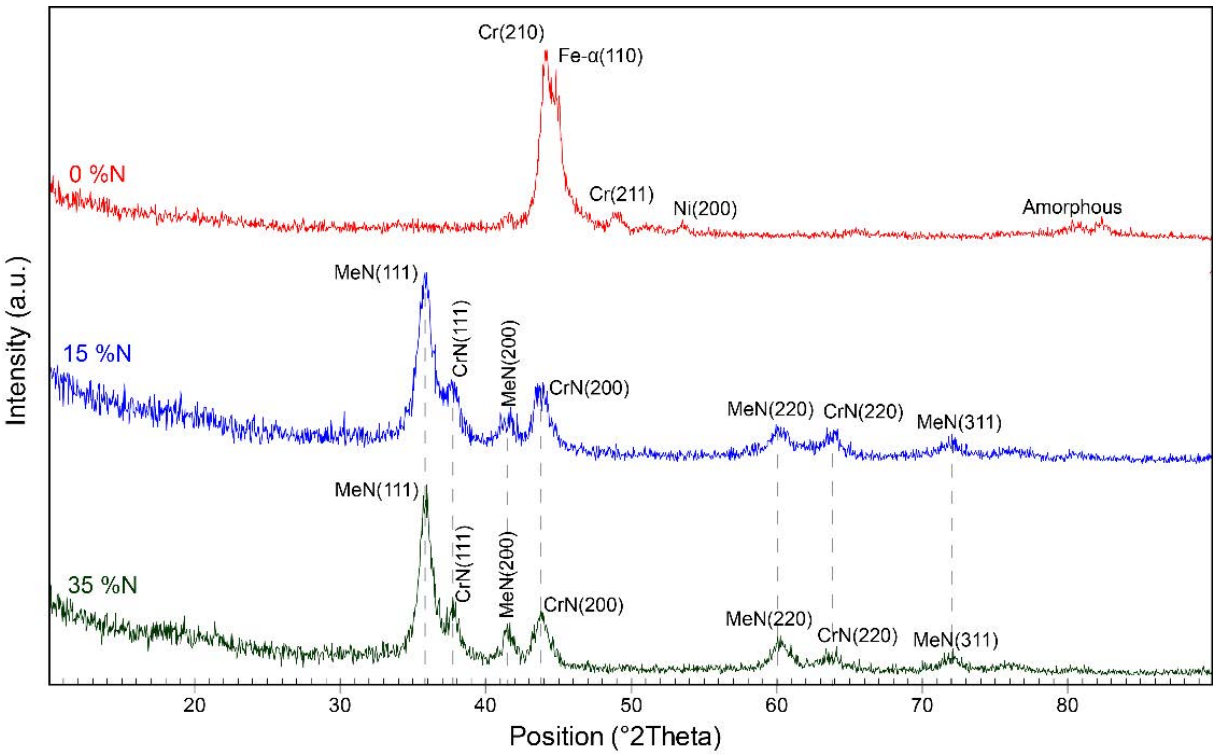

Figure 5.14: Grazing angle incidence XRD patterns of 304 stainless steel deposited layers with difrent nitrogen content. Acording (Kappaganthu and Y. Sun 2004), the MeN phase corresponds to an equiatomic metal/nitrogen ratio

the chemical analysis the CrN was known to be present in the layers. In addition, according with (Kappaganthu and Y. Sun 2004), with nearly equiatomic ratio of metal (Me) to nitrogen (N), MeN phase was obtained. That cubic MeN phase can be formed in the film when Me contains the basic compositions of the stainless steel target. A single MeN phase film can thus be fabricated with sufficient nitrogen doping to achieve the required Me/N atomic ratio (Kappaganthu and Y. Sun 2004). To be sure that our peaks correspond to the MeN phase, we also calculated the lattice parameter (see **Table5.10**). The two nitride layers had a value of $\sim 0.43\,\text{nm}$. If compared to the nitrogen-free austenite lattice parameter (0.36 nm), the calculated value is approximately 20% higher. As nitrogen atoms are incorporated into the structure an expanded fcc austenite (γN) phase, also known as the S-phase, is obtained. This phase is typical in other surface nitriding processes of steels. Nitrogen stabilizes the γN phase and increases its lattice parameter. Thus, this phase has lower reflection angles than nitrogen-free austenite. **Figure 5.15b** shows the evolution of the lattice parameter as a function of the atomic concentration of N. When a nitrogen threshold is exceeded (50 at.%), there is an abrupt change in its value. This suggests that the MeN phase is not a solid solution phase and the MeN phase is indeed different from the γN phase by nature. Since the MeN phase has a equiatomic metal/nitrogen composition, its detailed nomenclature can be written as ($Fe_{0.73}Cr_{0.18}Ni_{0.9}$), according to the composition of the stainless steel target (Kappaganthu and Y. Sun 2004; Kappaganthu and Y. Sun 2005). This nomenclature is valid when only the MeN phase is present in the layers. In our case, there is also the CrN phase, so it is recommended to identify in detail the MeN phase using the nomenclature $Fe_xCr_yNi_z$ x and z will most likely have values

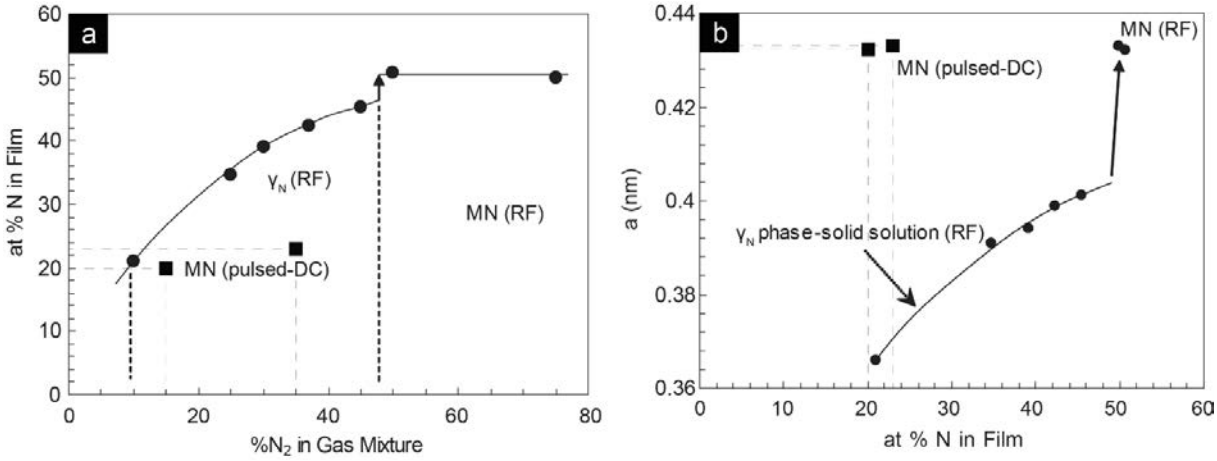

Figure 5.15: (a) Nitrogen concentration in film as a function of nitrogen gas composition in the sputtering gas mixture, (b) Variation of lattice parameter with nitrogen concentration in the fcc γN and MeN phases.Adapted from (Kappaganthu and Y. Sun 2004)

similar to the target, while y will be lower.

When we plot our results on the figures obtained by (Kappaganthu and Y. Sun 2004) (**Figure 5.15**), it is observed that our layers have the MeN phase at an atomic concentration N lower than the ones they reported. Under our sputtering conditions, in 304 stainless steel nitride layers there was a slight difference in at.% N as a function of N_2/Ar ratio. At the same time, there is a slight difference between the values of the lattice parameter as a function of the atomic concentration of N. It seems that the nitrogen threshold has been reached in the layers. It is necessary to prepare more layers using a smaller N_2/Ar ratio. Thus, when its chemical composition and crystalline structure will be studied, curves similar to those in **Figure 5.15b** can be obtained.

In general, the crystal size is larger in the layers deposited with pure Ar. Although at the 3/17 sccm/sccm N_2/Ar ratio, in the reflection (111), CrN grains size was 28.88 nm, which then decays to 7.07 nm when the ratio became 7/13 sccm/sccm of N_2/Ar ratio. This behaviour is strongly related with the thermal energy and the kinetic energy of the adatoms. In addition, the incorporation of nitrogen is known to decrease the energy and mobility of iron adatoms (Kappaganthu and Y. Sun 2005).

It should be noted that the MeN and CrN phases found in this work have been produced at room temperature. Which differs from the literature reviewed (Alresheedi and Krzanowski 2017; Kappaganthu and Y. Sun 2004; Kappaganthu and Y. Sun 2005; Saker et al. 1991). The layers that presented these phases were deposited at a temperature higher than the room temperature. Perhaps there can be two explanation for this fact. First, it may be that our cooling system (using water) did not sufficiently cool the substrate and it achieved thermodynamic conditions that favored the formation of the crystalline phases. However, although the temperature of the substrate was not monitored during the sputtering process, it can also be stated that the temperature was not enough to obtain large crystals. The other possible explanation is the type of power source used. All reference research was performed with a RF power source. However, we use a pulsed-DC power supply. Pulsed-DC technology has some advantages in comparison with RF. There is a higher power density and it is possible to control the frequency and duty cycle of the DC pulses. In addition, during the time of the negative pulse the sample can relax

Target	%N_2	hkl	Phase	Pos. (°2Th.)	d-spacing (Å)	FWHM (°2Th.)	a cal (Å)	a ref (Å)	Crystal size (nm)
SS304	0	210	Cr	44.12 ± 0.62	2.05 ± 0.03	0.81 ± 0.01	4.586	4.588	17.11 ± 0.24
		110	Alpha Fe	44.69 ± 2.01	2.03 ± 0.09	0.78 ± 0.04	2.865	2.886	17.62 ± 0.79
		211	Cr	48.98 ± 2.20	1.86 ± 0.08	0.83 ± 0.04	4.552	4.588	16.22 ± 0.73
		200	Ni	53.49 ± 1.61	1.71 ± 0.08	0.34 ± 0.02	3.423	3.450	38.67 ± 1.74
	15	111	MeN	35.86 ± 1.61	2.50 ± 0.11	2.65 ± 0.12	4.334	3.603	5.40 ± 0.24
		111	CrN	37.85 ± 1.70	2.37 ± 0.11	0.49 ± 0.02	4.114	4.140	28.88 ± 1.30
		200	MeN	41.71 ± 1.88	2.16 ± 0.10	4.00 ± 0.18	4.328	3.600	3.49 ± 0.16
		200	CrN	43.84 ± 1.97	2.06 ± 0.09	0.87 ± 0.04	4.127	4.140	15.91 ± 0.72
		220	MeN	60.11 ± 2.91	1.54 ± 0.07	1.37 ± 0.06	4.350	3.592	9.34 ± 0.42
		220	CrN	63.55 ± 2.86	1.46 ± 0.07	2.14 ± 0.10	4.137	4.140	5.87 ± 0.26
		311	MeN	72.20 ± 3.25	1.31 ± 0.06	3.87 ± 0.17	4.336	3.592	3.10 ± 0.14
	35	111	MeN	35.84 ± 1.61	2.50 ± 0.11	1.04 ± 0.05	4.336	3.603	13.81 ± 0.62
		111	CrN	37.6 ± 1.69	2.39 ± 0.11	2.01 ± 0.09	4.140	4.140	7.07 ± 0.32
		200	MeN	41.58 ± 1.87	2.17 ± 0.10	4.00 ± 0.18	4.340	3.600	3.50 ± 0.16
		200	CrN	43.84 ± 1.97	2.06 ± 0.09	0.90 ± 0.04	4.127	4.140	15.45 ± 0.70
		220	MeN	60.15 ± 2.71	1.54 ± 0.07	1.37 ± 0.06	4.347	3.592	9.38 ± 0.42
		220	CrN	63.37 ± 2.85	1.47 ± 0.07	4.00 ± 0.18	4.148	4.140	3.15 ± 0.14
		311	MeN	71.98 ± 3.24	1.31 ± 0.06	4.00 ± 0.16	4.347	3.592	3.01 ± 0.14
Al	40	100	AlN	33.07 ± 4.63	2.71 ± 0.38	2.84 ± 0.40	3.125	3.084	5.09 ± 0.71
		002	AlN	35.69 ± 5.00	2.51 ± 0.35	3.47 ± 0.49	3.125	3.084	4.13 ± 0.58

Table 5.11: Grazing angle incidence XRD peaks parameters of deposited layers

and thus reducing the stress before receiving the next pulse. This hypothesis is reinforced because all the layers have practically non-amorphous structures. It seems that the use of the pulsed-DC power supply made it possible to obtain stable layers with the CrN and MeN phases that other researchers obtained at higher temperatures.

The study of the crystalline structure of the thin sputtered layers, deposited inside the PEDRO reactor according to the conditions reported in **Table5.1**, has supplemented the information obtained by the XPS analysis. In general, the hypotheses raised in the previous section have been corroborated with the XRD results. For 304 stainless steel sputtered layers, it was found that the introduction of nitrogen influences the chemical composition and crystalline structure of the layers. With pure Ar, a rich layer was obtained in the compound Fe_xCr_y (possibly $Fe_{76}Cr_{24}$). In that layer there are also crystalline phases of Cr and Ni. On the other hand, the nitrided steel layers have two crystalline phases. One corresponds to the CrN and the other to a phase called MeN. The MeN phase possibly has a composition similar to that of the 304 stainless steel target, but low in chromium.

Figure 5.16 shows the grazing angle incidence XRD pattern of nitrided deposited layer. When comparing the diffraction pattern with the standard reference patterns, it was observed that (100) and (002) reflections at 33.07° and 35.69° corresponds to CrN. This is consistent with the results presented by (Moreira et al. 2011). However, they reported two prominent diffraction peaks at 35.9° and 37.8° corresponding to the (002) and (101) crystal planes of the hexagonal wurtzite phase of AlN. The main parameters that determine the preferred orientation are: (i) the nitrogen concentration in the gas mixture; (ii) the distance from the substrate to the target; (iii) the energy and concentration of the sputtering ions (Moreira et al. 2011). In addition, with regard to device applications it is desirable to develop AlN with a high degree of c-axis (002) orientation to obtain high values of electromechanical coupling factor k_t^2 (Clement et al. 2003).

Since the phase found presents a hexagonal unit cell, in addition to the lattice parameter a, it was necessary to calculate the lattice parameter c (cell height). Equation 5.3

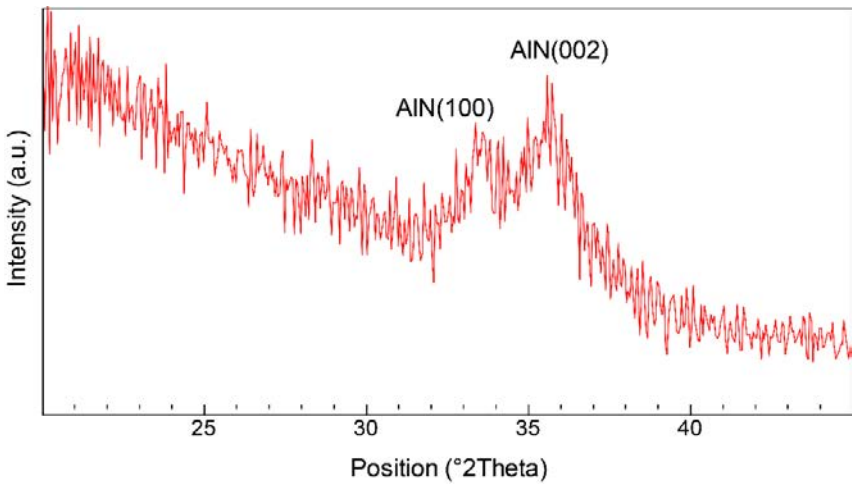

Figure 5.16: Grazing angle incidence XRD pattern of nitrided aluminum deposited layer

was used for this purpose.

$$\frac{1}{d-\text{spacing}^2} = \frac{4}{3}\left(\frac{h^2+hk+k^2}{a^2}\right) + \frac{l^2}{c^2} \tag{5.3}$$

The reference values for a and c are 3.084 and 4.948 Å, respectively. While the calculated values of a and c are 3.125 and 5.028 Å, respectively. The calculated values of the lattice parameters are slightly higher than those of the reference. This may be due to the fact that the CrN phase retains nitrogen atoms. This hypothesis is consistent with the results of the chemical analysis. In the high-resolution spectrum N 1s (**Figure 5.12b**), in addition to the signal from nitrides, a subpeak corresponding to pure nitrogen was also obtained. This is related to the low process temperature (Arrhenius relation) and also to the pulsed-DC power supply. Previously, we mentioned the advantages of this technology. According to our results, higher atomic concentration of N could be achieved compared to layers obtained with RF sources. In addition, it makes it possible to obtain layers with well-defined crystalline orientations and with low residual stress. On the other hand, no crystalline phases of Al_2O_3 or aluminum were observed in the nitrided aluminum layer analyzed. However, the chemical analysis found the presence of alumina on the surface. Most likely, the aluminum that did not form AlN reacted with oxygen from the atmosphere. An Al_2O_3 layer, a few nanometers thick, formed on the surface. This contamination, as mentioned above, benefits our diffusion barrier system.

Figure 5.17 shows the XRD patterns of the substrate and the diffusion barrier system as used for CNT growth. In this case, the signal from the thin layers was not noticeable. The aim of this study was to know the influence of the annealing process on the bulk material. Without annealing, the stainless steel substrate presents the austenitic (γ) and martensitic (α') phases.

These phases are characteristic of this material. The preferential growth orientations are similar to those found in the previous chapter. Martensite is a residual phase resulting from plastic deformation. In fact, it is known as strain induced martensite (Mallick et al. 2017). The development of the diffraction peaks with the temperature is coherent with the transformations that this material undergoes when it exceeds the recrystallization temperature. The parameters of the phases are reported in **Table5.12**. In the previous

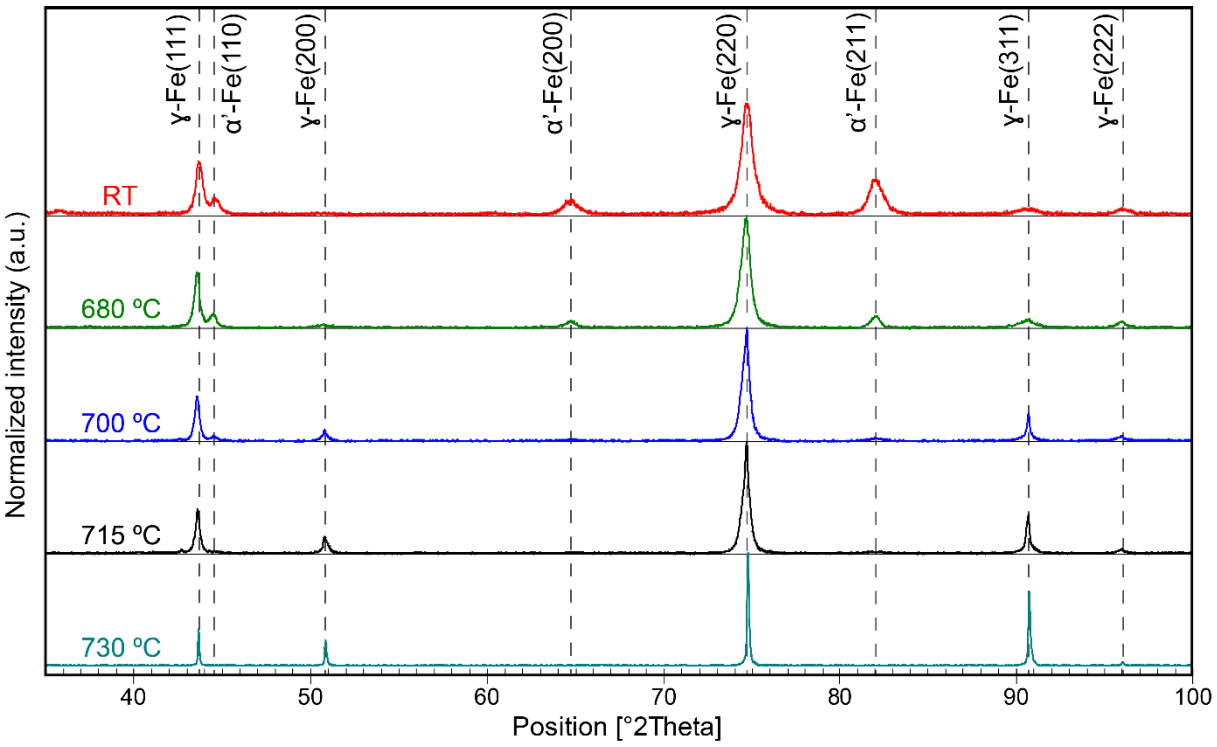

Figure 5.17: XRD patterns of 304 stainless steel substrate and diffusion barrier system at room temperature and different temperatures (like to the used during the CNTs growth)

chapter it was determined that for the substrate we use, the recrystallization temperature is below 650 °C.

For this chapter, all samples were annealed over that temperature. The range used was

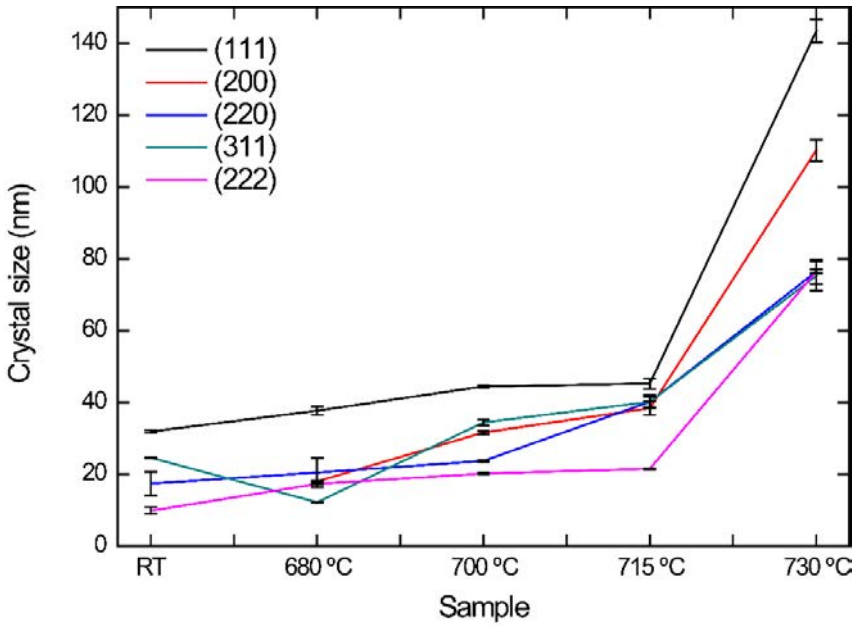

Figure 5.18: Austenitic crystal size development with temperature

	hkl	Phase	Pos. (°2Th.)	d-spacing (Å)	FWHM (°2Th.)	Crystal size (nm)
Room temperature	111	austenitic	43.70 ± 0.61	2.07 ± 0.03	0.43 ± 0.01	31.88 ± 0.45
	110	martensite	44.60 ± 0.71	2.03 ± 0.03	0.60 ± 0.01	23.13 ± 0.37
	200	austenitic				
	200	martensite	64.70 ± 1.10	1.44 ± 0.02	0.91 ± 0.02	13.81 ± 0.23
	220	austenitic	74.68 ± 14.30	1.27 ± 0.24	0.68 ± 0.13	17.4 ± 3.33
	211	martensite	82.06 ± 4.60	1.17 ± 0.07	0.80 ± 0.04	14.33 ± 0.80
	311	austenitic	90.49 ± 0.47	1.08 ± 0.01	0.44 ± 0.01	24.59 ± 0.13
	222	austenitic	96.03 ± 8.64	1.04 ± 0.09	0.84 ± 0.08	9.88 ± 0.89
680 °C	111	austenitic	43.58 ± 1.39	2.08 ± 0.07	0.37 ± 0.01	37.66 ± 1.21
	110	martensite	44.47 ± 0.40	2.04 ± 0.02	0.48 ± 0.01	29.06 ± 0.26
	200	austenitic	50.70 ± 0.48	1.80 ± 0.02	0.74 ± 0.01	18.04 ± 0.17
	200	martensite	64.72 ± 0.78	1.44 ± 0.02	0.61 ± 0.01	20.46 ± 0.25
	220	austenitic	74.62 ± 14.62	1.27 ± 0.25	0.58 ± 0.11	20.47 ± 4.01
	211	martensite	82.04 ± 1.42	1.17 ± 0.02	0.56 ± 0.01	20.21 ± 0.42
	311	austenitic	90.62 ± 0.70	1.08 ± 0.01	0.89 ± 0.01	12.22 ± 0.09
	222	austenitic	95.94 ± 0.86	1.04 ± 0.01	0.61 ± 0.01	17.31 ± 0.16
700 °C	111	austenitic	43.58 ± 0.39	2.08 ± 0.02	0.31 ± 0.01	44.45 ± 0.40
	110	martensite	44.51 ± 0.23	2.03 ± 0.01	0.31 ± 0.01	44.11 ± 0.23
	200	austenitic	50.81 ± 0.71	1.8 ± 0.03	0.42 ± 0.01	31.63 ± 0.44
	200	martensite	64.86 ± 1.10	1.44 ± 0.02	0.82 ± 0.01	15.29 ± 0.26
	220	austenitic	74.63 ± 0.90	1.27 ± 0.02	0.5 ± 0.01	23.72 ± 0.28
	211	martensite	82.03 ± 1.31	1.17 ± 0.02	0.82 ± 0.01	13.94 ± 0.22
	311	austenitic	90.69 ± 2.00	1.08 ± 0.02	0.32 ± 0.01	34.43 ± 0.76
	222	austenitic	95.91 ± 0.74	1.04 ± 0.01	0.52 ± 0.01	20.23 ± 0.16
715 °C	111	austenitic	43.61 ± 1.40	2.07 ± 0.07	0.31 ± 0.01	45.25 ± 1.45
	110	martensite				
	200	austenitic	50.83 ± 2.54	1.79 ± 0.09	0.35 ± 0.02	38.41 ± 1.92
	200	martensite				
	220	austenitic	74.64 ± 3.36	1.27 ± 0.06	0.47 ± 0.02	40.19 ± 1.81
	211	martensite	82.3 ± 0.43	1.17 ± 0.01	1.21 ± 0.01	9.39 ± 0.05
	311	austenitic	90.67 ± 3.17	1.08 ± 0.04	0.27 ± 0.01	40.19 ± 1.41
	222	austenitic	95.93 ± 0.74	1.04 ± 0.01	0.49 ± 0.01	21.56 ± 0.17
730 °C	111	austenitic	43.67 ± 0.96	2.07 ± 0.05	0.1 ± 0.01	143.3 ± 3.15
	110	martensite				
	200	austenitic	50.86 ± 1.32	1.79 ± 0.05	0.12 ± 0.01	110.2 ± 2.87
	200	martensite				
	220	austenitic	74.75 ± 3.36	1.27 ± 0.06	0.13 ± 0.01	76.43 ± 3.44
	211	martensite				
	311	austenitic	90.74 ± 4.99	1.08 ± 0.06	0.14 ± 0.01	75.24 ± 4.14
	222	austenitic	96.02 ± 0.74	1.04 ± 0.01	0.14 ± 0.01	76.43 ± 0.59

Table 5.12: XRD peaks parameters of bulk material

between 680 and 730 °C. The martensitic phase decreases as the annealing temperature increases. At 730 °C, no reflection of martensitic phases was recorded. The behaviour of the austenitic phase also corresponds to that observed in the previous chapter. In general, independent of the crystalline orientation, once the recrystallization temperature has been exceeded, the crystal size increases (**Figure 5.18**).

The only change observed, and perhaps very significant, is that the position of the (111), (200) and (311) reflections are almost constant. There are minimal displacements in their positions. This shows that the lattice parameters of the austenitic phase vary slightly

after the annealing process. The possible explanation is that the diffusion barrier system decreases the migration of atoms from alloying elements. In particular, the mobility of chromium is likely to decrease. This may allow the material to be more resistant to the harmful effects of a hydrogen atmosphere. To better understand the performance of the diffusion barrier system, prepared in this work, under a hydrogen atmosphere, it is necessary to make a more detailed study.

5.3.4 Deposition rate and electrical resistance

To determine the deposition rate, we used a glass substrate and profilometry measurements using a KLA Tencor, D-120. **Table5.13** contains the list of the deposition rate values of each layer. In addition, to perform **Figure 5.19**, additional samples were prepared to understand the development of the deposition rate with the percentage of N_2 flow rate. The deposition rate of the sputtered stainless steel layers decrease as the N_2 percentage increases. When the process pressure is constant (1 Pa), this change can be explained by the loss of efficiency associated to the decrease of Ar concentration during

Target	Flow ratio N_2/Ar (sccm)	N_2 %	Deposition rate (nm/min)
SS304	0/20	0	7.49 ± 0.15
	2/18	10	7.40 ± 0.02
	3/17	15	6.64 ± 0.13
	5/15	25	6.27 ± 0.11
	6/14	30	6.18 ± 0.07
	7/13	35	5.97 ± 0.06
Al	20/30	40	3.26 ± 0.10

Table 5.13: Deposition rate of nitrided SS304 and AlN layers at different percentage of N_2 flow rate

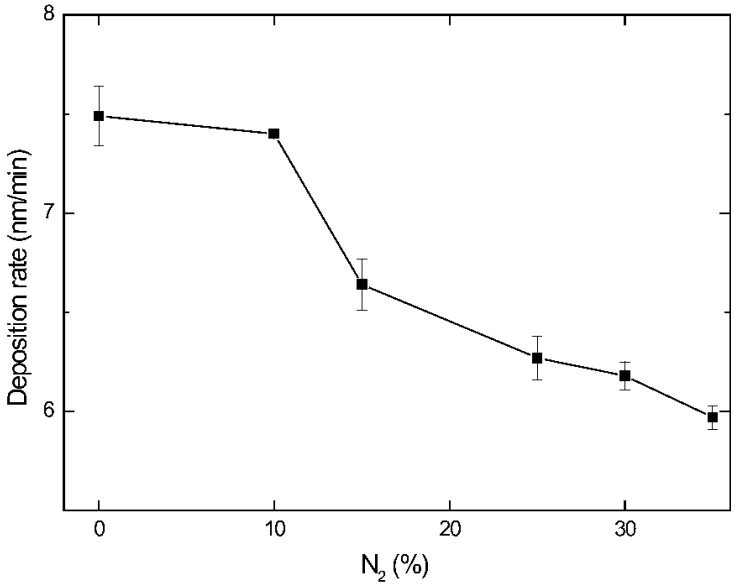

Figure 5.19: Evolution of deposition rate of nitrided SS304 layers vs. $N_2/(N_2 \equiv Ar)$ flow rate percentage

the sputtering process. In addition, when the N_2 percentage increases, it induces continued poisoning of the target (Baranowska et al. 2013). It should also be noted that the incorporation of nitrogen is known to decrease the energy and mobility of iron adatoms (Kappaganthu and Y. Sun 2005).

The deposit rate can be increased by increasing the pulsed-DC magnetron power. However, there is a risk that the internal stress of the layers will be high. This can lead to peeling-off of the layers. An interesting strategy to increase the deposit rate was proposed by (Kumar et al. 2000). They introduced hydrogen to the N_2/Ar mixture, in the range of 5 to 50%, which allowed to increase the deposition rate. According to (Moskalioviene and Galdikas 2015), this is due to two factors: (i) reduction of surface oxide due to chemical etching of oxygen by hydrogen and (ii) increase of NH radicals which become active nitrogen atoms on the steel surface, in other words, increase the amount of nitrogen adsorbed and diffused. High deposit rates are useful in applications where improving the mechanical properties of a surface is desired. For example, in applications where high resistance to abrasion, erosion or corrosion is required. For these cases, it is essential to have a thick layer. For our application, a thin transition layer was required between the substrate and the diffusion barrier. A gradient layer of approximately 190 nm thickness satisfies our needs.

We found that for AlN layer the deposition rate at 3 Pa was 3.26 nm/min. From the literature consulted it is known that the type of layer obtained, from an aluminum target and using a DC-magnetron sputtering technology, depends on several factors that are strongly correlated. Among those that outstand out, we have the percentage of reactive gas, the pressure at which the process is carried out, the power, the bias voltage and the temperature of the substrate (Borges et al. 2012; Iriarte et al. 2010; G. Ke et al. 2015; Moreira et al. 2011; Ren et al. 2015). Therefore, the values reported in the articles differ considerably. For example, at 2.1×10^{-2} and 5.4×10^{-2} Pa, (Borges et al. 2012) reported deposition rate of 35 and 63 nm/min, respectively. As mentioned for nitrided stainless steel layers, the reactive gas used in film preparation not only reacts with the sputtered material of the aluminum target, it also interacts with the surface of the cathode, gradually covering it with a layer of non metallic compound. The target is poisoned, the sputtering efficiency is lower than for the initial metal target (Baranowska et al. 2013; Borges et al. 2012). That is why, before the deposition of the nitrided layers, the surface of the targets used in our experiments was cleaned only by means an argon plasma. Thus, by repeating the process, similar deposition rates can be obtained.

On the other hand, the electrical resistivity of the films was determined using the four-point probe method (in linear geometry) and in a Van der Pauw geometry. The Keysight 2900 series Precision/Source Measuring Unit (SMU) was used to carry out the experiments. Silver paint was used to improve contact in the Van der Pauw test. Thus, an ohmic contact could be obtained between the tips and the layers under study. **Table5.14** summarizes the resistivity values obtained for each of the layers constituting the diffusion barrier system.

The resistivity values for nitrided stainless steel layers are two orders of magnitude above the value reported for bulk 304 stainless steel (see **Table5.2**). Nitrogen percentage governs the evolution of these values (see **Figure 5.20**). This behaviour is probably due to the obtaining of non-metallic nitrogen-rich phases in the layers (CrN), and also to the fact that the resistivity measurements were carried out in layers without annealing treatment. By subjecting the thin layers to annealing treatments, the size of the crystals is likely to increase and the number of grain boundaries to diminish. Although we did not measure the resistivity of annealed layers, it is probably lower than that of layers without

Target	Flow ratio N_2/Ar (sccm)	N_2 %	Resistivity (Ω.m)
SS304	0/20	0	$2.51 \times 10^{-6} \pm 1.24 \times 10^{-7}$
	2/18	10	$5.21 \times 10^{-6} \pm 2.58 \times 10^{-7}$
	3/17	15	$5.02 \times 10^{-6} \pm 3.77 \times 10^{-7}$
	5/15	25	$6.18 \times 10^{-6} \pm 3.69 \times 10^{-7}$
	6/14	30	$6.83 \times 10^{-6} \pm 4.33 \times 10^{-7}$
	7/13	35	$6.70 \times 10^{-6} \pm 5.86 \times 10^{-7}$
Al	20/30	40	$2.05 \times 10^{2} \pm 36.37$

Table 5.14: Resistivity of nitrided stainless steel and AlN layers grown by sputtering at different $N_2/(Ar+N_2)$ gas flow ratio

annealing treatment, because the increase of electrical mobility of free charge carriers due to the decrease the number of barriers associated to the grain boundaries. Of course, this is conditioned by the ratio between metallic and non metallic phases (Borges et al. 2012). In our case, during the CNT growth process, both the steel substrate and the diffusion barrier system, were annealed in the temperature range of 680 to 730 °C. It can be expected that the resistivity of the nitrided 304 stainless steel layers decreased as the temperatures increases.

In addition, the resistivity of the nitrided aluminum layer is nine orders of magnitude higher than that reported for stainless steel. However, this is seven orders of magnitude lower than that reported in the literature for pure AlN layers (Borges et al. 2012). Perhaps the layer that we obtained for this study has aluminum rich phases (Al + AlN) increasing the electrical conductivity of the system. Although there may also be traces of aluminum that oxidize when exposing the sample to the atmosphere. The variation of electrical properties with non-metallic over metallic atomic proportions can be explained by assuming that the electrical transport in the layer takes place through a series of channels formed by metallic grains. Some of the grains in a channel can be in contact and, in

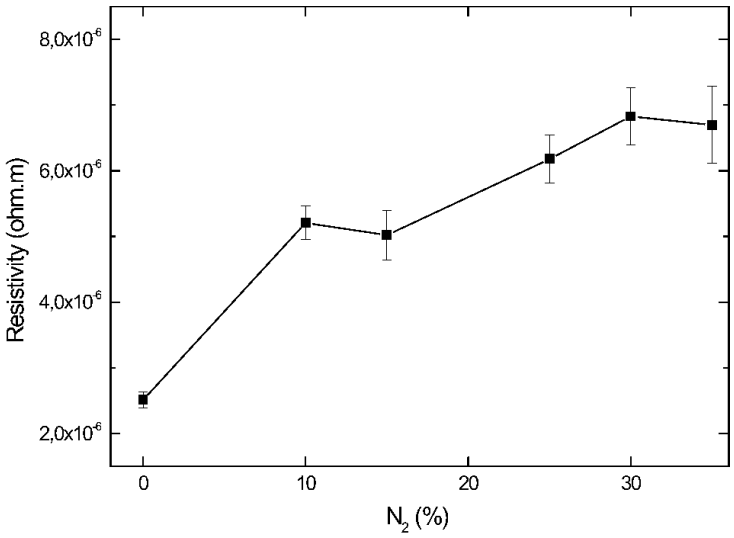

Figure 5.20: Development of resistivity with N_2 flow rate percentage for nitrided stainless steel layers

this case, current conduction is governed by constrictions between grains. However, other grains are separated by a thin insulating barrier, forming metal-insulator-metal (MIM) units and, in this case, electrical transport is controlled by tunneling processes, such as thermally activated tunneling and/or tunneling through localized states in the insulating layer (Canali et al. 1980; Kusy 1987). The resistivity of the nitrided aluminum layer, together with the results of the XPS and XRD analyses confirm its nature. It is a thin layer that contains AlN and also aluminum. This added to the presence of Al_2O_3 on the surface can improve the performance of the diffusion barrier.

5.3.5 Morphological characterization

In the experimental section, we mentioned that both the target and the substrate were made of 304 stainless steel with a thickness of 0.1 mm (**Figures 5.21a-b**). The deposition of the nitrided layers took place in an area of approximately 56 cm^2 (**Figure 5.21b**). The corners of those samples were not covered due to the configuration (frame) of our holder. Thus, in the four samples, which were obtained on the 56 cm^2 substrates, a small area of 304 stainless steel was not covered (**Figure 5.21c**). That "defect" made it possible to check the performance of the diffusion barrier system proposed in this chapter. At first glance it can be seen that the corner that lacks the nitrided layers shows a different color from the color observed in the area that has the nitrided layers (**Figure 5.21d**).

When these areas were examined with the scanning electron microscope (SEM) (Jeol

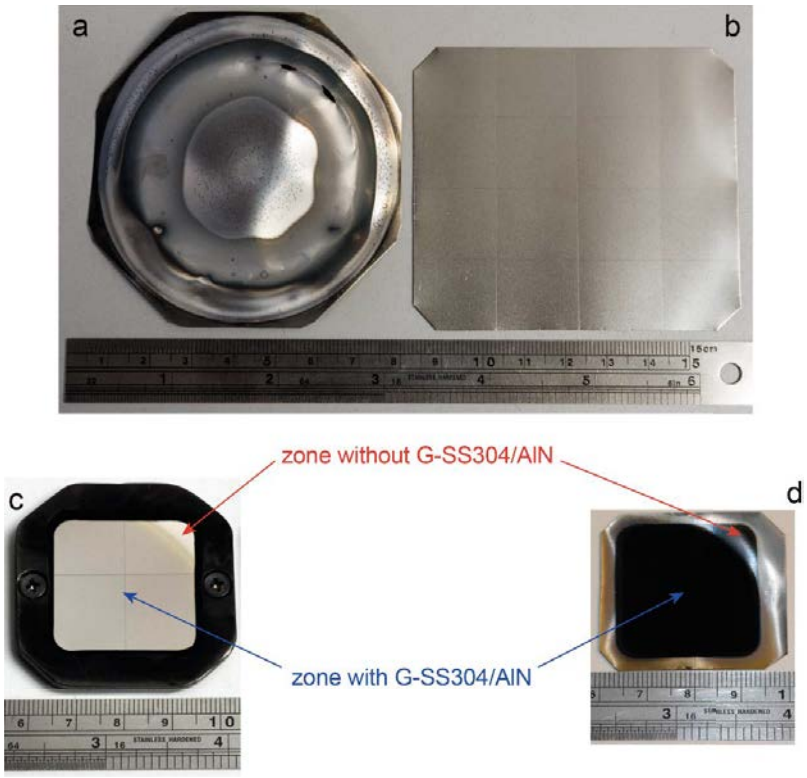

Figure 5.21: (a) Used SS304 target, after several deposition processes, (b) substrate of SS304 without diffusion barrier system, (c) Sample of SS304 with G−SS304/AlN before depositing the Fe layer, (d) Forest of CNTs. The thickness of the target and substrate is 0.1 mm

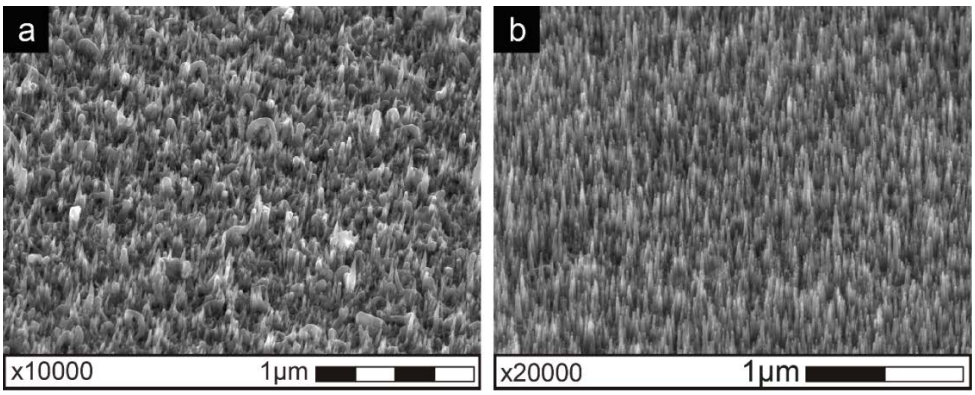

Figure 5.22: (a) SS304 surface without diffusion barrier system, (b) SS304 surface with diffusion barrier system. There is a CNTs forest

JSM 6510), the differences became even more evident. Structures with low order and variable morphology can be seen on the stainless steel (**Figure 5.22a**). Some of the structures observed may correspond to amorphous carbon and precipitated particles. It is clear that the catalytic activity of iron particles is severely affected when they are deposited directly on the surface of the steel. The native oxide layer of the stainless steel contaminates the catalyst particles (Masarapu and B. Wei 2007).

In contrast, **Figure 5.22b** shows nanostructures with a well-defined shape. These

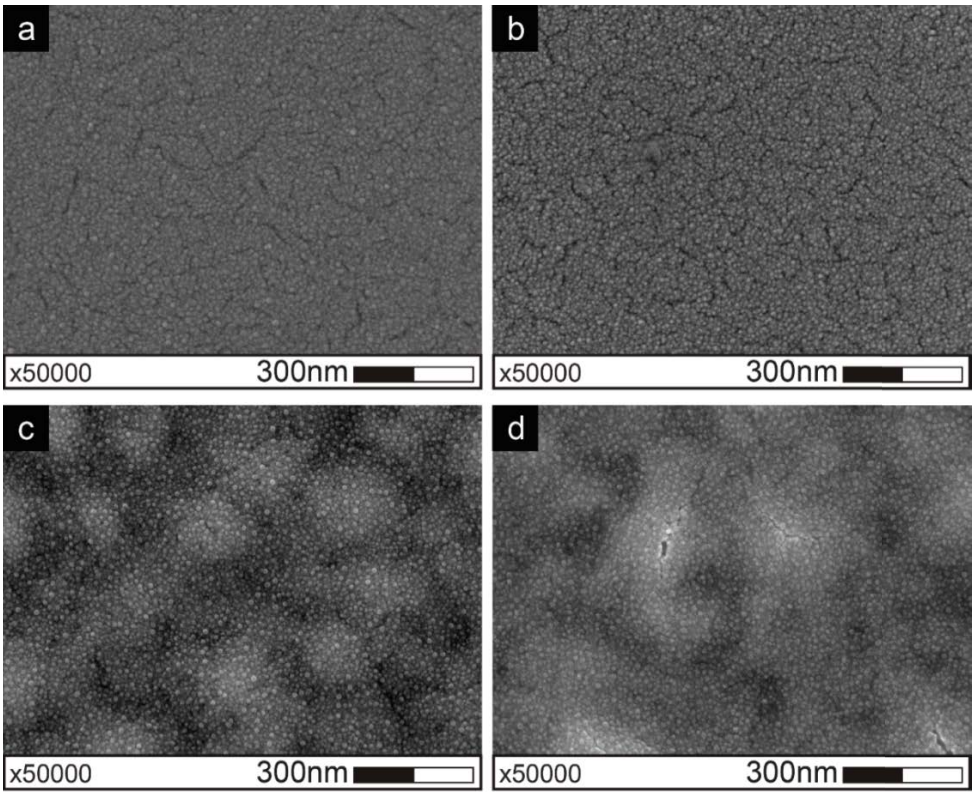

Figure 5.23: Iron nanoparticles on diffusion barrier system deposited over silicon wafers. The samples were annealing at 680 °C (a), 700 °C (b), 715 °C (c) and 730 °C (d)

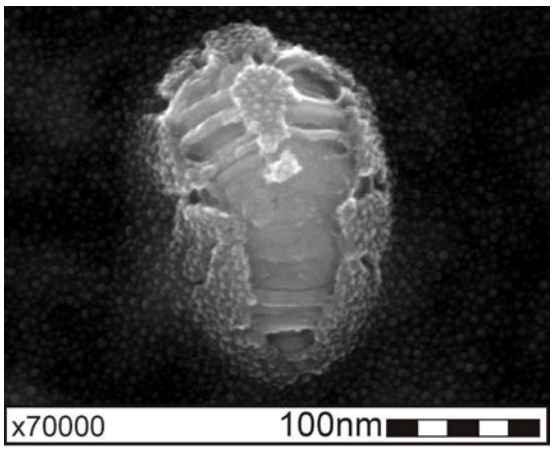

Figure 5.24: Precipitated particle on layers deposited over silicon wafer surface

form a uniform forest over the area covered with the diffusion barrier system. The differences identified imply that the diffusion barrier system performs the desired function. It prevents the diffusion of the catalyst into the substrate and allows it to form nanoislands to obtain uniform CNTs forests. Several samples were prepared to better understand the interaction of the catalyst with the diffusion barrier system. A first approach was to deposit the nitrided stainless steel and aluminum layers on silicon wafers. Then a thin layer of iron (catalyst) was deposited and finally annealed. The samples were heated to temperatures between 680 and 730 °C (**Figure 5.23**). The annealing process was stopped just before the introduction of acetylene (carbon precursor gas). Thus, it was possible to study the morphology and distribution of the nanoislands that formed on the surface before the CNTs begin to form.

In general, the distribution of iron nanoparticles was uniform on diffusion barrier surface. However, cracks can be seen in all SEM images (**Figures 5.23a-b**). Cracks may be due to the difference in the thermal expansion coefficient between the silicon substrate and the layers deposited by sputtering. Polished Si wafers were used instead of stainless steel because it is difficult to observe the nanoislands on SS304 with a roughness of tens of microns. In samples annealed at 715 and 730 °C (**Figures 5.23c-d**) there is some contrast between adjacent areas. That contrast may be due to the formation of valleys and small hills. The possible explanation for this phenomenon can be found in **Figure 5.24**. It seems that when the diffusion barrier is broken hydrogen promotes the formation of precipitates on the sputtered stainless steel thin layers. This fact was already mentioned in the previous chapter. If the thermodynamic conditions are favorable, the precipitated particles grow. This changes the initial flat surface into a rough surface. If precipitated particles grow enough, they can collapse the diffusion barrier system. **Figure 5.24** also provides some qualitative information about the mechanical behavior of the diffusion barrier system deposited by sputtering. What is observed is a layer that does not present a brittle behavior and has good adherence with the substrate.

On the other hand, the density and diameter of the iron nanoparticles was obtained using the ImageJ software. Thus, we noticed that as the temperature increases, the diameter of the nanoparticles increases slightly (see **Figure 5.25**). Although the variation is small, the increase in the diameter of nanoparticles can be understood as the effect of coalescence. Several studies have been carried out on this phenomenon. When the metal thin films are heated, the mobility of the atoms increases, the film coarsens and island

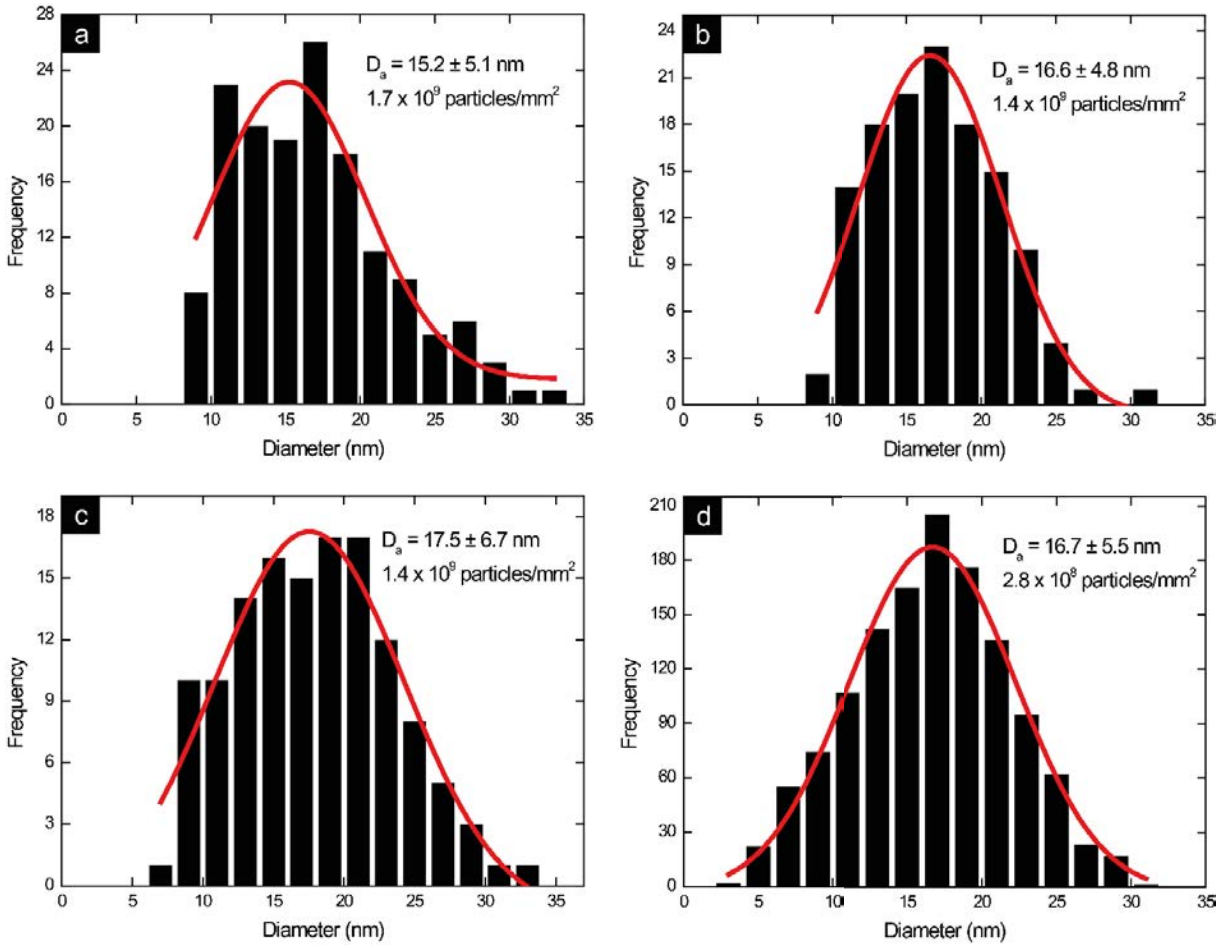

Figure 5.25: Development of iron nanoparticles diameter with annealing temperature. Iron was deposited on diffusion barrier system using silicon wafers as substrate. The samples were annealing at 680 (a), 700 (b), 715 (c) and 730 °C (d)

coalescence develops, driven by a complex mechanism that minimizes surface energy or free energy of the substrate/metal interface (Wen et al. 1996). The coarsening phenomenon can appear at temperature values lower than the metal melting point depending on the substrate interactions, annealing environment and the size effect which decreases the melting temperature (Qi et al. 2001). Bulk Fe melts at 1535 °C but the coarsening effect has been observed at temperature of about 270 °C (Signore et al. 2008). The slight increase in diameter directly influenced the density of the nanoislands. The density decreases when the annealing temperature increases. The obtained values were 1.7×10^9, 1.4×10^9, 1.4×10^9 and 2.8×10^8 nanoislands/mm^2 for 680, 700, 715 and 730 °C, respectively (**Figure 5.25**). The size of the nanoparticles mainly depends on the thickness of the iron film deposited at room temperature on the diffusion barrier. In this study we have chosen a thickness of 3 nm for the ultrathin film of iron.

The nanoislands obtained on the diffusion barrier system using 304 stainless steel as a support showed a similar behaviour. Although the contrast of the SEM images does not allow the form and distribution of the nanoislands to be properly appreciated, it is possible to differentiate them (**Figure 5.26**). However, the diameter and consequently the density of the nanoparticles was not the same. This was confirmed when the nanotube

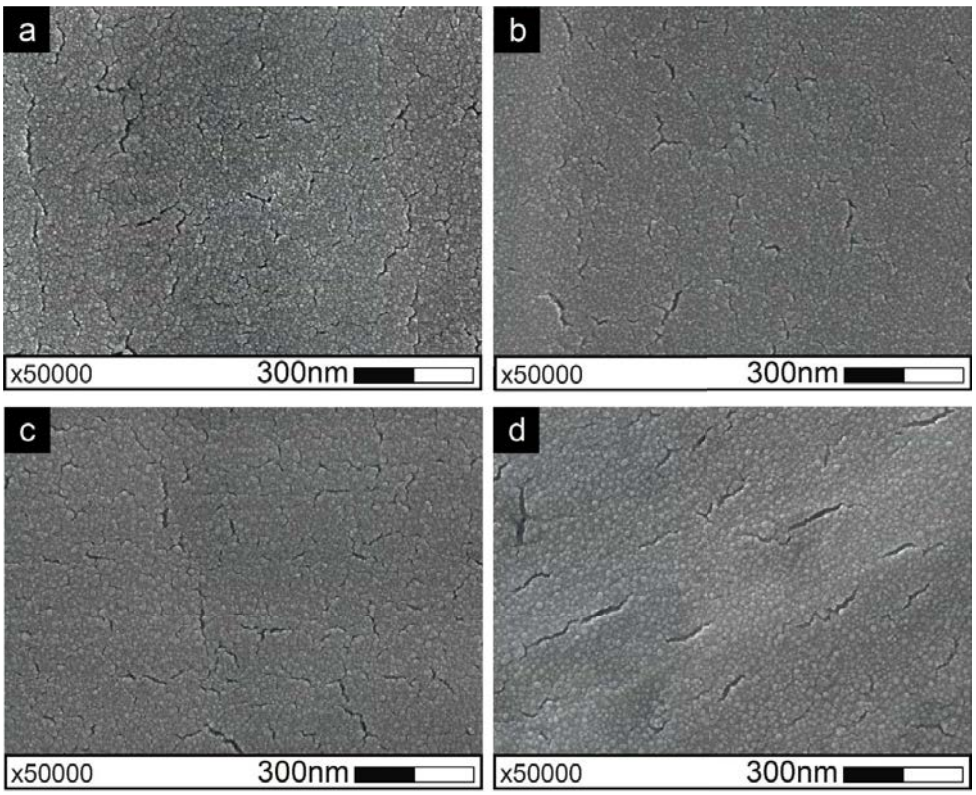

Figure 5.26: Iron nanoparticles on diffusion barrier system deposited over bulk SS304. The samples were annealed at 680 (a), 700 (b), 715 (c) and 730 °C (d)

forests were examined with the scanning electron microscope. In general, the diameter of the CNTs was larger than that obtained on the silicon wafers. As previously mentioned, the kinetic processes that occur in each system (Fe/AlN/G SS304/Si wafer and Fe/AlN/G−SS304/SS304 foil) were different. Although the most significant difference was that no precipitated particles were observed on the surfaces. This was useful in maintaining the integrity of the diffusion barrier system. Cracks were observed on the surface of all samples annealed between 680 and 730 °C. But unlike what happened to the silicon wafers, no collapse of the diffusion barrier system was observed. One possible explanation is that the observed cracks only affect the AlN layer, while the gradient layer acts as a hydrogen barrier that does not interact with the bulk material. This prevents particles (e.g. carbides) from precipitating on the surface. The proposed multilayer system, despite having cracks, fulfils its function of keeping the catalyst on the surface.

To complete this section, **Figure 5.27** summarizes the results obtained on 304 stainless steel. The densities of CNTs were lower than the value obtained for Fe particles on silicon wafers. The most homogeneous forest of CNTs was obtained at 680 °C (**Figures 5.27a-a'**). The average length of CNTs was 500 nm. Additionally, the diameter was between $20-25$ nm. At 730 °C (**Figures 5.27d-d'**) the CNTs forest showed a random morphology with diameters ranging from 30 to 70 nm and lengths between $600-1000$ nm. The CNTs obtained at 730 °C were longer than the others CNTs obtained at lower temperatures. The average diameter of these particles was bigger than the particles obtained at 680 °C because the high temperature produces coalescence of catalyst nanoislands. On the other hand, **Figures 5.27b-b'** show a mixed forest of CNTs. High percentage of these CNTs were similar to the CNTs obtained at 680 °C. **Figures 5.27c-c'** also showed a mixed forest

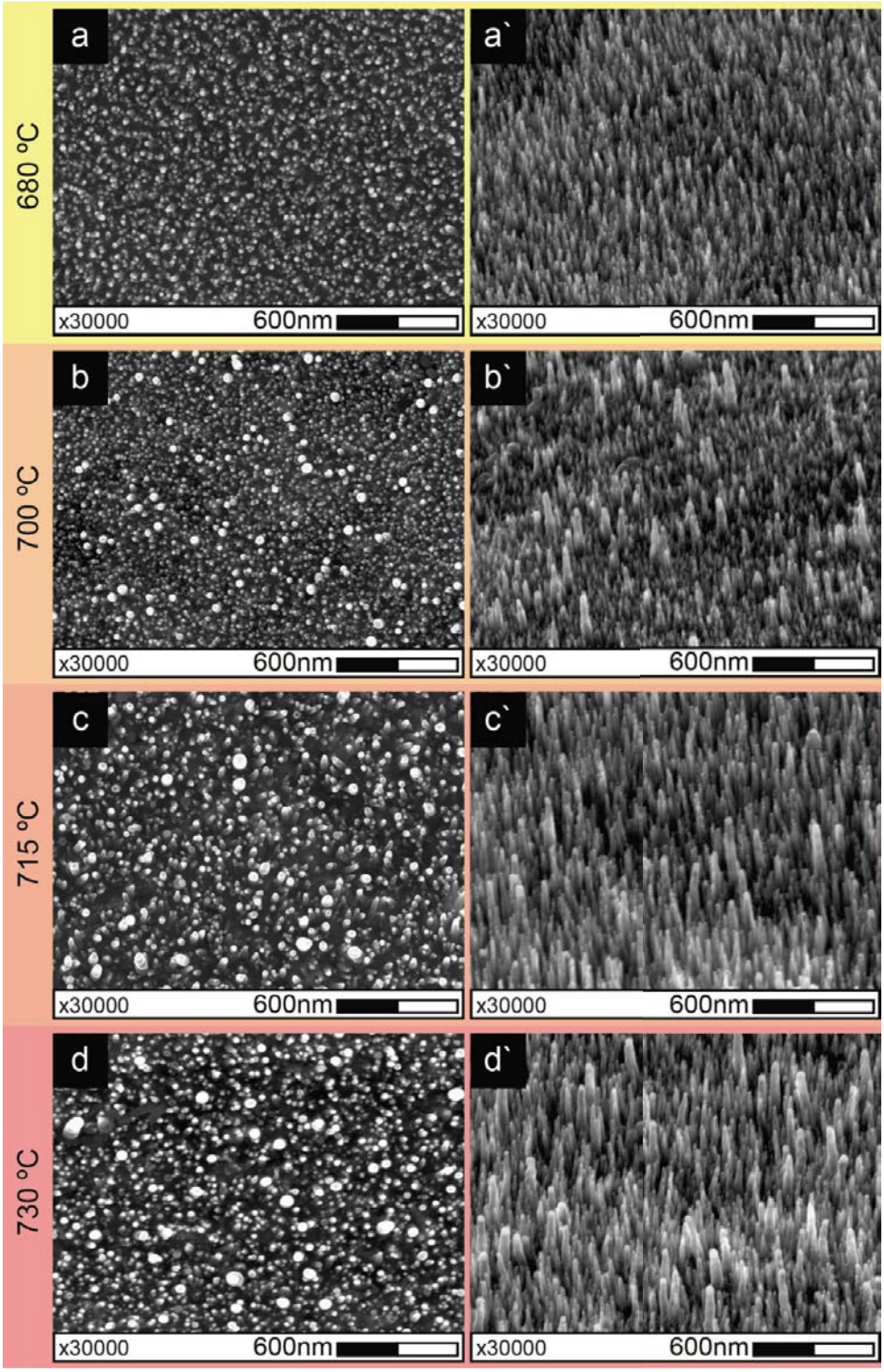

Figure 5.27: SEM images of CNTs forest obtained at different temperatures. a, b, c and d show the top view of CNTs. a', b', c' and d' show the tilted view of CNTs

of CNTs. Nevertheless, a low percentage of these CNTs obtained were similar to those obtained at 680 °C. This sequence of images shows the strong influence of temperature during carbon nanotube growth. (Grüneis et al. 2006) demonstrate that the growth rate of CNTs at eutectic temperature is higher in comparison with other temperatures. For

iron thin films, the eutectic temperature is around 732 °C (Harutyunyan et al. 2005). Our results are consistent with those works. At 730 °C, we got a higher growth rate.

5.3.6 Raman Shift Spectroscopy

Raman spectroscopy was performed to evaluate the quality of the forest of nanotubes using a micro Raman system (Horiba LabRam HR800, Japan). A green laser of 532 nm of wavelength, 0.5 mW of power and a 50LWD objective was used during the measurements. As can be seen in **Figure 5.28**, five peaks were used to fit the Raman spectra obtained. Four of these peaks (Gaussian curves) represent the graphitic sites of the samples (D"-band, D-band, G-band, D'-band), and one peak (Lorentzian curves) is assigned to the amorphous fraction (A-band) (Düngen et al. 2017). The Raman feature are given in **Table5.15**. D"-band is found around 1220 cm^{-1} and it is related to impurities in the graphite lattice (Shahzad Hussain, Amade, and Bertran 2014). The presence of the D-band in these materials is assigned to structural defects (probably edge defects in these cases) (Bokobza et al. 2015). The G ("Graphite") band at around 1585 cm^{-1} corresponding to an ideal graphitic lattice vibration mode with E_{2g} symmetry. Another first-order band accounting for structural disorder is the D' band at $\sim$ 1619 cm^{-1} which can be observed as a shoulder on the G-band. Like the G band, the D' band corresponds to a graphitic lattice mode with E_{2g} symmetry (Sadezky et al. 2005). Since A-band represents

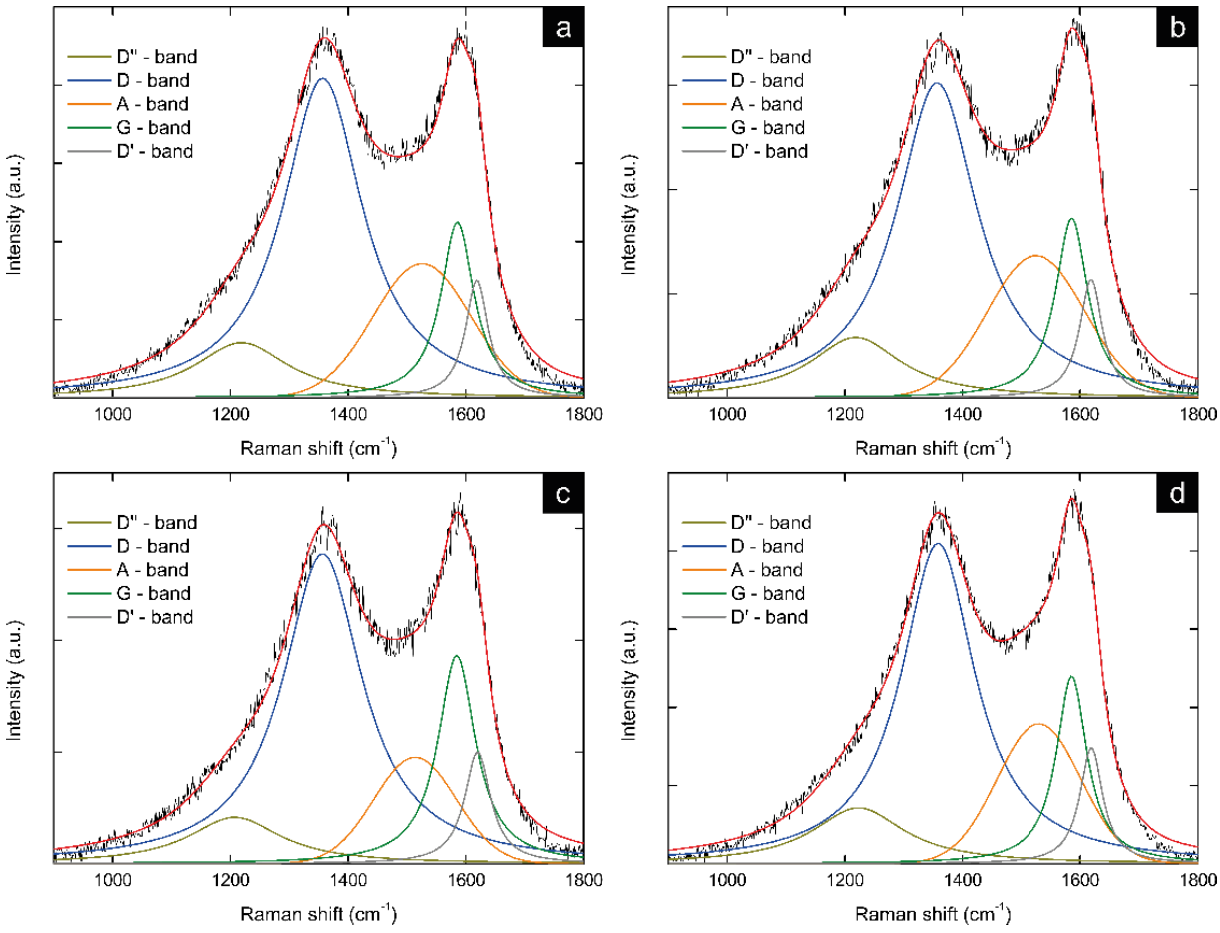

Figure 5.28: Raman spectra for CNTs at 680 °C (a), 700 °C (b) 715 °C (c) and 730 °C (d)

		D"	D	A	G	D'	I_D/I_G	$I_D/I_{D'}$
680 ℃	Position (cm^{-1})	1218.92 ± 8.23	1356.68 ± 1.19	1525.53 ± 8.13	1585.65 ± 2.44	1618.54 ± 1.84	1.82	2.71
	Intensity (a.u.)	1.41 ± 0.03	8.17 ± 0.16	3.43 ± 0.07	4.49 ± 0.09	3.01 ± 0.06		
	FWHM (cm^{-1})	193.48 ± 17.50	165.50 ± 6.88	196.37 ± 9.19	68.30 ± 7.12	46.86 ± 5.92		
700 ℃	Position (cm^{-1})	1218.35 ± 7.90	1356.53 ± 1.35	1525.26 ± 8.20	1586.03 ± 2.54	1618.71 ± 2.05	1.75	2.65
	Intensity (a.u.)	1.16 ± 0.02	6.04 ± 0.12	2.73 ± 0.05	3.45 ± 0.07	2.28 ± 0.05		
	FWHM (cm^{-1})	189.41 ± 17.50	167.14 ± 7.64	196.48 ± 9.71	66.41 ± 7.44	47.00 ± 6.45		
715 ℃	Position (cm^{-1})	1207.30 ± 8.26	1356.48 ± 1.45	1513.72 ± 7.62	1584.46 ± 2.96	1619.88 ± 2.51	1.49	2.78
	Intensity (a.u.)	0.83 ± 0.02	5.55 ± 0.11	1.91 ± 0.04	3.73 ± 0.07	2.00 ± 0.04		
	FWHM (cm^{-1})	190.90 ± 19.40	164.75 ± 6.44	165.18 ± 17.70	77.62 ± 6.00	53.64 ± 9.21		
730 ℃	Position (cm^{-1})	1223.00 ± 6.39	1358.39 ± 0.79	1530.21 ± 5.00	1585.93 ± 1.80	1619.23 ± 1.72	1.71	2.76
	Intensity (a.u.)	1.43 ± 0.03	8.19 ± 0.16	3.58 ± 0.07	4.80 ± 0.10	2.97 ± 0.06		
	FWHM (cm^{-1})	190.18 ± 13.35	152.59 ± 4.61	168.53 ± 7.78	63.08 ± 5.09	47.12 ± 6.02		

Table 5.15: Raman feature of CNTs obtained by PECVD

the amorphous carbon and according with our deconvolution processes, we can stablish that the samples analyzed in the present study exhibit amorphous carbon, as in previous chapter. Regardless of the temperature used during the growth of CNTs, the amount of amorphous carbon contained in the samples was high.

As discussed in Chapter 4, the type of amorphous carbon can be easily identified using the chart prepared by (Merlen et al. 2017). In this case, it can be observed that the amorphous carbon corresponds to nanocrsitaline graphite (nc-G) (see **Figure 5.29a**). In addition, when plotting the values of FWHM_D (Γ_D) and FWHM_G (Γ_G) in **Figure 5.29b**, it is estimated that the crystal size of the samples ranges from 1 to 10 nm.

The ratio between D and G bands intensities (I_D/I_G) evaluates the defects extension within CNTs and it increases as defects increase (Millie S. Dresselhaus et al. 2005; Osswald et al. 2007). This ratio was quite similar for the four samples which means that the temperature change does not affect strongly on the number of defects.

Finally, it can be said that the samples have a greater disorder, as previos chapter for PECVD samples. The value of $I_D/I_{D'}$ of CNTs samples on nitrided layers is below the minimum value determined by (Eckmann et al. 2012) for boundaries type defects in graphene sheets. Although it is not precisely graphene sheets, in the range $900 - 1800\,\text{cm}^{-1}$, Raman fingerprint of CNTs can be strongly affected by the amorphous carbon (nanocrystalline graphite). In between amorphous materials and perfect crystals, defects play a role in the disturbed Raman scattering process (Merlen et al. 2017). Note that the borders of the crystallites work as defects involved in the double resonance process, giving rise to the D and D' bands in the Raman spectra of nanographites (Cançado et al. 2007).

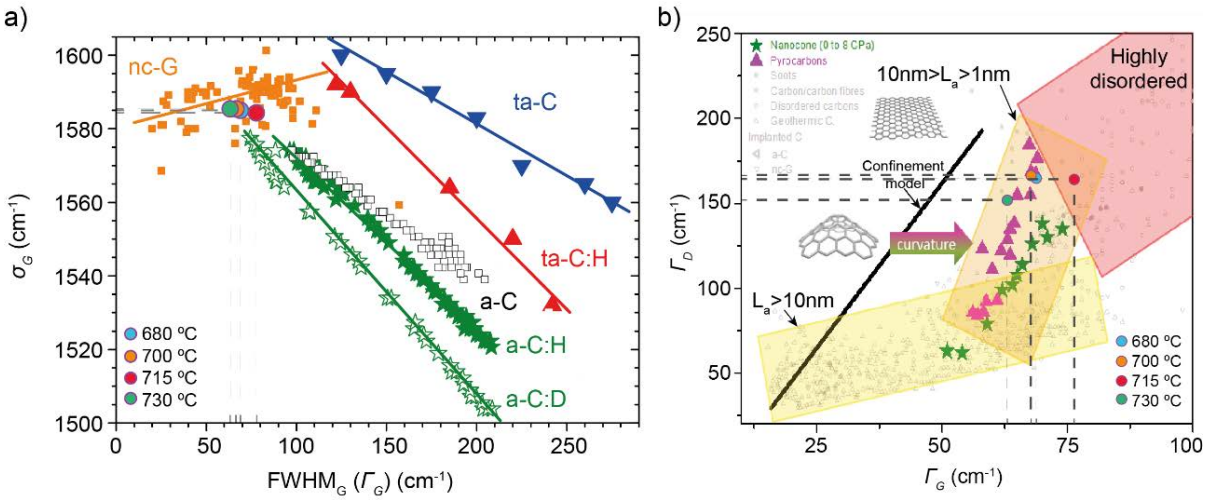

Figure 5.29: a) Plots of σ_G vs. Γ_G for nc-G and different amorphous carbons, b) Γ_D vs. Γ_G plot for a large variety of disordered aromatic carbons. Adapted from (Merlen et al. 2017)

5.4 Conclusions

An effective diffusion barrier system was obtained using a target of the same substrate material, i.e. 304 stainless steel and AlN. Using DC-magnetron sputtering, a gradient stainless steel layer was obtained. Its chemical composition and crystalline structure depend on the gas used during the sputtering process. By using only Ar gas, the predominant compound was rich in chrome and iron. This has a body centered cubic (bcc) crystal structure instead a face centered cubic (fcc) crystal structure of bulk material. However, by introducing nitrogen (in percentages between 15 and 35%) the chemical composition and crystalline structure of the layers change. Two phases have been found. One phase corresponds to CrN and the other is basically composed by alloy elements. The last one, that in the literature is reported as MeN, is cubic. In our case, we assume that MeN phase presents a chemical composition similar to that of the target, but poor in chromium. In addition, a nitrided aluminum layer was deposited on the gradient layer. Its chemical and crystalline study allowed to identify that the obtained layer is made up of AlN (wurtzite phase) and pure aluminum. On the other hand, the use of nitrogen during the sputtering process also modifies the deposition rate and resistivity of the nitrided layers. The performance of the diffusion barrier system on 304 stainless steel substrates was also tested. Samples that were annealed, despite cracks, allowed the catalyst to form nanoislands. Thus, it was possible to obtain a uniform forest of CNTs on 304 stainless steel by PECVD with a considerable percentage of amorphous carbon.

Chapter 6

Hybrid carbon-based materials supported in 304 stainless steel for supercapacitors

6.1 Introduction

Carbon-based nanostructured materials are suitable candidates for use in the manufacture of high power and high energy density storage systems (González et al. 2016). Their properties and characteristics have allowed them to become almost essential structures in the manufacture of new generation batteries and supercapacitors (Borenstein et al. 2017; Menea 2016). When manufacturing electrodes for supercapacitors, the use of carbon-based materials is not precisely because of their capacitance, since they have low volumetric capacitances (Borenstein et al. 2017), it is because they act as scaffolds to support materials with high capacitance. Basically, the researchers are looking for electrodes made of a composite material (nanostructured and three dimensional), with a high specific surface, good electrical conductivity, high chemical stability and high capacitance. Several research groups are working continuously to obtain electrodes with these characteristics. The essential contribution of carbon-based materials in the architecture described above are the three-dimensional nanoscale structure, high specific surface, good conductivity and chemical stability. For that, the use of like-carbon aerogels, activated carbons (ACs), carbon nanotubes (CNTs), graphene (Poonam et al. 2019), graphene nano walls (GNWs) (Amade et al. 2019), graphene composites and onion likecarbons (Borenstein et al. 2017) is commonly reported.

The high capacitance is provided by materials such as metal oxides. RuO_2, MnO_2, V_2O_5, Fe_3O_4, Co_3O_4, NiO and TiO_2 have been extensively investigated in the fields of electrochemical supercapacitors and hybrid devices (combining a batterytype electrode and a capacitive electrode) (Borenstein et al. 2017). We must take into account that the electrochemical performances of supercapacitors are mainly controlled by the structural and electrochemical properties of electrode materials (G. Wu et al. 2017). RuO_2 is the one with which the best capacitance results have been obtained. However, its high price and above all its toxicity relegate it to very specific applications (Borenstein et al. 2017; Shahzad Hussain, Amade, Jover, et al. 2013).

On the other hand, MnO_2 is the one who concentrates the attention of the researchers. Its low cost, low toxicity, excellent physicochemical properties, and environmental friendliness make this oxide the perfect candidate for a wide range of electrochemical applications including catalysis, biosensing, and energy storage (Pérez del Pino et al. 2017). However,

MnO_2 electrodes may suffer from limited capacity and power density due to their low conductivity. Hence, the integration of MnO_2 nanoparticles with conductive and high-surface carbonaceous materials may lead to a larger interfacial area between the MnO_2 particles and the electrolyte solution, resulting in enhanced electrochemical performance in terms of specific capacity, power and energy densities (W. Wei et al. 2011). Thus, the synergy that can be achieved between carbon-based materials and MnO_2 has led to results that were challenging less than 10 years ago. For example, some authors (Lei et al. 2019) reported that using carbon nanotubes (CNTs) randomly deposited on 316 stainless steel and coated with MnO_2 by electrodeposition, they achieved a nanocomposites with high areal capacitance of $492.5\,mF/cm^2$ ($615.6\,F/g$) at the current density of $0.5\,mA/cm_2$. They attribute this excellent electrochemical performance to the synergistic effects of high conductivity of graphenated CNTs and high pseudocapacitance of MnO_2 nanowires. On the other hand, an interesting architecture of multi-wall CNT/MnO_2 composite was designed by (L. Li et al. 2014), which was synthesized by the reduction of potassium permanganate under microwave irradiation. The electrochemical characterization of the CNT/MnO_2 (15% wt MnO_2) composite electrodes, in 1 M Na_2SO_4 aqueous solutions, shows a specific capacitance of $201\,F/g$. In this study, the CNTs were introduced together with the MnO_2 precursor. The uniformity achieved during the coating of the CNTs with MnO_2 is striking. Another approach to obtaining structures with MnO_2 and carbon-based materials is the incorporation of graphene sheets in the electrodes, as reported by (El-Kady et al. 2015). A three dimensional macroporous structure was obtained by laser reduction of graphene oxide (GO). Then, the graphene sheets were coated with MnO_2 by electrodeposition. According to their report, it was possible to obtain ultrahigh volumetric capacitance of over $1{,}100\,F/cm^3$. This corresponds to a specific capacitance of the constituent MnO_2 of $1{,}145\,F/g$, which is close to the theoretical value of $1{,}380\,F/g$. Also, hybrid structures between CNTs, graphene and MnO_2 were prepared. It is reported specific capacitance values between $236\,F/g$ (Y. Cheng et al. 2012) and $486.6\,F/g$ (Jin et al. 2013). In those works, the graphene and CNTs structures were randomly orientated. As we can see, there are several approaches that have been followed to obtain electrodes based on carbon-materials and MnO_2.

In this chapter, a new approach to produce electrodes based on carbonaceous materials and MnO_2 is presented. GNWs have been grown on vertically aligned CNTs forests using 304 stainless steel as substrate. Then MnO_2 was deposited on this hybrid structure by electrodeposition. Well-defined and homogeneously distributed oxide nanoparticles were obtained along the boundaries of GNWs. CNTs were obtained using iron nanoparticles, as catalyst material, on a nitrided diffusion barrier system. Plasma enhanced chemical vapor deposition (PECVD) was the process used to obtain CNTs, while GNWs were obtained by inductive coupled plasma–chemical vapor deposition (ICP-CVD). Furthermore, to contrast the performance of the hybrid structure CNTs/GNWs/MnO_2, manganese dioxide was deposited directly on the CNTs, thus we obtained the structure CNTs/MnO_2. We observe, by scanning electron microscope (SEM), that the carbon structure morphology strongly influences the geometry of the MnO_2 particles. In addition, the Raman spectra of the samples were obtained to know their structural fingerprint. SEM images with Raman spectra both confirmed the presence of MnO_2 on the carbon structures. In order to know the electrochemical performance of the electrodes, cyclovoltammetry (CV) and electrochemical impedance spectroscopy (EIS) were carried out. The charge/discharge test was not performed due to the instability of the electrodes during the electrochemical characterization. The instability of 304 stainless steel electrodes is discussed at the end of this chapter.

6.2 Experimental procedure

Following the process described in Chapter 5, a series of uniform CNTs forests were obtained on substrates of 9 cm^2 surface by PECVD process. As in that chapter, the substrate used was 304 stainless steel. Two approaches were used to decorate the nanostructures obtained. The first agreed to deposit manganese dioxide (MnO_2) directly on the CNTs. For that, the galvanostatic method was adopted. In this case a two electrode cell was used (Fan et al. 2008). The electrode was used as the cathode and a graphite electrode as the anode. Approximately 0.5 cm^3 of a 0.2 M $MnSO_4 \cdot H_2O$ solution was introduced drop wise through a hole in the anode during the deposition (**Figure 6.1**). The optimum conditions were found to be at a constant current of 1 $mA \cdot cm^{-2}$ (Shahzad Hussain, Amade, Jover, et al. 2013). Deposition time varied between 1 and 3 minutes. Since the as grown nanotubes obtained were highly hydrophobic, a post treatment with H_2O plasma was carried out, according with the process followed by (Shahzad Hussain, Amade, and Bertran 2014). Thus, a plasma of H_2O was generated during 60 s using an RF power supply (13.56 MHz, 75 W of power) at a pressure of 1.35 mbar. Thus, the functionalization process introduced different chemical groups containing oxygen, enhancing the wettability of the CNTs.

On the other hand, GNWs were grown on the CNTs forest. Graphene nanowalls where deposited using an inductively coupled plasma chemical vapor deposition (ICP-CVD) (13.56 MHz of frequency and 400 W of power) system, following the process reported by (Amade et al. 2019). The system consists of a long quartz tube (Vidrasa S.A., Ripollet, Spain) having a radio-frequency $\lambda/4$ resonator (homemade) with a cooper coil,

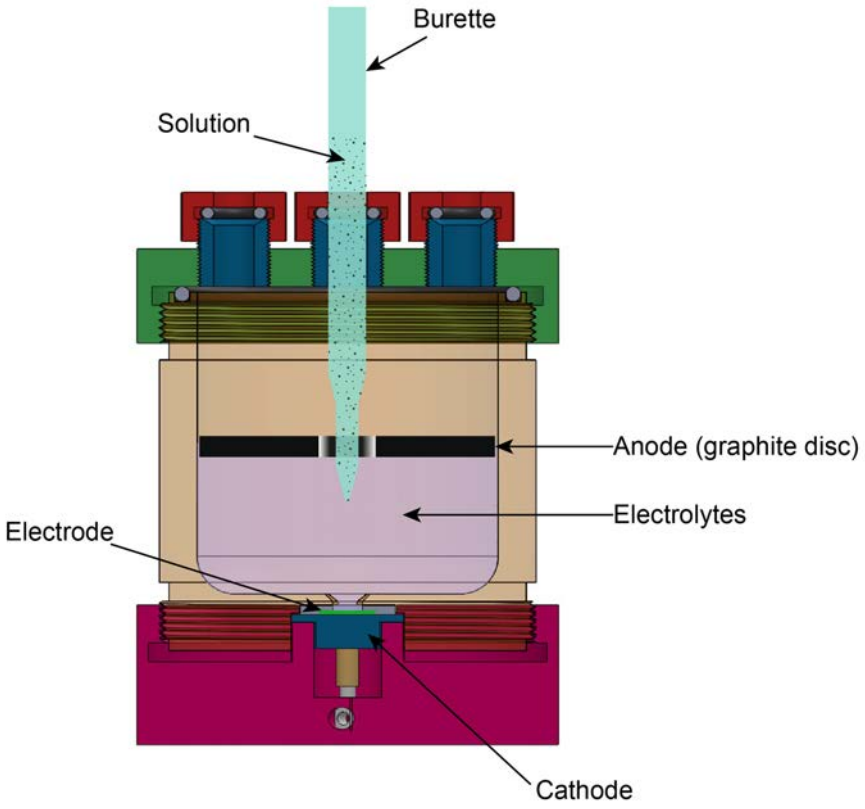

Figure 6.1: Configuration of the electrochemical cell for the electrodeposition of MnO_2

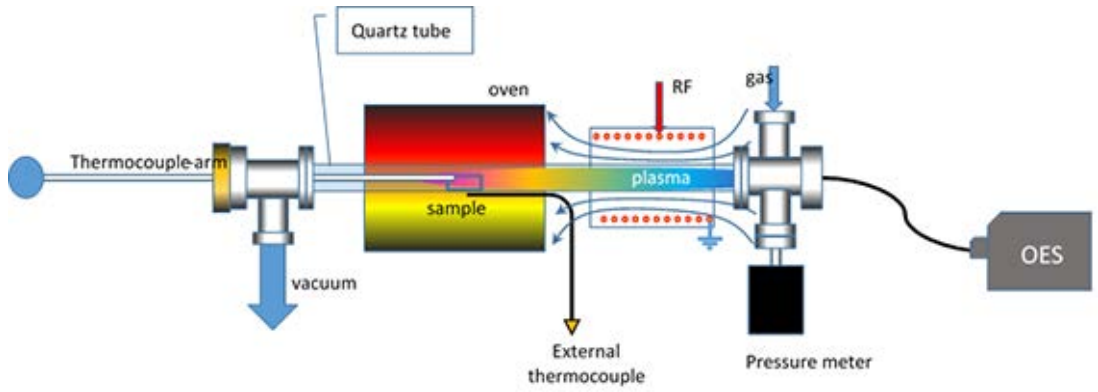

Figure 6.2: Schematic drawing of the ICP-CVD tubular reactor for producing carbon structures. The reactor is composed of a quartz tube, an oven and a coil connected to an RF power supply. The sample is placed in the middle of the oven. The system is evacuated with a primary rotatory pump and the pressure were analyzed with a pressure meter. The temperature is measured by means of two thermocouples. Different gases can be introduced through an inlet at one end of the quartz tube. OES: Optical Emission Spectroscopy device to study the emission of plasma generated species (Amade et al. 2019)

for producing remote plasma, and a tubular oven (PID Eng & Tech S.L., Madrid, Spain) working up to 1100 °C, 13 cm away from the quartz tube (**Figure 6.2**). The sample was placed inside the quartz tubular reactor, which was evacuated down to a pressure below 1 Pa and heated up to 750 °C. Then, pure methane (99.995%) was introduced as a precursor gas at one end of the quartz tube (10 sccm) and the pressure was maintained at 40 Pa. Under these conditions, plasma was ignited at an RF power of 400 W for 30 min. Lastly, the sample was cooled down to room temperature for 30 min. Like the CNTs, the GNWs are quite hydrophobic. Therefore, they were post-treated with oxygen plasma in order to become them hydrophilic. At room temperature, without breaking the vacuum, a RF plasma of O_2 (50 W of power and 0.4-0.5 mbar of pressure) was generated during 30 s. Subsequently, the hybrid carbon-based structure was also functionalized with MnO_2, following the same procedure described above.

The morphology of the nanostructures presents in the electrodes after the deposition of MnO_2, was studied by field emission scanning electron microscopy (FESEM) (FEI Nova NanoSEM 230, USA) equipped with an energy dispersive X-ray (EDX) detector.

Additionally, Raman spectroscopy was used to study the structural and chemical information of structures deposited on 304 stainless steel. HORIBA LabRam HR800 Japan system was used to perform this analysis. A green laser of wavelength 532 nm and power 0.5 mW and a 100× objective was used during the measurements.

Finally, the charge storage mechanism of the prepared electrodes was studied by means of cyclic voltammetry (CV) and electrochemical impedance spectroscopy (EIS) in a 1 M Na_2SO_4 aqueous solution using a potentiostat/galvanostat (AUTOLAB, PGSTAT30, USA). All experiments were carried out in a three electrode cell at 25 °C. An Ag/AgCl electrode (3M KCl internal solution) and a Pt-ring electrode were used as the reference and counter electrode, respectively. The materials developed for this investigation were used as the working electrode. The geometrical area of the working electrode was set to a constant value of 0.78 cm^2.

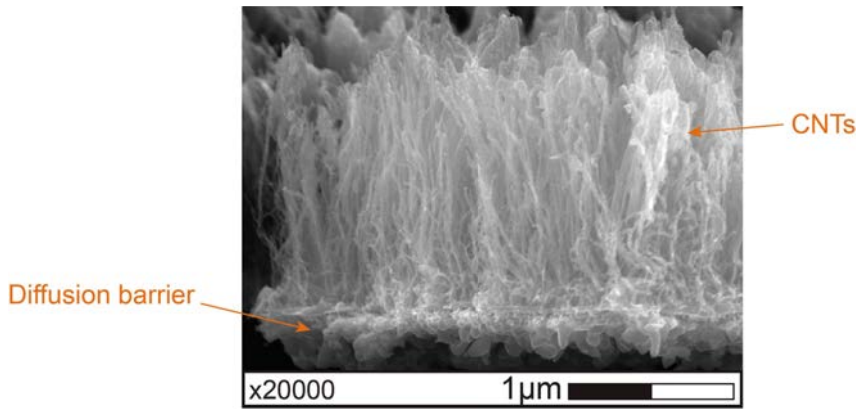

Figure 6.3: Lateral view of the CNTs, at the bottom there is a section of the nitrided layers

6.3 Results and discussion

6.3.1 Scanning electron microscope (SEM)

Figure 6.3 shows how the nanotubes are placed on the substrate. This image was obtained in the area near the cutting edge of the sample with CNTs and corresponds to a section of the nitrided layer system (diffusion barrier) that was detached from the substrate. The CNTs appear aligned vertically and unlike those shown in the previous chapters, they have higher density.

As mentioned in the previous section, GNWs were deposited on CNT forests (**Figures 6.4a-b**). The SEM images show that the hybrid structure obtained has two clearly differentiated zones (**Figures 6.4b**). The first, which acts as a support, corresponds to the vertically aligned CNTs. The second corresponds to GNWs that are attached to the top of the nanotubes. The high densities of CNTs limit their growth to that position. In addition, **Figures 6.4a** shows the dense and three-dimensional structure of GNWs, formed by randomly oriented graphene sheets. They present a catalyst-free growth, so they can be grown virtually on every substrate that withstand the synthesis temperature, around $600 - 730\,°C$. This structure presents a high specific surface, high conductivity,

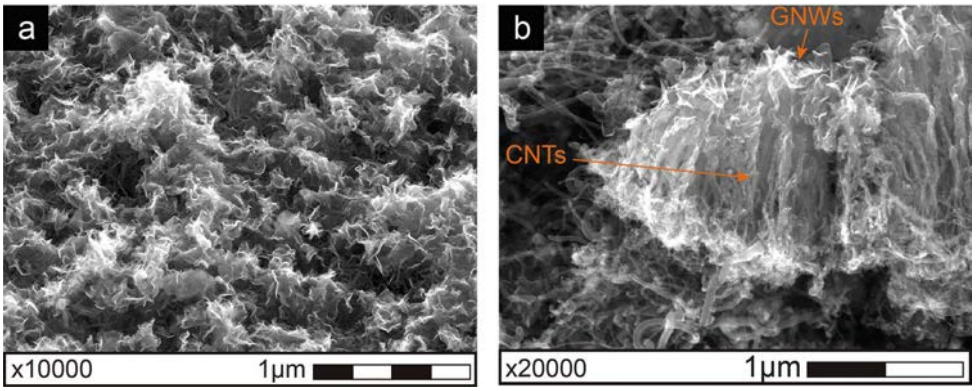

Figure 6.4: Graphene nanowalls deposited on CNTs (GNWs/CNTs structure). (a) top view of GNWs, (b) lateral view of hybrid structure

high density of reactive surface sites and a notable chemical stability, which makes GNWs an ideal candidate for supercapacitor applications (Chi et al. 2016; H. Wang et al. 2017). In fact, CNTs and GNWs are excellent materials for producing supercapacitor electrodes, mainly because both carbon-based materials can serve as a support (scaffold) for materials that have high capacitance.

In general, it could be said that the ideal architecture for supercapacitor electrodes must present nanostructurization, high specific surface, high chemical stability, high conductivity and of course high capacitance (Borenstein et al. 2017; W. Wei et al. 2011). If the selection of carbon-based support is adequate, the first four conditions are met. It is known that nanostructures such as CNTs or GNWs have high specific surface, high conductivity and chemical stability (Poonam et al. 2019). However, its capacitance, in comparison, for example, with some metallic oxides, is modest (González et al. 2016).

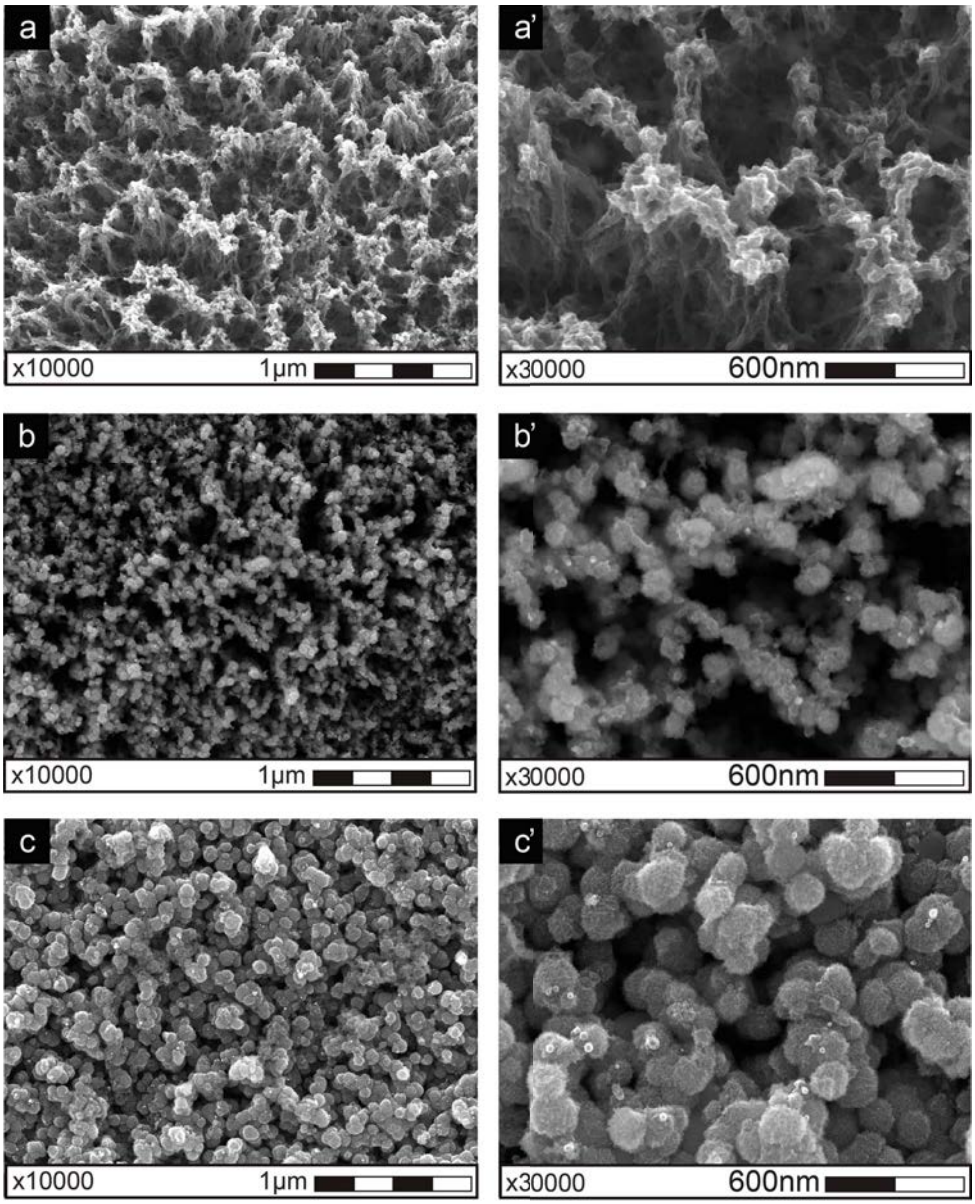

Figure 6.5: Top view of MnO_2 particles on CNTs deposited during 1 min (a, a'), 2 min (b, b'), 3 min (c, c')

The specific capacitance of carbon-based materials is greatly influenced by the purity and the morphology of the material (Pandolfo and Hollenkamp 2006). Several strategies have been reported to improve the capacitance of these nanostructures, such as producing composites with conductive polymers (Menea 2016) or doping them with nitrogen (H. Chen et al. 2013; Shahzad Hussain, Amade, H. Moreno, et al. 2014). In our case, we use another common approach to increase the capacitance of these carbon-based materials. We deposited MnO_2 by electrodeposition. This oxide presents an excellent pseudo capacitance and due to its characteristics (low-cost, abundance, environmentally friendly nature and low toxicity in comparison to other transition-metal oxides) it is widely used in the manufacture of supercapacitors (Beaudrouet et al. 2009; W. Wei et al. 2011).

The evolution of the MnO_2 particles deposited directly on the CNTs is shown in **Figure 6.5**. As deposition time increases, so does particle size. During the first minute of electrodeposition, the oxide particles were only deposited at the tips of the CNTs (**Figures 6.5a-a'**). From what we can see, they don't have a well-defined shape. These images also show that the orientation of the CNTs changed slightly. The tips of the CNTs came together and formed clusters. It is precisely in these regions that the MnO_2 particles grew. Probably, the pattern obtained in the CNTs is due to the surface tension generated when they were wet with electrolyte solution before electrodeposition. This behavior was also reported by (Fan et al. 2008). With two minutes of electrodeposition, the size of the MnO_2 particles increased (see **Figures 6.5b-b'**). The particles observed have the appearance of a sphere. These structures were also identified as a flower-like (Ni et al. 2009). In addition, particles not only grew at the tips of the CNTs, they also grew on the walls of the CNTs. This hypothesis is in agreement with that observed in **Figure 6.6**. The oxide particles grew on the walls of the peripheral CNTs of the clusters. Finally, after three minutes of electrodeposition, the manganese dioxide particles grew to diameters close to 400 nm. Those particles cover almost the entire exposed surface of the CNTs (see **Figures 6.5c-c'**). The composite material obtained between the CNTs and MnO_2 presented a threedimensional architecture. This means that the CNTs, obtained on 304 stainless steel, act as scaffolds for the oxide particles.

On the other hand, the surface of the GNWs/CNTs electrodes show a different morphology of the MnO_2 coating after the electrodeposition process (see **Figure 6.7**). After one minute of electrodeposition, well defined spherical oxide particles distributed over the whole structure were observed (see **Figures 6.7a-a'**). With two minutes of deposit, the particles maintained their shape and size, but their density increased. As can be seen in

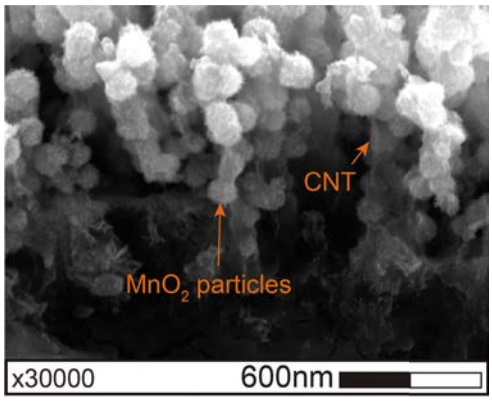

Figure 6.6: 45° view of the MnO_2 particles bonded to the walls of the CNTs

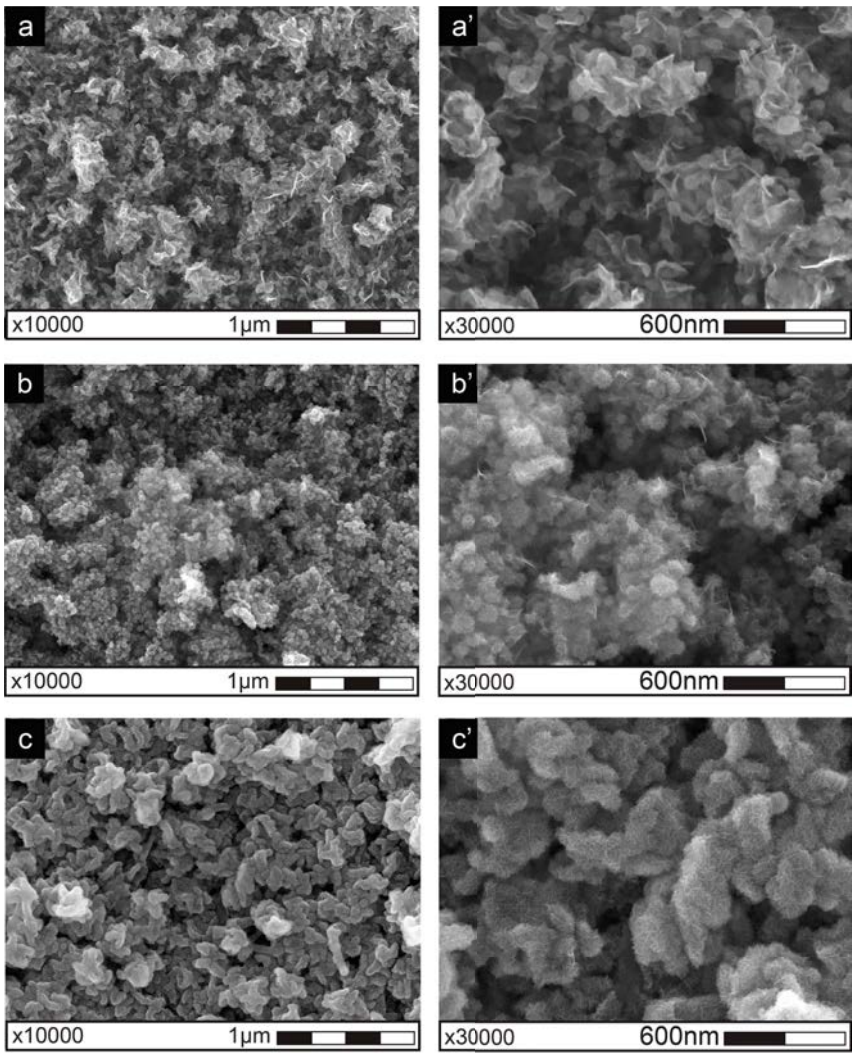

Figure 6.7: Top view of MnO_2 particles in GNWs/CNT electrodes. The electrodeposition process lasted 1 min (a, a'), 2 min (b, b'), 3 min (c, c')

Figures 6.7b-b', MnO_2 particles have a diameter of approximately 100 nm and they are quite close to each other. Eventually, after 3 minutes of electrodeposition, the graphene sheets become completely covered. In **Figures 6.7c-c'** the MnO_2 particles and the edges of the GNWs cannot be distinguished.

Figure 6.8 compares GNWs with and without MnO_2 coating. As the structure obtained with MnO_2/CNTs, the MnO_2/GNWs/CNTs structure is three-dimensional. However, the inclusion of GNWs has allowed a more uniform and smooth coating to be obtained on the surface of the graphene walls. Probably the main difference in particle/coating morphology of MnO_2 lies in the number of "defects" in the support material. These defects act as nucleation points for the MnO_2 particles. As CNTs are made up of concentric graphene tubes (MWCNTs), they have more crystalline defects at their tips. In addition, depending on the post-treatment applied to them (CNTs), there may also be defects in their external walls. But nevertheless, the GNWs have several defects per se (active edges) that promote the nucleation of manganese dioxide particles.

In order to contrast the influence of CNTs and GNWs on the morphology of oxide particles, MnO_2 was deposited directly on the surface of 304 stainless steel. The elec-

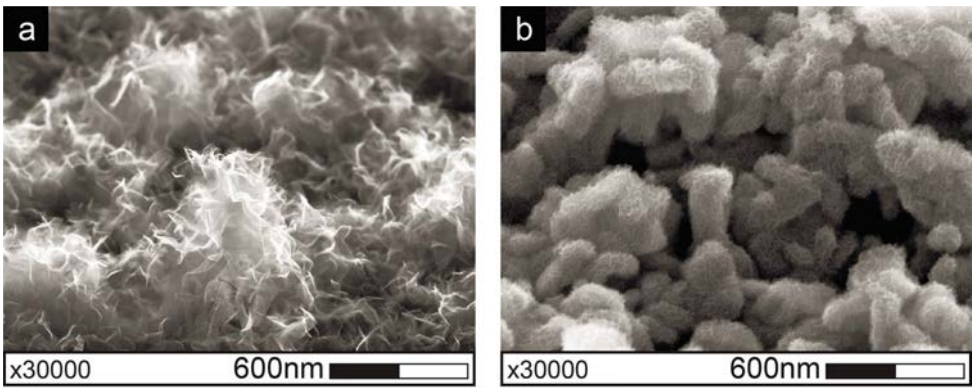

Figure 6.8: 45° view of GNWs supported by CNTs with (a) and without (b) MnO_2 coating

trodeposition process lasted 3 minutes. As can be seen in **Figure 6.9**, compared with carbon-based supports, the particle formation on the steel surface is not observed. Since the substrate had no mechanical preparation (grinding or polishing) it is observed that the MnO_2 coating follows the morphology of the surface where it was deposited. Aside from that detail, no three-dimensional structures are observed. Therefore, it can be stated that the carbon-based supports used in this study promote the formation of particles and/or coatings in three dimensions. Size and morphology are strongly related to the intrinsic properties and characteristics of each support material (specific surface, geometry, number of defects and porosity). Note that the surface of the CNTs and GNWs structures is mainly mesoporous (Borenstein et al. 2017).

For supercapacitor applications, the porosity of the electrode material is a crucial factor. With these materials an interesting synergy can be obtained in which the carbon matrix stabilizes the active nanoparticles, thus improving their charge storage capability and the latter moieties, in turn, stabilize the meso-porosity of the composite matrices, enabling us to obtain high rate capability (Borenstein et al. 2017). In our case, the integration of MnO_2 nanoparticles with conductive and high-surface carbonaceous materials produced a larger interfacial area between the MnO_2 particles and the electrolyte solution. It probably improved the electrochemical performance in terms of specific capacity, power and energy densities (W. Wei et al. 2011).

Figure 6.10 summarizes the steps followed to obtain the electrodes of this chapter.

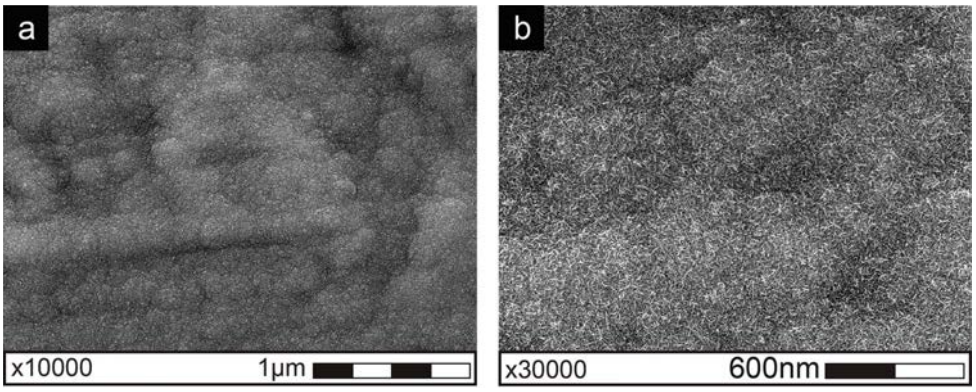

Figure 6.9: Top view of MnO_2 coating deposited directly on 304 stainless steel

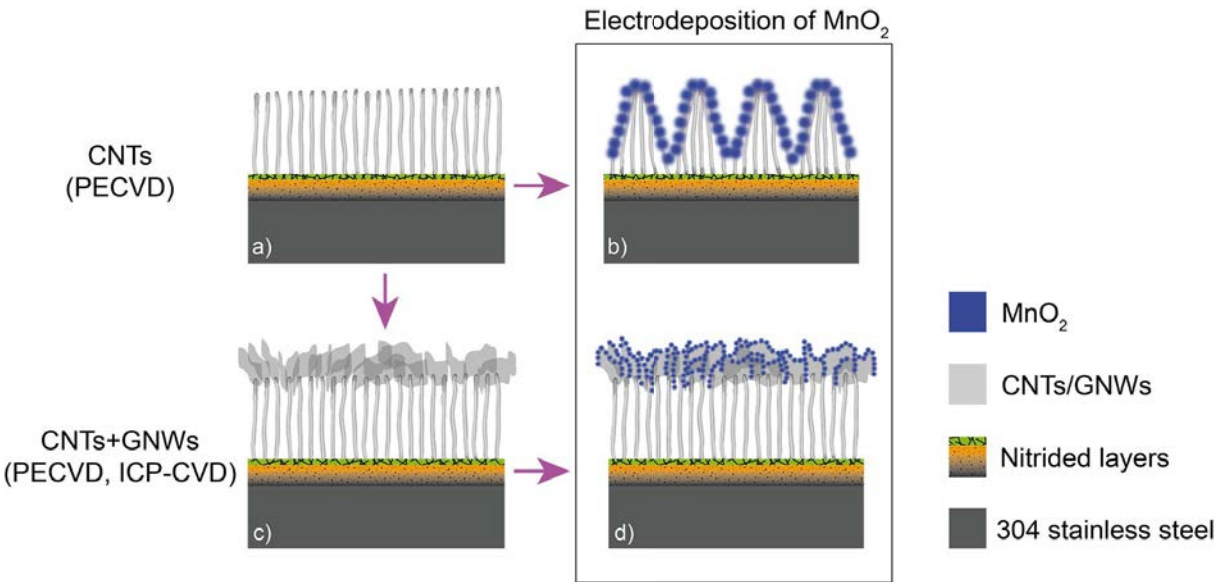

Figure 6.10: Electrode production process for supercapacitors followed in this work. (a) CNTs forest obtained by PECD, (b) MnO_2 deposited on CNTs by electrodeposition, (c) GNWs deposited by ICP-CVD on CNTs forest, (d) MnO_2 deposited on GNWs supported by CNTs

As we have already mentioned and according to the SEM images, the growth of the GNWs only takes place in the upper part of the CNTs. Despite this, it was possible to obtain threedimensional electrodes with MnO_2 coatings.

Something very important to note is that the SEM images of the MnO_2 structures were obtained in the samples after electrochemical characterization. (Shahzad Hussain, Amade, Jover, et al. 2013) compared the morphology of MnO_2 before and after electrochemical characterization. A clear change in structure was reported. However, the Mn structures obtained in this work were more similar to those reported by (Chang et al. 2008). They reported that Mn oxide, anodized under the CV condition, had the largest surface area, highest hydrous state, and lowest Mn valence state and showed the highest specific capacitance.

6.3.2 Energy dispersive X-ray analysis (EDX)

The chemical composition of the materials used was qualitatively identified by the energy dispersive X-ray detector (EDX). **Figure 6.11a** shows the typical spectrum of 304 stainless steel. All the peaks observed in the spectrum correspond to the alloying elements of that substrate. It should be noted that the untreated steel sample contained the native oxide layer. However, the peak corresponding to oxygen is not identified. This is probably due to the fact that the volume of material analyzed is approximately $1\,\mu m^3$, so the signal from the thin layer of native oxide ($\sim 2-3\,nm$) is masked.

On the other hand, the spectrum obtained from an electrode of CNTs and MnO_2 (1 minute of electrodeposition) is presented in **Figure 6.11b**. In addition to the alloying elements, it is possible to identify elements that were introduced during the electrode manufacturing process. Thus, Al forms part of the diffusion barrier system, S was surely provided by the electrolyte solution (Na_2SO_4). In addition, the peaks corresponding to Mn and O are observed. We believe that these signals correspond to the elements introduced

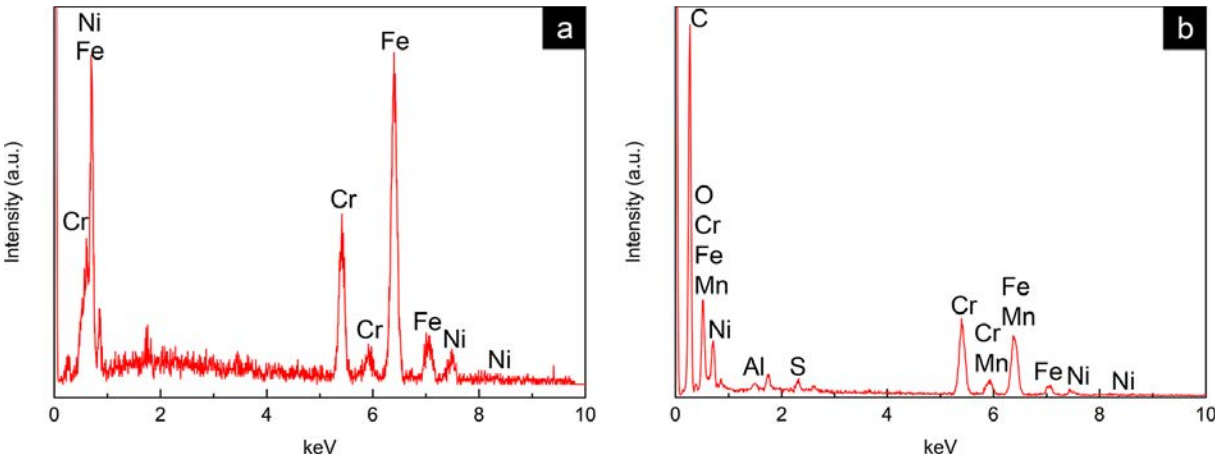

Figure 6.11: (a) EDX spectrum of 304 stainless steel, (b) EDX spectrum of electrode with carbon-based materials with MnO_2 deposited on 304 stainless steel

during the electrodeposition process. Under the conditions described herein, MnO_2 has already been obtained in our research group (Amade et al. 2019; Shahzad Hussain, Amade, Jover, et al. 2013). Besides, if we look at the C peak, it is the most intense. This probably corresponds to the signal coming from the CNTs.

6.3.3 Raman Shift Spectroscopy

Figure 6.12 shows the Raman spectra taken from samples of CNTs functionalized with MnO_2. These correspond to the samples after electrodeposition (1, 2 and 3 minutes) and after the electrochemical characterization. In addition, for reference purposes, the Raman spectrum of a sample containing only CNTs, functionalized by water plasma, has been included. In general, the spectra have the typical shape of broad D and G bands that are associated with multi-walled carbon nanotubes (MWCNTs). As already mentioned in the previous chapters, D-band ($\sim 1360\,cm^{-1}$) is related with disordered graphitic lattice and G band ($\sim 1580\,cm^{-1}$) is related with ideal graphitic lattice (Düngen et al. 2017). However, as already observed in the previous chapters, the broad peaks observed between 900 and $1800\,cm^{-1}$ hide the signal from other bands.

Following the deconvolution process presented by (Sadezky et al. 2005) it was possible to distinguish those bands. The curves used to fit the spectra, except for the A-band, were Lorentzians. A Gaussian type was used for the A band (see **Figure 6.13**). D'-band, like the D-band, is related with disordered graphitic lattice. These bands are activated by defects due to the breaking of the crystal symmetry that relax the Raman selection rules (Merlen et al. 2017). For Raman spectra of CNTs and MnO_2, this band is between 1616 and $1620\,cm^{-1}$ (see **Table6.1**).

In addition, considering the less intense bands, the D" band is present in the shoulder of the D band. It is a typical band of very defective samples (Merlen et al. 2017). In literature, this band is also denoted as D4 (Düngen et al. 2017; Sadezky et al. 2005). The samples of CNTs and MnO_2 present this band between 1214 and $1237\,cm^{-1}$. According with (Venezuela et al. 2011), it is mainly due to phonons associated to the KΓ direction in the Brillouin zone. As this band is related with very defective samples, (Couzi et al. 2016) determined the behavior of the D"band, by means the identification of two new bands (D*

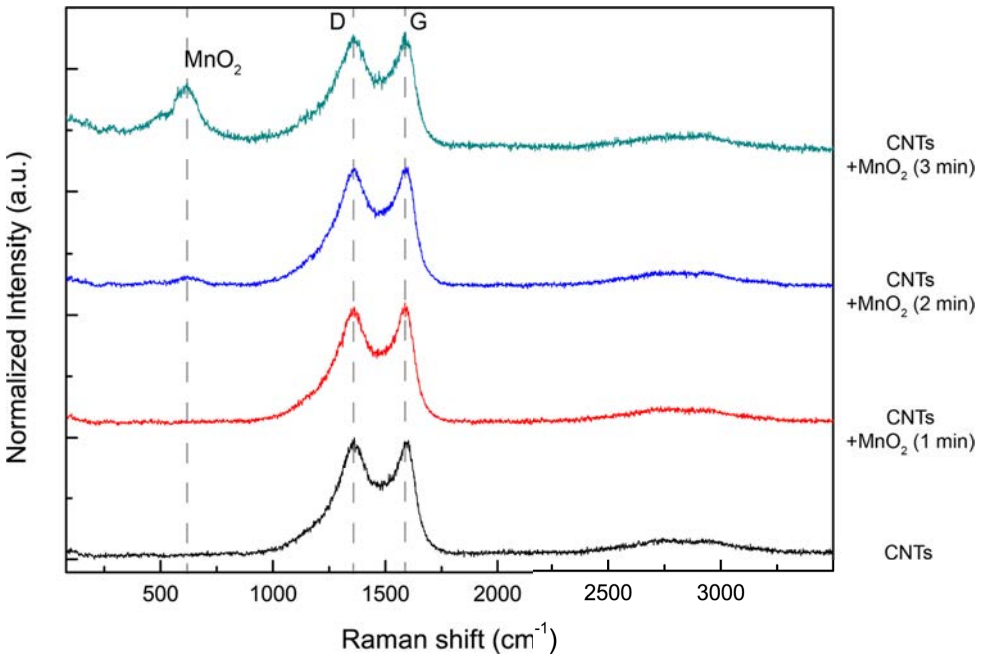

Figure 6.12: Raman spectra of MnO_2 deposited on CNTs by electrodeposition

and D**) lying close to the D"band on defective aromatic carbons (graphite nanoplatelets, heat treated glassy carbons, pyrograph nanofilaments, and multiwall nanotubes). Note that the D*, D**, and D" bands overlap, creating the wellknown D"-band often used to fit Raman spectra of soots (Merlen et al. 2017). In our case, for carbon nanotubes, the line shape of the D" mode is significantly broadened due to contributions from different tubes in or close to resonance with the excitation laser (Herziger et al. 2014). Note that the Raman intensity of the defect-induced lines (e.g., D, D', and D" bands) is proportional

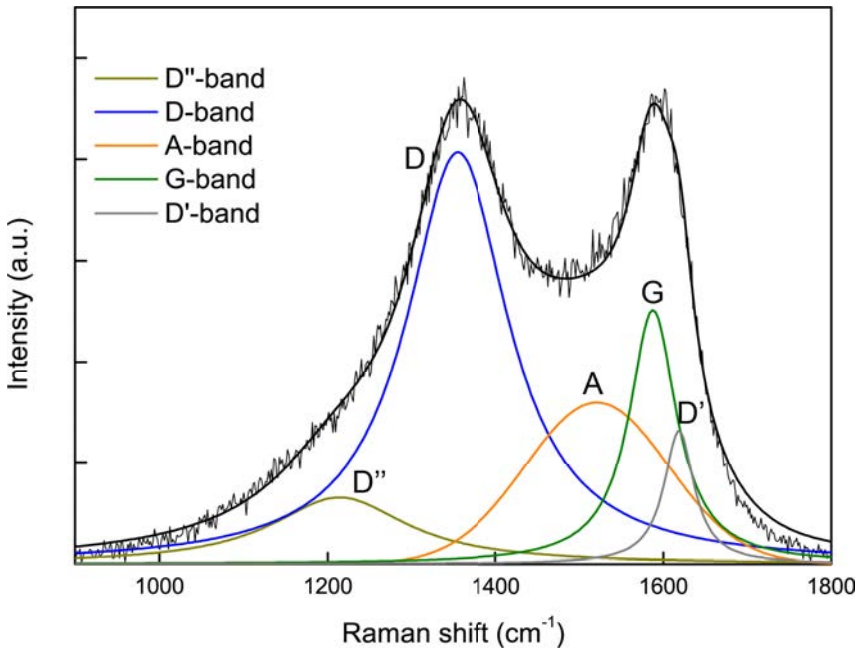

Figure 6.13: D and G band deconvolution for CNTs obtained by PECVD

		D"	D	A	G	D'	I_D/I_G	$I_D/I_{D'}$
CNTs	Position (cm^{-1})	1214.00 ± 7.72	1354.55 ± 0.94	1521.01 ± 7.88	1587.76 ± 2.32	1618.75 ± 1.88	1.62	3.07
	Intensity (a.u.)	1.32 ± 0.03	8.14 ± 0.16	3.21 ± 0.06	5.03 ± 0.10	2.65 ± 0.05		
	FWHM (cm^{-1})	196.29 ± 16.16	148.47 ± 5.13	201.31 ± 8.56	68.64 ± 6.16	43.44 ± 6.24		
$CNTs+MnO_2$ (1 min)	Position (cm^{-1})	1224.36 ± 7.32	1356.62 ± 0.77	1529.35 ± 4.67	1585.01 ± 2.05	1616.40 ± 2.28	1.67	3.16
	Intensity (a.u.)	1.62 ± 0.03	9.38 ± 0.19	4.03 ± 0.08	5.61 ± 0.11	2.97 ± 0.06		
	FWHM (cm^{-1})	203.86 ± 13.80	153.35 ± 4.55	156.38 ± 8.36	62.67 ± 4.96	48.04 ± 7.44		
$CNTs+MnO_2$ (2 min)	Position (cm^{-1})	1237.11 ± 6.24	1358.10 ± 0.76	1532.13 ± 4.17	1584.11 ± 1.71	1616.10 ± 1.30	1.94	2.48
	Intensity (a.u.)	2.39 ± 0.05	11.17 ± 0.22	5.27 ± 0.11	5.75 ± 0.12	4.51 ± 0.09		
	FWHM (cm^{-1})	195.23 ± 10.88	146.74 ± 4.69	179.78 ± 5.31	59.28 ± 5.16	43.76 ± 4.26		
$CNTs+MnO_2$ (3 min)	Position (cm^{-1})	1210.65 ± 17.03	1359.51 ± 1.09	1539.61 ± 7.09	1587.09 ± 3.03	1620.12 ± 2.79	1.80	2.78
	Intensity (a.u.)	1.28 ± 0.03	5.78 ± 0.12	2.32 ± 0.05	3.22 ± 0.06	2.08 ± 0.04		
	FWHM (cm^{-1})	355.43 ± 22.58	167.90 ± 6.70	156.49 ± 11.29	65.28 ± 7.67	50.11 ± 9.82		

Table 6.1: Raman feature of CNTs obtained by PECVD and decorated with MnO_2

to the average number of defects in the material (Venezuela et al. 2011). Thus, the ratio between the intensities of the D (I_D) and G (I_G) bands is a useful indicator of disordered graphitic lattice. As the I_D/I_G ratio decreases, so does the number of structural defects present in the CNTs (Shahzad Hussain, Amade, and Bertran 2014).

For CNTs and MnO_2 samples, there is no clear trend in the values of I_D/I_G ratio. The small increase in its value is perhaps more related to the characteristics of the CNTs on the substrate than to the addition of MnO_2. It should be remembered that the forests of CNTs were obtained on stainless steel, which influences the characteristics and morphology of the CNTs, even with the diffusion barrier system.

A-band in **Figure 6.13** is related to amorphous carbon (Düngen et al. 2017). It is also denoted as D3 (Sadezky et al. 2005). For "pure" amorphous carbons, the Raman spectra can be seen as simpler, because only a broad asymmetric band is seen close to 1500 cm^{-1}. However, this is incorrect, and for several reasons. First, many different kinds of amorphous carbon exist: sp^2 dominated ones (a−C), sp^3 dominated ones (ta−C, referring to tetrahedral amorphous carbon), one containing heteroatoms such as H (a−C:H, ta−C:H, an others) or N. Their structure and properties are related but widely varying. Second, as there is some aromatic carbon embedded in their structure, some resonance occurs (Merlen et al. 2017). In our case, with the deconvolution process, it was determined that all MnO_2/CNTs samples had amorphous carbon. However, A-band does not discriminate the type of amorphous carbon. Although there is a way to do it. This was demonstrated by (Pardanaud et al. 2014), who related the shift and width (FWHM) of the G band with the type of amorphous carbon. We have plotted the data obtained for our samples in **Figure 6.14**. According to this Figure, the amorphous carbon present in our samples correspond to nanocrystalline graphite (nc-G).

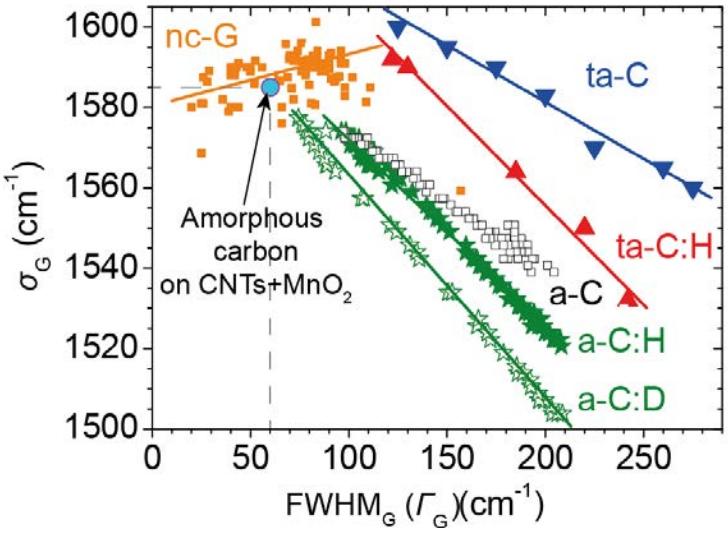

Figure 6.14: Plots of σG vs. ΓG for nc-G and different amorphous carbons. Data were recorded with λ_L=514 nm. Adapted from (Merlen et al. 2017)

If one uses FWHM_G (ΓG) as an indicator of local disorder close to sp^2 bonds in the material (which can be related to the size of the clusters and/or to the sp^3 content close to sp^2 bonds, one can use this parameter in order to have an idea of where is the sample situated in Ferrari's "three stage model". With this in mind, nc-G is more ordered than aC:H/D which are themselves more ordered than ta−C:H and ta−C. The presence of hydrogen systematically diminishes the shift of the G band (for ta−C/ta−C:H and a−C/ta−C:H) (Merlen et al. 2017).

So far, the results inherent to the CNTs have been presented and discussed. However, nothing has been said about the evolution of the observed peaks between 200 and 800 cm^{-1}. **Figure 6.15** shows that the Raman spectra for the sample of CNTs and

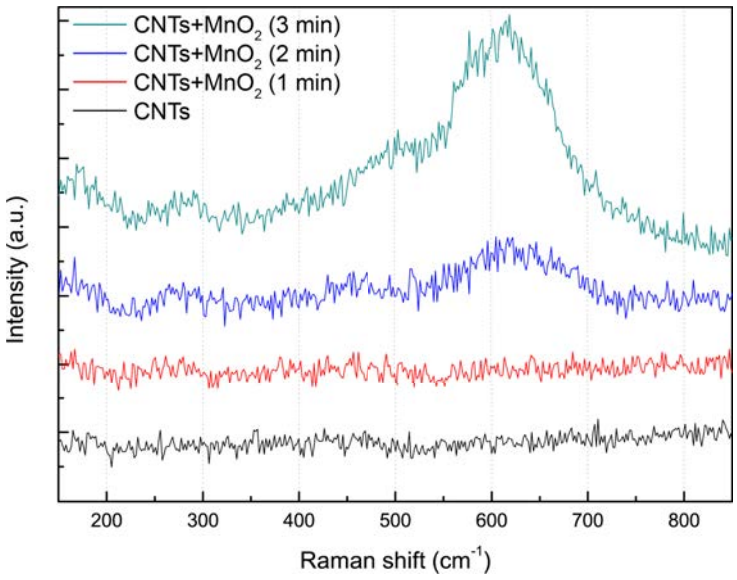

Figure 6.15: Raman spectra detail of MnO_2 deposited on CNTs by electrodeposition

$CNTs/MnO_2$, with 1 min of electrodeposition, are quite similar. In fact, there are no changes that can be reported. The small amount of manganese dioxide deposited during 1 min did not generate any Raman signatures. On the other hand, changes were observed in the Raman spectra corresponding to the samples with the highest amount of MnO_2 (deposited in 2 and 3 min). According to the SEM images presented in the previous section, these changes can be attributed to the presence of MnO_2 in the samples.

The peaks observed in the range $200-500\,cm^{-1}$ are assigned to distortion of Mn−O−Mn chains in MnO_2 octahedral lattices, while peaks in the range $500-650\,cm^{-1}$ are characteristic of Mn−O vibration in the basal plane of MnO_6 groups (Julien et al. 2003). MnO_2 Raman spectrum consists of three main distinguished peaks at 523, 576, and $650\,cm^{-1}$ and three smaller peaks, not always detected, at 392, 490, and $776\,cm^{-1}$ (Bernard 1993). In our case we can observe a broad peak at $\sim 620\,cm^{-1}$. In addition, in the spectrum of the sample with the greatest amount of manganese oxide, a shoulder at $\sim 500\,cm^{-1}$ is observed at that peak. There is also a small peak, nearly undetectable, around $280\,cm^{-1}$.

(Shahzad Hussain, Amade, Jover, et al. 2013) reported that after the electrochemical characterization process (with 2000 charge discharge cycles, in the range of 0 to 1 V), an intense and narrow peak emerged at $640\,cm^{-1}$ in the Raman spectrum. They assumed that dissolution of manganese species from the electrode in the solution and a slow phase transformation process from MnO_2 to Mn_3O_4 takes place during the constant current charge/discharge cycling owing to the irreversible redox reactions that occur in the region around 0 V. This hypothesis was supported by the chemical and morphological study of manganese before and after electrodeposition.

In the present study, the same electrodeposition process followed by (Shahzad Hussain, Amade, Jover, et al. 2013) was employed. However, the main difference is that charge/discharge electrochemical characterization could not be performed. The primary reason for this was that the electrodes under study were unstable. Only the studies of cyclovoltammetry and impedance were performed. This probably explains the gap of $20\,cm^{-1}$ between the highest intensity peaks obtained by (Shahzad Hussain, Amade,

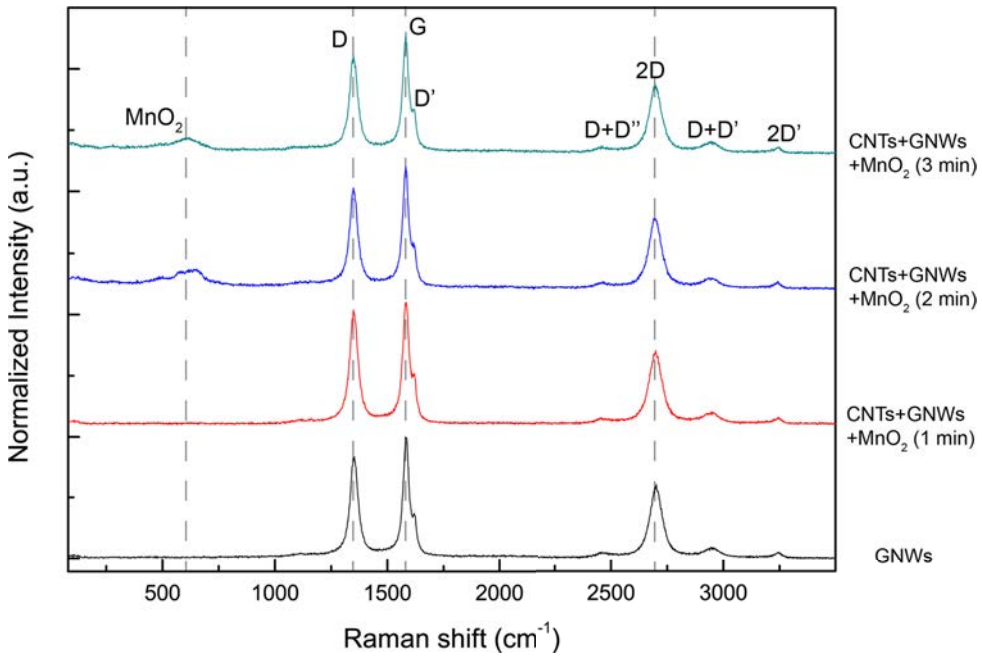

Figure 6.16: Raman spectra of MnO_2 deposited on GNWs supported by CNTs

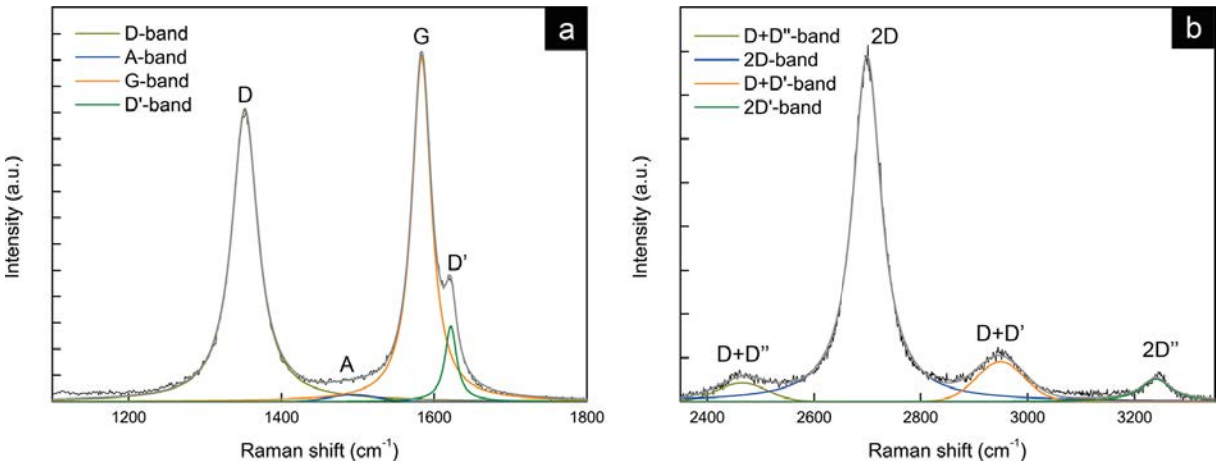

Figure 6.17: D and G band (a) and 2D band (b) deconvolution for GNWs supported by CNTs

Jover, et al. 2013) and the one shown in **Figure 6.15**. Since the time of use of the electrodes in the electrochemical characterization was shorter, the phase transformation from MnO_2 to Mn_3O_4 was not completed. This is consistent with what is observed in our SEM images. Only MnO_2 particles flower-like were observed. On the other hand, (Shahzad Hussain, Amade, Jover, et al. 2013) reported an evident change in morphology: from flower-like to needle-like shapes. The Raman spectra of the MnO_2 on GNWs supported by CNTs, in **Figure 6.16**, change considerably with respect to those observed in **Figure 6.12**. One of these differences is that the peaks between 900 and 1800 cm^{-1} are sharper. The deconvolution of the spectrum in that range was performed with four curves, three Lorentzians (D, G and D' bands) and one Gaussian (A band). It should be noted that band D" was not identified in the Raman signature of the hybrid material (see **Figure 6.17a**). This fact allows us to say that samples containing GNWs had fewer defects than CNT samples. In fact, the other peaks related with disordered graphitic lattice (D and D' band) decrease with respect to the intensity of the G band. The values of intensity, shift and width (FWHM) of the identified bands are provided in **Table6.2**. As mentioned before, the ratio between the intensities of the D (I_D) and G (I_G) bands is a useful indicator of disordered graphitic lattice.

For samples with CNTs/GNWs/MnO_2 the average value of the ratio I_D/I_G is 0.87, which if compared for samples of CNTs/MnO_2 (average value $I_D/I_G = 1.76$) is lower. The difference is considerable and is most likely due to the different amount of amorphous carbon present in the CNTs/MnO_2 samples. It seems that the PECVD process produced a higher amount of amorphous carbon (n-cG type) than the ICP-CVD process. This is demonstrated by A-band (related to amorphous carbon). **Table6.2** shows the parameters of A-band for CNTs/GNWs/MnO_2. It can be said that CNTs/MnO_2 samples present a greater disorder than CNTs/GNWs/MnO_2 samples. The disorder of the materials is directly related to the defects of the material (e.g. vacancies and boundaries). The $I_D/I_{D'}$ ratio is useful to know which type of defect is predominant in the materials. (Eckmann et al. 2012) showed for graphene that the $I_D/I_{D'}$ is very effective to discriminate between different kinds of defects: $I_D/I_{D'} = 3.5$, the minimum value, is found for boundaries, whereas $I_D/I_{D'}$ is close to 7 for vacancy like defects and up to 13 for sp^3 defects. The $I_D/I_{D'}$ ratio is interesting because, according to the resonance Raman theory, it is not sensitive to the number of defects but only to the type of defects (Merlen et al. 2017).

		D	A	G	D'	2D	I_D/I_G	$I_D/I_{D'}$	I_{2D}/I_G
GNWs	Position (cm^{-1})	1352.21 ± 0.07	1493.95 ± 3.85	1583.68 ± 0.06	1621.80 ± 0.20	2700.15 ± 0.09	0.85	3.85	0.60
	Intensity (a.u.)	22.19 ± 0.44	0.52 ± 0.01	26.21 ± 0.52	5.76 ± 0.12	15.78 ± 0.47			
	FWHM (cm^{-1})	41.20 ± 0.21	71.21 ± 9.78	30.53 ± 0.22	18.40 ± 0.67	64.54 ± 0.25			
CNTs+GNWs +MnO_2 (1 min)	Position (cm^{-1})	1351.08 ± 0.08	1486.96 ± 4.35	1582.96 ± 0.08	1620.61 ± 0.21	2697.78 ± 0.10	0.94	3.79	0.60
	Intensity (a.u.)	20.91 ± 0.42	0.37 ± 0.01	22.33 ± 0.45	5.52 ± 0.11	13.46 ± 0.40			
	FWHM (cm^{-1})	43.04 ± 0.23	52.17 ± 10.53	33.50 ± 0.25	18.08 ± 0.70	68.28 ± 0.29			
CNTs+GNWs +MnO_2 (2 min)	Position (cm^{-1})	1350.16 ± 0.14	1496.67 ± 7.41	1581.79 ± 0.12	1619.86 ± 0.39	2696.17 ± 0.10	0.84	3.87	0.62
	Intensity (a.u.)	16.76 ± 0.34	0.46 ± 0.01	20.07 ± 0.40	4.33 ± 0.09	12.37 ± 0.37			
	FWHM (cm^{-1})	44.19 ± 0.41	83.20 ± 19.29	31.65 ± 0.46	19.93 ± 1.34	66.51 ± 0.29			
CNTs+GNWs +MnO_2 (3 min)	Position (cm^{-1})	1349.99 ± 0.13	1493.71 ± 5.38	1581.84 ± 0.11	1620.01 ± 0.33	2697.37 ± 0.10	0.85	3.75	0.61
	Intensity (a.u.)	16.27 ± 0.33	0.47 ± 0.01	19.22 ± 0.38	4.34 ± 0.09	11.79 ± 0.35			
	FWHM (cm^{-1})	44.61 ± 0.37	73.47 ± 13.83	32.14 ± 0.40	18.92 ± 1.12	66.76 ± 0.30			

Table 6.2: Raman feature of GNWs supported by CNTs and decorated with MnO_2

The average value of $I_D/I_{D'}$ ratio for CNTs/GNWs/MnO_2 samples is 3.81. Therefore, according to (Eckmann et al. 2012), it can be said that the defects that prevail in these samples are boundaries type. This makes sense, since in the SEM images it was observed that the GNWs, supported by CNTs, had a large number of edges (nanowalls), which also acted as nucleation points for the MnO_2 particles. On the other hand, the average value of $I_D/I_{D'} = 2.87$ of CNTs/MnO_2 samples is below the minimum value determined by Eckmann et al. for graphene. This may be influenced by the fact that the Raman fingerprint of the material, in the range $900 - 1800\,cm^{-1}$, was strongly affected by the amorphous carbon (nanocrystalline graphite). In between amorphous materials and perfect crystals, defects play a role in the disturbed Raman scattering process (Merlen et al. 2017). Note that the borders of the crystallites work as defects involved in the double-resonance process, giving rise to the D and D' bands in the Raman spectra of nanographites (Cançado et al. 2007).

Another difference that can be observed between the Raman spectra of CNTs/MnO_2 and CNTs/GNWs/MnO_2 are the peaks in the range $2350-3300\,cm^{-1}$ (see **Figure 6.17b**). Those peaks represent the signature of the multi-layer graphene (A. C. Ferrari et al. 2006). The most intense peak corresponds to the 2D-band. This band is due to TO phonons around the K point in the Brillouin zone, and it is active due to the double resonance mechanism (Reich and Thomsen 2004). It must be taken into account that for the $D-$ band, a phonon and a defect are involved. For the 2D-band, only two phonons (without defect) are necessary. This explains why the 2D-band is always visible, even for defect free samples (Merlen et al. 2017). As it has different electronic structures close to the K point, and because the double resonance mechanism connects phonons to the electronic structure, the shift, shape (composed of several overlapped bands), and intensity of the 2- band(s) can be used to distinguish from monolayer up to 5–10 stacked layers. The relative intensity ratio between the 2D and G bands was also found to be

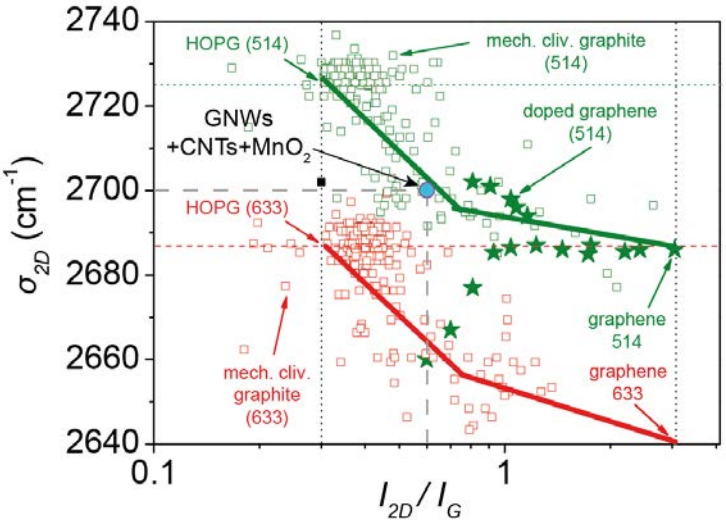

Figure 6.18: 2D band shift as a function of I_{2D}/I_G for laser wavelengths of 514 and 633 nm. Adapted from (Merlen et al. 2017)

dependent on the number of layers: I_{2D}/I_G is close to 3 for monolayer graphene, and falls down to 0.3 for highly oriented pyrolytic graphite (HOPG). The Raman plot σ2D versus I_{2D}/I_G (see **Figure 6.18**) can be used to rapidly have an idea of the quality of the graphene samples handled (Merlen et al. 2017).

For our samples, the average value of I_{2D}/I_G is 0.61 and the shift of the G-band is around 2700 cm^{-1}. By plotting these data in **Figure 6.18**, it can be seen that the CNTs/GNWs/MnO_2 samples are between the structure of the HOPG and the monolayer graphene. These results are consistent with the results previously presented in our research group. In the paper of (Amade et al. 2019), it was reported that the nano walls have few nanometer thick (around 10 graphene layers).

To continue the discussion of the Raman spectra, in **Figure 6.17b** it is also possible to distinguish three weak bands that are close to 2D-band. In the literature these 2D subbands are denominated D+D", D+D' and 2D' and are found at $\sim$ 2460, $\sim$ 2940 and $\sim$ 3230 cm^{-1}, respectively (Merlen et al. 2017). It is worth mentioning that for spectrum fitting in the range 2350$-$3300 cm^{-1}, two Lorentzian (2D and 2D' band) and two Gaussian (D+D", D+D' band) curves were used. Today, the number and origin of the 2D sub-bands have been understood for multilayer graphene (A. C. Ferrari et al. 2006) in the framework of the double resonance mechanism and more complex things can occur such as folding (Podila et al. 2012), misorientation (Poncharal et al. 2008), and stacking faults that can modify the intensities and shape (Merlen et al. 2017). The presence of these 2D sub-bands confirms the structure of the hybrid material that has been obtained in this work: the CNTs support GNWs that are composed of few folded layers of graphene and whose orientation and distribution is random.

If the values of FWHM are reviewed for both CNTs/MnO_2 and CNTs/GNWs/MnO_2 samples (see **Table6.1** and **Table6.2**), it can be seen that there is some variation in their values. This can be attributed to the crystalline quality of the carbon structures. Because of defects implied in this model, Raman spectroscopy can be used to characterize how a graphenic material is far from its crystalline state (Merlen et al. 2017). The values of crystallite size (L_a) for the CNTs/MnO_2 samples is less than that of the CNTs/GNWs/MnO_2 samples. This can be seen graphically in **Figure 6.19**. We have plotted the values of ΓD

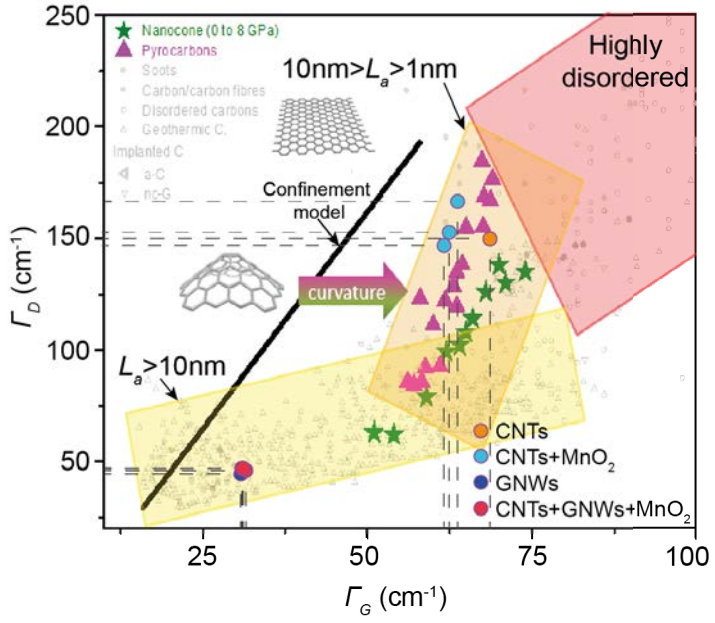

Figure 6.19: ΓD vs. ΓG plot for a large variety of disordered aromatic carbons (Merlen et al. 2017)

and ΓG on chart prepared by (Merlen et al. 2017). In this chart the FWHM values of the D and G bands are related. Depending on the characteristic size of the aromatic domain, the data are grouped in three different areas: the lowest rectangle with La higher than roughly 10 nm, the intermediate region with L_a in the range of few to 10 nm, and the higher one with La close to 1 nm. For CNTs/MnO_2 sample L_a is in the range of $1-10$ nm and for CNTs/GNWs/MnO_2 sample $L_a > 10$ nm. This makes sense, the CNTs/MnO_2 samples, which have more amorphous carbon and therefore more defects, have a smaller

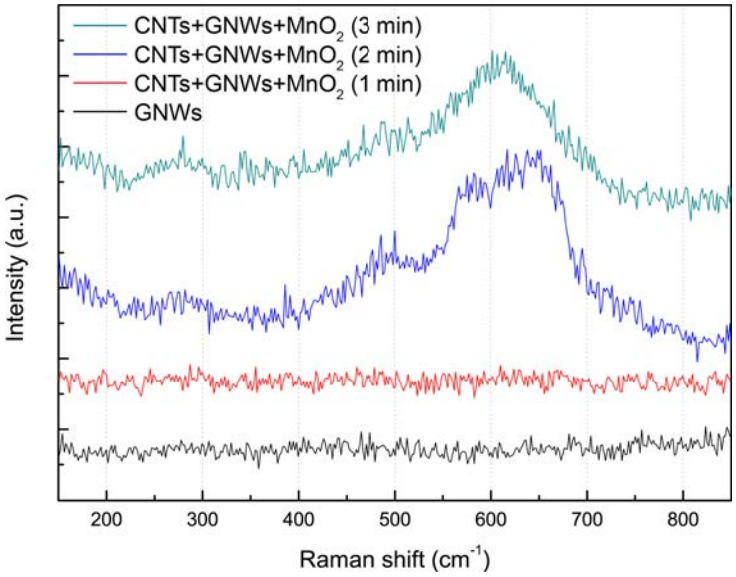

Figure 6.20: Raman spectra detail of MnO_2 deposited by electrodeposition on GNWs/CNTs

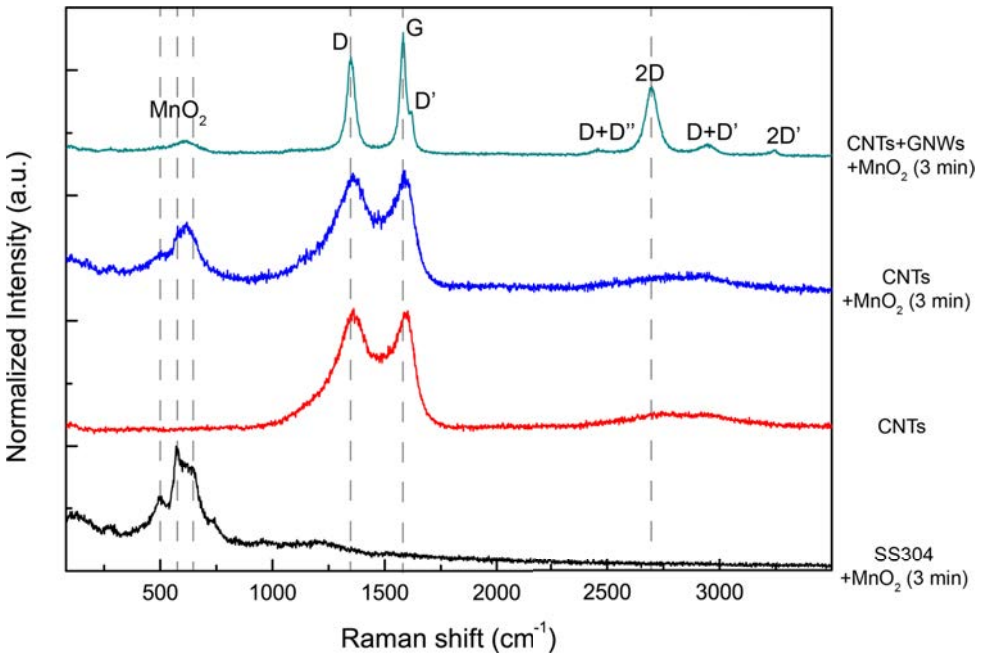

Figure 6.21: Raman spectra comparison

crystal size than that CNTs/GNWs/MnO_2 sample, which have less amorphous carbon. Besides, this is in accordance with the established by the I_D/I_G ratio, the CNTs/MnO_2 samples have a greater degree of disorder than the CNTs/GNWs/MnO_2 samples.

With respect to the influence of MnO_2 on the Raman spectra of the MnO_2/GNWs/CNTs samples, a behavior similar to that of the MnO_2/CNTs samples was observed. In **Figure 6.20**, the oxide free sample has a spectrum identical to that of the sample obtained after one minute of electrodeposition. In the spectra of the samples that had oxide deposited for 2 min and 3 min, MnO_2 peaks appear in the range of $200 - 800\,cm^{-1}$. Like the MnO_2/CNTs samples, the charge/discharge electrochemical characterization was not performed due to the instability of the electrodes. So, the shift and shape of the peaks can be attributed to an incomplete transformation from MnO_2 to Mn_3O_4 (Shahzad Hussain, Amade, Jover, et al. 2013). In addition, we presume that the intensity of the peaks attributed to the MnO_2 is related with the size of the particles deposited during electrodeposition. In the samples containing GNWs there were more defects (borders) for the nucleation of the particles. Thus, the diameter of the MnO_2 particles obtained during 2 and 3 min was quite similar (~ 100 nm). The only thing that changed between the two samples was the particle density. If we compare this with the Raman spectrum of the MnO_2/CNTs samples, where the particle size increased with the electrodeposition time, we can see that the intensity of the peaks in the range $200 - 800\,cm^{-1}$ effectively depends on the size of the MnO_2 particles. This hypothesis is consistent with the SEM images. As the MnO_2 particles become bigger, so is the intensity of the MnO_2 peak in the Raman spectra.

To finish this section, **Figure 6.21** is included, which compares the Raman spectrum of the CNTs, MnO_2/CNTs and MnO_2/GNWs/CNTs samples. In addition, the Raman spectrum of the 304 stainless steel sample coated with MnO_2 has been included. All spectra belong to the samples that were coated with manganese dioxide by electrodeposition during 3 minutes. With the exception of the sample of CNTs, which is used as a reference. The Raman fingerprints of each sample are conclusive. This characterization technique

allowed to discriminate in detail the characteristics of the samples. The presence of amorphous carbon in the CNTs gives a specific fingerprint to these spectrums, with broad D and G bands. On the other hand, the low amount of amorphous carbon in the GNWs produced a spectrum with sharp and intense D and G bands, which also present the 2D band, characteristic of multilayer graphene. Finally, the Raman spectrum of MnO_2 on 304 stainless steel confirms the versatility of this technique to distinguish between materials that are different from carbon-based materials.

6.3.4 Electrochemical characterization

As previously mentioned, a three-electrode cell configuration was used with Ag/AgCl as the reference electrode, a Pt ring as the counter electrode and the carbon-based nanostructured samples as the working electrode. Bare MnO_2 electrodeposited on SS substrate during 3 minutes and bare CNTs were also analyzed for comparison. All measurements were performed in a 1 M Na_2SO_4 aqueous solution at room temperature.

The average areal capacitance of the samples was obtained from the cyclic voltammograms according to the following equation:

$$C = \frac{q_a + |q_c|}{2A\Delta V} \tag{6.1}$$

where C is the areal capacitance in $mF \cdot cm^{-2}$, q_a and q_c are the anodic and cathodic charges in mC, respectively. A is the geometric area of the electrode in cm^2 and ΔV the applied voltage window in V.

The cyclic voltammograms of the samples present typical rectangular shapes characteristic of a capacitive behavior. Overlapped with the rectangular shape two redox peaks appear for the CNTs samples with 1 and 2 minutes of MnO_2 deposition, which almost disappear after 3 minutes deposition of manganese dioxide (**Figure 6.22**). These peaks are presumably related with the fact that Fe catalyst is present on the tips of the

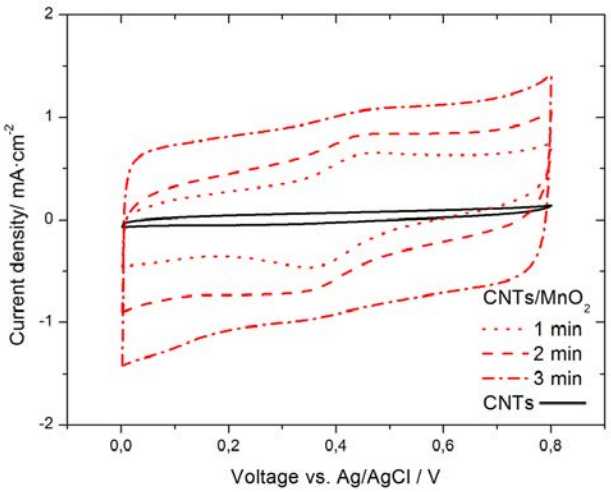

Figure 6.22: Cyclic voltammograms of CNTs and CNTs/MnO_2 nanocomposites with MnO_2 electrodeposited during 1,2 and 3 minutes. Scan rate: $50\,mV \cdot s^{-1}$

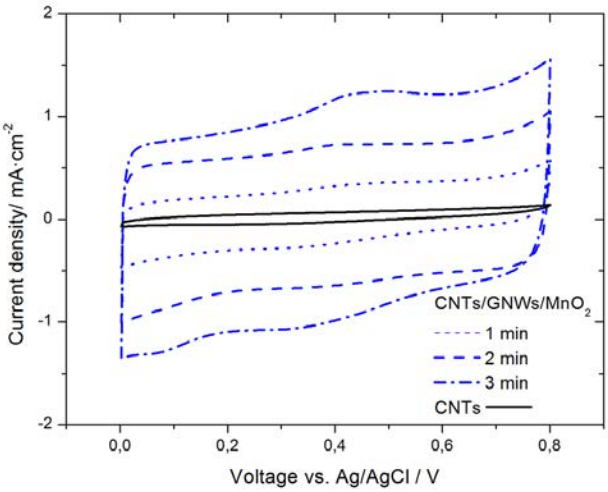

Figure 6.23: Cyclic voltammograms of CNTs and CNTs/GNWs/MnO_2 nanocomposites with MnO_2 electrodeposited during 1,2 and 3 minutes. Scan rate: $50\,\mathrm{mV}\cdot\mathrm{s}^{-1}$

CNTs, which, at short deposition times, might not be covered with manganese dioxide and thus, exposed to the electrolyte. Alternatively, the redox peaks might also be due to oxidation/reduction processes of Fe from the SS substrate. Cyclic voltammograms of CNTs/GNWs/MnO_2 samples also present the typical rectangular shape (**Figure 6.23**).

In this case, no redox peaks due to Fe are expected, since no catalyst has been used during the process, and the density of GNWs is such, that the electrolyte does not reach the substrate. Clearly, the capacitance increases with deposition time for both CNTs

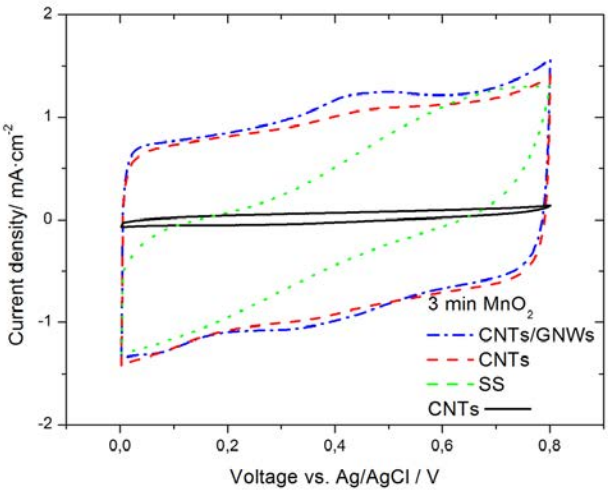

Figure 6.24: Cyclic voltammograms of CNTs, CNTs/GNWs/MnO_2, CNTs/MnO_2 and MnO_2 electrodeposited during 3 minutes. Scan rate: $50\,\mathrm{mV}\cdot\mathrm{s}^{-1}$

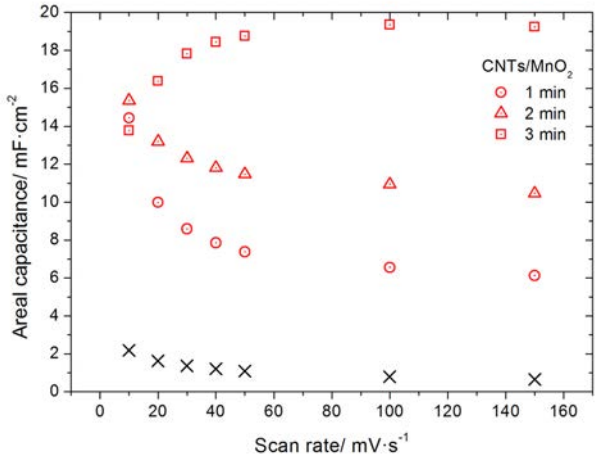

Figure 6.25: Areal capacitance versus scan rate for CNTs/MnO_2 nanocomposites at different manganese dioxide deposition times compared to bare CNTs

and CNTs/GNWs samples, which means that after 3 minutes we are still increasing the contact area between electrolyte and manganese dioxide. The sample with bare MnO_2 has a more resistive behavior due to the smaller surface area and thicker layer of manganese dioxide (**Figure 6.24**).

Therefore, the carbon nanostructuring of the samples allows faster charging and discharging of the electrodes due to reduced oxide thickness and increased surface area in contact with the electrolyte. The capacitance as a function of scanning rate follows a similar trend; as the MnO_2 deposition time increases, so does the capacitance. In addition, unexpected behavior appears with increased deposition time. Namely, an increase of the capacitance with the scan rate (**Figures 6.25, 6.26 and 6.27**). Typically, the capacitance decreases with the scanning rate due to the limitation of the proton diffusion processes through the oxide layer. This unexpected behavior has been previously reported

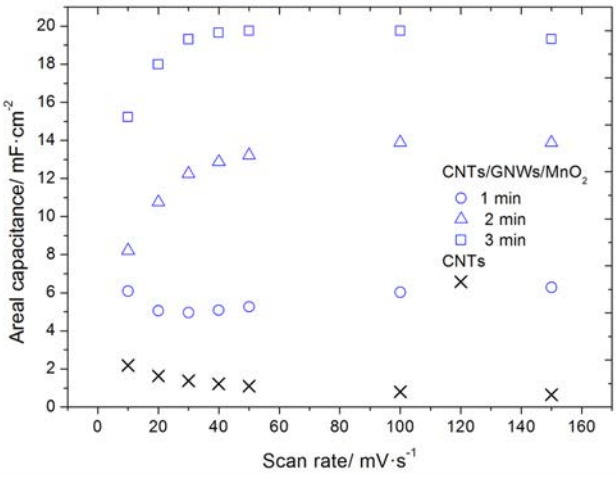

Figure 6.26: Areal capacitance versus scan rate for CNTs/GNWs/MnO_2 nanocomposites at different manganese dioxide deposition times compared to bare CNTs

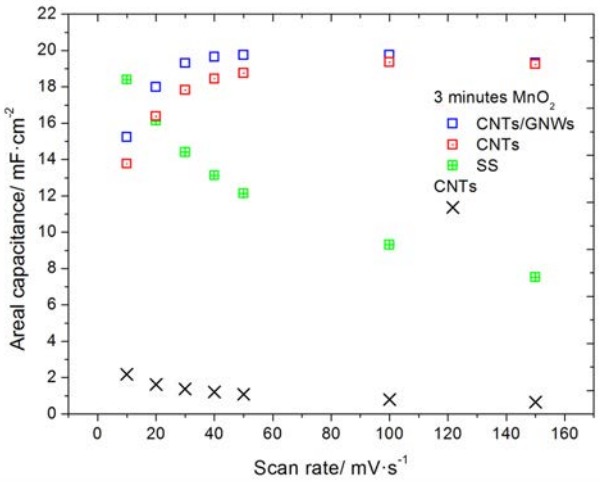

Figure 6.27: Areal capacitance versus scan rate for CNTs/GNWs/MnO_2, CNTs/MnO_2 and MnO_2 electrodeposited during 3 minutes, and bare CNTs

and attributed to an excellent contact between the porous collector (GNWs or CNTs in this case) and the oxide that allows an efficient access of both electrons and ions to afford a fast redox reaction at high scanning rates (Amade et al. 2019; Lang et al. 2011). In the case of CNTs (**Figure 6.25**) the capacitance decreases with the scanning rate at small deposition times. It is assumed that under these conditions nanotubes are not completely covered by oxide and therefore both carbon nanotubes and oxide contribute to total capacitance. The porous forest of carbon nanotubes produces a slow ionic diffusion and, consequently, a decrease in capacity with the scanning rate. Once the top of the forest is completely covered with a thin layer of oxide, fast redox reactions take place at high scanning rates.

In the case of CNTs/GNWs (**Figure 6.26**) nucleation of MnO_2 results in a thin and homogeneous layer right from the beginning, which allows fast diffusion and redox reactions. Compared to bare MnO_2 and CNTs, the nanostructured samples show higher capacitance at high scan rates, which is related with fast charge/discharge processes and high stability (**Figure 6.27**).

$$C = \frac{q_a + |q_c|}{2m\Delta V} \tag{6.2}$$

MnO_2 mass deposited on the carbon nanostructures during 1, 2 and 3 min was 0.04, 0.06 and 0.12,mg, respectively. These quantities were deposited on both the CNTs and CNTs/GNWs electrodes during the electrodeposition process. With Equation 6.2, the specific capacitance of the electrodes could be determined. Note that m is the mass of CNTs/MnO_2 and CNTs/GNWs/MnO_2 composite in grams. Thus, for a scanning rate of $50\,mV{\cdot}s^{-1}$, the calculated values for the CNTs/MnO_2 electrodes with MnO_2 deposit for 1, 2 and 3 min were 83, 100 and $130\,F{\cdot}g^{-1}$, respectively. While for CNTs/GNWs/MnO_2 electrodes were: 58, 100 and 115 $F{\cdot}g^{-1}$. The fact that the nanocomposites CNTs/MnO_2 and CNTs/GNWs/MnO_2 have similar capacitance values confirms the supposition that only the top layer of the nanotubes contributes to the capacitance. The electrolyte is not able to reach the bottom due to either the manganese dioxide layer or the highly dense GNWs growing on the CNTs.

Electrochemical impedance spectroscopy was performed by applying an alternating

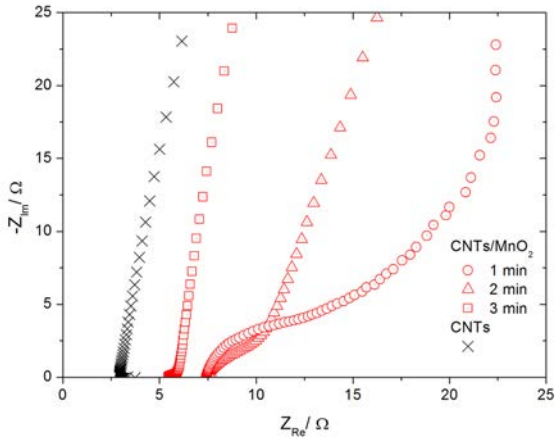

Figure 6.28: Impedance spectra of CNTs/MnO_2 and bare CNTs samples

voltage of 10 mV between 0.1 Hz and 100 kHz. This technique provides more information on the electrochemical processes that take place at the interfaces and the bulk of electrode materials. An equivalent circuit can be found describing the different processes such as load transfer resistance, diffusion or capacitance. However, this is beyond the scope of this work, and only interception with the x-axis, which is related to electrochemical series resistance (ESR), will be comment. The ESR is the result of all the contact resistances, electrolyte resistance and electrode resistances that are present in our system and is a crucial parameter for fast charge/discharge rates. In the case of CNTs this resistance increases once MnO_2 is deposited, due to the additional resistance of the oxide layer (**Figure 6.28**).

However, the ESR for the MnO_2 layer deposited for 3 minutes is lower than that of the minute deposited. The reason is supposed to be due to the slow diffusion of ions through the porous nanotube forest, but fast electron transport through the nanotubes once the top of the forest is covered with the oxide. Another possibility could be the oxidation of

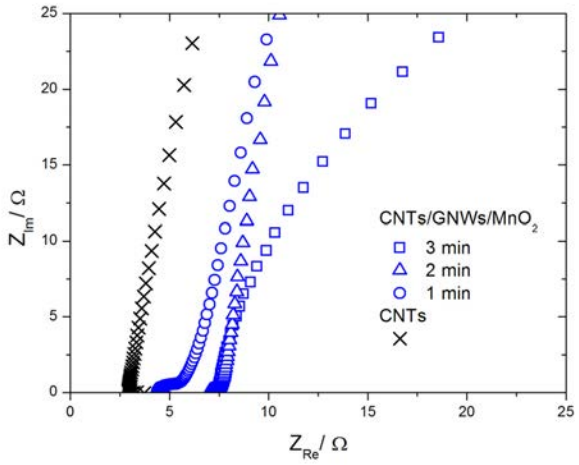

Figure 6.29: Impedance spectra of CNTs/GNWs/MnO_2 and bare CNTs samples

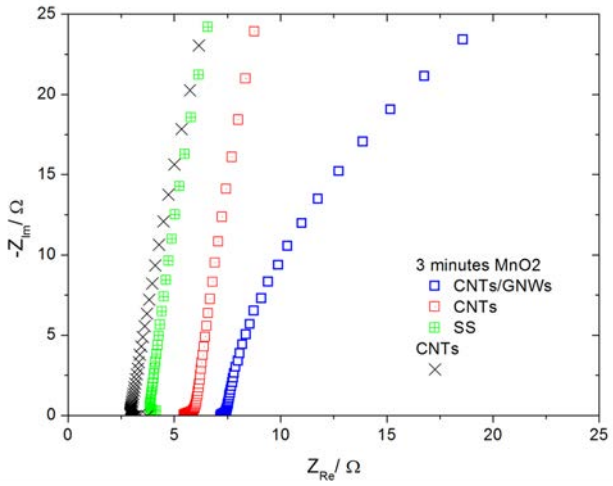

Figure 6.30: Impedance spectra of CNTs/MnO_2, CNTs/GNWs/MnO_2 , bare CNTs and bare SS/MnO_2 samples

the substrate by the electrolyte and the corresponding increase of its resistance. For low MnO_2 deposition, this effect is expected to be more important. In the case of GNWs the trend is opposite, which means that from the beginning the oxide layer is covering the surface of the GNWs, and with the increase of the MnO_2 deposition time the oxide layer becomes thicker and therefore more resistive (**Figure 6.29**).

Finally, when comparing the samples with 3 minutes MnO_2 deposition with the bare substrate reference sample, the ESR seems to be smaller for the latter (**Figure 6.30**). However, the substrate of this sample was not heated and pre-treated as during the growth of CNTs and GNWS. Consequently, the series resistance is smaller for this sample. The ESR values of the samples are between 4 and 7.5 Ω which still needs to be improved in order to achieve fast charge/discharge rates.

6.3.5 Alternative electrode architecture and oxidation problems

In order to improve the capacitance of the electrodes, during the development of this research, it was looked for a long time to improve the architecture of the electrodes for the supercapacitors. The main challenge (at least that's what was believed) was to control the density of the nanostructures, especially the CNTs density, in order to functionalize and decorate them. An architecture caught our attention and its repeatability was acceptable.

Using the method described in Chapter 4, a low-density of CNTs forest was obtained. The separation between each nanotube was enough to grow GNWs. This can be seen in Figure 31. These hybrid structures were obtained on 304 stainless steel surfaces without the use of diffusion barriers or external catalyst. The alloy elements of steel, mainly iron, made it possible to obtain CNTs with surprising uniformity. The GNWs were then obtained by the ICP-CVD technology.

The hybrid nanostructures were promising because the steel surface was not pretreated (chemical or mechanical) (see **Figure 6.31a**). As it can be seen, regardless of the rolling direction (surface roughness), the forest of the hybrid structure spreads evenly over the whole surface. This fact is important from the point of view of scalability, as the time to obtain these nanostructures was significantly reduced. With the plus that it could be obtained on a cheap substrate compared to other flexible substrates (e.g. copper foil, nickel

		D"	D	A	G	D'	2D	I_D/I_G	$I_D/I_{D'}$	I_{2D}/I_G
CNTs	Position (cm^{-1})	1205.34 ± 10.90	1357.77 ± 2.10	1522.97 ± 15.89	1587.24 ± 4.43	1618.49 ± 3.23		1.64	3.16	
	Intensity (a.u.)	1.21 ± 0.02	6.06 ± 0.12	2.42 ± 0.05	3.70 ± 0.07	1.92 ± 0.04				
	FWHM (cm^{-1})	215.12 ± 22.58	173.25 ± 10.36	205.78 ± 15.50	80.80 ± 10.23	49.72 ± 11.18				
CNTs+GNWs	Position (cm^{-1})		1346.72 ± 0.05	1482.28 ± 3.65	1578.78 ± 0.08	1617.38 ± 0.24	2690.94 ± 0.09	1.35	6.09	0.80
	Intensity (a.u.)		93.82 ± 1.88	1.47 ± 0.03	69.27 ± 1.39	15.40 ± 0.31	55.71 ± 1.67			
	FWHM (cm^{-1})		34.98 ± 0.15	56.66 ± 8.86	32.59 ± 0.26	18.54 ± 0.80	61.08 ± 0.25			

Table 6.3: Raman feature of GNWs supported by CNTs (Direct growth)

and graphite paper). Another advantage of this process is the good adhesion between the CNTs and the substrate (see **Figure 6.31b**). As no diffusion barrier is used, CNT forests have better contact with the substrate surface. In addition, if the density of the CNTs (which support other structures) is adequate, it is possible to coat them with GNWs (**Figure 6.31c**) and then deposit other materials (e.g. metal oxides). **Figure 6.31d** shows a GNWs/CNT completely coated by MnO_2 particles deposited by electrodeposition. Raman characterization allowed to analyze the hybrid structures obtained by direct growth. Perhaps what can be highlighted in the Raman fingerprint of those GNWs/CNTs

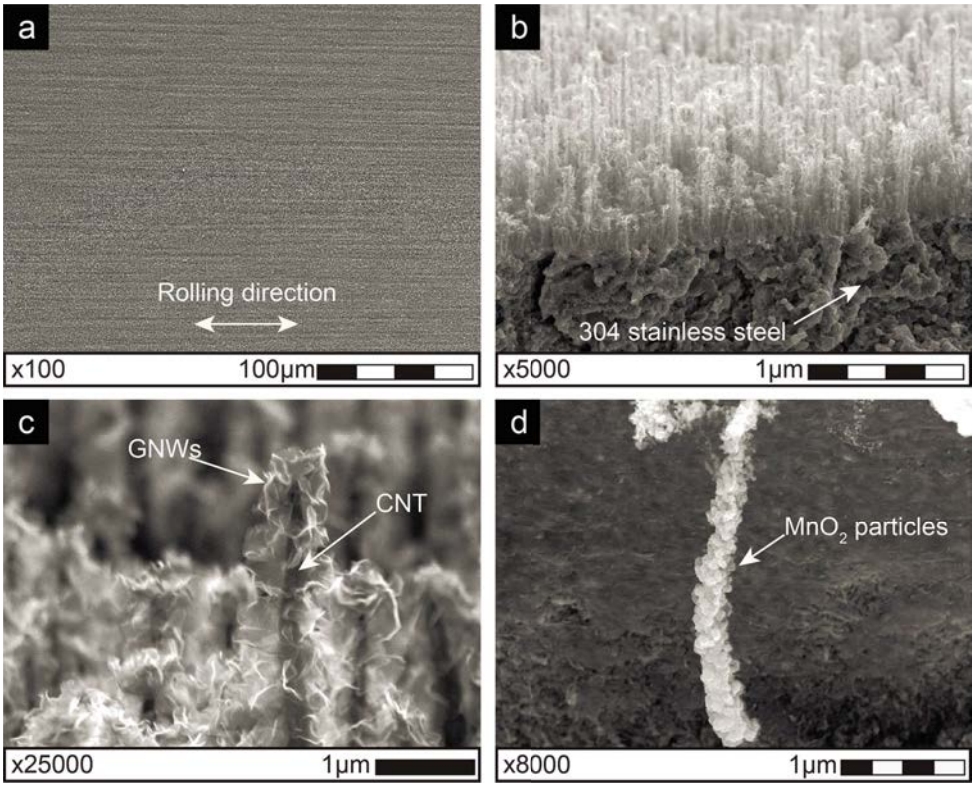

Figure 6.31: GNWs/CNTs directly growth on 304 stainless steel. (a) Top view of hybrid forest, the arrows indicate the rolling direction of the sheet metal. (b) 45° view of GNWs/CNTs, (c) Detail of CNT decorated with GNWs, (d) GNWs/CNT hybrid structure completely decorated with MnO_2 particles

structure is that the D-band has a higher intensity than the G-band (see **Figure 6.32**). In addition, calculating $I_D/I_{D'}$ gives a value of 6.09. According to (Eckmann et al. 2012), this can be attributed to the vacancy prevalence. Furthermore, if we look at the values of the I_D/I_G ratio in **Table6.3**, the difference in the disorder degree is not as large as in the samples analyzed in the previous sections. This may be explained by the fact that in these samples, the density of the GNWs is not as high compared to the samples where the GNWs are at the tip of the CNTs. However, the fact of having a larger degree of disorder (defects) favors the functionalization of the structures.

It is important to note that the value of the I_{2D}/I_G ratio is higher than those reported in **Table6.2**. This may be because GNWs have fewer stacked graphene layers. In fact, if we look at **Figure 6.18** we can see that with the values of I_{2D}/I_G (0.80) and FWHM of 2D-band (2690.94 cm^{-1}) the point obtained is displaced towards the zone with the lowest number of graphene layers. This is very attractive because there is more graphene surface to be functionalized with, for example, manganese oxide.

6.3.6 Consideration of the electrochemical effects of 304 stainless steel

For much of the time, in our research group we dedicated to improving the process of obtaining CNTs and GNWs. However, a serious drawback was hidden. The negative effects that the process to obtain these structures was producing on 304 stainless steel substrates were not considered. When the electrochemical characterization of the electrodes was attempted, the results were not as expected. This was repeated for both direct growth and diffusion barrier samples. Samples obtained by direct growth were the most problematic. By discarding several factors (e.g. stability of nanostructures, contact between nanostructures and substrate, electrochemical cell design) we begin to suspect the substrate. Immediately we decided to review the literature concerning the effects of 304 stainless steel exposure to hydrogen-rich atmospheres.

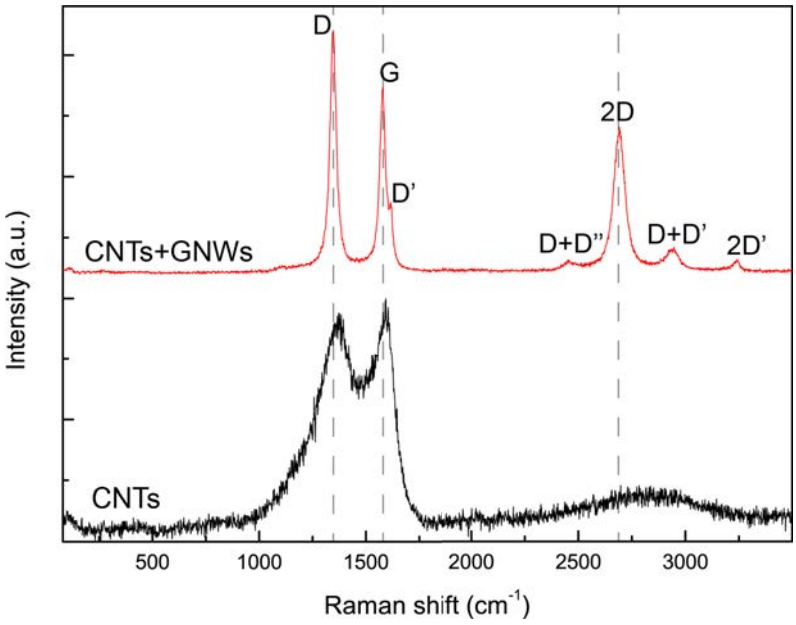

Figure 6.32: Raman spectra of GNWs supported by CNTs (Direct growth)

Austenitic stainless steels in general are materials that are commonly used in chemically aggressive environments (Akita et al. 2015). In fact, this was one of the reasons why we selected this material: its chemical stability. However, it was not taken into account that 304 stainless steel exposed to thermal processes (between 500 and 800 °C) and under an atmosphere rich in H_2 is significantly deteriorated (Nikulin et al. 2010). Several effects that are described in the literature were observed in our electrodes. For example, in direct growth process of CNTs, the embrittlement of the material was detected. When the material was cut without any treatment, a certain resistance to cutting was distinguished. This ductile material under shear stress is first plastically deformed and then separated (William D. Callister and Rethwisch 2013). But, when the substrate (with CNTs) was cut, it was observed that the material had no more resistance to cutting and behaved like a brittle material. As steel's ductility decreased, so did its flexibility. Very likely that behavior may be due to hydrogen embrittlement (Han et al. 1998; Marchi et al. 2005). Furthermore, this behaviour may be related to excessive crystal growth and decarburization phenomena (Han et al. 1998). In Chapter 4 it was observed that the 304 stainless steel went through a recrystallization process. The size of the crystals increased with temperature. In addition, it was observed that there is a process of decarburization of the material. In the direct growth process, a thick layer of carbides forms on the surface of the 304 stainless steel. With the use of nitrided layers decarburization phenomena was eliminated. The nitride layers acted as a diffusion barrier and also protected the substrate from the hydrogen rich-atmosphere.

But without a doubt, the low corrosion resistance of electrodes (304 stainless steel supporting nanostructures) was the phenomenon that generated the most problems for us. Regardless of the process employed to obtain the electrodes, premature oxidation processes always occurred during their electrochemical characterization. A possible explanation for electrodes obtained by direct growth (Chapter 4) was the sensitization degree of the steel (Marchi et al. 2005; Nikulin et al. 2010). The formation of chromium carbides, on the surface and on the grain boundaries, generates Cr depleted zones. Note that chromium is the main alloying element that provides to stainless steels their corrosion resistance qualities by combining with oxygen to form a thin, transparent chromium-oxide protective film on the surface (Nikulin et al. 2010). If the Cr% (in weight) drops under ∼11%, the corrosion resistance of the material also drops. This behavior is well summarized in **Figure 6.33**. In addition, as the material has a different chemical composition (chromium carbides, and Cr depleted regions), zones with different corrosion potential are also formed (E_{corr}). Depending on the value of E_{corr}, these zones may be anodic or cathodic, which in the presence of an electrolyte (e.g. sodium sulfate) eventually form a galvanic cell (S. Li and Hihara 2012; Shi et al. 2017). Thus, the corrosion process begins. Checking the galvanic series (Schweitzer 2007), the materials with the highest E_{corr} are the anodic areas. In our case, the corrosion acts in the Cr depleted regions.

On electrodes with nitrided layers of 304 stainless steel, very probably the same thing happens. That is, there are anodic and cathodic zones that when exposed to an electrolyte form a galvanic cell. In Chapter 5 it was determined that through the sputtering process, layers with different crystalline phases were obtained. Depending on the percentage of N introduced during the sputtering process, a CrN phase was formed, and a second phase was composed of the other alloying elements of the steel (Fe, Ni, Mn). In that case, the CrN is the cathodic part and the Fe rich phase is the anodic part. In this way, from this situation, the rest of phases are exposed to the electrolyte when the layer of AlN is cracked. It is necessary to mention that the electrodes with nitrided layers were more stable during the electrochemical characterization. This can be attributed to the fact

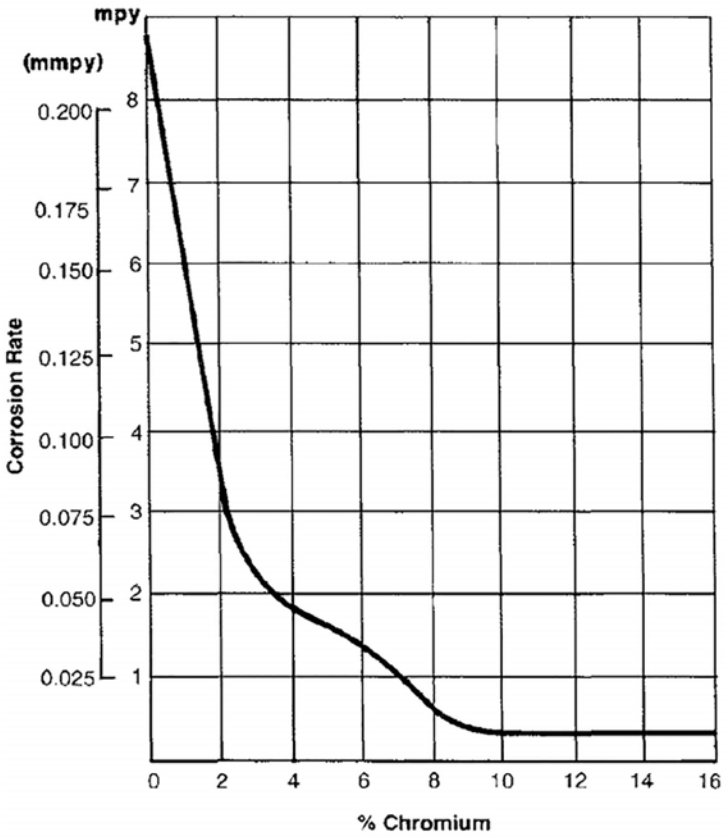

Figure 6.33: Effect of chromium content on corrosion rate (in normal atmosphere) (Nikulin et al. 2010). Mils per year or (mpy) is used to give the corrosion rate in a pipe, a pipe system or other metallic surfaces

that corrosion processes are localized and not generalized (as in direct growth process). Localized corrosion processes are also known as pitting corrosion (Frankel 2013; Shi et al. 2017).

In general, it can be said that the corrosion processes that took place in our electrodes correspond to galvanic corrosion. The corrosion occurs when two regions, with different potentials, are in electrical contact while immersed in an electrically conducting corrosive liquid. Because the regions have different natural potentials in the liquid, a current will flow from the anode (more electronegative) material to the cathode (more electropositive), which will increase the corrosion on the anode, see **Figure 6.34**.

When a metal is corroding two processes occur. One is the dissolution of metal at the anode (e.g. iron):

$$\mathrm{Fe} \rightarrow \mathrm{Fe}^{2+} + 2\mathrm{e} \tag{6.3}$$

This must be balanced by a cathodic reaction. Most practical cases of galvanic corrosion occur in solutions containing dissolved oxygen and in most neutral and alkaline liquids the primary cathodic reaction is the reduction of dissolved oxygen:

$$\mathrm{O_2} + 2\mathrm{H_2O} + 4\mathrm{e} \rightarrow 4\mathrm{OH} \tag{6.4}$$

In acid liquids the cathodic reaction is often the reduction of hydrogen ions to hydrogen gas:

$$2\mathrm{H}^{+} + 2\mathrm{e} \rightarrow \mathrm{H_2} \tag{6.5}$$

Other cathodic reactions can occur in deaerated environments and one example is liquids containing hydrogen sulphide. There is a range of partially oxidised sulphur species (e.g. thiosulphate, dithionate etc.) and reduction of one or more of these species can be the principle cathodic reaction in corrosion (Francis 2000).

To test the hypothesis that electrode instability during electrochemical characterization was a consequence of substrate corrosion, we decided to use Raman spectroscopy. Thus, Raman spectra were obtained from samples with nitrided layers that were electrochemically characterized. It is important to mention that the Raman characterization was carried out three days after the electrochemical characterization. **Figure 6.35** presents two of these spectra, which correspond to the samples with the highest percentage of MnO_2, and compares them with the Raman spectra of the samples already discussed in the previous section (obtained immediately after electrochemical characterization). As you can see, the spectra have changed. When reviewing the literature, it seems that the shift where the new peaks appear (250, 510, 700 and 1380 cm^{-1}) coincide with the vibration modes generated by rust phases (oxides and hydroxides) (Colomban et al. 2008; S. Li and Hihara 2012; Oh et al. 1998). The peak shapes are not like those of a Gaussian peak, nor are they narrow, perhaps due to the masking effect produced by different species.

Among the rust phases that usually arise in this type of corrosion are: goethite (αFeOOH), haematite (Fe_2O_3), akaganeite ($\beta-$FeOOH(Cl)), lepidocrocite ($\gamma-$FeOOH), maghemite ($\gamma-Fe_2O_3$) and magnetite (Fe_3O_4) (Colomban et al. 2008; S. Li and Hihara 2012). The formation of various rust phases in different locations was possibly due a synergistic effect of oxygen gradients in the droplets and the variation of local pH environments (S. Li and Hihara 2012). In our case, although we do not know exactly the type of oxide or hydroxide present on the surface (due to masking of the peaks in the spectrum), the Raman spectra confirmed the presence of rust on our samples. In addition, in order to know the morphology of this rust, some SEM images of the electrodes with nitrided layers were taken. Structures such as those shown in **Figure 6.36** were found. They are structures that in scale surpass those that we obtained by PECVD and by ICP-CVD. Their morphology differs considerably from that of CNTs and GNWs. In addition, it was observed that, in some electrode areas, there was a total collapse of the diffusion barrier (possibly by pitting corrosion processes).

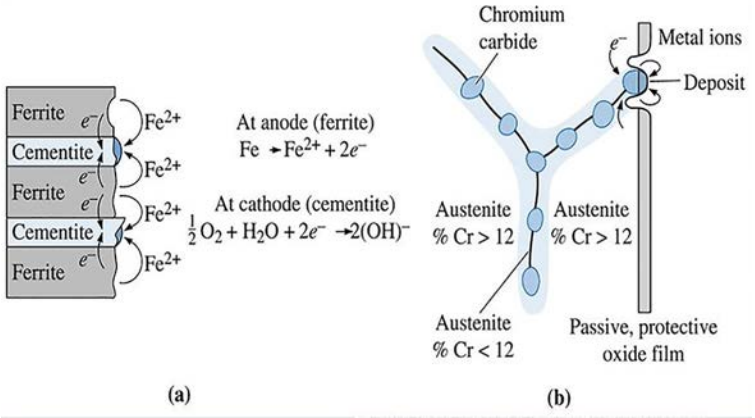

Figure 6.34: Example of micro galvanic cells in two phase alloys. (a) In steel, ferritic is anodic to cementite. (b) In austenitic stainless steel, precipitation of chromium carbide makes the low chromium austenite in the grain boundaries anodic

Raman characterization and SEM images allowed us to confirm our hypothesis: the corrosion resistance of 304 stainless steel decreases considerably after thermal processes, in a hydrogen-rich atmosphere, to which it is subjected to obtain carbon nanostructures by PECVD and/or ICP-CVD. A more detailed study of 304 stainless steel corrosion could be carried out, such as studying the chemical composition of rust or optimizing the diffusion barriers (with Ni, Ti, Cr). However, from what has been found so far, this material alone is not suitable for this application. At least not to be subjected to processes that are used in obtaining CNTs and GNWs. In fact, this coincides with the revised literature. This type of steel is very susceptible to forming chromium carbides at high temperatures. As already mentioned, the formation of chromium carbides produces poor chromium zones which, under the presence of an electrolyte, can act as anodic zones. Thus, giving rise to the creation of micro galvanic cells. On the other hand, by using a diffusion barrier system with nitrided layers, corrosion problems were also obtained. Nitrided layers of 304 stainless steel also had galvanic and cathodic zones. This led to localized corrosion processes, which in the end also affect the electrochemical performance of the electrodes.

As alternatives to 304 stainless steel, other ferrous alloys that are less susceptible to thermal processes can be looked for. The main aim is to ensure that the stainless steel character of the material is not damaged after the thermal processes to which it is subjected. This basically means ensuring that the thin layer of Cr_2O_3 is on the surface and that it is continuous (no cracks). In many processes, isothermal (constant temperature) conditions are not maintained and process temperatures vary. Expansion differences between the base metal and the protective film (or scale) during heating and cooling can cause cracking and spalling of the protective scale. This allows the oxidizing media to attack the exposed metal surface (Nikulin et al. 2010). **Figure 6.37** shows the influence of Ni on scaling resistance of some stainless steels. It should be noted that the most susceptible is 304 steel while the most stable is 310 series steel. Scaling resistance means that nickel reduces the thermal expansion differential between the base metal and the oxide film and thereby reducing stresses at the base metal-oxide interface during cooling. As we

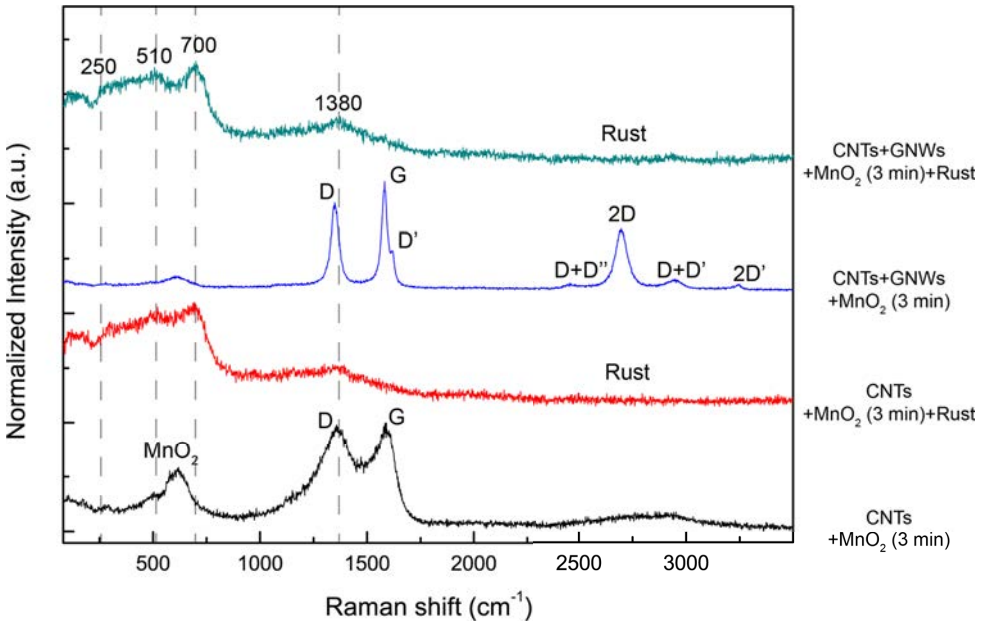

Figure 6.35: Raman spectra before and after corrosion process on stainless steel electrodes

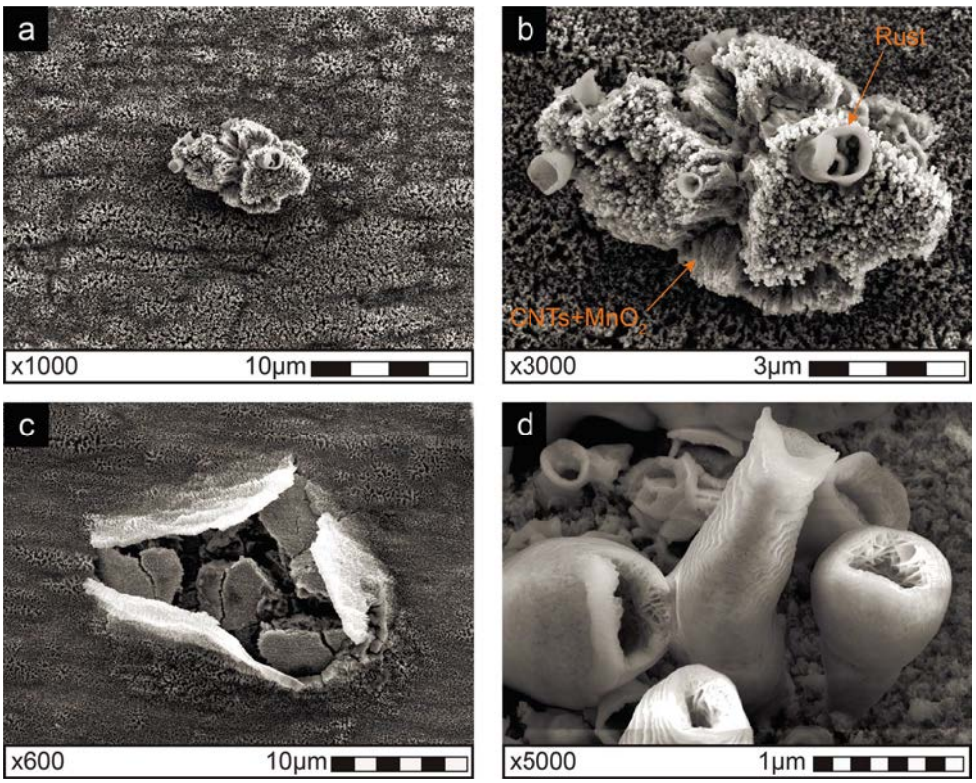

Figure 6.36: Corrosion process on stainless steel electrodes. (a) Top view of forest of CNTs+MnO_2 with rust, (b) detail of rust structure, (c) collapse of diffusion barrier system, (d) Rust structures on electrodes

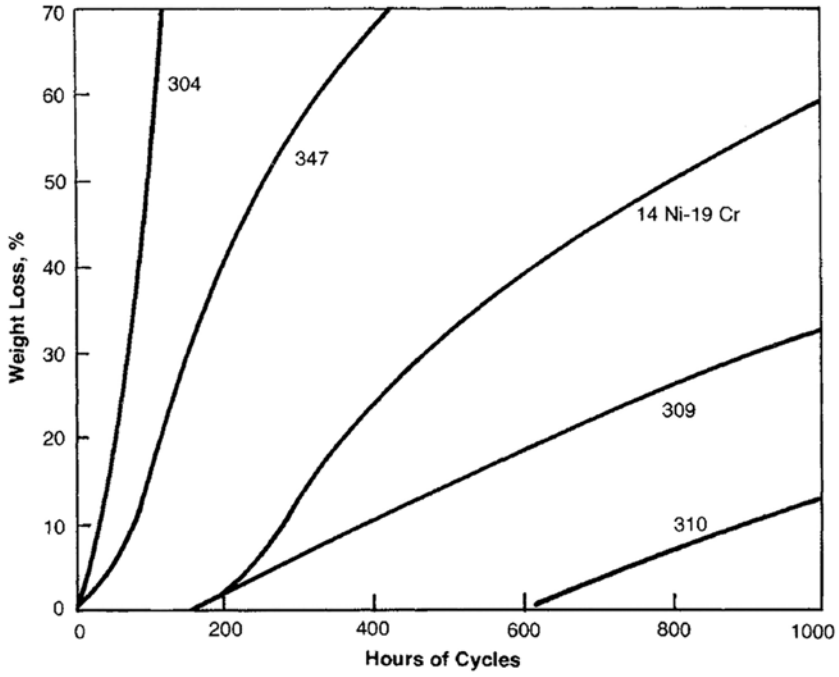

Figure 6.37: Scaling resistance of some iron-chromium-nickel alloys in cycling-temperature conditions at 982 °C (Nikulin et al. 2010)

can see, 310 stainless steel is an option that should be considered for the manufacture of electrodes. Even if it is desired to ensure that carbide formation will not occur, the 310S series can be selected. This particular series has a lower carbon content, which according to the standards further reduces the possibility of chromium carbide formation.

6.4 Conclusions

In this work, hybrid structures of carbon-based materials have been obtained through PECVD and ICP-CVD processes. In addition, MnO_2 particles were successfully deposited on these structures using electrodeposition. As demonstrated, the size of the MnO_2 particles depends on the type of defects present in the nanostructures. Regardless of the time of electrodeposition, particles of $\sim 100\,nm$ with good distribution were obtained at the borders of the GNWs. The borders, which are crystalline defects, acted as nucleation points for the oxide particles. While in CNTs, with less borders, the size of the oxide particles depended on the time spent in electrodeposition. It was curious how the orientation of the CNTs changes after the electrodeposition process. This fact, which is summarized in Figure 6.10, was not observed when the CNTs were coated with GNWs. The pattern formed is considered to originate from the surface tension generated when the samples come into contact with the electrolyte solution prior to the electrodeposition process. The Raman characterization allowed to obtain the fingerprint of the CNTs, GNWs, MnO_2 and even of the rust that formed on the electrodes after the electrochemical characterization. The deconvolution of the Raman spectra of CNTs and GNWs provided more details of the nature of these nanostructures. Thus, it was determined that the large amount of amorphous carbon present in CNTs corresponds to nanocrystalline graphite (nc-G) type. In addition, it was found that GNWs have few stacked layers of graphene (about 10) and that they have boundary type defects. The degree of disorder in the CNTs is greater than that of the GNWs, that fact can be attributed to the large amount of amorphous carbon on the samples. In the case of the Raman rust fingerprint, although spectra with well-defined peaks were not obtained, based on the literature consulted and the SEM images, it can be concluded that the structures observed correspond to iron oxides and/or iron hydroxides. It was evidenced that the functionalization of carbon-based nanostructures with MnO_2 improves their electrochemical performance. Thus, CNTs without MnO_2 presented an areal capacitance of around $1\,mF/^2$, while when decorated with MnO_2 and GNWs/MnO_2 that value rises to $20\,mF/cm^2$. If the mass of CNTs/MnO_2 and CNTs/GNWs/MnO_2 is considered, the capacitance value is around $120\,F{\cdot}g^{-1}$. Unexpected behavior appears with increased deposition time. Namely, an increase of the capacitance with the scan rate. Typically, the capacitance decreases with the scanning rate due to the limitation of the proton diffusion processes through the oxide layer. This unexpected behavior has been previously reported and attributed to an excellent contact between the porous collector (CNTs) and the oxide that allows an efficient access of both electrons and ions to afford a fast redox reaction at high scanning rates. The performance of the electrodes also depends on the stability of the substrate during electrochemical characterization. The instability of the electrode is explained by the fact that 304 stainless steel loses its resistance to corrosion after the thermal processes used to obtain the nanostructures. Several corrosion processes can take place on the substrate surface when it is exposed to slightly corrosive environments (e.g. sodium sulfate, water and ambient humidity). The best option to avoid these recurring problems is to look for another substrate. 310S stainless steel, with high chromium and nickel content, is an option.

Conclusions

In this study we focused on obtaining CNTs on 304 stainless steel foil (0.1 mm thick). Today we understand more the advantages and disadvantages of using this ferrous alloy to produce electrodes for supercapacitors. This substrate was selected for being a conductive material, for its flexibility and above all, in standard conditions, for its high corrosion resistance. Corrosion resistance is a critical point during electrochemical characterization as it prevents the substrate from reacting with the electrolyte.

To accomplish the objectives of this thesis, several systems of the CNTs reactor have been optimized. Thus, the technological drawbacks found during the preliminary experiments were satisfactorily resolved. This allowed us to considerably improve the processes of obtaining CNTs on different substrates. Therefore, reproducibility was significantly improved by the precise control of temperature, pressure and gas composition during the growth processes. In addition, the reactor's load capacity was increased: the new system like-carrousel allowed four samples to be placed inside the main chamber of the reactor at the same time.

In general, two approaches were used to obtain carbon nanotubes (CNTs) forests on the surface of this conductive material. The first was to obtain CNTs directly on the surface of the steel. While the second was to use a diffusion barrier system that prevents the catalyst from diffusing into the substrate. For both approaches, the processes used to obtain CNTs were plasma enhanced chemical vapor deposition (PECVD) and water assisted chemical vapor deposition (WACVD). In addition, it should be noted that there was no mechanical preparation (grinding and polishing) of the 304 stainless steel surfaces. Uniform CNTs forests were obtained over an area of 9 cm^2.

We have grown CNTs directly on 304 stainless steel without catalyst layer, through a specific thermal and plasma process of the substrate. This process has been carried out by two steps:

The reduction of the native oxide layer from the stainless steel surface to improve the electric contact of the carbon nanostructures. The native Cr_2O_3 layer was completely removed with a hydrogen-argon plasma in the temperature range 600 to 730 °C. The OES spectra allowed us to estimate that during the first 60 s, after plasma started, the oxide layer was completely reduced. Firestone Abbot curves proved that during 5 minutes of process also modified the roughness of the substrate.

The precipitation of metal carbides on the surface of 304 stainless steel promotes multiple nucleation of CNTs in the carbide microparticles surface. Between 600 and 650 °C the most common carbides were Fe_3C and $(FeCr)_7C_3$. In contrast, at 700 and 730 °C, the carbide found was Cr_7C_3 and in low proportion $(FeCr)_7C_3$ and Fe_3C. Another thing to note is that precipitated carbides formed a porous thick layer on the surface,

under which there probably was a depleted chromium zone.

Special attention must be paid to the time and temperature used in the reduction and CNTs growth process on this material. In particular to prevent that their flexibility and corrosion resistance are affected, because a prolonged exposure can severely change the properties of the material. In this sense, as the temperature increases, the size of the internal crystals also increases as a result of the recrystallization temperature (600 − 650 °C) being exceeded.

MWCNTs forests directly on the reduced surface of 304 stainless steel were grown with no external catalyst deposition. The amount of iron in the carbide layer obtained at 730 °C was enough to act as a catalyst.

CNTs obtained by WACVD have better crystallinity than those obtained by PECVD, although with random orientation. This was evidenced through the deconvolution of Raman spectra. The identified bands in both PECVD and WACVD samples were: D" ($1200\,cm^{-1}$), D ($1350\,cm^{-1}$), A ($1500\,cm^{-1}$), G ($1580\,cm^{-1}$) and D' ($1620\,cm^{-1}$). It has been demonstrated that PECVD samples contain more amorphous carbon in nanocrystalline graphite form.

In a second approach, uniform forest of CNTs was grown on nitrided stainless steel layers previously deposited on 304 stainless steel substrates. For that an aluminum nitride (AlN) thin layer was deposited as a diffusion barrier before the catalyst ultrathin layer.

In this second approach, a new diffusion barrier system has been developed based on an interface layer having a gradient nitrogen composition, starting from 0 to 35% of nitrogen content in 304 stainless steel alloy. Nitrided layer show two crystalline phases. One phase corresponds to chromium nitride (CrN) and the other is basically composed by alloy elements (MeN).

The percentage of nitrogen has allowed produce a highly efficient buffer layer to support the AlN diffusion barrier based on a suitable tuning of its thermal expansion coefficient.

The use of this kind of diffusion barrier with resistivities of $200\,\Omega{\cdot}m$ does not limit the current through the contact between metal and carbon nanostructures in a significative way, because series resistance increases in a very low value ($34\,\Omega{\cdot}m/cm^2$).

The results show that the temperature used for the growth of the CNTs influenced their morphology (length and diameter), but did not influence the amount of amorphous carbon present in the samples.

New hybrid carbon nanostructures were developed for application to supercapacitors.

The CNTs were decorated with graphene nanowalls (GNWs) using PECVD and ICP-CVD, respectively.

One of the main advantages of this hybrid carbon nanostructures is the important increase of the number of surface defects becoming nucleation centers for the metal oxides used in the supercapacitor electrodes.

Two three-dimensional hybrid metal oxide carbon nanostructures have been developed for supercapacitor applications. One of MnO_2 electrodeposited on CNTs and other with MnO_2 electrodeposited on CNTs decorated by GNWs.

The functionalization of carbon-based nanostructures with MnO_2 improves their electrochemical performance. The electrochemical characterization of these structures has shown a factor of twenty increment in the areal capacitance of MnO_2-functionalized structures compared to naked carbon nanostructures.

Appendix

Below is a list of the samples produced during this work. Deposit parameters and also some general comments are included. The nomenclature used to identify the samples is explained in the following figure.

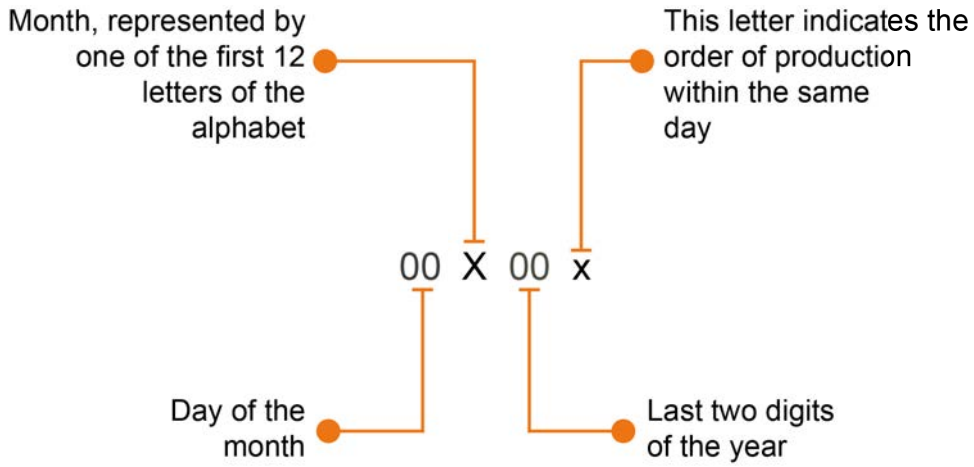

Detailed drawings of the different components designed and built for the repowering of the CNT reactor are also included. Finally, the detailed drawings of the new electrochemical cell have been attached.

Sample code	Substrate	Objective	Sample code (PEDRO)	Result	Catalyst Deposition										CNTs growth																General comments
					Plasma source	Target	Previous vacuum (Pa)	Gas 1	Flux (sccm)	Pressure reactor (mbar)	Time (s)	Deposition rate (nm/s)	Power (W)	VBias (V)	Gas	Flux (sccm)	P (mbar)	Ramp time (s)	Hold time (s)	Tfinal (ºC)	Plasma source	Gas 1	Flux (sccm)	Pressure (mbar)	Gas 2	Flux (sccm)	Pressure (mbar)	Power (W)	VBias (V)	Deposition time (s)	
19L16a.pdf	SS304+Ni+Ti+AlN	Deposition of CNTs	16L1501	Success	RF	Fe	1.3*10^-4	Ar	128	0.02	25.00	0.04	60.00	97.00	H2	100	2	500	120	600	RF	NH3	100	0.8	C2H2	50	1	50	342	1200	
20L16a.pdf	SS304+Ni+Ti+AlN	Deposition of CNTs	16L1501	Failure	RF	Fe	1.5*10^-4	Ar	128	0.02	25.00	0.04	60.00	98.00	H2	100	2	500	120	600	RF	NH3	100	0.8	C2H2	50	1	50	357	1200	
20A17b.pdf	Si	Deposition of CNTs		Failure	RF	Fe	2.5*10^-4	Ar	128	0.02	87.00	0.04	60.00	96.7	H2	100	2	750	120	680	RF	NH3	100	0.8	C2H2	50	1	50	372	900	
23A17a-Fe calibration.pdf	Glass	Determination of deposition rate		Success	RF	Fe	2.5*10^-4	Ar	128	0.02	600.00		60.00	106.1	This was the first sputtering process using the new Fe traget where it was contaminated.																
23A17a.pdf	Si	Deposition of CNTs		Failure	RF	Fe	2.5*10^-4	Ar	128	0.0195	87.00	0.04	60.00	96.7	H2	100	2	750	120	680	RF	NH3	100	0.8	C2H2	50	1	50	372	900	
23A17b-Fe calibration.pdf	Glass	Determination of deposition rate		Failure	RF	Fe	2.5*10^-4	Ar	128	0.0194	900.00		60.00	106.2	The water cooling system of the target was not opened																
23A17d.pdf	SS304+Ni+Ti+AlN	Deposition of CNTs	16L1901	Failure	RF	Fe	2.9*10^-4	Ar	128	0.0193	90.00	0.04	60.00	105.5	H2	100	2	675	120	700	RF	NH3	100	0.8	C2H2	50	1	50	396	1200	
13B17a.pdf	Si	Deposition of CNTs		Failure	RF	Fe	3.2*10^-4	Ar	128	0.0194	200.00	0.015	60.00	102.00	H2	100	2	750	120	680	RF	NH3	100	0.8	C2H2	50	1	50	397	900	
13B17b.pdf	Si	Deposition of CNTs		Success	RF	Fe	4.7*10^-4	Ar	128	0.0194	233.00	0.015	60.00	101.3	H2	100	2	750	120	680	RF	NH3	100	0.8	C2H2	50	1	50	378	900	
15B17b-Fe calibration.pdf	Glass	Determination of deposition rate		Success	RF	Fe	3.5*10^-4	Ar	128	0.0195	1200.00		60.00	98.00																	
15B17c-Fe calibration.pdf	Glass	Determination of deposition rate		Success	RF	Fe	3.7*10^-4	Ar	128	0.0197	1200+1200		60.00	97.00																	
16B17b.pdf	Si	Deposition of CNTs		Success	RF	Fe	3.5*10^-4	Ar	128	0.0194	62.00	0.04	60.00	-97.00	H2	100	2	750	120	680	RF	NH3	100	0.8	C2H2	50	1	50	374-384	900	
17B17b.pdf	Si	Deposition of CNTs		Success	RF	Fe	2.3*10^-4	Ar	128	0.0194	39.00	0.026	60.00	98.7	H2	100	2	750	120	680	RF	NH3	100	0.8	C2H2	50	1	50	-381	900	
23B17b.pdf	SS+Ni+Ti+AlN	Deposition of CNTs	17A2001	Success	RF	Fe	4.5*10^-4	Ar	128	0.0199	62.00	0.026	60.00	-96.00	H2	100	2	750	120	700	RF	NH3	100	0.8	C2H2	50	1	50	367	900	
02C17b.pdf	SS+Ni+Ti+AlN	Deposition of CNTs	17C0102	Success	RF	Fe	3.8*10^-4	Ar	128	0.0199	40.00	0.026	60.00	-96.00	H2	100	2	750	120	680	RF	NH3	100	0.8	C2H2	50	1	50	367	900	
03C17a.pdf	SS+Ni+Ti+AlN	Deposition of CNTs	17C0102	Success	RF	Fe	3.8*10^-4	Ar	128	0.02	40.00	0.026	60.00	100.00	H2	100	2	750	120	680	RF	NH3	100	0.8	C2H2	50	1	50	332	900	
08C17b.pdf	SS+Ni+Ti+TaN	Deposition of CNTs	17C0301	Success	RF	Fe	3.5*10^-4	Ar	128	0.02	62.00	0.026	60.00	96.3	H2	100	2	750	120	680	RF	NH3	100	0.8	C2H2	50	1	50	355	900	
13C17a.pdf	SS+gradientSS+AlN	Deposition of CNTs	17C0901	Success	RF	Fe	3.4*10^-4	Ar	128	0.0199	62.00	0.026	60.00	-98.00	H2	100	2	750	120	700	RF	NH3	100	0.8	C2H2	50	1	50	-352	900	
15C17c.pdf	Si	Deposition of CNTs		Success	RF	Fe	4.6*10^-4	Ar	128	0.0199	62.00	0.04	60.00	-95.5	H2	100	2	750	120	680	RF	NH3	100	0.8	C2H2	50	1	50	370-329	900	
					N2 plasma treatment: Flow rate= 100sccm, Pressure= 0.5mbar, RF power=50W, P(inc)= 50.34, P(ref)= 0.1-1.71, Plasma time= 120s, bias voltage=220-290V																										
12D17a (calibration Al).pdf	Glass	Deposition of CNTs		Success	RF	Al	1.9*10^-4	Ar	42 (58)	0.0103	600.00		120.00	-190.00	Cleaning Al target: Flux Ar=42 (58) sccm, Preactor=0.0103 mbar, time=300(s), Power=120W, Power in=121.08W, Powe ref=9.64W, Vbias=-189V																
12D17b (calibration Al2O3).pdf	Glass	Deposition of CNTs		Success	RF	Al	2.8*10^-4	Ar	37 (51)	0.0109	600.00		120.00	-184.00	Cleaning Al target: Flux Ar=42 sccm, Preactor=0.0103 mbar, time=600(s), Power=120W, Power in=121.08W, Powe ref=6.64W, Vbias=-189V																
12D17c (calibration Al2O3).pdf	Glass	Deposition of CNTs		Success	RF	Al	2.8*10^-4	Ar	37 (51)	0.0107	600.00		120.00	-180.00	Cleaning Al target: Flux Ar=42 sccm, Preactor=0.0102 mbar, time=600(s), Power=120W, Power in=119.53W, Powe ref=6.16W, Vbias=-139, Load=6.8, Tune=7.02																
12D17c.pdf	Si+Al2O3	Deposition of CNTs	17D0706	Failure	RF	Fe	2.8*10^-4	Ar	128	0.0203	50.00	0.04	60.00	-97.00	H2	100	2	750	120	600	CVD	NH3	100	0.8	C2H2	50	10,132	-	-	1800	
					We used water assisted CVD with this sample. the annealing tempereature was 600C but the CVD temperature was 700C. The circular scale is devided to 25 lines The water was opened with a scale 21																										
18D17a (Al2O3).pdf	Glass	Deposition of CNTs		Success	RF	Al	2.8*10^-4	Ar	37 (51)	0.0107	600.00		120.00	-182.00	Cleaning Al target: Flux Ar=42 sccm, Preactor=0.0102 mbar, time=600(s), Power=120W, Power in=119.53W, Powe ref=6.16W, Vbias=-139V																
18D17a.pdf	Si+Al2O3	Deposition of CNTs	17D0706	Success	RF	Fe	2.8*10^-4	Ar	128	0.0203	50.00	0.04	60.00	-98.2	H2	100	2	750	120	600	CVD	NH3	100	0.8	C2H2	50	10,132	-	-	1800	
					We used water assisted CVD with this sample. the annealing tempereature was 600C but the CVD temperature was 700C. The circular scale is devided to 25 lines. The water was opened with a scale 21																										
19D17a (Al2O3).pdf	Glass	Deposition of CNTs		Success	RF	Al	2.8*10^-4	Ar	8.6 (12.5)	0.0033	900.00	0.016	120.00	-185.00	Cleaning Al target: Flux Ar=42 sccm, Preactor=0.0102 mbar, time=600(s), Power=120W, Power in=119.53W, Powe ref=6.16W. Vbias=-139V																
21D17a (Depth profile XPS).pdf	SS+gradientSS+AlN	Annealing	17D2001	Success	RF	Fe	2.5*10^-4	Ar	128	0.0201	62.00	0.04	60.00	-96.9	H2	100	2	750	120	680	RF	NH3	100	0.8	C2H2	0	0				
21D17b (Depth profile XPS).pdf	SS+gradientSS+AlN	Annealing	17D2001	Success	RF	Fe	4.7*10^-4	Ar	128	0.0201	62.00	0.04	60.00	-99.5	H2	100	2	750	120	680											
21D17c (Depth profile XPS).pdf	SS+gradientSS+AlN	Annealing	17D2001	Success	RF	Fe	3.9*10^-4	Ar	128	0.0201	62.00	0.04	60.00	-99.3	H2	100	2	750	120	700											

Sample code	Substrate	Objective	Sample code (PEDRO)	Result	Catalyst Deposition										CNTs growth																General comments
					Plasma source	Target	Previous vacuum (Pa)	Gas 1	Flux (sccm)	Pressure reactor (mbar)	Time (s)	Deposition rate (nm/s)	Power (W)	VBias (V)	Gas	Flux (sccm)	P (mbar)	Ramp time (s)	Hold time (s)	Tfinal (ºC)	Plasma source	Gas 1	Flux (sccm)	Pressure (mbar)	Gas 2	Flux (sccm)	Pressure (mbar)	Power (W)	VBias (V)	Deposition time (s)	
21D17d (Depth profile XPS).pdf	SS+gradientSS+AlN	Annealing	17D2001	Success	RF	Fe	3.7*10^-4	Ar	128	0.0201	62.00	0.04	60.00	-99.4	H2	100	2	750	120	715											
21D17e (Depth profile XPS).pdf	SS+gradientSS+AlN	Determination of deposition rate	17D2101	Success	RF	Fe	3.4*10^-4	Ar	128	0.0202	62.00	0.04	60.00	-99.1																
21D17f (Depth profile XPS).pdf	SS+gradientSS+AlN	Annealing	17D2101	Success	RF	Fe	3.3*10^-4	Ar	128	0.0201	62.00	0.04	60.00	-97.9	H2	100	2	750	120	730											
21D17g (Depth profile XPS).pdf	SS+gradientSS+AlN	Deposition of CNTs	17D2101	Success	RF	Fe	4.7*10^-4	Ar	128	0.0201	62.00	0.04	60.00	-98.00	H2	100	2	750	120	600	CVD	NH3	100	0.8	C2H2	50	1			1200	We used water assisted CVD with this sample. the annealing tempereature was 600C but the CVD temperature was 730C. The circular scale is devided to 25 lines. The water was opened with a scale 21
22F17b (similar 21D17g) WACVD.pdf	SS+gradientSS+AlN	Deposition of CNTs	17F1601	Failure	RF	Fe	4.7*10^-4	Ar	128	0.0201	62.00	0.04	60.00	-97.3	H2	100	2	750	120	600	CVD	NH3	100	0.8	C2H2	50	1			1200	We used water assisted CVD with this sample. the annealing tempereature was 600C but the CVD temperature was 730C. The circular scale is devided to 25 lines. The water was opened with a scale 21
23F17b (similar 21D17g) WACVD.pdf	SS+gradientSS+AlN	Deposition of CNTs	17F1601	Failure	RF	Fe	5.5*10^-4	Ar	128	0.0206	62.00	0.04	60.00	-95.9	H2	100	2	750	120	600	CVD	NH3	100	0.8	C2H2	50	1			1200	We used water assisted CVD with this sample. the annealing tempereature was 600C but the CVD temperature was 730C. The circular scale is devided to 25 lines
23F17c (similar 21D17g) WACVD.pdf	SS+gradientSS	Deposition of CNTs	17F2201	Failure	RF	Fe	5.3*10^-4	Ar	128	0.0206	62.00	0.04	60.00	-95.5	H2	100	2	750	120	600	CVD	NH3	100	0.8	C2H2	50	1			1200	We used water assisted CVD with this sample. the annealing tempereature was 600C but the CVD temperature was 730C. The circular scale is devided to 25 lines
26F17b (Fe calibration)-old target.pdf	Glass	Determination of deposition rate		Success	RF	Fe	4.6*10^-4	Ar	128	0.0203	900.00		60.00	-93.8																
26F17c (Fe calibration) old target.pdf	Glass	Determination of deposition rate		Success	RF	Fe	4.8*10^-4	Ar	128	0.0207	1800.00		60.00	-95.3, -94.5																
27F17c (similar 21D17g) WACVD.pdf	SS+gradientSS+AlN	Deposition of CNTs	17F2601	Failure	RF	Fe	5.5*10^-4	Ar	128	0.0206	62.00	0.04	60.00	-101.5	H2	100	2	750	120	600	CVD	NH3	100	0.8	C2H2	50	1			1200	We used water assisted CVD with this sample. the annealing tempereature was 600C but the CVD temperature was 730C. The circular scale is devided to 25 lines
13G17b (Al2O3).pdf	Si	Deposition of CNTs		Success	RF	Al	4.2*10^-4	Ar	8.6 (12.5)	0.0033	635.00	0.016	120.00	-105.00	Cleaning Al target: Flux Ar=42 sccm, Preactor=0.0102 mbar, time=600(s), Power=150W, Power in=150.96W, Powe ref=67.25W, Vbias=-117V															
17G17b (Al2O3-Grid).pdf	Al2O3	Deposition of CNTs		Failure	RF	Fe	5.1*10^-4	Ar	128	0.0200	45.00	0.044	60.00	-100.7	H2	100	2	750	120	600		NH3	100	0.8	C2H2	50	1			1800	We used water assisted CVD with this sample. the annealing tempereature was 600C but the CVD temperature was 700C. The circular scale is devided to 25 lines
18G17a (Al2O3).pdf	SS304+G SS304	Deposition of CNTs	17F2201	Success	RF	Al	2.7*10^-4	Ar	12.1 (17)	0.0043	600.00	0.016	120.00	-102.00	Cleaning Al target: Flux Ar=42 sccm, Preactor=0.0102 mbar, time=600(s), Power=120W, Power in=119.8W, Power ref=46.40W, Vbias=-102V															
18G17a (WACVD).pdf	SS304+G SS304+Al2O3	Deposition of CNTs	17F2201	Success	RF	Al	3.6*10^-4	Ar	128	0.0200	45.00	0.04	60.00	-101.00	H2	100	2	750	120	600		NH3	100	0.8	C2H2	50	1			1800	We used water assisted CVD with this sample. the annealing tempereature was 600C but the CVD temperature was 730C. The circular scale is devided to 25 lines
18G17b (Al2O3).pdf	SS304+G SS304	Deposition of CNTs		Success	RF	Al	2.7*10^-4	Ar	8.6 (12.5)	0.0033	600.00	0.016	120.00	-102.00	Cleaning Al target: Flux Ar=42 sccm, Preactor=0.0102 mbar, time=600(s), Power=120W, Power in=119.8W, Power ref=46.40W, Vbias=-102,V															
18G17b (WACVD).pdf	SS304+G SS304+Al2O3	Deposition of CNTs	17F2201	Success	RF	Al	3.5*10^-4	Ar	8.6 (12.5)	0.033	635.00	0.044	120.00	-101.00	H2	100	2	750	120	600		NH3	100	0.8	C2H2	50	1			1800	Cleaning Al target: Flux Ar=42 sccm, Preactor=0.0103 mbar, time=600(s), Power=120W, Power in=119.50W, Power ref=39.64W, Vbias=-105V Fe Sputtering: Flux Ar=90 sccm (via H2), Preactor=0.0202 mbar, time=45 (s), Power=60W, Power in=59.42W, Powe ref=0.83W, Vbias=-101.3V We used water assisted CVD with this sample. the annealing tempereature was 600C but the CVD temperature was 730C. The circular scale is devided to 25 lines The water was opened with a scale 21
21G17a (Al2O3-Grid).pdf	Al2O3	Deposition of CNTs		Success	RF	Fe	4.7*10^-4	Ar	90 (128)	0.02	45.00	0.044	60.00	-100.7	H2	100	2	750	120	600		NH3	100	0.8	C2H2	50	1			1800	We used water assisted CVD with this sample. The annealing temperature was 600C but the CVD temperature was 730C. The circular scale is divided to 25 lines
13I17c (test-Si).pdf	Si	Deposition of CNTs		Failure	RF	Fe	4.7*10^-4	Ar	65 (128)	0.019	45.00	0.044	60.00	-107.00	H2	100	2	750	120	600	RF	NH3	100	0.8	C2H2	50	1	50	-344	900	
15I17a (test-Si).pdf	Si	Deposition of CNTs		Success	RF	Fe	4.2*10^-4	Ar	66 (128)	0.0202	45.00	0.044	60.00	-116.00	H2	100	2	750	120	600	RF	NH3	100	0.8	C2H2	50	1	50	-303	900	
27I17a (DLC).pdf	Glass	Deposition of CNTs		Success			3.4*10^-4														RF	CH4	40	0.3				100	-508	600	
27I17b (DLC).pdf	Glass	Deposition of CNTs		Failure			4.4*10^-4														RF	CH4 (C2H2 ch.)	50 (mfc 80)	0.5				120	-1114	600	

Sample code	Substrate	Objective	Sample code (PEDRO)	Result	Catalyst Deposition										CNTs growth																	General comments
					Plasma source	Target	Previous vacuum (Pa)	Gas 1	Flux (sccm)	Pressure reactor (mbar)	Time (s)	Deposition rate (nm/s)	Power (W)	VBias (V)	Gas	Flux (sccm)	P (mbar)	Ramp time (s)	Hold time (s)	Tfinal (ºC)	Plasma source	Gas 1	Flux (sccm)	Pressure (mbar)	Gas 2	Flux (sccm)	Pressure (mbar)	Power (W)	VBias (V)	Deposition time (s)	
27I17c (DLC).pdf	SS304+G-SS304+AlN	Deposition of CNTs	17F2701	Failure			3.4*10^-4													RF	CH4 (C2H2 ch.)	50 (mfc 80)	0.5				120	-1145	600	
27I17d (DLC).pdf	SS304+G-SS304+AlN	Deposition of CNTs	17F2701	Success			3.4*10^-4													RF	CH4 (C2H2 ch.)	40 (mfc 64.7)	0.3				100	-1223	600	
04J17a (Al2O3).pdf	Al2O3	Other		Success	RF	Al	2.7*10^-4	Ar	12.1 (17)	0.0043	600.00	0.016	120.00	-102.00	Cleaning Al target: Flux Ar=42 sccm, Preactor=0.0098 mbar, time=600(s), Power=120W, Power in=120.62W, Power ref=45.50W, Vbias=-101,V																
04J17a (Al2O3-Grid).pdf	Al2O3	Deposition of CNTs		Success	RF	Fe	3.5*10^-4	Ar	128	0.0198	90s / 4nm	0.047	60.00	-99.00	H2	100	2	750	120	600		H2	100	0.8	C2H2	50	1			900	H plasma under P=1mbar, 50 sccm, and 100W, for 5 min. Load: 5.98 /Tune: 9.72. Bias voltage (V): -380V Difussion barrier of 10nm of Al2O3. We used water assisted CVD with this sample. The annealing temperature was 600C but the CVD temperature was 730C. The circular scale is divided to 25 lines. The water was opened with a scale 21
04J17b (Shahzad).pdf	Si+Al2O3+Ni	Deposition of CNTs		Success			3.5*10^-4								H2	50	0.5	1200	300	680	RF	H2	100	0.8	C2H2	50	1	50	322	900	The H2 plasma was done during the annealing process under P=0.5mbar, 50 sccm, and 30W using another RF power supply. On Si: 10nm of Al2O3 and 10nm Ni
06J17a (Al2O3).pdf	Al2O3	Other		Success	RF	Al	2.7*10^-4	Ar	12.1 (17)	0.0043	600.00	0.016	120.00	-94.00	Cleaning Al target: Flux Ar=42 sccm, Preactor=0.0098 mbar, time=600(s), Power=120W, Power in=118.87W, Power ref=48.62W, Vbias=-100V																
06J17a (Al2O3-Grid).pdf	Al2O3	Deposition of CNTs		Success	RF	Fe	3.4*10^-4	Ar	128	0.0198	64s / 3nm	0.047	60.00	-105.00	H2	100	2	750	120	600		H2	100	0.8	C2H2	50	1			900	H plasma under P=1mbar, 50 sccm, and 100W, for 5 min. Load: 6.44 /Tune: 9.72. Bias voltage (V): -272 (unstable plasma) H plasma under P=1mbar, 50 sccm, and 90W, for 5 min. Load: 5.98 /Tune: 9.72. Bias voltage (V): -401V Difussion barrier of 10nm of Al2O3. We used water assisted CVD with this sample. The annealing temperature was 600C but the CVD temperature was 730C. The circular scale is divided to 25 lines The water was opened with a scale 21
10J17a (Al2O3).pdf	Al2O3	Other		Success	RF	Al	1.9*10^-4	Ar	12.1 (17)	0.0043	600.00	0.016	120.00	-97.00	Cleaning Al target: Flux Ar=42 sccm, Preactor=0.0098 mbar, time=600(s), Power=120W, Power in=118.87W, Power ref=48.62W, Vbias=-101V																
10J17a (Al2O3-Grid).pdf	Al2O3	Deposition of CNTs		Success	RF	Fe	5.5*10^-4	Ar	67 (128)	0.0198	64s / 3nm	0.047	60.00	-105.00	H2	100	2	750	120	600		H2	100	0.8	C2H2	50	1			900	H plasma under P=1mbar, 50 sccm, and 90W, for 5 min. Load: 5.98 /Tune: 9.72. Bias voltage (V): -408 Difussion barrier of 10nm of Al2O3. We used water assisted CVD with this sample. The annealing temperature was 600C but the CVD temperature was 730C. The circular scale is divided to 25 lines. The water was opened with a scale 21
16J17a (Al2O3).pdf	SS304 (grid)	Other		Success	RF	Al	1.9*10^-4	Ar	12.1 (17)	0.0043	1250.00	0.016	120.00	-93.00	Cleaning Al target: Flux Ar=42 sccm, Preactor=0.0098 mbar, time=600(s), Power=120W, Power in=118.87W, Power ref=48.62W, Vbias=-102V																
16J17a (SS304-Grid).pdf	SS304 (grid)	Deposition of CNTs		Success	RF	Fe	5.5*10^-4	Ar	67 (128)	0.0198	64s / 3nm	0.047	60.00	-104.7	H2	100	2	750	120	600	RF	H2	100	0.8	C2H2	50	1	50	-389	900	N2 plasma treatment: bias voltage=-602V, Pressure= 0.1mbar, RF power=75W, Plasma time= 120s, P(inc)= 76, P(ref)= 0.04
17J17a (AlN).pdf	Si wafer	Other		Success	RF	Al	2.6*10^-4	Ar	12.1 (17)	0.0043	1250.00	0.016	120.00	-93.00	Cleaning Al target: Flux Ar=42 sccm, Preactor=0.0098 mbar, time=600(s), Power=120W, Power in=119.35W, Power ref=42.40W, Vbias=-106V																
18J17a (Al2O3).pdf	SS304 (grid)	Other		Success	RF	Al	1.9*10^-4	Ar	12.1 (17)	0.0043	1250.00	0.016	120.00	-93.00	Cleaning Al target: Flux Ar=42 sccm, Preactor=0.0098 mbar, time=600(s), Power=120W, Power in=120.31W, Power ref=39.98W, Vbias=-105.8V																
18J17a (SS304-Grid).pdf	SS304 (grid)	Deposition of CNTs		Success	RF	Fe	5.5*10^-4	Ar	128	0.0198	64s / 3nm	0.047	60.00	-104.7	H2	100	2	750	120	600	RF	H2	100	0.8	C2H2	50	1	50	-389	900	N2 plasma treatment: bias voltage=-602V, Pressure= 0.1mbar, RF power=75W, Plasma time= 120s, P(inc)= 76, P(ref)= 0.04, Load=5.42, Tune= 0.4
19J17a (Al2O3-Grid).pdf	Al2O3	Deposition of CNTs		Success	RF	Fe	4.0*10^-4	Ar	128	0.02	85.00	0.047	60.00	-103.5	H2	100	2	750	120	600		NH3	100	0.8	C2H2	50	1			1800	H plasma under P=1mbar, 50 sccm, and 90W, for 5 min. Load: 6 /Tune: 9.70. Bias voltage (V): -440 We used water assisted CVD with this sample. The annealing temperature was 600C but the CVD temperature was 730C. The circular scale is divided to 25 lines.The water was opened with a scale 21
24J17a (H2O Plasma)-IBEC.pdf	Si	H2O Plasma		Success	RF	Fe	4.8*10^-4	Ar	128	0.0203	64 (3nm)	0.047	60.00	-106.4	H2	100	2	750	120	680	RF	NH3	100	0.8	C2H2	50	1	50	354	900	Water plasma treatment: bias voltage=-275V, Pressure= 135 Pa (1,35mbar), RF power=75W, Plasma time= 120s, P(inc)= 73.82, P(ref)= 16.20,
25J17a (similar15B17d)-ICMAB.pdf	Si+AlN	Deposition of CNTs	17J2401	Success	RF	Fe	3.4*10^-4	Ar	128	0.0208	64s/ 3nm	0.047	60.00	-108.3	H2	100	2	750	120	680	RF	NH3	100	0.8	C2H2	50	1	50	-334	900	
30J17a (similar15B17d)-ICMAB.pdf	Si+AlN	Deposition of CNTs		Success	RF	Fe	3.4*10^-4	Ar	128	0.0208	64s/ 3nm	0.047	60.00	-108.1	H2	100	2	750	120	680	RF	NH3	100	0.8	C2H2	50	1	50	-334	1200	

Sample code	Substrate	Objective	Sample code (PEDRO)	Result	Catalyst Deposition										CNTs growth																	General comments
					Plasma source	Target	Previous vacuum (Pa)	Gas 1	Flux (sccm)	Pressure reactor (mbar)	Time (s)	Deposition rate (nm/s)	Power (W)	VBias (V)	Gas	Flux (sccm)	P (mbar)	Ramp time (s)	Hold time (s)	Tfinal (ºC)	Plasma source	Gas 1	Flux (sccm)	Pressure (mbar)	Gas 2	Flux (sccm)	Pressure (mbar)	Power (W)	VBias (V)	Deposition time (s)	
02K17a (Al2O3-Grid).pdf	Al2O3	Deposition of CNTs		Success	RF	Fe	3.7*10^-4	Ar	128	0.02	85.00	0.047	60.00	-105.5	H2	100	2	750	120	600		NH3	100	0.8	C2H2	50	1			1800	
															H plasma under P=1mbar, 50 sccm, and 90W, for 5 min. Load: 6 /Tune: 9.70. Bias voltage (V): -406V/ Pref=11.39(W)/Pinc=90.04(W) We used water assisted CVD with this sample. The annealing temperature was 600C but the CVD temperature was 730C. The circular scale is divided to 25 lines.The water was opened with a scale 21																	
02K17b (Ash).pdf	SS mesh+AlN	Deposition of CNTs	17K0201	Failure	RF	Fe	6.2*10^-4	Ar	128	0.0201	64.00	0.047	60.00	-105	H2	100	2	750	120	680	CVD	NH3	100	0.8	C2H2	50	1	50		900	
03K17a(Ash).pdf	SS mesh+AlN	Deposition of CNTs	17K0201	Failure	RF	Fe	4.8*10^-4	Ar	128	0.0201	64.00	0.047	60.00	-106.5/-105.7	H2	100	2	750	120	680	CVD	NH3	100	0.8	C2H2	50	1	60	1.006	900	
03K17b(ICMAB).pdf	Si+G-SS304+AlN	Deposition of CNTs	17K0301	Success	RF	Fe	5.9*10^-4	Ar	128	0.0201	64.00	0.047	60.00	-103.8/-103.7	H2	100	2	750	120	680	CVD	NH3	100	0.8	C2H2	50	1	60	-350	600	
03K17c(Ash).pdf	SS mesh+Al2O3	Deposition of CNTs	17K0202	Success	RF	Fe	5.9*10^-4	Ar	128	0.0201	64.00	0.047	60.00	-103.7/-103.4	H2	100	2	750	120	680	CVD	NH3	100	0.8	C2H2	50	1	50	-310	900	
06K17a(ICMAB).pdf	Si+G-SS304+AlN	Deposition of CNTs	17K0301	Failure	RF	Fe	2.6*10^-4	Ar	128	0.019	64.00	0.047	60.00	-106.8	H2	100	2	750	120	680	CVD	NH3	100	0.8	C2H2	50	1	60	1.022	600	
06K17b(Ash).pdf	SS mesh+Al2O3	Deposition of CNTs	17K0601	Success	RF	Fe	4.9*10^-4	Ar	128	0.0206	64.00	0.047	60.00	-106.3/-105.8	H2	100	2	750	120	680	CVD	NH3	100	0.8	C2H2	50	1	50	-332	900	
06K17c(Ash).pdf	SS mesh+Al2O3	Deposition of CNTs	17K0601	Success	RF	Fe	4.3*10^-4	Ar	128	0.0197	64.00	0.047	60.00	-106.8	H2	100	2	750	120	680	CVD	NH3	100	0.8	C2H2	50	1	50	-332	900	
08K17a(ICMAB).pdf	Si+G-SS304+AlN	Deposition of CNTs	17K0301	Success	RF	Fe	2.7*10^-4	Ar	128	0.0198	64.00	0.047	60.00	-106.4/-105.6	H2	100	2	750	120	680	CVD	NH3	100	0.8	C2H2	50	1	50	1.013	300	PECVD process was stable.
08K17b(ICMAB).pdf	Si+G-SS304+AlN	Deposition of CNTs	17K0301	Success	RF	Fe	3.7*10^-4	Ar	128	0.0193	64.00	0.047	60.00	-104.6/-104.1	H2	100	2	750	120	680	CVD	NH3	100	0.8	C2H2	50	1	50	1.009	300	PECVD process was stable.
08K17c(ICMAB).pdf	Si+G-SS304+AlN	Deposition of CNTs	17K0301	Success	RF	Fe	4.2*10^-4	Ar	128	0.0193	64.00	0.047	60.00	-104.1/-103.7	H2	100	2	750	120	680	CVD	NH3	100	0.8	C2H2	50	1	50	1.015	300	PECVD process was stable.
08K17d(ICMAB).pdf	Si+G-SS304+AlN	Deposition of CNTs	17K0301	Success	RF	Fe	5.8*10^-4	Ar	128	0.0193	64.00	0.047	60.00	-104.1/-103.6	H2	100	2	750	120	680	CVD	NH3	100	0.8	C2H2	50	1	50	0.997	300	PECVD process was stable.
09K17a(Ash-AlN).pdf	SS mesh+AlN	Deposition of CNTs	17K0201	Failure	RF	Fe	3.6*10^-4	Ar	128	0.0197	85 (4nm)	0.047	60.00	-106.5/-105.4	H2	100	2	750	120	680	CVD	NH3	100	0.8	C2H2	50	1	50	-332	600	PECVD process was unstable.
09K17b(Fe calibration).pdf	Si wafer	Deposition of CNTs		Success	RF	Fe	8.5*10^-4	Ar	128	0.0197	600.00		60.00	-103.9/																	PECVD process was unstable.
09K17c(Ash-Al2O3).pdf	SS mesh+Al2O3	Deposition of CNTs	17K0202	Success	RF	Fe	3.0*10^-4	Ar	128	0.0201	64 (3nm)	0.047	60.00	-103.7/-103.6	H2	100	2	750	120	680	CVD	NH3	100	0.8	C2H2	50	1	50	-327	1200	PECVD process was unstable.
10K17a(Ash-Al2O3).pdf	SS mesh+Al2O3	Deposition of CNTs	17K1001	Success	RF	Fe	4.2*10^-4	Ar	128	0.0207	64 (3nm)	0.047	60.00	-104.8/-104.0	H2	100	2	750	120	680	RF	NH3	100	0.8	C2H2	50	1			1200	CVD process was unstable.
10K17b(Ash-Al2O3).pdf	SS mesh+Al2O3	Deposition of CNTs	17K1001	Success	RF	Fe	3.2*10^-4	Ar	128	0.0207	64 (3nm)	0.047	60.00	-104.4/-103.7	H2	100	2	750	120	680	RF	NH3	100	0.8	C2H2	50	1	50	-309	1200	PECVD process was stable but the reflected power was high.
13K17a(Si wafer a-b-c-d).pdf	Si+AlN (a-b-c-d)	Deposition of CNTs	17K1002	Success	RF	Fe	1.9*10^-4	Ar	128	0.0213	64.00	0.047	60.00	-104.2	H2	100	2	750	120	680	CVD	NH3	100	0.8	C2H2	50	1	50	-310	300	PECVD process was stable.
13K17b(Si wafer a-b-c-d).pdf	Si+AlN (a-b-c-d)	Deposition of CNTs	17K1301	Success	RF	Fe	5.2*10^-4	Ar	128	0.0213	64.00	0.047	60.00	-104.3/-103.2	H2	100	2	750	120	680	CVD	NH3	100	0.8	C2H2	50	1	50	0.875	300	PECVD process was stable. The bias voltage was low when starting the process
14K17a(Si wafer Al).pdf	Si+Al	Annealing	17K1401	Success			5.2*10^-4								H2	100	2	300	120	300											
16K17a(Ash-Al2O3).pdf	SS mesh+Al2O3	Deposition of CNTs	17K1402	Success	RF	Fe	2.2*10^-4	Ar	128	0.0214	64 (3nm)	0.047	60.00	-105.3/-104.4	H2	100	2	750	120	680	RF	NH3	100	0.8	C2H2	50	1	50	0.389	1200	PECVD process was unstable.
17K17a(Si wafer Al).pdf	Si+Al	Annealing	17K1401	Success			2.2*10^-4								H2	100	2	120	600	400											
23K17a(SS+G-ss+AlN).pdf	SS+G-SS+AlN	Deposition of CNTs		Success	RF	Fe	5.3*10^-4	Ar	128	0.0193	64.00	0.047	60.00		H2	100	2	750	120	680	CVD	NH3	100	0.8	C2H2	50	1	50	-395	300	PECVD process was stable. Sputtering process was unstable, high reflected power.
23K17b(Si wafer-test).pdf	Si wafer	Deposition of CNTs		Success	RF	Fe	5.3*10^-4	Ar	128	0.0193	64.00	0.047	60.00	-106.5	H2	100	2	750	120	680	CVD	NH3	100	0.8	C2H2	50	1	50	-395	300	PECVD process was stable. Sputtering process was unstable, high reflected power.

Sample code	Substrate	Objective	Sample code (PEDRO)	Result	Catalyst Deposition										CNTs growth																	General comments
					Plasma source	Target	Previous vacuum (Pa)	Gas 1	Flux (sccm)	Pressure reactor (mbar)	Time (s)	Deposition rate (nm/s)	Power (W)	VBias (V)	Gas	Flux (sccm)	P (mbar)	Ramp time (s)	Hold time (s)	Tfinal (ºC)	Plasma source	Gas 1	Flux (sccm)	Pressure (mbar)	Gas 2	Flux (sccm)	Pressure (mbar)	Power (W)	VBias (V)	Deposition time (s)	
24K17a (Al2O3-Grid).pdf	Al2O3-grid	Deposition of CNTs		Failure	RF	Fe	4.4*10^-4	Ar	128	0.021	21 (1nm)	0.047	60.00	-109.7/108.8	H2	100	2	750	120	600		NH3	100	0.8	C2H2	50	1			1800	
															H plasma under P=1mbar, 50 sccm, and 90W, for 300(s). Load: 3.8 /Tune: 9.73. Bias voltage (V): -410/-442V. Pref=3.94(W)/Pinc=89.29(W) We used water assisted CVD with this sample. The annealing temperature was 600C but the CVD temperature was 730C. The circular scale is divided to 25 lines The water was opened with a scale 21																		
24K17b (Al2O3-Grid).pdf	Al2O3-grid	Deposition of CNTs		Success	RF	Fe	4.4*10^-4	Ar	128	0.0201	43 (2nm)	0.047	60.00	-107.0/105.3	H2	100	2	750	120	600		H2	100	0.8	C2H2	50	1			1800	
															H plasma under P=1mbar, 50 sccm, and 90W, for 300(s). Load: 3.8 /Tune: 9.73. Bias voltage (V): -413/-454V. Pref=8.89(W)/Pinc=89.41(W) We used water assisted CVD with this sample. The annealing temperature was 600C but the CVD temperature was 730C. The circular scale is divided to 25 lines The water was opened with a scale 21. (Program Ultra_v2, with H2)																		
28K17a (Al2O3-Grid).pdf	Al2O3-grid	Deposition of CNTs		Success	RF	Fe	3.0*10^-4	Ar	128	0.0201	43 (2nm)	0.047	60.00	-107.0/105.3	H2	100	2	750	120	600		H2	100	0.8	C2H2	50	1			3600	
															H plasma under P=1mbar, 50 sccm, and 90W, for 300(s). Load: 3.8 /Tune: 9.73. Bias voltage (V): -413/-454. Pref=8.89(W)/Pinc=89.41(W). We used water assisted CVD with this sample. The annealing temperature was 600C but the CVD temperature was 730C. The circular scale is divided to 25 lines. The water was opened with a scale 21.(Program Ultra_v2, with H2)																		
28K17b (Shahzad).pdf	Si	Deposition of CNTs		Failure	RF	Fe	4.1*10^-4	Ar	128	0.0208	64s/ 3nm	0.047	60.00	-106.2/-105.1	H2	100	2	750	120	680	RF	NH3	100	0.8	C2H2	50	1	50	-562	10	
28K17c (Shahzad).pdf	Si	Deposition of CNTs		Success	RF	Fe	3.4*10^-4	Ar	128	0.0208	64s/ 3nm	0.047	60.00	-105.00	H2	100	2	750	120	680	RF	NH3	100	0.8	C2H2	50	1	50	-530	10	
28K17d (Shahzad).pdf	Si	Deposition of CNTs		Success	RF	Fe	3.4*10^-4	Ar	128	0.0208	64s/ 3nm	0.047	60.00	-105.8	H2	100	2	750	120	680	RF	NH3	100	0.8	C2H2	50	1	50	-570	5	
29K17a(Ash-Al2O3).pdf	SS mesh+Al2O3	Deposition of CNTs	17K2802	Success	RF	Fe	2.9*10^-4	Ar	128	0.0207	64 (3nm)	0.047	60.00	-106.3/-106.5	H2	100	2	750	120	680	RF	NH3	100	0.8	C2H2	50	1	50	-309	1200	PECVD process was unstable. The amonia tank was empty.
29K17b (Si wafer+Al2O3 pattern).pdf	Si wafer+Al2O3 pattern	Deposition of CNTs		Success	RF	Fe	5.4*10^-4	Ar	128	0.0201	43 (2nm)	0.047	60.00	-103.5	H2	100	2	750	120	600		H2	100	0.8	C2H2	50	1			600	
															We used water assisted CVD with this sample. The annealing temperature was 600C but the CVD temperature was 730C. The circular scale is divided to 25 lines The water was opened with a scale 21 (Program Ultra_v2, with H2)																		
01L17a(Ash-Al2O3).pdf	SS mesh+Al2O3	Deposition of CNTs	17K2802	Success	RF	Fe	2.9*10^-4	Ar	128	0.0207	64 (3nm)	0.047	60.00	-107/-106.9	H2	100	2	750	120	600		NH3	100	0.8	C2H2	50	1			1200	
															We used water assisted CVD with this sample. The annealing temperature was 600C but the CVD temperature was 730C. The circular scale is divided to 25 lines. The isopropanol was opened with a scale 21 (Program Ultra_v2, with H2)																		
01L17b (graphite sheet).pdf	graphite sheet	Deposition of CNTs		Failure	RF	Fe	6.2*10^-4	Ar	128	0.0201	43 (2nm)	0.047	60.00	-105.1/103.6	H2	100	2	750	120	600		H2	100	0.8	C2H2	50	1			3600	
															H plasma under P=1mbar, 50 sccm, and 90W, for 300(s). Load: 3.83 /Tune: 9.73. Bias voltage (V): -423/-464V. Pref=1.26(W)/Pinc=90.06(W) We used water assisted CVD with this sample. The annealing temperature was 600C but the CVD temperature was 730C.The circular scale is divided to 25 lines. The water was opened with a scale 21 (Program Ultra_v2, with H2)																		
05L17a (CNTs+Si annealing).pdf	CNTs+Si	Annealing		Success			1.6*10^-4											750	7200	680												
12L17a (graphite sheet).pdf	graphite sheet	Deposition of CNTs		Failure	RF	Fe	7.6*10^-4	Ar	135	0.0194	64 (3nm)	0.047	60.00	-106.6/104.3	H2	100	2	750	120	600		H2	100	0.8	C2H2	50	1			3600	
															H plasma under P=1mbar, 50 sccm, and 90W, for 300(s). Load: 3.83 /Tune: 9.73. Bias voltage (V): -406/-485. Pref=1.26(W)/Pinc=90.06(W) We used water assisted CVD with this sample. The annealing temperature was 600C but the CVD temperature was 730C. The circular scale is divided to 25 lines The water was opened with a scale 21 (Program Ultra_v2, with H2)																		
12L17b (Si wafer+Al2O3 pattern).pdf	Si wafer+Al2O3 pattern	Deposition of CNTs	17L1201	Success	RF	Fe	3.7*10^-4	Ar	135	0.0201	43 (2nm)	0.047	60.00	-103.5/-104.2	H2	100	2	750	120	600		H2	100	0.8	C2H2	50	1			600	
															We used water assisted CVD with this sample. The annealing temperature was 600C but the CVD temperature was 730C. The circular scale is divided to 25 lines																		
15L17a (graphite sheet).pdf	graphite sheet	Deposition of CNTs		Failure	RF	Fe	5.9*10^-4	Ar	7	0.021	64 (3nm)	0.047	60.00	-107.3/105.6	H2	100	2	750	120	600		H2	100	0.8	C2H2	50	1			600	
															H plasma under P=1mbar, 50 sccm, and 90W, for 300(s). Load: 3.80 /Tune: 9.12. Bias voltage (V): -400/-440. Pref=1.26(W)/Pinc=90.06(W) DLC under P=0.3mbar, 40 sccm (CH4 via C2H2), and 100W, for 53(s). Load: 3.82 /Tune: 9.69. Bias voltage (V): -633/-637 Pref=16.4(W)/Pinc=99.75(W) We used water assisted CVD with this sample. The annealing temperature was 600C but the CVD temperature was 730C. The circular scale is divided to 25 lines The water was opened with a scale 21 (Program Ultra_v2, with H2)																		
18L17a (Arevik-Shahzad).pdf	Si	Deposition of CNTs		Success	RF	Fe	3.6*10^-4	Ar	7	0.0205	64s/ 3nm	0.047	60.00	-105.2/-104.4	H2	100	2	750	120	680	RF	NH3	100	0.8	C2H2	50	1	50	-400	10	
19L17a (CNTs+Si annealing).pdf	CNTs+Si	Annealing		Success			1.9*10^-4											750	7200	680												
09A18a (graphite sheet).pdf	graphite sheet	Deposition of CNTs		Success	RF	Fe	5.9*10^-4	Ar	135	0.021	64 (3nm)	0.047	60.00	-105.1/103.8	H2	100	2	750	120	600	RF	NH3	100	0.8	C2H2	50	1	50	-382	600	
															H plasma under P=1mbar, 50 sccm, and 90W, for 300(s). Load: 3.80 /Tune: 9.25. Bias voltage (V): -407/-442 Pref=0.28(W)/Pinc=89.64(W)																		
01C18a (PECVD-CNTs-Si wafer).pdf	Si	Deposition of CNTs		Success	RF	Fe	4.2*10^-4	Ar	135	0.0202	64 (3nm)	0.047	60.00	-106.0/-104.6	H2	100	2	750	120	680		NH3	100	0.8	C2H2	50	1	50	-398V	900	

Sample code	Substrate	Objective	Sample code (PEDRO)	Result	Catalyst Deposition										CNTs growth																	General comments
					Plasma source	Target	Previous vacuum (Pa)	Gas 1	Flux (sccm)	Pressure reactor (mbar)	Time (s)	Deposition rate (nm/s)	Power (W)	VBias (V)	Gas	Flux (sccm)	P (mbar)	Ramp time (s)	Hold time (s)	Tfinal (ºC)	Plasma source	Gas 1	Flux (sccm)	Pressure (mbar)	Gas 2	Flux (sccm)	Pressure (mbar)	Power (W)	VBias (V)	Deposition time (s)		
23C18a (SS304+G-SS304+CNTs).pdf	SS304+G-SS304+AlN	Deposition of CNTs	17F2601	Failure	RF	Fe	2.5*10^-4	Ar	135	0.0202	78 (3nm)	0.0383	60.00	-106.1/-105	H2	100	2	750	120	730	RF	NH3	100	0.8	C2H2	50	1	50	0.993	900		NH3 flow: 13.8% (operation test)
02D18a (SS304+CNTs).pdf	SS304	Deposition of CNTs		Success											H2	100	2	750	120	680	RF	NH3	100	0.8	C2H2	50	1	50	-407	600		
															Vacuum: 3.8*10^-4 (Pa) Annealing: Tfinal (ºC)730// H2(sccm)100/ P(mbar)2// Ramp time(s)900/ Hold time(s)30/ H2(sccm)50/ P(mbar)0.8/ Purge time(s)30// RFpower(W)90/ Ar(sccm)50/ Base pressure(mbar)1/ Time(s)300// Load: 3.88 /Tune: 9.72//Bias voltage (V):-570/-585 //Pref=3.72(W)/Pinc=89.7(W) PROGRAM: Ultra_v1-H2-Ar//FILE: c:\temp\02d18aht.txt																		
03D18a (SS304+CNTs).pdf	SS304	Deposition of CNTs		Success											H2	100	2	750	120	680		NH3	100	0.8	C2H2	50	1			600		
															Vacuum: 4.4*10^-4 (Pa) Annealing: Tfinal (ºC)730// H2(sccm)100/ P(mbar)2// Ramp time(s)900/ Hold time(s)30/ H2(sccm)50/ P(mbar)0.8/ Purge time(s)30// RFpower(W)90/ Ar(sccm)50/ Base pressure(mbar)1/ Time(s)300// Load: 4.15 /Tune: 9.72//Bias voltage (V):-569/-570 //Pref=0.68(W)/Pinc=89.8(W) PROGRAM: Ultra_v1-H2-Ar//FILE: c:\temp\03d18aht.txt We used water assisted CVD with this sample. the annealing tempereature was 600C but the CVD temperature was 730C. The circular scale is devided to 25 lines The water was opened with a scale 21																		
06D18a (SS304+CNTs).pdf	SS304	Deposition of CNTs		Success			7.6*10^-4								H2	100	2	750	120	730	RF	NH3	100	0.8	C2H2	50	1	50	1.018	600		
															Vacuum: 4.8*10^-4 (Pa) Annealing: Tfinal (ºC)730// H2(sccm)100/ P(mbar)2// Ramp time(s)900/ Hold time(s)30/ H2(sccm)50/ P(mbar)0.8/ Purge time(s)30// RFpower(W)90/ Ar(sccm)50/ Base pressure(mbar)1/ Time(s)300// Load: 3.88 /Tune: 9.72//Bias voltage (V):-545/-565 //Pref=0.737(W)/Pinc=89.7(W) PROGRAM: Ultra_v1-H2-Ar//FILE: c:\temp\06d18aht.txt																		
09D18a (ref 15C17b)(SS304+GSS304+AlN).pdf	SS+SSgradient+AlN	Deposition of CNTs	18D0501-3	Success	RF	Fe	4.7*10^-4	Ar	135	0.0199	78 (3nm)	0.0383	60.00	-104.1/-103.6	H2	100	2	750	120	730	RF	NH3	100	0.8	C2H2	50	1	50	1.064	900		
18D18a (SS304+CNTs).pdf	SS304	Deposition of CNTs		Success			5.9*10^-4								H2	100	2	750	120	730	RF	NH3	100	0.8	C2H2	50	1	50	1.041	600		
															Vacuum: 4.5*10^-4 (Pa) Annealing: Tfinal (ºC)400// H2(sccm)100/ P(mbar)2// Ramp time(s)494 / Hold time(s)30 / H2(sccm)50 / P(mbar)0.8 / Purge time(s)30// RFpower(W)90/ Ar(sccm)50/ Base pressure(mbar)1/ Time(s)300// Load: 3.92 /Tune: 9.15//Bias voltage (V):-378/-420 //Pref=2(W)/Pinc=90(W) PROGRAM: Ultra_v1-H2-Ar//FILE: c:\temp\18d18aht.txt																		
18D18b (SS304+CNTs).pdf	SS304	Deposition of CNTs		Success			5.9*10^-4								H2	100	2	750	120	730	RF	NH3	100	0.8	C2H2	50	1	50	1.026	600		
															Vacuum: 4.4*10^-4 (Pa) Annealing: Tfinal (ºC)500// H2(sccm)100/ P(mbar)2// Ramp time(s)617 / Hold time(s)30 / H2(sccm)50 / P(mbar)0.8 / Purge time(s)30// RFpower(W)90/ Ar(sccm)50/ Base pressure(mbar)1/ Time(s)300// Load: 4.12/Tune: 9.15//Bias voltage (V):-454/-470 //Pref=0.291(W)/Pinc=89.6(W) PROGRAM: Ultra_v1-H2-Ar//FILE: c:\temp\18d18bht.txt																		
18D18c (SS304+CNTs).pdf	SS304	Deposition of CNTs		Success			5.9*10^-4								H2	100	2	750	120	730	RF	NH3	100	0.8	C2H2	50	1	50	1.034	600		
															Vacuum: 5.5*10^-4 (Pa) Annealing: Tfinal (ºC)600// H2(sccm)100/ P(mbar)2// Ramp time(s)741 / Hold time(s)30 / H2(sccm)50 / P(mbar)0.8 / Purge time(s)30// RFpower(W)90/ Ar(sccm)50/ Base pressure(mbar)1/ Time(s)300// Load: 4.04/Tune: 9.38//Bias voltage (V):-508/-540 //Pref=2.88(W)/Pinc=89(W) PROGRAM: Ultra_v1-H2-Ar//FILE: c:\temp\18d18cht.txt																		
19F18a (SS304+CNTs).pdf	SS304	Deposition of CNTs		Success			7.6*10^-4								H2	100	2	750	120	730	RF	NH3	100	0.8	C2H2	50	1	50	1.014	600		
															Vacuum: 5.5*10^-4 (Pa) Annealing: Tfinal (ºC)730// H2(sccm)100/ P(mbar)2// Ramp time(s)900/ Hold time(s)30/ H2(sccm)50/ P(mbar)0.8/ Purge time(s)30// RFpower(W)90/ Ar(sccm)50/ Base pressure(mbar)1/ Time(s)300// Load: 4.16 /Tune: 9.72//Bias voltage (V):-590/-535 //Pref=0.737(W)/Pinc=90.1(W) PROGRAM: Ultra_v1-H2-Ar//FILE: c:\temp\19f18aht.txt																		
19F18b (SS304+CNTs).pdf	SS304	Deposition of CNTs		Success			5.9*10^-4								H2	100	2	750	120	730	RF	NH3	100	0.8	C2H2	50	1	50	1.014	600		
															Vacuum: 6.3*10^-4 (Pa) Annealing: Tfinal (ºC)730// H2(sccm)100/ P(mbar)2// Ramp time(s)183/ Hold time(s)30/ H2(sccm)50/ P(mbar)0.8/ Purge time(s)30// RFpower(W)90/ Ar(sccm)50/ Base pressure(mbar)1/ Time(s)400// Load: 4.16 /Tune: 9.72//Bias voltage (V):-500/-553 //Pref=0.633(W)/Pinc=89.7(W) PROGRAM: Ultra_v1-H2-Ar//FILE: c:\temp\19f18bht.txt WACVD: during the last 10min. 15 (scale manual valve)																		
20F18a (SS304+CNTs).pdf	SS304	Deposition of CNTs		Success			4.9*10^-4								H2	100	2	750	120	730	RF	NH3	100	0.8	C2H2	50	1	50	1.025	600		
															Vacuum: 3.8*10^-4 (Pa) Annealing: Tfinal (ºC)730// H2(sccm)100/ P(mbar)2// Ramp time(s)900/ Hold time(s)30/ H2(sccm)50/ P(mbar)0.8/ Purge time(s)30// RFpower(W)90/ Ar(sccm)50/ Base pressure(mbar)1/ Time(s)400// Load: 4.2 /Tune: 9.7//Bias voltage (V):-562/-544 //Pref=1(W)/Pinc=89.7(W) PROGRAM: Ultra_v1-H2-Ar//FILE: c:\temp\20f18aht.txt																		
20F18b (SS304+CNTs).pdf	SS304	Deposition of CNTs		Failure			5.5*10^-4								H2	100	2	750	120	730	RF	NH3	100	0.8	C2H2	50	1	60	1.011	600		
															Vacuum: 5.1*10^-4 (Pa) Annealing: Tfinal (ºC)730// H2(sccm)100/ P(mbar)2// Ramp time(s)900/ Hold time(s)30/ H2(sccm)50/ P(mbar)0.8/ Purge time(s)30// RFpower(W)90/ Ar(sccm)50/ Base pressure(mbar)1/ Time(s)300// Load: 3.78 /Tune: 7.7//Bias voltage (V):-202 //Pref=9.9(W)/Pinc=90.5(W) PROGRAM: Ultra_v1-H2-Ar//FILE: c:\temp\20f18bht.txt PROBLEMS WITH THE BIAS VOLTAGE																		

Sample code	Substrate	Objective	Sample code (PEDRO)	Result	Catalyst Deposition										CNTs growth																	General comments
					Plasma source	Target	Previous vacuum (Pa)	Gas 1	Flux (sccm)	Pressure reactor (mbar)	Time (s)	Deposition rate (nm/s)	Power (W)	VBias (V)	Gas	Flux (sccm)	P (mbar)	Ramp time (s)	Hold time (s)	Tfinal (ºC)	Plasma source	Gas 1	Flux (sccm)	Pressure (mbar)	Gas 2	Flux (sccm)	Pressure (mbar)	Power (W)	VBias (V)	Deposition time (s)					
20F18c (SS304+CNTs).pdf	SS304	Deposition of CNTs		Failure			7.5*10^-4								H2	100	2	750	120	730	RF	NH3	100	0.8	C2H2	50	1	60	1.007	600			
															Vacuum: 6.8*10^-4 (Pa) Annealing: Tfinal (ºC)730// H2(sccm)100/ P(mbar)2// Ramp time(s)900/ Hold time(s)30/ H2(sccm)50/ P(mbar)0.8/ Purge time(s)30// RFpower(W)90/ Ar(sccm)50/ Base pressure(mbar)1/ Time(s)300// Load: 4.1 /Tune: 9.7//Bias voltage (V):-675/-606 //Pref=5.12(W)/Pinc=89.7(W) PROGRAM: Ultra_v1-H2-Ar//FILE: c:\temp\20f18cht.txt																											
21F18a (SS304+CNTs).pdf	SS304	Deposition of CNTs		Failure			5.1*10^-4								H2	100	2	750	120	730	RF	NH3	100	0.8	C2H2	50	1	50	1.023	600			
															Vacuum: 5.5*10^-4 (Pa) Annealing: Tfinal (ºC)730// H2(sccm)100/ P(mbar)2// Ramp time(s)900/ Hold time(s)30/ H2(sccm)50/ P(mbar)0.8/ Purge time(s)30// RFpower(W)90/ Ar(sccm)50/ Base pressure(mbar)1/ Time(s)300// Load: 4.1 /Tune: 9.7//Bias voltage (V):-555/-593 //Pref=0.436(W)/Pinc=90.3(W) PROGRAM: Ultra_v1-H2-Ar//FILE: c:\temp\21f18aht.txt																											
09G18a (SS304)(Surface morphology,XPS,XRD) .pdf	SS304	Study of surface morphology and chemical compostion.		Success											Vacuum: 5.5*10^-4 (Pa) Annealing: Tfinal (ºC)730// H2(sccm)100/ P(mbar)2// Ramp time(s)900/ Hold time(s)30/ H2(sccm)50/ P(mbar)0.8/ Purge time(s)30// Heating rate=48,7 (ºC/min) RFpower(W)90/ Ar(sccm)50/ Base pressure(mbar)1/ Time(s)300// Load: 4.10 /Tune: 9.70//Bias voltage (V):-589/-566 //Pref=1.51(W)/Pinc=89.4(W) PROGRAM: Ultra_v1-H2-Ar//FILE: c:\temp\09g18aht.txt																											
09G18b (SS304)(Surface morphology,XPS,XRD) .pdf	SS304	Study of surface morphology and chemical compostion.		Success											Vacuum: 5.3*10^-4 (Pa) Annealing: Tfinal (ºC)700// H2(sccm)100/ P(mbar)2// Ramp time(s)862/ Hold time(s)30/ H2(sccm)50/ P(mbar)0.8/ Purge time(s)30// Heating rate=48,7 (ºC/min) RFpower(W)90/ Ar(sccm)50/ Base pressure(mbar)1/ Time(s)300// Load: 3.86 /Tune: 9.70//Bias voltage (V):-583/-571 //Pref=1.84(W)/Pinc=89.6(W) PROGRAM: Ultra_v1-H2-Ar//FILE: c:\temp\09g18bht.txt																											
09G18c (SS304)(Surface morphology,XPS,XRD) .pdf	SS304	Study of surface morphology and chemical compostion.		Success											Vacuum: 5.1*10^-4 (Pa) Annealing: Tfinal (ºC)650// H2(sccm)100/ P(mbar)2// Ramp time(s)801/ Hold time(s)30/ H2(sccm)50/ P(mbar)0.8/ Purge time(s)30// Heating rate=48,7 (ºC/min) RFpower(W)90/ Ar(sccm)50/ Base pressure(mbar)1/ Time(s)300// Load: 3.86 /Tune: 9.70//Bias voltage (V):-545/-544 //Pref=1.72(W)/Pinc=89.9(W) PROGRAM: Ultra_v1-H2-Ar//FILE: c:\temp\09g18cht.txt																											
09G18d (SS304)(Surface morphology,XPS,XRD) .pdf	SS304	Study of surface morphology and chemical compostion.		Success											Vacuum: 5.8*10^-4 (Pa) Annealing: Tfinal (ºC)600// H2(sccm)100/ P(mbar)2// Ramp time(s)739/ Hold time(s)30/ H2(sccm)50/ P(mbar)0.8/ Purge time(s)30// Heating rate=48,7 (ºC/min) RFpower(W)90/ Ar(sccm)50/ Base pressure(mbar)1/ Time(s)300// Load: 3.90 /Tune: 9.70//Bias voltage (V):-530/-525//Pref=0.488(W)/Pinc=89.6(W) PROGRAM: Ultra_v1-H2-Ar//FILE: c:\temp\09g18cht.txt																											
10G18a (SS304+CNTs).pdf	SS304	Deposition of CNTs		Success			4.2*10^-4								H2	100	2	750	120	730	RF	NH3	100	0.8	C2H2	50	1	50	1.01	600			
															Vacuum: 4.4*10^-4 (Pa) Annealing: Tfinal (ºC)730// H2(sccm)100/ P(mbar)2// Ramp time(s)900/ Hold time(s)30/ H2(sccm)50/ P(mbar)0.8/ Purge time(s)30// Heating rate=48,7 (ºC/min) RFpower(W)90/ Ar(sccm)50/ Base pressure(mbar)1/ Time(s)300// Load: 3.90 /Tune: 9.70//Bias voltage (V):-640/-580 //Pref=1.49(W)/Pinc=90.4(W) PROGRAM: Ultra_v1-H2-Ar//FILE: c:\temp\10g18aht.txt Previous vacuum:6.5*10^-4 A: Water plasma treatment: bias voltage=-332/-339V, Pressure= 135 Pa (1,35mbar), RF power=75W, Plasma time= 60s, P(inc)= 75.71, P(ref)= 1.01, Tune: 9.73 Load:4.08 B: Water plasma treatment: bias voltage=-328/-340V, Pressure= 135 Pa (1,35mbar), RF power=75W, Plasma time= 90s, P(inc)= 76.04, P(ref)= 0.78, Tune: 9.73 Load:4.08 C: Water plasma treatment: bias voltage=-314/-320V, Pressure= 135 Pa (1,35mbar), RF power=75W, Plasma time= 120s, P(inc)= 75.71, P(ref)= -0.10, Tune: 9.73 Load:4.05																											
12G18a (SS304)(Surface morphology,XPS,XRD) .pdf	SS304	Study of surface morphology and chemical compostion.		Success											Vacuum: 4.7*10^-4 (Pa) Annealing: Tfinal (ºC)730// H2(sccm)100/ P(mbar)2// Ramp time(s)900/ Hold time(s)30/ H2(sccm)100/ P(mbar)0.8/ Purge time(s)30// Heating rate=48,7 (ºC/min) RFpower(W)90/ Ar(sccm)0/ Base pressure(mbar)1/ Time(s)300// Load: 3.78 /Tune: 9.72//Bias voltage (V):-725/-710 //Pref=35.6(W)/Pinc=89.6(W) PROGRAM: Ultra_v1-H2-Ar//FILE: c:\temp\12g18aht.txt																											
12G18b (SS304)(Surface morphology,XPS,XRD) .pdf	SS304	Study of surface morphology and chemical compostion.		Success											Vacuum: 5.7*10^-4 (Pa) Annealing: Tfinal (ºC)730// H2(sccm)100/ P(mbar)2// Ramp time(s)900/ Hold time(s)30/ H2(sccm)75/ P(mbar)0.8/ Purge time(s)30// Heating rate=48,7 (ºC/min) RFpower(W)90/ Ar(sccm)25/ Base pressure(mbar)1/ Time(s)300// Load: 4.02/Tune: 9.73//Bias voltage (V):-714/-678 //Pref=5.38(W)/Pinc=89.9(W) PROGRAM: Ultra_v1-H2-Ar//FILE: c:\temp\12g18bht.txt																											
12G18c (SS304)(Surface morphology,XPS,XRD) .pdf	SS304	Study of surface morphology and chemical compostion.		Success											Vacuum: 5.3*10^-4 (Pa) Annealing: Tfinal (ºC)730// H2(sccm)100/ P(mbar)2// Ramp time(s)900/ Hold time(s)30/ H2(sccm)25/ P(mbar)0.8/ Purge time(s)30// Heating rate=48,7 (ºC/min) RFpower(W)90/ Ar(sccm)75/ Base pressure(mbar)1/ Time(s)300// Load: 4.08/Tune: 9.7//Bias voltage (V):-613/-545 //Pref=3.82(W)/Pinc=90.2(W) PROGRAM: Ultra_v1-H2-Ar//FILE: c:\temp\12g18bht.txt																											
10I18a (SS304+CNTs).pdf	SS304	Deposition of CNTs		Failure			3.5*10^-4								H2	100	2	750	120	730	RF	NH3	100	0.8	C2H2	50	1	50	1.012	600			
															Vacuum: 3.0*10^-4 (Pa) Annealing: Tfinal (ºC)730// H2(sccm)100/ P(mbar)2// Ramp time(s)900/ Hold time(s)30/ H2(sccm)50/ P(mbar)0.8/ Purge time(s)30// RFpower(W)90/ Ar(sccm)50/ Base pressure(mbar)1/ Time(s)300// Load: 4 /Tune: 9.74//Bias voltage (V):-545/-565 //Pref=0.498(W)/Pinc=90.4(W) PROGRAM: Ultra_v1-H2-Ar//FILE: c:\temp\10i18aht.txt																											

Sample code	Substrate	Objective	Sample code (PEDRO)	Result	Catalyst Deposition										CNTs growth																	General comments
					Plasma source	Target	Previous vacuum (Pa)	Gas 1	Flux (sccm)	Pressure reactor (mbar)	Time (s)	Deposition rate (nm/s)	Power (W)	VBias (V)	Gas	Flux (sccm)	P (mbar)	Ramp time (s)	Hold time (s)	Tfinal (ºC)	Plasma source	Gas 1	Flux (sccm)	Pressure (mbar)	Gas 2	Flux (sccm)	Pressure (mbar)	Power (W)	VBias (V)	Deposition time (s)					
14I18a (SS304+CNTs).pdf	SS304	Deposition of CNTs		Failure			6.5*10^-4								H2	100	2	750	120	730	RF	NH3	100	0.8	C2H2	50	1	50	1.038	600					Vacuum: 6.1*10^-4 (Pa) Annealing: Tfinal (ºC)730// H2(sccm)100/ P(mbar)2// Ramp time(s)900/ Hold time(s)30/ H2(sccm)50/ P(mbar)0.8/ Purge time(s)30// RFpower(W)90/ Ar(sccm)50/ Base pressure(mbar)1/ Time(s)300// Load: 3.92 /Tune: 9.74//Bias voltage (V):-605/-600 //Pref=3.28(W)/Pinc=90(W) / 46.7 V / 26.0 A (resistance power source) PROGRAM: Ultra_v1-H2-Ar//FILE: c:\temp\14i18aht.txt
17I18a (SS304+CNTs).pdf	SS304	Deposition of CNTs		Success			5.8*10^-4								H2	100	2	750	120	730	RF	NH3	100	0.8	C2H2	50	1	45	1.005	600					Vacuum: 4.3*10^-4 (Pa) Annealing: Tfinal (ºC)730// H2(sccm)100/ P(mbar)2// Ramp time(s)900/ Hold time(s)30/ H2(sccm)50/ P(mbar)0.8/ Purge time(s)30// RFpower(W)80/ Ar(sccm)50/ Base pressure(mbar)1/ Time(s)300// Load: 4.12 /Tune: 9.70//Bias voltage (V):-531/-552 //Pref=2.91(W)/Pinc=80.2(W) / 47.5 V / 26.3 A (resistance power source) PROGRAM: Ultra_v1-H2-Ar//FILE: c:\temp\17i18aht.txt COOL DOWN time: 10 (min)
17I18c (SS304)(Surface morphology study).pdf	SS304	Study of surface morphology.		Success																														Vacuum: 6.9*10^-4 (Pa) Annealing: Tfinal (ºC)730// H2(sccm)100/ P(mbar)2// Ramp time(s)900/ Hold time(s)30/ H2(sccm)50/ P(mbar)0.8/ Purge time(s)30// Heating rate=48,7 (ºC/min) RFpower(W)90/ Ar(sccm)50/ Base pressure(mbar)1/ Time(s)300// Load: 3.84 /Tune: 9.70//Bias voltage (V):-571/-594//Pref=3.86(W)/Pinc=89.2(W) PROGRAM: Ultra_v1-H2-Ar//FILE: c:\temp\17i18cht.txt
17I18d (SS304)(Surface morphology study).pdf	SS304	Study of surface morphology.		Success																														Vacuum: 6.1*10^-4 (Pa) Annealing: Tfinal (ºC)730// H2(sccm)100/ P(mbar)2// Ramp time(s)900/ Hold time(s)30/ H2(sccm)50/ P(mbar)0.8/ Purge time(s)30// Heating rate=48,7 (ºC/min) RFpower(W)90/ Ar(sccm)50/ Base pressure(mbar)1/ Time(s)500// Load: 3.84 /Tune: 9.70//Bias voltage (V):-570/-580//Pref=3.2(W)/Pinc=89.2(W) PROGRAM: Ultra_v1-H2-Ar//FILE: c:\temp\17i18dht.txt
18I18a (SS304+CNTs).pdf	SS304	Deposition of CNTs		Failure			5.5*10^-4								H2	100	2	750	120	730	RF	NH3	100	0.8	C2H2	50	1	50	0.995	600					Vacuum: 3.0*10^-4 (Pa) Annealing: Tfinal (ºC)730// H2(sccm)100/ P(mbar)2// Ramp time(s)900/ Hold time(s)30/ H2(sccm)50/ P(mbar)0.8/ Purge time(s)30// RFpower(W)90/ Ar(sccm)50/ Base pressure(mbar)1/ Time(s)600// Load: 3.84 /Tune: 9.70//Bias voltage (V):-631/-573/-600 //Pref=4.51(W)/Pinc=89.9(W) / 46.2 V / 25.9 A (resistance power source) PROGRAM: Ultra_v1-H2-Ar//FILE: c:\temp\18i18aht.txt COOL DOWN time: 10 (min)
19I18b (SS304+CNTs).pdf	SS304	Deposition of CNTs		Failure			6.7*10^-4								H2	100	2	750	120	730	RF	NH3	100	0.8	C2H2	50	1	45	1.015	600					Vacuum: 4.4*10^-4 (Pa) Annealing: Tfinal (ºC)730// H2(sccm)100/ P(mbar)2// Ramp time(s)900/ Hold time(s)30/ H2(sccm)50/ P(mbar)0.8/ Purge time(s)30// RFpower(W)90/ Ar(sccm)50/ Base pressure(mbar)1/ Time(s)500// Load: 3.84 /Tune: 9.70//Bias voltage (V):-585/-555/-585 //Pref=4.79(W)/Pinc=89.6(W) / 46.2 V / 25.9 A (resistance power source) PROGRAM: Ultra_v1-H2-Ar//FILE: c:\temp\19i18bht.txt COOL DOWN time: 10 (min)
19I18c (SS304+CNTs).pdf	SS304	Deposition of CNTs		Success			7.2*10^-4								H2	100	2	750	120	730	RF	NH3	100	0.8	C2H2	50	1	40	1	600					Vacuum: 6.0*10^-4 (Pa) Annealing: Tfinal (ºC)730// H2(sccm)100/ P(mbar)2// Ramp time(s)900/ Hold time(s)30/ H2(sccm)50/ P(mbar)0.8/ Purge time(s)30// RFpower(W)80/ Ar(sccm)50/ Base pressure(mbar)1/ Time(s)500// Load: 3.84 /Tune: 9.70//Bias voltage (V):-587/-531/-556 //Pref=7.61(W)/Pinc=79.5(W) / 44.4 V / 25.0 A (resistance power source) PROGRAM: Ultra_v1-H2-Ar//FILE: c:\temp\19i18cht.txt COOL DOWN time: 10 (min)
19I18d (SS304+CNTs).pdf	SS304	Deposition of CNTs		Failure			6.9*10^-4								H2	100	2	750	120	730	RF	NH3	100	0.8	C2H2	50	1	35	0.881	600					Vacuum: 6.2*10^-4 (Pa) Annealing: Tfinal (ºC)730// H2(sccm)100/ P(mbar)2// Ramp time(s)900/ Hold time(s)30/ H2(sccm)50/ P(mbar)0.8/ Purge time(s)30// RFpower(W)75/ Ar(sccm)50/ Base pressure(mbar)1/ Time(s)500// Load: 3.84 /Tune: 9.70//Bias voltage (V):-650/-533/-562 //Pref=7.61(W)/Pinc=79.5(W) / 48.03 V / 26.9 A (resistance power source) PROGRAM: Ultra_v1-H2-Ar//FILE: c:\temp\19i18dht.txt COOL DOWN time: 10 (min)
20I18a (SS304+CNTs).pdf	SS304	Deposition of CNTs		Failure			4.9*10^-4								H2	100	2	750	120	730	RF	NH3	100	0.8	C2H2	50	1	40	0.995	600					Vacuum: 3.7*10^-4 (Pa) Annealing: Tfinal (ºC)730// H2(sccm)100/ P(mbar)2// Ramp time(s)900/ Hold time(s)30/ H2(sccm)50/ P(mbar)0.8/ Purge time(s)30// RFpower(W)80/ Ar(sccm)50/ Base pressure(mbar)1/ Time(s)500// Load: 3.84 /Tune: 9.70//Bias voltage (V):-686/-544/-569 //Pref=4.06(W)/Pinc=80.1(W) / 44.8V / 25.9 A (resistance power source) PROGRAM: Ultra_v1-H2-Ar//FILE: c:\temp\20i18aht.txt COOL DOWN time: 10 (min)
01J18a (PECVD-test).pdf	Si	Deposition of CNTs		Success	RF	Fe	6.5*10^-4	Ar	135	0.021	75.00	0.04	60.00	-123.00	H2	100	2	750	120	680	RF	NH3	100	0.8	C2H2	50	1	50	-1.02	600					
01J18b (WACVD-test).pdf	Si	Deposition of CNTs		Failure	RF	Fe	6.6*10^-4	Ar	135	0.021	25.00	0.04	60.00	-121.7/-122.5	H2	100	2	750	120	600/730		NH3	100	0.8	C2H2	50	1			300					I used water assisted CVD with this sample. the annealing tempereature was 600ºC but the CVD temperature was 730ºC.The circular scale is devided to 25 lines. The water was opened with a scale 20
03J18a (SS304)(Surface morphology study).pdf	SS304	Study of surface morphology.		Success																														///////Vacuum: 2.8*10^-4 (Pa) Annealing: Tfinal (ºC)730// H2(sccm)100/ P(mbar)2// Ramp time(s)900/ Hold time(s)30/ H2(sccm)50/ P(mbar)0.8/ Purge time(s)30// Heating rate=48,7 (ºC/min) RFpower(W)60/ Ar(sccm)50/ Base pressure(mbar)1/ Time(s)500// Load: 4.10 /Tune: 9.74//Bias voltage (V):-593/-514/-640//Pref=3/15.4 (W)/Pinc=59.9(W) ////////Power supply:V=46.94V//I=27.2A PROGRAM: Ultra_v1-H2-Ar//FILE: c:\temp\03j18aht.txt

Sample code	Substrate	Objective	Sample code (PEDRO)	Result	Catalyst Deposition										CNTs growth																General comments
					Plasma source	Target	Previous vacuum (Pa)	Gas 1	Flux (sccm)	Pressure reactor (mbar)	Time (s)	Deposition rate (nm/s)	Power (W)	VBias (V)	Gas	Flux (sccm)	P (mbar)	Ramp time (s)	Hold time (s)	Tfinal (ºC)	Plasma source	Gas 1	Flux (sccm)	Pressure (mbar)	Gas 2	Flux (sccm)	Pressure (mbar)	Power (W)	VBias (V)	Deposition time (s)	
03J18b (SS304)(Surface morphology study).pdf	SS304	Study of surface morphology.		Success																											///////Vacuum: 3.8*10^-4 (Pa) Annealing: Tfinal (ºC)730// H2(sccm)100/ P(mbar)2// Ramp time(s)900/ Hold time(s)30/ H2(sccm)50/ P(mbar)0.8/ Purge time(s)30// Heating rate=48,7 (ºC/min) RFpower(W)70/ Ar(sccm)50/ Base pressure(mbar)1/ Time(s)300// Load: 3.98 /Tune: 9.74//Bias voltage (V):-582/-548/-556//Pref=2.8 (W)/Pinc=70(W) ///////Power supply:V=46.94V//I=27.2A PROGRAM: Ultra_v1-H2-Ar//FILE: c:\temp\03j18bht.txt
03J18c (SS304)(Surface morphology study).pdf	SS304	Study of surface morphology.		Success																											///////Vacuum: 4.1*10^-4 (Pa) Annealing: Tfinal (ºC)730// H2(sccm)100/ P(mbar)2// Ramp time(s)900/ Hold time(s)30/ H2(sccm)50/ P(mbar)0.8/ Purge time(s)30// Heating rate=48,7 (ºC/min) RFpower(W)80/ Ar(sccm)50/ Base pressure(mbar)1/ Time(s)300// Load: 3.98 /Tune: 9.74//Bias voltage (V):-648/-573/-582//Pref=4.42 (W)/Pinc=80.2(W) ///////Power supply:V=46.10V//I=26.4A PROGRAM: Ultra_v1-H2-Ar//FILE: c:\temp\03j18cht.txt
03J18d (SS304+CNTs).pdf	SS304	Deposition of CNTs		Failure			4.7*10^-4								H2	100	2	750	120	730	RF	NH3	100	0.8	C2H2	50	1	40	1.059	600	///////Vacuum: 3.3*10^-4 (Pa) Annealing: Tfinal (ºC)730// H2(sccm)100/ P(mbar)2// Ramp time(s)900/ Hold time(s)30/ H2(sccm)50/ P(mbar)0.8/ Purge time(s)30// Heating rate=48,7 (ºC/min) RFpower(W)60/ Ar(sccm)50/ Base pressure(mbar)1/ Time(s)500// Load: 4.10 /Tune: 9.74//Bias voltage (V):-574/-528/-533//Pref=2.93 (W)/Pinc=60.1(W) ///////Power supply:V=50.09V//I=28.5A PROGRAM: Ultra_v1-H2-Ar//FILE: c:\temp\03j18aht.txt COOL DOWN time: 15 (min)
15J18b (SS304+CNTs).pdf	SS304	Deposition of CNTs		Success											H2	100	2	750	120	680	RF	NH3	100	0.8	C2H2	50	1	50	1.044	600	Vacuum: 2.9*10^-4 (Pa) Annealing: Tfinal (ºC)730// H2(sccm)100/ P(mbar)2// Ramp time(s)900/ Hold time(s)30/ H2(sccm)50/ P(mbar)0.8/ Purge time(s)30// RFpower(W)80/ Ar(sccm)50/ Base pressure(mbar)1/ Time(s)300// Load: 4.0/Tune: 9.7//Bias voltage (V):-588/-530/-552 //Pref=1.35(W)/Pinc=80.3(W) PROGRAM: Ultra_v1-H2-Ar//FILE: c:\temp\15j18bht.txt
22J18b (SS304+CNTs).pdf	SS304	Deposition of CNTs		Success			4.9*10^-4								H2	100	2	750	120	650	RF	NH3	100	0.8	C2H2	50	1	60	-414	600	Vacuum: 5.4*10^-4 (Pa) Annealing: Tfinal (ºC)750// H2(sccm)100/ P(mbar)2// Ramp time(s)900/ Hold time(s)30/ H2(sccm)100/ P(mbar)0.8/ Purge time(s)30// RFpower(W)90/ Ar(sccm) 0/ Base pressure(mbar)1/ Time(s) 300// Load: 3.88 /Tune: 9.70//Bias voltage (V):-651/-685 //Pref=16.2(W)/Pinc=80(W) / PROGRAM: Ultra_v1-H2-Ar//FILE: c:\temp\22j18bht.txt COOL DOWN time: 60 (min)
22K18b (SS304+CNTs).pdf	SS304	Deposition of CNTs		Success			2.7*10^-4								H2	100	2	750	500	730	RF	NH3	100	1	C2H2	50	1	50	1.028	1800	///Reduction of native oxide/// T(ºC)730// H2(sccm)100/ P(mbar)2// External power supply: Load: 70%/Tune: 37%//Bias voltage (V):-417/-428 /Pref=0 (W)/Pinc=80(W) /////// Power supply (graphite heater):57.3V/30.7 A
23K18a (SS304+CNTs).pdf	SS304	Deposition of CNTs		Success			4.6*10^-4								H2	100	1	900	120	730	RF	NH3	100	0.8	C2H2	50	1	50	-0	1800	///Reduction of native oxide/// T(ºC)730// H2(sccm)100/ P(mbar)1// External power supply: Load: 85%/Tune: 34%//Bias voltage (V):-557/-561 /Pref=0 (W)/Pinc=90(W) /////// Power supply (graphite heater):57.3V/30.7 A
23K18b (SS304+CNTs).pdf	SS304	Deposition of CNTs		Success			5.5*10^-4								H2	100	1	900	120	730	RF	NH3	100	0.8	C2H2	50	1	50	1.03	1800	///Reduction of native oxide/// T(ºC)730// H2(sccm)100/ P(mbar)1// External power supply: Load: 85%/Tune: 34%//Bias voltage (V):-570/-573 /Pref=0 (W)/Pinc=90(W) /////// Power supply (graphite heater):57.3V/30.7 A
24a19a (SS304+CNTs).pdf	SS304	Deposition of CNTs		Success			2.2*10^-4								H2	100	1	780	620	650/730	RF	NH3	100	0.8	C2H2	50	1	50	1.101	1800	///Reduction of native oxide/// T(ºC)650// H2(sccm)100/ P(mbar)2// Bias voltage (V):-430/-460/ /Pref=0 (W)/Pinc=160(W) // time (s): 500////// Temperature (C): 650ºC 120s with H2(stabilize)+500s with H2(reduction) Power supply (graphite heater):51.1V/30.7 A Note: the annealing and H2 Plasma were achieved at 650ºC but the PECVD at 730ºC
24a19b (SS304+CNTs).pdf	SS304	Deposition of CNTs		Success			2.9*10^-4								H2	100	1	780	1200	650/730	RF	NH3	100	0.8	C2H2	50	1	50	1.014	1800	///Reduction of native oxide/// T(ºC)650// H2(sccm)100/ P(mbar)2// Bias voltage (V):-449/-461/ /Pref=0 (W)/Pinc=160(W) // time (s): 500////// Temperature (C): 650ºC 200s with H2(stabilize)+500s with H2(reduction)+500s with H2(nucleation??) Power supply (graphite heater):51.1V/30.7 A Note: the annealing and H2 Plasma were achieved at 650ºC but the PECVD at 730ºC
24a19c (SS304+CNTs).pdf	SS304	Deposition of CNTs		Success			3.4*10^-4								H2	100	1	780	200/500 /500	650/650	RF	NH3	100	0.8	C2H2	50	1	50	0.981	1800	///Reduction of native oxide/// T(ºC)650// H2(sccm)100/ P(mbar)2// Bias voltage (V):-454/-469/ /Pref=0 (W)/Pinc=160(W) // time (s): 500////// Temperature (C): 650ºC 200s with H2(stabilize)+500s with H2(reduction)+500s with NH3(nucleation??) Power supply (graphite heater):41.8V/24.4 A (nucleation??) Note: the annealing and H2 Plasma were achieved at 650ºC but the PECVD at 650ºC

Sample code	Substrate	Objective	Sample code (PEDRO)	Result	Catalyst Deposition										CNTs growth																		General comments
					Plasma source	Target	Previous vacuum (Pa)	Gas 1	Flux (sccm)	Pressure reactor (mbar)	Time (s)	Deposition rate (nm/s)	Power (W)	VBias (V)	Gas	Flux (sccm)	P (mbar)	Ramp time (s)	Hold time (s)	Tfinal (ºC)	Plasma source	Gas 1	Flux (sccm)	Pressure (mbar)	Gas 2	Flux (sccm)	Pressure (mbar)	Power (W)	VBias (V)	Deposition time (s)					
25a19a (SS304+CNTs).pdf	SS304	Deposition of CNTs		Success			2.1*10^-4								H2	100	1	780	1200	650/730	RF	NH3	100	0.8	C2H2	50	1	50	1.043	1800					////Reduction of native oxide/// T(ºC)650// H2(sccm)100/ P(mbar)2// Bias voltage (V):-454/-457/ /Pref=0 (W)/Pinc=160(W) // time (s): 500////// Temperature (C): 650ºC 200s with H2(stabilize)+500s with H2(reduction)+500s with NH3(nucleation??) Power supply (graphite heater):41.8V/24.4 A (nucleation??) Note: the annealing and H2 Plasma were achieved at 650ºC but the PECVD at 730ºC
29a19a (SS304+CNTs).pdf	SS304	Deposition of CNTs		Success			3.6*10^-4								H2	100	1	780	200/500 /500	650/680	RF	NH3	100	0.8	C2H2	50	1	50	1.003	1800					////Reduction of native oxide/// T(ºC)650// H2(sccm)100/ P(mbar)2// Bias voltage (V):-454/-460/ /Pref=0 (W)/Pinc=160(W) // time (s): 500////// Temperature (C): 650ºC 200s with H2(stabilize)+500s with H2(reduction)+500s with H2(nucleation??) Power supply (graphite heater):43.14/24.9 A (reduction)////45.66/26.4 A (nucleation??) Note: the annealing and H2 Plasma were achieved at 650ºC but the PECVD at 680ºC
29a19b (SS304+CNTs).pdf	SS304	Deposition of CNTs		Success			2.8*10^-4								H2	100	1	780	200/500 /500	650/730	RF	NH3	100	0.8	C2H2	50	1	50	1.138	1800					////Reduction of native oxide/// T(ºC)650// H2(sccm)100/ P(mbar)2// Bias voltage (V):-446/-467/ /Pref=0 (W)/Pinc=160(W) // time (s): 500////// Temperature (C): 650ºC 200s with H2(stabilize)+500s with H2(reduction)+500s with NH3(nucleation??) Power supply (graphite heater):42.34/27.8A (reduction)////45.66/26.4 A (nucleation??) Note: the annealing and H2 Plasma were achieved at 650ºC but the PECVD at 730ºC
29a19c (SS304+CNTs).pdf	SS304	Deposition of CNTs		Success			3.3*10^-4								H2	100	1	780	620	650/730	RF	NH3	100	0.8	C2H2	50	1	50	1.077	1800					////Reduction of native oxide/// T(ºC)650// H2(sccm)100/ P(mbar)2// Bias voltage (V):-441/-461/ /Pref=0 (W)/Pinc=160(W) // time (s): 500////// Temperature (C): 650ºC 120s with H2(stabilize)+500s with H2(reduction) Power supply (graphite heater):44.6.1V/26.1 A Note: the annealing and H2 Plasma were achieved at 650ºC but the PECVD at 730ºC. The first 600 s was for PECVD, then was for WACVD (20 lines - valve scale).
31a19a (SS304+CNTs).pdf	SS304	Deposition of CNTs		Success			2.1*10^-4								NH3	100	1	780	200/500 /500	650/730	RF	NH3	100	0.8	C2H2	50	1	50	1.034	1800					////Reduction of native oxide/// T(ºC)650// H2(sccm)100/ P(mbar)2// Bias voltage (V):-342/-334/ /Pref=0 (W)/Pinc=160(W) // time (s): 500////// Temperature (C): 650ºC 200s with NH3(stabilize)+500s with NH3(reduction)+500s with NH3(nucleation??) Power supply (graphite heater):42.34/27.8A (reduction)////45.66/26.4 A (nucleation??) Note: the annealing and NH3 Plasma were achieved at 650ºC but the PECVD at 730ºC
19C19a (SS304)(reduction-OES).pdf	SS304	Study of surface morphology and chemical compostion.		Failure																														Vacuum: 2.8*10^-4 (Pa) Annealing: Tfinal (ºC)730// H2(sccm)100/ P(mbar)2// Ramp time(s)900/ Hold time(s)30/ H2(sccm)50/ P(mbar)0.8/ Purge time(s)30// Heating rate=48,7 (ºC/min) RFpower(W)90/ Ar(sccm)50/ Base pressure(mbar)1/ Time(s)300// Load: 4.45 /Tune: 6.08//Bias voltage (V):-680/-220//Pref=1.24(W)/Pinc=90.2(W) PROGRAM: Ultra_v1-H2-Ar//FILE: c:\temp\19c19aht.txt
21C19a (SS304)(reduction-OES).pdf	SS304	Study of reduction process		Success																														Vacuum: 3.0*10^-4 (Pa) Annealing: Tfinal (ºC)730// H2(sccm)100/ P(mbar)2// Ramp time(s)900/ Hold time(s)30/ H2(sccm)50/ P(mbar)0.8/ Purge time(s)30// Heating rate=48,7 (ºC/min) RFpower(W)90/ Ar(sccm)50/ Base pressure(mbar)1/ Time(s)300// Load: 4.45 /Tune: 6.08//Bias voltage (V):-565/-587//Pref=1.24(W)/Pinc=90.2(W) PROGRAM: Ultra_v1-H2-Ar//FILE: c:\temp\21c19aht.txt
21C19b (SS304)(reduction-OES).pdf	SS304	Study of reduction process		Success																														Vacuum: 4.1*10^-4 (Pa) Annealing: Tfinal (ºC)730// H2(sccm)100/ P(mbar)2// Ramp time(s)900/ Hold time(s)30/ H2(sccm)50/ P(mbar)0.8/ Purge time(s)30// Heating rate=48,7 (ºC/min) RFpower(W)90/ Ar(sccm)50/ Base pressure(mbar)1/ Time(s)300// Load: 4.58/Tune: 4.80//Bias voltage (V):-679/-585//Pref=7.18(W)/Pinc=90.4(W) PROGRAM: Ultra_v1-H2-Ar//FILE: c:\temp\21c19bht.txt
21C19c (SS304)(reduction-OES).pdf	SS304	Study of reduction process		Success																														Vacuum: 5.9*10^-4 (Pa) Annealing: Tfinal (ºC)RT// H2(sccm)100/ P(mbar)2// RFpower(W)150/ Ar(sccm)50/ Base pressure(mbar)1/ Time(s)300// Load: 4.35/Tune: 5.18//Bias voltage (V):-326/-450//Pref=5.83(W)/Pinc=150.4(W) PROGRAM: Ultra_v1-H2-Ar//FILE: c:\temp\21c19cht.txt
23D19a-SS304+GSS304+AlN (ref.15C17b PECVD).pdf	SS+SSgradient+AlN	Deposition of CNTs	17F1601	Failure	RF	Fe	2.5*10^-4	Ar	128	0.0199	67 (2nm)	0.03	60.00	0.99	H2	100	2	750	120	730	RF	NH3	100	0.8	C2H2	50	1	50	370-329	900					
23D19b-SS304+GSS304+AlN (ref.15C17b PECVD).pdf	SS+SSgradient+AlN	Deposition of CNTs	17F2701	Failure	RF	Fe	3.4*10^-4	Ar	128	0.0199	67 (2nm)	0.03	60.00	-106.8	H2	100	2	750	120	730	RF	NH3	100	0.8	C2H2	50	1	50	1.109	900					
24D19a-SS304+GSS304+AlN (ref.15C17b PECVD).pdf	SS+SSgradient+AlN	Deposition of CNTs	19D2301	Success	RF	Fe	2.7*10^-4	Ar	128	0.0199	83 (2.5nm)	0.03	60.00	-105.4/106.9	H2	100	2	750	120	730	RF	NH3	100	0.8	C2H2	50	1	50	1.018	900					

Sample code	Substrate	Objective	Sample code (PEDRO)	Result	Catalyst Deposition										CNTs growth																General comments
					Plasma source	Target	Previous vacuum (Pa)	Gas 1	Flux (sccm)	Pressure reactor (mbar)	Time (s)	Deposition rate (nm/s)	Power (W)	VBias (V)	Gas	Flux (sccm)	P (mbar)	Ramp time (s)	Hold time (s)	Tfinal (ºC)	Plasma source	Gas 1	Flux (sccm)	Pressure (mbar)	Gas 2	Flux (sccm)	Pressure (mbar)	Power (W)	VBias (V)	Deposition time (s)	
24D19b-SS304+GSS304+AlN (ref.15C17b PECVD).pdf	SS+SSgradient+AlN	Deposition of CNTs	19D2301	Success	RF	Fe	5.6*10^-4	Ar	128	0.0199	83 (2.5nm)	0.03	60.00	-102.8/103.1	H2	100	2	750	120	730	RF	NH3	100	0.8	C2H2	50	1	50	1	900	
															I forgot to start the roots pump during the annealing, hold time and the first seconds of PECVD (30s) Water plasma treatment: bias voltage=-227/-238V, Pressure= 135 Pa (1,35mbar), RF power=75W, Plasma time= 60s, P(inc)= 74.65, P(ref)= 3.55, Tune: 5.20 Load:4.48																		
24D19c-SS304+GSS304+AlN (ref.15C17b PECVD).pdf	SS+SSgradient+AlN	Deposition of CNTs	19D2301	Success	RF	Fe	5.1*10^-4	Ar	128	0.0199	83 (2.5nm)	0.03	60.00	-100.9/101.6	H2	100	2	750	120	730	RF	NH3	100	0.8	C2H2	50	1	50	0.98	900	
															Water plasma treatment: bias voltage=-236/-244V, Pressure= 135 Pa (1,35mbar), RF power=75W, Plasma time= 60s, P(inc)= 74.96, P(ref)= 5.23, Tune: 5.20 Load:4.48																		
24D19d-SS304+GSS304+AlN (ref.15C17b PECVD).pdf	SS+SSgradient+AlN	Deposition of CNTs	19D2301	Success	RF	Fe	5.1*10^-4	Ar	128	0.0199	83 (2.5nm)	0.03	60.00	-102.9/102.2	H2	100	2	750	120	730	RF	NH3	100	0.8	C2H2	50	1	50	1.019	900	
															Water plasma treatment: bias voltage=-242/-250V, Pressure= 135 Pa (1,35mbar), RF power=75W, Plasma time= 60s, P(inc)= 74.89, P(ref)= 7.68, Tune: 5.20 Load:4.48																		
24D19e-SS304+GSS304+AlN (ref. 21D17g WACVD).pdf	SS+gradientSS+AlN	Deposition of CNTs	19D2402	Success	RF	Fe	4.3*10^-4	Ar	128	0.0201	67 (2nm)	0.03	60.00	-101.9/-102.5	H2	100	2	750	120	600	CVD	NH3	100	0.8	C2H2	50	1			1800	
															We used water assisted CVD with this sample. the annealing tempereature was 600 ºC but the CVD temperature was 730 ºC. The circular scale is devided to 25 lines The water was opened with a scale 5.																		
25D19a-SS304+GSS304+AlN (H2O Plasma 23D19b)-SEM-RAMAN.pdf	SS+SSgradient+AlN+Fe+CNTs	H2O plasma	17F2701	Success	RF	Fe	3.4*10^-4	Ar	128	0.0199	67 (2nm)	0.03	60.00	-106.8	H2	100	2	750	120	730	RF	NH3	100	0.8	C2H2	50	1	50	1.109	900	
															Water plasma treatment: bias voltage=-262/-269V, Pressure= 135 Pa (1,35mbar), RF power=75W, Plasma time= 60s, P(inc)= 75.16, P(ref)= 0.36, Tune: 7.40 Load:4.60																		
25D19b-SS304+GSS304+AlN (WACVD).pdf	SS+gradientSS+AlN	Deposition of CNTs	19D2402	Success	RF	Fe	5.9*10^-4	Ar	128	0.0201	67 (2nm)	0.03	60.00	-105.7/-104.1	H2	100	2	750	120	600	CVD	NH3	100	0.8	C2H2	50	1			600	
															We used water assisted CVD with this sample. the annealing tempereature was 600 ºC but the CVD temperature was 730 ºC. The circular scale is devided to 25 lines																		
06E19a-SS304+GSS304+AlN.pdf	SS+SSgradient+AlN	Deposition of CNTs	19D2404	Success	RF	Fe	4.7*10^-4	Ar	128	0.0199	83 (2.5nm)	0.03	60.00	-102.2/102.8	H2	100	2	750	120	730	RF	NH3	100	0.8	C2H2	50	1	50	1.022	900	
06E19b-SS304+GSS304+AlN.pdf	SS+SSgradient+AlN	Deposition of CNTs	19D2404	Success	RF	Fe	3.3*10^-4	Ar	128	0.0199	83 (2.5nm)	0.03	60.00	-99.8/100.1	H2	100	2	750	120	730	RF	NH3	100	0.8	C2H2	50	1	50	1.008	900	
13E19a-SS304+CNTs (H2O plasma).pdf	SS+CNTs	H2O plasma	23K18b (CNTs reactor)	Success			3.4*10^-4								Water plasma treatment: bias voltage=-237/-248V, Pressure= 135 Pa (1,35mbar), RF power=75W, Plasma time= 60s, P(inc)= 75.11, P(ref)= 2.82, Tune: 5.20 Load:4.48																		

Feedthroughs drawings

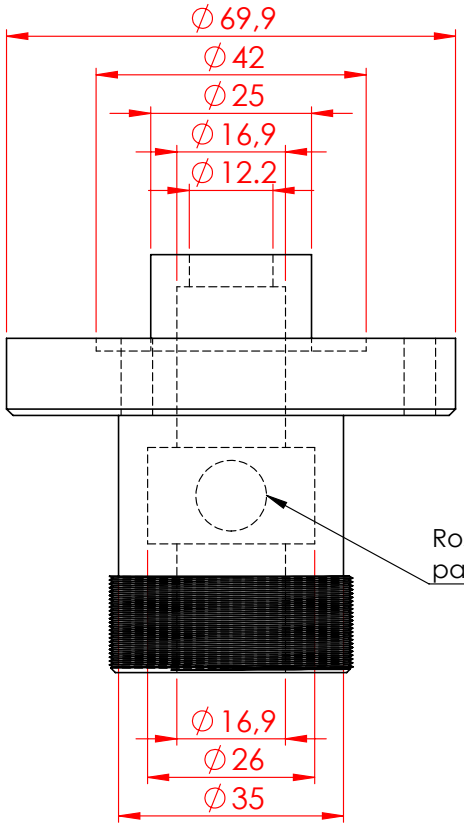

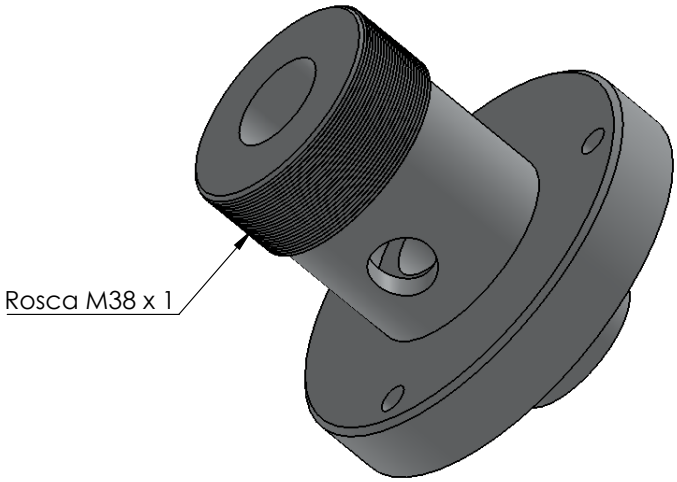

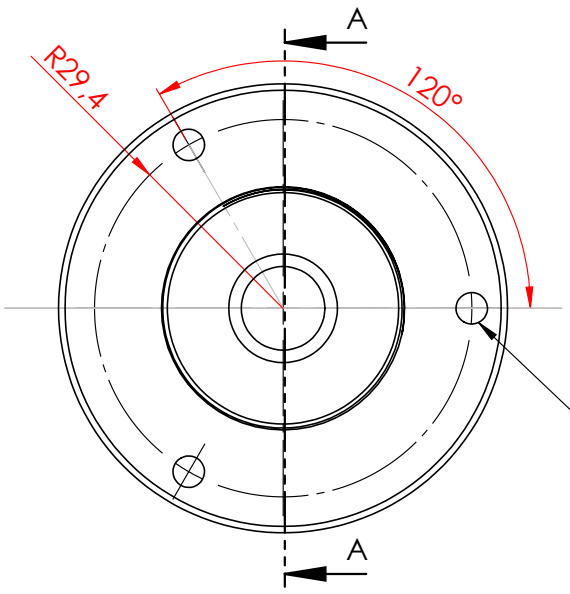

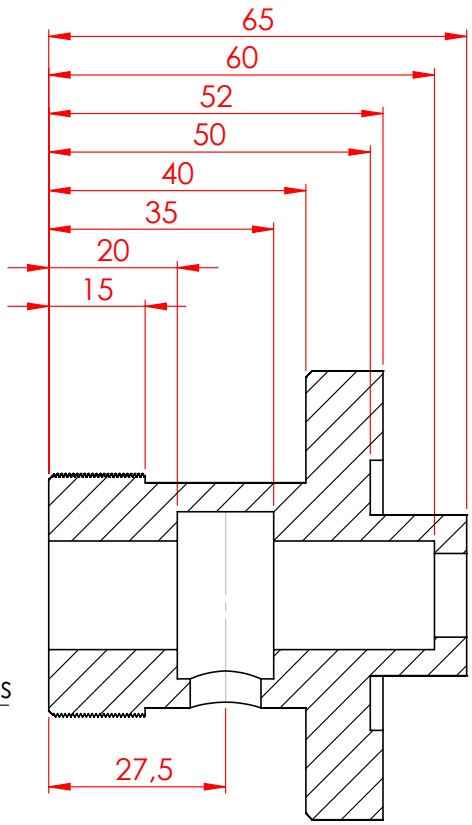

SECCIÓN A-A
ESCALA 1 : 1

NOTAS:
Todas las dimensiones están en mm.
Tolerancia general: ±0.1 mm / ±0.2°

TÍTULO:
Estructura
Pasamuros 12mm

MATERIAL:
Acero inox. 304

FEMAN-UB

A4

Espesor:N/A

ESCALA:1:2

CANTIDAD: 1

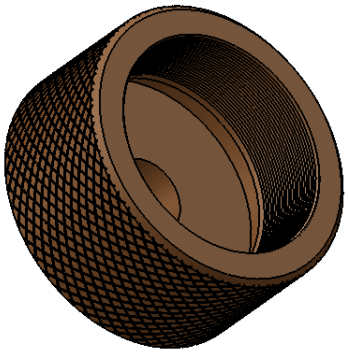

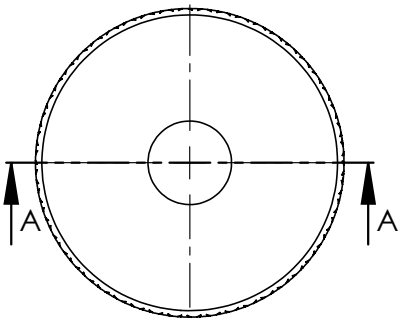

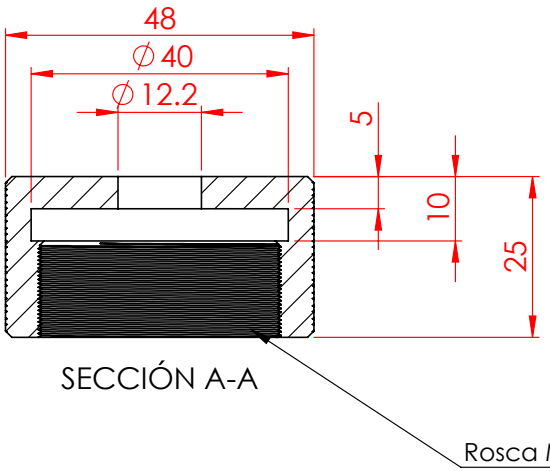

NOTAS:
Todas las dimensiones están en mm.
Tolerancia general: ±0.1 mm / ±0.2°

TÍTULO:
Tapa-Pasamuros 12mm

MATERIAL:
Bronce

FEMAN-UB

A4

Espesor: N/A

ESCALA:1:1

CANTIDAD: 1

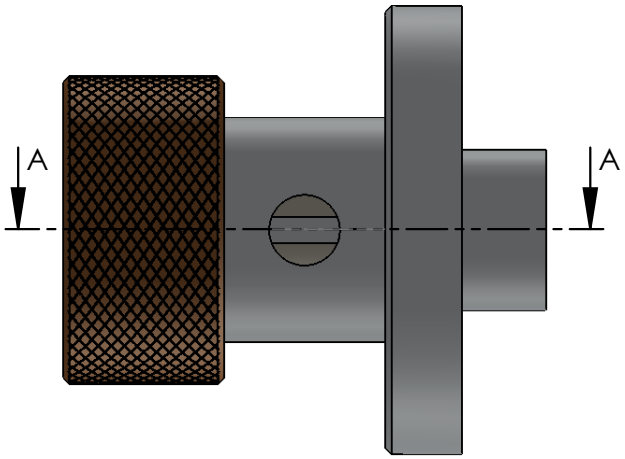

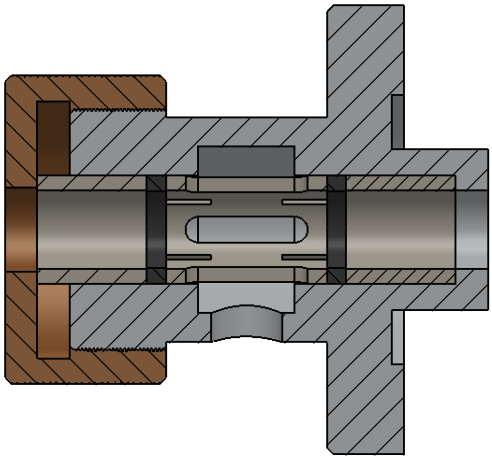

SECCIÓN A-A
ESCALA 1 : 1

NOTAS:
Todas las dimensiones están en mm.
Tolerancia general: ±0.1 mm / ±0.2°

TÍTULO:
Ensamblaje Pasamuros 12mm

MATERIAL:
Acero-Latón-Teflón

FEMAN-UB

A4

Espesor: N/A

ESCALA:1:2

CANTIDAD: 1

Carousel system drawings

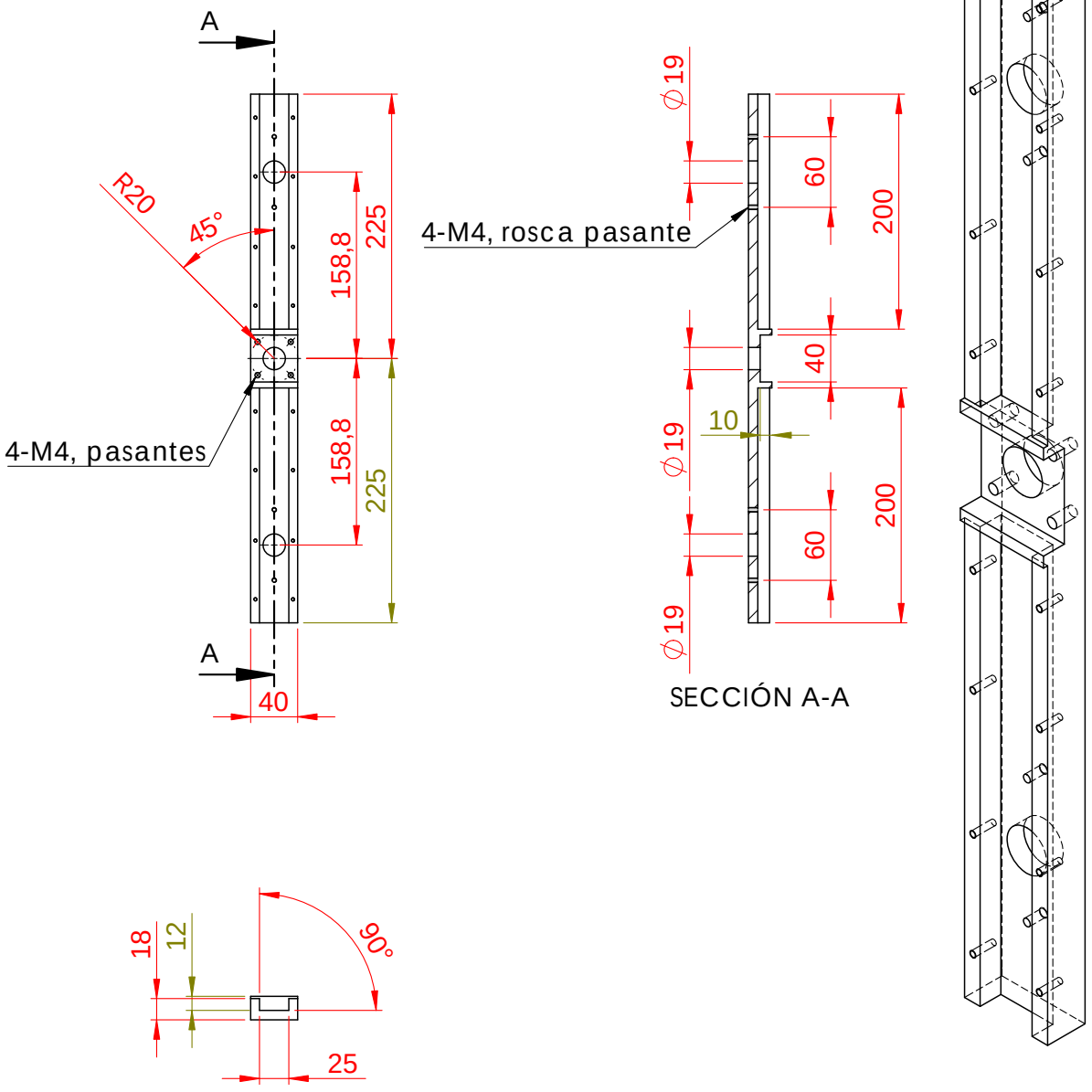

NOTAS: Todas las dimensiones están en mm.	**TÍTULO:** Barra soporte 1	
MATERIAL: Acero inoxidable 304	FEMAN-UB	A4
Espesor: N/A	ESCALA:1:5	CANTIDAD: 1

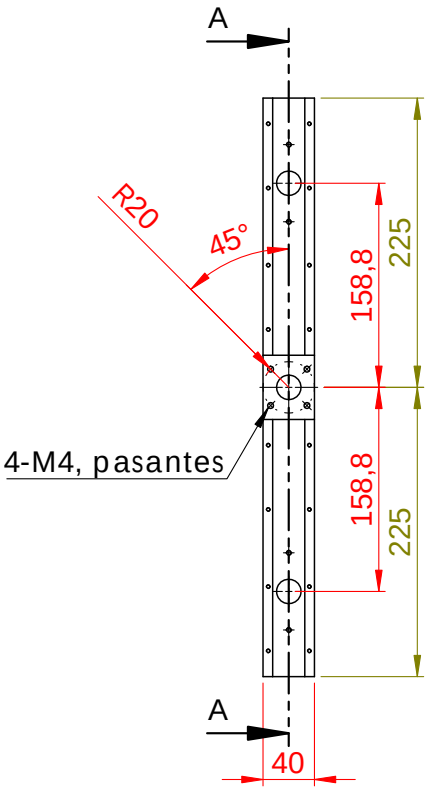

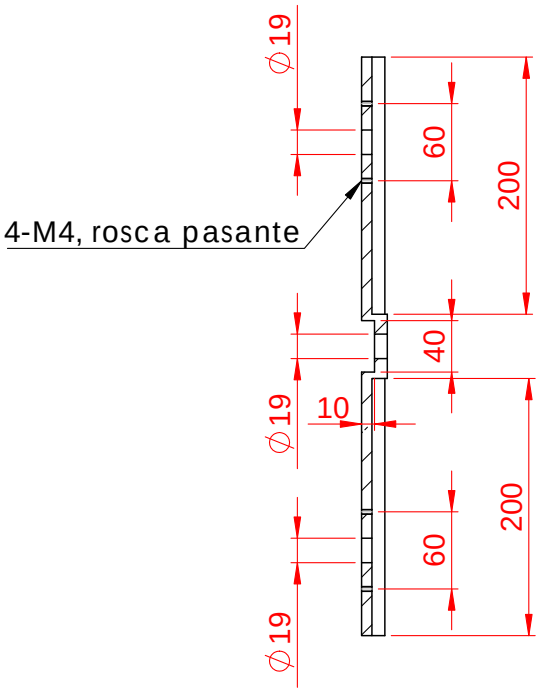

SECCIÓN A-A

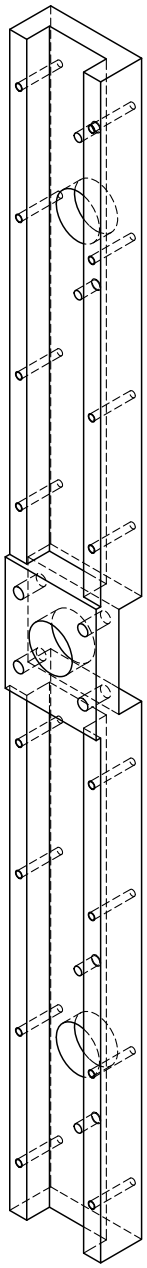

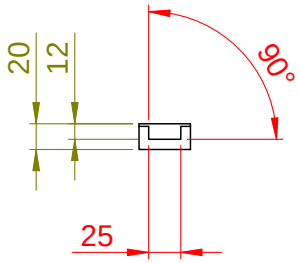

NOTAS:
Todas las dimensiones están en mm.

TÍTULO:
Barra soporte 2

MATERIAL:
Acero inoxidable 304

FEMAN-UB

A4

Espesor: N/A

ESCALA:1:5

CANTIDAD: 1

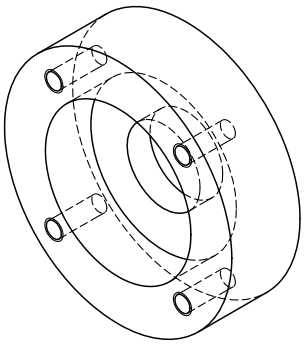

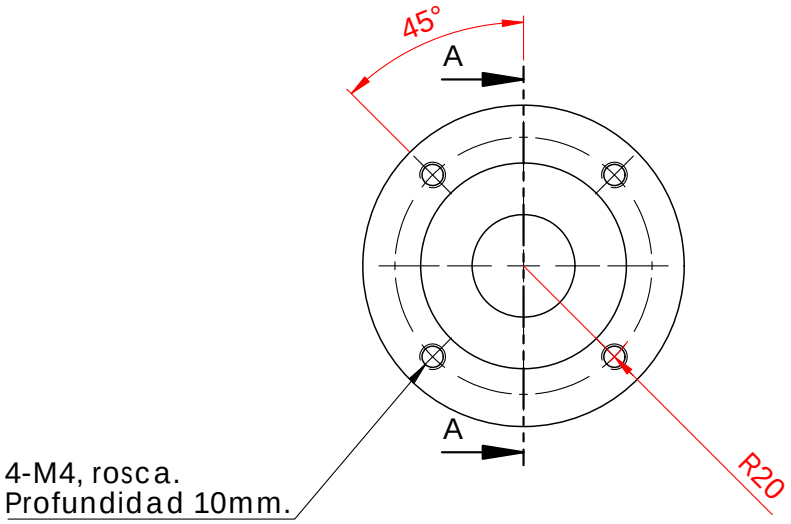

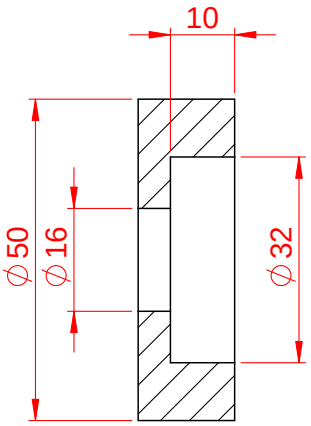

SECCIÓN A-A

NOTAS: Todas las dimensiones están en mm.	**TÍTULO:** Porta rodamiento-sup	
MATERIAL: Acero inoxidable 304	FEMAN-UB	A4
Espesor: N/A	ESCALA:1:1	CANTIDAD: 1

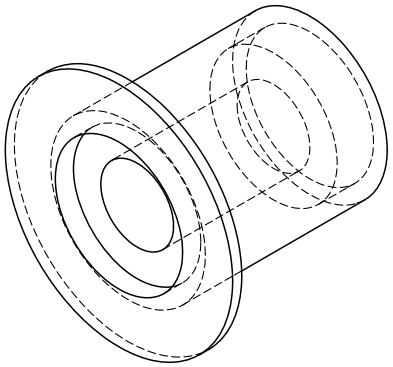

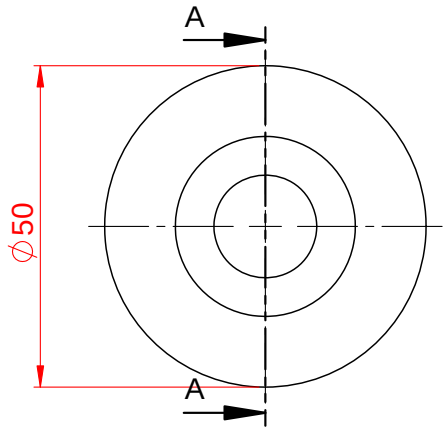

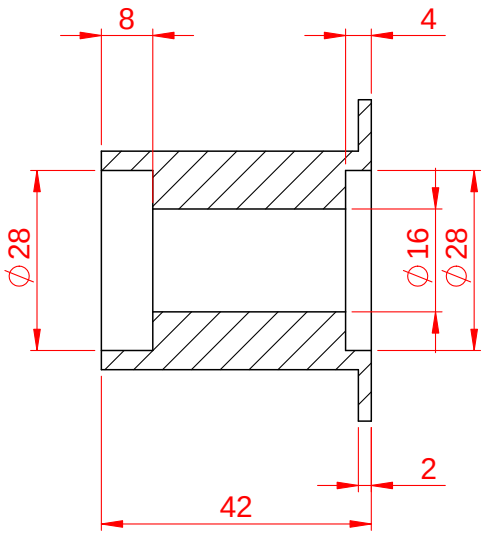

SECCIÓN A-A

NOTAS:
Todas las dimensiones están en mm.

TÍTULO:
Porta rodamientos-RS

MATERIAL:
Acero inoxidable 304

FEMAN-UB

A4

Espesor: N/A

ESCALA:1:1

CANTIDAD: 1

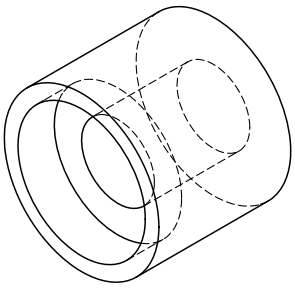

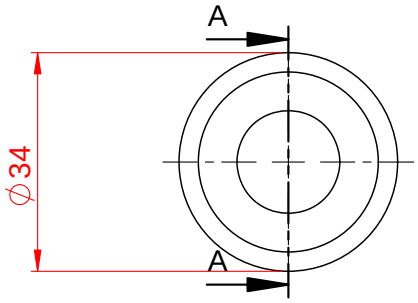

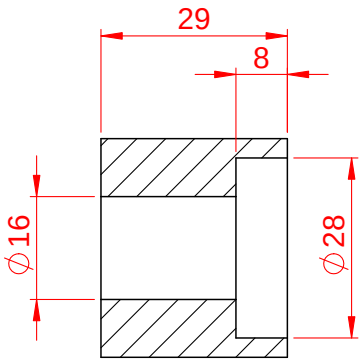

SECCIÓN A-A

NOTAS: Todas las dimensiones están en mm.	**TÍTULO:** Porta rodamientos-RI	
MATERIAL: Acero inoxidable 304	FEMAN-UB	A4
Espesor: N/A	ESCALA:1:1	CANTIDAD: 1

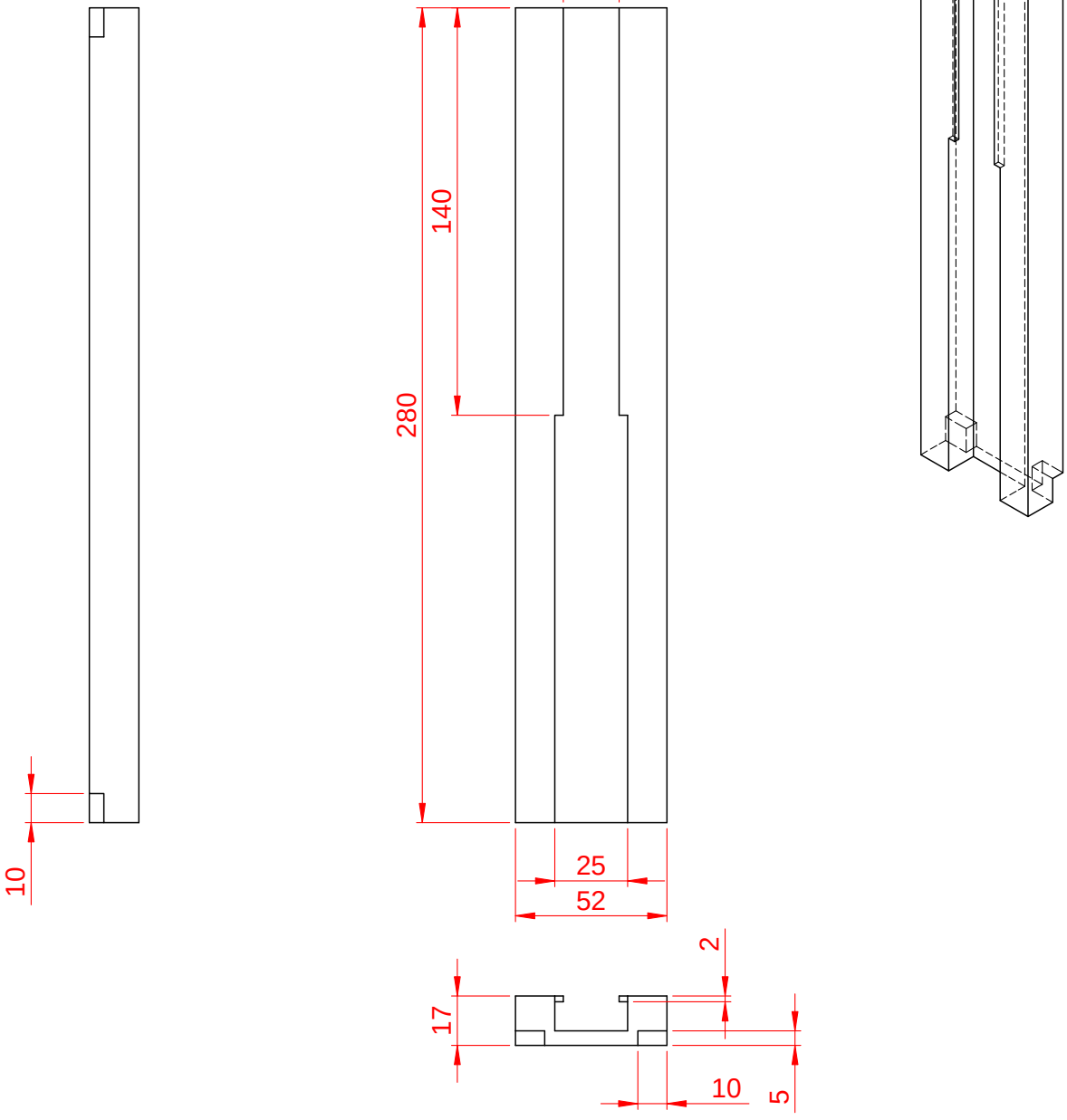

NOTAS:
Todas las dimensiones están en mm.

TÍTULO:
Riel -precamara

MATERIAL:
Aluminio

FEMAN-UB

A4

Espesor: N/A

ESCALA:1:2

CANTIDAD: 1

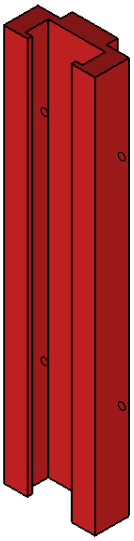

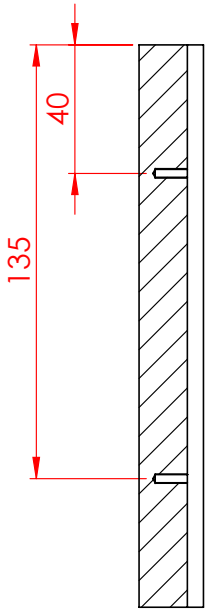

SECCIÓN A-A

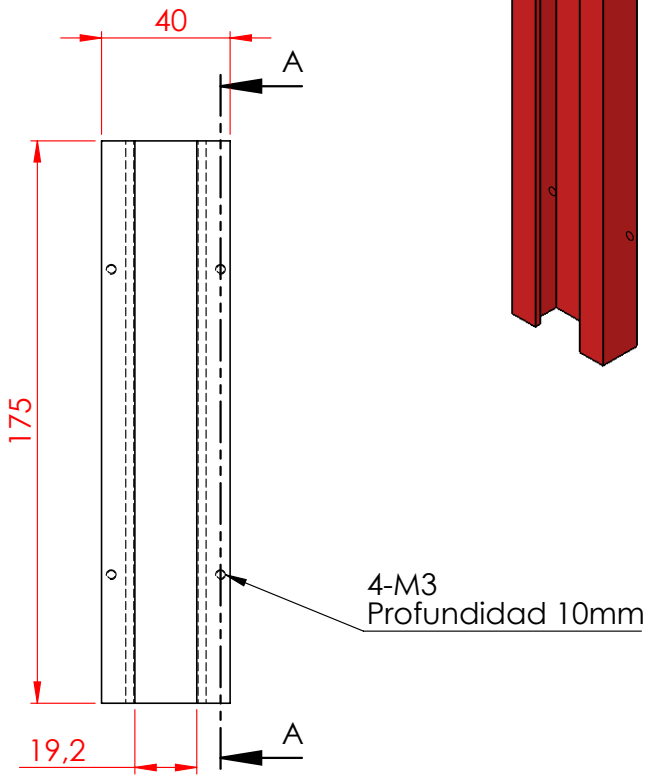

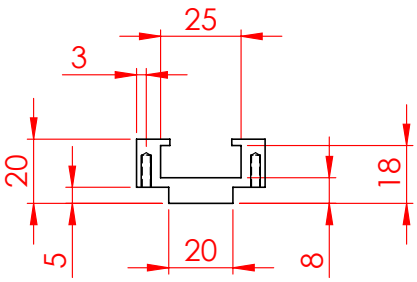

NOTAS:
Todas las dimensiones están en mm.
Tolerancia general: ±0.1 mm / ±0.2°

TÍTULO:
Riel reactor

MATERIAL:
Acero inox. 304

FEMAN-UB

A4

Espesor: N/A

ESCALA:1:2

CANTIDAD: 1

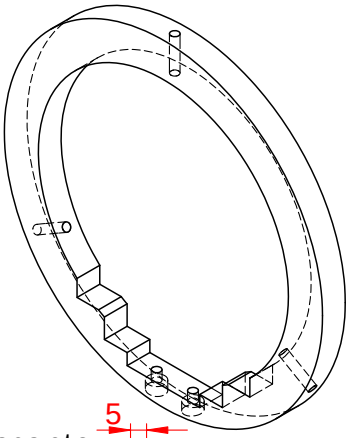

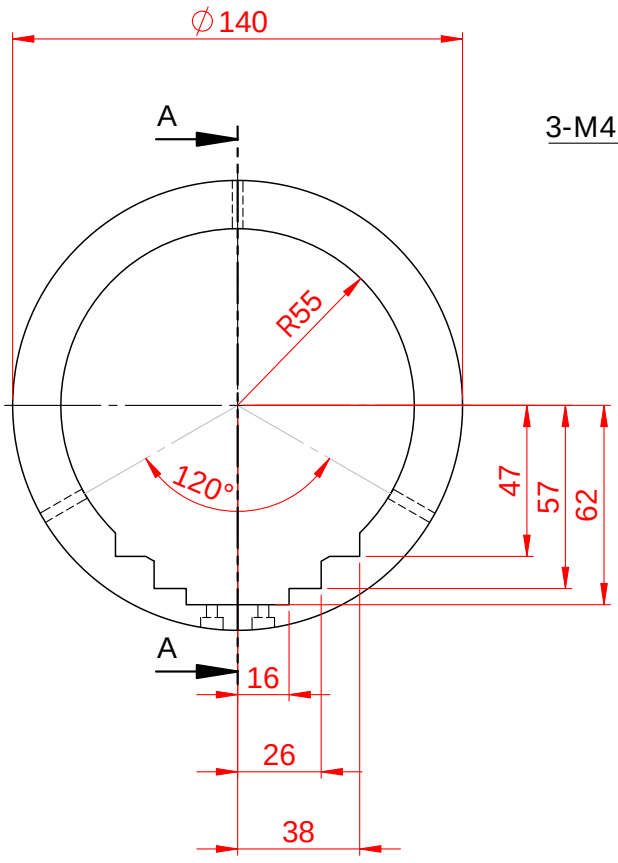

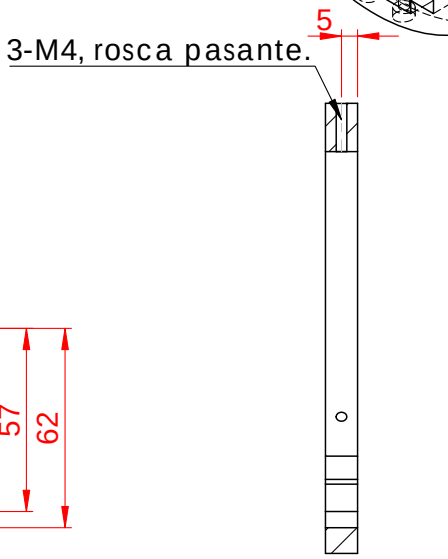

SECCIÓN A-A

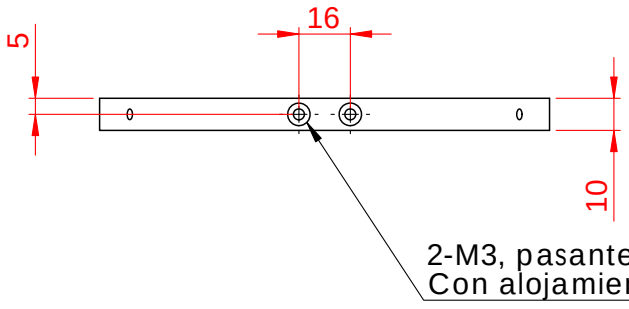

NOTAS: Todas las dimensiones están en mm.	**TÍTULO:** Anclaje-rieles-pre	
MATERIAL: Aluminio	FEMAN-UB	A4
Espesor: 10 mm	ESCALA:1:2	CANTIDAD: 2

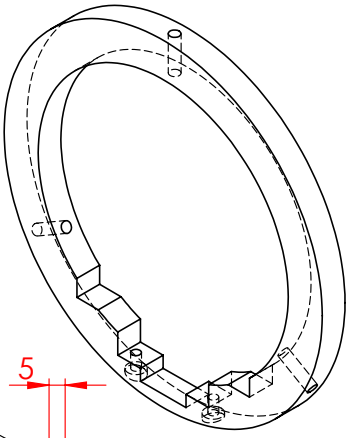

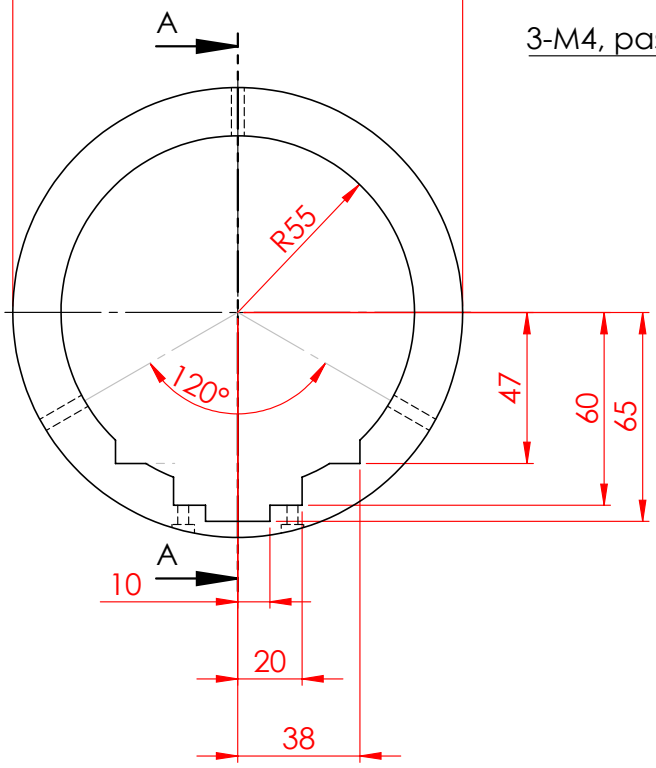

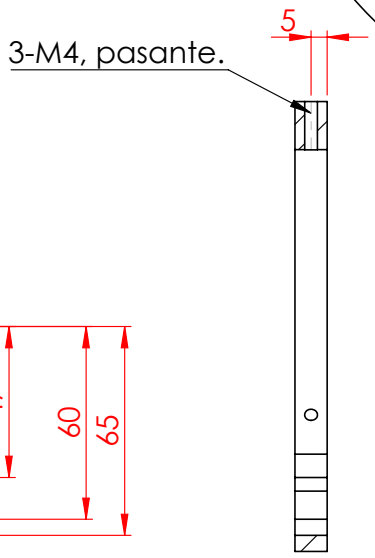

SECCIÓN A-A

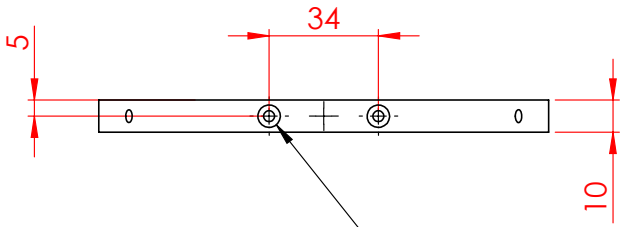

2-Ø3.25, pasantes.
Con alojamiento para cabeza de tornillo M3.

NOTAS: Todas las dimensiones están en mm. Tolerancia general: ±0.1 mm / ±0.2°	**TÍTULO:** Anclaje-riel reactor	
MATERIAL: Acero inox. 304	FEMAN-UB	A4
Espesor: 10 mm	ESCALA:1:2	CANTIDAD: 2

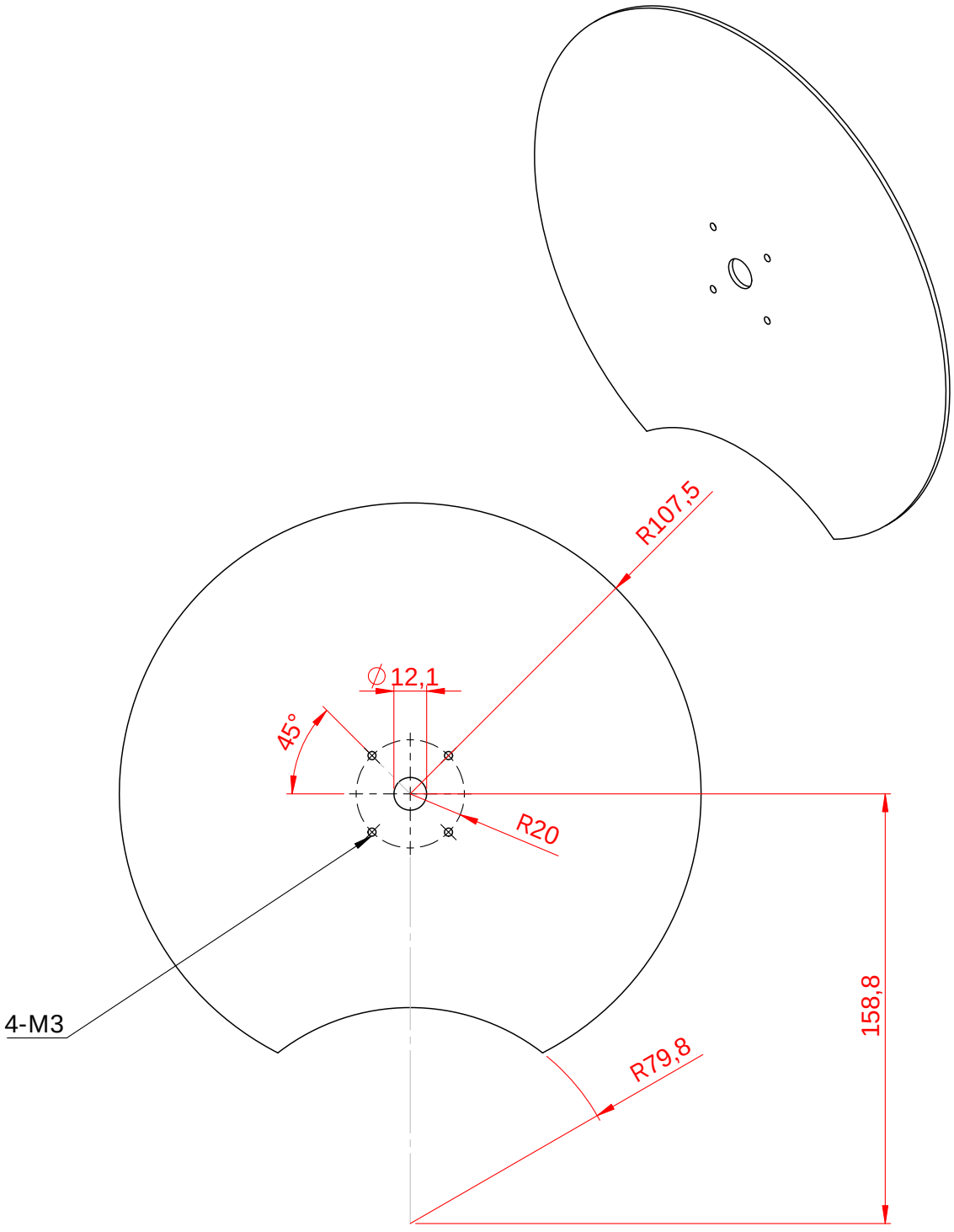

NOTAS: Todas las dimensiones están en mm.	**TÍTULO:** Disco protector	
MATERIAL: Acero inoxidable 304	FEMAN-UB	A4
Espesor: 2	ESCALA:1:2	CANTIDAD: 1

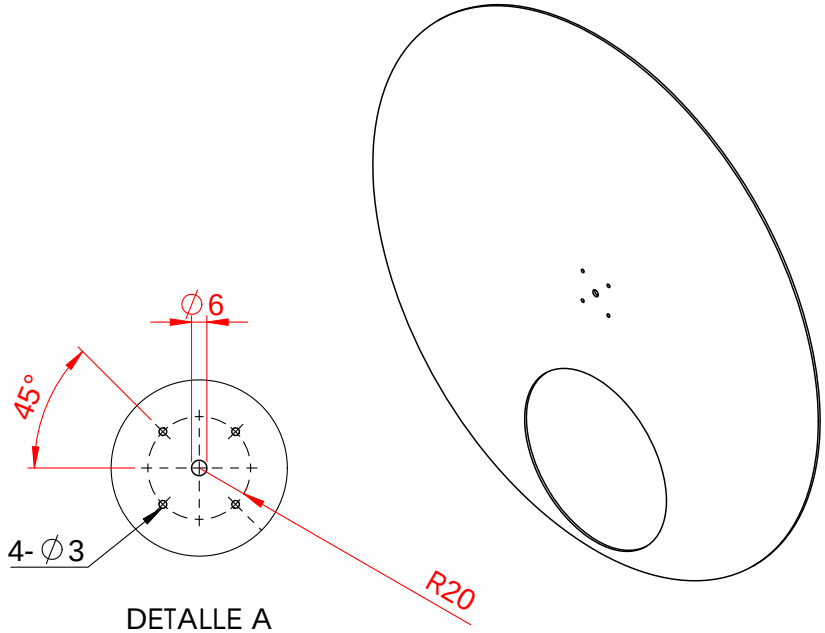

DETALLE A
ESCALA 2 : 5

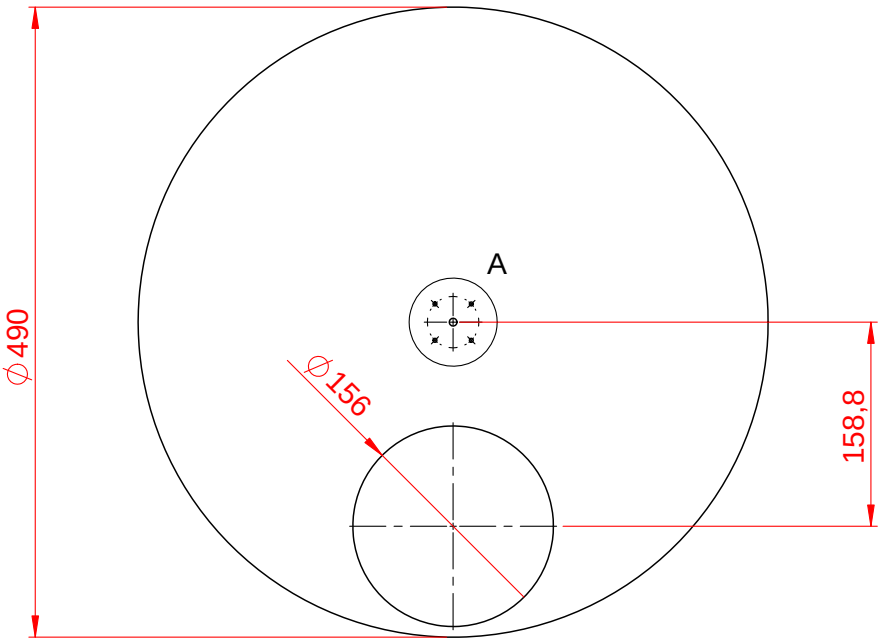

NOTAS:
Todas las dimensiones están en mm.

TÍTULO:
Disco

MATERIAL:
Acero inoxidable 304

FEMAN-UB

A4

Espesor: 2

ESCALA:1:5

CANTIDAD: 1

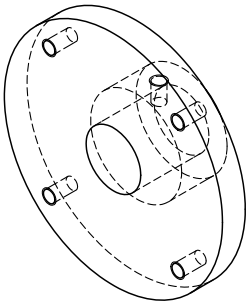

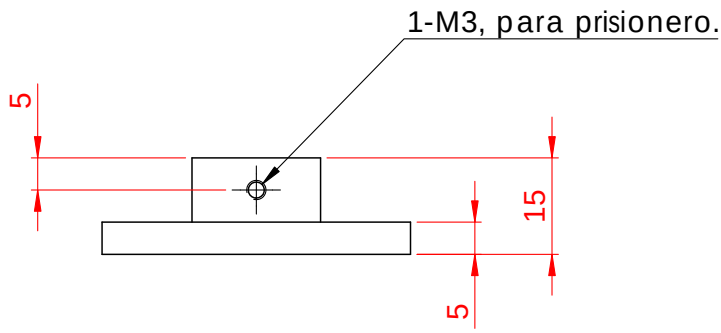

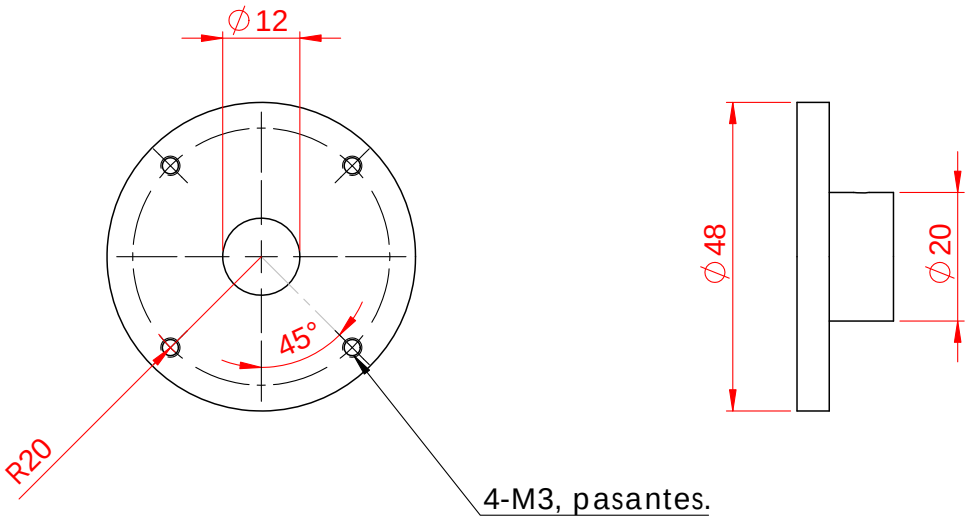

NOTAS:
Todas las dimensiones están en mm.

TÍTULO:
Acople discos

MATERIAL:
Acero inoxidable 304

FEMAN-UB

A4

Espesor: N/A

ESCALA:1:1

CANTIDAD: 2

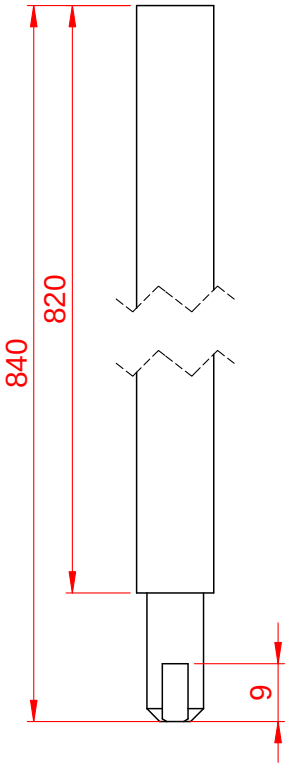

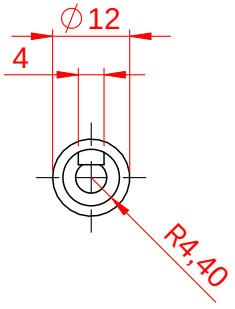

NOTAS: Todas las dimensiones están en mm.	**TÍTULO:** Eje-lock	
MATERIAL: Acero inoxidable 304	FEMAN-UB	A4
Espesor: N/A	ESCALA:1:10	CANTIDAD: 1

Clutch system drawings

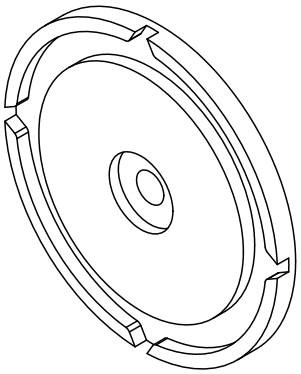

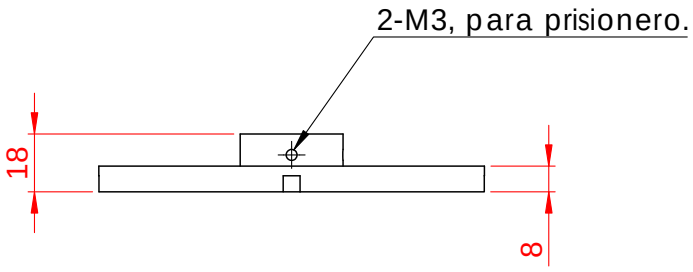

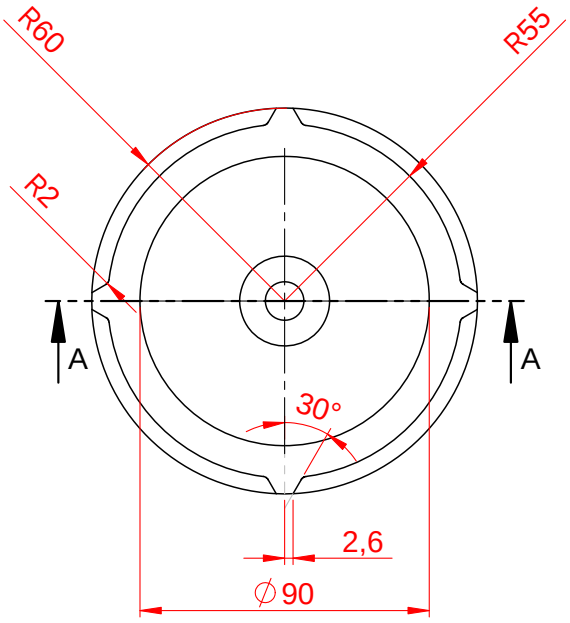

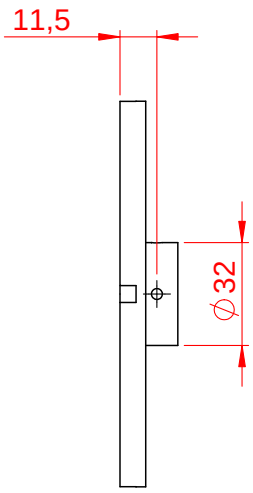

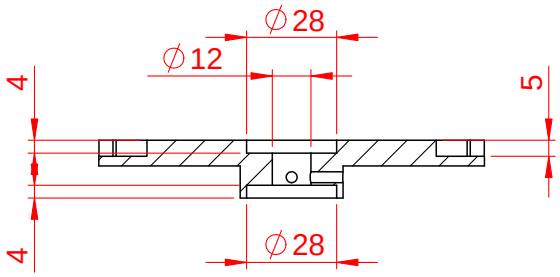

SECCIÓN A-A

NOTAS: Todas las dimensiones están en mm.	**TÍTULO:** Disco-lock	
MATERIAL: Acero inoxidable 304	FEMAN-UB	A4
Espesor: N/A	ESCALA:1:2	CANTIDAD: 1

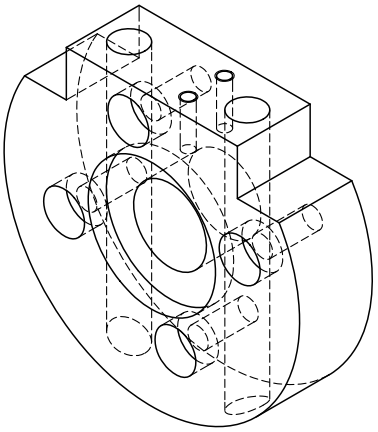

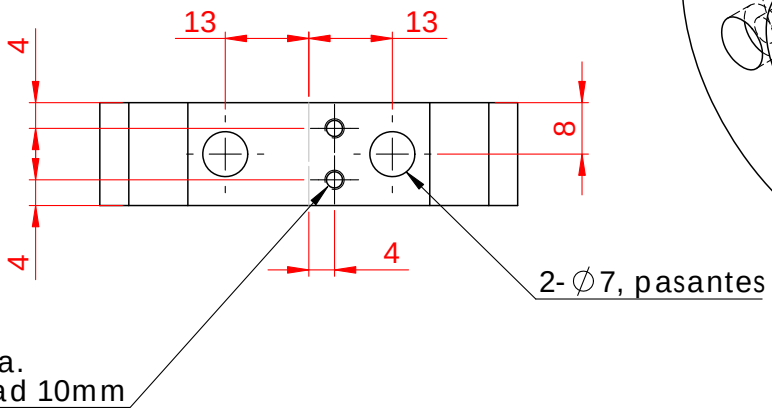

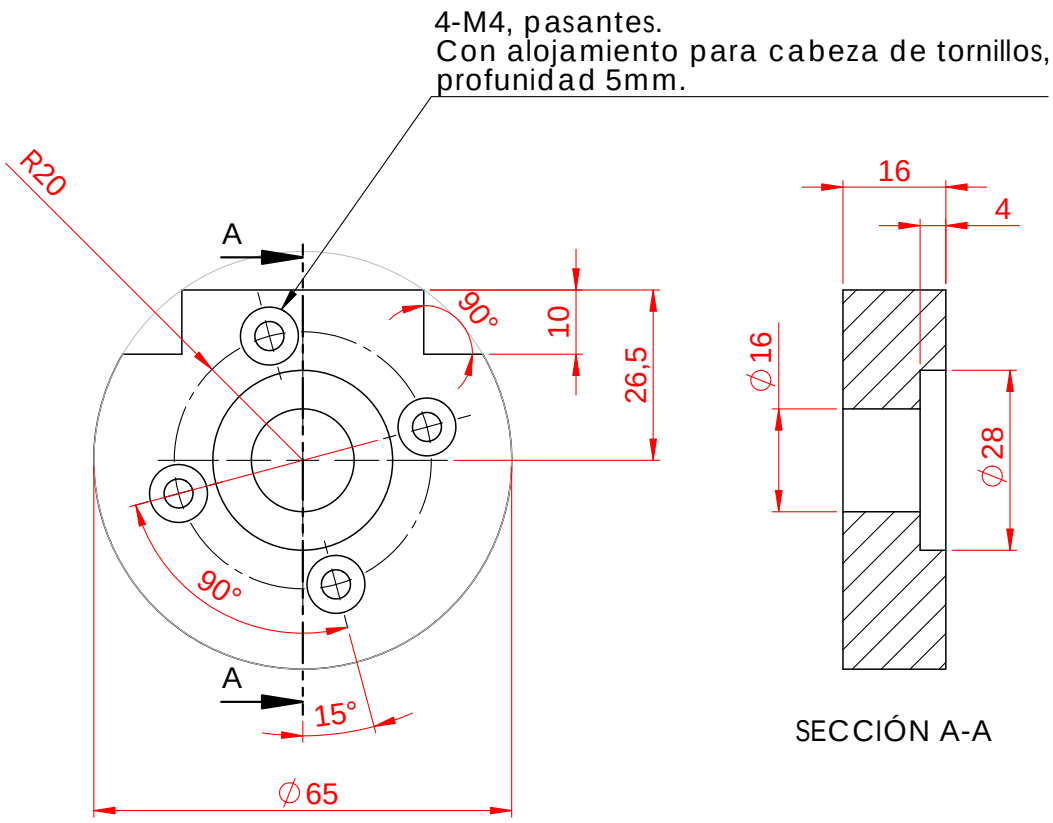

NOTAS: Todas las dimensiones están en mm.	**TÍTULO:** Lock-rodamiento	
MATERIAL: Acero inoxidable 304	FEMAN-UB	A4
Espesor: N/A	ESCALA:1:1	CANTIDAD: 1

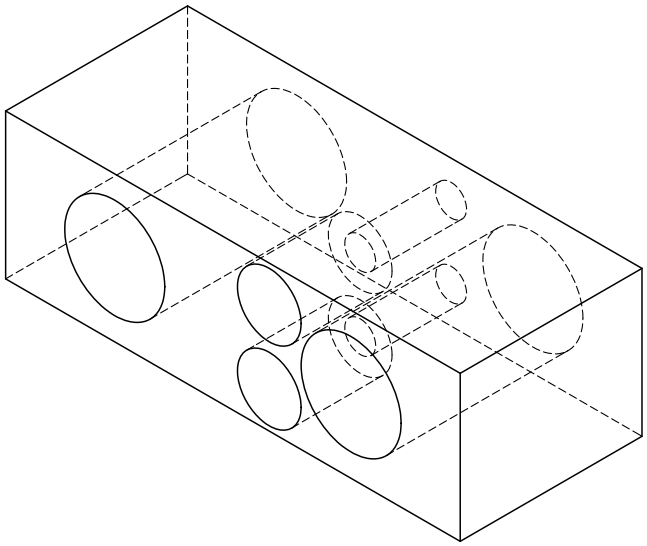

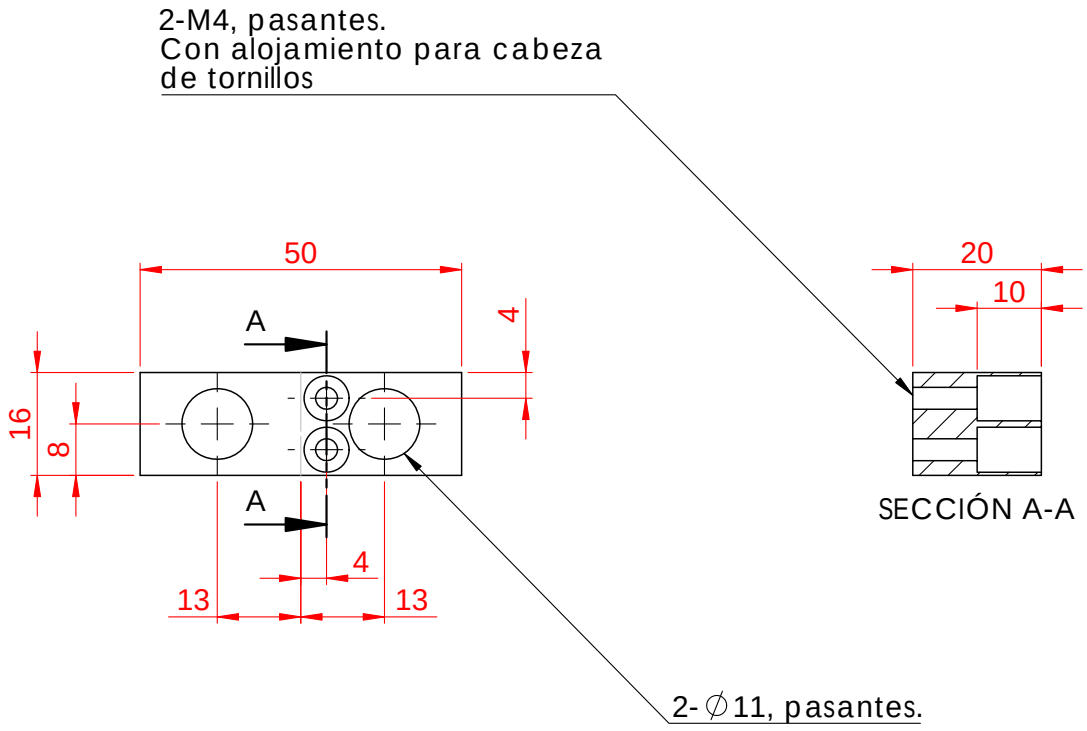

NOTAS: Todas las dimensiones están en mm.	**TÍTULO:** Base Lock	
MATERIAL: Acero inoxidable 304	FEMAN-UB	A4
Espesor: N/A	ESCALA:1:1	CANTIDAD: 1

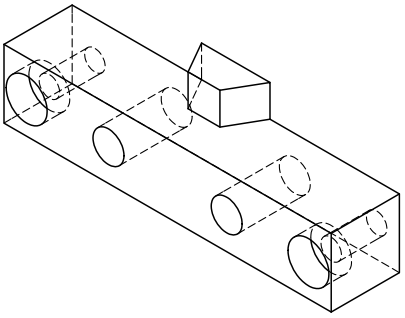

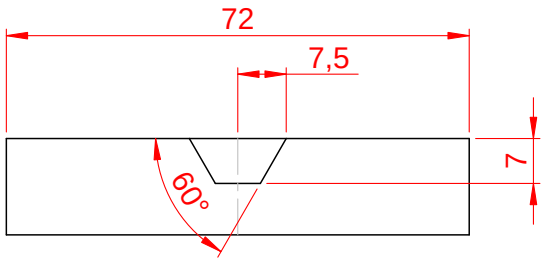

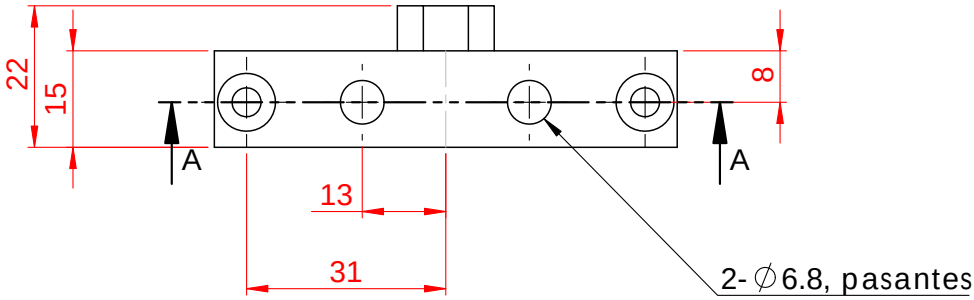

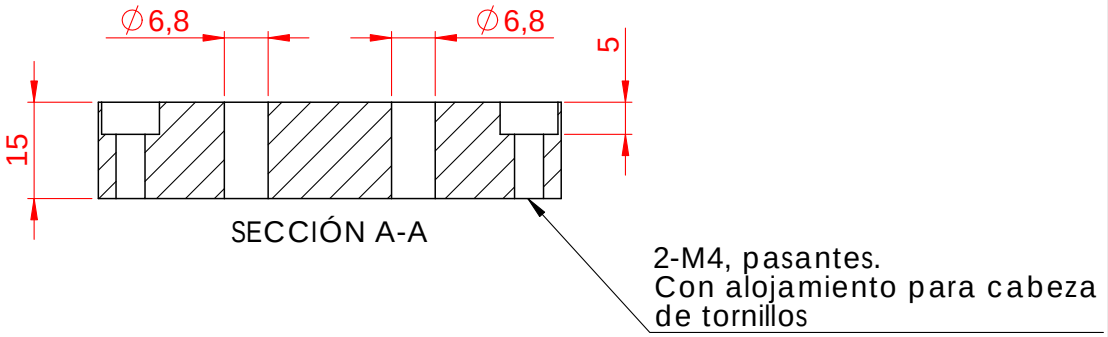

NOTAS: Todas las dimensiones están en mm.	**TÍTULO:** Lock	
MATERIAL: Acero inoxidable 304	FEMAN-UB	A4
Espesor: N/A	ESCALA:1:1	CANTIDAD: 1

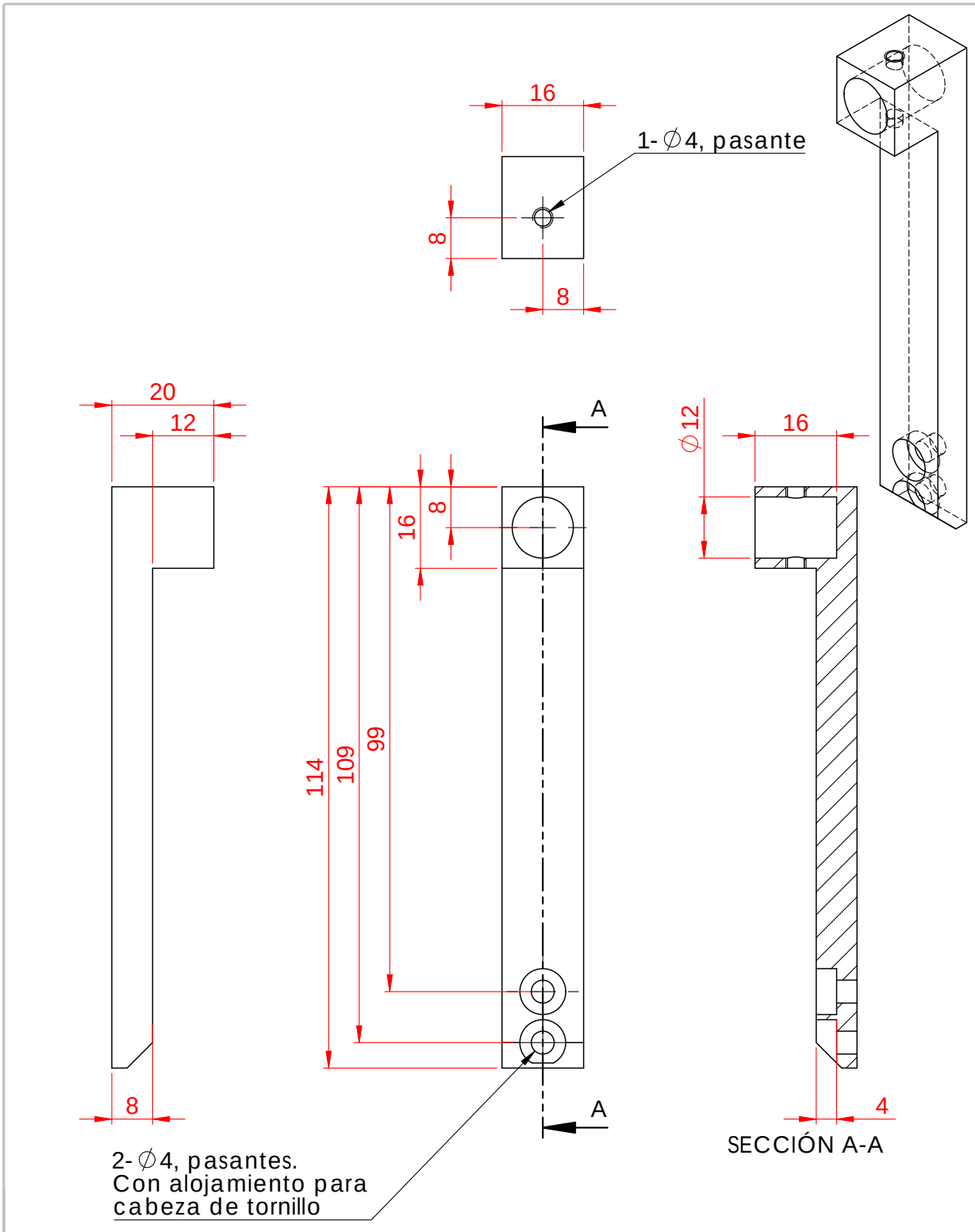

NOTAS: Todas las dimensiones están en mm.	**TÍTULO:** Barra 1	
MATERIAL: Acero inoxidable 304	FEMAN-UB	A4
Espesor: N/A	ESCALA:1:1	CANTIDAD: 1

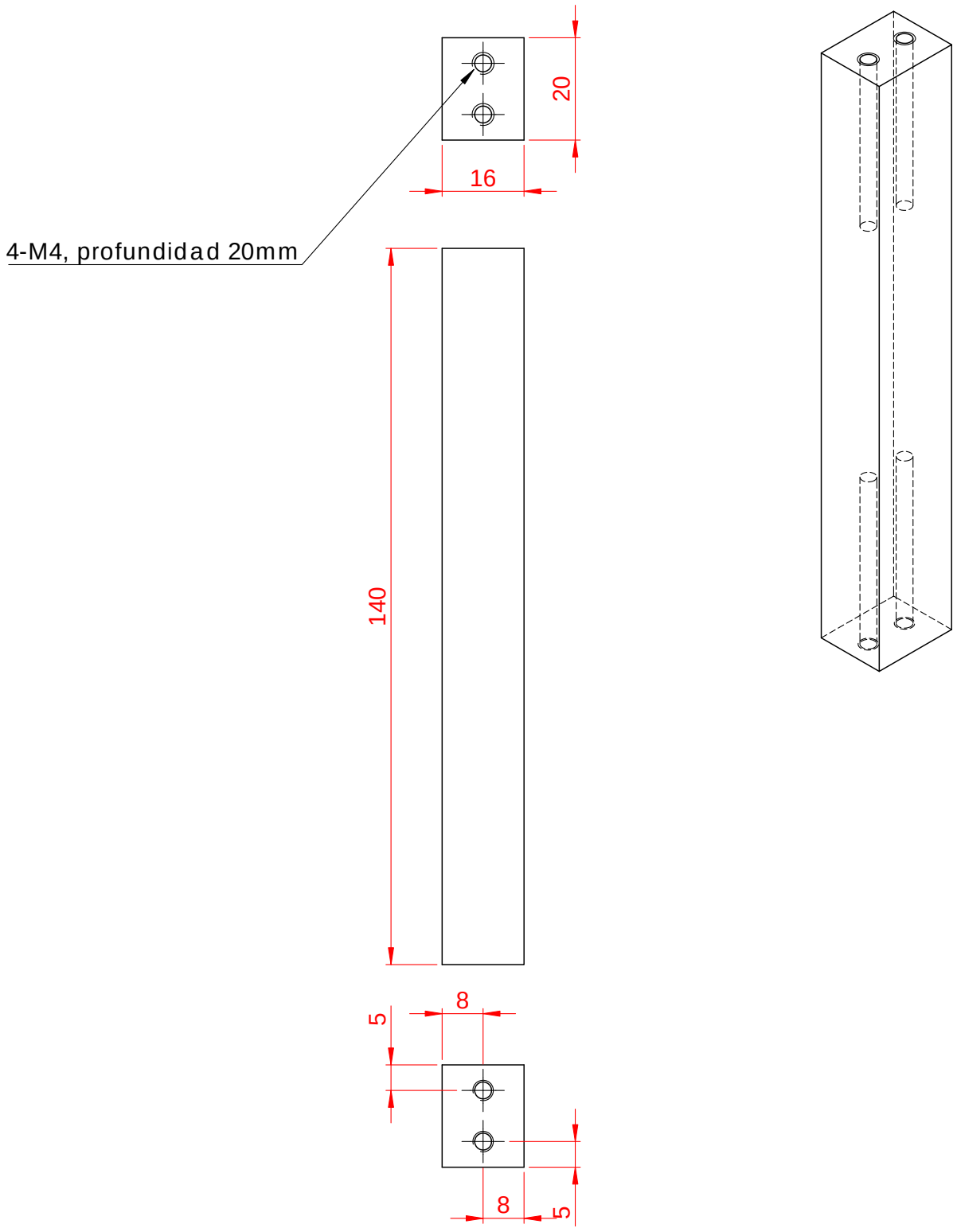

NOTAS:
Todas las dimensiones están en mm.

TÍTULO:
Barra 2

MATERIAL:
Acero inoxidable 304

FEMAN-UB

A4

Espesor: N/A

ESCALA:1:1

CANTIDAD: 1

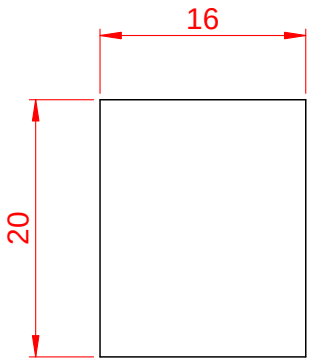

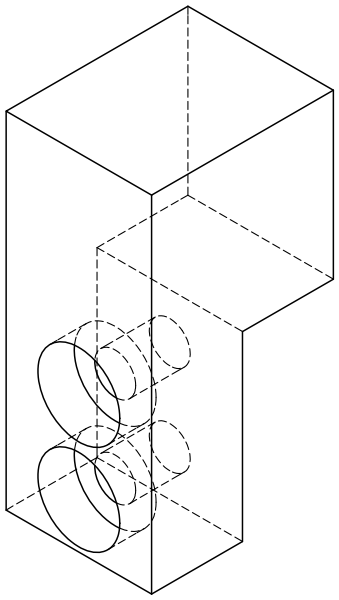

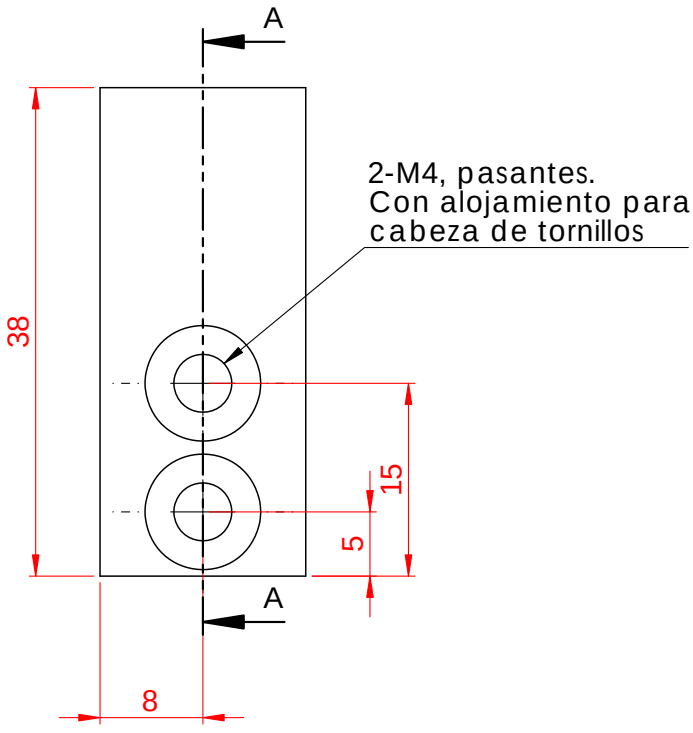

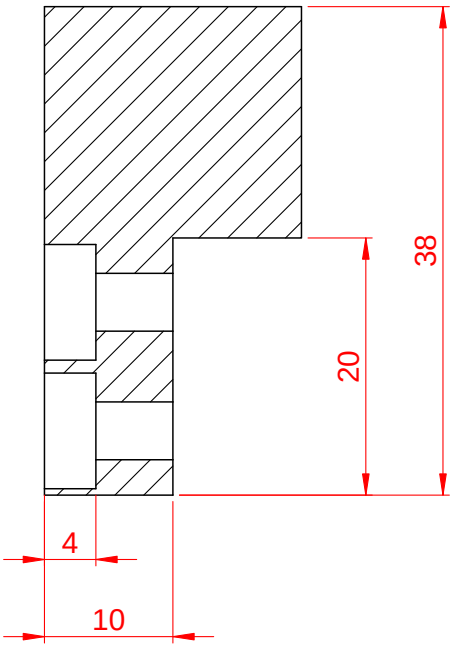

SECCIÓN A-A

NOTAS: Todas las dimensiones están en mm.	**TÍTULO:** Barra 3	
MATERIAL: Acero inoxidable 304	FEMAN-UB	A4
Espesor: N/A	ESCALA:2:1	CANTIDAD: 1

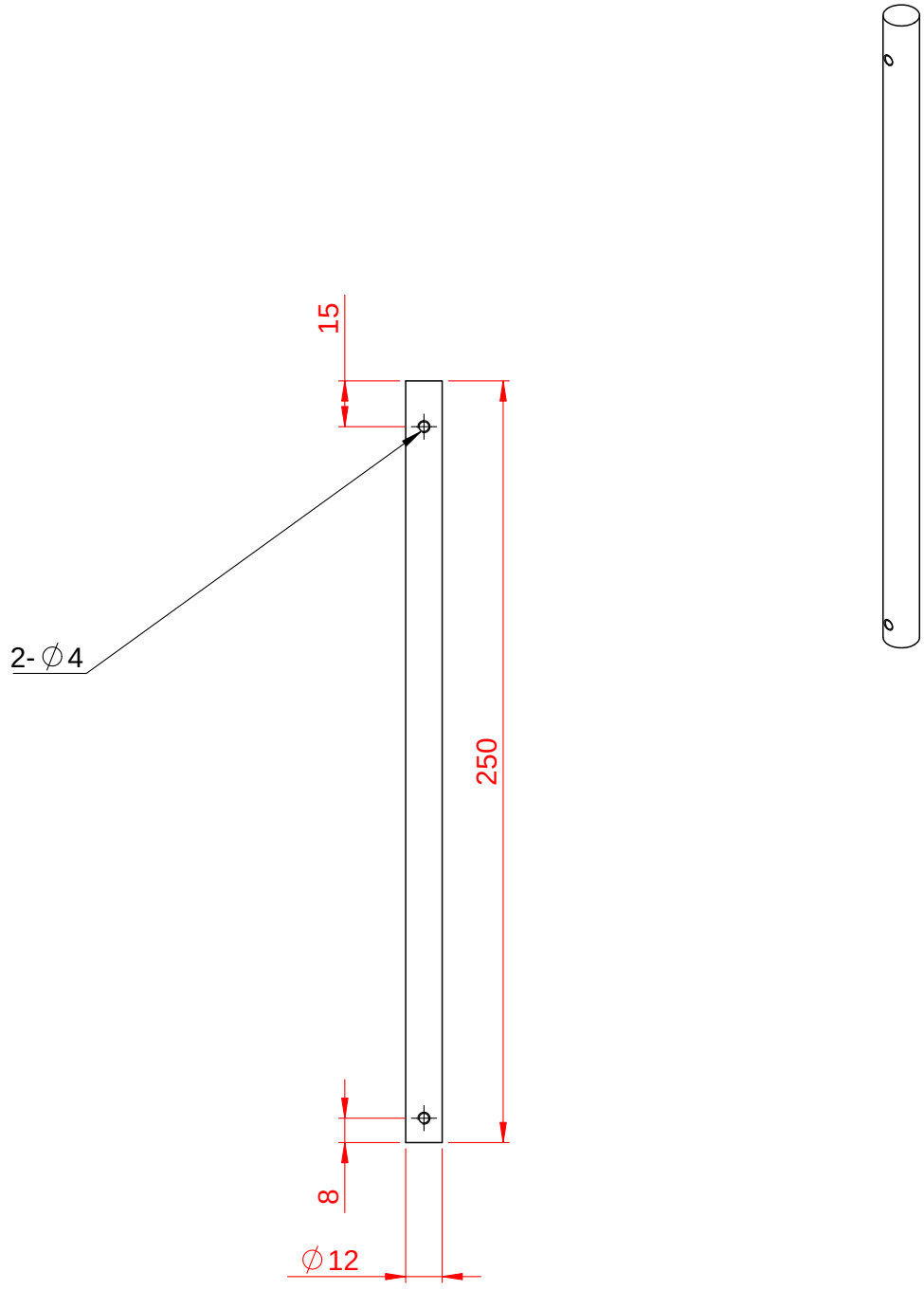

NOTAS: Todas las dimensiones están en mm.	**TÍTULO:** Eje	
MATERIAL: Acero inoxidable 304	FEMAN-UB	A4
Espesor: N/A	ESCALA:1:2	CANTIDAD: 1

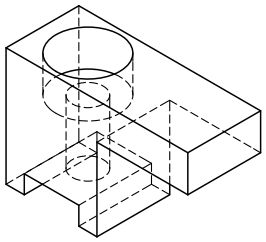

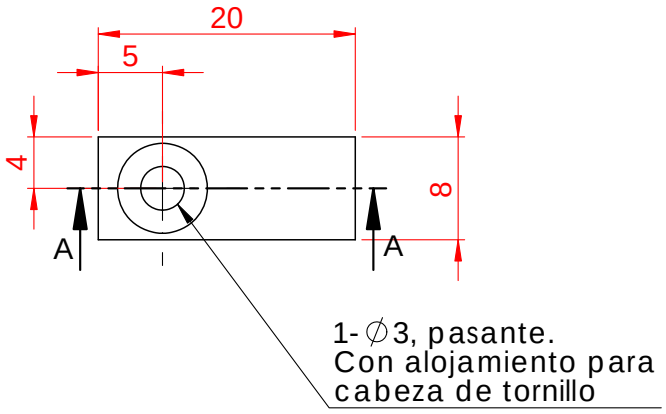

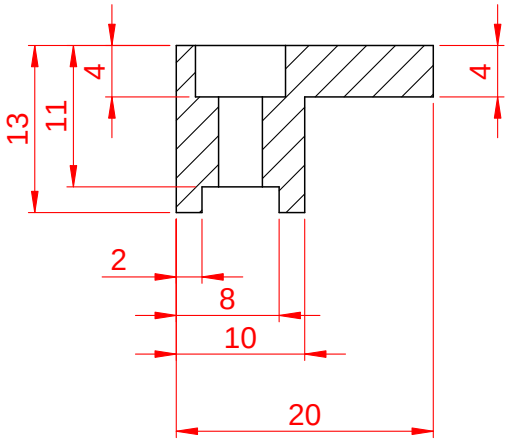

SECCIÓN A-A

NOTAS: Todas las dimensiones están en mm.	**TÍTULO:** Seguro	
MATERIAL: Acero inoxidable 304	FEMAN-UB	A4
Espesor: N/A	ESCALA:2:1	CANTIDAD: 1

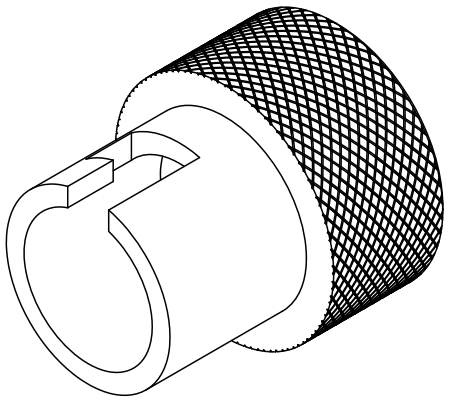

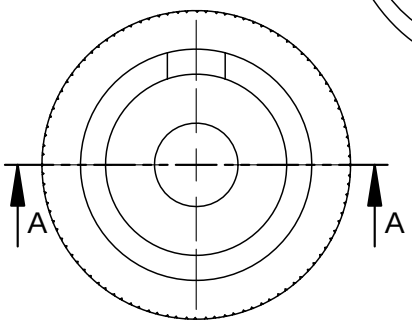

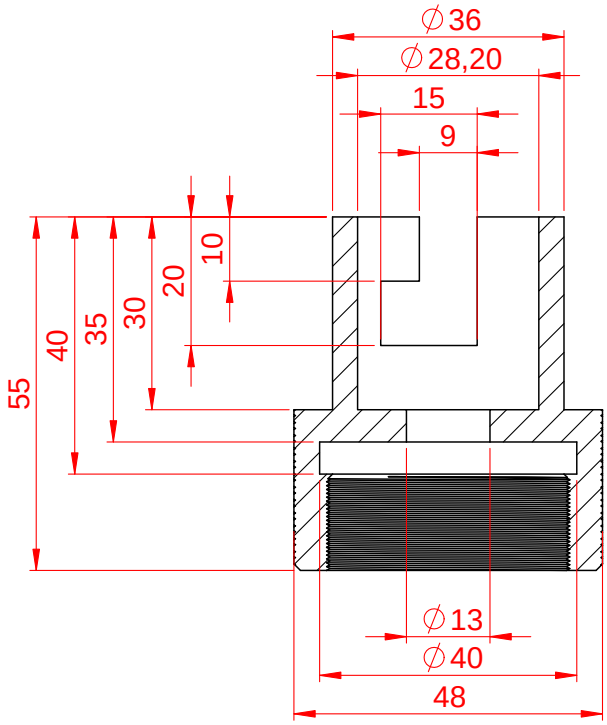

SECCIÓN A-A

NOTAS: Todas las dimensiones están en mm.	**TÍTULO:** Tapa-Seguro	
MATERIAL: Latón	FEMAN-UB	A4
Espesor: N/A	ESCALA:1:1	CANTIDAD: 1

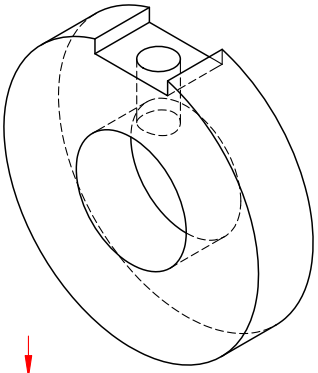

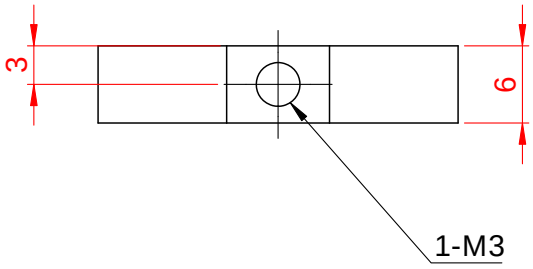

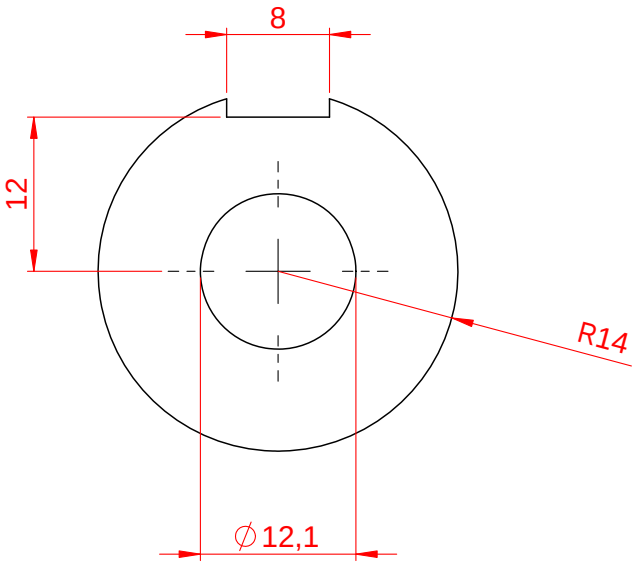

NOTAS: Todas las dimensiones están en mm.	**TÍTULO:** Seguro 1	
MATERIAL: Acero inoxidable 304	FEMAN-UB	A4
Espesor: N/A	ESCALA:2:1	CANTIDAD: 1

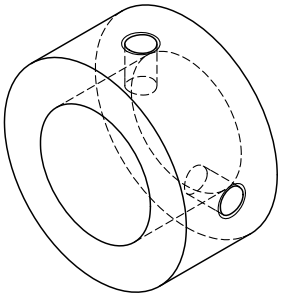

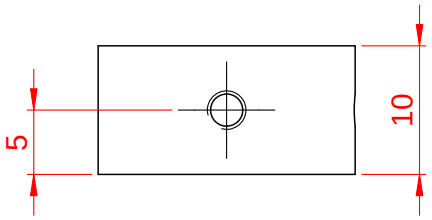

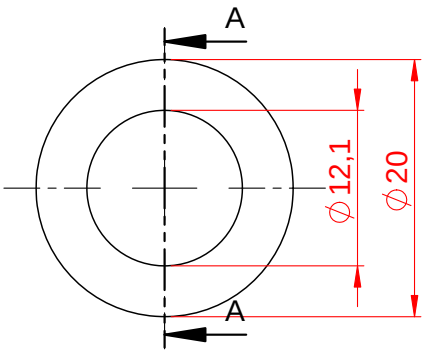

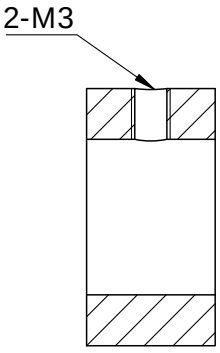

SECCIÓN A-A

NOTAS: Todas las dimensiones están en mm.	**TÍTULO:** Seguro Eje 12mm	
MATERIAL: Acero inoxidable 304	FEMAN-UB	A4
Espesor: N/A	ESCALA:2:1	CANTIDAD: 4

Position control system drawings

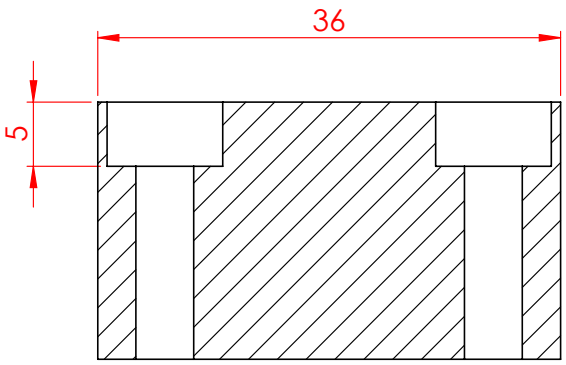

SECCIÓN A-A

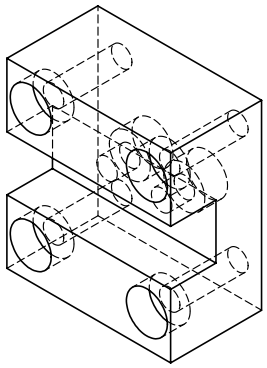

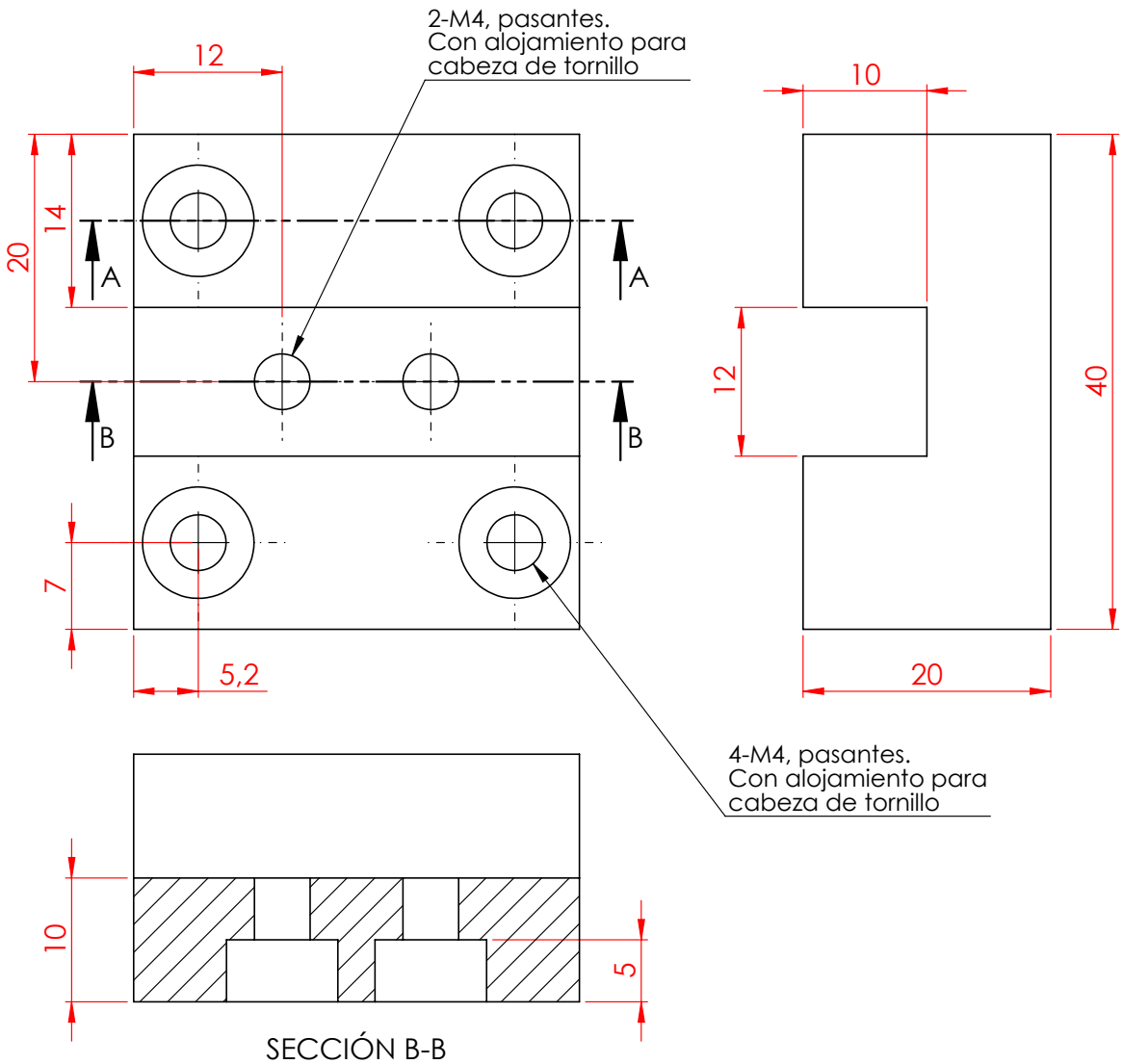

SECCIÓN B-B

NOTAS: Todas las dimensiones están en mm.	**TÍTULO:** Acople-guía	
MATERIAL: Aluminio	FEMAN-UB	A4
Espesor: 20 mm	ESCALA:2:1	CANTIDAD: 2

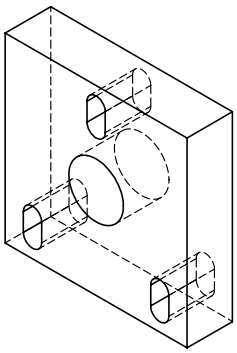

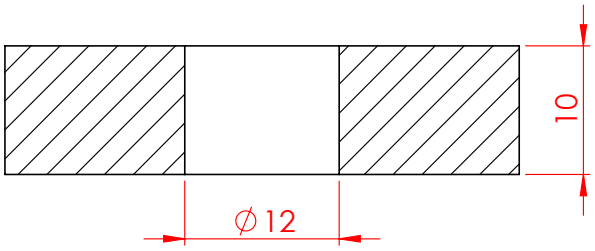

SECCIÓN A-A

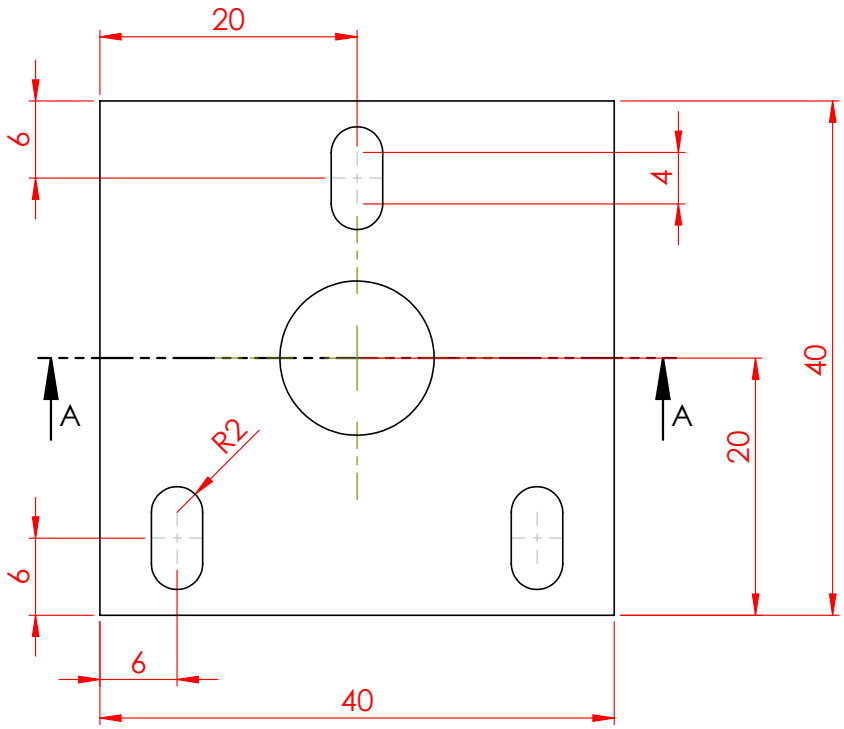

NOTAS:
Todas las dimensiones están en mm.

TÍTULO:
Anclaje Base 2

MATERIAL:
Aluminio

FEMAN-UB

A4

Espesor: 10 mm

ESCALA:2:1

CANTIDAD: 1

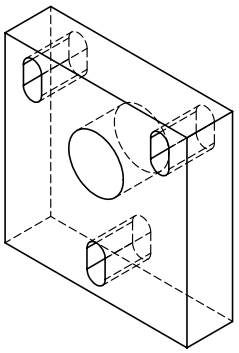

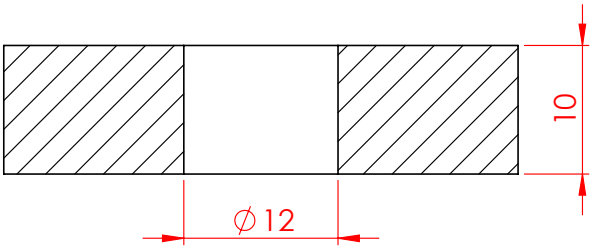

SECCIÓN A-A

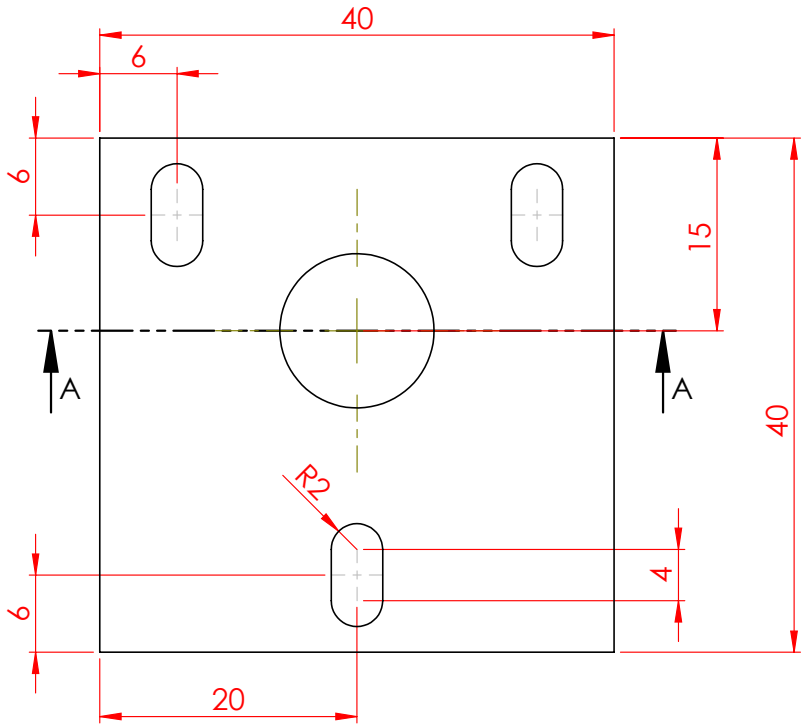

NOTAS:
Todas las dimensiones están en mm.

TÍTULO:
Anclaje Base 1

MATERIAL:
Aluminio

Espesor: 10 mm

FEMAN-UB

A4

ESCALA:2:1

CANTIDAD: 1

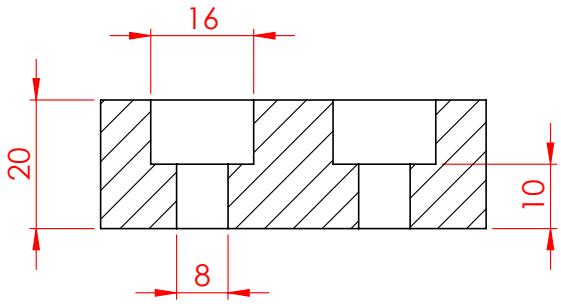

SECCIÓN A-A

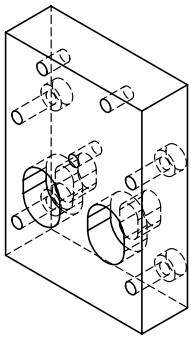

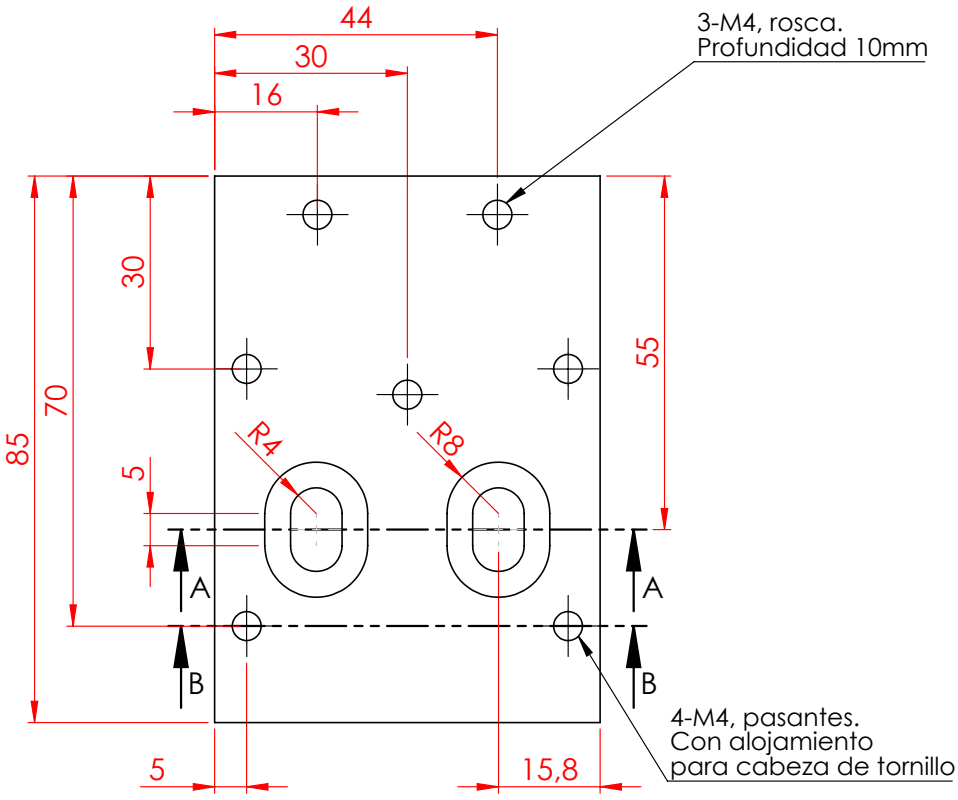

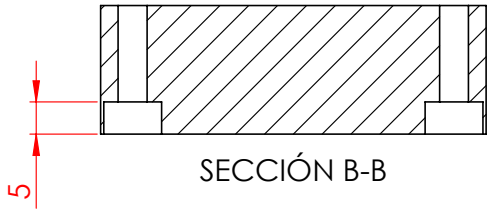

SECCIÓN B-B

NOTAS: Todas las dimensiones están en mm.	**TÍTULO:** Base 1	
MATERIAL: Aluminio	FEMAN-UB	A4
Espesor: 20 mm	ESCALA:1:1	CANTIDAD: 1

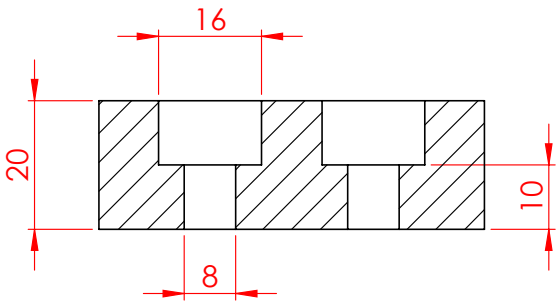

SECCIÓN A-A

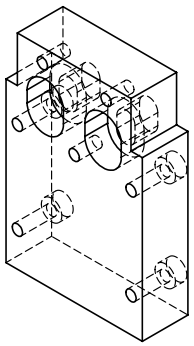

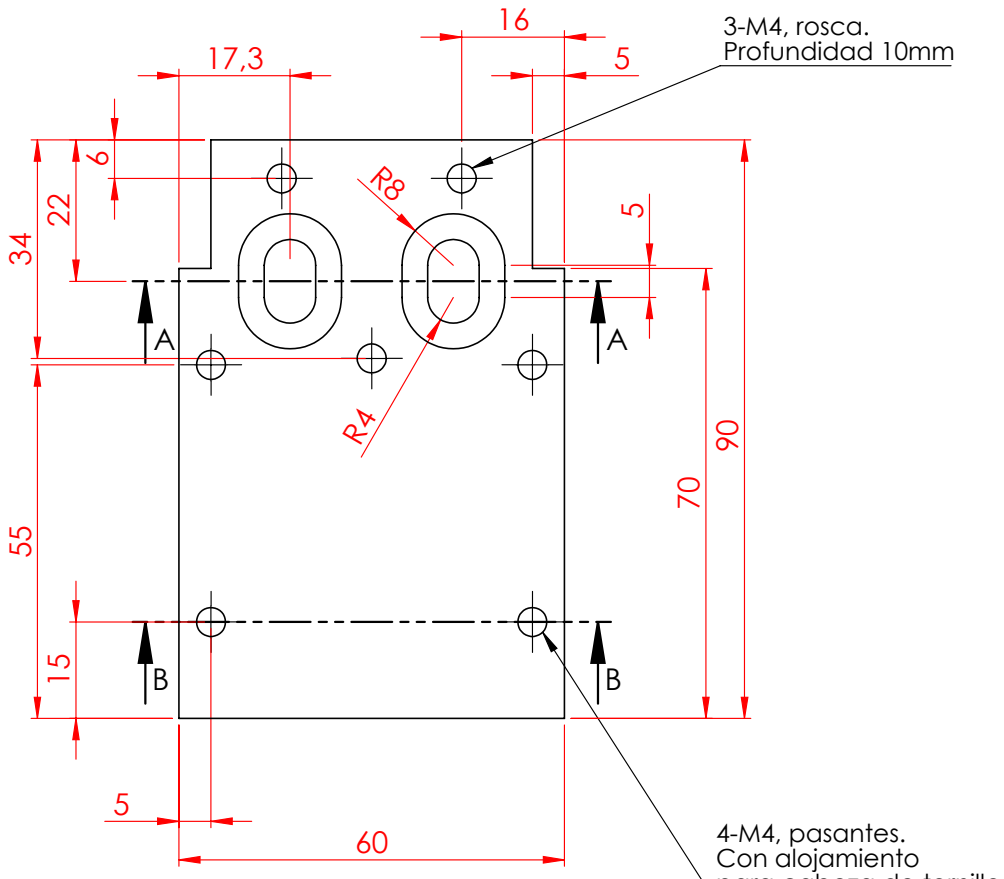

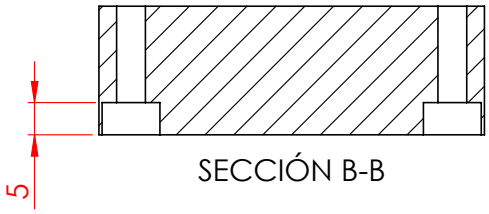

SECCIÓN B-B

NOTAS: Todas las dimensiones están en mm.	**TÍTULO:** Base 2	
MATERIAL: Aluminio	FEMAN-UB	A4
Espesor: 20 mm	ESCALA:1:1	CANTIDAD: 1

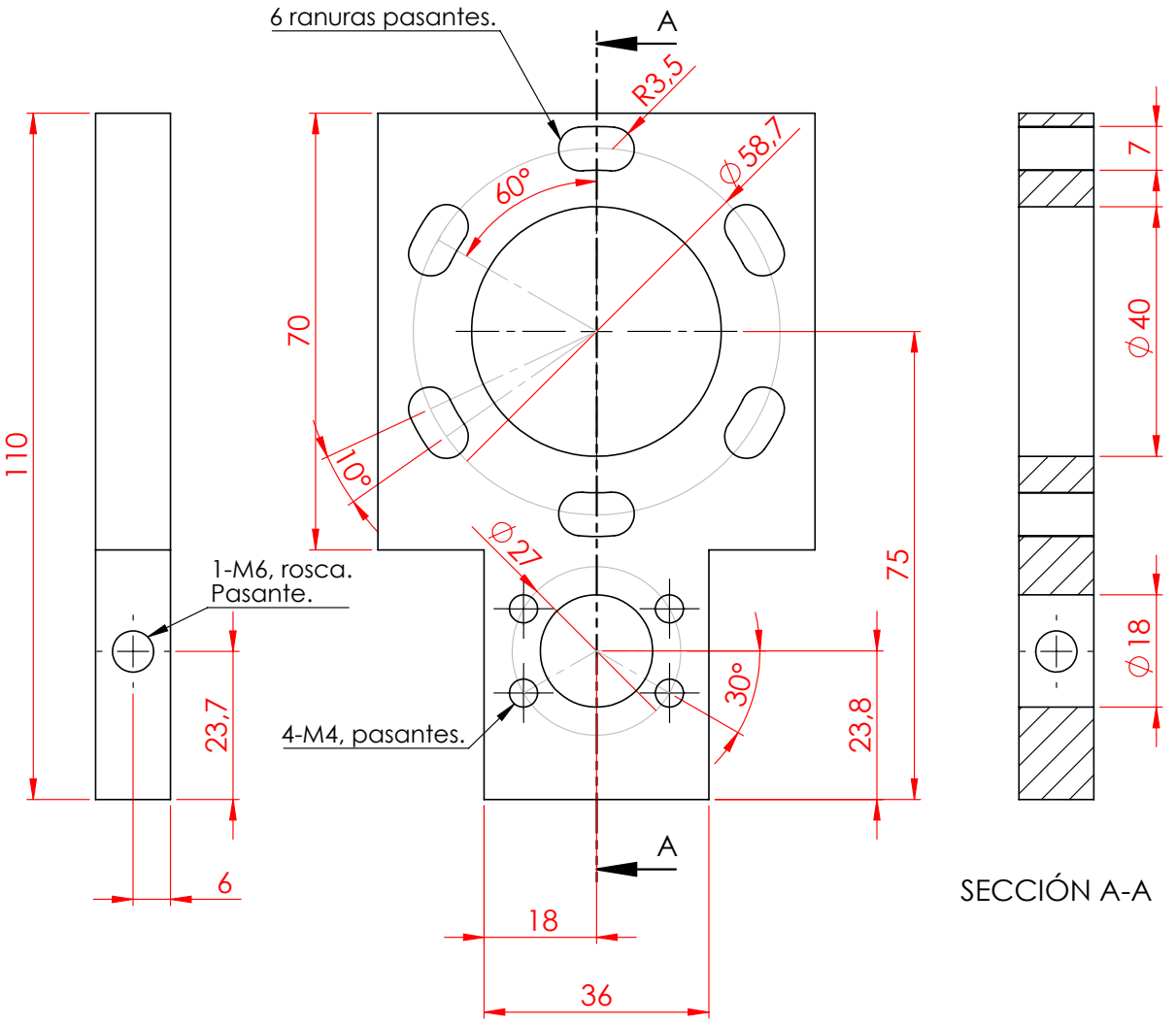

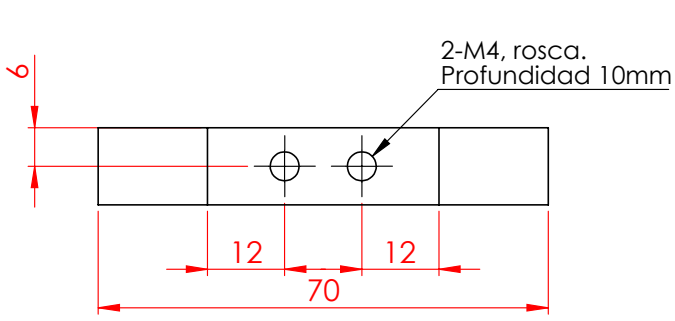

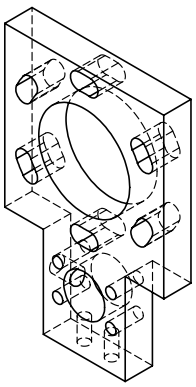

NOTAS: Todas las dimensiones están en mm.	**TÍTULO:** Brida-acople 1	
MATERIAL: Aluminio	FEMAN-UB	A4
Espesor: 12 mm	ESCALA:1:1	CANTIDAD: 1

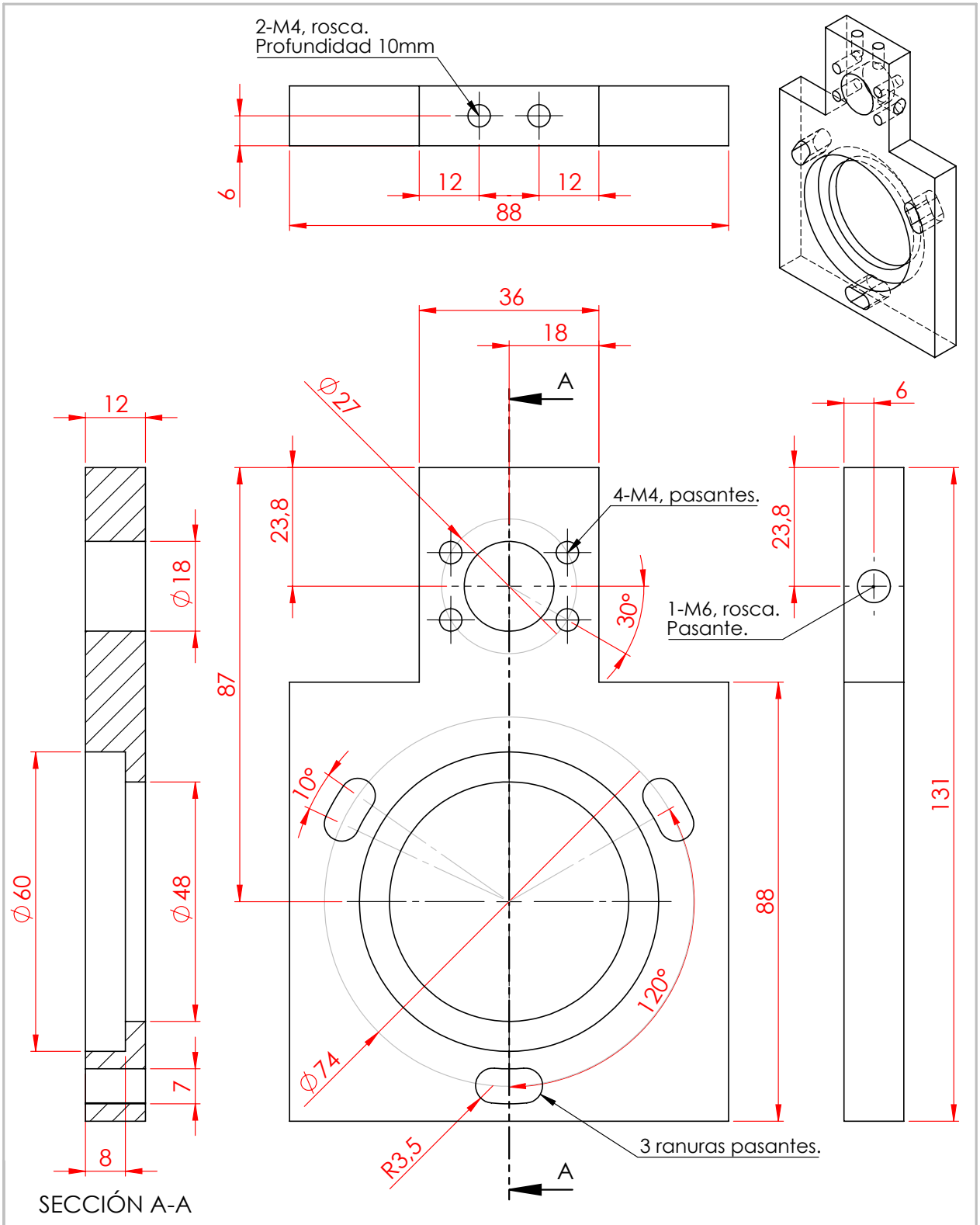

NOTAS: Todas las dimensiones están en mm.	**TÍTULO:** Brida-acople 2	
MATERIAL: Aluminio	FEMAN-UB	A4
Espesor: 12 mm	ESCALA:1:1	CANTIDAD: 1

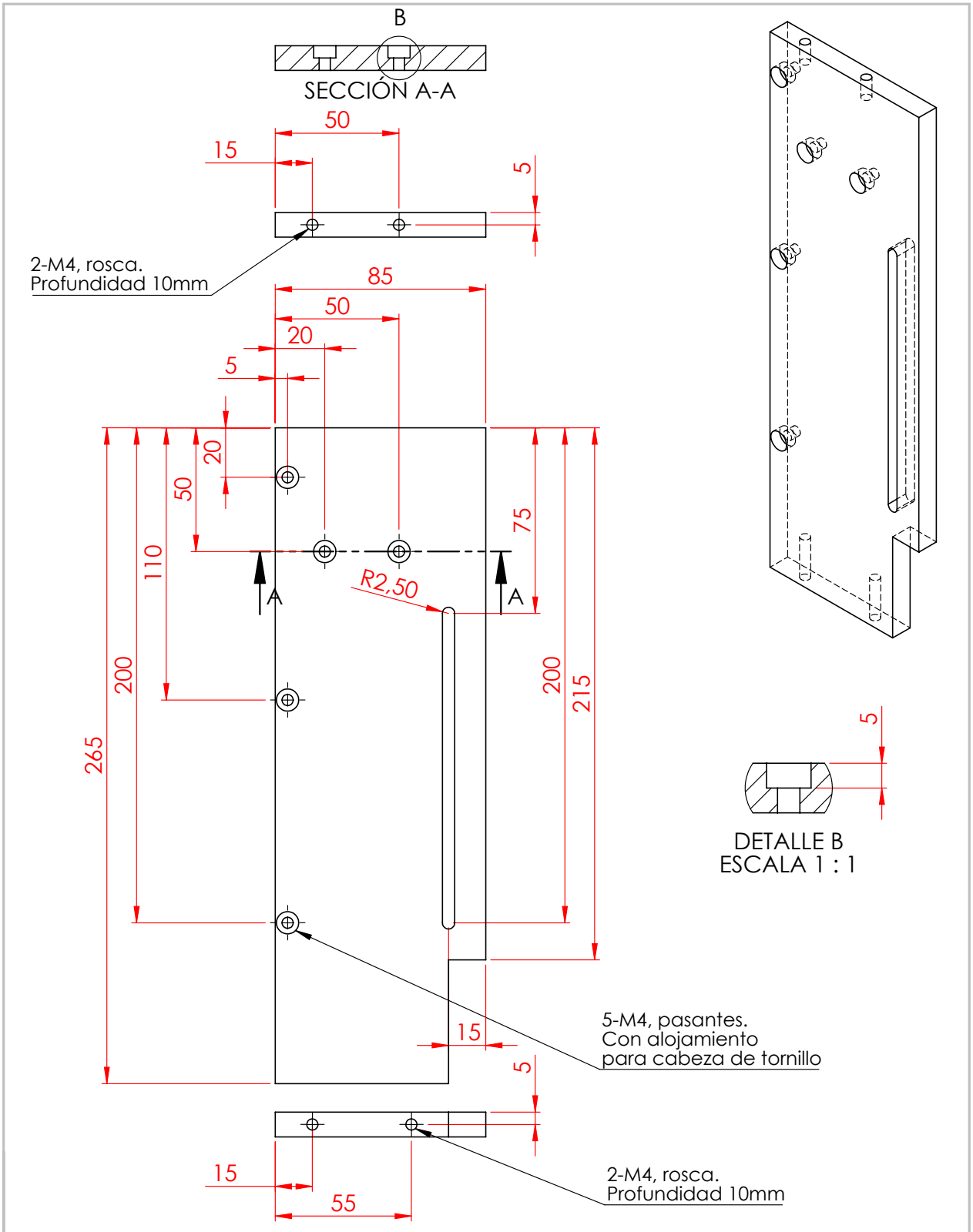

NOTAS:
Todas las dimensiones están en mm.

TÍTULO:
Lateral-Derecha-2

MATERIAL:
Aluminio

Espesor: 10 mm

FEMAN-UB

A4

ESCALA:1:2

CANTIDAD: 1

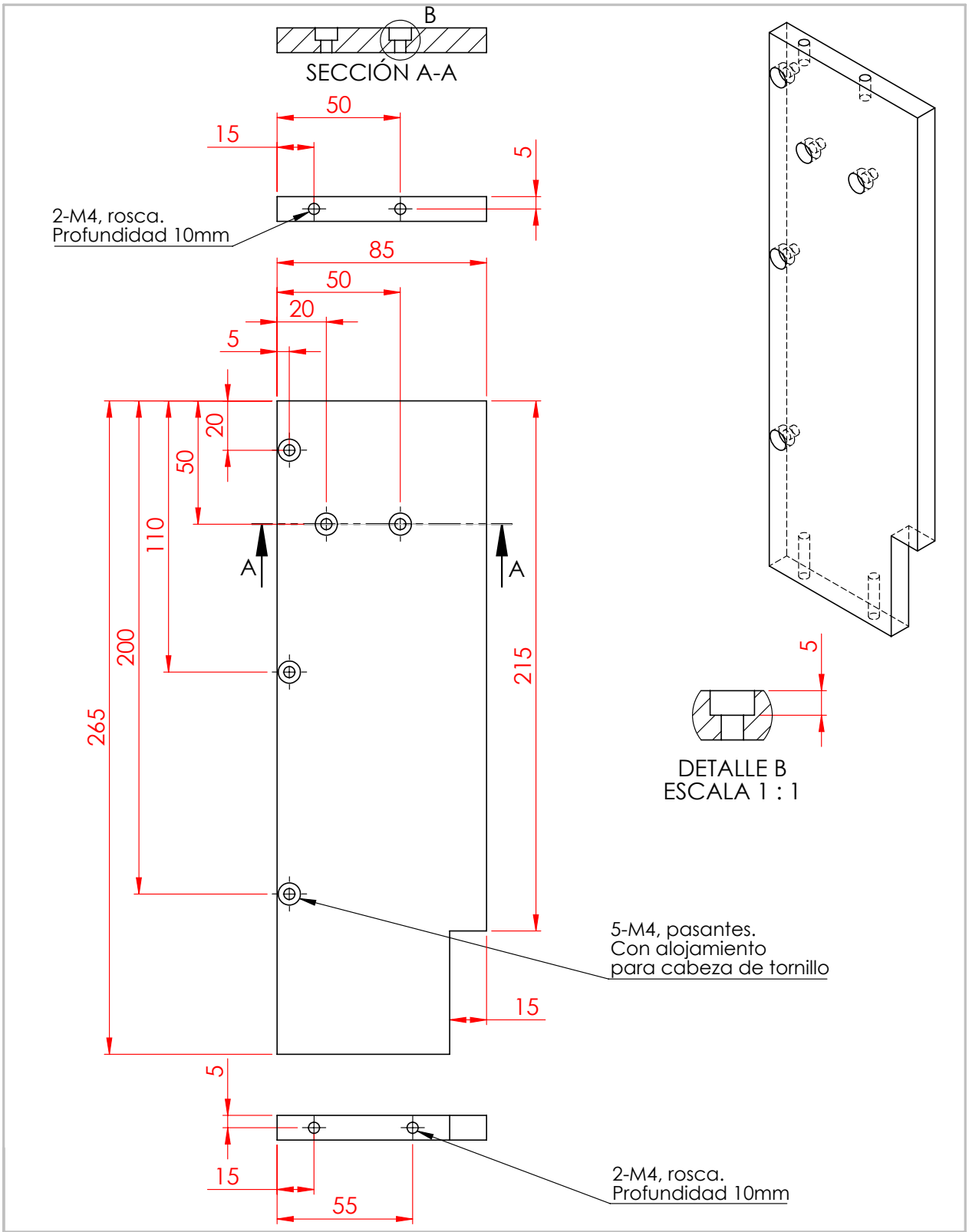

NOTAS:
Todas las dimensiones están en mm.

TÍTULO:
Lateral Derecha 1

MATERIAL:
Aluminio

FEMAN-UB

A4

Espesor: 10 mm

ESCALA:1:2

CANTIDAD: 1

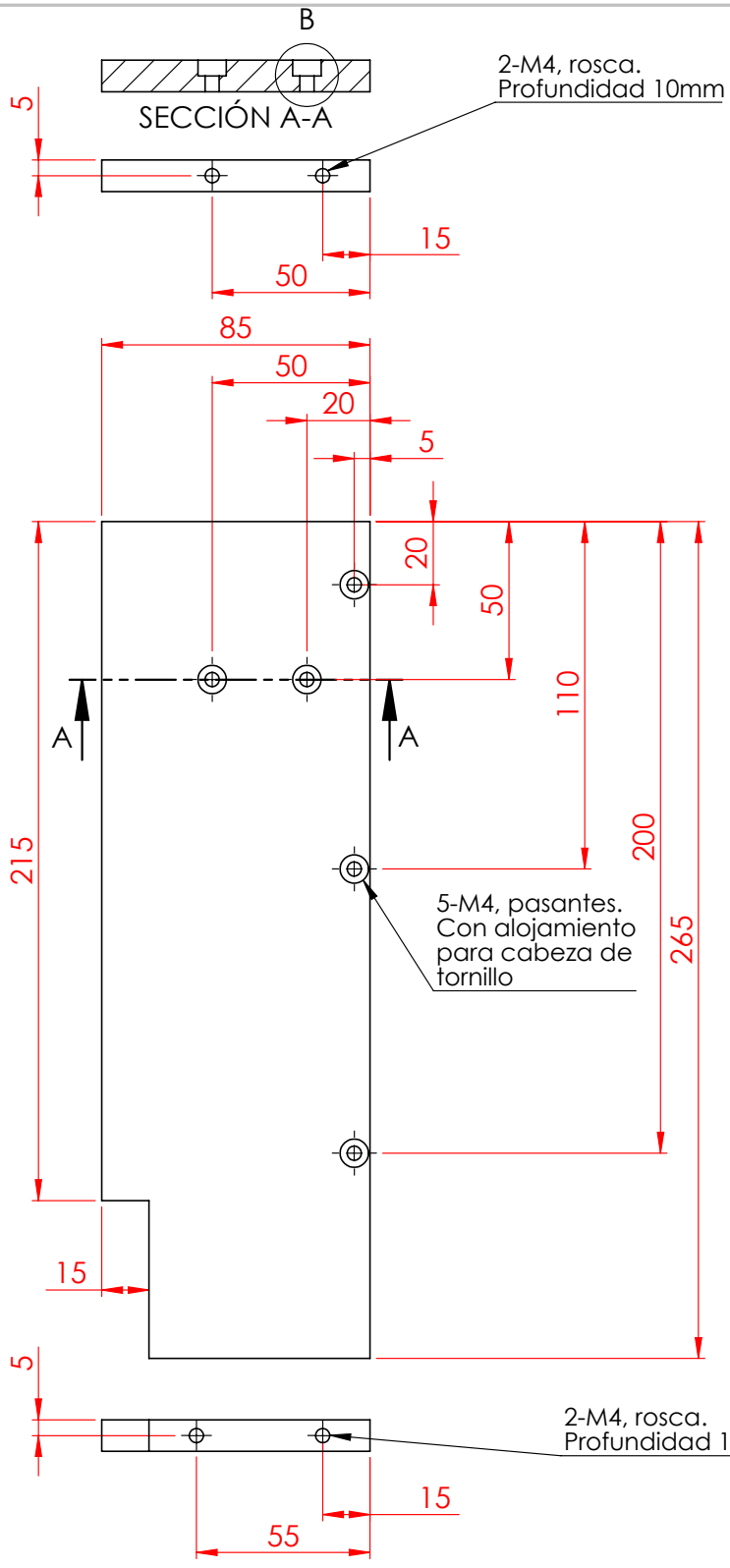

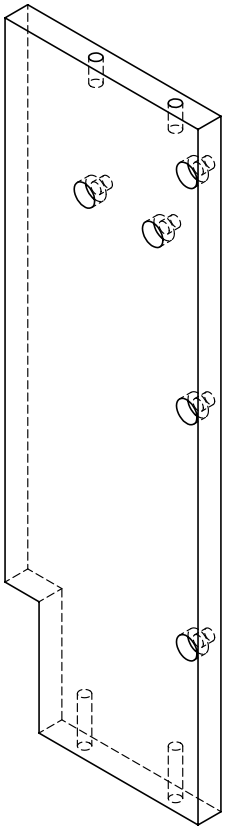

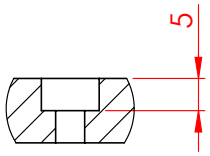

DETALLE B
ESCALA 1 : 1

NOTAS:
Todas las dimensiones están en mm.

TÍTULO:
Lateral-Izquierda 2

MATERIAL:
Aluminio

FEMAN-UB

A4

Espesor: 10 mm

ESCALA:1:2

CANTIDAD: 1

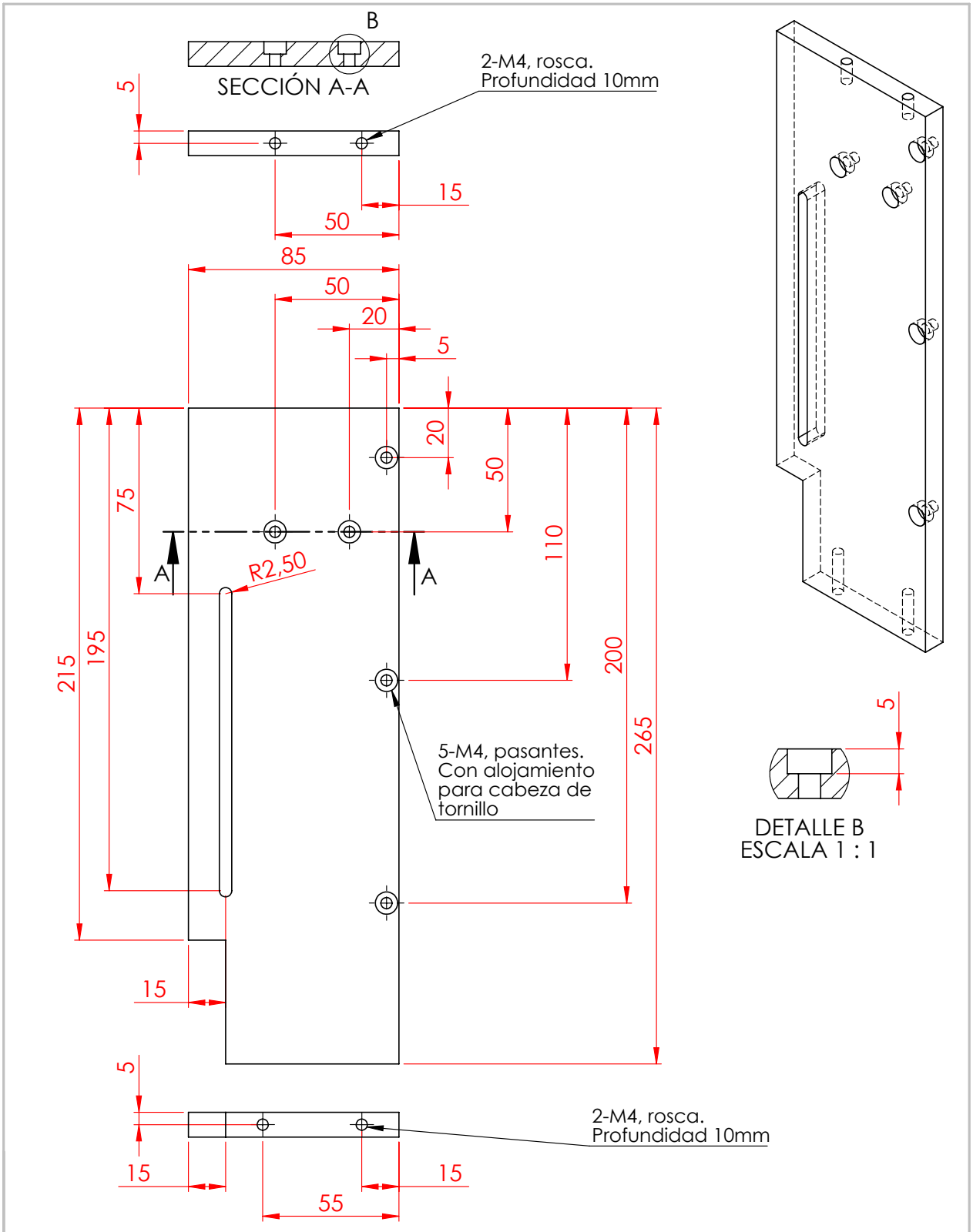

NOTAS:
Todas las dimensiones están en mm.

TÍTULO:
Lateral Izquierda 1

MATERIAL:
Aluminio

Espesor: 10 mm

FEMAN-UB

A4

ESCALA:1:2

CANTIDAD: 1

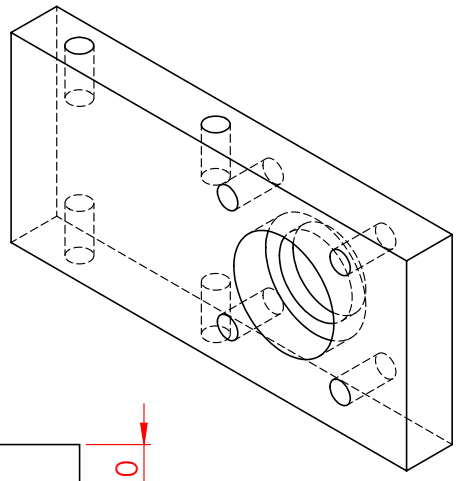

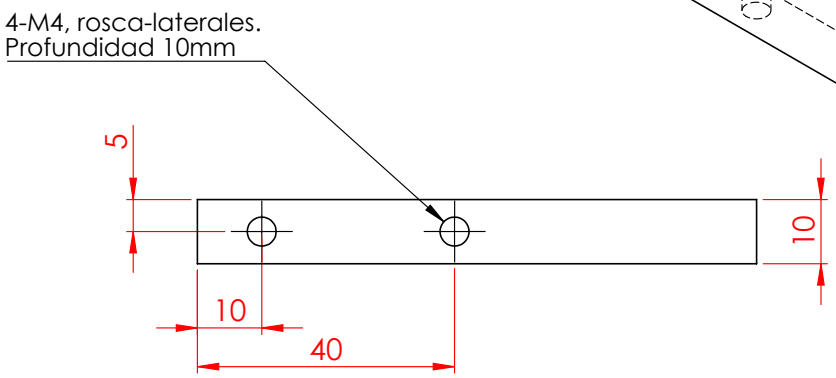

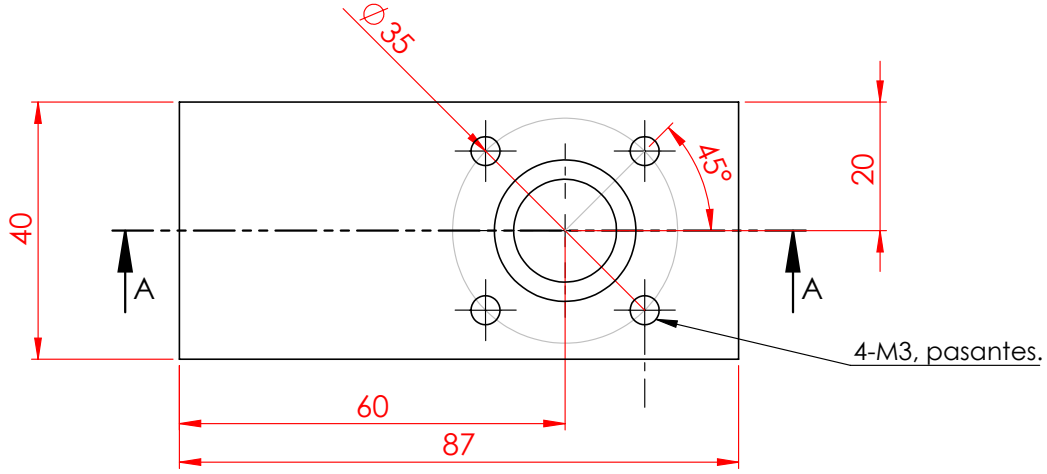

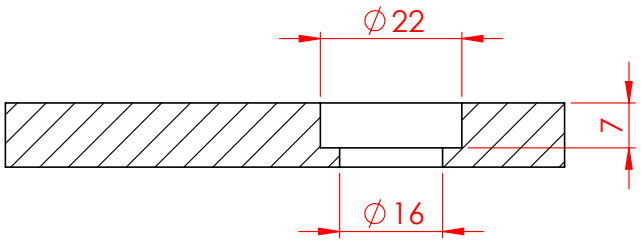

SECCIÓN A-A

NOTAS:
Todas las dimensiones están en mm.

TÍTULO:
Superior husillo

MATERIAL:
Aluminio

FEMAN-UB

A4

Espesor: 10 mm

ESCALA:1:1

CANTIDAD: 2

SECCIÓN A-A

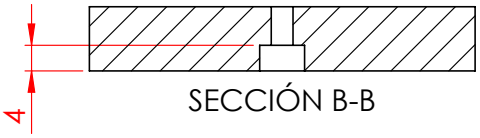

SECCIÓN B-B

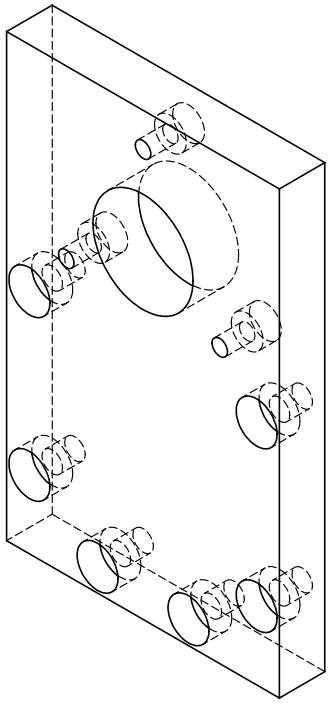

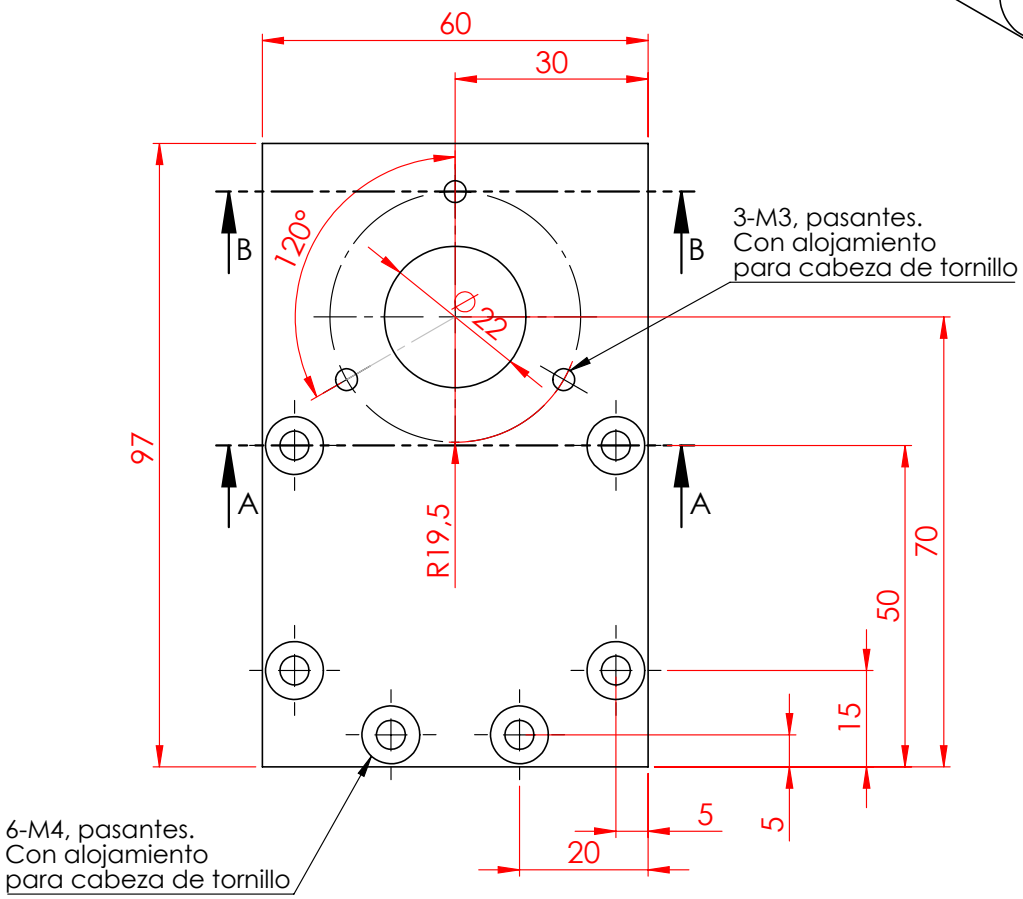

NOTAS:
Todas las dimensiones están en mm.

TÍTULO:
Superior Motor

MATERIAL:
Aluminio

Espesor: 10 mm

FEMAN-UB

A4

ESCALA:1:1

CANTIDAD: 2

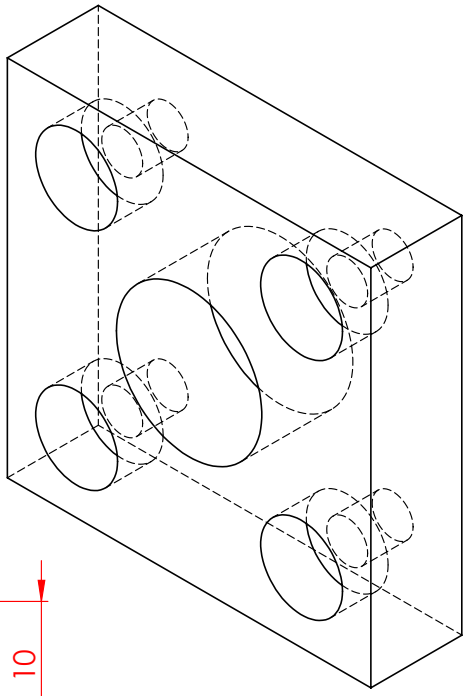

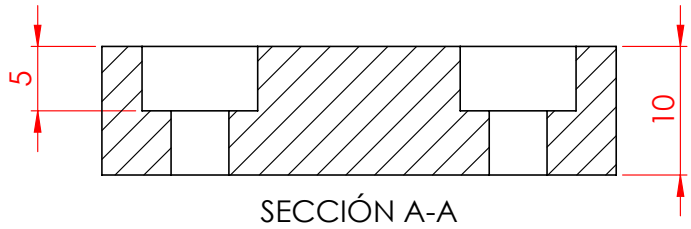

SECCIÓN A-A

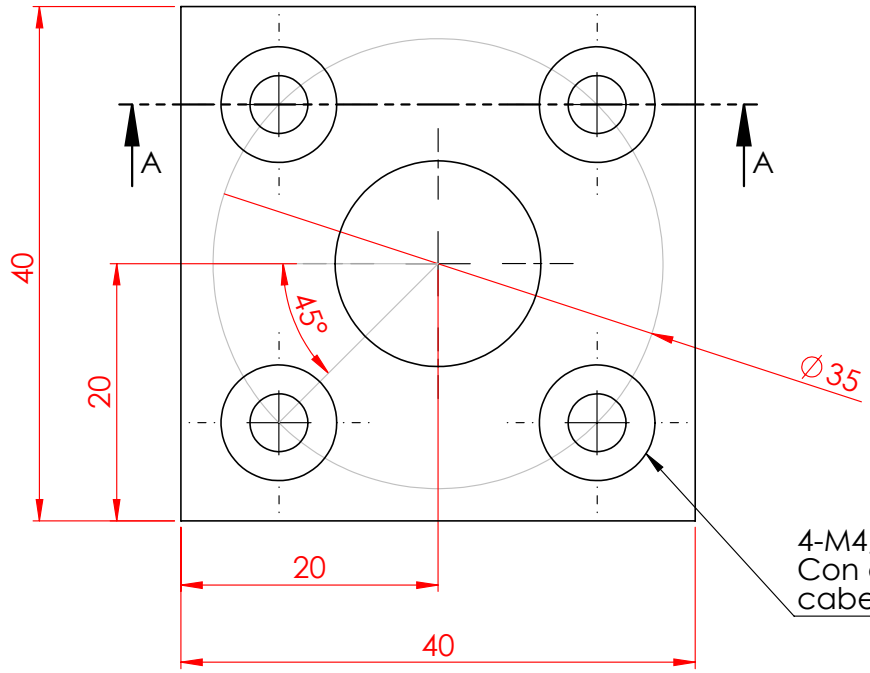

4-M4, pasantes.
Con alojamiento para cabeza de tornillo.

NOTAS:
Todas las dimensiones están en mm.

TÍTULO:
Tapa Rodamiento

MATERIAL:
Aluminio

Espesor: 10 mm

FEMAN-UB

A4

ESCALA:2:1

CANTIDAD: 2

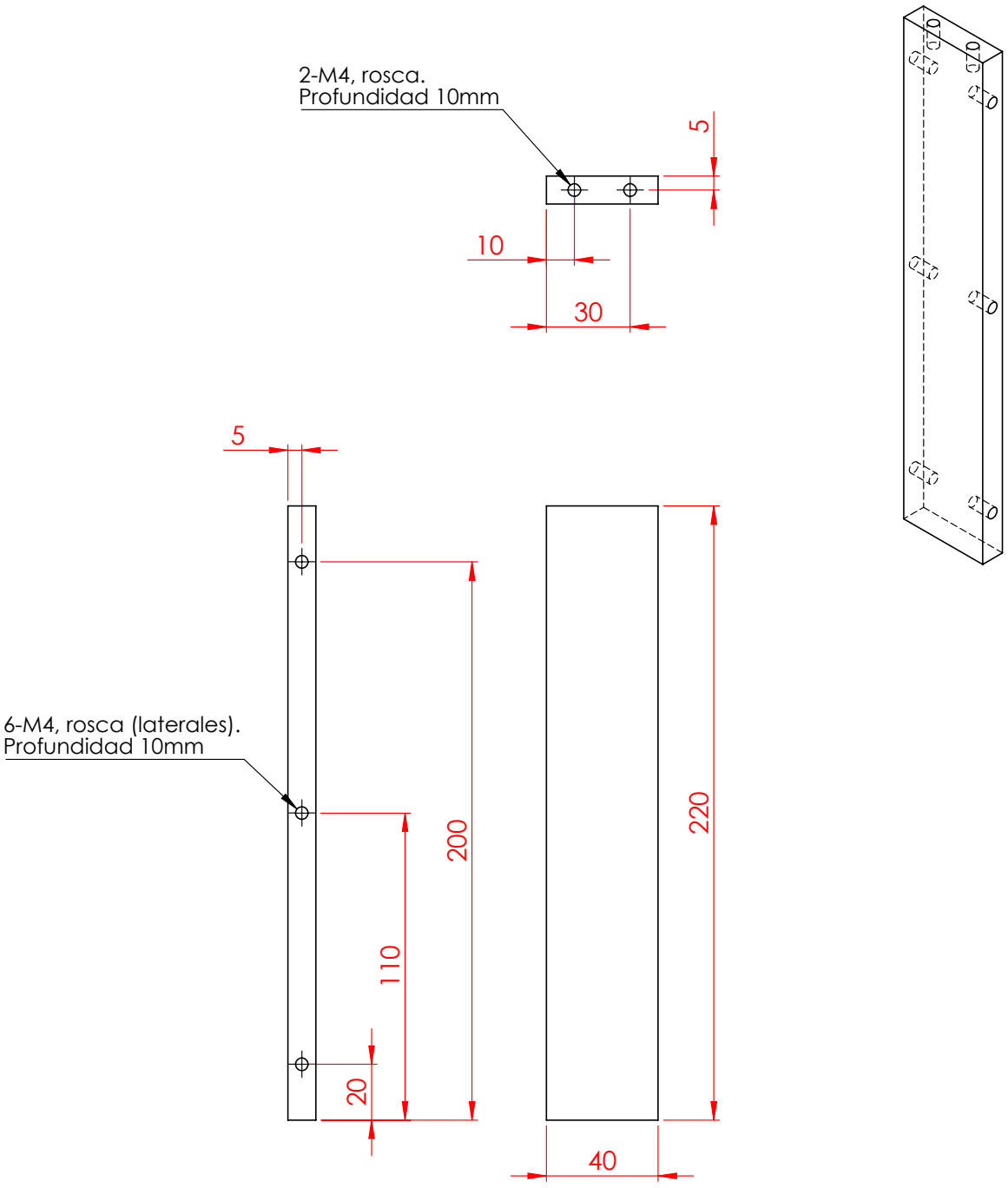

NOTAS:
Todas las dimensiones están en mm.

TÍTULO:
Unión guía

MATERIAL:
Aluminio

Espesor: 10 mm

FEMAN-UB

A4

ESCALA:1:2

CANTIDAD: 2

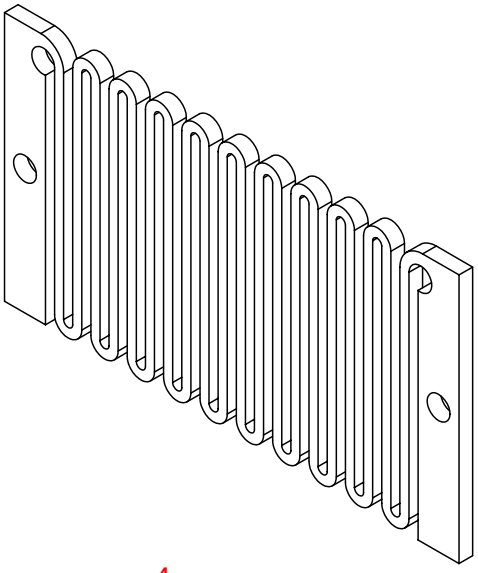

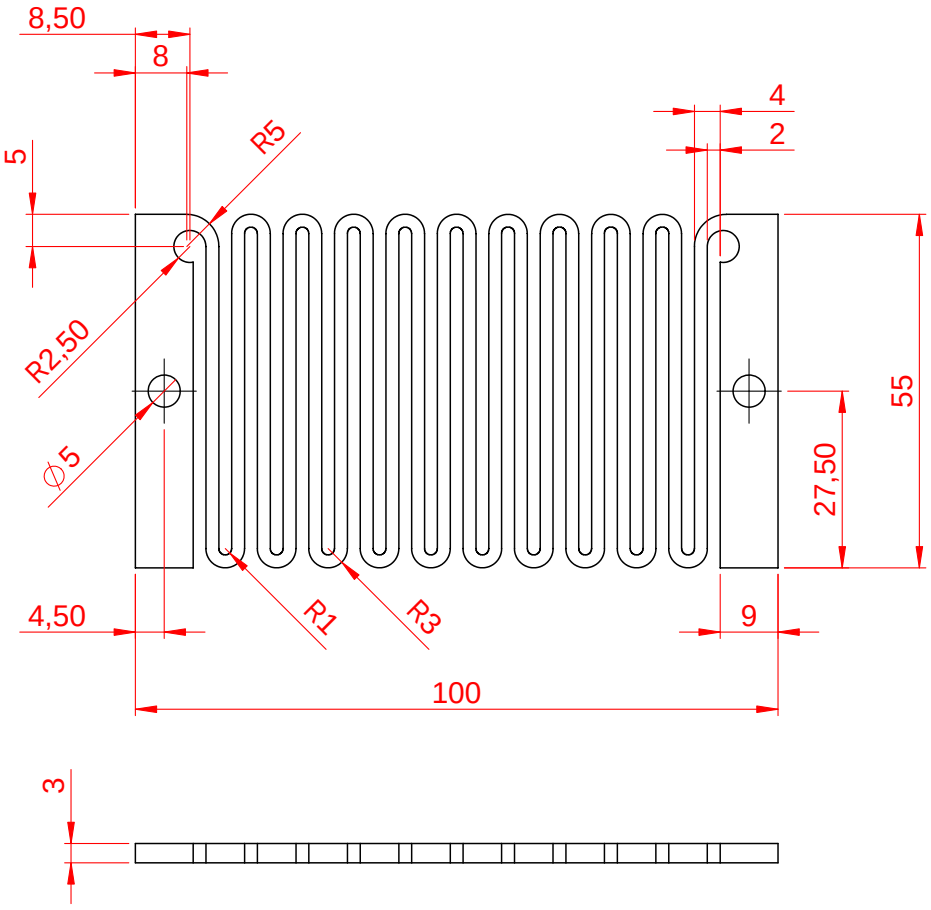

NOTAS: Todas las dimensiones están en mm.	**TÍTULO:** Resistencia Grafito	
MATERIAL: Grafito	FEMAN-UB	A4
Espesor: N/A	ESCALA:1:1	CANTIDAD: 6

Holder system drawings

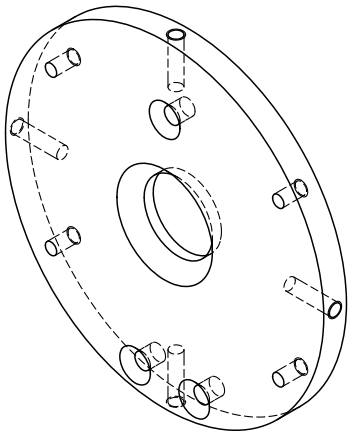

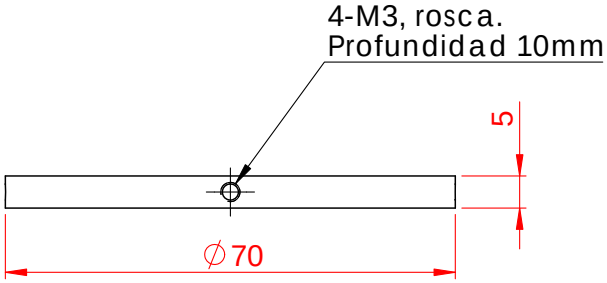

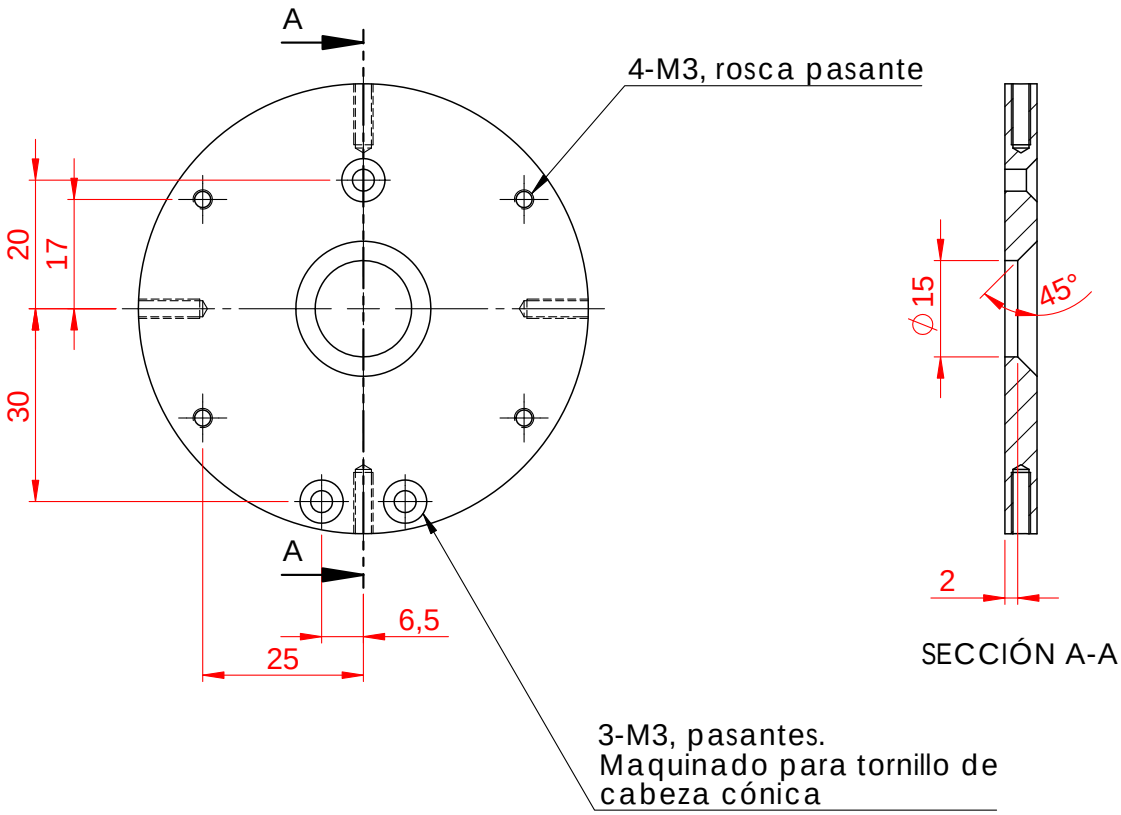

NOTAS: Todas las dimensiones están en mm.	**TÍTULO:** Base-holder	
MATERIAL: Acero inoxidable 304	FEMAN-UB	A4
Espesor: N/A	ESCALA:1:1	CANTIDAD: 4

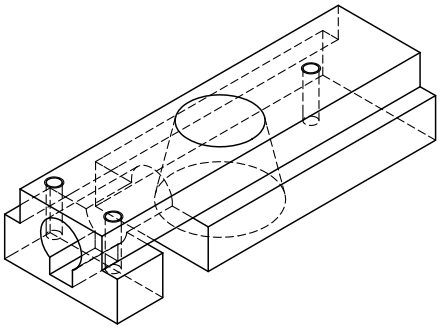

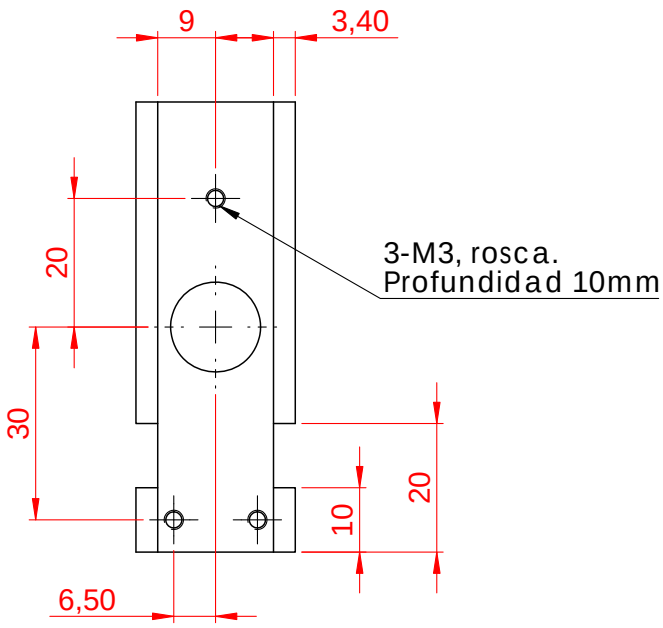

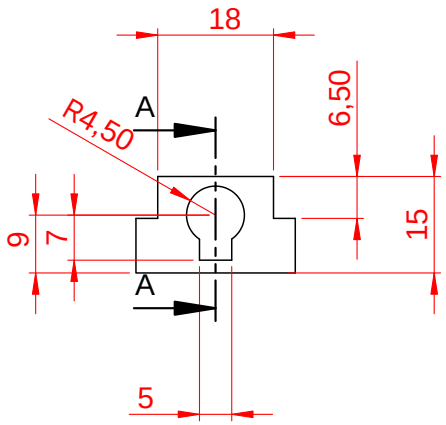

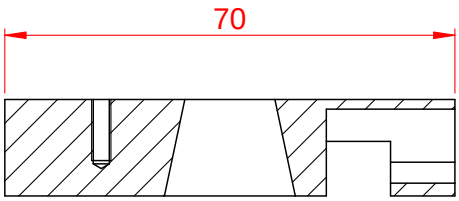

SECCIÓN A-A

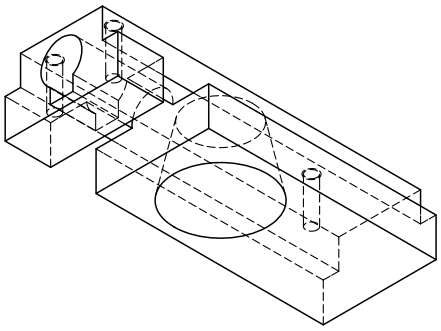

NOTAS:
Todas las dimensiones están en mm.

TÍTULO:
Base Holder

MATERIAL:
Acero inoxidable 304

FEMAN-UB

A4

Espesor: N/A

ESCALA:1:1

CANTIDAD: 4

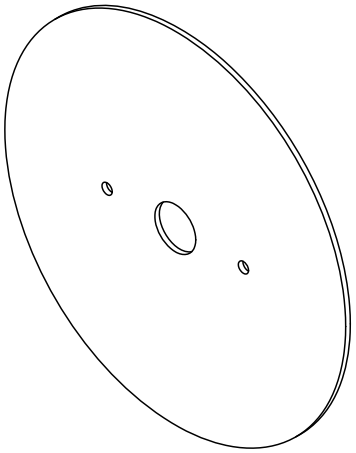

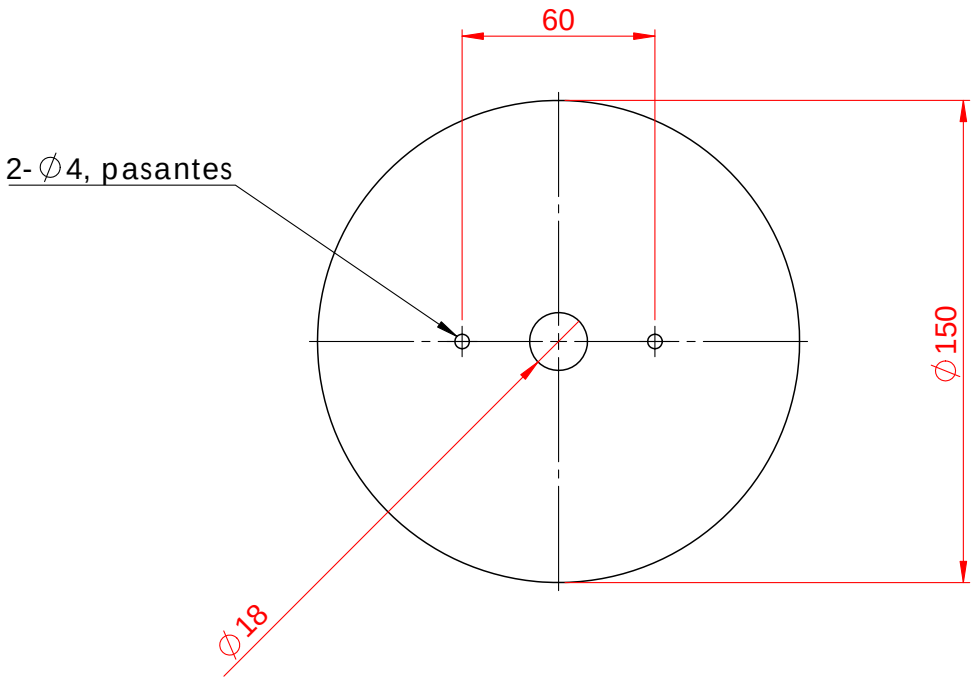

NOTAS: Todas las dimensiones están en mm.	**TÍTULO:** Disco pantalla	
MATERIAL: Acero inoxidable 304	FEMAN-UB	A4
Espesor: 2	ESCALA:1:2	CANTIDAD: 4

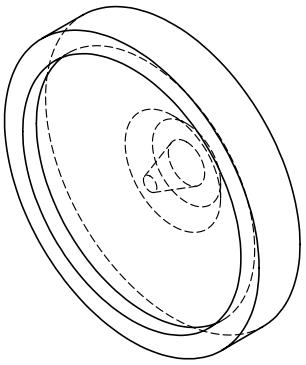

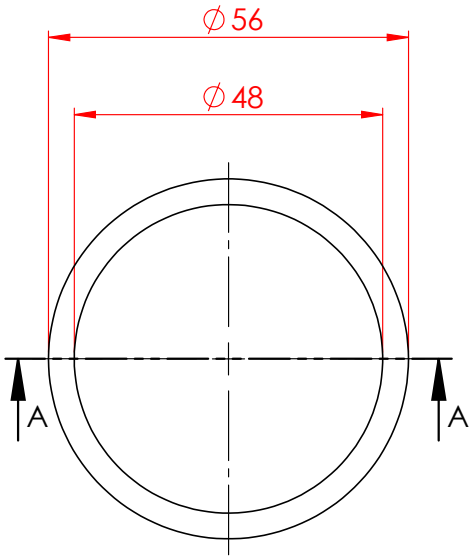

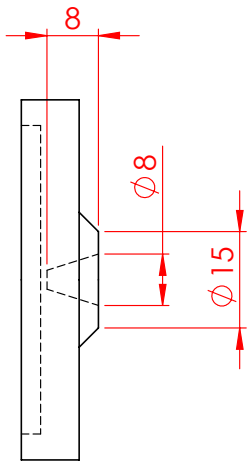

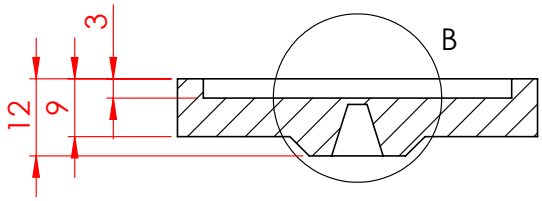

SECCIÓN A-A

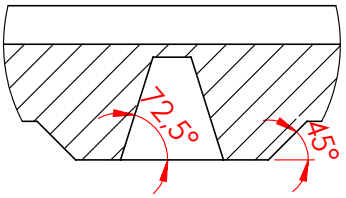

DETALLE B
ESCALA 2 : 1

NOTAS: Todas las dimensiones están en mm.	**TÍTULO:** Grafito-base	
MATERIAL: Grafito	FEMAN-UB	A4
Espesor: N/A	ESCALA:1:1	CANTIDAD: 6

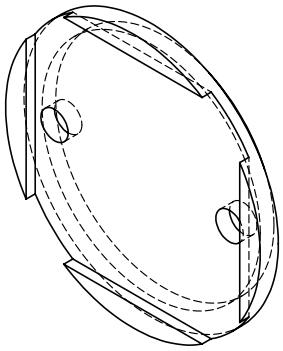

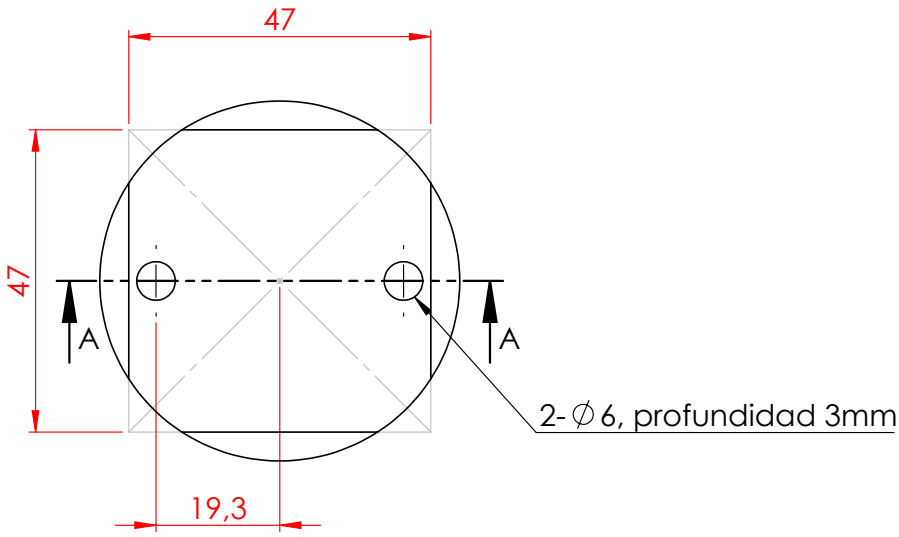

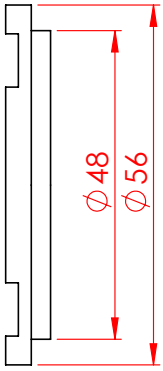

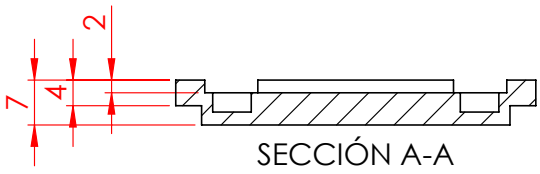

NOTAS: Todas las dimensiones están en mm.	**TÍTULO:** Grafito-PM1	
MATERIAL: Grafito	FEMAN-UB	A4
Espesor: N/A	ESCALA:1:1	CANTIDAD: 6

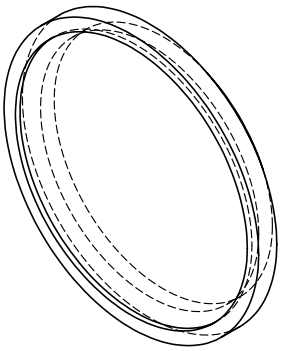

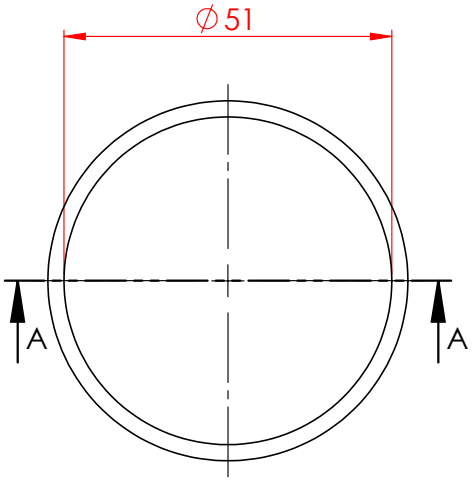

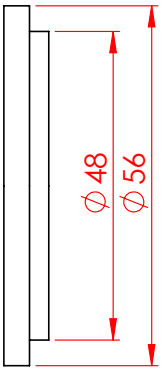

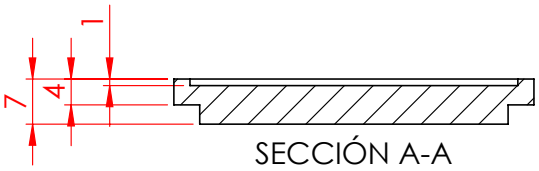

SECCIÓN A-A

NOTAS: Todas las dimensiones están en mm.	**TÍTULO:** Grafito-PM2	
MATERIAL: Grafito	FEMAN-UB	A4
Espesor: N/A	ESCALA:1:1	CANTIDAD: 6

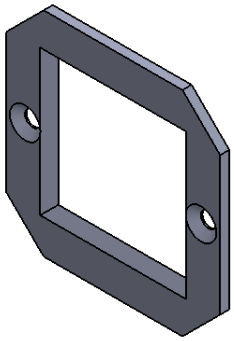

SECCIÓN A-A

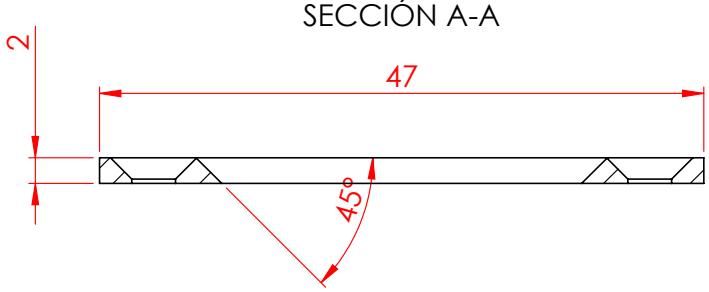

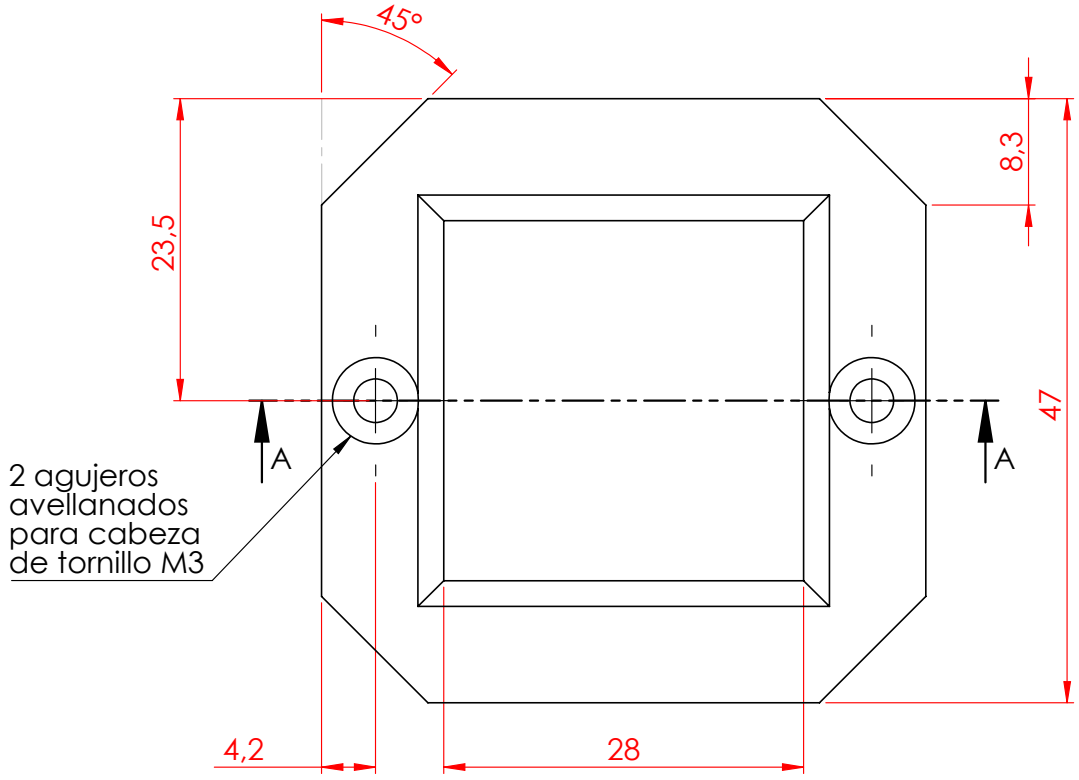

NOTAS: Todas las dimensiones están en mm. Tolerancia general: ±0.1 mm / ±0.2°	**TÍTULO:** Porta muestras superior	
MATERIAL: Acero inox. 304	FEMAN-UB	A4
Espesor: 2 mm	ESCALA:2:1	CANTIDAD: 5

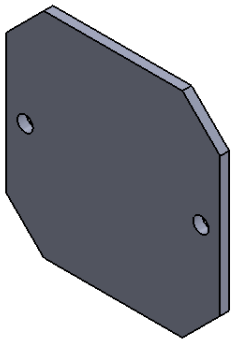

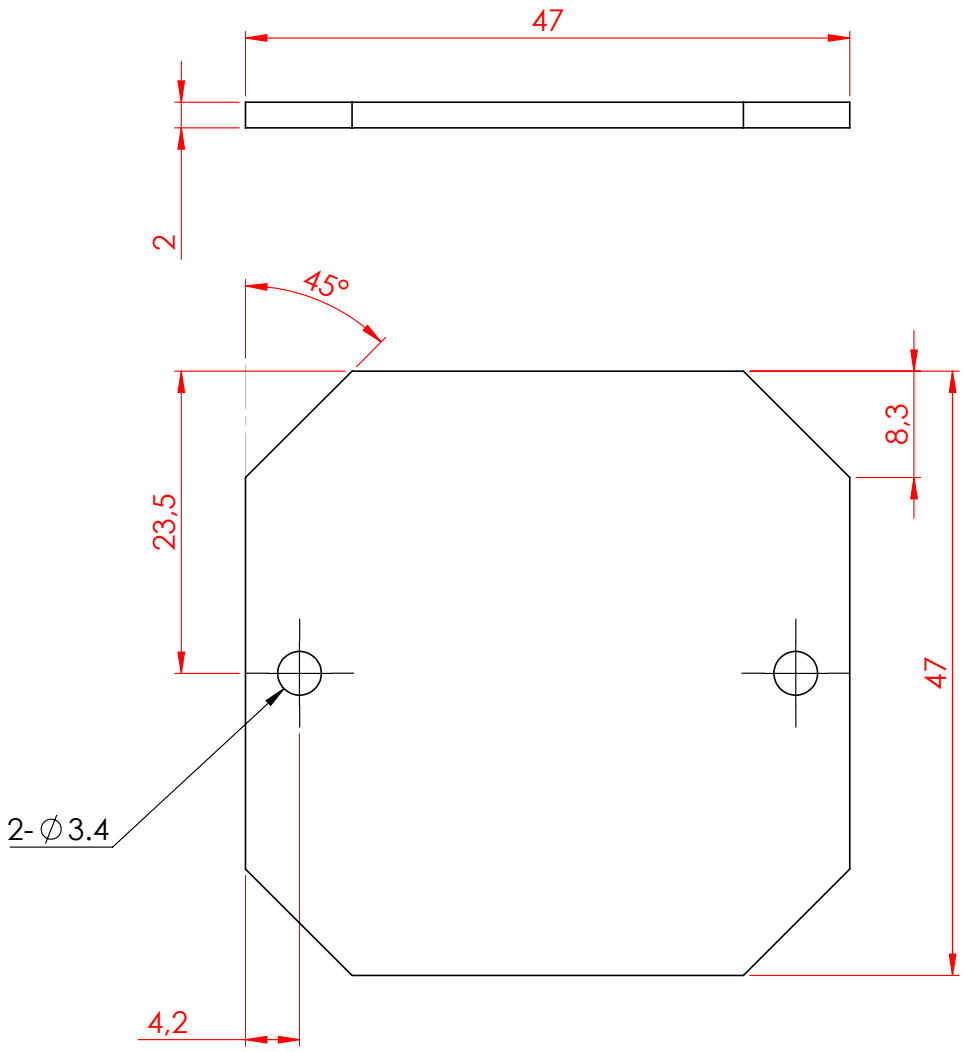

NOTAS: Todas las dimensiones están en mm. Tolerancia general: ±0.1 mm / ±0.2°	**TÍTULO:** Porta muestras inferior	
MATERIAL: Acero inox. 304	FEMAN-UB	A4
Espesor: 2 mm	ESCALA:2:1	CANTIDAD: 5

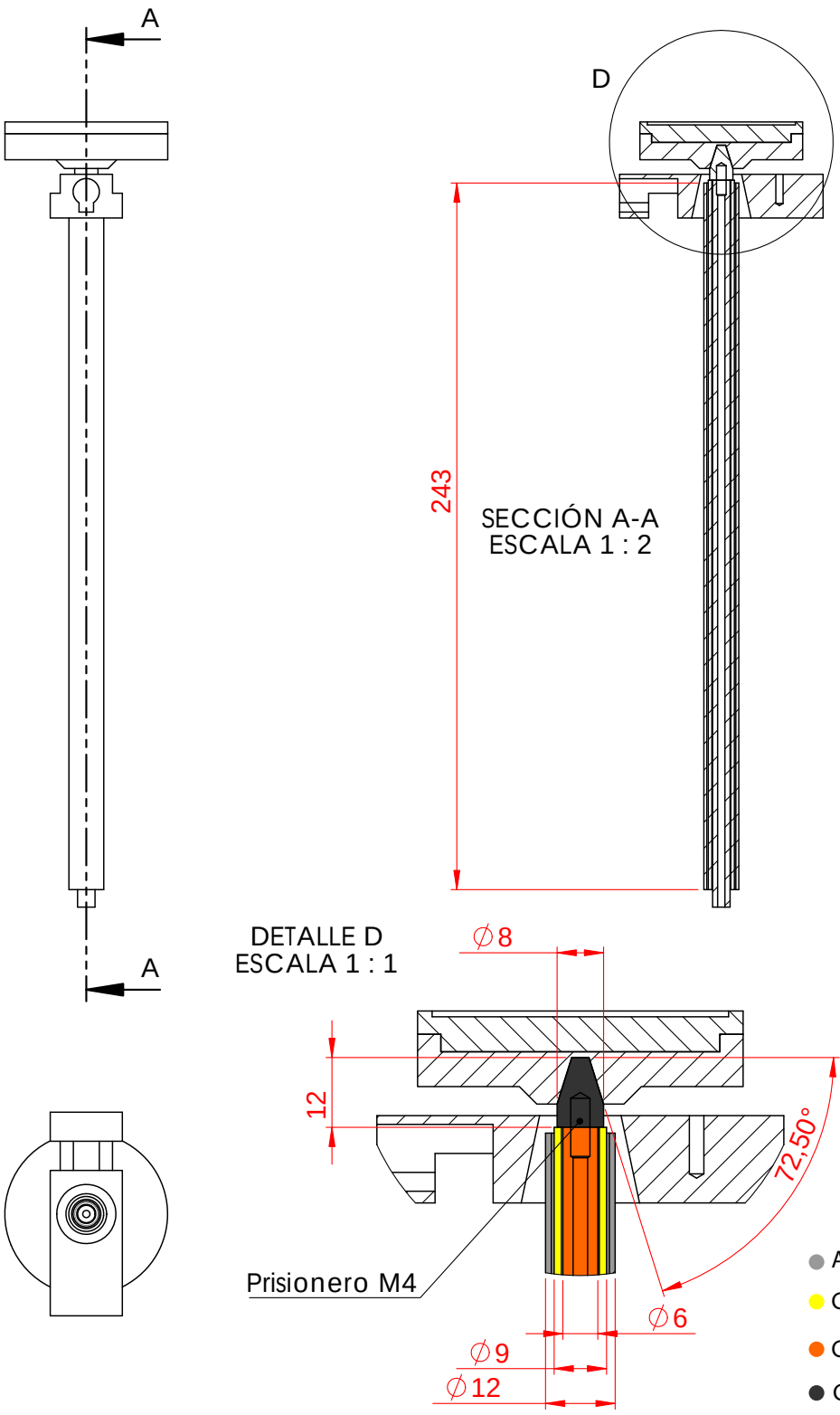

NOTAS:
Todas las dimensiones están en mm.

TÍTULO:
Electrodo PECVD

MATERIAL:
Acero inox-cerámica-cobre-grafito

FEMAN-UB

A4

Espesor: N/A

ESCALA:1:5

CANTIDAD: 1

Electrochemical cell drawings

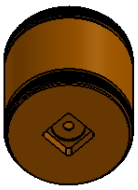

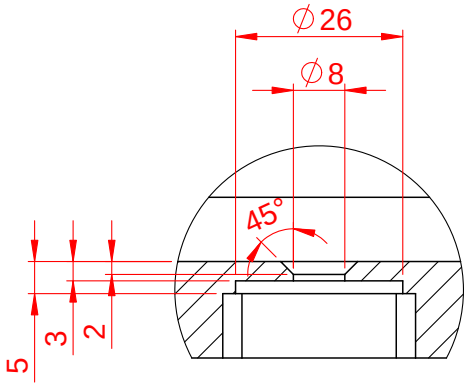

DETALLE B
ESCALA 1 : 1

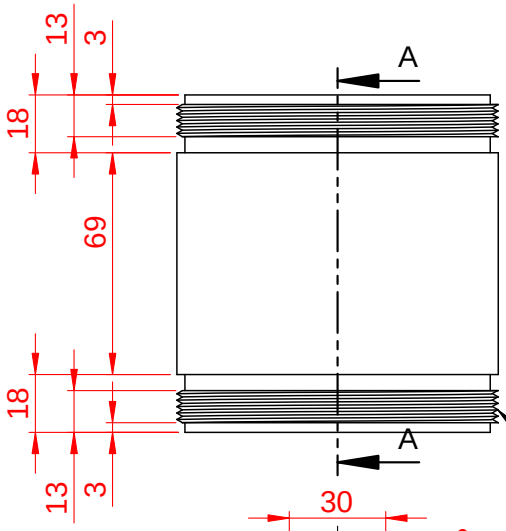

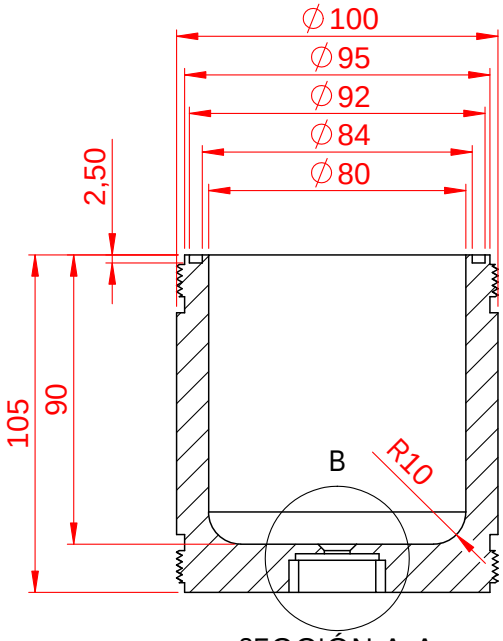

SECCIÓN A-A

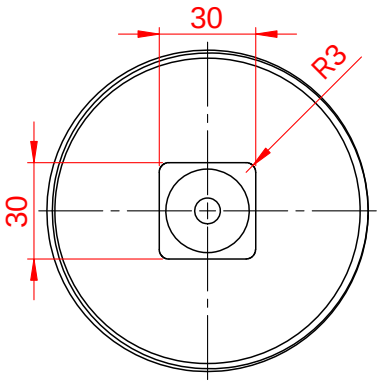

Rosca con paso de 2mm

NOTAS: Todas las dimensiones están en mm.	**TÍTULO:** Recipiente	
MATERIAL: PVC	FEMAN-UB	A4
Espesor: N/A	ESCALA:1:2	CANTIDAD: 2

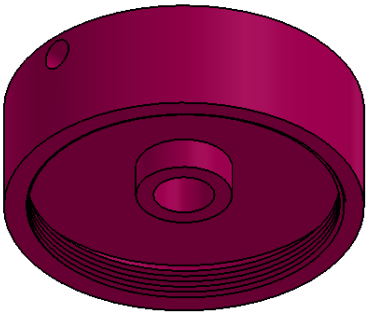

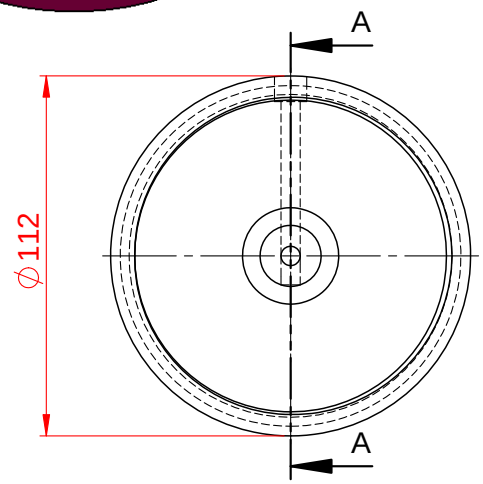

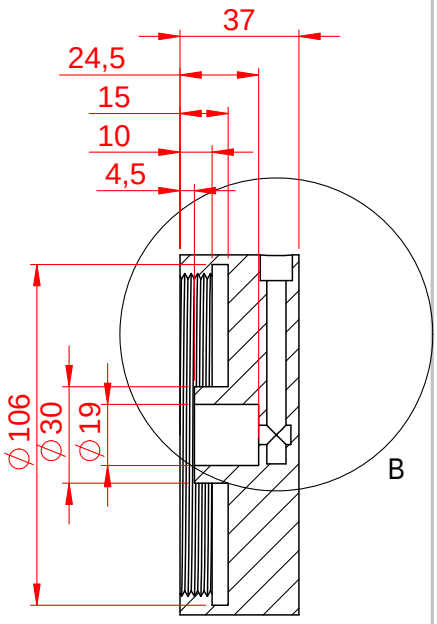

SECCIÓN A-A

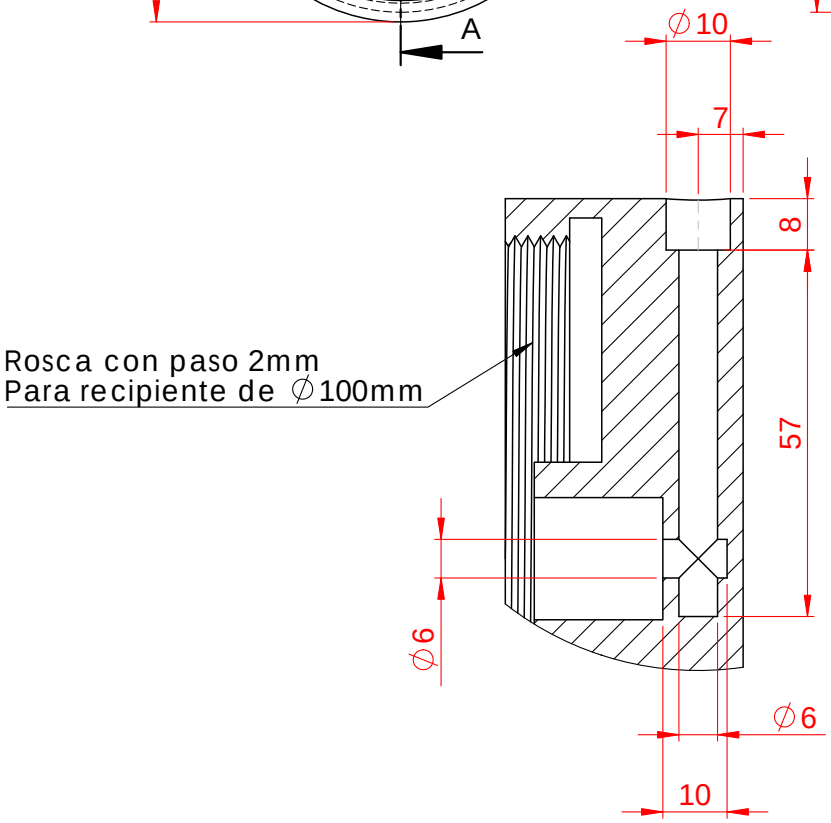

DETALLE B
ESCALA 1 : 1

NOTAS: Todas las dimensiones están en mm.	**TÍTULO:** Tapa inferior	
MATERIAL: PVC	FEMAN-UB	A4
Espesor: N/A	ESCALA:1:2	CANTIDAD: 2

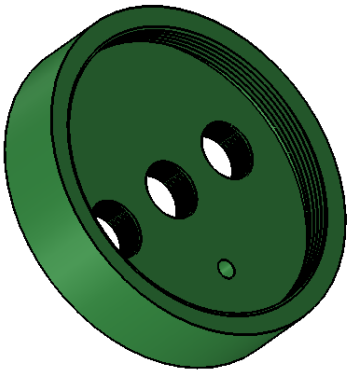

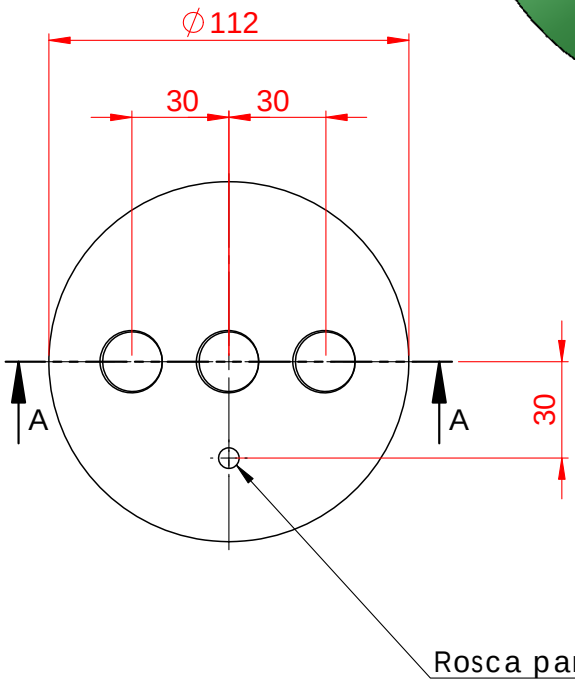

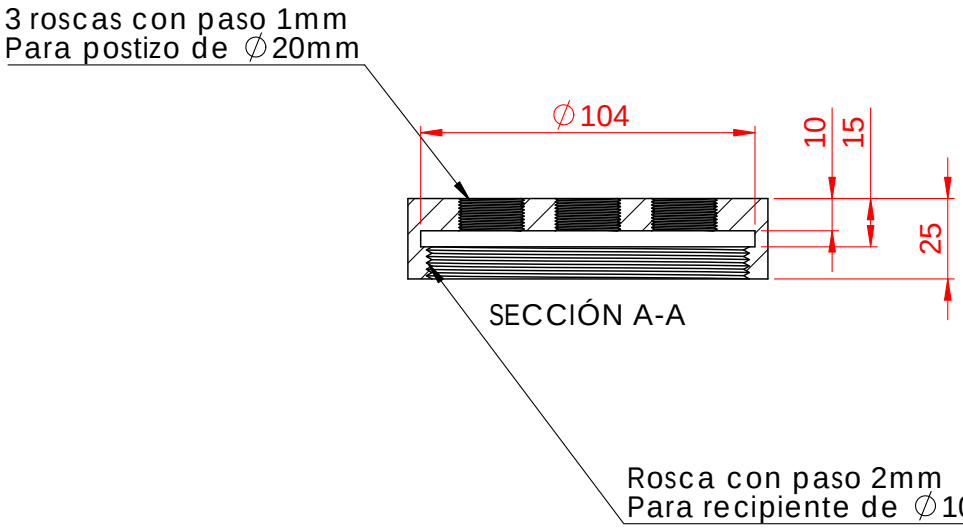

NOTAS: Todas las dimensiones están en mm.	**TÍTULO:** Tapa superior	
MATERIAL: PVC	FEMAN-UB	A4
Espesor: N/A	ESCALA:1:2	CANTIDAD: 2

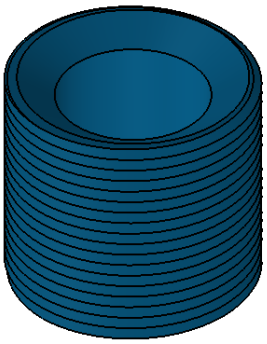

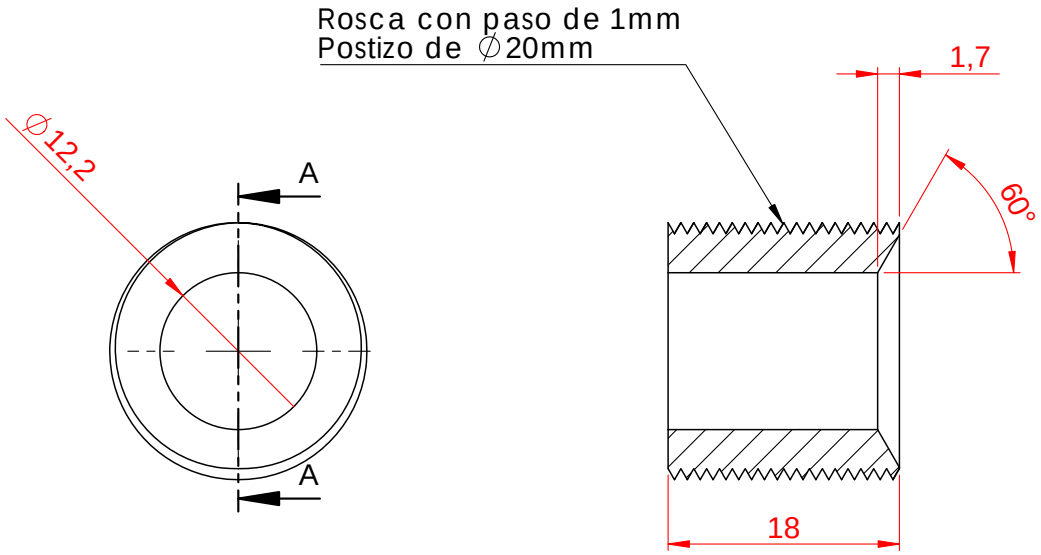

SECCIÓN A-A

NOTAS: Todas las dimensiones están en mm.	**TÍTULO:** Postizo	
MATERIAL: PVC	FEMAN-UB	A4
Espesor: N/A	ESCALA:2:1	CANTIDAD: 6

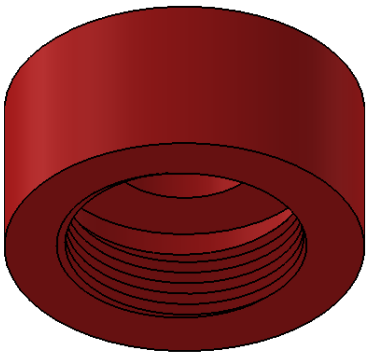

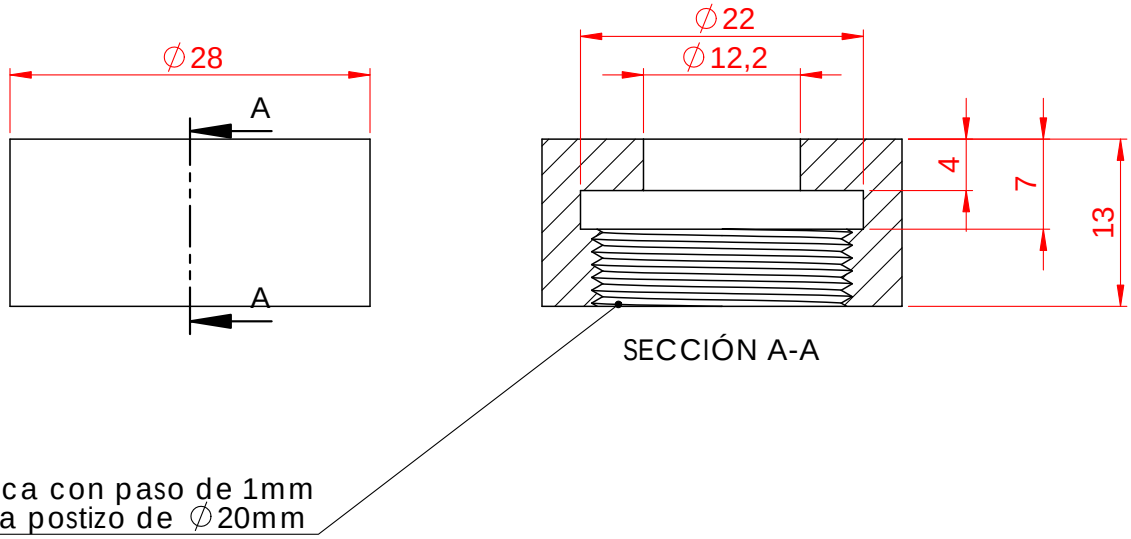

NOTAS: Todas las dimensiones están en mm.	**TÍTULO:** Tapa postizo	
MATERIAL: PVC	FEMAN-UB	A4
Espesor: N/A	ESCALA:2:1	CANTIDAD: 6

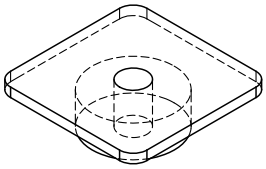

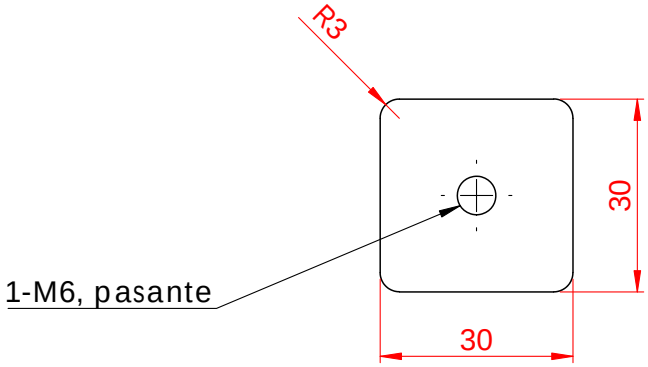

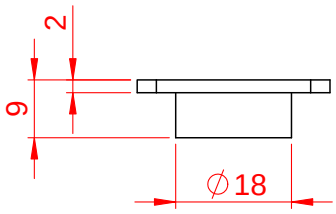

NOTAS:
Todas las dimensiones están en mm.

TÍTULO:
Porta muestras

MATERIAL:
Acero inoxidable 304

FEMAN-UB

A4

Espesor: N/A

ESCALA:1:1

CANTIDAD: 2

Bibliography

ACS. (2019). C.V. Raman The Raman Effect - Landmark. Retrieved from https://www-acs-org.sire.ub.edu/content/acs/en/education/whatischemistry/landmarks/ramaneffect.html

Adamska, M., & Narkiewicz, U. (2017). Fluorination of Carbon Nanotubes - A Review. *Journal of Fluorine Chemistry*, *200*(July), 179–189. doi:10.1016/j.jfluchem.2017.06.018

Akita, M., Uematsu, Y., Kakiuchi, T., Nakajima, M., Tsuchiyama, T., Bai, Y., & Isono, K. (2015). Effect of sensitization on corrosion fatigue behavior of type 304 stainless steel annealed in nitrogen gas. *Materials Science and Engineering A*, *640*, 33–41. doi:10.1016/j.msea.2015.05.080

Albella, J. (2018). *Thin films and surface modification of materials*. Madrid: Consejo Superior de Investigaciones Científicas.

Alresheedi, F. I., & Krzanowski, J. E. (2017). Structure and morphology of stainless steel coatings sputter-deposited in a nitrogen/argon atmosphere. *Surface and Coatings Technology*, *314*, 105–112. doi:10.1016/j.surfcoat.2016.09.063

Amade, R., Muyshegyan-Avetisyan, A., González, J. M., del Pino, A. P., György, E., Pascual, E., ... Serra, E. B. (2019). Super-capacitive performance of manganese dioxide/graphene nano-walls electrodes deposited on stainless steel current collectors. *Materials*, *12*(3), 1–13. doi:10.3390/ma12030483

AmericanLaboratory. (2010). X-ray Photoelectron Spectroscopy (XPS) for Energy-Related Device Characterization. Retrieved from https://www.americanlaboratory.com/914-Application-Notes/532-X-ray-Photoelectron-Spectroscopy-XPS-for-Energy-Related-Device-Characterization/

An, J., Zhan, Z., & Zheng, L. (2016). *Controllable Synthesis of Carbon Nanotubes*. doi:10.1016/B978-0-323-41481-4.00001-0

Ando, Y., Zhao, X., Sugai, T., & Kumar, M. (2004). Growing carbon nanotubes. *Materials Today*, *7*(10), 22–29. doi:10.1016/s1369-7021(04)00446-8

Angstrom Sciences. (2019). Sputtering Power Supply – Types of Sputtering Power – Pulsed – RF. Retrieved from https://www.angstromsciences.com/sputtering-power-supply

Antunes, E. F., Lobo, A. O., Corat, E. J., & Trava-Airoldi, V. J. (2007). Influence of diameter in the Raman spectra of aligned multi-walled carbon nanotubes. *Carbon*, *45*(5), 913–921. doi:10.1016/j.carbon.2007.01.003

Baker, R. T. K., Yates, D. J. C., & Dumesic, J. A. (2009). Filamentous Carbon Formation over Iron Surfaces, 1–21. doi:10.1021/bk-1983-0202.ch001

Baranowska, J., Fryska, S., & Suszko, T. (2013). The influence of temperature and nitrogen pressure on S-phase coatings deposition by reactive magnetron sputtering. *Vacuum*, *90*(1), 160–164. doi:10.1016/j.vacuum.2012.03.054

Bard, A. (2001). *Electrochemical methods, fundamentals and applications*.

Barr, T. L., & Seal, S. (2002). Nature of the use of adventitious carbon as a binding energy standard. *Journal of Vacuum Science & Technology A: Vacuum, Surfaces, and Films*, *13*(3), 1239–1246. doi:10.1116/1.579868

Beaudrouet, E., Le Gal La Salle, A., & Guyomard, D. (2009). Nanostructured manganese dioxides: Synthesis and properties as supercapacitor electrode materials. *Electrochimica Acta*, *54*(4), 1240–1248. doi:10.1016/j.electacta.2008.08.072

Béguin, F., Presser, V., Balducci, A., & Frackowiak, E. (2014). Carbons and electrolytes for advanced supercapacitors. *Advanced Materials*, *26*(14), 2219–2251. doi:10.1002/adma.201304137

Bellani, S., Antognazza, M. R., & Bonaccorso, F. (2019). Carbon-Based Photocathode Materials for Solar Hydrogen Production. *Advanced Materials*, *31*(9), 1–33. doi:10.1002/adma.201801446

Bernard, M.-C. (1993). Electrochromic Reactions in Manganese Oxides. *Journal of The Electrochemical Society*, *140*(11), 3065. doi:10.1149/1.2220986

Bethune, D. S., Kiang, C. H., De Vries, M. S., Gorman, G., Savoy, R., Vazquez, J., & Beyers, R. (1993). Cobalt-catalysed growth of carbon nanotubes with single-atomic-layer walls. *Nature*, *363*(6430), 605–607. doi:10.1038/363605a0

Biesinger, M. C. [M. C.], Brown, C., Mycroft, J. R., Davidson, R. D., & McIntyre, N. S. (2004). X-ray photoelectron spectroscopy studies of chromium compounds. *Surface and Interface Analysis*, *36*(12), 1550–1563. doi:10.1002/sia.1983

Biesinger, M. (2018). X-ray Photoelectron Spectroscopy (XPS) Reference Pages: Aluminum. Retrieved from http://www.xpsfitting.com/search/label/Aluminum

Biesinger, M. C. [Mark C.], Payne, B. P., Grosvenor, A. P., Lau, L. W., Gerson, A. R., & Smart, R. S. C. (2011). Resolving surface chemical states in XPS analysis of first row transition metals, oxides and hydroxides: Cr, Mn, Fe, Co and Ni. *Applied Surface Science*, *257*(7), 2717–2730. doi:10.1016/j.apsusc.2010.10.051

Bogacz, W., Lemanowicz, M., Al-Rashed, M. H., Nakonieczny, D., Piotrowski, T., & Wójcik, J. (2017). Impact of roughness, wettability and hydrodynamic conditions on the incrustation on stainless steel surfaces. *Applied Thermal Engineering*, *112*, 352–361. doi:10.1016/j.applthermaleng.2016.10.076

Bokobza, L., Bruneel, J.-L., & Couzi, M. (2015). Raman Spectra of Carbon-Based Materials (from Graphite to Carbon Black) and of Some Silicone Composites. *C*, *1*(1), 77–94. doi:10.3390/c1010077

Bonaccorso, F., Bongiorno, C., Fazio, B., Gucciardi, P. G., Maragò, O. M., Morone, A., & Spinella, C. (2007). Pulsed laser deposition of multiwalled carbon nanotubes thin films. *Applied Surface Science*, *254*(4), 1260–1263. doi:10.1016/j.apsusc.2007.08.045

Borenstein, A., Hanna, O., Attias, R., Luski, S., Brousse, T., & Aurbach, D. (2017). Carbon-based composite materials for supercapacitor electrodes: A review. *Journal of Materials Chemistry A*, *5*(25), 12653–12672. doi:10.1039/c7ta00863e

Borges, J., Martin, N., Barradas, N. P., Alves, E., Eyidi, D., Beaufort, M. F., ... Marques, L. (2012). Electrical properties of AlN xO y thin films prepared by reactive magnetron sputtering. *Thin Solid Films*, *520*(21), 6709–6717. doi:10.1016/j.tsf.2012.06.062

Boss, C., & Fredeen, K. (1997). *Concepts, instrumentation, and techniques in Inductively Coupled Plasma Optical Emission Spectrometry* (Second). Perkin Elmer.

Boutry, C. M., Sun, W., Strunz, T., Chandrahalim, H., & Hierold, C. (2010). Development and characterization of biodegradable conductive polymers for the next generation of RF bio-resonators. *2010 IEEE International Frequency Control Symposium, FCS 2010*, *2*(1), 258–261. doi:10.1109/FREQ.2010.5556332

Bower, C., Zhu, W., Jin, S., & Zhou, O. (2000). Plasma-induced alignment of carbon nanotubes. *Applied Physics Letters*, *77*(6), 830–832. doi:10.1063/1.1306658

Bronikowski, M. J., Willis, P. A., Colbert, D. T., Smith, K. A., & Smalley, R. E. (2002). Gas-phase production of carbon single-walled nanotubes from carbon monoxide via the HiPco process: A parametric study. *Journal of Vacuum Science & Technology A: Vacuum, Surfaces, and Films*, *19*(4), 1800–1805. doi:10.1116/1.1380721

Brown, B., Parker, C. B., Stoner, B. R., & Glass, J. T. (2011). Growth of vertically aligned bamboo-like carbon nanotubes from ammonia/methane precursors using a platinum catalyst. *Carbon*, *49*(1), 266–274. doi:10.1016/j.carbon.2010.09.018

Bruker. (2019). OES - Optical Emission Spectrometry. Retrieved from https://www.bruker.com/products/x-ray-diffraction-and-elemental-analysis/optical-emission-spectrometry.html

Buj Corral, I., Calvet, J. V., & Salcedo, M. C. (2010). Use of roughness probability parameters to quantify the material removed in plateau-honing. *International Journal of Machine Tools and Manufacture*, *50*(7), 621–629. doi:10.1016/j.ijmachtools.2010.02.007

Canali, C., Malavasi, D., Morten, B., Prudenziati, M., & Taroni, A. (1980). Piezoresistive effects in thick-film resistors. *Journal of Applied Physics*, *51*(6), 3282–3288. doi:10.1063/1.328035

Cançado, L. G., Jorio, A., & Pimenta, M. A. (2007). Measuring the absolute Raman cross section of nanographites as a function of laser energy and crystallite size. *Physical Review B - Condensed Matter and Materials Physics*, *76*(6), 1–7. doi:10.1103/PhysRevB.76.064304

CasaXPS. (2013). XPS Spectra, 1–77. Retrieved from www.casaxps.com

CasaXPS. (2018). CasaXPS: Processing Software for XPS, AES, SIMS and More. Retrieved from http://www.casaxps.com

Cavanagh, H. D., Jester, J.-V., & Petroll, W. M. (1994). The future development of confocal microscopy. *16*(5), 261–261. doi:10.1002/sca.4950160502

Chakrapani, N., Wei, B., Carrillo, A., Ajayan, P. M., & Kane, R. S. (2004). Capillarity-driven assembly of two-dimensional cellular carbon nanotube foams. *Proceedings of the National Academy of Sciences of the United States of America*, *101*(12), 4009–12. doi:10.1073/pnas.0400734101

Chalupa, D. C., Morrow, P. E., Oberdörster, G., Utell, M. J., & Frampton, M. W. (2004). Ultrafine particle deposition in subjects with asthma. *Environmental health perspectives*, *112*(8), 879–82. doi:10.1289/ehp.6851

Chandler, D. (2015). Chemical Vapor Deposition. *MIT News*, (595), 64–88. Retrieved from https://news.mit.edu/2015/explained-chemical-vapor-deposition-0619

Chang, J. K., Huang, C. H., Tsai, W. T., Deng, M. J., & Sun, I. W. (2008). Ideal pseudocapacitive performance of the Mn oxide anodized from the nanostructured and amorphous Mn thin film electrodeposited in BMP-NTf2 ionic liquid. *Journal of Power Sources*, *179*(1), 435–440. doi:10.1016/j.jpowsour.2007.12.084

Cheaptubes. (2019). Carbon-Nanotube-Masterbatch-ABS. Retrieved from https://cheaptubes.com/wp-content/uploads/2015/09/Carbon-Nanotube-Masterbatch-ABS.jpg

Chen, H., Sun, F., Wang, J., Li, W., Qiao, W., Ling, L., & Long, D. (2013). Nitrogen doping effects on the physical and chemical properties of mesoporous carbons. *Journal of Physical Chemistry C*, *117*(16), 8318–8328. doi:10.1021/jp4017773

Chen, R. J., Franklin, N. R., Kong, J., Cao, J., Tombler, T. W., Zhang, Y., & Dai, H. (2001). Molecular photodesorption from single-walled carbon nanotubes. *Applied Physics Letters*, *79*(14), 2258–2260. doi:10.1063/1.1408274

Chen, Y., & Zhang, J. (2014). Chemical vapor deposition growth of single-walled carbon nanotubes with controlled structures for nanodevice applications. *Accounts of Chemical Research*, *47*(8), 2273–2281. doi:10.1021/ar400314b

Cheng, Q. F., Wang, J. P., Wen, J. J., Liu, C. H., Jiang, K. L., Li, Q. Q., & Fan, S. S. (2010). Carbon nanotube/epoxy composites fabricated by resin transfer molding. *Carbon*, *48*(1), 260–266. doi:10.1016/j.carbon.2009.09.014

Cheng, Y., Lu, S., Zhang, H., Varanasi, C. V., & Liu, J. (2012). Synergistic effects from graphene and carbon nanotubes enable flexible and robust electrodes for high-performance supercapacitors. *Nano Letters*, *12*(8), 4206–4211. doi:10.1021/nl301804c

Chi, Y. W., Hu, C. C., Huang, K. P., Shen, H. H., & Muniyandi, R. K. (2016). Manipulation of defect density and nitrogen doping on few-layer graphene sheets using the plasma methodology for electrochemical applications. *Electrochimica Acta*, *221*, 144–153. doi:10.1016/j.electacta.2016.10.093

Choi, K. S., Cho, Y. S., Hong, S. Y., Park, J. B., & Kim, D. J. (2001). The role of ammonia treatment in the alignment of the carbon nanotubes synthesized with Ni and Fe via thermal chemical vapor deposition. *Journal of the Korean Physical Society*, *39*(December), S7–S10.

Ci, L., Wei, J., Wei, B., Liang, J., Xu, C., & Wu, D. (2001). Carbon nanofibers and single-walled carbon nanotubes prepared by the floating catalyst method. *Carbon*, *39*(3), 329–335. doi:10.1016/S0008-6223(00)00126-3

Clement, M., Iborra, E., Sangrador, J., Sanz-Hervás, A., Vergara, L., & Aguilar, M. (2003). Influence of sputtering mechanisms on the preferred orientation of aluminum nitride thin films. *Journal of Applied Physics*, *94*(3), 1495–1500. doi:10.1063/1.1587267

Colomban, P., Cherifi, S., & Despert, G. (2008). Raman identification of corrosion products on automotive galvanized steel sheets. *Journal of Raman Spectroscopy*, *39*(7), 881–886. doi:10.1002/jrs.1927

Conway, B. E. (1991). Transition from "Supercapacitor" to "Battery" Behavior in Electrochemical Energy Storage. *Journal of The Electrochemical Society*, *138*(6), 1539. doi:10.1149/1.2085829

Correa-Duarte, M. A., Wagner, N., Rojas-Chapana, J., Morsczeck, C., Thie, M., & Giersig, M. (2004). Fabrication and biocompatibility of carbon nanotube-based 3D networks as scaffolds for cell seeding and growth. *Nano Letters*, *4*(11), 2233–2236. doi:10.1021/nl048574f. arXiv: arXiv:1011.1669v3

Couzi, M., Bruneel, J. L., Talaga, D., & Bokobza, L. (2016). A multi wavelength Raman scattering study of defective graphitic carbon materials: The first order Raman spectra revisited. *Carbon*, *107*, 388–394. doi:10.1016/j.carbon.2016.06.017

Creighton, J., & Ho, P. (2001). Introduction to Chemical Vapour Deposition. *Chemical Vapor Deposition (#06682G)*, *2*(595), 1–28. doi:10.1007/978-1-84882-894-0_1

Crystalimpact. (2019). Rietveld Refinement. Retrieved from https://www-acs-org.sire.ub.edu/content/acs/en/education/whatischemistry/landmarks/ramaneffect.html

De Jong, W. H., & Borm, P. J. A. (2008). Drug delivery and nanoparticles:applications and hazards. *International journal of nanomedicine*, *3*(2), 133–49. Retrieved from http://www.ncbi.nlm.nih.gov/pubmed/18686775%7B%5C%%7D0Ahttp://www.pubmedcentral.nih.gov/articlerender.fcgi?artid=PMC2527668

De Los Arcos, T., Wu, Z. M., & Oelhafen, P. (2003). Is aluminum a suitable buffer layer for carbon nanotube growth? *Chemical Physics Letters*, *380*(3-4), 419–423. doi:10.1016/j.cplett.2003.09.057

Department of Applied Physics UB. (2001). Electrical Conductivity and Hall Effect in a Semiconductor. Barcelona: Laboratory Guide.

Dervishi, E., Li, Z., Watanabe, F., Xu, Y., Saini, V., Biris, A. R., & Biris, A. S. (2009). Thermally controlled synthesis of single-wall carbon nanotubes with selective diameters. *Journal of Materials Chemistry*, *19*(19), 3004–3012. doi:10.1039/b822469b

Detroye, M., Reniers, F., Buess-Herman, C., & Vereecken, J. (1999). AES-XPS study of chromium carbides and chromium iron carbides. *Applied Surface Science*, *144-145*, 78–82. doi:10.1016/S0169-4332(98)00769-7

Devia, D. M., Rodriguez-Restrepo, L. V., & Restrepo-Parra, E. (2015). Methods Employed in Optical Emission Spectroscopy Analysis: a Review. *Ingeniería y Ciencia*, *11*(21), 239–267. doi:10.17230/ingciencia.11.21.12

Dexmat. (2018). CNT products. Retrieved from https://dexmat.com/cnt-products/

Di, J., Hu, D., Chen, H., Yong, Z., Chen, M., Feng, Z., ... Li, Q. (2012). Ultrastrong, foldable, and highly conductive carbon nanotube film. *ACS Nano*, *6*(6), 5457–5464. doi:10.1021/nn301321j

Di, J., Yong, Z., Yao, Z., Liu, X., Shen, X., Sun, B., ... Li, Q. (2013). Robust and aligned carbon nanotube/titania core/shell films for flexible tco-free photoelectrodes. *Small*, *9*(1), 148–155. doi:10.1002/smll.201201168

Di, J., Yong, Z., Zheng, X., Sun, B., & Li, Q. (2013). Aligned carbon nanotubes for high-efficiency Schottky solar cells. *Small*, *9*(8), 1367–1372. doi:10.1002/smll.201202995

Dresselhaus, M. S. [M. S.], Dresselhaus, G., & Saito, R. (1995). Physics of carbon nanotubes. *Carbon*, *33*(7), 883–891. doi:10.1016/0008-6223(95)00017-8

Dresselhaus, M., Lin, Y., Rabin, O., Jorio, A., Souza Filho, A., Pimenta, M., ... G. (2012). Nanowires and Nanotubes. *23*, 129–140.

Dresselhaus, M. S. [Millie S.], Dresselhaus, G., Saito, R., & Jorio, A. (2005). Raman spectroscopy of carbon nanotubes. doi:10.1016/j.physrep.2004.10.006

Düngen, P., Prenzel, M., Stappen, C. V., Pfänder, N., Heumann, S., & Schlögl, R. (2017). Investigation of Different Pre-Treated Multi-Walled Carbon Nanotubes by Raman Spectroscopy. *Materials Sciences and Applications*, *08*(08), 628–641. doi:10.4236/msa.2017.88044

Dupin, J. C., Gonbeau, D., Vinatier, P., & Levasseur, A. (2000). Systematic XPS studies of metal oxides, hydroxides and peroxides. *Physical Chemistry Chemical Physics*, *2*(6), 1319–1324. doi:10.1039/a908800h

Dutrow, B. (2019). X-ray Powder Diffraction (XRD). Retrieved from https://serc.carleton.edu/research%7B%5C_%7Deducation/geochemsheets/techniques/XRD.html

Ebbesen, T., & Ajayan, P. (1992). Large-scale synthesis of carbon nanotubes. *Nature*, *358*, 220–222.

Eckmann, A., Felten, A., Mishchenko, A., Britnell, L., Krupke, R., Novoselov, K. S., & Casiraghi, C. (2012). Probing the nature of defects in graphene by Raman spectroscopy. *Nano Letters*, *12*(8), 3925–3930. doi:10.1021/nl300901a

Eun, K., & Myung, H. (2007). Cytotoxic Effects of Nanoparticles Assessed. *Journal of Microbiology and Biotechnology*, *17*, 1573–1578.

Fan, Z., Chen, J., Zhang, B., Liu, B., Zhong, X., & Kuang, Y. (2008). High dispersion of γ-MnO2 on well-aligned carbon nanotube arrays and its application in supercapacitors. *Diamond and Related Materials*, *17*(11), 1943–1948. doi:10.1016/j.diamond.2008.04.015

Feliu, S., & Pérez-Revenga, M. L. (2004). Effect of the presence of alloying elements in interstitial-free and low-carbon steels on their surface composition after annealing in reducing atmospheres (dew point = -30 °C). *Metallurgical and Materials*

Transactions A: Physical Metallurgy and Materials Science, *35 A*(7), 2039–2050. doi:10.1007/s11661-004-0152-2

Feliu, S., & Pérez-Revenga, M. L. (2005). Correlation between the surface chemistry of annealed if steels and the growth of a galvanneal coating. *Acta Materialia*, *53*(9), 2857–2866. doi:10.1016/j.actamat.2005.03.003

Ferrari, A. C., Meyer, J. C., Scardaci, V., Casiraghi, C., Lazzeri, M., Mauri, F., ... Geim, A. K. (2006). Raman spectrum of graphene and graphene layers. *Physical review letters*, *97*(18), 187401. doi:10.1103/PhysRevLett.97.187401

Ferrari, A., & Robertson, J. (2000). Interpretation of Raman spectra of disordered and amorphous carbon A. *Physical Review B*, *61*(20), 14 095–14 107.

Firme, C. P., & Bandaru, P. R. (2010). Toxicity issues in the application of carbon nanotubes to biological systems. *Nanomedicine: Nanotechnology, Biology, and Medicine*, *6*(2), 245–256. doi:10.1016/j.nano.2009.07.003

Forbes. (2018). The U.S.-China Trade War And Global Economic Dominance. Retrieved from https://www.forbes.com/sites/yuwahedrickwong/2018/09/11/the-u-s-china-trade-war-and-global-economic-dominance/%7B%5C#%7D3142d2fb256a

Francis, R. (2000). *Guides to Good Practice in Corrosion Control*, National Physical Laboratory. Retrieved from https://www.npl.co.uk/special-pages/guides/bimetallic-guide.pdf

Frankel, G. (2013). Pitting Corrosion of Metals. *Corrosion*, *19*(8), 261t–268t. doi:10.5006/0010-9312-19.8.261

Franklin, A. D. (2013). The road to carbon nanotube transistors. *Nature*, *498*, 443–444. doi:10.1016/S0769-2617(86)80238-6

Franklin, A. D., Luisier, M., Han, S. J., Tulevski, G., Breslin, C. M., Gignac, L., ... Haensch, W. (2012). Sub-10 nm carbon nanotube transistor. *Nano Letters*, *12*(2), 758–762. doi:10.1021/nl203701g

Fredi, G., Jeschke, S., Boulaoued, A., Wallenstein, J., Rashidi, M., Liu, F., ... Asp, L. E. (2018). Graphitic microstructure and performance of carbon fibre Li-ion structural battery electrodes. *Multifunctional Materials*, *1*(1), 015003. doi:10.1088/2399-7532/aab707

Fridman, A. (2008). *Plasma Chemistry*. doi:10.1017/CBO9780511546075

Futaba, B. D. N., Goto, J., Yasuda, S., Yamada, T., Yumura, M., & Hata, K. (2009). General Rules Governing the Highly Efficient Growth of Carbon Nanotubes, 4811–4815. doi:10.1002/adma.200901257

García Cespedez, J. (2008). *Nanotubos de carbono: síntesis , caracterización y aplicaciones* (Doctoral dissertation, Universitat de Barcelona).

García-Céspedes, J., Thomasson, S., Teo, K. B., Kinloch, I. A., Milne, W. I., Pascual, E., & Bertran, E. (2009). Efficient diffusion barrier layers for the catalytic growth of carbon nanotubes on copper substrates. *Carbon*, *47*(3), 613–621. doi:10.1016/j.carbon.2008.10.045

Ghasemi, A., Amiri, H., Zare, H., Masroor, M., Hasanzadeh, A., Beyzavi, A., ... Hamblin, M. R. (2017). Carbon nanotubes in microfluidic lab-on-a-chip technology: current trends and future perspectives. *Microfluidics and Nanofluidics*, *21*(9), 1–19. doi:10.1007/s10404-017-1989-1

González, A., Goikolea, E., Barrena, J. A., & Mysyk, R. (2016). Review on supercapacitors: Technologies and materials. *Renewable and Sustainable Energy Reviews*, *58*, 1189–1206. doi:10.1016/j.rser.2015.12.249

Graphenea. (2019). Graphene Oxide (Chemically Exfoliated). Retrieved from https://www.graphenea.com/collections/graphene-oxide

Grüneis, A., Kramberger, C., Grimm, D., Gemming, T., Rümmeli, M. H., Barreiro, A., ... Büchner, B. (2006). Eutectic limit for the growth of carbon nanotubes from a thin iron film by chemical vapor deposition of cyclohexane. *Chemical Physics Letters*, *425*(4-6), 301–305. doi:10.1016/j.cplett.2006.05.057

Guo, L., Shanov, V., & Singh, R. N. (2005). Growth of carbon nanotubes by microwave plasma chemical vapor deposition (MPCVD). *Ceramic Transactions*, *159*(August 2000), 177–183. doi:10.1063/1.1319529

Gupta, R. P., & Sen, S. K. (1975). Calculation of multiplet structure of core ¡math display="inline"¿ ¡mi¿p¡/mi¿ ¡/math¿ -vacancy levels. II. *Physical Review B*, *12*(1), 15–19. doi:10.1103/PhysRevB.12.15. arXiv: arXiv:1011.1669v3

Gupta, T. (2018). *Carbon: The Black, the Gray and the Transparent*. doi:978-3-319-66405-7

Han, G., He, J., Fukuyama, S., & Yokogawa, K. (1998). Effect of strain-induced martensite on hydrogen environment embrittlement of sensitized austenitic stainless steels at low temperatures. *Acta Materialia*, *46*(13), 4559–4570. doi:10.1016/S1359-6454(98)00136-0

Harris, J., Youngman, R., & Teller, R. (1990). On the nature of the oxygen-related defect in aluminum nitride. *Materials Research Society*, *5*(8), 1763–1773.

Harutyunyan, A. R., Tokune, T., & Mora, E. (2005). Liquid as a required catalyst phase for carbon single-walled nanotube growth. *Applied Physics Letters*, *87*(5), 1–3. doi:10.1063/1.2005395

Harvey, D. (2019). Analytical Chemistry-Electrochemical Methods. (pp. 1–115). Retrieved from https://chem.libretexts.org/Bookshelves/Analytical%7B%5C_%7DChemistry/Book%7B%5C%%7D3A%7B%5C_%7DAnalytical%7B%5C_%7DChemistry%7B%5C_%7D2.0%7B%5C_%7D(Harvey)

Hata, K., Futaba, D. N., Mizuno, K., & Namai, T. (2004). Water-Assisted Highly Efficient Synthesis of Impurity-Free Single-Walled Carbon Nanotubes. *306*(November), 1362–1365.

Hedayati, O., Korei, N., Adeli, M., & Etminanbakhsh, M. (2017). Microstructural evolution and interfacial diffusion during heat treatment of Hastelloy/stainless steel bimetals. *Journal of Alloys and Compounds*, *712*, 172–178. doi:10.1016/j.jallcom.2017.04.080

Heimann, R. B., Evsyukov, S. E., & Koga, Y. (1997). Carbon allotropes: A suggested classification scheme based on valence orbital hybridization. *Carbon*, *35*(10-11), 1654–1658. doi:10.1016/S0008-6223(97)82794-7

Hernadi, K., Fonseca, A., Nagy, J. B., Bernaerts, D., & Lucas, A. A. (1996). Fe-catalyzed carbon nanotube formation. *Carbon*, *34*(10), 1249–1257. doi:10.1016/0008-6223(96)00074-7

Herziger, F., Tyborski, C., Ochedowski, O., Schleberger, M., & Maultzsch, J. (2014). Double-resonant la phonon scattering in defective graphene and carbon nanotubes. *Physical Review B - Condensed Matter and Materials Physics*, *90*(24), 1–6. doi:10.1103/PhysRevB.90.245431

Herzog, E., Casey, A., Lyng, F. M., Chambers, G., Byrne, H. J., & Davoren, M. (2007). A new approach to the toxicity testing of carbon-based nanomaterials-The clonogenic assay. *Toxicology Letters*, *174*(1-3), 49–60. doi:10.1016/j.toxlet.2007.08.009

Hofmann, S., Kleinsorge, B., Ducati, C., & Robertson, J. (2003). Controlled low-temperature growth of carbon nanofibres by plasma deposition. *New Journal of Physics*, *5*. doi:10.1088/1367-2630/5/1/153

Holzwarth, U., & Gibson, N. (2011). The Scherrer equation versus the 'Debye-Scherrer equation'. *Nature Nanotechnology*, *6*(9), 534–534. doi:10.1038/nnano.2011.145

Hughes, M. (2014). What Is Sputtering? Magnetron Sputtering? Retrieved from http://www.semicore.com/what-is-sputtering

Hussain, S. [S.], Amade, R., Jover, E., & Bertran, E. (2012). Functionalization of carbon nanotubes by water plasma. *Nanotechnology*, *23*(38). doi:10.1088/0957-4484/23/38/385604

Hussain, S. [Shahzad]. (2014). *Carbon Nanotubes Deposited by Hot Wire Plasma CVD and water assisted CVD for Energetic and Environmental Applications* (Doctoral dissertation, Barcelona University).

Hussain, S. [Shahzad], Amade, R., & Bertran, E. (2014). Study of CNTs structural evolution during water assisted growth and transfer methodology for electrochemical applications. *Materials Chemistry and Physics*, *148*(3), 914–922. doi:10.1016/j.matchemphys.2014.08.070

Hussain, S. [Shahzad], Amade, R., Jover, E., & Bertran, E. (2013). Water Plasma Functionalized CNTs/MnO 2 Composites for Supercapacitors. *The Scientific World Journal*, *2013*, 1–8. doi:10.1155/2013/832581

Hussain, S. [Shahzad], Amade, R., Moreno, H., & Bertran, E. (2014). RF-PECVD growth and nitrogen plasma functionalization of CNTs on copper foil for electrochemical applications. *Diamond and Related Materials*, *49*, 55–61. doi:10.1016/j.diamond.2014.08.006

Hye, R. B., Lim, H., Hyun, J. S., & Hee, C. C. (2007). A synthesis of high purity single-walled carbon nanotubes from small diameters of cobalt nanoparticles by using oxygen-assisted chemical vapor deposition process. *Bulletin of the Korean Chemical Society*, *28*(11), 2056–2060. doi:10.5012/bkcs.2007.28.11.2056

Ibidi. (2019). Confocal Microscopy: Principle & Applications. Retrieved from https://ibidi.com/content/216-confocal-microscopy

Iijima, S., & Ichihashi, T. (1993). Single-shell carbon nanotubes of 1-nm diameter. *Nature*, *363*(6430), 603–605. doi:10.1111/j.1753-4887.1971.tb07294.x. arXiv: arXiv:1011.1669v3

Inagaki, M., Kang, F., Toyoda, M., & Konno, H. (2014). *Advanced Materials Science and Engineering of Carbon*. Oxford.

Iriarte, G. F., Rodríguez, J. G., & Calle, F. (2010). Synthesis of c-axis oriented AlN thin films on different substrates: A review. *Materials Research Bulletin*, *45*(9), 1039–1045. doi:10.1016/j.materresbull.2010.05.035

Ji, X., Zhang, W., Li, X., Yu, H., & Dong, H. (2017). A novel hybrid method combining ASP with PECVD for in-situ low temperature synthesis of vertically aligned carbon nanotube films. *Diamond and Related Materials*, *77*(January), 16–24. doi:10.1016/j.diamond.2017.05.008

Jiang, K., Wang, J., Li, Q., Liu, L., Liu, C., & Fan, S. (2011). Superaligned carbon nanotube arrays, films, and yarns: A road to applications. *Advanced Materials*, *23*(9), 1154–1161. doi:10.1002/adma.201003989

Jiang, M., Qi, Y., Liu, H., & Chen, Y. (2018). The Role of Nanomaterials and Nanotechnologies in Wastewater Treatment: a Bibliometric Analysis. *Nanoscale Research Letters*, *13*. doi:10.1186/s11671-018-2649-4

Jiang, Y., Wang, H., Shang, X. F., Li, Z. H., & Wang, M. (2009). Influence of NH3 atmosphere on the growth and structures of carbon nanotubes synthesized by the arc-discharge method. *Inorganic Materials*, *45*(11), 1237–1239. doi:10.1134/s0020168509110090

Jin, Y., Chen, H., Chen, M., Liu, N., & Li, Q. (2013). Graphene-patched CNT/MnO2 nanocomposite papers for the electrode of high-performance flexible asymmetric supercapacitors. *ACS Applied Materials and Interfaces*, *5*(8), 3408–3416. doi:10.1021/am400457x

Jinlong, L., Hongyun, L., & Tongxiang, L. (2015). The grain size and special boundary dependence of corrosion resistance in 304 austenitic stainless steels. *Materials Chemistry and Physics*, *163*, 496–500. doi:10.1016/j.matchemphys.2015.08.004

Jose, F., Ramaseshan, R., Dash, S., Bera, S., Tyagi, A. K., & Raj, B. (2010). Response of magnetron sputtered AlN films to controlled atmosphere annealing. *Journal of Physics D: Applied Physics*, *43*(7), 075304. doi:10.1088/0022-3727/43/7/075304

Julien, C., Massot, M., Baddour-Hadjean, R., Franger, S., Bach, S., & Pereira-Ramos, J. P. (2003). Raman spectra of birnessite manganese dioxides. *Solid State Ionics*, *159*(3-4), 345–356. doi:10.1016/S0167-2738(03)00035-3

Jung, N., Kwon, S., Lee, D., Yoon, D. M., Park, Y. M., Benayad, A., ... Park, J. S. (2013). Synthesis of chemically bonded graphene/carbon nanotube composites and their application in large volumetric capacitance supercapacitors. *Advanced Materials*, *25*(47), 6854–6858. doi:10.1002/adma.201302788

Jurečka, S., Imamura, K., Matsumoto, T., & Kobayashi, H. (2018). Investigation of morphological and optical properties of nanostructured layers formed by the SSCT etching of silicon. *Applied Surface Science*, *461*(August), 72–77. doi:10.1016/j.apsusc.2018.08.099

El-Kady, M. F., Ihns, M., Li, M., Hwang, J. Y., Mousavi, M. F., Chaney, L., ... Kaner, R. B. (2015). Engineering three-dimensional hybrid supercapacitors and microsupercapacitors for high-performance integrated energy storage. *Proceedings of the National Academy of Sciences*, *112*(14), 4233–4238. doi:10.1073/pnas.1420398112

Kaech, A. (2013). *An Introduction to Electron Microscopy Instrumentation , Imaging and Preparation*. Retrieved from http://www.zmb.uzh.ch/static/bio407/assets/Script%7B%5C_%7DAK%7B%5C_%7D2014.pdf

Kandalkar, S. G., Dhawale, D. S., Kim, C. K., & Lokhande, C. D. (2010). Chemical synthesis of cobalt oxide thin film electrode for supercapacitor application. *Synthetic Metals*, *160*(11-12), 1299–1302. doi:10.1016/j.synthmet.2010.04.003

Kang, L. X., Li, D., Yong, Z. Z., Zhang, X. H., & Li, Q. (2016). Growth of Aligned Carbon Nanotubes and Their Applications. *Industrial Applications of Carbon Nanotubes*, 381–403. doi:10.1016/B978-0-323-41481-4.00013-7

Kang, S. J., Kocabas, C., Ozel, T., Shim, M., Pimparkar, N., Alam, M. A., ... Rogers, J. A. (2007). High-performance electronics using dense, perfectly aligned arrays of single-walled carbon nanotubes. *Nature Nanotechnology*, *2*(4), 230–236. doi:10.1038/nnano.2007.77

Kappaganthu, S. R., & Sun, Y. [Y.]. (2004). Formation of an MN-type cubic nitride phase in reactively sputtered stainless steel-nitrogen films. *Journal of Crystal Growth*, *267*(1-2), 385–393. doi:10.1016/j.jcrysgro.2004.03.066

Kappaganthu, S. R., & Sun, Y. [Y.]. (2005). Influence of sputter deposition conditions on phase evolution in nitrogen-doped stainless steel films. *Surface and Coatings Technology*, *198*(1-3 SPEC. ISS.), 59–63. doi:10.1016/j.surfcoat.2004.10.047

Ke, G., Tao, Y., Lu, Y., Bian, Y., Zhu, T., Guo, H., & Chen, Y. (2015). Highly c-axis oriented AlN film grown by unbalanced magnetron reactive sputtering and its electrical properties. *Journal of Alloys and Compounds*, *646*, 446–453. doi:10.1016/j.jallcom.2015.05.174

Ke, Q., & Wang, J. (2016). Graphene-based materials for supercapacitor electrodes – A review. *Journal of Materiomics*, *2*(1), 37–54. doi:10.1016/j.jmat.2016.01.001

Keithley. (2012). Application Note Se ries Performing van der Pauw Sheet Resistance Measurements Using the. *Application Note Series*, (3180).

Keraudy, J., García Molleja, J., Ferrec, A., Corraze, B., Richard-Plouet, M., Goullet, A., & Jouan, P. Y. (2015). Structural, morphological and electrical properties of nickel oxide thin films deposited by reactive sputtering. *Applied Surface Science*, *357*, 838–844. doi:10.1016/j.apsusc.2015.08.199

Kerber, S. J., & Tverberg, J. (2000). STAINLESS. (November), 33–36.

Keyence. (2019). What Is Surface Area Roughness? Retrieved from https://www.keyence.com/ss/products/microscope/roughness/surface

Kiamahalleh, M. V., Zein, S. H. S., Najafpour, G., Sata, S. A., & Buniran, S. (2012). Multiwalled Carbon Nanotubes Based Nanocomposites for Supercapacitors: a Review of Electrode Materials. *Nano*, *07*(02), 1230002. doi:10.1142/s1793292012300022

Kong, D., Xiao, Z., Gao, Y., Zhang, X., Guo, R., Huang, X., ... Zhi, L. (2019). Sp 2 -carbon dominant carbonaceous materials for energy conversion and storage. *Materials Science and Engineering R: Reports*, *137*(September 2018), 1–37. doi:10.1016/j.mser.2018.10.001

Korneva, G. (2008). *Functionalization of carbon nanotubes* (Doctoral thesis, Drexel University).

Kovalevsky, J., & Quinn, T. J. (2004). The international system of units (SI). *Comptes Rendus Physique*, *5*(8 SPEC.ISS.), 799–811. doi:10.1016/j.crhy.2004.07.002

Kumar, S., Baldwin, M. J., Fewell, M. P., Haydon, S. C., Short, K. T., Collins, G. A., & Tendys, J. (2000). The effect of hydrogen on the growth of the nitrided layer in r.f.-plasma-nitrided austenitic stainless steel AISI 316. *Surface and Coatings Technology*, *123*(1), 29–35. doi:10.1016/S0257-8972(99)00393-X

Kusy, A. (1987). An equivalent network for resistance and temperature coefficient of resistance versus temperature and composition of thick resistive films. *Journal of Applied Physics*, *62*(4), 1324–1334. doi:10.1063/1.339659

Lacerda, R. G., Teh, A. S., Yang, M. H., Teo, K. B. K., Rupesinghe, N. L., Dalal, S. H., ... Legagneux, P. (2004). Growth of highly-quality single-wall carbon nanotubes without amorphous carbon formation. *Applied Physics Letters*, *84*(2), 269–271. doi:10.1063/1.1639509

Lang, X., Hirata, A., Fujita, T., & Chen, M. (2011). Nanoporous metal/oxide hybrid electrodes for electrochemical supercapacitors. *Nature Nanotechnology*, *6*(4), 232–236. doi:10.1038/nnano.2011.13

Lebreton, F., Abolmasov, S. N., Silva, F., & Roca I Cabarrocas, P. (2016). In situ photoluminescence study of plasma-induced damage at the a -Si:H/c-Si interface. *Applied Physics Letters*, *108*(5). doi:10.1063/1.4941298

Lee, C. C., Wang, D. T., & Choi, W. S. (2006). Design and construction of a compact vacuum furnace for scientific research. *Review of Scientific Instruments*, *77*(12). doi:10.1063/1.2402910

Lee, J. Y., Punkkinen, M. P., Schönecker, S., Nabi, Z., Kádas, K., Zólyomi, V., ... Kwon, S. K. (2018). The surface energy and stress of metals. *Surface Science*, *674*(January), 51–68. doi:10.1016/j.susc.2018.03.008

Lehman, J. H., Terrones, M., Mansfield, E., Hurst, K. E., & Meunier, V. (2011). Evaluating the characteristics of multiwall carbon nanotubes. *Carbon*, *49*(8), 2581–2602. doi:10.1016/j.carbon.2011.03.028

Lei, R., Zhang, H., Fang, Q., Ni, H., & Gu, H. (2019). MnO 2 nanowires electrodeposited on freestanding graphenated carbon nanotubes as binder-free electrodes with enhanced supercapacitor performance. *Materials Letters*, *249*, 140–142. doi:10.1016/j.matlet.2019.04.063

Lekawa-Raus, A., Patmore, J., Kurzepa, L., Bulmer, J., & Koziol, K. (2014). Electrical properties of carbon nanotube based fibers and their future use in electrical wiring. *Advanced Functional Materials*, *24*(24), 3661–3682. doi:10.1002/adfm.201303716

Lepró, X., Lima, M. D., & Baughman, R. H. (2010a). Spinnable carbon nanotube forests grown on thin, flexible metallic substrates. *Carbon*, *48*(12), 3621–3627. doi:10.1016/j.carbon.2010.06.016

Lepró, X., Lima, M. D., & Baughman, R. H. (2010b). Spinnable carbon nanotube forests grown on thin, flexible metallic substrates. *Carbon*, *48*(12), 3621–3627. doi:10.1016/j.carbon.2010.06.016

Li, L., Hu, Z. A., An, N., Yang, Y. Y., Li, Z. M., & Wu, H. Y. (2014). Facile synthesis of MnO 2 /CNTs composite for supercapacitor electrodes with long cycle stability. *Journal of Physical Chemistry C*, *118*(40), 22865–22872. doi:10.1021/jp505744p

Li, L. F., & Celis, J. P. (2004). Intergranular corrosion of 304 stainless steel pickled in acidic electrolytes. *Scripta Materialia*, *51*(10), 949–953. doi:10.1016/j.scriptamat.2004.07.022

Li, Q., Zhang, X., DePaula, R. F., Zheng, L., Zhao, Y., Stan, L., ... Zhu, Y. T. (2006). Sustained growth of ultralong carbon nanotube arrays for fiber spinning. *Advanced Materials*, *18*(23), 3160–3163. doi:10.1002/adma.200601344

Li, S., & Hihara, L. H. (2012). In situ Raman spectroscopic identification of rust formation in Evans' droplet experiments. *Electrochemistry Communications*, *18*(1), 48–50. doi:10.1016/j.elecom.2012.02.014

Li, Y. [Yan], Cui, R., Ding, L., Liu, Y., Zhou, W., Zhang, Y., ... Liu, J. (2010). How catalysts affect the growth of single-walled carbon nanotubes on substrates. *Advanced Materials*, *22*(13), 1508–1515. doi:10.1002/adma.200904366

Li, Y. [Yang], Xu, G., Zhang, H., Li, T., Yao, Y., Li, Q., & Dai, Z. (2015). Alcohol-assisted rapid growth of vertically aligned carbon nanotube arrays. *Carbon*, *91*, 45–55. doi:10.1016/j.carbon.2015.04.035

Li, Z. Q., Lu, C. J., Xia, Z. P., Zhou, Y., & Luo, Z. (2007). X-ray diffraction patterns of graphite and turbostratic carbon. *Carbon*, *45*(8), 1686–1695. doi:10.1016/j.carbon.2007.03.038

Lieber, C. M., Odom, T. W., Huang, J.-L., & Kim, P. (1998). Atomic structure and electronic properties of single-walled carbon nanotubes. *Nature*, *391*(6662), 62–64. doi:10.1038/34145. arXiv: 9903215v1 [arXiv:cond-mat]

Liu, H., Li, S., Zhai, J., Li, H., Zheng, Q., Jiang, L., & Zhu, D. (2004). Self-assembly of large-scale micropatterns on aligned carbon nanotube films. *Angewandte Chemie - International Edition*, *43*(9), 1146–1149. doi:10.1002/anie.200351988

Liu, K., Jiang, K., Feng, C., Chen, Z., & Fan, S. (2005). A growth mark method for studying growth mechanism of carbon nanotube arrays. *Carbon*, *43*(14), 2850–2856. doi:10.1016/j.carbon.2005.06.002

Liu, K., Sun, Y. [Yinghui], Chen, L., Feng, C., Feng, X., Jiang, K., ... Fan, S. (2008). Controlled growth of super-aligned carbon nanotube arrays for spinning continuous unidirectional sheets with tunable physical properties. *Nano Letters*, *8*(2), 700–705. doi:10.1021/nl0723073

Liu, W., Zhang, X., Xu, G., Bradford, P. D., Wang, X., Zhao, H., ... Zhu, Y. (2011). Producing superior composites by winding carbon nanotubes onto a mandrel under

a poly(vinyl alcohol) spray. *Carbon*, *49*(14), 4786–4791. doi:10.1016/j.carbon.2011.06.089

Loiseau, A., Gavillet, J., Ducastelle, F., Thibault, J., Stéphan, O., Bernier, P., & Thair, S. (2003). Nucleation and growth of SWNT: TEM studies of the role of the catalyst. *Comptes Rendus Physique*, *4*(9), 975–991. doi:10.1016/j.crhy.2003.10.022

Lothongkum, G., Chaikittisilp, S., & Lothongkum, A. W. (2003). XPS investigation of surface films on high Cr-Ni ferritic and austenitic stainless steels. *218*, 202–209. doi:10.1016/S0169-4332(03)00600-7

Lu, C., & Liu, J. (2006). Controlling the Diameter of Carbon Nanotubes in Chemical Vapor Deposition Method by Carbon Feeding. *Journal of Physical Chemistry B*, *110*(41), 20254–20257. doi:10.1021/jp0632283

Lucideon. (2019). Scanning Electron Microscopy, Energy Dispersive X-Ray Analysis (SEM EDX EDA) — Lucideon. Retrieved from https://www.lucideon.com/testing-characterization/techniques/sem-edx

Machala, Z., Janda, M., Hensel, K., Jedlovský, I., Leštinská, L., Foltin, V., ... Morvová, M. (2007). Emission spectroscopy of atmospheric pressure plasmas for bio-medical and environmental applications. *Journal of Molecular Spectroscopy*, *243*(2), 194–201. doi:10.1016/j.jms.2007.03.001

Makowski, T., & Fortuniak, W. (2015). Applied Surface Science Conductive hydrophobic hybrid textiles modified with carbon nanotubes. *357*, 1007–1014. doi:10.1016/j.apsusc.2015.09.132

Mallick, P., Tewary, N. K., Ghosh, S. K., & Chattopadhyay, P. P. (2017). Microstructure-tensile property correlation in 304 stainless steel after cold deformation and austenite reversion. *Materials Science and Engineering A*, *707*(September), 488–500. doi:10.1016/j.msea.2017.09.070

Marchi, C. S., Laboratories, S. N., Marchi, C. S., Somerday, B. P., Laboratories, S. N., Laboratories, S. N., ... Company, L. M. (2005). Austenitic Stainless Steels Type 304 & 304L Fe-19Cr-10Ni. (code 2101).

Markets&Markets. (2019). Carbon Nanotubes (CNT) Market. Retrieved from https://www.marketsandmarkets.com/Market-Reports/carbon-nanotubes-139.html

Masarapu, C., & Wei, B. (2007). Direct growth of aligned multiwalled carbon nanotubes on treated stainless steel substrates. *Langmuir*, *23*(17), 9046–9049. doi:10.1021/la7012232

Maser, W. K., Muñoz, E., Benito, A. M., Martínez, M. T., De La Fuente, G. F., Maniette, Y., ... Sauvajol, J. L. (1998). Production of high-density single-walled nanotube material by a simple laser-ablation method. *Chemical Physics Letters*, *292*(4-6), 587–593. doi:10.1016/S0009-2614(98)00776-3

Mattox, D. M. (2009). *Handbook of Physical Vapor Deposition (PVD) Processing (Second Edition)*. doi:10.1016/B978-0-8155-2037-5.00025-3

Menea, F. (2016). Electrochemical Techniques for Characterization and Detection Application of Nanostructured Carbon Composite. *Intechopen*, *1*(Nanosurface), 23. doi:http://dx.doi.org/10.5772/57353

Meng, F., Zhang, X., Xu, G., Yong, Z., Chen, H., Chen, M., ... Zhu, Y. (2011). Carbon nanotube composite films with switchable transparency. *ACS Applied Materials and Interfaces*, *3*(3), 658–661. doi:10.1021/am200114r

Merlen, A., Buijnsters, J., & Pardanaud, C. (2017). *A Guide to and Review of the Use of Multiwavelength Raman Spectroscopy for Characterizing Defective Aromatic Carbon Solids: from Graphene to Amorphous Carbons*. doi:10.3390/coatings7100153

Mešić, B. (2010). Highly conductive electrodes as diffusion barrier for high temperature applications, 149.

Meurig Thomas, J., & Midgley, P. A. (2004). High-resolution transmission electron microscopy: the ultimate nanoanalytical technique. *Chem. Commun.* (11), 1253–1267. doi:10.1039/b315513g

Meyyappan, M., Delzeit, L., Cassell, A., & Hash, D. (2003). Carbon nanotube growth by PECVD: A review. *Plasma Sources Science and Technology*, *12*(2), 205–216. doi:10.1088/0963-0252/12/2/312

Michael Keidar, & Beilis, I. I. (2013). *Plasma Engineering Plasma Engineering Applications from Aerospace to*.

Milne, W. I., Lacerda, R. G., Teo, K. B. K., Hash, D. B., Bell, M. S., & Meyyappan, M. (2006). Carbon nanotubes by plasma-enhanced chemical vapor deposition. *Pure and Applied Chemistry*, *78*(6), 1117–1125. doi:10.1351/pac200678061117

Mischler, S., Mathieu, H. J., & Landolt, D. (1988). The investigation of passive films on iron—chromium alloys by AES and XPS. *Surface and Interface Analysis*, *12*(7), 429–429. doi:10.1002/sia.740120712

Mittemeijer, E., & Scardi, P. (2004). *Diffraction Analysis of the Microstructure of Materials*. doi:10.1007/978-3-662-06723-9

Mitutoyo. (2014). Surface Finish Analysis Overview.

Moreira, M. A., Doi, I., Souza, J. F., & Diniz, J. A. (2011). Electrical characterization and morphological properties of AlN films prepared by dc reactive magnetron sputtering. *Microelectronic Engineering*, *88*(5), 802–806. doi:10.1016/j.mee.2010.06.045

Moreno, H. A., Hussain, S., Amade, R., & Bertran, E. (2014). Growth and functionalization of CNTs on stainless steel electrodes for supercapacitor applications. *Materials Research Express*, *1*(3), 035050. doi:10.1088/2053-1591/1/3/035050

Moskalioviene, T., & Galdikas, A. (2015). The Effect of Hydrogen on Plasma Nitriding of Austenitic Stainless Steel: Kinetic Modeling. *Metallurgical and Materials Transactions A: Physical Metallurgy and Materials Science*, *46*(12), 5588–5595. doi:10.1007/s11661-015-3183-y

Motamedi, P., & Cadien, K. (2014). XPS analysis of AlN thin films deposited by plasma enhanced atomic layer deposition. *Applied Surface Science*, *315*(1), 104–109. doi:10.1016/j.apsusc.2014.07.105

Moulder, J. F., Stickle, W. F., Sobol, P. E., & Bomben, K. D. (1992). Handbook of Photoelectron Spectroscopy. *Physical Electronics, Inc., Eden Prairie, Minnesota*. doi:10.1002/sia.740030412

Mozetič, M., Vesel, A., Kovač, J., Zaplotnik, R., Modic, M., & Balat-Pichelin, M. (2015). Formation and reduction of thin oxide films on a stainless steel surface upon subsequent treatments with oxygen and hydrogen plasma. *Thin Solid Films*, *591*, 186–193. doi:10.1016/j.tsf.2015.02.007

Myscope. (2019). MyScope Outreach. Retrieved from https://myscopeoutreach.org/

Nanakoudis, A. (2018). EDX analysis with a scanning electron microscope (SEM): how does it work? Retrieved from https://blog.phenom-world.com/edx-analysis-scanning-electron-microscope-sem

Ni, J., Lu, W., Zhang, L., Yue, B., Shang, X., & Lv, Y. (2009). Low-Temperature Synthesis of Monodisperse 3D Manganese Oxide Nanoflowers and Their Pseudocapacitance Properties. *Journal Of Physical Chemistry C*, *113*(1), 54–60. doi:10.1021/jp806454r

Nicolet, M. (1978). Diffusion Barrier in thin films. *Films, Thin Solid Sequoia, Elsevier*, *52*, 415–443.

Nikulin, I., Kaibyshev, R., & Skorobogatykh, V. (2010). High temperature properties of an austenitic stainless steel. *Journal of Physics: Conference Series*, *240*. doi:10.1088/1742-6596/240/1/012071

NIST-Database. (2012). NIST X-ray Photoelectron Spectroscopy (XPS) Database, Version 3.5. Retrieved from https://srdata.nist.gov/xps/Default.aspx

Oh, S. J., Cook, D., & Townsend, H. (1998). Characterization of iron oxides commonly formed as corrosion products on steel. Old Dominion University,Bethlehem Steel Corporation.

Olympus. (2019). Confocal Microscopy. Retrieved from https://www.olympus-lifescience.com/en/microscope-resource/primer/techniques/confocal/confocalintro/

Osswald, S., Havel, M., & Gogotsi, Y. (2007). Monitoring oxidation of multiwalled carbon nanotubes by Raman spectroscopy. (April), 728–736. doi:10.1002/jrs

Pandolfo, A. G., & Hollenkamp, A. F. (2006). Carbon properties and their role in supercapacitors. *Journal of Power Sources*, *157*(1), 11–27. doi:10.1016/j.jpowsour.2006.02.065. arXiv: caps19

Parak, W. J., Nel, A. E., & Weiss, P. S. (2015). Grand Challenges for Nanoscience and Nanotechnology. *ACS Nano*, *9*(7), 6637–6640. doi:10.1021/acsnano.5b04386

Pardanaud, C., Martin, C., & Roubin, P. (2014). Multiwavelength Raman spectroscopy analysis of a large sampling of disordered carbons extracted from the Tore Supra tokamak. *Vibrational Spectroscopy*, *70*, 187–192. doi:10.1016/j.vibspec.2013.12.004

Parkansky, N., Boxman, R. L., Alterkop, B., Zontag, I., Lereah, Y., & Barkay, Z. (2004). Single-pulse arc production of carbon nanotubes in ambient air. *Journal of Physics D: Applied Physics*, *37*(19), 2715–2719. doi:10.1088/0022-3727/37/19/015

ParticleAnalytical. (2019). X-Ray Diffraction – XRD. Retrieved from https://particle.dk/methods-analytical-laboratory/xrd-analysis/

Patrick, J. W. (1995). Porosity in Carbons: Characterization and Applications. *Porosity in Carbons*, 253.

Payling, R., & Larkins, P. (2002). Book Review. *Spectrochimica Acta Part B: Atomic Spectroscopy*, *57*(2), 381–383. doi:https://doi.org/10.1016/S0584-8547(01)00378-0

Pérez del Pino, A., György, E., Pascual, E., Pantoja-Suárez, F., Amade, R., Bertran-Serra, E., ... Alshaikh, I. (2017). Laser-driven coating of vertically aligned carbon nanotubes with manganese oxide from metal organic precursors for energy storage. *Nanotechnology*, *28*(39), 395405. doi:10.1088/1361-6528/aa81b1

Pfeiffer. (2019a). Overview of vacuum. Retrieved from https://www.pfeiffer-vacuum.com/en/know-how/introduction-to-vacuum-technology/general/overview-of-vacuum/

Pfeiffer. (2019b). Types of flow. Retrieved from https://www.pfeiffer-vacuum.com/en/know-how/introduction-to-vacuum-technology/fundamentals/types-of-flow/

Phatak, O. (2018). Isotopes of Carbon. Retrieved from https://sciencestruck.com/isotopes-of-carbon

PhysicalElectronics. (2019). X-Ray Photoelectron Spectroscopy (XPS) Surface Analysis Technique. Retrieved from https://www.phi.com/surface-analysis-techniques/xps-esca.html

Pierson, H. (1999). *Handbook of chemical vapour deposition*. doi:10.1016/B978-081551432-9.50006-1

Plasma-Therm. (2019). PECVD. Retrieved from http://www.plasma-therm.com/pecvd.html

Poco. (2015). Properties and Characteristics of Graphite for Industrial Application. Poco Graphite Company.

Podila, R., Rao, R., Tsuchikawa, R., Ishigami, M., & Rao, A. M. (2012). Raman spectroscopy of folded and scrolled graphene. *ACS Nano*, *6*(7), 5784–5790. doi:10.1021/nn302331p

Poncharal, P., Ayari, A., Michel, T., & Sauvajol, J.-L. (2008). Raman spectra of misoriented bilayer graphene. *Physical Review B*, *78*(11), 1–4. doi:10.1103/physrevb.78.113407

Poonam, Sharma, K., Arora, A., & Tripathi, S. K. (2019). Review of supercapacitors: Materials and devices. *Journal of Energy Storage*, *21*(October 2018), 801–825. doi:10.1016/j.est.2019.01.010

Porter, A. L., & Youtie, J. (2009). Where does nanotechnology belong in the map of science? *Nature Nanotechnology*, *4*(9), 534–536. doi:10.1038/nnano.2009.207

Prasek, J., Drbohlavova, J., Chomoucka, J., Hubalek, J., Jasek, O., Adam, V., & Kizek, R. (2011). Methods for carbon nanotubes synthesis - Review. *Journal of Materials Chemistry*, *21*(40), 15872–15884. doi:10.1039/c1jm12254a

Qi, Y., Çain, T., Johnson, W. L., & Goddard, W. A. (2001). Melting and crystallization in Ni nanoclusters: The mesoscale regime. *Journal of Chemical Physics*, *115*(1), 385–394. doi:10.1063/1.1373664

Reibold, M., Paufler, P., Levin, A., Kochmann, W., Pätzke, N., & Meyer, D. (2006). Carbon nanotubes in an ancient Damascus sabre. *Nature*, 1. Retrieved from https://www-nature-com.sire.ub.edu/articles/444286a.pdf

Reich, S., & Thomsen, C. (2004). Raman spectroscopy of graphite Raman spectroscopy of graphite. *Philosophical transactions of the royal society A*, (April), 2271–2288.

Ren, P., Zhu, S., & Wang, F. (2015). Microstructural stability of AlN diffusion barrier for nanocomposite Ni + CrAlYSiHfN coating on single crystal superalloy at high temperatures. *Applied Surface Science*, *359*, 420–425. doi:10.1016/j.apsusc.2015.10.096

Rigaku. (2019). Grazing Incidence X-ray Diffraction (GIXRD) analysis of thin film material. Retrieved from https://www.rigaku.com/en/products/xrd/ultima/app029

Romero, P., Oro, R., Campos, M., Torralba, J. M., & De Villoria, R. G. (2015). Simultaneous synthesis of vertically aligned carbon nanotubes and amorphous carbon thin films on stainless steel. *Carbon*, *82*(100), 31–38. doi:10.1016/j.carbon.2014.10.020

Rossnagel, S. M., Westwood, W. D., & Haber, J. J. (1990). *Handbook of plasma processing technology: fundamentals, etching, deposition, and surface interactions*.

Rümmeli, M. H., Schäffel, F., Kramberger, C., Gemming, T., Bachmatiuk, A., Kalenczuk, R. J., ... Pichler, T. (2007). Oxide-driven carbon nanotube growth in supported catalyst CVD. *Journal of the American Chemical Society*, *129*(51), 15772–15773. doi:10.1021/ja0779405

Sabat, K. C., Rajput, P., Paramguru, R. K., Bhoi, B., & Mishra, B. K. (2014). Reduction of oxide minerals by hydrogen plasma: An overview. *Plasma Chemistry and Plasma Processing*, *34*(1), 1–23. doi:10.1007/s11090-013-9484-2

Sadezky, A., Muckenhuber, H., Grothe, H., Niessner, R., & Pöschl, U. (2005). Raman microspectroscopy of soot and related carbonaceous materials: Spectral analysis and structural information. *Carbon*, *43*(8), 1731–1742. doi:10.1016/j.carbon.2005.02.018

Sahay, C., & Ghosh, S. (2018). Understanding surface quality: Beyond average roughness (Ra). *ASEE Annual Conference and Exposition, Conference Proceedings*, *2018-June*.

Saito, R., Hofmann, M., Dresselhaus, G., Jorio, A., & Dresselhaus, M. S. (2011). Raman spectroscopy of graphene and carbon nanotubes. *Advances in Physics*, *60*(3), 413–550. doi:10.1080/00018732.2011.582251

Saito, T., Ohshima, S., Okazaki, T., Ohmori, S., Yumura, M., & Iijima, S. (2008). Selective Diameter Control of Single-Walled Carbon Nanotubes in the Gas-Phase Synthesis. *Journal of Nanoscience and Nanotechnology*, *8*(11), 6153–6157. doi:10.1166/jnn.2008.sw23

Saker, A., Leroy, C., Michel, H., & Frantz, C. (1991). Properties of sputtered stainless steel-nitrogen coatings and structural analogy with low temperature plasma nitrided layers of austenitic steels. *Materials Science and Engineering A*, *140*(100), 702–708. doi:10.1016/0921-5093(91)90500-M

Schweitzer, P. (2007). *Fundamentals of Metallic Corrosion*. New York: Taylor and Francis Group, LLC.

Seah, C.-M., Chai, S.-P., & Mohamed, A. R. (2011). Synthesis of aligned carbon nanotubes. *Carbon*, *49*(14), 4613–4635. doi:10.1016/j.carbon.2011.06.090

Shatynski, S. R. (1979). The thermochemistry of transition metal carbides. *Oxidation of Metals*, *13*(2), 105–118. doi:10.1007/BF00611975

Shenderova, O. A., Zhirnov, V. V., & Brenner, D. W. (2002). Carbon nanostructures. *Critical Reviews in Solid State and Materials Sciences*, *27*(3-4), 227–356. doi:10.1080/10408430208500497

Shi, Y., Yang, B., & Liaw, P. (2017). Corrosion-Resistant High-Entropy Alloys: A Review. *Metals*, *7*(2), 43. doi:10.3390/met7020043

Shulaker, M. M., Hills, G., Patil, N., Wei, H., Chen, H. Y., Wong, H. S., & Mitra, S. (2013). Carbon nanotube computer. *Nature*, *501*(7468), 526–530. doi:10.1038/nature12502

Signore, M. A., Rizzo, A., Rossi, R., Piscopiello, E., Di Luccio, T., Capodieci, L., ... Giorgi, R. (2008). Role of iron catalyst particles density in the growth of forest-like carbon nanotubes. *Diamond and Related Materials*, *17*(11), 1936–1942. doi:10.1016/j.diamond.2008.04.016

Singh, C., Shaffer, M. S., & Windle, A. H. (2003). Production of controlled architectures of aligned carbon nanotubes by an injection chemical vapour deposition method. *Carbon*, *41*(2), 359–368. doi:10.1016/S0008-6223(02)00314-7

Smits, F. M. (1958). Measurement of Sheet Resistivities with the Four-Point Probe. *Bell System Technical Journal*, *37*(3), 711–718. doi:10.1002/j.1538-7305.1958.tb03883.x

Speakman, S. (2011a). Basics of X-Ray Powder Diffraction. Boston: Massachusetts Institute of Technology. Retrieved from http://prism.mit.edu/xray/Basics%20of%20X-Ray%20Powder%20Diffraction.pdf

Speakman, S. (2011b). Estimating Crystallite Size Using XRD. Massachusetts Institute of Technology. Retrieved from http://prism.mit.edu/xray/oldsite/CrystalSizeAnalysis.pdf

Speakman, S. (2011c). Introduction to X-Ray Powder Diffraction Data Analysis. Boston: Massachusetts Institute of Technology. Retrieved from http://prism.mit.edu/xray/introduction%20to%20xrpd%20data%20analysis.pdf

Stephen, O., & Nigel, S. (2014). Current and future trends in vacuum process technology — Solid State Technology. Retrieved from https://electroiq.com/2009/10/current-and%7B%5C_%7Dfuture/

Stopar, K., Drobne, D., Eler, K., & Bartol, T. (2016). Citation analysis and mapping of nanoscience and nanotechnology: identifying the scope and interdisciplinarity of research. *Scientometrics*, *106*(2), 563–581. doi:10.1007/s11192-015-1797-x

Stramel, A. A., Gupta, M. C., Lee, H. R., Yu, J., & Edwards, W. C. (2010). Pulsed laser deposition of carbon nanotube and polystyrenecarbon nanotube composite thin films. *Optics and Lasers in Engineering*, *48*(12), 1291–1295. doi:10.1016/j.optlaseng.2010.06.002

Sumlo Iijima. (1991). Helical microtubules of graphitic carbon. *Nature*, *354*(354), 56–58.

Sun, X., Sun, H., Li, H., & Peng, H. (2013). Developing polymer composite materials: Carbon nanotubes or graphene? *Advanced Materials*, *25*(37), 5153–5176. doi:10.1002/adma.201301926

Sundgren, J. E., Johansson, B. O., & Karlsson, S. E. (1983). Kinetics of nitride formation on titanium targets during reactive sputtering. *Surface Science*, *128*(2-3), 265–280. doi:10.1016/S0039-6028(83)80031-4

Terwagne, G., Hody, H., & Colaux, J. (2003). Structural and quantitative analysis of stainless steel coatings deposited by DC-magnetron sputtering in a reactive atmosphere. *Surface and Coatings Technology*, *174-175*(03), 383–388. doi:10.1016/S0257-8972(03)00594-2

Tessonnier, J. P., & Su, D. S. (2011). Recent progress on the growth mechanism of carbon nanotubes: A review. *ChemSusChem*, *4*(7), 824–847. doi:10.1002/cssc.201100175

Thapa, A., Neupane, S., Guo, R., Jungjohann, K. L., Pete, D., & Li, W. (2018). Direct growth of vertically aligned carbon nanotubes on stainless steel by plasma enhanced chemical vapor deposition. *Diamond and Related Materials*, *90*(September), 144–153. doi:10.1016/j.diamond.2018.10.012

ThermoFisher. (2019). Thermo Scientific XPS: What is XPS. Retrieved from https://xpssimplified.com/whatisxps.php

UDEL. (2019). Carbon Nanotube-Based Sensing Composites. Retrieved from https://sites.udel.edu/nsf-cmmi-cnt-shm/the-basics/

VacAero. (2015). Conductance in Vacuum Pumping Systems. Retrieved from https://vacaero.com/information-resources/vacuum-pump-technology-education-and-training/1025-conductance-in-vacuum-pumping-systems.html

Vacuum Daily.net. (2011). Vacuum technology in constant evolution - Vacuumdaily.net. Retrieved from http://www.vacuumdaily.net/2011/06/vacuum-technology-in-constant-evolution/

Van der Pauw, L. (1958). A method of measuring the resistivity and Hall coefficient on lamellae of arbitrary shape. *Philips Technical Review*, *13*(1), 1–9.

Varshney, D., Weiner, B. R., & Morell, G. (2010). Growth and field emission study of a monolithic carbon nanotube/diamond composite. *Carbon*, *48*(12), 3353–3358. doi:10.1016/j.carbon.2010.05.025

Venezuela, P., Lazzeri, M., & Mauri, F. (2011). Theory of double-resonant Raman spectra in graphene: Intensity and line shape of defect-induced and two-phonon bands. *Physical Review B - Condensed Matter and Materials Physics*, *84*(3), 1–25. doi:10.1103/PhysRevB.84.035433

Vesel, A., Mozetic, M., & Balat-Pichelin, M. (2016). Reduction of a thin chromium oxide film on Inconel surface upon treatment with hydrogen plasma. *Applied Surface Science*, *387*, 1140–1146. doi:10.1016/j.apsusc.2016.06.098

Walker, M. (2019). What is Magnetron Sputtering? Retrieved from https://www.wisegeek.com/what-is-magnetron-sputtering.htm

Wang, B., Poa, C. H., Wei, L., Li, L. J., Yang, Y., & Chen, Y. (2007). (n,m) selectivity of single-walled carbon nanotubes by different carbon precursors on Co-Mo catalysts. *Journal of the American Chemical Society*, *129*(29), 9014–9019. doi:10.1021/ja070808k

Wang, B., Wei, L., Yao, L., Li, L. J., Yang, Y., & Chen, Y. (2007). Pressure-induced single-walled carbon nanotube (n,m) selectivity on Co-Mo catalysts. *Journal of Physical Chemistry C*, *111*(40), 14612–14616. doi:10.1021/jp0762525

Wang, H., Gao, E., Liu, P., Zhou, D., Geng, D., Xue, X., ... Yu, G. (2017). Facile growth of vertically-aligned graphene nanosheets via thermal CVD: The experimental and theoretical investigations. *Carbon*, *121*, 1–9. doi:10.1016/j.carbon.2017.05.074

Wang, J.-T., Chen, C., Wang, E., & Kawazoe, Y. (2015). A New Carbon Allotrope with Six-Fold Helical Chains in all-sp2 Bonding Networks. *Scientific Reports*, *4*(1), 4339. doi:10.1038/srep04339

Wang, X. K., Lin, X. W., Dravid, V. P., Ketterson, J. B., & Chang, R. P. H. (1995). Carbon nanotubes synthesized in a hydrogen arc discharge. *Applied Physics Letters*, *66*(18), 2430–2432. doi:10.1063/1.113963

Wang, Y., Li, M., Gu, Y., Zhang, X., Wang, S., Li, Q., & Zhang, Z. (2015). Tuning carbon nanotube assembly for flexible, strong and conductive films. *Nanoscale*, *7*(7), 3060–6. doi:10.1039/c4nr06401a

Wei, W., Cui, X., Chen, W., & Ivey, D. G. (2011). Manganese oxide-based materials as electrochemical supercapacitor electrodes. *Chemical Society Reviews*, *40*(3), 1697–1721. doi:10.1039/c0cs00127a

Weinhold, F., & Landis, R. (2005). *Valency and Bonding: A Natural Bond Orbital Donor Acceptor Perspective*. Cambridge, London: Cambridge University. Press.

Wen, J. M., Evans, J. W., Bartelt, M. C., Burnett, J. W., & Thiel, P. A. (1996). Coarsening mechanisms in a metal film: From cluster diffusion to vacancy ripening. *Physical Review Letters*, *76*(4), 652–655. doi:10.1103/PhysRevLett.76.652

Weston, G. (1985). Fundamentals of vacuum science and technology. *Ultrahigh Vacuum Practice*, *1*, 1–21. doi:10.1016/B978-0-408-01485-4.50004-0

William D. Callister, J., & Rethwisch, D. G. (2013). Materials science.

Winter, M., & Brodd, R. J. (2004). What are batteries, fuel cells, and supercapacitors? *Chemical reviews*, *104*(10), 4245–69. doi:10.1021/cr020730k

Wu, G., Tan, P., Wang, D., Li, Z., Peng, L., Hu, Y., ... Chen, W. (2017). High-performance Supercapacitors Based on Electrochemical-induced Vertical-aligned Carbon Nanotubes and Polyaniline Nanocomposite Electrodes. *Scientific Reports*, *7*(December 2016), 1–8. doi:10.1038/srep43676

Wu, Z., Song, T., & Sun, B. (2017). Carbon-Based Materials Used for Perovskite Solar Cells. *ChemNanoMat*, *3*(2), 75–88. doi:10.1002/cnma.201600312

Wyczalek, F. (2006). Energy and Environmental Sustainability or Collapse. (June, p. 12). doi:10.2514/6.2006-4070

Xie, S. S., Qian, L. X., Chang, B. H., Zou, B. S., Zhou, W. Y., & Zhao, R. A. (1996). Large-Scale Synthesis of Aligned Carbon Nanotubes. *Science*, *274*(5293), 1701–1703.

Xu, Y., Dervishi, E., Biris, A. R., & Biris, A. S. (2011). Chirality-enriched semiconducting carbon nanotubes synthesized on high surface area MgO-supported catalyst. *Materials Letters*, *65*(12), 1878–1881. doi:10.1016/j.matlet.2011.03.040

Xu, Z., Yan, T., & Ding, F. (2015). Atomistic simulation of the growth of defect-free carbon nanotubes. *Chemical Science*, *6*(8), 4704–4711. doi:10.1039/c5sc00938c

Yang, J., Esconjauregui, S., Sugime, H., Makaryan, T., Hallam, T., Duesberg, G. S., & Robertson, J. (2014). Comparison of carbon nanotube forest growth using AlSi, TiSiN, and TiN as conductive catalyst supports. *Physica Status Solidi (B) Basic Research*, *251*(12), 2389–2393. doi:10.1002/pssb.201451162

Yang, K. L., & Yang, R. T. (1986). The accelerating and retarding effects of hydrogen on carbon deposition on metal surfaces. *Carbon*, *24*(6), 687–693. doi:10.1016/0008-6223(86)90176-4

Yang, S. T., Wang, X., Jia, G., Gu, Y., Wang, T., Nie, H., ... Liu, Y. (2008). Long-term accumulation and low toxicity of single-walled carbon nanotubes in intravenously exposed mice. *Toxicology Letters*, *181*(3), 182–189. doi:10.1016/j.toxlet.2008.07.020

Yang, X., Wang, X., Ling, X., & Wang, D. (2017). Enhanced mechanical behaviors of gradient nano-grained austenite stainless steel by means of ultrasonic impact treatment. *Results in Physics*, *7*, 1412–1421. doi:10.1016/j.rinp.2017.04.002

Zhang, L. [Linlin], Wang, Y., Niu, Z., & Chen, J. (2019). Advanced nanostructured carbon-based materials for rechargeable lithium-sulfur batteries. *Carbon*, *141*, 400–416. doi:10.1016/j.carbon.2018.09.067

Zhang, L. [Liwen], Wang, X., Xu, W., Zhang, Y., Li, Q., Bradford, P. D., & Zhu, Y. (2015). Strong and Conductive Dry Carbon Nanotube Films by Microcombing. *Small*, *11*(31), 3830–3836. doi:10.1002/smll.201500111

Zheng, J. P. (1997). The Limitations of Energy Density for Electrochemical Capacitors. *Journal of The Electrochemical Society*, *144*(6), 2026. doi:10.1149/1.1837738

Zhi, M., Xiang, C., Li, J., Li, M., & Wu, N. (2013). Nanostructured carbon–metal oxide composite electrodes for supercapacitors: a review. *Nanoscale*, *5*(1), 72–88. doi:10.1039/C2NR32040A. arXiv: 1005.0853

Zhu, H., Wei, J., Wang, K., & Wu, D. (2009). Applications of carbon materials in photovoltaic solar cells. *Solar Energy Materials and Solar Cells*, *93*(9), 1461–1470. doi:10.1016/j.solmat.2009.04.006

Trajectory of the author

EDUCATION

Escuela Politécnica Nacional, Ecuador *September 2008*
Degree in Mechanical Engineering

Universitat de Barcelona, Spain *July 2013*
Master in Nanoscience and Nanotechnology

PREVIOUS ACTIVITIES

Escuela Politécnica Nacional May 2014 - Present
Assistant Professor, Department of Materials, Faculty of Mechanical Eng. Quito, Ecuador

Gartec S.A – Pruftechnik A.G. May 2011 - May 2012
Technical Support Engineer *Quito, Ecuador*

Conduto S.A. May 2010 - April 2011
Project Control Engineer *Orellana, Ecuador*

Sudamerica Energy Sudamer S.A. - OCP November 2008 - November 2009
Cathodic Protection Supervisor of the main Ecuadorian oil pipeline *Quito, Ecuador*

STAYS IN RESEARCH CENTRES

Research institute	Department of Applied Physics, Faculty of Physics, ENPHOCAMAT Group, Institute of Nanoscience and Nanotechnology, Universitat de Barcelona
Location	Barcelona
Country	Spain
Year	2015
Duration	3 years and 8 months
Research line	Carbon based materials-metal oxide systems for supercapacitors
Research institute	Department of Applied Physics, Faculty of Physics, FEMAN Group, Universitat de Barcelona
Location	Barcelona
Country	Spain
Year	2013
Duration	6 months
Research line	Diamond-like carbon thin films formed on martensitic steel surface

MATERIAL PRODUCTION TECHNIQUES

Technique	Plasma enhanced chemical vapor deposition (PECVD)
Technique	Chemical vapor deposition (CVD)
Technique	Magnetron Sputtering-Physical vapor deposition (PVD)
Technique	Heat treatments
CNTs reactor	With two heads of magnetron sputtering (PVD) and one CVD/PECVD/WACVD station. PVD: physical vapor deposition CVD: chemical vapor deposition PECVD: plasma enhanced chemical vapor deposition WACVD: water assisted chemical vapor deposition
Thin films reactor	With on head of magnetron sputtering (PVD) and one head of PECVD. PVD: physical vapor deposition PECVD: plasma enhanced chemical vapor deposition

CHARACTERIZATION TECHNIQUES

Technique	Scanning electron microscope (SEM)
Technique	Transmission electron microscope (TEM)
Technique	Atomic force microscope (AFM)
Technique	Confocal microscope
Technique	Raman spectroscopy
Technique	X-ray photoelectron spectroscopy (XPS)
Technique	X-ray diffraction (XRD)
Technique	Profilometer
Technique	Calotest
Technique	Nanotribometer
Technique	Contact angle meter
Technique	Van der Pauw and four probe methods
Technique	Electrochemical characterization

CONFERENCES

Title	Native oxide film reduction on stainless steel for direct growth of carbon nanotubes
Location	Grand Hotel Tiziano, Lecce
Country	Italy
Date	05/09/2018
Title of the event	Trends in Nanotechnology International Conference (TNT2018)
Title	Growth of carbon nanotubes on stainless steel using nitrided multi-layer as diffusion barrier
Location	Pontificie Universidad Católica del Ecuador-Quito
Country	Ecuador
Date	30/08/2017
Title of the event	Nanoscience and Nanotechnology Week in Ecuador
Title	Diamond-like carbon thin films formed on martensitic steel surface
Location	Institute of High National Studies-Quito
Country	Ecuador
Date	04/06/2014
Title of the event	First International Congress on Biomedical Engineering and Mathematical Modelling in Biosciences

Title	Diamond-like carbon: applications
Location	Escuela Politécnica Nacional-Quito
Country	Ecuador
Date	23/09/2014
Title of the event	Seminar on New Composite Materials and Nanostructured Materials
Title	The superhydrophobic and superhydrophilic surfaces and their study in insects and plants of the northern sierra of Ecuador, industrial applications
Location	Università degli Studi di Milano, Milano
Country	Italy
Date	25/01/2013
Title of the event	II Forum of Ecuadorian Students in Europe

PUBLICATIONS IN JOURNALS

Authors	A. Pérez del Pino; E. György; I. Alshaikh; F. Pantoja-Suárez; J.L. Andújar; E. Pascual; R. Amade; E. Bertran-Serra
Title	Laser-driven coating of vertically aligned carbon nanotubes with manganese oxide from metal organic precursors for energy storage
Magazine	909342 - Nanotechnology
Electronic link	https://iopscience.iop.org/article/10.1088/1361-6528/aa81b1/meta
Authors	Pantoja-Suarez, L.; Morales, M.; Andujar, J.L.; Esteve, J.; Segarra, M.; Bertran, E.
Title	Plackett-Burman experimental design for pulsed-DC-plasma deposition of DLC coatings
Magazine	216574 - arXiv
Electronic link	http://arxiv.org/abs/1507.04267

CONGRESS CONTRIBUTIONS

Authors	Fernando Pantoja-Suárez, Islam Alshaikh, Joan Martí-González, Arevik Musheghyan Avetisyan, Roger Amade, José Luis Andujar, Esther Pascual and Enric Bertran-Serra
Title	Carbon-based materials growth process effect on 304 stainless steel substrates
Type of participation	Poster
Congress	Nano Spain Conference 2019
Location	Parc Científic de Barcelona, Barcelona
Country	Spain
Date	May 28-31, 2019

Authors	Pantoja-Suárez, F.; Alshaikh, I.; Amade, R.; Andújar, J.L.; Pascual, E.; Bertran-Serra, E.
Title	Surface analysis of gradient stainless steel buffer layer to support aluminium nitride diffusion barrier for carbon nanotubes growth
Type of participation	Poster
Congress	Trends in Nanotechnology International Conference (TNT2017)
Location	TU Dresden Auditorium Center, Dresden
Country	Germany
Date	June 5-9, 2017

Authors	Pantoja-Suárez, F.; Alshaikh, I.; Amade, R.; Andújar, J.L.; Pascual, E.; Bertran-Serra, E.
Title	Gradient stainless steel buffer layer to support aluminium nitride diffusion barrier for carbon nanotubes growth
Type of participation	Poster
Congress	26th International Conference on Metallurgy and Materials (METAL 2017)
Location	Hotel Voronez I, Brno
Country	Czech Republic
Date	May 24-26, 2017

Authors	Pantoja-Suárez, F.; Alshaikh, I.; Amade, R.; Andujar, J.L.; Pascual, E.; Bertran, E.
Title	Thin AlN diffusion barrier for carbon nanotubes growth over stainless steel substrate
Type of participation	Poster
Congress	10th Anniversary IN2UB, Universitat de Barcelona
Location	Col-legi Oficial de Metges de Barcelona, Barcelona
Country	Spain
Date	26th January 2017

Authors	Luis F. Pantoja S.; Enric Bertran
Title	Diamond-like carbon thin films formed on martensitic steel surface
Type of participation	Poster
Congress	First International Congress of Biomedical Engineering and Mathematical Modeling in Biosciences
Location	Institute of High National Studies-Quito
Country	Ecuador
Date	04/06/2014

Authors	Luis F.; Pantoja S.; Enric Bertran
Title	Morphology and wear resistance of DLC thin films deposited on steel surface by PECVD
Type of participation	Poster
Congress	International Congress of Metallurgy and Materials SAM-CONAMET / IBEROMAT 2014
Location	Universidad del Litoral, Santa Fe
Country	Argentina
Date	October 21-24, 2014

PROJECTS

Project/Contract Title	Materials by energy, photonics & Catalysis (ENPHOCAMAT)
Type of Programme	SGRC - Ajuts de Suport als Grups de Recerca de Catalunya (SGR)
Funding Administration	AGAU - Agència de Gestió d'Ajuts Universitaris i de Recerca (Agència de Gestió d'Ajuts Universitaris i de Recerca (AGAUR))
Number of project	2017SGR1086
Duration	from 2017 to 2019
Responsible researcher(s)	Enric Bertran Serra
Keywords	028723 - Catàlisi / 025251 - Nanomaterials / 032866 - MAPLE / 050125 - Tractament tèrmic / 213552 - PVD / 015952 - CVD

Project/Contract Title	Nanocomposites Carbon hybrids and metal oxides for application in supercapacitors
Type of Programme	NENE - National Energy Program
Funding Administration	MCOC - Ministry of Economy and Competitiveness
Number of project	ENE2014-56109-C3-1-R
Duration	from 2015 to 2017
Responsible researcher(s)	Enric Bertran Serra; Esther Pascual Miralles
Keywords	026401 - Nanocomposites / 003239 - Hybrids / 010369 - Carbon

Project/Contract Title	Synthesis of CNS (VACNTs and GNWs) in flexible metal tapes and study of their electrochemical properties after functionalization with metal oxide composite materials
Type of Programme	NENE - National Energy Program
Funding Administration	MCOC - Ministry of Economy and Competitiveness
Number of project	ENE2017-89210-C2-2-R
Duration	from 2018 to 2020
Responsible researcher(s)	Enric Bertran Serra; Esther Pascual Miralles
Keywords	054973 - CNTs / 054972 - GNWs / 004855 - Metal Oxides / 010442 - ICP / 015952 - CVD

Resumen en español

La capacidad de los seres humanos para estudiar, manipular y comprender la materia a escala nanométrica nos ha permitido desarrollar materiales que pueden combinar propiedades físicas, químicas, ópticas, magnéticas y mecánicas que los materiales a granel no poseen. Uno de los materiales que despertó el interés en el mundo de la Nanociencia y la Nanotecnología fueron los nanotubos de carbono (CNTs por sus siglas en inglés). Estas nanoestructuras ya habían sido reportadas hace más de cuarenta años, pero no es hasta principios de los años 90 que el Dr. Sumio Iijima logra producirlas en condiciones estables en su laboratorio. A partir de ese momento, los recursos dedicados a la investigación y producción de estos materiales basados en el carbono fueron en aumento. Aunque hoy en día no captan el mismo interés científico que hasta 2010, su importancia en el mundo científico y especialmente en el mercado es relevante. De hecho, ya que la tecnología para la producción de CNTs a escala industrial ha madurado, estos se encuentran en un gran número de aplicaciones, tales como en el refuerzo de polímeros, actuando como andamiajes para el crecimiento de tejidos artificiales, en la fabricación de tintas conductoras o como parte de los electrodos para baterías y de los supercondensadores de nueva generación. Es precisamente en esta última aplicación donde el interés científico se ha centrado con especial atención. Junto con otros materiales a base de carbono, como el grafeno, son excelentes materiales de soporte para materiales con alta capacitancia. Los grupos de investigación y las empresas de todo el mundo están invirtiendo muchos recursos en la obtención de electrodos que tienen una arquitectura tridimensional a nanoescala y cuya superficie específica es elevada.

En ese sentido, el objetivo de este trabajo fue sintetizar CNTs sobre la superficie de un material flexible y conductor: el acero inoxidable 304. Nos centramos en la optimización de los procesos de crecimiento mediante el depósito químico en fase de vapor asistido por plasma (PECVD por sus siglas en inglés) y el depósito químico en fase de vapor asistido por agua (WACVD por sus siglas en inglés) con y sin la contribución de material de catalizador externo. Además, como se verá en el desarrollo de este trabajo, hubo un esfuerzo importante para entender los efectos que los procesos térmicos, necesarios para el crecimiento de CNTs, producen sobre las propiedades del acero. Especialmente la influencia en la resistencia a la corrosión, ya que el uso final de los CNTs en acero inoxidable es la fabricación de electrodos expuestos a ambientes corrosivos.

El Capítulo 1, a modo de introducción, aborda el tema de la Nanociencia y la Nanotecnología. También se describe brevemente la clasificación de los materiales a base de carbono. Una extensa sección del capítulo se utiliza para cubrir los diferentes procesos de fabricación de CNTs. Además, también se incluyen los mecanismos de crecimiento comúnmente utilizados para explicar el crecimiento de los CNTs. La parte final del capítulo incluye algunas de las propiedades y aplicaciones en las que se utilizan estas nanoestructuras. Se citan algunos problemas de salud que pueden producirse por la ma-

nipulación inadecuada de estos materiales nanoestructurados.

La descripción experimental se incluye en el Capítulo 2. En general, se presentan algunos de los principios fundamentales de la tecnología de vacío y de plasma, pilares básicos de los procesos utilizados para el crecimiento de los CNTs. Una serie de procesos de deposición química en fase de vapor (CVD por sus siglas en inglés) y de deposición física en fase de vapor (PVD por sus siglas en inglés), como la pulverización catódica (magnetron sputtering) o PECVD, están explicados en detalle. La descripción de los dos reactores utilizados durante este trabajo, así como los cambios realizados en los mismos, se incluye al final del capítulo. También se incluye el proceso de recalibración del sistema de control de temperatura PID, que desempeña un papel importante en el control de la temperatura del proceso de crecimiento de los CNTs.

Todas las técnicas de caracterización utilizadas en este trabajo se describen en el Capítulo 3. Se incluyen los conceptos básicos de cada una de las técnicas. La caracterización del sustrato y las nanoestructuras obtenidas por PECVD y WACVD incluyó mediciones eléctricas, ópticas, espectroscópicas y de difracción de rayos-X.

El Capítulo 4 muestra los parámetros y resultados de crecimiento de los CNTs directamente sobre el acero inoxidable. La capa de óxido nativa del acero se eliminó sin necesidad de procesos mecánicos ni químicos. Además, no se utilizó ningún catalizador externo. En su reemplazo fueron utilizados los elementos de aleación del acero. Se presenta un estudio detallado de los efectos causados en el sustrato de acero por el proceso de reducción de la capa de óxido nativa. Los resultados de la caracterización del sustrato y de los CNTs mediante diferentes técnicas microscópicas, espectroscópicas y de difracción de rayos-X han sido incluidos. La actividad catalítica del sustrato ha sido demostrada tanto por PECVD como por WACVD.

El proceso de obtención de bosques uniformes de CNTs sobre un sistema de barrera de difusión obtenido a partir de capas delgadas nitruradas se describe en el Capítulo 5. En este capítulo se presenta la caracterización de las capas nitruradas obtenidas a partir de un blanco de acero inoxidable 304 y un blanco de aluminio, por pulverización catódica. Su composición química, la estructura cristalina, la velocidad de deposición y la resistividad eléctrica se discuten en esta sección. También se incluyen los resultados de la dependencia de la morfología de los CNTs en función de la temperatura a la que crecen. Las técnicas de caracterización utilizadas fueron la espectroscopía de fotoelectrones emitidos por rayos-X, la difracción de rayos-X, las medidas de resistividad por el método Van der Pauw, la medición de espesores con perfilómetro y la caracterización Raman de las estructuras de carbono.

Finalmente, en el Capítulo 6 se muestran los resultados de la caracterización electroquímica de los electrodos obtenidos durante esta investigación. Los CNTs obtenidos por el proceso descrito en el Capítulo 5 fueron caracterizados electroquímicamente. Además, los resultados obtenidos se comparan con otros de muestras de CNTs decoradas con nanoparedes de grafeno (GNWs por sus siglas en inglés) y funcionalizados con dióxido de manganeso (MnO_2). En este capítulo se muestra que los CNTs pueden ser utilizados como andamios para otras estructuras. Incluye el estudio de la influencia del tiempo de deposición en la formación de nanopartículas de MnO_2 y cómo la morfología del sustrato influye en su nucleación. La parte final del capítulo trata el tema de la inestabilidad de los electrodos durante la caracterización electroquímica. En esta sección se incluyen los resultados de la microscopía electrónica de barrido y de la caracterización Raman que permitieron identificar los productos de la corrosión del electrodo.

Principales resultados

Hoy en día entendemos mejor las ventajas y desventajas de utilizar el acero inoxidable 304 para producir electrodos de supercondensadores. Este sustrato fue seleccionado por ser un material conductor, por su flexibilidad y, sobre todo, en condiciones estándar, por su alta resistencia a la corrosión. La resistencia a la corrosión es un punto crítico durante la caracterización electroquímica, ya que evita que el sustrato reaccione con el electrolito.

Para lograr los objetivos de esta tesis, se han optimizado varios sistemas del reactor de CNTs. Así, los inconvenientes tecnológicos encontrados durante los experimentos preliminares se resolvieron satisfactoriamente. Esto nos permitió mejorar considerablemente los procesos de obtención de CNTs en diferentes sustratos. Por lo tanto, la reproducibilidad mejoró significativamente gracias al control preciso de la temperatura, la presión y la composición del gas durante los procesos de crecimiento. Además, se aumentó la capacidad de carga del reactor: el nuevo sistema similar a un carrusel permitió colocar cuatro muestras dentro de la cámara principal del reactor al mismo tiempo.

En general, se utilizaron dos enfoques para obtener bosques de nanotubos de carbono en la superficie de este material conductor. La primera fue obtener CNTs directamente en la superficie del acero. Mientras que el segundo fue utilizar un sistema de barrera de difusión que evita que el catalizador se difunda en el sustrato. Para ambos enfoques, los procesos utilizados para obtener CNTs fueron el depósito químico en fase de vapor asistido por plasma (PECVD) y el depósito químico en fase de vapor asistido por agua (WACVD). Además, debe señalarse que no hubo preparación mecánica (desbastado o pulido) de la superficie del acero inoxidable 304. Se obtuvieron bosques uniformes de CNTs en un área de $9\,\mathrm{cm}^2$.

Hemos obtenido CNTs directamente sobre acero inoxidable 304 sin capa de catalizador, a través de un proceso térmico y de plasma específico del sustrato. Este proceso se ha llevado a cabo en dos etapas:

La reducción de la capa de óxido nativo de la superficie de acero inoxidable para mejorar el contacto eléctrico de las nanoestructuras de carbono. La capa nativa de Cr_2O_3 fue completamente eliminada con un plasma de argón e hidrógeno en el rango de temperatura de 600 a 730 °C. El espectro de OES nos permitió estimar que durante los primeros 60 s, después de que el plasma comenzara, la capa de óxido fue completamente eliminada. Las curvas de Firestone Abbot demostraron que durante los 5 minutos de proceso también se modificó la rugosidad del sustrato.

La precipitación de carburos metálicos en la superficie del acero inoxidable 304 promueve la nucleación múltiple de CNTs en la superficie de las micropartículas de carburo. Entre 600 y 650 °C, los carburos más comunes fueron el Fe_3C y el $(FeCr)_7C_3$. En contraste, entre 700 y 730 °C, el carburo encontrado fue de Cr_7C_3 y un bajo porcentaje de $(FeCr)_7C_3$ y Fe_3C. Otra de las cosas a tener en cuenta es que los carburos precipitados formaron una capa porosa y gruesa en la superficie, bajo la cual probablemente había una zona empobrecida en cromo.

Se debe prestar especial atención al tiempo y la temperatura utilizados en el proceso de reducción y crecimiento de los CNTs en este material. En particular para evitar que su flexibilidad y resistencia a la corrosión se vean afectadas, ya que una exposición prolongada puede alterar gravemente las propiedades del material. En este sentido, a medida que la temperatura aumenta, el tamaño de los cristales internos también lo hace como resultado

de que se sobrepasa la temperatura de recristalización ($600 - 650\,°C$).

Se han obtenido bosques de nanotubos de carbono multicapa (MWCNT por sus siglas en inglés) directamente en la superficie reducida de acero inoxidable 304 sin deposición externa de catalizadores. La cantidad de hierro en la capa de carburo obtenida a 730 °C fue suficiente para actuar como catalizador.

Los CNTs obtenidos por WACVD tienen mejor cristalinidad que los obtenidos por PECVD, aunque con orientación aleatoria. Esto se evidenció a través de la deconvolución de los espectros Raman. Las bandas identificadas en las muestras de PECVD y WACVD fueron: D" ($1200\,cm^{-1}$), D ($1350\,cm^{-1}$), A ($1500\,cm^{-1}$), G ($1580\,cm^{-1}$) y D' ($1620\,cm^{-1}$). Se ha demostrado que las muestras de PECVD contienen más carbono amorfo en forma de grafito nanocristalino.

El segundo enfoque consistió en el crecimiento de un bosque uniforme de CNTs sobre capas de acero inoxidable nitruradas previamente depositadas sobre sustratos de acero inoxidable 304. Para ello se depositó una fina capa de nitruro de aluminio (AlN) como barrera de difusión antes de la capa ultrafina del catalizador.

En este segundo enfoque, se ha desarrollado un nuevo sistema de barrera de difusión basado en una capa de interfaz con una composición de nitrógeno en gradiente, a partir de 0 a 35% de contenido de nitrógeno en una aleación de acero inoxidable 304. La capa nitrurada presenta dos fases cristalinas. Una fase corresponde al nitruro de cromo (CrN) y la otra está compuesta básicamente por elementos de aleación (MeN).

El porcentaje de nitrógeno ha permitido producir una capa de amortiguamiento altamente eficiente para soportar la barrera de difusión de AlN basada en una adecuada sintonización de su coeficiente de expansión térmica.

El uso de este tipo de barrera de difusión con resistividades de 200 $\Omega{\cdot}m$ no limita la corriente a través del contacto entre nanoestructuras metálicas y de carbono de forma significativa, ya que la resistencia en serie aumenta en un valor muy bajo ($34\,\Omega{\cdot}m/cm^2$).

Los resultados muestran que la temperatura utilizada para el crecimiento de los CNTs influyó en su morfología (longitud y diámetro), pero no en la cantidad de carbono amorfo presente en las muestras.

Se han desarrollado nuevas nanoestructuras híbridas de carbono para su aplicación en supercondensadores.

Los CNTs fueron decorados con nanoparedes de grafeno (GNWs) usando PECVD y plasma de acoplamiento inductivo-CVD (ICP-CVD por sus siglas en inglés), respectivamente.

Una de las principales ventajas de esta nanoestructura híbrida de carbono es el importante aumento del número de defectos superficiales que se convierten en centros de nucleación de los óxidos metálicos utilizados en los electrodos de supercondensadores.

Se han desarrollado dos nanoestructuras híbridas tridimensionales de óxido metálico y carbono para aplicaciones de supercondensadores. Uno de MnO_2 electrodepositado en CNTs y otro con MnO_2 electrodepositado en CNTs decorados por GNWs.

La funcionalización de nanoestructuras de carbono con MnO_2 mejora su rendimiento electroquímico. La caracterización electroquímica de estas estructuras ha mostrado un factor de incremento de veinte en la capacitancia superficial de las estructuras funcionalizadas con MnO_2 en comparación con las nanoestructuras de carbono sin MnO_2.